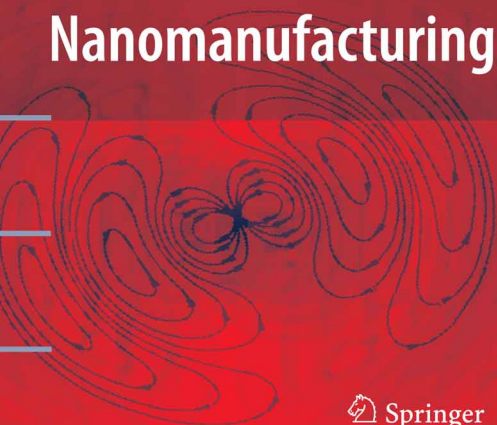


Mark J. Jackson



Micro and Nanomanufacturing



 Springer

MICRO AND NANOMANUFACTURING

MICRO AND NANOMANUFACTURING

Mark J. Jackson, M.Eng, Ph.D
Purdue University



Mark J. Jackson
Purdue University
West Lafayette, Indiana
USA

Micro and Nanomanufacturing

Library of Congress Control Number: 2006932032

ISBN 0-387-25874-4

e-ISBN 0-387-26132-X

ISBN 978-0387-25874-4

e-ISBN 978-0-387-26132-4

Printed on acid-free paper.

© 2007 Springer Science+Business Media, LLC

All rights reserved. This work may not be translated or copied in whole or in part without the written permission of the publisher (Springer Science+Business Media, LLC, 233 Spring Street, New York, NY 10013, USA), except for brief excerpts in connection with reviews or scholarly analysis. Use in connection with any form of information storage and retrieval, electronic adaptation, computer software, or by similar or dissimilar methodology now known or hereafter developed is forbidden.

The use in this publication of trade names, trademarks, service marks and similar terms, even if they are not identified as such, is not to be taken as an expression of opinion as to whether or not they are subject to proprietary rights.

9 8 7 6 5 4 3 2 1

springer.com

Printed in the United States

Contents

1. Principles of Micro- and Nanofabrication	1
1.1 Introduction	1
1.2 Material Removal Rates	47
1.3 Conclusions	51
1.4 Problems	51
References	52
2. Microfabrication Using X-ray Lithography	55
2.1 Introduction	55
2.2 X- ray Lithography	58
2.3 Synchrotron Radiation	59
2.4 Microfabrication Process	62
2.5 Methods of Resist Application	83
2.6 Exposure	85
2.7 Problems	95
References	96
3. Manufacturing High Aspect Ratio Microstructures	99
3.1 Introduction	99
3.2 Dry Etching	99
3.3 Plasma Etching Processes	100
3.4 Characteristics of the Plasma	102
3.5 Etching of Microstructures	103
3.6 Micromachining High Aspect Ratio Microstructures	120
3.7 Micromolding	120
3.8 Micromolding Processes	121
3.9 Micromolding Tools	128
3.10 Micromold Design	131
3.11 Micromolding Applications	131
3.12 Limitations of Micromolding	132
3.13 Fabrication of Moving Microstructures	132
3.14 Conclusions	138
3.15 Problems	138
References	139

4.	Meso-micromachining	143
4.1	Introduction	143
4.2	Size Effects in Micromachining	144
4.3	Mechanism for Large Plastic Flow	177
4.4	Inhomogeneous Microstrains	178
4.5	Origins of the Size Effect	180
4.6	Meso-machining Processes	182
4.7	Problems	188
	References	188
5.	Mechanical Micromachining	191
5.1	Introduction	191
5.2	Microfluidic Systems	191
5.3	Theory of Micromachining	195
5.4	Experimental Micromachining	208
5.5	Micromachining Tool Design	221
5.6	High-Speed Air Turbine Spindles	226
5.7	Mechanical Design of Rotors	233
5.8	Discussion	250
5.9	Conclusions	251
5.10	Future Developments	252
5.11	Problems	253
	References	253
6.	Microgrinding	255
6.1	Introduction	255
6.2	Grinding Wheels	261
6.3	Conventional Grinding Processes	275
6.4	Precision Grinding Processes	279
6.5	Ultra Precision Grinding	299
6.6	Conclusions	314
6.7	Problems	315
	References	315
7.	Diamond Micro Cutting Tools	323
7.1	Introduction	323
7.2	Properties of Diamond	325
7.3	History of Diamond	326
7.4	CVD Diamond Technology	332
7.5	CVD Diamond Processes	332

7.6	Treatment of Substrate	337
7.7	Modification of HFCVD Process	343
7.8	Nucleation and Growth	345
7.9	Deposition on 3-D Substrates	356
7.10	Wear of Diamond	364
7.11	Time-Modulated CVD Diamond	372
7.12	Conclusions	381
7.13	Problems	382
	References	382
8.	Laser Micro- and Nanofabrication	387
8.1	Introduction	387
8.2	Laser Fundamentals	387
8.3	Laser Microfabrication	403
8.4	Laser Nanofabrication	464
8.5	Conclusions	472
8.6	Problems	473
	References	473
9.	Micromachining Using Water Droplets	475
9.1	Introduction	475
9.2	Theory of Pulsed Liquid Impact	476
9.3	Impact by Water Drops	480
9.4	Modeling Machining Thresholds	482
9.5	Comparative Results	493
9.6	Material Removal Rates	497
9.7	Design of Water-Based Tools	499
9.8	Analysis of Space Frame	500
9.9	Mode Shapes of Tetrahedral Structure	504
9.10	Conclusions	516
9.11	Problems	518
	References	519
10.	Diamond Nanogrinding	521
10.1	Introduction	521
10.2	Piezoelectric Nanogrinding	522
10.3	Stress Analysis in Nanogrinding Grains	524
10.4	Fracture Dominated Wear Model	534
10.5	Nanogrinding	535
10.6	Porous Nanogrinding Tools	545
10.7	Laser Dressing of Tools	569
10.8	Future Directions	587

	10.9 Problems	588
	References	589
11.	Nanomachining	591
	11.1 Introduction	591
	11.2 Nanometric machining	592
	11.3 Theoretical Basis of Nanomachining	595
	11.4 Implementation	612
	11.5 Conclusions	631
	11.6 Problems	632
	References	632
12.	Micro- and Nanomanufacturing	635
	12.1 Introduction	635
	12.2 Micromanufacturing	635
	12.3 Nanomanufacturing	648
	12.4 Commercialization Issues of Micro and Nanotechnologies	672
	12.5 Future Developments	683
	12.6 Problems	684
	References	685
	Subject Index	687

Preface

When Nobel Laureate Richard Feynman presented his vision on miniaturization at the California Institute of Technology in 1959, he promoted a scientific curiosity in what is now known as “nanotechnology”. His revolutionary vision was captured in a paper published in the February 1960 issue of Caltech’s journal, *“Engineering and Science”*. In this paper, Feynman speaks about controlling and manipulating atoms and constructing products atom-by-atom, and molecule-by-molecule. Feynman described the scaling down of lathes and drilling machines, and talks about drilling holes, turning, molding, stamping parts, and so forth. Even in 1959, Feynman described the need for micro- and nanomanufacturing as the basis for creating a microscopic world that would benefit mankind. Since the 1960s, Feynman’s vision has created the basis for the foundation of the semiconductor industry and within the last decade, has rapidly contributed to the development of micro electro- mechanical systems (MEMS). At the same institution, President Bill Clinton talked about the exciting promise of nanotechnology in January 2000, and later announced an ambitious national nanotechnology initiative (NNI) that was enacted in 2001 with a budget of \$497 million to promote nanoscale research that would benefit society. Nanotechnology encompasses technology performed at the nanoscale that has real-world applications. Nanofabrication includes methods that manipulate atoms and molecules to produce single artifacts to produce sub micron-sized components and systems. Nanomanufacturing is a challenge presented to us to produce single-nanoscale artifacts in a mass production fashion that obviously produces the accompanying economies of scale. Nanotechnology will have a profound effect on our society that will lead to breakthrough discoveries in materials and manufacturing, electronics, medicine, healthcare, the environment, sustainability, energy, biotechnology, information technology, national security, and prevention of the spread of global terrorism. Nanotechnology will lead the next industrial revolution.

The purpose of this book is to present information and knowledge on the emerging field of micro- and nanomanufacturing. The book is written in the spirit of scientific endeavor outlined by Richard Feynman, who stated that one of the greatest challenges to scientists in the field of miniaturization is the manufacture of tiny objects using techniques such as turning, molding, stamping, and drilling. The book presents information on subjects such as fabrication, molding, lithography, machining, milling, water drop machining, self assembly, manipulation, cutting, to name but a few.

The book should serve as a text for undergraduate and graduate courses in micro- and nanomanufacturing in subject areas such as mechanical engineering, materials science, physics, chemistry, and electrical and electronic engineering. The structure of the book is based on matter provided by many colleagues and the author wishes to thank Professor Waqar Ahmed, University of Ulster, U.K., Htet Sein, Manchester Metropolitan University, Grant Robinson, Purdue University, Luke Hyde, Purdue University, David Tolfree, Daresbury Laboratory, U.K., Emeritus Professor Milton Shaw, Arizona State University, Professor V. C. Venkatesh, Malaysia University of Technology, Sam McSpadden, Oak Ridge National Laboratory, Professor Kai Cheng, Brunel University, U.K., and Dr. Xun Luo, Cranfield University, U.K., for helping construct a source of knowledge and information on micro- and nanomanufacturing and for granting the author permission to use such matter.

The author expects that the textbook will stimulate further interest in this field of nanotechnology and hopes that there still is, “plenty of room at the bottom”.

Mark J. Jackson
Purdue University

1. Principles of Micro- and Nanofabrication

1.1 Introduction

Innovations in the area of micro and nanofabrication have created opportunities to manufacture structures at the nanometer and millimeter scales. These opportunities can be used to fabricate electronic, optical, magnetic, and chemical/biological devices ranging from sensors to computation and control systems. In this chapter, we introduce the dominant micro and nanofabrication techniques that are currently used to fabricate structures in the nanometer scale up to the millimeter scale. The first part of this chapter focuses on microfabrication of MEMS and semiconductor devices as an example of microfabrication. Next, the chapter focuses on nanofabrication techniques including several top-down and bottom-up techniques. Again, we use semiconductor devices as an example that shows the promising techniques that can be used to manufacture nanofabricated structures.

Most micro and nanofabrication techniques were developed by the semiconductor industry. The semiconductor industry has grown rapidly in the past 30 years, which is driven by the microelectronics revolution. The desire to place many transistors on to a silicon wafer has demanded innovative ways to fabricate electronic circuits and to fit more and more electronic devices into a smaller workable area. Early transistors were made from germanium but are now predominantly silicon, with the remainder made from gallium arsenide. While gallium arsenide has high electron mobility compared to silicon, it has low hole mobility, a poor thermal oxide, less stability during thermal processing, and much higher defect density than silicon. Silicon is the material of choice for most electronic application but gallium arsenide is useful for circuits that operate at high speeds with low-to-moderate levels of integration. This type of

material is used for analog circuits operating at speeds in excess of 10^9 Hz. The performance of integrated circuits can be increased by placing transistors closer together and by depositing transistors in a precise way. The minimum feature size has reduced at an astonishing rate over the past thirty years. Figure 1.1 shows the reduction in the feature sizes as a function of the number of transistors per chip using conventional lithographic techniques. Figure 1.2 shows a single strand of human hair and an array of transistors on a single piece of silicon to reveal the relative size of transistors that can be accommodated on a piece of silicon.

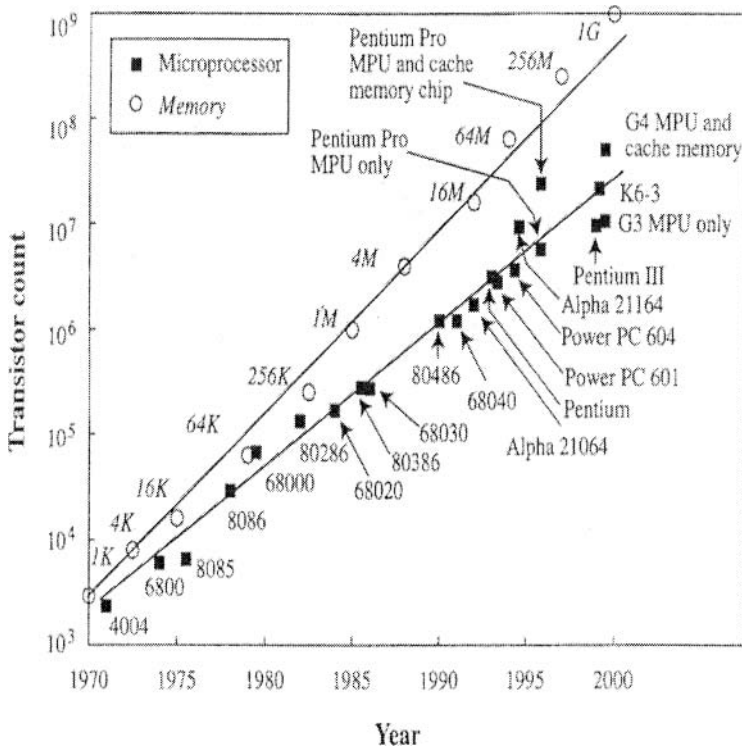


Fig. 1.1. Transistor count per chip as a function of time [1]

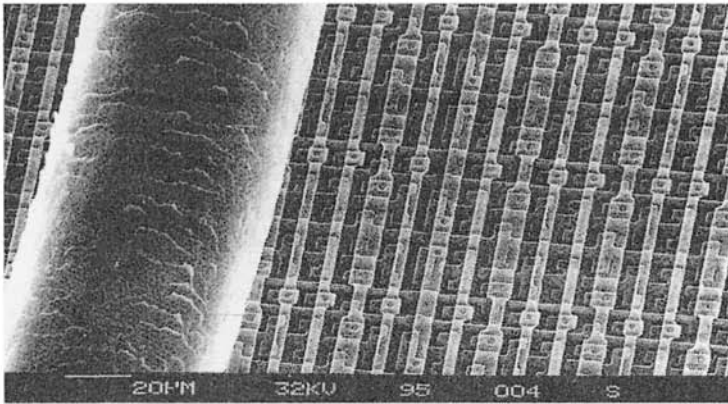


Fig. 1.2. Scanning electron micrograph of an integrated circuit chip in the mid-1980s. The human hair to the left of the image provides an indication of the relative size of the transistor wires [1]

Microfabrication begins when a set of photomasks are provided to the integrated circuit fabricator. The photomasks are physical representations of the design of the circuits to be manufactured in accordance with the rules of layout. A silicon wafer provides the basis of the integrated circuit. Wafers are processed using a grinding process that produces a flat surface that is still conductive at this stage. The wafer is insulated by growing a thermal oxide layer so that leakage of current between transistors is prevented. A conducting layer is deposited that will be used for producing transistors. Several techniques have been developed for depositing insulating and conducting layers such as sputtering, physical vapor deposition using a magnetron, chemical vapor deposition (CVD), and epitaxial growth of layers using techniques such as metal oxide CVD, molecular beam epitaxy, and chemical beam epitaxy. The conducting layer is divided up into individual resistors. Individual resistors are deposited to the wafer using photolithographic techniques. Further processing is required that forms the integrated circuit and uses techniques such as pattern transfer, etching, deposition, and growth. These same techniques have also been used to create a plethora of microscale products in silicon-based materials for applications other than integrated circuits.

1.1.1 Microfabrication of MEMS and Semiconductor Devices

Traditionally, integrated circuits have been manufactured using microfabrication techniques that have been classified as machining processes. Figure 1.3 shows the standard route followed to produce an integrated circuit. The same flowchart can be used for producing any microscale product produced using silicon-based materials. The chart shows the basic functions that are composed of initially cleaning the substrate, applying a thin film using many deposition techniques, applying lithographic techniques to apply mask material, etching to form the required shape of the microscale features, removal of the mask material using chemical or plasma etching, then finally characterizing the nature of the created structure. The final microstructures are then separated from the initial substrate material and released for quality control.

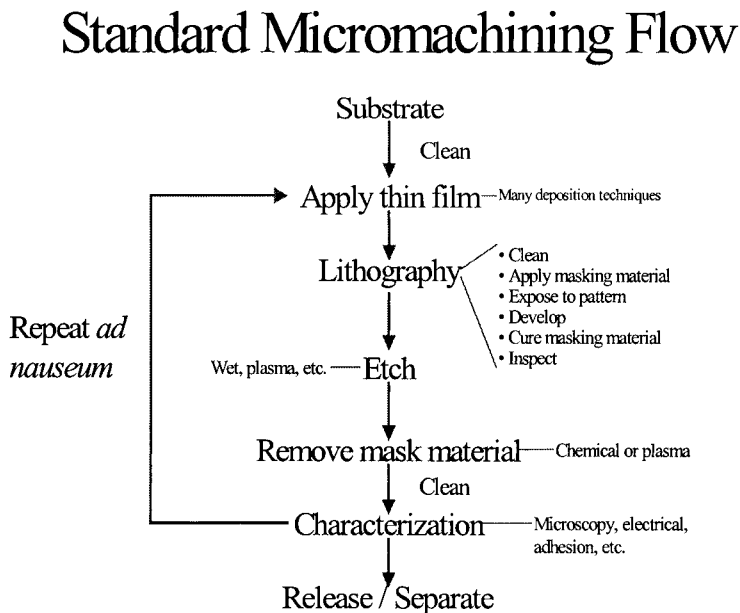


Fig. 1.3. Standard micromachining flow chart showing various processing steps

The basics of microfabrication are shown in Figs. 1.4 – 1.6 and show that fabrication at the microscale is made up of three basic regimes, i.e., addition, multiplication, and subtraction. The addition phase involves adding a thin film coating to the substrate material. This can take the form of electroplating or spray coating a liquid film to the substrate and allowing it to dry, or a thin film can be created by oxidation or doping in an atmospheric chamber. Other methods include fusion bonding a solid to the substrate, or using low- and high-pressure vacuum techniques to bond a thin coating to the substrate. The process of feature multiplication also takes many forms and is a process step necessary to create microscale features, particularly channeled features that are used in micro and nanofluidic devices.

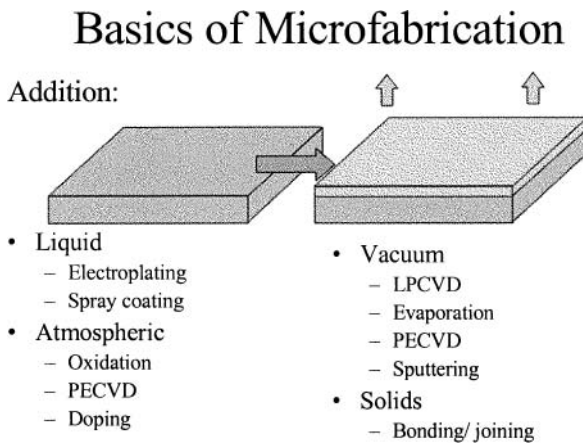
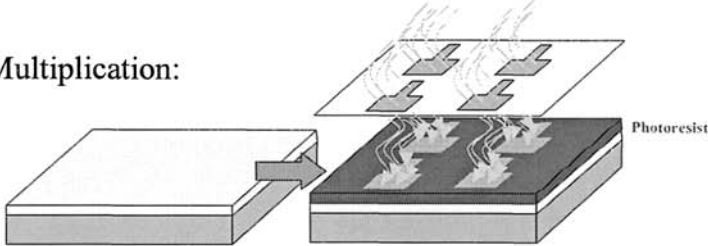


Fig. 1.4. Microfabrication by the addition of a thin solid film

Multiplication of features can be performed using a number of processes such as direct writing of features using electron beam, ion beam, and atomic force microscopic techniques. Contact lithography is another popular technique for depositing features in addition to new methods of micro/nanoscale feature generation using microstamping processes.

Basics of Microfabrication

Multiplication:

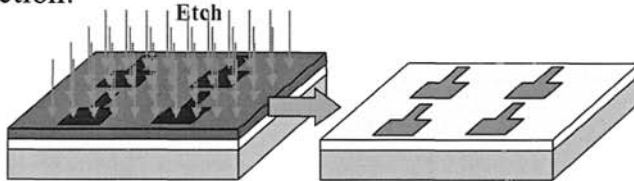


- Photolithography
 - Contact
 - Projection
- Direct write
 - E-beam, ion beam, AFM
- Microstamping
 - Molecular films
 - Transfer of masking/structural layers

Fig. 1.5. Microfabrication by the multiplication of a thin solid film

Basics of Microfabrication

Subtraction:

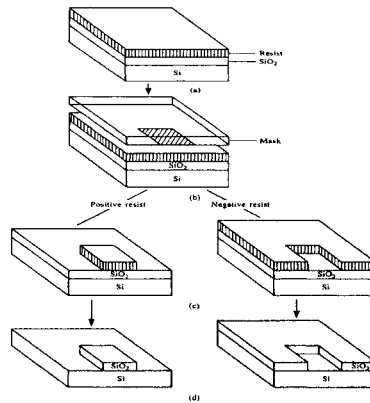


- Liquids
 - Chemical reactions
- Gases
 - Chemical etchants
- Focused beams
 - Ion mill
 - Excimer lasers
- Plasma
 - Plasma chemical etch, sputter etch
 - Reactive Ion Etch
- Mechanical
 - Polishing/Chemical mechanical polishing

Fig. 1.6. Microfabrication by the subtraction of parts of a thin solid film

Subtraction of material to create features can be performed using a variety of techniques shown in Fig. 1.6. In materials other than silicon, subtraction processes can include mechanical micromilling, laser ablation, water micromachining, and a great number of other processes. These processes can remove material at much higher material removal rates and are discussed further in subsequent chapters in this textbook. Combinations of all of these techniques can be used to produce features of different size, shape, and scale. The standard way of creating features on single pieces of silicon is being surpassed by new microfabrication processes that achieve improved performance of individual devices. The standard way of producing integrated circuits is shown in Fig. 1.7, which shows the process of depositing a thin film on the surface of silicon, which is selectively removed by etching processes that produce wells or channels with known geometry owing to the texture of the silicon crystal.

Conventional IC Fabrication Process



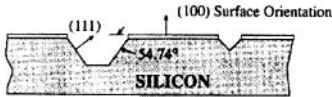
Source: *Introduction to Microelectronics Fabrication*, Volume V, Modular Series on Solid State Devices, by R.C Jaeger, edited by G.W. Neudeck and R.F. Pierret. © 1988 by Addison-Wesley Publishing Company. Reprinted by permission.

Fig. 1.7. Typical fabrication process for an integrated circuit [2]

Crystal Plane Effects on Etching

- Example: (100): (110): (111) on Si
 - Etch rates of 400:600:1 for KOH, depending on mixture

ANISOTROPIC WET ETCHING: (100) SURFACE



ANISOTROPIC WET ETCHING: (110) SURFACE

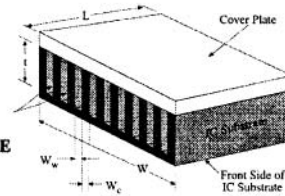
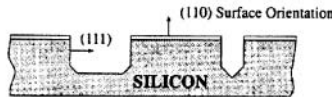
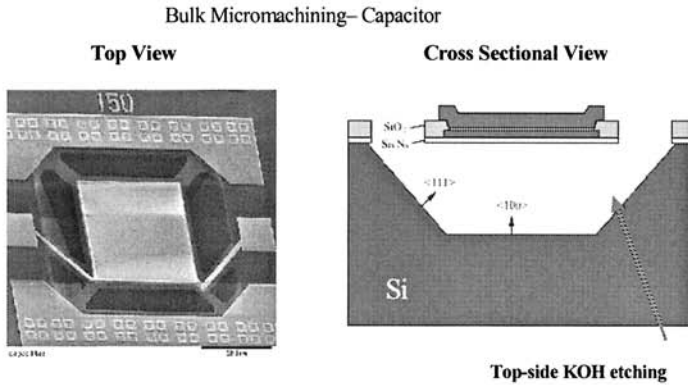


Fig. 1.8. Crystal plane etching on (100), (110), and (111) planes of silicon using KOH etchant. The figure shows the shape of the channel produced in silicon by bulk micromachining [2]

The removal of silicon in certain directions of crystal planes is known as bulk micromachining [2]. Figure 1.8 shows the characteristic planes of silicon etched by using KOH etchant. The shape of the channel, or trench, produced is fixed by the way atoms are arranged in known directions.

The process of bulk micromachining to produce electronic devices such as capacitors is shown in Fig. 1.9. Here, (a) the feature is cleaned to prepare the substrate for deposition of the mask, (b) the mask is etched using KOH etchant, and (c) the substrate is etched to produce a deep trench. Trenches for microfluidic devices made from silicon can be produced in this way, but the shape of the trench is controlled by the way atoms are arranged in crystallographic planes.



Y. Sun, H. van Zeijl, J.L. Tauritz and R.G.F. Baets, "Suspended Membrane Inductors and Capacitors for Application in Silicon MMICs," Microwave and Millimeter-wave Monolithic Circuits Symposium Digest of Papers, IEEE, 1996, pp. 99-102.

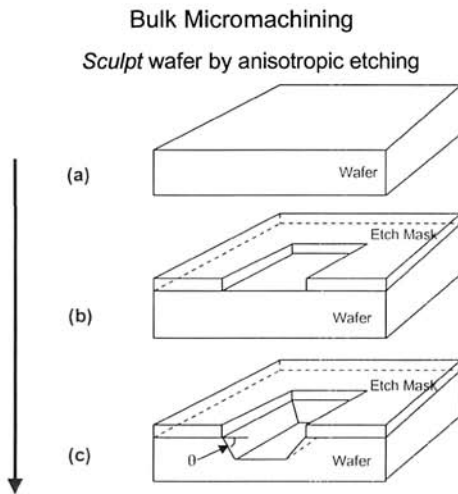
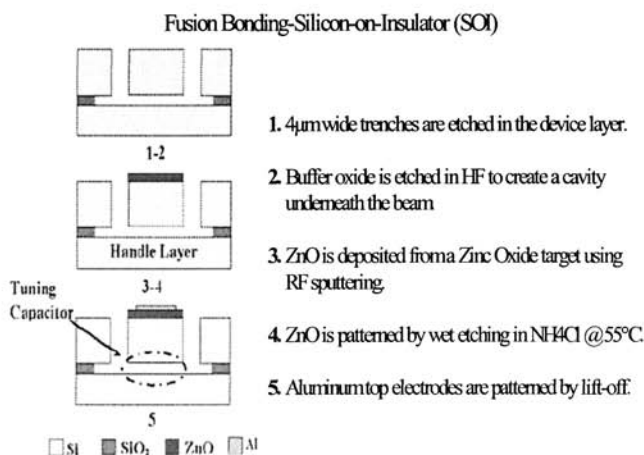


Fig. 1.9. Bulk micromachining by anisotropic etching to produce features such as a capacitor [3]

Another method used for bonding thin films to silicon substrates is fusion bonding. Figure 1.10 shows the basic principle used for bonding silicon on an insulator material to create a voltage tunable, piezo-electrically transduced SCS resonator (Fig. 1.11). Figure 1.11

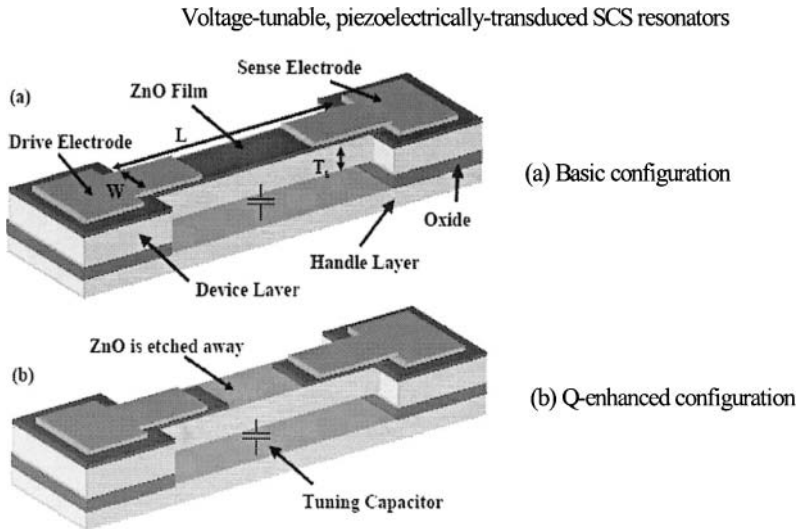
shows the basic construction of the resonator, and also shows how etching a thin ZnO film can create a Q-enhanced resonating device. This process can also be used for creating stepped features in micro-fluidic devices and other micromachined products.



Piazza, G., R. Abdolvand, and F. Ayazi, Voltage-Tunable Piezoelectrically-Transduced Single-Crystal Silicon Resonators on SOI Substrate," 2003 IEEE MEMS Conference, Kyoto, Japan, Kyoto, Japan, January 19 - 23, 2003, pp 149-152.

Fig. 1.10. Fusion bonding of silicon on an insulator showing the various steps of the process [4]

The formation of the trench in the previous application can take a long time to produce when using wet etchants. One way of increasing the aspect ratio of a trench to make it deeper is to reactively ion etch the substrate to produce a deeper feature. This principle of this process is shown in Fig. 1.12. The etching speed is typically 1 – 2 microns per minute, which is slow compared to mechanical micromilling processes and laser-based micromachining processes. The formation of features in engineering materials such as steel, copper, and aluminum alloys is usually achieved by using the aforementioned processes.



Piazza, G., R. Abdolvand, and F. Ayazi, Voltage-Tunable Piezoelectrically-Transduced Single-Crystal Silicon Resonators on SOI Substrate," 2003 IEEE MEMS Conference, Kyoto, Japan, Kyoto, Japan, January 19 - 23, 2003, pp 149-152.

Fig. 1.11. Voltage tunable, piezoelectrically-transduced SCS resonator showing the manufacturing process used to produce the Q-enhanced configuration [4]

Deep reactive ion etching is a way of producing masters for manufacturing products on the mass scale. When coupled with micro molding techniques, a wide variety of microproducts can be produced. Deep reactive ion etching of deep trenches is used to produce tunable capacitors. Figure 1.13 shows such an application. This type of process is discussed in detail in Chapter 3.

Deep Reactive Ion Etching

Robert Bosch GmbH, Patent 5501893, March 26, 1996

- Etch-resistant polymer in sidewalls allows bottom to be etched to achieve high aspect ratio

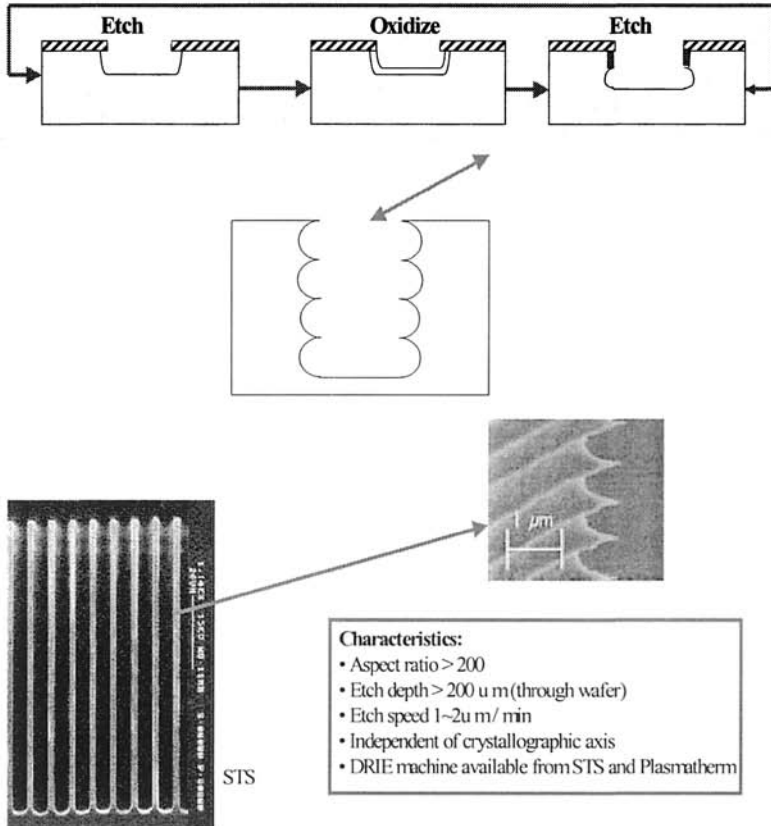


Fig. 1.12. Deep reactive ion etching of silicon substrate to produce trenches with aspect ratios greater than 200 at an etching speed of 1 - 2 μm per minute [5]

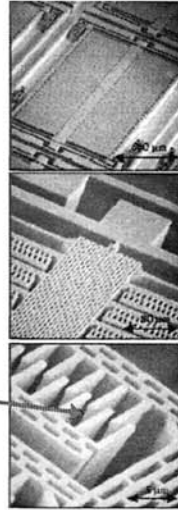
Deep Reactive Ion Etching—Applications

Robert Bosch GmbH, Patent 5501893, March 26, 1996

Interdigitated Area-Tuning Variable Capacitor

- Increased capacitance
- Single crystal silicon → Low-stress structures
- Large tuning range

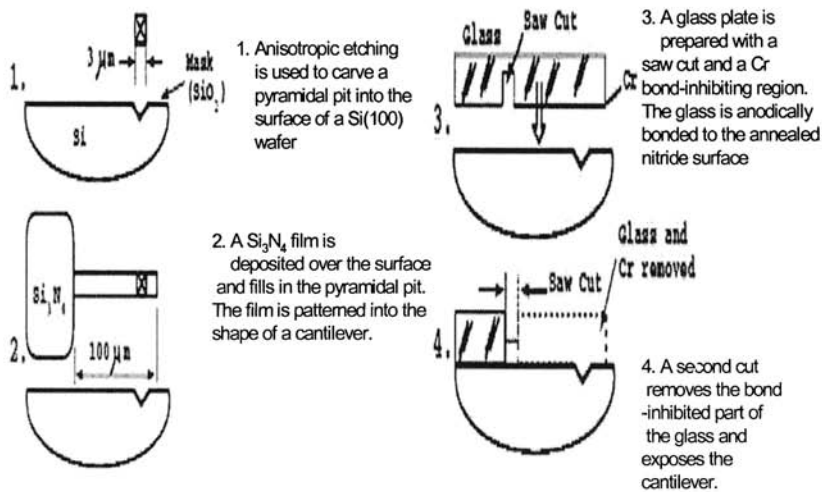
$$C = \frac{\epsilon A}{d}$$

J.J. Yao, *Topical Review: RF MEMS from a Device Perspective*, J. Micromech. Microeng. 10 (2000) R9-R38.**Fig. 1.13.** Area tunable variable capacitors [6]

In the field of nanofabrication, microfabrication processes can be used to make cantilever probes for atomic force microscopes that can be used for multiplying features on silicon and other materials by direct writing. The subsequent chapters of this book explain how microfabrication techniques have been developed to produce single products through fabrication, and also explain how multiple micro-products can be produced through manufacturing. An example of how microfabrication can produce nanofabrication tools is shown in Fig. 1.14. A cantilever made from silicon and glass is etched to produce the features required to produce a probe that is required to directly write to the surface of the substrate. This type of cantilever can be used to produce nanofabricated features that are discussed at length in the next section.

When producing the cantilever, anisotropic etching is used to form the pit into the (100) surface of the silicon wafer.

Cantilever Probe Microfabrication



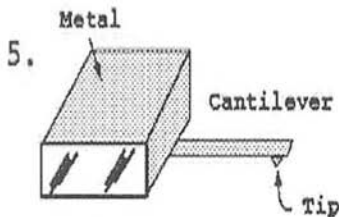
<http://www.physics.mcgill.ca/spm/MagFM/microfab.html>

Fig. 1.14. Initial stages of fabrication of a cantilever probe

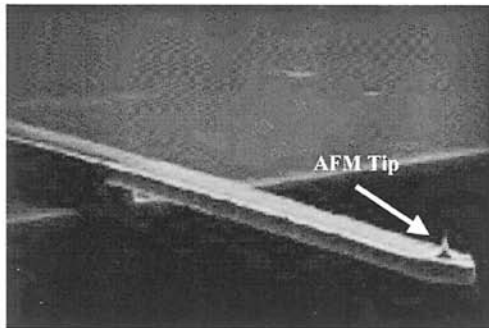
A silicon nitride film is deposited to the surface and fills the pit created by etching. The beam of the tip is prepared by using a glass plate from which the silicon is etched away to leave a silicon nitride cantilever beam that is connected to a metal block.

In addition to producing nanofabrication tools for the manipulation of single atoms or clusters of atoms and molecules, the semiconductor industry began producing field effect transistors with nanoscale features in the year 2000. The Pentium 4 microprocessor contains some 42 million transistors connected to each other on a single piece of silicon. To do this, silicon grown via the Czochralski process no longer produces a defect free substrate for the deposition of nanoscale transistors. Producers of silicon wafers routinely deposit a defect free single crystal silicon layer using a gaseous deposition technique.

Cantilever Probe Microfabrication



5. Silicon is etched away leaving the Si₃N₄ microcantilever attached to the edge of the glass block. The reverse side of the cantilever is coated with a reflective metal coating for the deflection detector.



<http://www.physics.mcgill.ca/spm/MagFM/microfab.html>

Fig. 1.15. Cantilever probe used for direct writing to a substrate

Engineers also deposit an oxide layer with low capacitance prior to the deposition of the thin silicon layer. This is known as silicon-on-insulator technology, which increases the speed transistors can be switched on and off. Another novel way of increasing the speed further still is to slightly strain the silicon lattice by forming a silicon-germanium blend that increases the mobility of electrons. To insulate the gate of the transistor, traditionally a thin layer of silicon dioxide has been deposited to conventional substrates. A material with a high dielectric constant is being developed to replace the use of silicon dioxide. Hafnium oxide and strontium titanate are likely contenders that will allow the gate oxide layer to be slightly thicker without compromising the switching ability of the transistor. This is

achieved by atomic layer deposition. The first-generation nanoscale field effect transistor is shown in Fig. 1.16.

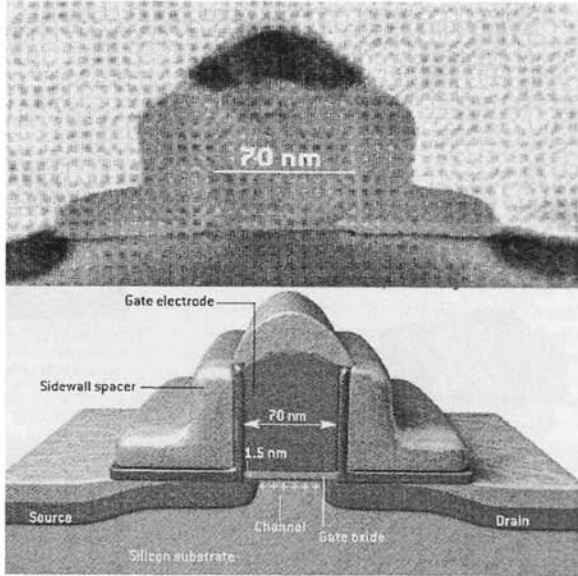


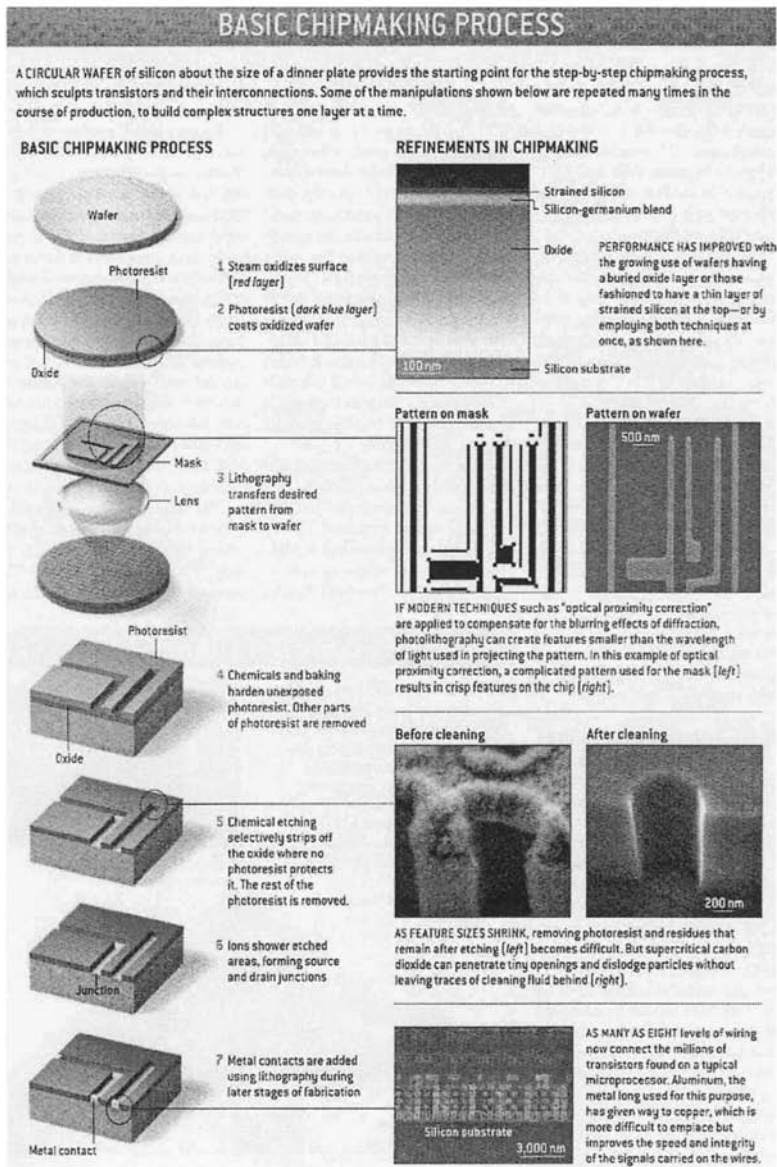
Fig. 1.16. The first generation of nanoscale field effect transistor [7]

After the gate insulators have been deposited, parts of the structure must be selectively removed to achieve the appropriate pattern on the silicon wafer. The lithographic procedure developed so far is needed to create transistors and their interconnections. The process of lithography traditionally created difficulties when feature sizes were smaller than the wavelength of light used to deposit small features to the silicon substrate. Since 2000, features in the range of 70 nm have been created using ultraviolet light that has a wavelength of 248 nm. Figure 1.17 shows the basic manufacturing process for producing microprocessors that employ nanoscale field effect transistors. To achieve this resolution, methods such as optical proximity correction, phase-shifting masks, and excimer lasers have been used to correct the aberrations. The latest technique employed using light with a wavelength of 193 nm produces features in the range of 50 nm. The next step is to use ‘soft’ x-rays such as extreme ultraviolet light, but difficulties occur using this technique because mate-

rials absorb light at extreme ultraviolet wavelengths and lenses become opaque; therefore projection would be aided by the use of multilayered mirrors. The solution to manufacturing at the nanoscale lies in the ability to pattern using mechanical techniques such as soft lithography and nanoimprint lithography.

Semiconductor manufacturers are also using a technique called “immersion lithography” that was developed in 2004 to overcome the diffraction limit imposed by optical lithography. Here, the process works by channeling water through the gap between the imaging machine and the photoresist that coats a semiconductor wafer, thereby improving the resolution of features on the chip and the depth of focus. As the stage that holds the wafer moves, the water supply is channeled away from the surface of the wafer (Fig. 1.18). Using this technology will reduce the resolution to 32 nm that will be required for the 2011 generation of chips. The use of sapphire lenses in the immersion lithographic technique is predicted to reduce the resolution further to 25 nm, i.e., 25 nm distance between transistors, for the 2015 generation of chips. Further advances to reduce the resolution further will require the use of extreme ultra-violet lithography, which is projected to reduce the resolution to 13 nm. However, the mechanical techniques provide great promise for future generations of chips employing techniques such as soft lithography and nanoimprinting. Figure 1.18 shows the principle of immersion lithography as shown in *Scientific American* (July 2005).

This monograph presents fabrication and manufacturing processes that can be used for materials other than silicon. The purpose of this book is to introduce the reader to micro- and nanoscale manufacturing processes so that an informed choice of selecting manufacturing processes can be made for products other than those used in the semiconductor industry. This initial chapter introduces the reader to micro- and nanofabrication processes that have already been developed for the purpose of building micro- and nanoscale products. Subsequent chapters will focus on emerging processes that may prove useful for the manufacture of future micro- and nanoscale products.



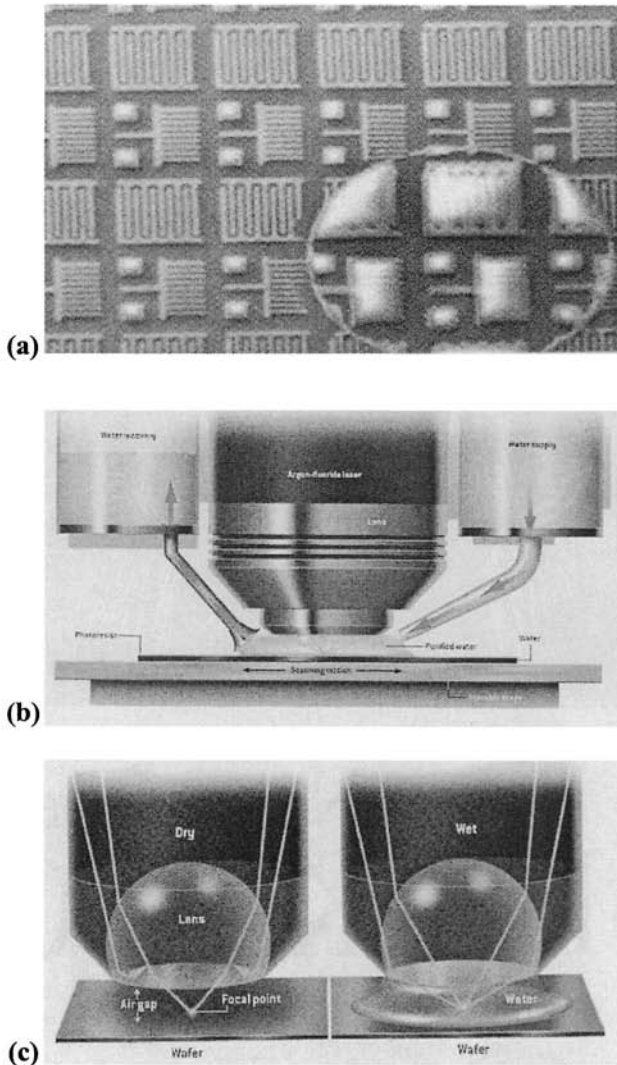
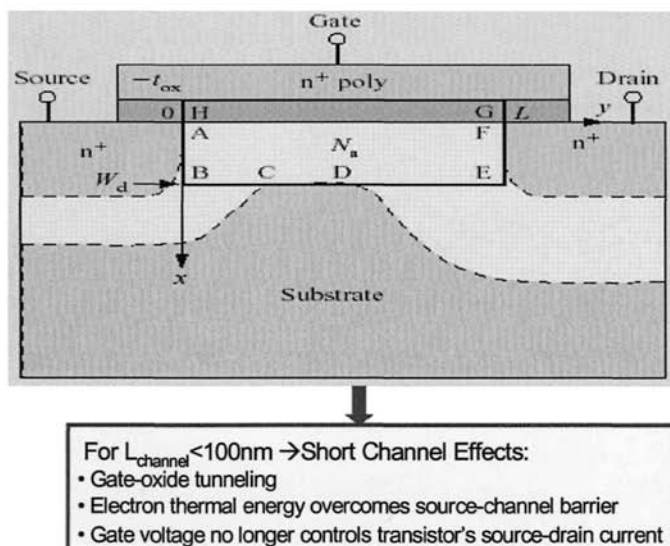


Fig. 1.18. Schematic diagram of the immersion lithographic process: (a) water drop showing change in resolution; (b) process showing the supply and extraction of water between lens and silicon wafer; and (c) principle of light reflection between air gap and liquid drop showing position of focal point on chip and path of reflected light waves. (Reproduced courtesy of *Scientific American* – “Shrinking circuits with water” by G. Stix, July 2005.)

1.1.2 Nanofabrication of Semiconductor Devices

Nanofabrication Using Soft Lithography

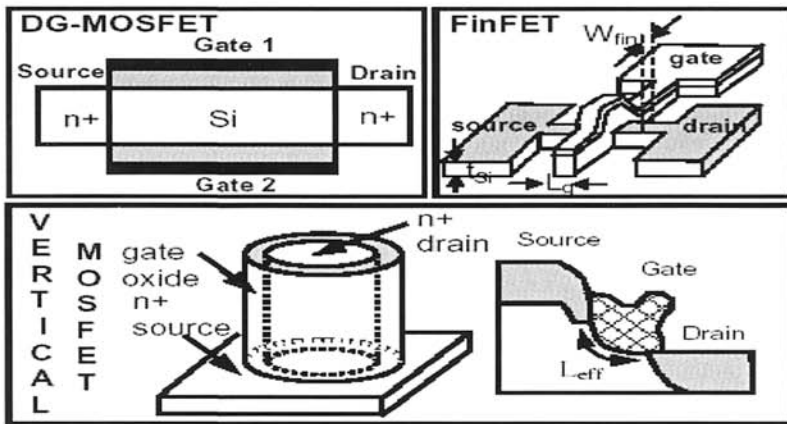
Nanofabrication has developed from a direct requirement to increase the density of transistors to a single piece of silicon. However, nanofabrication can be used to develop products other than for the semiconductor industry. In the first instance, nanofabrication is being developed to construct devices such as resonant tunneling diodes and transistors, and single-electron transistors and carbon nanotube transistors. The most common type of transistor being developed for use at the nanoscale is the field effect transistor. Figure 1.19 shows such a transistor and also its physical features such as source, drain, and gate, and each component of the fabricated transistor in relation to the substrate.



Y.. Taur,
IBM
J. Res. &
Dev.
,vol. 46, No.
2/3, 2002

Fig. 1.19. Schematic diagram of the field effect transistor [8]

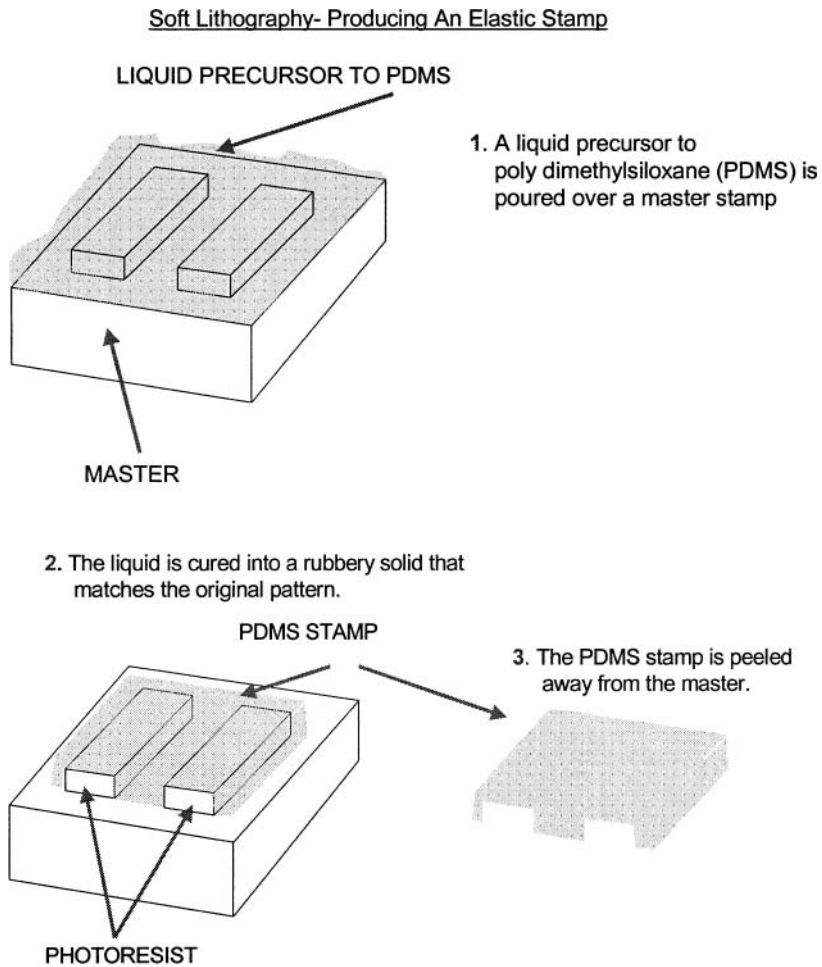
For very short channels of less than 100 nm, gate oxide tunneling effects occur where gate voltages no longer control the transistor's source-drain current flow. The challenge for nanofabrication of these devices is to deposit materials in a physical way that will faithfully reproduce device function. Figure 1.20 shows the physical layout of different types of field effect transistor.



A.M. Ionescu, et al. "Few Electron Devices: Towards Hybrid CMOS-SET Integrated Circuits," 39th Design Automation Conference (DAC) 2002, pp. 88-93, June, New Orleans, Louisiana, USA

Fig. 1.20. Physical layout of various field effect transistors [9]

A very simple and novel way of reproducing nanoscale features is to use a technique known as soft lithography. In soft lithography, a liquid known as polydimethylsiloxane is poured on a master pattern of the feature to be produced. The liquid cures to form a "rubbery" solid that can be peeled over the master pattern to reveal a very simple mold that can be attached to a stamp. Figure 1.21 shows the basic principle of soft lithography. The basis of nanoelectronic fabrication of field effect transistors using the soft lithographic technique has been demonstrated using a process known as microcontact printing. In the self-assembly process, a stamp is coated with a solution of molecules known as thiols. Thiols then self-assemble on contact with a thin gold film that has been deposited to the silicon substrate.

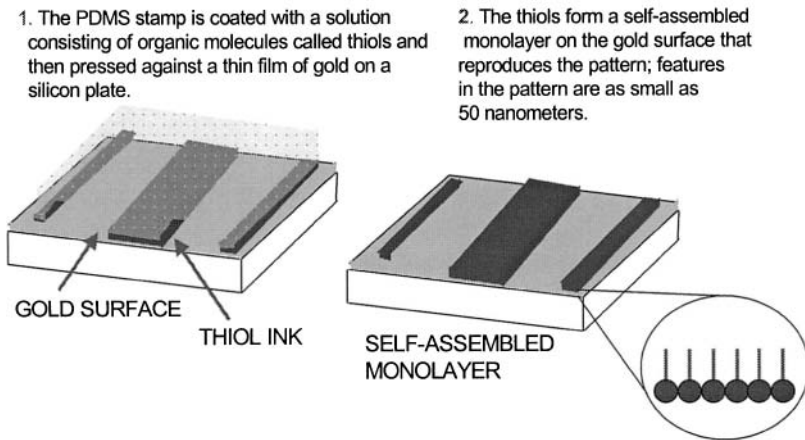


Whitesides & Love, Scientific American, Sept. 2001

Fig. 1.21. Principle of the soft lithography technique [10]

Figure 1.22 shows the basic principle of the process of micro-contact printing of a self-assembled monolayer on a gold film. The process has also been used to deposit GaAs and AlGaAs to silicon substrates to produce nanoscale transistors. Figure 1.23 shows a schematic view of a field effect transistor produced using soft lithography. Figure 1.24 shows the process steps required to produce such structures. Gate lengths and widths are of the order of 20 to 50 μm .

Soft Lithography-Microcontact Printing



Whitesides & Love, Scientific American, Sept. 2001

Fig. 1.22. Principle of microcontact printing using the soft lithography process [10]

The process of using the soft lithography technique is also used to replicate extremely fine features that can be attached to micro- and mesoscale products in order to provide localized functionality on larger scale surfaces. The technique has the potential to transform engineering products such as bearings and other contact surfaces to reduce wear and improve product reliability.

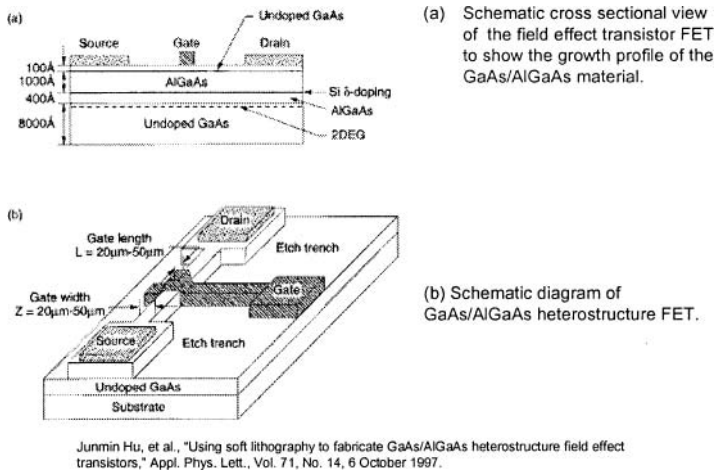


Fig. 1.23. Schematic diagram of a GaAs/AlGaAs field effect transistor produced using soft lithography [11]

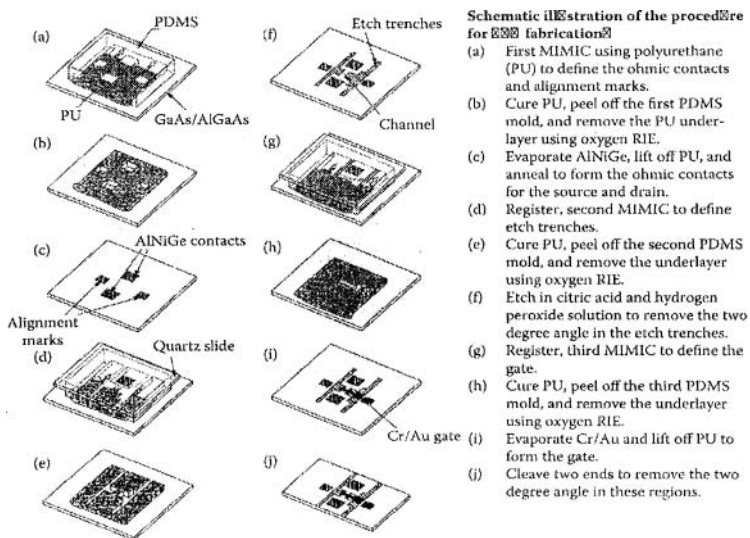
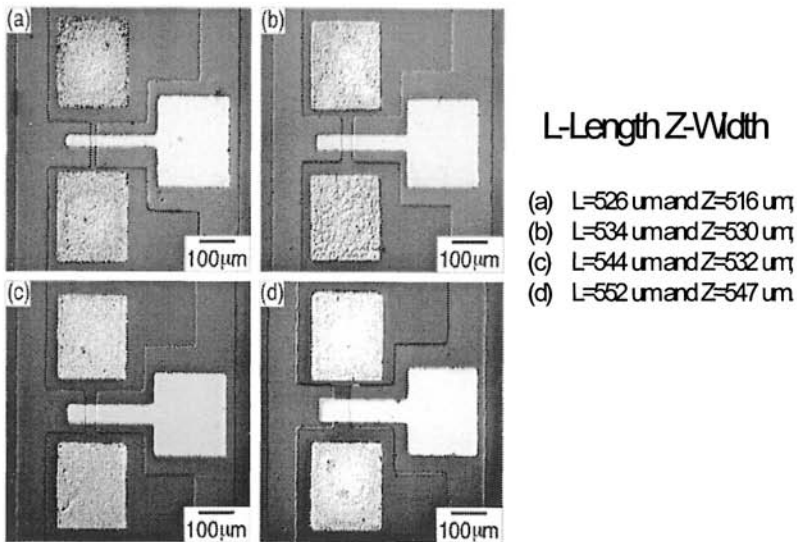


Fig. 1.24. Schematic illustration of the manufacturing procedure for producing a field effect transistor using soft lithography [11]

The procedure for fabricating a set of field effect transistors involves defining the resistive contacts and the alignment tracks by micromolding in capillaries using polyurethane liquid. The second process involves curing the polyurethane, then peeling off the PDMS mold, and removing the polyurethane base layer using the oxygen RIE process. The ohmic contacts for source and drain are produced by evaporating AuNiGe to the surface and removing the remaining polyurethane. Once annealed, the etch trenches are defined by etching with citric acid and hydrogen peroxide. The gate is then produced by evaporating a thin Cr/Au layer to the surface. The product is a set of nanostructured field effect transistors produced using soft lithography processes. Figure 1.25 shows the physical layout of the field effect transistors produced using this process.



Jumin Hu, et al., "Using soft lithography to fabricate GaAs/AlGaAs heterostructure field effect transistors," *Appl. Phys. Lett.*, Vol. 71, No. 14, 6 October 1997.

Fig. 1.25. Micrographs of field effect transistors with various gate lengths L and gate widths Z fabricated by soft lithography [11]

The fabrication of nanoelectronic features using soft lithography is at an early stage but promises to overcome the limitations experienced using optical methods of lithography, such as overcoming the diffraction limit observed in photolithography.

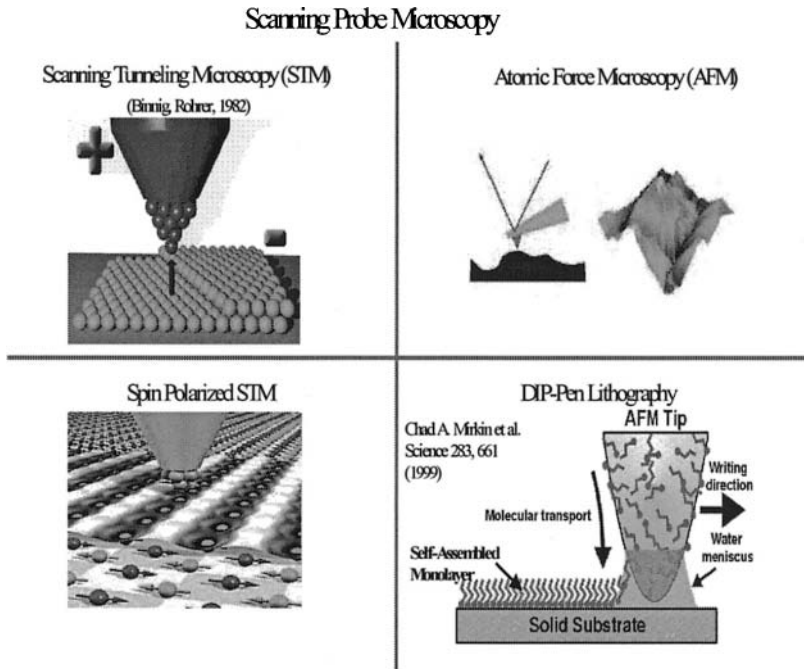
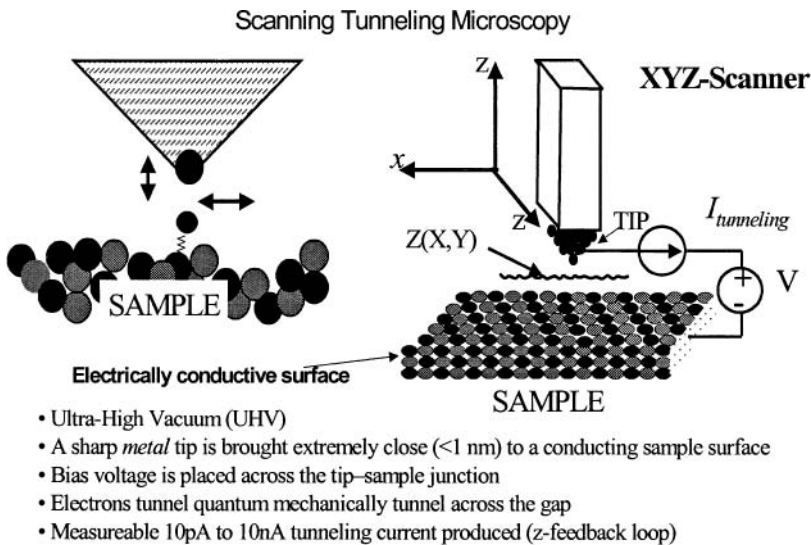


Fig. 1.26. Manipulative techniques used for nanofabrication

Nanofabrication Using Manipulative Techniques

Nanofabrication using manipulative techniques is a promising way of producing nano-based electronic components using processes such as scanning tunneling microscopy, atomic force microscopy, spin-polarized scanning tunneling microscopy, and dip pen nanolithography. Figure 1.26 shows the difference between these manipulative techniques. Scanning tunneling microscopy is a process that relies on a very sharp tip connected to a cantilever beam to

touch a surface composed of atoms that is electrically conductive. It is a process that is conducted in an ultrahigh vacuum where a sharp metal tip is brought into extremely close contact (less than 1 nm) with a conducting surface (Fig. 1.27). A bias voltage is applied to the tip and the sample junction where electrons tunnel quantum-mechanically across the gap. A feedback current is monitored to provide feedback and is usually in the range between 10 pA and 10 nA. The applied voltage is such that the energy barrier is lowered so that electrons can tunnel through the air gap. The tip is chemically polished or ground, and is made of materials such as tungsten, iridium, or platinum-iridium.



Franz J. Giessibl, "Advances in atomic force microscopy,"
[Online]: xxx.lanl.gov, arXiv:cond-mat/0305119 v1 6 May 2003.

Fig. 1.27. Basic principle of operation of the scanning tunneling microscope [12]

There are two modes of operation: (1) topography mode in which the tip scans in the x-y plane where the tunneling current is

kept constant and; (2) constant height mode where the tip is scanned in the x - y plane at constant depth and the tunneling current is modulated.

Figures 1.28 and 1.29 show images of quantum “corrals” on the surfaces of copper (111) and silver (111) that demonstrates the observations of ripples of electronic density distribution for surface electrons afforded by scanning tunneling microscopy. These observations are for conductive surfaces only. Non-conductive surfaces can still be imaged but require a technique known as atomic force microscopy, which is a powerful technique that can be used to fabricate structures at the nanoscale.

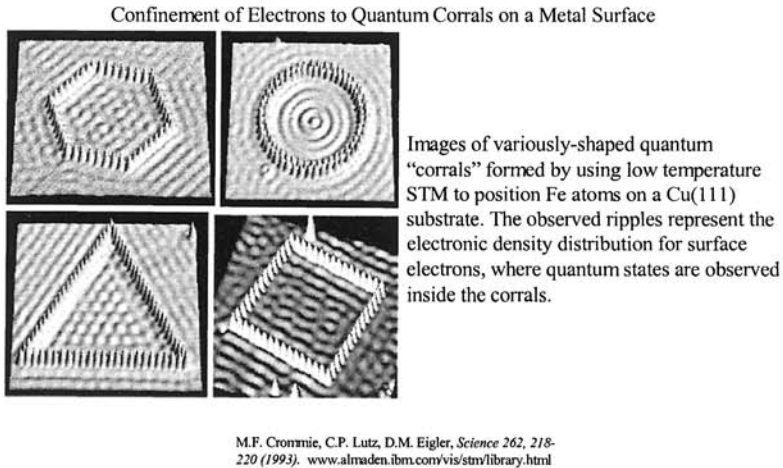
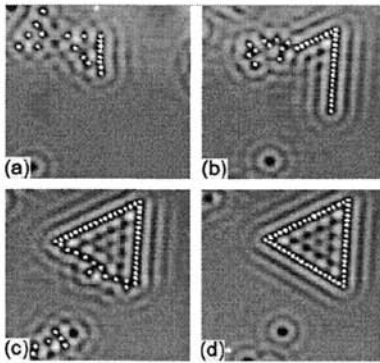


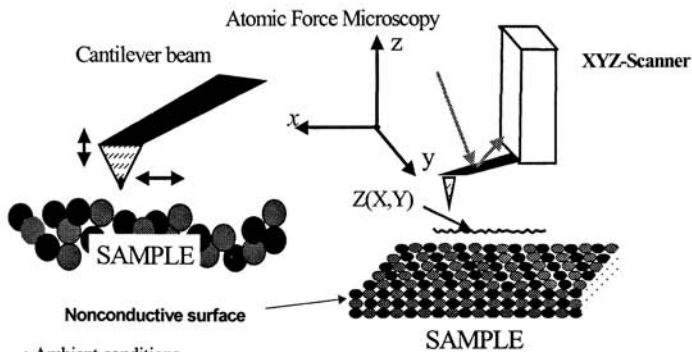
Fig. 1.28. Images of quantum “corrals” formed by positioning atoms on a (111) copper substrate [13]



Sequence of low-temperature STM images ($49 \text{ nm} \times 49 \text{ nm}$) showing the construction of a triangular "corral" composed of Ag atoms on a Ag(111) substrate.

K.-F. Braun, K.-H. Rieder, Phys. Rev. Lett. 88, 096801 (2002).

Fig. 1.29. Sequence of low-temperature images showing the construction of a triangular "corral" of silver atoms on a (111) surface of silver [14]



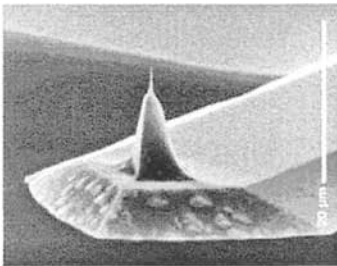
- Ambient conditions
- A sharp tip at end of cantilever beam is brought into contact with sample surface
- Surface is scanned by cantilever beam, like phonograph's stylus
- Beam's low spring constant allows small forces ($\sim 10^{-9} \text{ N}$) to be resolved
- Beam's deflection is monitored via laser beam reflection
- Feedback mechanism if force between tip and sample

Franz J. Giessibl, "Advances in atomic force microscopy,"
[Online]: xxx.lanl.gov, arXiv:cond-mat/0305119 v1 6 May 2003.

Fig. 1.30. Principle of atomic force microscopy on a non-conductive surface [12]

The atomic force microscope (AFM) is used in ambient conditions and in ultrahigh vacuum, and a sharp tip connected to a cantilever beam is brought into contact with the surface of the sample (Fig. 1.30). The surface is scanned, causing the beam to deflect, which is monitored by a scanning laser beam. The tip is micro-machined from materials such as silicon (Figs. 1.31 and 1.32), tungsten, diamond, iron, cobalt, samarium, iridium, or cobalt-samarium permanent magnets.

Silicon Cantilever with Integrated Tip

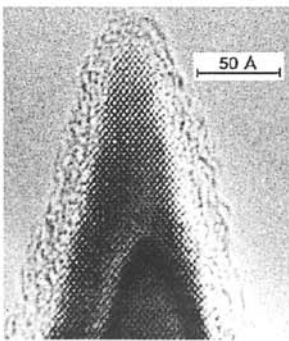


Scanning electron micrograph of a micromachined silicon cantilever with an integrated tip pointing in the [001] crystal direction.

Nanosensors, 2002, POINTPROBE sensors, Nanosensors AG, NANOSENSORS GmbH und Co. KG, Koogstraat 4, 25870 Norderfriedrichskoog, Germany.

Fig. 1.31. Silicon cantilever beam with integrated tip (Courtesy of Nanosensors)

Silicon Cantilever with Integrated Tip



Transmission Electron Micrograph of an extremely sharp silicon tip

Marcus, R., T. Ravi, T. Gmitter, K. Chin, D. Liu, W. Orvis, D. Ciarlo, C. Hunt, and J. Trujillo, 1990, "Formation of silicon tips with 1 nm radius", *Appl. Phys. Lett.* 56(3), 236-238.

Fig. 1.32. Transmission electron micrograph of an AFM tip [15]

The cantilever beam and tip are controlled by certain physical laws and as such possess a spring constant, k , and a resonant frequency, f_0 . The tip and cantilever experience a displacement force that is dominated by surface tension in ambient conditions (AFM mode), and chemical, van der Waals, and electrostatic forces in vacuum (STM mode). In summary, the modes of operation of the AFM are static and dynamic. In static AFM, the force between tip and surface is variable and non-linear compared to the surface-tip distance. Figure 1.33 shows the basic principle of operation in the static mode. The figure shows the contact mode, non-contact mode, and the intermittent dynamic modes and explains the differences between them.

Advances in the use of atomic force microscopy are reviewed by Giessibl [12] who presents an overview of the development of the technique and how it can be used for imaging and manipulation of small-scale features.

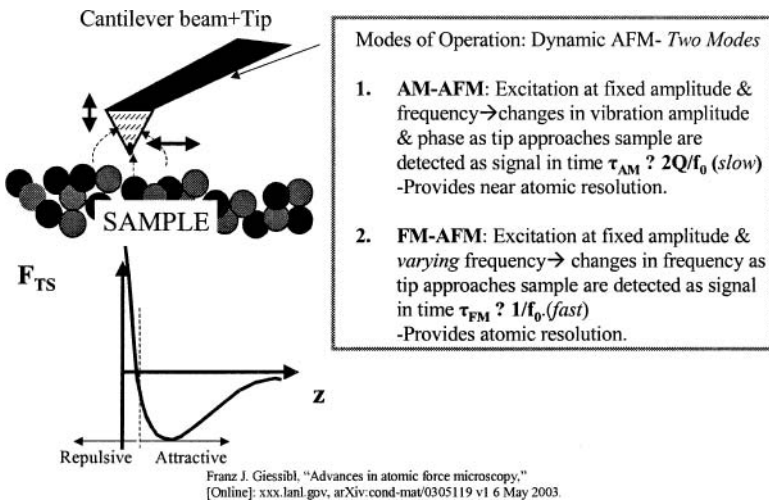
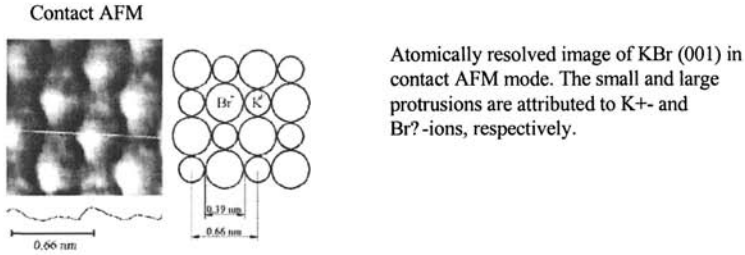
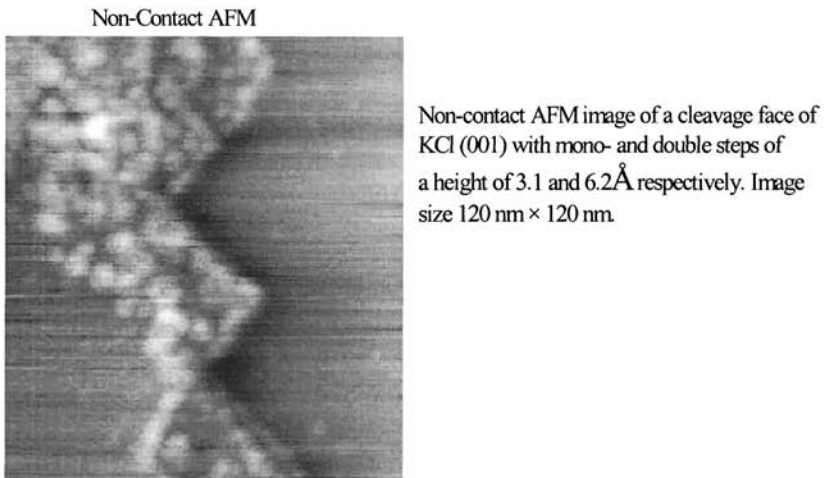


Fig. 1.33. Modes of operation of the atomic force microscope [12]



Giessibl, F. J. and G. Binnig, 1992b, "True atomic resolution on KBr with a low-temperature atomic force microscope in ultrahigh vacuum", *Ultramicroscopy* 42-44, 281-286.

Fig. 1.34. Atomic resolution of KBr surface using an AFM in ultrahigh vacuum [16]



Giessibl, F. J. and B. M. Trafts, 1994, "Piezoresistive cantilevers utilized for scanning tunneling and scanning force microscope in ultrahigh vacuum", *Rev. Sci. Instrum.* 65, 1923-1929.

Fig. 1.35. Non-contact AFM image of a cleavage face of potassium chloride showing distinctive variations in height [17]

The contact mode shows provides images of atomically resolved surfaces such as the potassium bromide surface (001) shown in Fig. 1.34. Here, the small and large protrusions are attributed to K^+ and Br^- ions. The tip exerts a large normal and lateral force in the repulsive regime when the tip is scanning the surface of the potassium bromide layer. Figure 1.35 shows the image generated by the non-contact dynamic AFM imaging regime. The tip oscillates above the sample in the attractive force range, which tends to avoid the noise and force deflections associated with the repulsive range. The image shows distinctive variations in height that can be used to manipulate features at the nanoscale in three dimensions. This technique can be used to manipulate nanotubes and other forms of carbon to construct nanoproducts. There are two modes of operation for the dynamic AFM (Fig. 1.36): AM-AFM; in which excitation of the cantilever-tip is done at a fixed amplitude and frequency, and FM-AFM where excitation is performed at fixed amplitude and a varying frequency. AM-AFM provides near atomic resolution (Fig. 1.37), whereas FM-AFM provides absolute atomic resolution (Fig. 1.38).

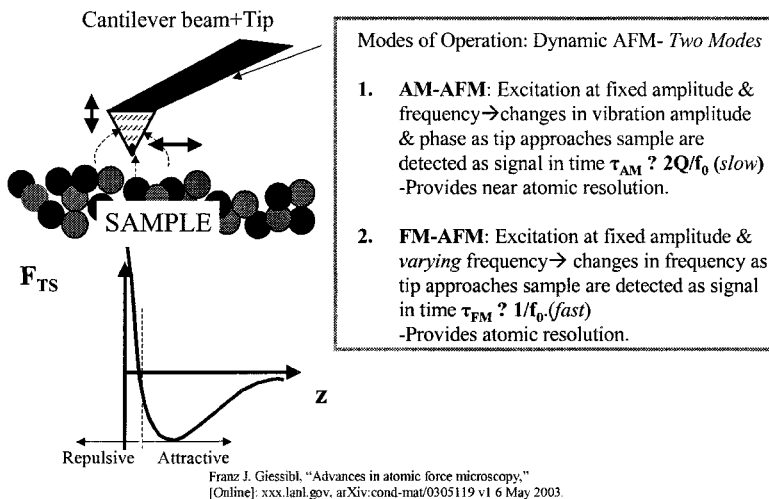
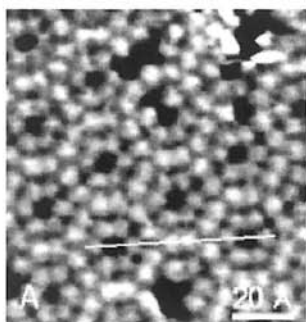


Fig. 1.36. Modes of operation of the dynamic AFM [12]

AM-AFM



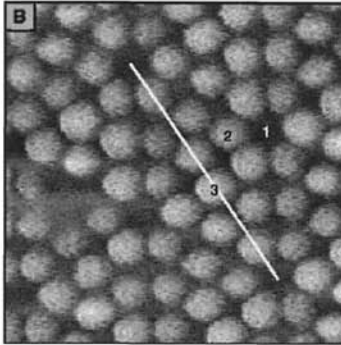
AFM image of the silicon with AM mode. Image size $100^{\circ}\text{A} \times 100^{\circ}\text{A}$. The grey scale in the image corresponds to a height difference of 1\AA .

Erlandsson, R., L. Olsson, and P. Martensson, 1997, "Inequivalent atoms and imaging mechanisms in ac-mode atomic-force microscopy of $\text{Si}(111)7\times 7$ ", *Phys. Rev. B* 54, R8309–R8312.

Fig. 1.37. AFM image of silicon surface (111) in the AM-AFM mode [18]

The coupling of the FM-AFM mode of operation with the ability to deposit colloids of nanoconducting particles allows the AFM to take part in constructing three-dimensional nanoscale products through fabrication. This can be performed by using a process called electrostatic trapping. The fabrication of single-electron transistors using the AFM is shown in Fig. 1.39. In this figure, nanoparticles are pushed into position using the cantilever beam and tip to deposit the particles in the correct position to form the conductive island between drain, gate and source. The attraction of the particles is aided by electrostatic trapping (Fig. 1.40). A commercial instrument that can be used for nanofabrication using the AFM principle is one provided by the Veeco Metrology Group (Fig. 1.41). This piece of equipment can be used to fabricate nanoscale features such as single-electron transistors with a little modification. The instrument can also be used to manipulate carbon nanotubes to construct conducting three-dimensional devices (Figs. 1.42 and 1.43).

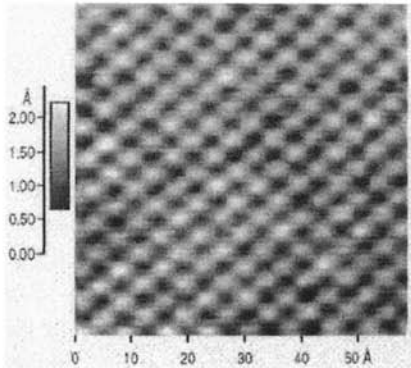
FM-AFM



6 nm×6 nm constant frequency shift image ($f = 738$ Hz, rms error 1.15 Hz, scan speed 2 nm/s). The labels 1, 2, and 3 indicate the position of frequency distance measurements

Lantz, M., H. J. Hug, R. Hoffmann, P. van Schendel, P. Kappenberger, S. Martin, A. Baratoff, and H.-J. Güntherodt, 2001, "Quantitative Measurement of Short-range Chemical Bonding Forces", *Science* 291, 2580–2583.

FM-AFM



First FM-AFM image of an insulator (KCl) with true atomic resolution.

Parameters: $k = 17$ N/m, $f_0 = 114$ kHz,
 $A = 34$ nm, $f = 70$ Hz and
 $Q = 28\,000$

Patrin, J., 1995, Atomic resolution of an insulator by noncontact AFM, Presentation at the 12th International Conference on Scanning Tunneling Microscopy 1995 (Snowmass, Colorado, USA).

Fig. 1.38. AFM Image of potassium chloride with absolute atomic resolution operating in the FM-AFM mode [19,20]

Building a Single-Electron Transistor by AFM Nanomanipulation.

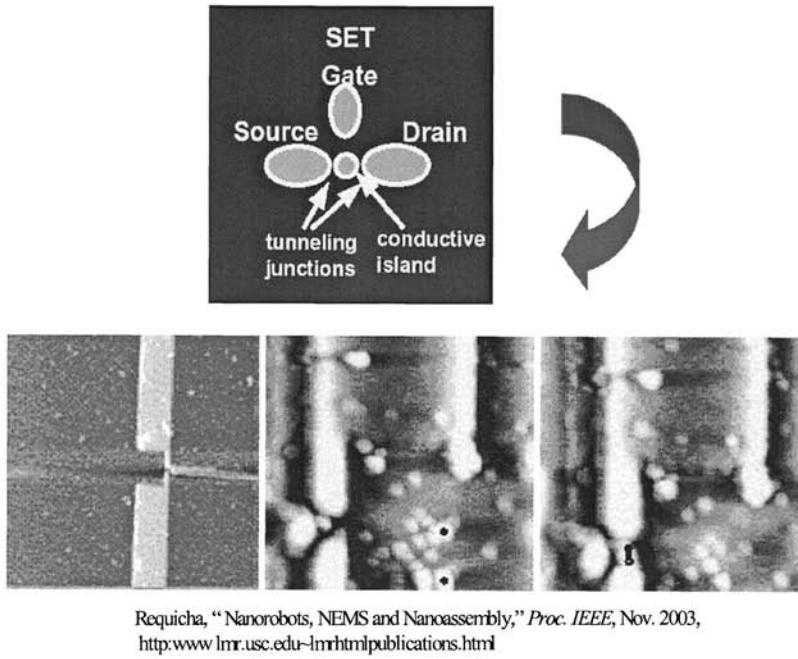
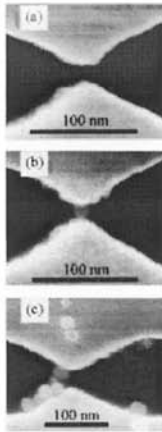


Fig. 1.39. Construction of a single-electron transistor aided by pushing the particles using an AFM tip and trapping the particles by electrostatic trapping [21]

Figure 1.39 shows the construction of a single-electron transistor, which is aided by physically pushing the particles using an atomic force microscope tip and trapping the particles by electrostatic trapping. The process can be used on larger scale features where there is a requirement to specifically engineer a surface to provide a known functionality such as a non-stick surface. AFM is a process capable of reproducing small, but highly functional surfaces.



(a) Pt electrodes (white) separated by a 14 nm gap.

(b) After ET, the same electrodes are bridged by a single 17 nm Pd particle.

(c) Another example where three Pd colloids are trapped across a 26 nm gap.

A. Bezryadin, C. Dekker, G. Schmid, "Electrostatic trapping of single conducting nanoparticles between nanoelectrodes," *Appl. Phys. Lett.* 71 (9), 1 September 1997

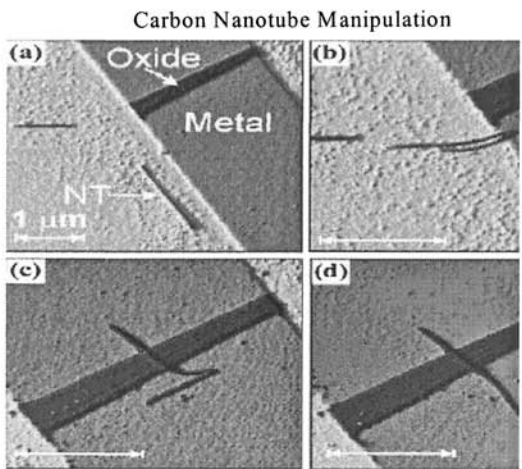
Fig. 1.40. Electrostatic trapping of palladium colloids between two nanoelectrodes [22]



Instrument optimized for high resolution force measurements and topographic imaging.

By C.B. Prater, P.G. Maivald, K.J. Kjoller, M.G. Heaton, "Probing Nano-Scale Forces with the Atomic Force Microscope," *Application Note 08*, Digital Instruments/ Veeco Metrology Group.

Fig. 1.41. Veeco instrument for probing nanoscale features (Courtesy of Veeco Metrology Group)



P. Avouris et al., Appl. Surf. Sci 141, 201-209 (1999).

Fig. 1.42. Carbon nanotube manipulation using the atomic force microscope [23]

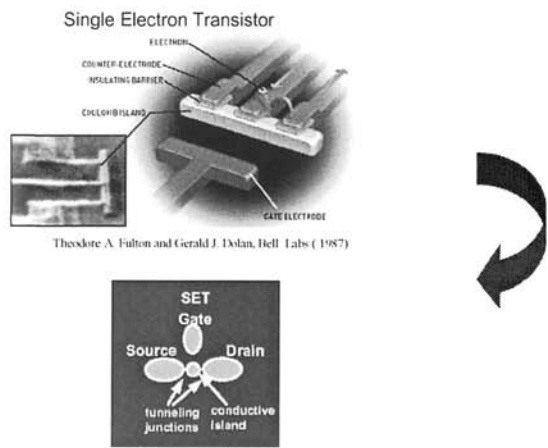
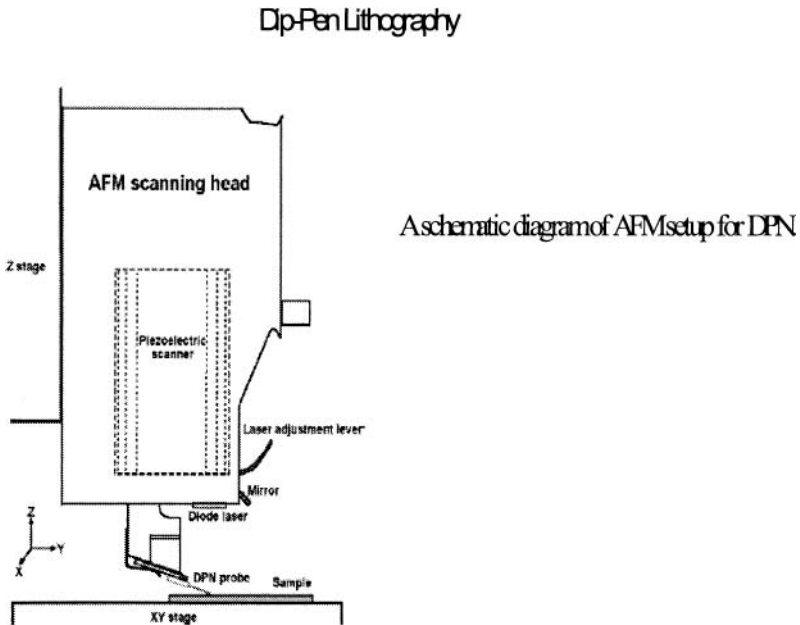


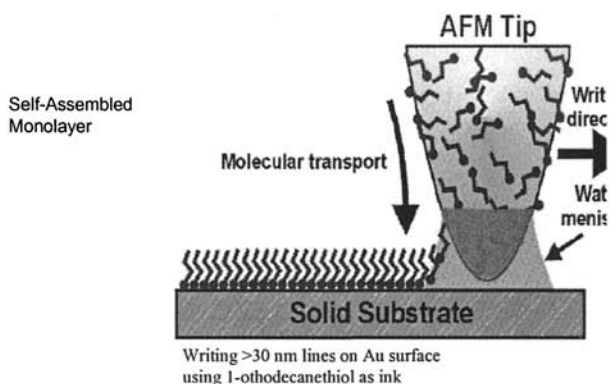
Fig. 1.43. Single-electron transistor constructed using carbon nanotubes (Courtesy of Bell Laboratories)

The atomic force microscope can be adapted to perform dip pen nanolithography by adding a dip pen nanoprobe to the tip of the AFM. Figure 1.44 shows the schematic diagram that allows nanofabrication of three-dimensional products to occur using self-assembled molecules (SAM) or colloids of nanoparticles.



X Wang, D Bullen, J. Zou, K. Ryu, C. Liu, S.-W. Chung, and C. A. Mirkin,
 "Linear Probe Arrays for Dip-Pen Nanolithography"

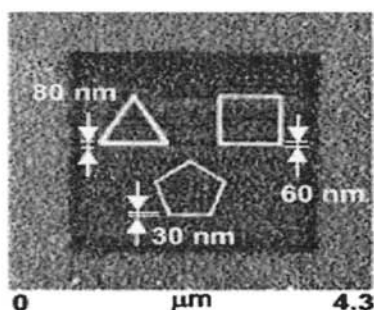
Fig. 1.44. Schematic diagram showing the AFM adapted for dip pen nanolithography [24]



Van Crocker, Jr, The Dip Pen Nanolithography™ (DPN™) Process, *Nanoink presentation*, April 7, 2003.

Fig. 1.45. Principle of forming a self-assembled monolayer using dip pen nanolithography

In the dip pen mode, the AFM is operated in the ambient condition so that the monolayer film of SAMs is deposited from tip to substrate in a controlled manner. It seems logical that reservoirs of self-assembled molecules are provided in order to speed up the process of nanofabrication. Figure 1.46 shows the type of nanolayers deposited using the dip pen nanolithographic technique.



AFMs are used in contact mode in ambient conditions, a monolayer film of adsorbed water usually connects the tip and sample. Some researchers have thought of using this property to transfer SAMs from reservoirs down the tip to the substrate

S. Hong, J. Zhu, C.A. Mirkin, *Science* **286**, pp. 523-525, 1999.

Fig. 1.46. Dip pen nanolithography of self-assembled monolayers

assembled monolayers. The process is likely to be developed into a nanomanufacturing process with the addition of many contacting probes containing reservoirs of colloidal fluids. One of the major uses of this technique is the deposition and positioning of carbon nanotubes and other structures of carbon in order to produce electronic components and other functional and structural products made from the new forms of carbon.

Nanofabrication Using Carbon Nanomaterials

A carbon nanotube is based on a two-dimensional graphene sheet. With reference to Fig. 1.47, (a) the chiral vector is defined on the hexagonal lattice as $\mathbf{Ch} = n\hat{\mathbf{a}}_1 + m\hat{\mathbf{a}}_2$, where $\hat{\mathbf{a}}_1$ and $\hat{\mathbf{a}}_2$ are unit vectors, and n and m are integers. The chiral angle, q , is measured relative to the direction defined by $\hat{\mathbf{a}}_1$. This diagram has been constructed for $(n, m) = (4, 2)$, and the unit cell of this nanotube is bounded by OAB'B. To form the nanotube, imagine that this cell is rolled up so that O meets A and B meets B', and the two ends are capped with half of a fullerene molecule. Different types of carbon nanotubes have different values of n and m .

With reference Fig. 1.47, (b) zigzag nanotubes correspond to $(n, 0)$ or $(0, m)$ and have a chiral angle of 0° , armchair nanotubes have (n, n) and a chiral angle of 30° , while chiral nanotubes have general (n, m) values and a chiral angle of between 0° and 30° . According to the theory, nanotubes can either be metallic (green circles) or semi-conducting (blue circles). Simple construction of a one-dimensional carbon nanotube is shown in Fig. 1.48.

Carbon nanotubes can be manufactured by arc discharge, laser ablation, and chemical vapor deposition methods in the form of multiwall carbon nanotubes (MWCNT), or single-wall carbon nanotubes (SWCNT). Figure 1.49 shows the structure of a multi-wall carbon nanotube. The properties of such CNT's are shown in Tables 1.1 and 1.2.

Applications: One-Dimensional Conduction

Carbon Nanotubes

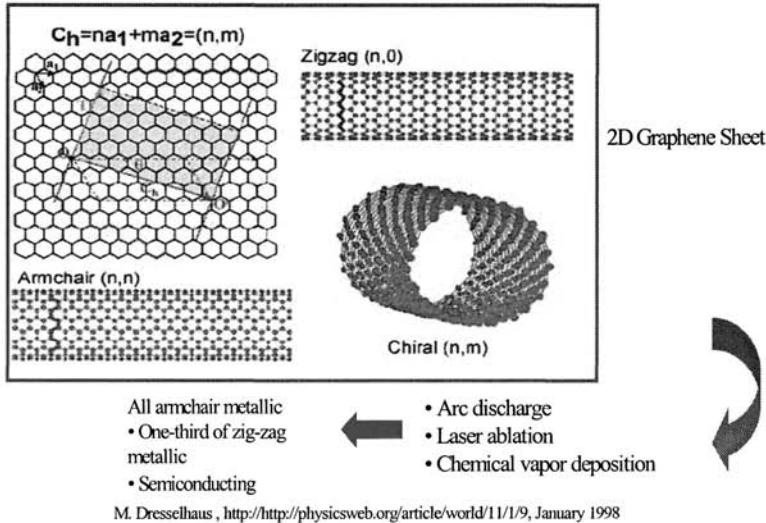


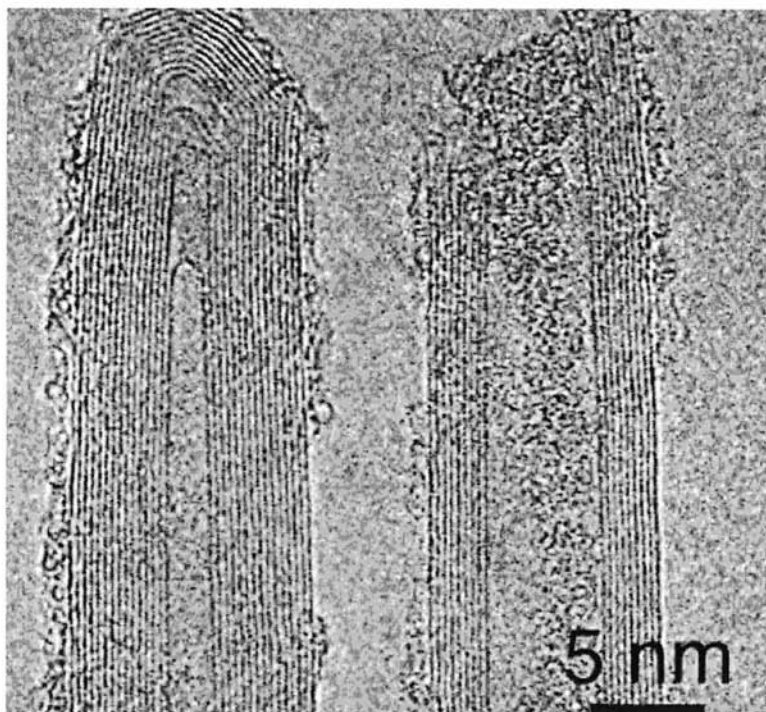
Fig. 1.48. One-dimensional conducting carbon nanotubes [25]

Carbon nanotubes are nanomaterials that possess high strength and thermal properties and can be designed to be conducting and semiconducting materials. This makes them particularly suited to be made into probes for AFM cantilever beams and for the construction of carbon nanotube transistors.

The preparation of carbon nanotube tipped AFM probes begins by anisotropically etching silicon to form deep pits for nanotubes of carbon to grow. Once etched, a catalyst is deposited that promotes the growth of the nanotubes. Direct growth by placing in a chemical vapor deposition chamber allows the nanotubes to grow and form the AFM probe.

The probe is then bonded to a silicon cantilever and the manufacturing regime is shown in Fig. 1.50. Figure 1.51 shows the single-wall carbon nanotubes grown from the silicon cantilever probe. Carbon nanotubes are also used as vacuum tube lighting elements because they emit light at relatively low currents, which makes them environmentally friendly devices.

Multi-Wall Carbon Nanotubes (MWCNT)



<http://physicsweb.org/article/world/13/6/8>

Fig. 1.49. Multi-wall carbon nanotube structure (Courtesy of Physicsweb.org)

Table 1.1. Properties of Carbon Nanotubes [26]

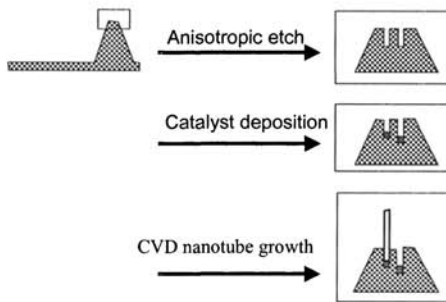
Property	Item	Data
Geometrical	Layers	Single/multiple
	Aspect ratio	10-1000
	Diameter	04 nm-100 nm
	Length	Several μm to several cm
Mechanical	Young's modulus	1T Pa (steel: 0.2T Pa)
	Tensile strength	45 G Pa (steel: 2 G Pa)
	Density	1.33 - 1.4g/cm ³
Electronic	Conductivity	Metallic/semi-conductor
	Current capacity	1 TA/cm ³ (Cu:1GA/cm ³)
	Field emission	1 - 3V active phosphorus
Thermal	Heat transmission	>3kW/mK

Table 1.2. Applications of carbon nanotubes [26]

State	Device	Main properties applied
Bulk/array	Composite	High strength, conductivity, etc.
	Field emission devices	High current density
	Electrochemical devices	Large surface area
	Fuel cells	Large surface area
Individual	Nanoelectronics: wire, electronics, diodes, transistor, switch, memory, etc.	Small sizes, semiconducting/metallic
	NEMS	Well defined properties

Applications: AFM Tips

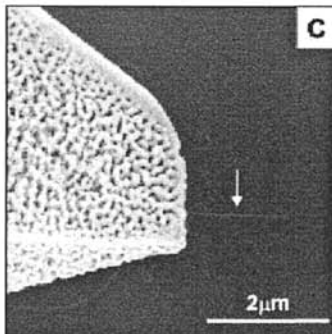
CVD nanotube tip preparation approach.



C. L. Cheung, J. H. Hafner, and C. M. Lieber, "Carbon nanotube atomic force microscopy tips: Direct growth by chemical vapor deposition and application to high-resolution imaging," *PNAS*, April 11, 2000 vol. 97 no. 8 p 3813

Fig. 1.50. Deposition of carbon nanotubes to manufacture AFM probes [27]

CVD nanotube tip preparation approach.



Field emission SEM image of SWNT bundles grown from a Si cantilever tip assembly.

C. L. Cheung, J. H. Hafner, and C. M. Lieber, "Carbon nanotube atomic force microscopy tips: Direct growth by chemical vapor deposition and application to high-resolution imaging," *PNAS*, April 11, 2000 vol. 97 no. 8 p 3813

Fig. 1.51. CVD nanotube assembly grown from a silicon cantilever probe [27]

Applications: Carbon Nanotube Transistors

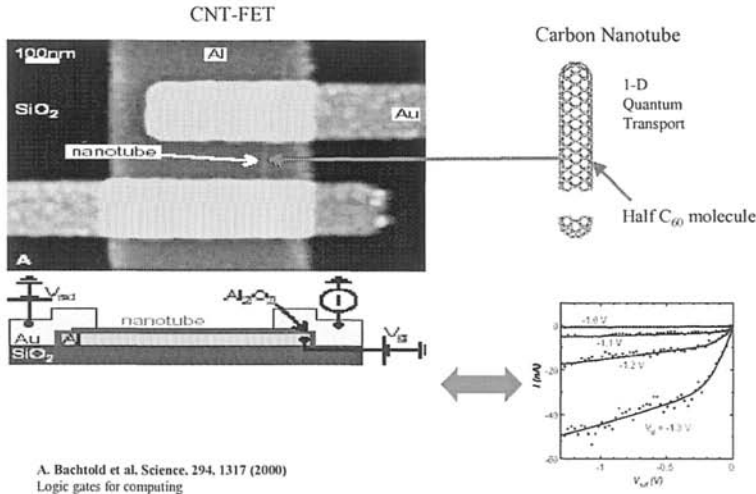


Fig. 1.52. Logic gates for computing using a carbon nanotube that has been pushed into place using the atomic force microscope [28]

AFM probes are currently being employed to construct semiconducting elements such as carbon nanotube logic inverters and carbon nanotube transistors using the cantilever beam and tip to push carbon nanotubes into place after depositing them close to the source, drain, and gate of the transistor (Figs. 1.52 - 1.54). This makes the AFM a manipulative nanofabricating tool that is currently solving the very problems created by scaling down the size of electronic devices to the nanoscale.

1.2 Material Removal Rates

There are two variables associated with measuring material removal rates in micro and nanofabrication:

Applications: Carbon Nanotube Transistors

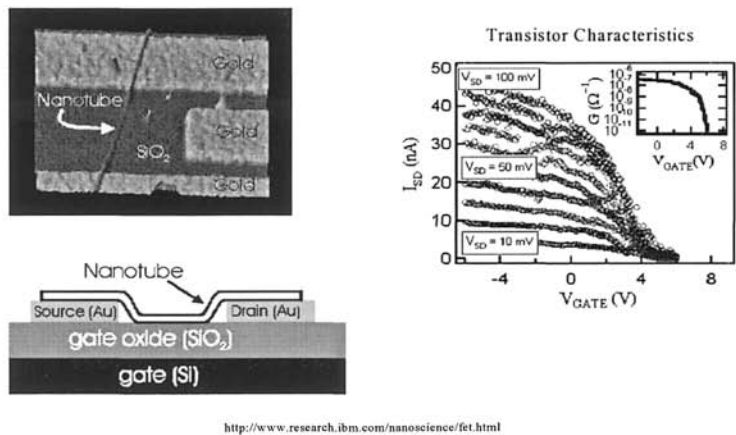
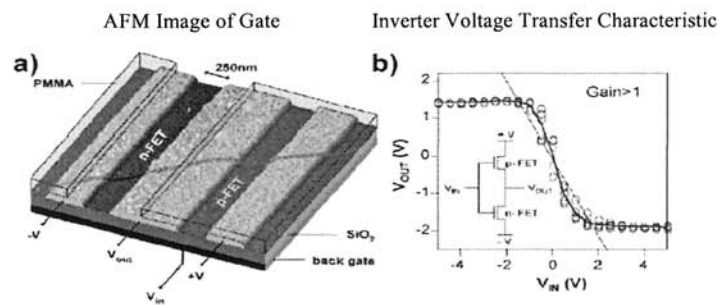


Fig. 1.53. Carbon nanotube transistor showing transistor characteristics. Courtesy of IBM

Applications: CNT Logic Inverter



V. Derycke, R. Martel, J. Appenzeller, and Ph. Avouris, "Carbon Nanotube Inter- and Intramolecular Logic Gates," Nano Lett., Vol. 1, pp. 453-456, 2001.

Fig. 1.54. Carbon nanotube logic inverter [29]

(1) the speed at which lithographic processes can be carried measured as the area processed per unit time, and (2) the rate of pattern transfer as measured by the depth removed per unit time.

1.2.1 Lithography

For optical lithography, the rate of area covered is measured in wafers per hour. For 200 mm diameter wafers, typical values are between 30 and 60 per hour for deposition of 250 nm feature sizes.

Electron beam lithography is much slower than optical lithography and is typically measured in hours per wafer and depends on the complexity of the pattern to be created. There are a number of variables to be considered: pattern density, fill factor, and the ultimate resolution required. The required resolution determines the diameter of the beam, which is two to five times smaller than the minimum feature size. An approximate expression for the writing time, T , for a pattern is:

$$T = \frac{FF \cdot A \cdot S}{i} \quad (1.1)$$

Where FF is the fill factor, A is the total area to be covered, S is the sensitivity, and I is the beam current. The beam current is related to the spot diameter, d , by:

$$i = \frac{B \cdot \pi^2 \cdot d^2 \cdot \alpha^2}{4} \quad (1.2)$$

Where B is the electron source brightness, and α is the beam's semi-angle at the substrate, which is typically 1 to 10 mrad. The brightness depends on the electron source, and this can be a thermionic source such as LaB_6 , or a field emission source whose brightness is typically $10^8 \text{ Acm}^{-2}\text{sr}^{-1}$. The field emission sources have higher speed and provide smaller spot sizes. Fill factors are between 2% and 50% giving area coverage rates of 2 to 100 cm^2 per hour.

1.2.2. Pattern Transfer

Deposition rates are usually 10 to 100 nm/min and depend upon the system used and the type of materials deposited.

Dry etch rates depend on the type of structure being etched and its aspect ratio. Table 1.3 shows the effects of using different etches including etch rates, etch depths, feature sizes that can be dry etched, etch system used, type of etch gas used, and mask used with the type of material to be etched. Most semiconductors and MEMS etching is carried out using plasma based systems, although wet etches are frequently used. Table 1.4 shows the characteristics of frequently used wet etching solutions.

Table 1.3. Dry etch rates for various micro- and nanomachined materials

Material etched	Mask material	Etch gas	Etch system	Etch rate (nm/min)	Depth (μm)	Feature size (μm)
Si	600nm photoresist	ICP	SF_6/CHF_3	680	0.5	0.5
Si	2.8 μm SiO_2	BCl_3/Cl_2	RIE	200	48	10
Si	15nm Au	SiCl_4	RIE	140	0.06	0.015
Polycrystalline Si	Tetraethoxysilane	HBr	ECR	230	0.4	0.3
	BPTEOS					
GaAs	40 nm Cr	$\text{Cl}_2/\text{C}_4\text{H}_8$	ECR	460	2.3	0.2
AlGaAs	40 nm Cr	$\text{Cl}_2/\text{C}_4\text{H}_8$	ECR	280	1.4	0.2
InGaAs	100 nm NiCr	Cl_2/Ar	RIE	90	3	2
InGaAs	20/50nm Ti/Ni	Cl_2/Ar	ICP	250	0.4	0.1
Au	500nm SiO_2	Cl_2	ECR	250	0.4	1
AlCu (0.5%Cu)	Photoresist	BCl_3/Cl_2	ICP	1000	0.7	0.4
W/WSi _x	Resist	SF_6/Ar	RIE	100	0.4	0.3
W	45nm Ni	SF_6	ECR	120	0.45	0.2
W	50nm PMMA	SF_6/O_2	RIE	50	0.05	0.03
NiMnSb	Photoresist	SF_6/Ar	ICP	>1000	0.5	1.2
$\text{YBa}_2\text{Cu}_3\text{O}_{7-x}$	50nm C	Ion	Ar	25	0.1	0.2
		beam milling				
SiO_2	300nm polycrystalline Si	$\text{C}_4\text{F}_8/\text{O}_2/\text{Ar}$	M-RIE	600	1	0.06
Si_3N_4	50nm Ti	C_2F_6	ECR	25	0.1	0.03
Diamond	Al	CF_4/O	RIE	0.78	0.3	0.01
Polyimide	NiCr	O_2	RIE	3	0.6	0.1

Table 1.4. Wet etch rates for various micro- and nanomachined materials

Material etched	Mask material	Wet etchant	Etch rate (nm/min)	Comments
SiO ₂	Resist	HF	50	
Si ₃ N ₄	Resist	H ₃ PO ₄	10	
Al	Resist	HNO ₃ /CH ₃ CO OH/H ₃ PO ₄ /H ₂ O	35	
Si	SiO ₂	KOH	600	Used at 80°C, anisotropic. Stops etching on (111) plane
GaAs	Resist	H ₂ SO ₄ /H ₂ O ₂ / H ₂ O	800	Anisotropic etch

1.3 Conclusions

Micro- and nanofabrication is a challenge brought about by scaling down the size of transistors so that microprocessors can run faster and more efficiently. However, the development of these fabricating techniques will have a positive effect of producing products other than semiconductors and microprocessors. These techniques have yet to be exploited by the automotive, aerospace, healthcare, and many other industries that have yet to invent and manufacture micro- and nanofabricated products.

1.4 Problems

1. Describe the materials used in the semiconductor industry.
2. Explain the process of micromachining. Use a flowchart to show your answer.

3. Explain how deep trenches are machined in silicon.
4. Illustrate how microcapacitors are manufactured.
5. Show how cantilever probes for AFM applications are manufactured using deep reactive ion etching.
6. Describe and illustrate the basic chipmaking process.
7. What is soft lithography? How does soft lithography overcome the problems encountered using optical lithography?
8. Show how field effect transistors are manufactured using soft lithographic techniques.
9. Explain the operation of a scanning tunneling microscope.
10. What is an atomic force microscope? Explain its modes of operation.
11. Explain how carbon nanotubes can be used to make field effect transistors.
12. Describe the properties of carbon nanotubes.
13. How are carbon nanotubes used to make AFM probes?
14. Show how a field effect transistor, variable area capacitor, and electronic resonators are manufactured.

References

1. Campbell SA, The Science and Engineering of Microelectronic Fabrication - 2nd Edition, Oxford Series in Electrical Engineering - Oxford University Press, 2005.
2. Yeager RC, Introduction to Microelectronic Fabrication, Volume V, Modular Series on Solid State Devices – edited by Neudeck and Pierret, Addison Wesley Press, Reading, MA, 1988.
3. Sun Y, H. von Zeigl, J. L. Tauritz, R. Baets, Suspended Membrane Inductors and Capacitors for Application in Silicon MMCs, Microwave and Monolithic Circuits Symposium Digest of Papers, IEEE, p.p. 99-102, 1996.
4. Piazza GR, R. Abdolvand, and F. Ayazi, Voltage-Tunable, Piezoelectrically-Transduced Single Crystal Silicon Resonators on SOI Substrates, 2003 IEEE MEMS Conference, Kyoto, Japan, p.p. 149-152, 2003.

5. Deep Reactive Ion Etching Patent Number 5501893, Robert Bosch GmbH, 1996.
6. Yao JJ, Topical Review: RF MEMS from a Device Perspective, *Journal of Micromechanics and Microengineering*, **10**, R9-R38, 2000.
7. Hutcheson GD, The First Nanochips, *Scientific American*, p.p. 76-83, April 2004.
8. Taur Y, *IBM Journal of Research and Development*, **46**, 2/3, 2002.
9. Ionescu AM et al., Few Electron Devices – Towards Hybrid CMOS-SET Integrated Circuits, *Proc. 39th Design and Automation Conference*, New Orleans, USA, p.p. 88-93, 2002.
10. Whitesides GM and Love JC, The Art of Building Small, *Scientific American – Special Issue on Nanotechnology*, p.p. 39-47, September 2001.
11. Hu J et al., Using Soft Lithography to Fabricate GaAs/AlGaAs Heterostructure Field Effect Transistors, *Applied Physics Letters*, **71**, (14), October 1997.
12. Giessibl FJ, *Advances in Atomic Force Microscopy*, Accessed on line at: xxx.lanl.gov/arXiv:cond-mat/0305119. Accessed December 2005.
13. Crommie MF, Lutz CP, Eigler DM, *Science*, **262**, 218-220, 1993.
14. Braun KF and Reider KH, *Phys. Rev. Lett*, **88**, 096801, 2002.
15. Marcus R, Ravi T, Gmitter K, Chin K, Liu D, Orvis W, Ciarlo D, Hunt C, Trujillo J, Formation of Silicon Tips with 1nm Radius, *Appl. Phys. Lett.*, **56**, (3), 236-238, 1990.
16. Giessibl FJ and Binnig G, True Atomic Resolution on KBr with a Low Temperature Atomic Force Microscope in Ultra High Vacuum, *Ultramicroscopy*, **42-44**, 281-286, 1992.
17. Giessibl FJ and Trafas BM, Piezoresistive Cantilevers Utilized for Scanning Tunneling and Scanning Force Microscopes in Ultra High Vacuum, *Rev. Sci. Instrum.*, **65**, 1923-1929, 1994.
18. Erlandsson R, Olsson L, and Martensson P, Inequivalent Atoms and Imaging Mechanisms in AC-Mode Atomic Force Microscopy, *Phys. Rev. B.*, **54**, R8309-R8312. 1994.
19. Lantz M, Hug HJ, Hoffman P, van Schendel P, Kappenberger P, Martin S, Baratoff A, and Gunderrodt H, Quantitative Measurement of Short-Range Chemical Bonding Forces, *Science*, **291**, 2580-2583, 2001.

20. Patrin J, Atomic Resolution of an Insulator by Non-contact AFM, 12th International Conference on Scanning Tunneling Microscopy, Colorado, 1995.
21. Requicha A, Nanorobots, NEMS, and Nanoassembly, Proceedings of the IEEE Special issue on nanoelectronics and nanoprocessing, **91**, (11), p.p. 1922-1933, November 2003. www-lmr.usc.edu/~lmr/html/publications.html. Accessed December 2005.
22. Bezyadin A, Dekker C, Schmid G, Electrostatic Trapping of Single Conducting Nanoparticles Between Nanoelectrodes, *Appl. Phys. Lett.*, **71**, (9), September 1997.
23. Avouris P et al., *Applied Surf. Sci.*, **141**, 210-209, 1999.
24. Wang X, Bullen D, Zou J, Ryu K, Chung SW, and Mirkin CA, Linear Arrays for Dip Pen Nanolithography, *Materials Research Bull.*, **26**, (7), p.p. 535-538, July 2001.
25. Dresselhaus M, January 1998 – Website accessed December 2005. <http://physicsweb.org/article/world/11/1/9>.
26. Fukuda H, Arai J, and Dong K, Assembly of Nanodevices with Carbon Nanotubes Through Nanorobotic Manipulators, *Proc. IEEE*, **91**, (11), p.p. 1803-1818, November 2003.
27. Cheung CL, Hafner J, Lieber CM, Carbon Nanotube Atomic Force Microscopy Tips: Direct Growth By Chemical Vapor Deposition and Application to High Resolution Imaging, *PNAS*, **97**, (8), p. 3813, April 11, 2000.
28. Bachtold A et al., *Science*, **294**, p.1317, 2000.
29. Derycke V, Martel R, Appenzeller J, and Avouris P, Carbon Nanotube Inter and Intramolecular Logic Gates, *Nano Letters*, **1**, p.p. 453-456, 2001.

2. Microfabrication Using X- ray Lithography

2.1 Introduction

During the last decade there has been a rapid development in micro-fabrication technology driven by the market need for low-cost consumer products such as portable telecommunications equipment, computers, and healthcare diagnostics. Much of the technology used for these is based on production of silicon semiconductors and microchips. Interest in non-silicon-based technologies started to grow back in the early 1980s with the development of a German fabrication process known as LIGA, an acronym for Lithography (Lithographie), electroplating (Galvanoformung), molding (Abformung) [1, 2]. It originated at the Karlsruhe Nuclear Research Laboratory in Germany. Since then a number of groups, mainly in Germany and the United States have been active in developing the process to make precision microcomponents for a range of innovative products such as microspectrometers, fiber-optic wave guides, micro-reactors and microfluidic devices. A few of these have been manufactured on a large scale and placed on the market. LIGA was often used to fabricate the components, which were then integrated with others into the end product. High costs are often associated with the integration and packaging of the final product.

The most active groups developing and using the LIGA process are the Sandia National Laboratories at Livermore, the Center for Advanced Microstructures and Devices (CAMD) at the Louisiana State University at Baton Rouge, in the United States, Institut für Mikrostrukturtechnik (FZK) Karlsruhe and Antwenderzentrum BESSY, Berlin in Germany. In addition the work done in the United Kingdom at Central Microstructure Facility at the CCLRC's Rutherford Appleton Laboratory using the national synchrotron at Dares-

bury as part of a European network program has advanced fabrication techniques in mask and resist development. A small start in commercialization has been made by two companies in the United States, Axsun and International Mezzo, which provides commercial LIGA services.

Progress in commercialization has been slow owing to the absence of fast prototyping and large-scale manufacturing capabilities, and the lack of established design rules and standards. This situation was recently reviewed at a workshop at the COMS2004 conference in Edmonton. The delegates decided to form an International LIGA Interest Group to bring together major researchers, practitioners, manufacturers, and users into an international network to provide mechanisms for communication to solve the problems and be an incentive for commercialization.

Since 1980 numerous reports and papers on the development and use of the LIGA process have been published and are too numerous to be listed here. A more recent overview of the current status of this process was given by Hruby at the HARMST Conference in 2003 [3], and commercialization issues were reviewed recently by Tolfree at COMS2004 [4] and Goettert at COMS2004 [5].

The latest market survey [6] indicated that a global market valued in excess \$40 billion is emerging for microproducts. The increased interest in nanotechnology driven by the prospect of producing new non-silicon-based materials with unique properties, has increased market estimates to over a \$1trillion. Micro-nanomanufacturing is now a key value-added element in many sectors of industry.

The boundaries between nanotechnology and microtechnology may be blurred, but there is a degree of commonality in the techniques and equipment involved in both - but they are, in essence and in application, very different. It is at the nano not the micro scale that the physical and chemical properties of materials change. Microfabrication is essentially a top-down technology but at the nano-scale, either top-down or bottom-up techniques can be used, and the latter are significantly different. Many products require a variety of top-down processes for their manufacture. For example, the common CD has data pits about 500 nm wide and 125 nm deep formed

in a plastic disc. The read-write heads are very precise mechanisms that require a number of electro-mechanical processes.

Extensive papers and reviews on microfabrication technologies have been published. Two examples are: "The Fundamentals of Microfabrication" by Madou 2002 [7], and 'Microfabrication using Synchrotron Radiation' by Tolfree in 1998 [8]. These and others can be found in the literature and on internet sites, cover most of the relevant principles and issues associated with the development and exploitation of the technologies. It was therefore decided to restrict the content on this chapter to microfabrication using lithographic X-ray techniques. This technique is known as deep X-ray lithography (DXRL), is like all lithographic processes, ultimately limited in line-width by the wavelength of the illuminating radiation. The conversion from a 2-D pattern to a 3-D structure is dependent on a number of factors, which are examined below.

There are multiple types of lithography, including UV, deep UV, X-ray and electron-beam lithography. Currently, for non-silicon-based materials, the highest precision can be achieved using DXRL with very parallel, high-energy x-rays from a synchrotron radiation source (SRS). It is the increased access provided by the large number (>80) of synchrotrons now operating world wide, coupled to availability of low-solubility resists, thus reducing exposure time that has encouraged a greater interest in DXRL. This technique still has to find a wider community of users outside of research but it will have a significant role to play in the range of tools and processes required to develop a micro-nanotechnology (MNT)-based industry.

Micro-nanotechnology (MNT) is pervasive and will have an impact, sometimes disruptive, on almost every industry sector and through the generation of new products and systems, on the society in general. The universal use of the mobile telephone and ink-jet printer are two well-known examples. The availability of a vast range of new consumer and industrial products such as sensors, embedded transducers and actuators, displays, health care diagnostics etc. will revolutionize the way people will live and work in the future.

2.2 X- ray Lithography

2.2.1. History

International Business Machines (IBM) first combined electrodeposition and x- ray lithography in 1969. They made high-aspect ratio metal structures by plating gold patterns of 20 μm in thickness in a resist that had been exposed to x- rays. The IBM work was an extension of through-mask plating, also pioneered by IBM in 1969, and was directed toward the fabrication of thin film magnetic recording heads. A historical background of lithography was provided by Cerrina [9].

The development of the LIGA process referred to above required small slotted nozzles for uranium isotope separation [10] to be produced. Since then, the X- ray lithographic technique has been developed to fabricate a variety of microstructures in materials [11 - 19]. The potential of LIGA for the development of microsystems was reviewed by Bacher [20]. Essentially, a three-step process, the LIGA technique can be used to make 3D microstructures.

By adding molding techniques the broader implications of x- ray lithography as a means of low-cost manufacturing of a wide variety of microparts with unprecedented accuracy from various materials can be realised. In Germany, x- ray lithography was originally developed outside of the semiconductor industry.

Early pioneering work in the use of synchrotron radiation for microfabrication was carried out by Professor Guckel at the University of Wisconsin in the United States. This included use of the LIGA technique to develop micromotors [21-24]. Guckel repositioned the field in light of semiconductor process capabilities and brought it closer to standard manufacturing processes.

2.3 Synchrotron Radiation (SR)

2.3. General Characteristics

The radiation emitted by relativistic electrons when traversing a magnetic field can be understood from purely classical electromagnetic theory. Its properties can be expressed by basic equations that are used in the design of synchrotron radiation sources [25-32]. A basic introduction to synchrotron radiation sources is given by Marks [33] and a general review that provides details on the subject by Turner [34]. The power of the emitted radiation is inversely proportional to the mass of the charged particle, so electrons yield useful quantities of radiation in the visible and X- ray regions of the electromagnetic spectrum.

Centripetal acceleration of highly relativistic charged particles in a magnetic bending field results in the tangential emission of synchrotron radiation over a wide spectrum at every point of the curved particle trajectory. Considering only electrons, the emission pattern is essentially determined by that of a single circulating electron.

With reference to Fig. 2.1, the radiation pattern emitted by relativistic electrons can be transformed into the laboratory reference frame, resulting in its being compressed in a narrow forward cone, tangential with respect to the electrons' circular path. This natural collimation is an important characteristic property of synchrotron radiation. As the electron beam sweeps out the curved path, a continuous fan of radiation results in the horizontal plane while the distribution in the vertical plane is highly collimated.

The opening half-angle of the emission cone of radiation is wavelength-dependent [35], its angular distribution can be approximated by a Gaussian distribution, the width of which is related to the kinetic energy, E , and the rest energy (mc^2). The natural divergence δ_n is given by:

$$\delta_n = (mc^2)/E \quad (2.1)$$

The divergence is an important parameter when considering the use of synchrotron radiation sources for deep x-ray lithography. This has to be as low as possible but is limited to the practical values obtainable for E , which are in the range (1.5-3) GeV for typical national sources, resulting in values for the natural divergence between 0.2 and 0.3 mrad in the x-ray region.

The continuous emission of radiation excites particle oscillations that give rise to a finite extension of the particle beam and corresponding angular deviations with respect to the ideal trajectory. Since the direction of photon emission follows the instantaneous particle direction, an additional angular width, δ_p , results, which is independent of the natural divergence and when added to the natural divergence it forms the total angular width of the synchrotron radiation and is given by:

$$s_{tot} = (\delta n^2 + \delta p^2)^{1/2} \quad (2.2)$$

The electron beam emittance is determined by the particular design of the synchrotron but can be optimized to be similar in magnitude to the natural divergence. A typical value for s_{tot} is in the range 0.3-0.4 mrad that leads to a vertical intensity distribution of the beam. At a distance of 10 m from the emission point and with a typical beam width of 3-4 mm, the beam is seen as a broad radiation fan in the horizontal direction. In calculating the above, the finite width of the beam has been ignored but could be important at the location of the lithography station on an external beam line on a synchrotron. When the beam width is taken into account, the product of beam size, W , and its angular width, δ_t , is given by the emittance, E :

$$E = W\delta_t \quad (2.3)$$

2.3.2 Spectral Characteristics

Owing to both longitudinal and transverse oscillations of the circulating electrons, individual components in the frequency spectrum become smeared out, resulting in a continuous spectrum of radiation

being emitted from the infra-red to wavelengths shorter than a critical wavelength, λ_c , in the hard x- ray region.

The spectrum shape is characterized by the electron energy, the beam current and the magnetic field in the accelerator [36]. The spectral distribution from a small elemental arc of radius, R , along the electron orbit can be described in terms of a critical wavelength, λ_c , Angstrom.

$$\lambda_c = 18.6/BE^2 \quad (2.4)$$

Where E is the electron energy (GeV), B is the bending field (Tesla). The critical wavelength is a useful parameter for characterising emission. It represents the value of wavelength that equally divides the total integrated photon energy. Since the spectrum extends into long wavelengths and the photon energy is inversely proportional to wavelength, the critical wavelength is near the short wavelength end of the spectrum. A typical spectrum from a dipole magnet in which the emission is integrated over the complete fan of radiation is shown in Fig. 2.1. For a source of fixed radius, the radiated power varies as the fourth power of the electron energy.

2.3.3 Spectral Brilliance and Brightness

The finite size of the electron beam and the correlation between individual electrons and their orbits is characterized by phase space distributions.

The photon flux radiated by the source can be described by a number of different parameters. The spectral flux is the number of photons/s/mrad horizontal emitted into a 0.1% bandwidth, the emission being integrated fully in the vertical plane.

The brightness is the spectral flux per mrad vertical; it therefore has units of photons/s/mrad² per 0.1% bandwidth. Where the incident beam is focused on a sample, and the source area becomes important, the concept of brilliance, the brightness per unit source area, is used. This has units of photons/s/mrad²/mm² per 0.1% bandwidth.

The value of brightness or brilliance for any particular synchrotron is dependent on the design of the accelerator and particularly its magnet lattice, a high value of brilliance being required for good resolution [37]. The quality of the radiation source is therefore characterized by its spectral brilliance and the spectral distribution of the emission.

Brightness can be increased by the use of insertion devices such as wigglers and undulators, placed in straight sections of the storage ring. These devices have a periodic magnetic structure and therefore produce an oscillatory path of the electrons with enhancement and modification of the radiation. The theory associated with these devices is given in [38,39].

The enhanced penetrating power and beam intensity of the higher energy X- rays resulting from the use of wigglers enables the production of deeper molds, thus facilitating the manufacture of 3D microstructures. Using data from the Daresbury synchrotron source, parameters required for deep lithography using wiggler radiation were calculated by using software developed at Daresbury Laboratory in the United Kingdom.

It should be noted that a beryllium window can withstand a 1 atmosphere pressure differential across a small diameter (<1 inch). For large area exposures, windows up to 6 cm in diameter have been developed. Beryllium windows age with x- ray exposure and must be replaced periodically. This is one of the limitations of using external X- ray beams and adds to the overall operational cost.

2.4 Microfabrication Process

2.4.1 General

An overview of microlithography, micromachining, and microfabrication has been given in a SPIE Handbook [9]. Methods exist for fabricating microstructures but the use of deep X- ray lithography and the LIGA process referred to above provides the highest dimension precision.

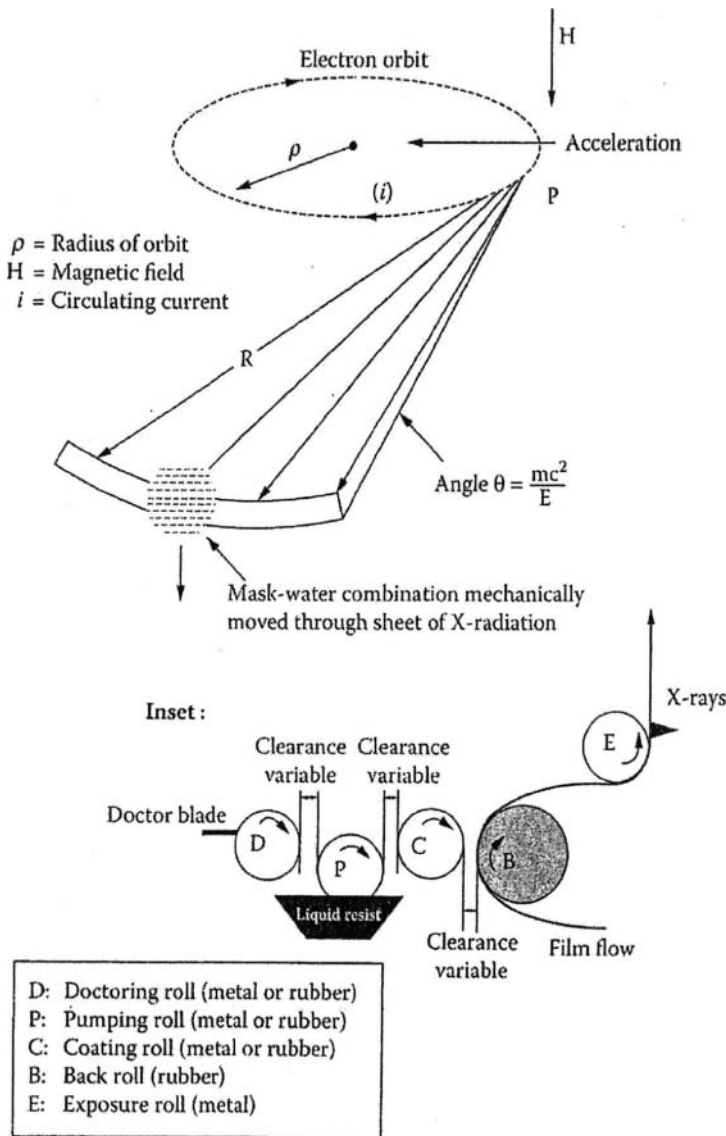


Fig. 2.1. Schematic of an x-ray exposure station with a synchrotron radiation source. The x-ray radiation opening angle, θ , is tangential to the path of the electron describing a line on an intersecting substrate. (M. Madou, "Fundamentals of Microfabrication", 2nd edition, 2002, CRC Press [7])

However, limitations in the materials that can be used and the relatively high cost of the process from prototyping to large-scale manufacture of components has restricted its wider use. The development of new resists, (SU8) increased knowledge of the process, and the wider availability of synchrotron storage rings has awakened renewed interest in LIGA as a viable process technology. The current support for nanotechnology has also raised questions about the boundaries that can be reached for top-down processing.

2.4.2 LIGA Process

LIGA is a three-step process (Fig. 2.2). Although here, we consider x-ray based lithography, UV-LIGA and Laser-LIGA techniques have also reached an advanced stage of development. UV-LIGA in particular has encouraged the production of a negative resist known as SU-8 that can also be used in X-ray lithography owing to its increased radiation sensitivity over more commonly used polymethylmethacrylate (PMMA) resists, thus reducing exposure time and subsequent costs.

The penetrating power of X-rays compared to other longer wavelength radiations allows the fabrication of structures that have vertical dimensions from hundreds of microns to millimeters and horizontal dimensions as small as microns. These 3-D microstructures with high aspect ratios offer a range of microcomponents for many useful applications.

2.4.3 Lithography Steps

The first step using x-ray lithography involves exposing a thick layer of resist through a patterned mask to a high-energy beam of x-rays from a synchrotron. The pattern is etched into the resist substrate by the use of x-rays. A chemical solvent is used to dissolve away the damaged material, resulting in a negative relief replica of the mask pattern. Certain metals can be electrodeposited into the re-

sist mold. After removal of the resist, a freestanding metal structure is produced. The metal structure may be a final product, or serve as a mold insert for precision plastic molding. Molded plastic parts may then be final products or lost molds. The plastic mold retains the same shape, size, and form as the original resist structure but is produced quickly. The plastic lost mold may subsequently metal parts in a secondary process, or generate ceramic parts using a slip casting process.

2.4.4 X- ray Lithography

X- ray lithography is basically a shadow printing process in which patterns coated on a mask are transferred into a third dimension in a resist material, normally PMMA. This is subsequently chemical process to dissolve away the volume of material damaged by the x-rays. The quality of the remaining structure is dependent on the beam exposure, the precision of patterning on the mask and the purity and processing of the resist material. Beyond exposure it is the precision of electroforming and micromolding processes that determines the quality of the final product.

Micromachining techniques are changing manufacturing approaches for a wide variety of small parts. Frequently, semiconductor batch microfabrication methods are considered along with traditional serial machining methods. In this sense, x- ray lithography and pseudo x- ray lithography processes are classed as hybrid technologies, bridging semiconductor and classical manufacturing technologies. The ability of x- ray lithography and pseudo x- ray lithography for creating a wide variety of shapes from different materials makes these methods similar to classical machining, with the added benefit of high aspect ratios and absolute tolerances that are possible using lithography and other high-precision mold fabrication techniques.

2.4.5 X- ray Masks

Good quality, radiation resistant masks are an essential element in lithography. To be highly transmissive to x- rays, the mask substrate must be a low-Z (atomic number) thin membrane.

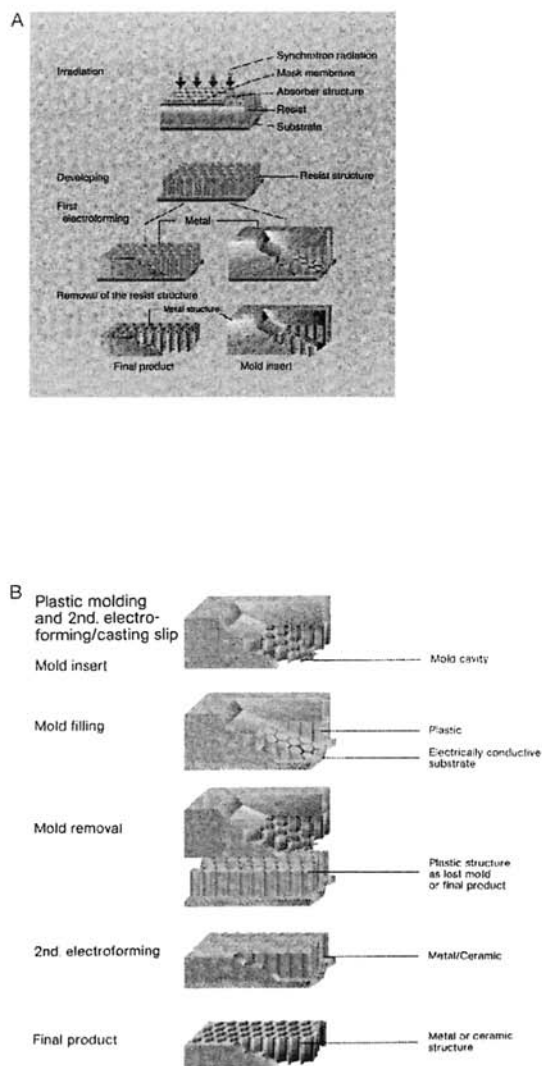


Fig. 2.2. (A) Basic x-ray exposure: (1) x-ray deep-etch lithography and, (2) primary electroforming process. (B) Plastic molding and secondary electroforming process. (From Lehr and Schmidt, "The LiGA Technique", IMM GmbH, Mainz-Hechstein, 1995)

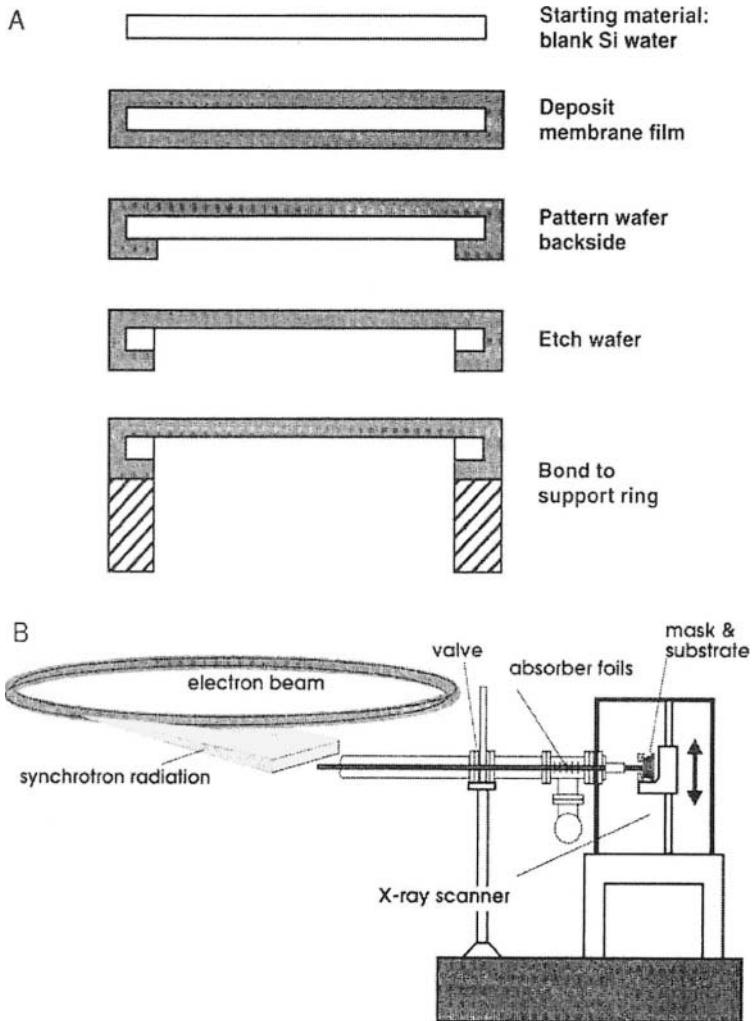


Fig. 2.3. Schematic of a typical x- ray mask (A) and mask and substrate assembly in an x- ray scanner (B). (From M. Madou, "Fundamentals of Microfabrication", 2nd Edition, 2002, CRC Press [7])

Table 2.1. Comparison of masks for use in x- ray lithography and the semiconductor industry.

Feature	Semiconductor lithography	X- ray lithography
Transparency	$\geq 50\%$	$\geq 80\%$
Absorber thickness	$\pm 1 \mu\text{m}$	$10 \mu\text{m}$ or higher
Field size	$50 \times 50 \text{ mm}^2$	$100 \times 100 \text{ mm}^2$
Radiation resistance	$= 1$	$= 100$
Surface roughness	$< 0.1 \mu\text{m}$	$< 0.5 \mu\text{m}$
Waviness	$< \pm 1 \mu\text{m}$	$< \pm 1 \mu\text{m}$
Dimensional stability	$< 0.05 \mu\text{m}$	$< 0.1\text{--}0.3 \mu\text{m}$
Residual membrane stress	$\sim 10^8 \text{ Pa}$	$\sim 10^8 \text{ Pa}$

X- ray masks should withstand many exposures without distortion, must be aligned with respect to the sample, and must be rugged. Possible x- ray mask architecture and its assembly with a substrate in an x- ray scanner are shown in Fig. 2.3. The mask shown here has three major components: an absorber, a membrane or mask blank, and a frame. The absorber contains the information to be imaged onto the resist. It is composed of a material with a high atomic number (Z); often gold is used that is patterned to a membrane material with a low Z . The high- Z material absorbs x- rays, whereas the low- Z material transmits x- rays.

The frame is robust in relation to the membrane/absorber assembly so that the whole can be handled. The requirements for x- ray masks in x- ray lithography differ substantially from those for the semiconductor industry. A comparison is presented in Table 2.1.

The main difference lies in the thickness of the absorber. To achieve high contrast, a very thick absorber ($>10\ \mu\text{m}$ vs. $1\ \mu\text{m}$) and highly transparent mask blanks (transparency $>80\%$) must be used because of the low resist sensitivity and the great depth of the resist. Another difference focuses on the radiation stability of membrane and absorber. For conventional optical lithography, the supporting substrate is a relatively thick, optically flat piece of glass or quartz highly transparent to optical wavelengths. It provides a highly stable ($>10^6\ \mu\text{m}$) basis for the thin ($0.1\ \mu\text{m}$) chrome absorber pattern. In contrast, the x- ray mask consists of a very thin membrane (2 to $4\ \mu\text{m}$) of low-Z material carrying a high-Z thick absorber pattern. A single exposure in x- ray lithography results in an exposure dose 100 times higher than in the semiconductor case.

2.4.6 Mask Materials

The low-Z membrane material in an x- ray mask must have a transparency for rays with a critical wavelength, λ_c , from 0.2 to 0.6 nm of at least 80% and should not scatter those rays. To avoid pattern distortion, the residual stress, σ_r , in the membrane should be less than $10^6\ \text{N/m}^2$. Mechanical stress in the absorber pattern can cause in-plane distortion of the supporting thin membrane, requiring a high Young's modulus for the membrane material. During one typical lithography step, the masks may be exposed to $1\ \text{MJ/cm}^2$ of x- rays. Since most membranes must be very thin for optimal transparency, a compromise has to be found among transparency, strength, and form stability. Important x- ray membrane materials are listed in Table 2.2. The higher radiation dose in x- ray lithography prevents the use of BN and compound mask blanks that incorporate a polyimide layer. Those mask blanks are perfectly appropriate for classical semiconductor lithography work but will not do for x- ray lithography processes. Mask blanks of metals such as titanium (Ti) and beryllium were specifically developed for x- ray lithography applications because of their resistance to radiation breakdown. In comparing titanium and beryllium membranes, beryllium can have a much greater membrane thickness, d , and still be adequately trans-

parent. For example, a membrane transparency of 80%, essential for adequate exposure of a 500 μm thick PMMA resist layer, is obtained with a thin 2 μm titanium film, whereas, with beryllium, a thick 300 μm membrane achieves the same result. The thicker beryllium membrane permits easier processing and handling. In addition, beryllium has a greater Young's modulus E than titanium and, since it is the product of E and d that determines the amount of mask distortion, distortions due to absorber stress should be much smaller for beryllium blanks. Beryllium is an excellent membrane material for x-ray lithography because of its high transparency and excellent damage resistance. Stoichiometric silicon nitride (Si_3N_4) used in x-ray mask membranes may contain numerous oxygen impurities, absorbing x-rays and thus producing heat. This heat often suffices to prevent the use of nitride as a good x-ray lithography mask. Single-crystal silicon masks have been made (1 cm square and 0.4 μm thick, and 10 cm square and 2.5 μm thick) by electro-chemical etching techniques. For Si and Si_3N_4 , Young's modulus is quite low compared with CVD-grown diamond and SiC films, with a Young's modulus as high as three times. Higher stiffness materials are more desirable, because the internal stresses of the absorbers, which can distort mask patterns, are less of an issue. Unfortunately, diamond and SiC membranes are also the most difficult to produce.

Table 2.2. Comparison of membrane materials for x-ray masks

Material	X-ray transparency	Observations
Silicon	0 (50% transmission at 5.5 μm thickness).	Single-crystal silicon, stacking faults cause scattering to occur, material is brittle.
SiC	0 (50% transmission at 2.3 μm thickness).	Amorphous with resistance to fracture.
Diamond	0 (50% transmission at 4.6 μm thickness).	High stiffness and transparency

The requirements on the absorber are high attenuation (>10 dB), stability under radiation over an extended period of time, negligible distortion, ease of patterning, and low microstructural defect density. Typical absorber materials are listed in Table 2.3. Gold is used most commonly; tungsten and other materials are used infrequently. In the semiconductor industry, an absorber thickness of $0.5 \mu\text{m}$ might be sufficient, whereas x- ray lithography deals with thicker layers of resist, requiring a thicker absorber material to maintain the same resolution.

Table 2.3. Comparison of absorber materials for x- ray masks

Material	Observations
Gold	Not the best stability (grain growth), low stress, electroplating only, defects repairable (thermal exp coefficient $14.2^\circ\text{C}^{-1} 10^{-6}$) ($0.7 \mu\text{m}$ for 10 dB).
Tungsten	Refractory and stable, special care is needed for stress control, dry etchable, repairable (thermal exp coefficient $4.5^\circ\text{C}^{-1} 10^{-6}$) ($0.8 \mu\text{m}$ for 10 dB).
Tantalum	Refractory and stable, special care is needed for stress control, dry etchable, repairable.
Alloys	Easier stress control, greater thickness needed to obtain 10 dB.

Figure 2.4 illustrates how x- rays, with a characteristic wavelength of 0.55 nm , are absorbed along their trajectory through a Kapton pre-absorber filter, an x- ray mask, and resist. The low-energy portion of the synchrotron radiation is absorbed mainly in the top portion of the resist layer, since absorption increases with increasing wavelength. The Kapton pre-absorber filters out much of the low-energy radiation to prevent over exposure of the top surface of the resist. The x- ray dose at which the resist gets damaged, D_{dm} , and the dose required for development of the resist, D_{dv} , as well as the

“threshold dose” at which the resist starts dissolving in a developer, D_{th} , are all indicated in Fig. 2.4. In the areas under the absorber pattern of the x-ray mask, the absorbed dose must stay below the threshold dose, D_{th} . Otherwise, the structures partly dissolve, resulting in poor feature definition. From Fig. 2.4, we can deduce that the height of the gold absorbers must exceed $6\text{ }\mu\text{m}$ to reduce the absorbed radiation dose of the resist under the gold pattern to below the threshold dose, D_{th} . In Fig. 2.5, the necessary thickness of the gold absorber patterns of an x-ray mask is plotted as a function of the thickness of the resist to be patterned; the Au must be thicker for thicker resist layers and for shorter characteristic wavelengths, λ_c , of the x-ray radiation. To pattern a 500 nm high structure with a λ_c of 0.225 nm , the gold absorber must be more than $11\text{ }\mu\text{m}$ in height.

Exposure of more extreme photoresist thickness requires x-ray photon energies that are significantly higher. At 3000 eV , the absorption length in PMMA roughly measures $100\text{ }\mu\text{m}$, which enables the above-mentioned $500\text{ }\mu\text{m}$ exposure depth. Using $20,000\text{ eV}$ photons results in absorption lengths of 1 cm . PMMA structures up to 10 cm thick have been exposed this way. A high-energy mask for high-energy exposures has a gold absorber $50\text{ }\mu\text{m}$ thick and a blank membrane of $400\text{ }\mu\text{m}$ thickness of silicon. An absorption contrast of 400 when exposing a $1000\text{ }\mu\text{m}$ thick PMMA sheet can be obtained. An advantage of using such thick silicon blank membranes is that larger resist areas can be exposed, since it does not depend on a fragile membrane-absorber combination.

2.4.7 Single-layer Absorber Fabrication

To make a mask with gold absorber structures of a height above $10\text{ }\mu\text{m}$, one must first succeed in structuring a resist of that thickness. The height of the resist should be higher than the absorber itself so as to accommodate the electrodeposited metal in between the resist features. Currently, no means to structure a resist of that height with sufficient accuracy and perfect verticality of the walls exists, unless x-rays are used.

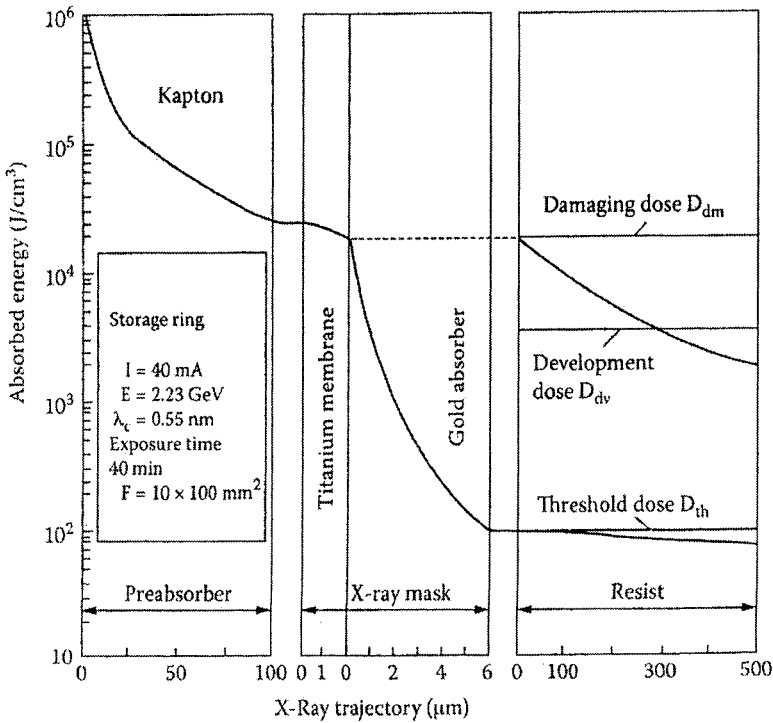


Fig. 2.4. Absorbed energy along the x-ray trajectory including a 500 μm thick PMMA specimen, x-ray mask, and a Kapton pre-absorber. (From P. Bley, W. Menz, W. Bacher, K. Feit, M. Harmening, H. Hein, J. Mohr, W. Schomberg and K. Stark, "Application of the LiGA Process in the Fabrication of 3-D Structures", 4th International Symposium on Microprocess Conference, Japan, 1991, p.p. 384-389)

Different procedures for producing x-ray masks with thicker absorber layers using a two-stage lithography process have been developed. First, an intermediate mask is made with photo or electron-beam lithography. This intermediate mask starts with a 3 μm thick resist layer, in which case the needed line-width accuracy and photoresist wall steepness of printed features are achievable. After gold plating in between the resist features and stripping of the resist, this intermediate mask is used to write a pattern with x-rays in a thicker resist, say 20 μm thick. After electrodepositing and resist stripping, the actual x-ray mask (that is, the master mask) is obtained.

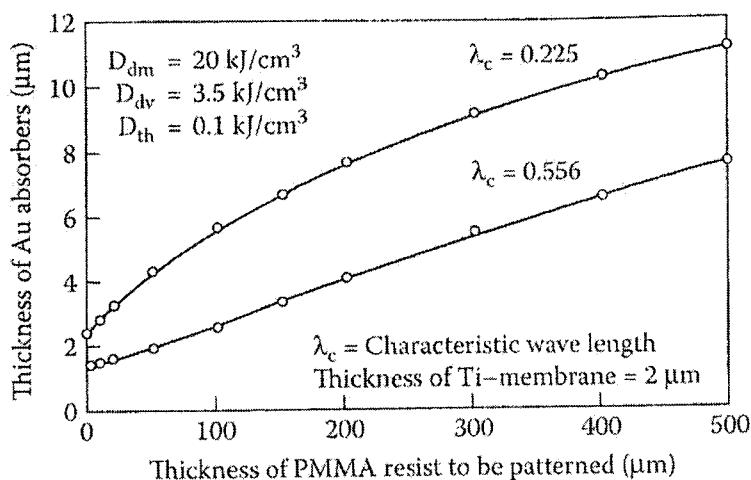


Fig. 2.5. Minimum thickness of gold absorbers used for the x- ray mask. (From P. Bley, W. Menz, W. Bacher, K. Feit, M. Harmening, H. Hein, J. Mohr, W. Schomberg and K. Stark, "Application of the LiGA Process in the Fabrication of 3-D Structures", 4th International Symposium on Microprocess Conference, Japan, 1991, p.p. 384-389)

Since hardly any accuracy is lost in the copying of the intermediate mask with x- rays to obtain the master mask, it is the intermediate mask quality that determines the ultimate quality of the x- ray lithographic-produced microstructures. The structuring of the resist in the intermediate mask is handled with optical techniques when the requirements of the x- ray lithography structures are less stringent. The minimal lateral dimensions for optical lithography in a $3 \mu\text{m}$ thick resist typically measure about $2.5 \mu\text{m}$. Under optimal conditions, a wall angle of 88° is achievable. With electron beam lithography, a minimum lateral dimension of less than $1 \mu\text{m}$ is feasible. The most accurate pattern transfer is achieved through reactive ion etching of a tri-level resist system. In this approach, a 3 to $4 \mu\text{m}$ thick polyimide resist is first coated to the titanium or beryllium membrane, followed by a coat of 10 to 15 nm titanium deposited with magnetron sputtering. The thin layer of titanium is an excellent

etch mask for the polyimide; in the optimized oxygen plasma, the titanium etches 300 times slower than the polyimide. To structure the thin titanium layer itself, a $0.1\text{ }\mu\text{m}$ thick optical resist is used. Since this top resist layer is so thin, excellent lateral tolerances result. The thin Ti layer is patterned with optical photolithography and etched in the argon plasma. After the thin titanium layer is etched, exposing the polyimide locally, an oxygen plasma helps to structure the polyimide down to the titanium or beryllium membrane. Lateral dimensions of $0.3\text{ }\mu\text{m}$ can be obtained in this fashion. Patterning the top resist layer with an electron beam increases the accuracy of the three-level resist method even further. Electrodeposition of gold on the titanium or beryllium membrane and stripping of the resist finishes the process of making the intermediate x-ray lithography mask. To make a master mask, this intermediate mask is printed by x-ray radiation onto a PMMA-resist-coated master mask. The PMMA thickness corresponds to a bit more than the desired absorber thickness. Since the resist layer thickness is in the 10 to $20\text{ }\mu\text{m}$ range, a synchrotron x-ray wavelength of 0.1 nm is adequate for the making of the master mask. A further improvement in x-ray lithography mask making is to fabricate intermediate and master mask on the same substrate, greatly reducing the risk for deviations in dimensions caused, for example, by temperature variations during printing.

2.4. Alignment of X- ray Mask to Substrate

The mask and resist-coated substrate must be properly registered to each other before they are put in an x-ray scanner. Alignment of an x-ray mask to the substrate is a problem, since no visible light can pass through most x-ray membranes. To solve this problem windows are etched in a titanium x-ray membrane. Diamond membranes have a potential advantage here, as they are optically transparent and enable easy alignment for multiple irradiations without a need for etched holes.

Figure 2.6 illustrates an alternative, x-ray alignment system involving capacitive pickup between conductive metal fingers on the mask and ridges on a small substrate area; Silicon in this case (U.S.

Patent 4,607,213 [Registered in 1986] and 4,654,581 [Registered in 1987]). When using multiple groups of ridges and fingers, two axis lateral and rotational alignment become possible.

Another alternative may involve liquid nitrogen-cooled Si (Li) x-ray diodes as alignment detectors, eliminating the need for observation with visible light. A procedure has been developed to eliminate the need for an x-ray mask membrane. Unlike conventional masks, the so-called x-ray transfer mask does not treat a mask as an independent unit. The technique is based on forming an absorber pattern directly on the resist surface forming a conformal, self-aligned, or transfer mask. An example process is shown in Fig. 2.7. In this sequence, a transfer mask plating base is first prepared on the PMMA substrate plate by evaporating 0.7 nm of chromium (as adhesion layer) followed by 50 nm of gold using an electron beam evaporator.

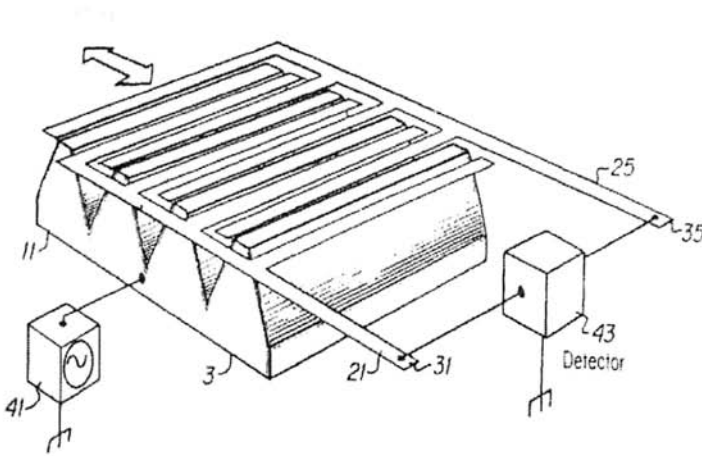


Fig. 2.6. Mask alignment system in x-ray lithography. Invention described by U.S. Patents 4,654,581 (Registered in 1987) and 4,607,213 (Registered in 1986)

A 3 μm thick layer of standard Novolak-based resist is then applied over the plating base and exposed in contact mode through an optical mask using an ultraviolet exposure station. Three microme-

ters of electroplated gold on the exposed plating base further completes the transfer mask.

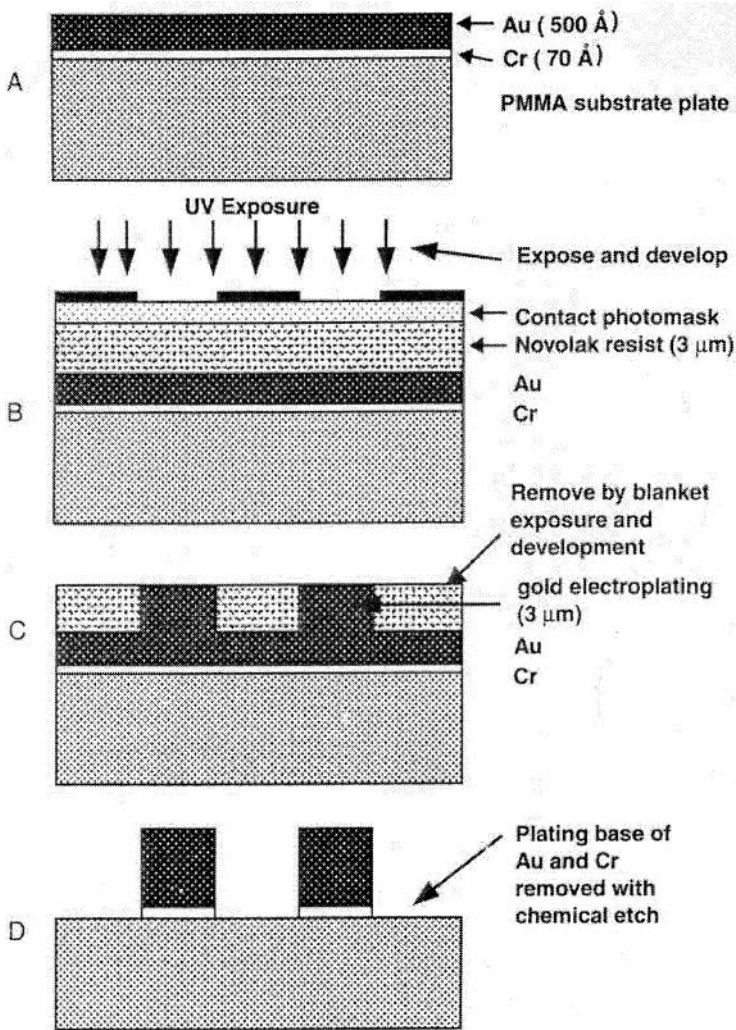


Fig. 2.7. Sample transfer mask formation. (From M. Madou, 'Fundamentals of Microfabrication', 2nd edition, 2002, CRC Press [7])

A blanket exposure and subsequent development remove the remaining resist. The 50 nm of Au plating base is dissolved by a dip of 20 to 30 s in a solution of potassium iodide (5%) and iodine (1.25%) in water; the Cr adhesion layer is removed by a standard chromium etch.

Fabrication of the transfer mask can thus be performed using standard lithography equipment available at almost any lithography shop. Depending on the resolution required, the x-ray transfer mask can be fabricated using known photon, electron beam, or x-ray lithography techniques. The patterning of the PMMA resist with a self-aligned mask is accomplished in multiple steps of exposure and development.

An example of a cylindrical resonator made this way is shown in Fig. 2.8. Each exposure/development step involves an exposure dose of about 8 to 12 J/cm². Subsequent 5-min development steps remove ~30 μ m of PMMA. In seven steps, a self-supporting 1.5 mm thick PMMA resist is patterned to a depth of more than 200 μ m. The resist pattern shown in Fig. 2.8 is 230 μ m thick and exhibits a 2 μ m gap between the inner cylinder and the pickup electrodes (aspect ratio is 100:1). The resonator pattern was produced using soft (1 nm length) x-rays and a 3 μ m thick Au absorber only.

Forming of the transfer mask directly on the sample surface creates several additional new opportunities; besides *in situ* development, etching, and deposition, these include exposure of samples with curved surfaces and dynamic deformation of a sample surface during the exposure (hemispherical structures for lenses are possible this way). The authors summarize the advantages of the transfer mask method as follows:

- Alleviates the difficulty in fabricating fragile mask membranes;
- Avoids alignment requirements during successive exposure steps;
- Reduces exposure time and absorber thickness for the same exposure source;
- Enhances pattern transfer fidelity, since there is almost no proximity gap;

- Avoids thermal deformation caused by exposure heat;
- Increases photoresist development rate by step-wise elevated exposure dose.

2.4.9 Choice of Resist Substrate

In the x- ray lithography process, the primary substrate, or base plate, must be a conductor or an insulator coated with a conductive top layer. A conductor is required for subsequent electrodeposition. Some examples of primary substrates that have been used successfully are Al, austenite steel plate, Si wafers with a thin Ti or Ag/Cr top layer, and copper plated with gold, titanium, or nickel.

Other metal substrates as well as metal-plated ceramic, plastic, and glass plates have been employed. It is important that the plating base provide good adhesion for the resist. For that purpose, prior to applying the x- ray resist on copper or steel, the surface sometimes is mechanically roughened by micro grinding with corundum or other abrasive media.

During chemical preconditioning, a titanium layer, sputter-deposited onto the polished metal base plate (e.g., a Cu plate), is oxidized for a few minutes in a solution of 0.5 M NaOH and 0.2 M H₂O₂ at 65 °C. The oxide produced typically measures 30 nm thick and exhibits a micro rough surface instrumental to securing resist to the base plate. The Ti adhesion layer may further be covered with a thin nickel seed layer (~15 nm) for electroless or electroplating of nickel. When using a highly polished Si surface, adhesion promoters need to be added to the resist. A substrate of special interest is a processed silicon wafer with integrated circuits. Integrating the x- ray lithography process with semiconductor circuitry on the same wafer will create additional x- ray lithographic applications. The rear surface of electrodeposited micro devices is attached to the primary substrate but can be removed from the substrate if required. In the latter case, the substrate may be treated chemically, or electro-chemically, to intentionally induce poor adhesion. Ideally, excellent adhesion exists between substrate and resist, and poor adhesion exists between the electroplated structure and the plating base. Achieving these two contradictory demands is one of the main challenges in x- ray lithography.

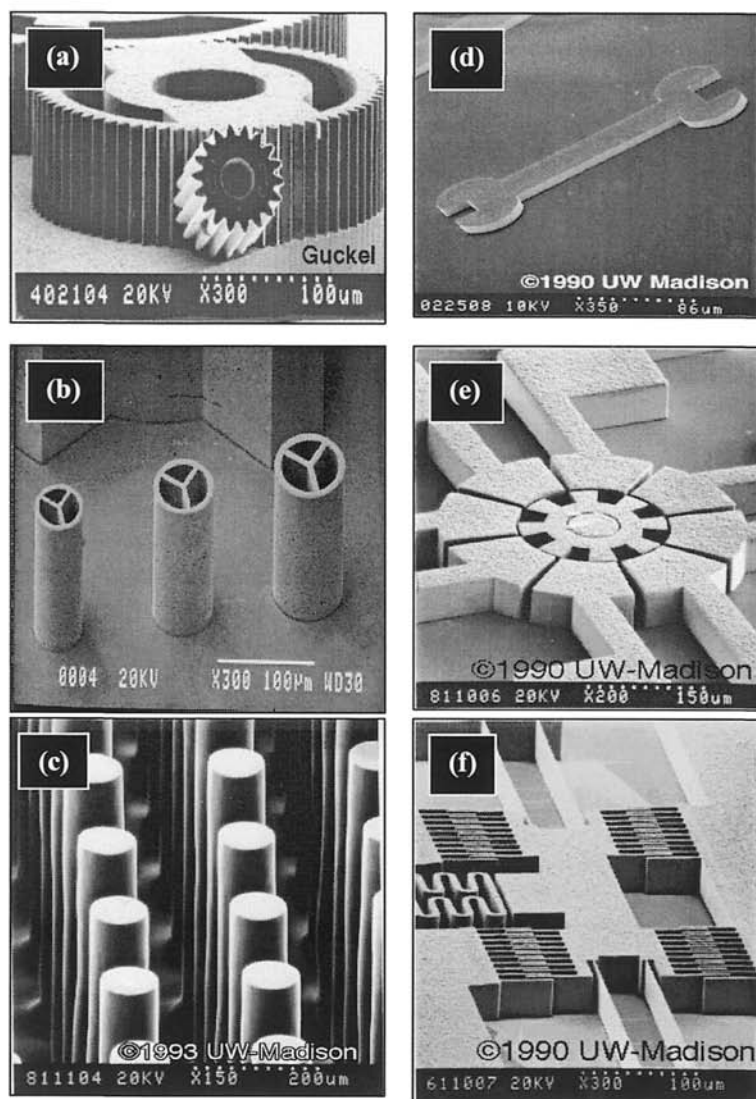


Fig. 2.8. SEM micrographs of microstructures made by the transfer mask method and multiple exposure/development steps: (a) gear and mechanism; (b) hollow pillars; (c) high aspect ratio pillars; (d) wrench; (e) metering device; and (f) comb drive (Courtesy of the University of Wisconsin at Madison)

2.4.10 Resist Requirements

An x- ray resist ideally should have high sensitivity to x- rays, high resolution, resistance to dry and wet etching, thermal stability of greater than 140 °C, and a matrix or resin absorption of less than $0.35 \mu\text{m}^{-1}$ at the wavelength of interest. These requirements are only those for semiconductor production with x- ray lithography. To produce high-aspect-ratio microstructures with high lateral tolerances an additional set of requirements is required. The unexposed resist must be absolutely insoluble during development. This means that a high contrast (γ) is required. The resist must also exhibit very good adhesion to the substrate and be compatible with the electro-forming process. The latter imposes a resist glass transition temperature (T_g) greater than the temperature of the electrolyte bath used to electrodeposit metals between the resist features remaining after development (say, at 60 °C). To avoid mechanical damage to the microstructures induced by stress during development, the resist layers should exhibit low internal stresses. If the resist structure is the end product of the fabrication process, further specifications depend on the application itself, for example, optical transparency and refractive index for optical components or large mechanical yield strength for load-bearing applications. Owing to excellent contrast and good process stability known from electron beam lithography, PMMA is the preferred resist for deep-etch synchrotron radiation lithography. Two major concerns with PMMA as the x- ray lithography resist are a rather low lithographic sensitivity of about 2 J/cm^2 at a wavelength λ_c of 0.84 nm and a susceptibility to stress cracking. For example, even at shorter wavelengths, $\lambda_c = 0.5 \text{ nm}$, over 90 min of irradiation are required to structure a $500 \mu\text{m}$ thick resist layer with an average ring storage current of 40 mA and a power consumption of 2 MW at the 2.3-GeV ELSA synchrotron. The internal stress arising from the combination of a polymer and a metallic substrate can cause cracking in the microstructures during development, a phenomenon PMMA is especially prone to. X- ray resists explored for lithographic applications include poly(lactides), for example, poly(lactide-co-glycolide) (PLG); polymethacrylimide (PMI); polyoxymethylene (POM); and polyalkensulfone (PAS). PLG is a new positive resist that is more sensitive to x- rays by a

factor of 2 to 3 compared with PMMA. From the comparison of different resists for deep x- ray lithography in Table 2.4, PLG emerges as the most promising x- ray lithography resist. POM, a promising mechanical material, may also be suited for medical applications given its biocompatibility. All of the resists shown in Table 2.6 exhibit significantly enhanced sensitivity compared to PMMA, and most exhibit reduced stress corrosion. Negative x- ray resists have inherently higher sensitivities compared to positive x- ray resists, although their resolution is limited by swelling. Poly(glycidyl methacrylate-co-ethyl acrylate) (PGMA), a negative electron beam resist has also been used in x- ray lithography. In general, resist materials sensitive to electron beam exposure also display sensitivity to x- rays and function in the same fashion; materials positive in tone for electron beam radiation typically are also positive in tone for x- ray radiation. A strong correlation exists between the resist sensitivities observed with these two radiation sources, suggesting that the reaction mechanisms might be similar for both types of irradiation. More common x- ray resists from the semiconductor industry are reviewed in Table 2.5.

Table 2.4. Properties of resists for deep x- ray lithography

Feature	PMMA	POM	PAS	PMI	PLG
Sensitivity	-	+	++	0	0
Resolution	++	0	--	+	++
Sidewall smoothness	++	--	--	+	++
Stress corrosion	-	++	+	-	+
Adhesion on substrate	+	+	+	-	+

Note: PMMA = poly(methylmethacrylate), POM = polyoxymethylene, PAS = Polyalkensulfone, PMI = polymethacrylimide, PLG = poly(lactide-co-glycolide). ++ = excellent; + = good; 0 = reasonable; - = bad; -- = very bad.

2.5 Methods of Resist Application

2.5.1 Multiple Spin Coats

Different methods to apply ultra thick layers of PMMA have been studied. In the case of multi-layer spin coating, high interfacial stresses between the layers can lead to extensive crack propagation upon developing the exposed resist.

Table 2.5. Resist materials used for electron beam and x- ray lithography processes.

Novolak- based resist	EBL sensitivity ($\mu\text{C}/\text{cm}^2$)	EBL contrast	XRL sensitivity (mJ/cm^2)	XRL contrast
PMMA	100	2.0	6500	2.0
PBS	1	2.0	170	1.3
EBR-9	1.2	3.0		
Ray-PF			125	*
COP	0.5	0.8	100	1.1
GMCIA	7.0	1.7		
DCOPA			14	1.0
Novolak based	200-500	2-3	750-2000	~

*Indicates that the value is process dependent.

2.5.2 Commercial PMMA Sheets

High molecular weight PMMA is commercially available as pre-fabricated plate and several groups have employed freestanding or bonded PMMA resist sheets for producing x-ray lithography structures. After overcoming the initial problems encountered when attempting to glue PMMA foils to a metallic base plate with adhesives, this has become the preferred method in several laboratories.

2.5.3 Casting of PMMA

PMMA also can be purchased in the form of a casting resin. In a typical procedure, PMMA is *in situ* polymerized from a solution of 35 wt% PMMA of a mean molecular weight of anywhere from 100,000 g/mol up to 10^6 g/mol in methylmethacrylate (MMA). Polymerization at room temperature takes place with benzoyl peroxide (BPO) catalyst as the hardener (radical builder) and dimethylaniline (DMA) as the initiator. The oxygen content in the resin, inhibiting polymerization, and gas bubbles, inducing mechanical defects, are reduced by degassing while mixing the components in a vacuum chamber at room temperature and at a pressure of 100 mbar for 2 to 3 min. In a practical application, resin is dispensed on a base plate provided with shims to define pattern and thickness and subsequently covered with a glass plate to avoid oxygen absorption.

2.5.4 Resist Adhesion

Smooth surfaces such as Si wafers with an average roughness, R_a , smaller than 20 nm pose additional adhesion challenges that are often solved by modifying the resist itself. To promote adhesion of resist to polished untreated surfaces, such as a metal-coated Si wafers, coupling agents must be used to chemically attach the resist to the substrate. An example of such a coupling agent is methacryloxypropyl trimethoxy silane (MEMO). With 1 wt% of MEMO added to the casting resin, excellent adhesion results. The adherence is brought about by a siloxane bond between the silane and the hydrolyzed oxide layer of the metal. The integration of this coupling agent in the polymer matrix is achieved via the double bond of the

methacryl group of MEMO. Hydroxyethyl methacrylate (HEMA) can improve PMMA adhesion to smooth surfaces, but higher concentrations are needed to obtain the same adhesion improvement. Silanization of polished surfaces prior to PMMA casting, instead of adding adhesion promoters to the resin, did not seem to improve the PMMA adhesion. In the case of PMMA sheets, as mentioned before, one option is solvent bonding of the layers to a substrate. In another approach, Galhotra et al. [40] mechanically clamped the exposed and developed self-supporting PMMA sheet onto a 1.0 mm thick Ni sheet for subsequent Ni plating.

2.5.5 Stress-Induced Cracks in PMMA

The internal stress arising from the combination of a polymer on a metallic substrate can cause cracking in the microstructures during development. To reduce the number of stress-induced cracks, both the PMMA resist and the development process must be optimized. Detailed measurements of the heat of reaction, the thermomechanical properties, the residual monomer content, and the molecular weight distribution during polymerization and soft baking have shown the necessity to produce resist layers with a high molecular weight and with only a very small residual monomer content.

2.6. Exposure

2.6.1 Optimal Wavelength

For a given polymer, the lateral dimension variation in a x- ray lithography microstructure could, in principle, result from the combined influence of several mechanisms. These include Fresnel diffraction, the range of high-energy photoelectrons generated by the x-rays, the finite divergence of synchrotron radiation, and the time evolution of the resist profiles during the development process. The theoretical results demonstrate that the effect of Fresnel diffraction (edge diffraction), which increases as the wavelength increases, and the effect of secondary electrons in PMMA, which increases as the

wavelength decreases, lead to minimal structural deviations when the characteristic wavelength ranges between 0.2 and 0.3 nm (assuming an ideal development process and no x-ray divergence). To fully utilize the accuracy potential of a 0.2 to 0.3 nm wavelength, the local divergence of the synchrotron radiation at the sample site should be less than 0.1 mrad. Under these conditions, the variation in critical lateral dimensions likely to occur between the ends of a 500 μm high structure due to diffraction and secondary electrons is estimated to be 0.2 μm . The estimated Fresnel diffraction and secondary electron scattering effects are shown as a function of characteristic wavelength in Fig. 2.9.

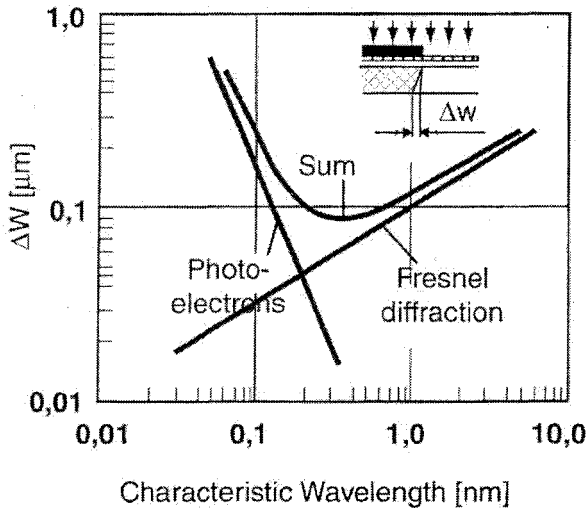


Fig. 2.9. Fresnel diffraction and photoelectron generation as a function of characteristic wavelength, λ_c , and the resulting lateral dimension variation (ΔW). (From W. Menz and P. Bley, "Microsystems for Engineers", VCH Publishers, Germany, 1993)

Using cross-linked PMMA, or linear PMMA with a unimodal and extremely high molecular weight distribution (peak molecular weight greater than 1,000,000 g/mol), the experimentally determined lateral tolerances on a test structure as shown in Fig. 2.10 are 55 nm

per 100 μm resist thickness, in good agreement with the 0.2 μm over 500 μm expected on a theoretical basis. These results are obtained only when a resist/developer system with a ratio of the dissolution rates in the exposed and unexposed areas of approximately 1000 is used. The use of resist layers, not cross-linked and displaying a relatively low bimodal molecular weight distribution, as well as the application of excessively strong solvents such as used to develop thin PMMA resist layers in the semiconductor industry, lead to more pronounced conical shape in the test structure of Fig. 2.10. An illustration of the effect of molecular weight distribution on lateral geometric tolerances is that linear PMMA with a peak molecular weight below 300,000 g/mol shows structure tolerances of up to 0.15 $\mu\text{m}/100 \mu\text{m}$. To obtain the best tolerances requires a PMMA with a very high molecular weight, also a pre-requisite for low stress in the developed resist. Finally, if the synchrotron beam is not parallel to the absorber wall but at an angle greater than 50 mrad, greater angles may result.

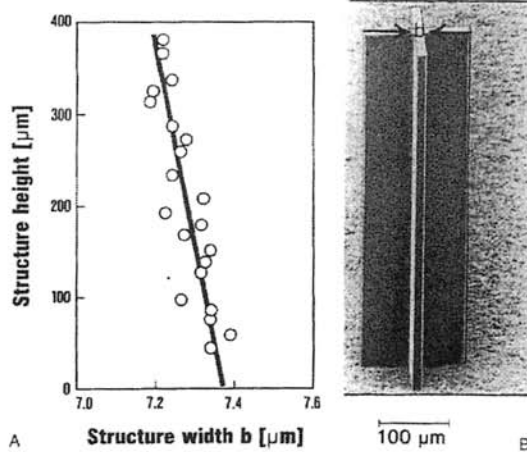


Fig. 2.10. Structural tolerances. (A) SEM micrograph of a test structure to determine conical shape. (B) Structural dimensions as a function of structure height. The tolerances of the dimensions are within 0.2 μm over the total structure height of 400 μm (From J. Mohr, W. Ehrfeld, and D. Munchmeyer, in *J. Vac. Sci. Technol.*, Volume B6, 1988, p.p. 2264-2267)

2.6.2 Deposited Dose

The x-ray irradiation of PMMA reduces the average molecular weight. For one-component positive resists, this lowering of the average molecular weight causes the solubility of the resist in the developer to increase dramatically. The average molecular weight making dissolution possible is a sensitive function of the type of developer used and the development temperature. The molecular weight distribution, measured after resist exposure, is unimodal with peak molecular weights ranging from 3000 g/mol to 18,000 g/mol, dependent on the dose deposited during irradiation.

The peak molecular weight increases nearly linearly with increasing resist depth; that is, decrease of the absorbed dose. Fig. 2.11A illustrates a typical bimodal molecular weight distribution of PMMA before radiation, exhibiting an average molecular weight of 600,000. The gray region in this figure indicates the molecular weight region where PMMA readily dissolves; that is, below the 20,000 g/mol level for the temperature and developer used.

Since the fraction of PMMA with a 20,000 molecular weight is very small in non-irradiated PMMA, the developer hardly attacks the resist at all. After irradiation with a dose D_{dv} of 4 kJ/cm³, the average molecular weight becomes low enough to dissolve almost all of the resist (Fig. 2.11B). With a dose D_{dm} of 20 kJ/cm³, all of the PMMA dissolves swiftly (Fig. 2.11C). At a dose above D_{dm} , the microstructures are destroyed by the formation of bubbles. It follows that to dissolve PMMA completely and to make defect-free microstructures, the radiation dose for the specific type of PMMA used must lie between 4 and 20 kJ/cm³.

These two numbers also lock in a maximum value of 5 for the ratio of the radiation dose at the top and bottom of a PMMA structure. To make this ratio as small as possible, the soft portion of the synchrotron radiation spectrum is usually filtered out by a pre-absorber (for example, a 100 μ m thick polyimide foil [Kapton]) to reduce differences in dose deposition in the resist.

2.6.3 Stepped and Slanted Microstructures

For many applications, stepped or inclined resist sidewalls are very useful – consider, for instance, the fabrication of multi-level devices or prisms or, more basic yet, angled resist walls to facilitate the release of molded parts. Using stepped absorber layers on a single mask to make stepped multilevel microstructures is not always very well resolved.

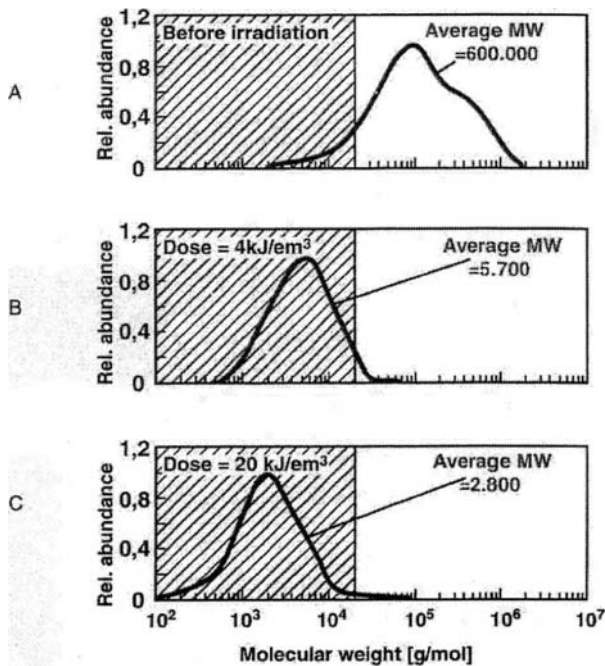


Fig. 2.11. Molecular weight distribution of PMMA before (A) and after irradiation with 4 (B) to 20 kJ/cm³ (C). The shaded areas indicate the domain in which PMMA is minimally 50% dissolved (From W. Menz and P. Bley, “Microsystems for Engineers”, VCH Publishers, Germany, 1993)

To make better-resolved stepped features, one can first relief print a PMMA layer, for example, by using a Ni mold insert made

from a first x- ray mask. Subsequently, the relief structure may be exposed to synchrotron radiation to further pattern the polymer layer through a precisely adjusted second x- ray mask. To carry out this process, a two-layer resist system needs to be developed consisting of a top PMMA layer that fulfills the requirement of the relief printing process, and a bottom layer that fulfills the requirements for x- ray lithography. The bottom resist layer promotes high molecular weight and adhesion, while the top PMMA layer is of lower molecular weight and contains an internal mold-release agent. This process sequence, combining plastic impression molding with x- ray lithography, is illustrated in Fig. 2.12. The two-step resist then facilitates the fabrication of a mold insert by electroforming, which can be used for the molding of two-step plastic structures. Extremely large structural heights can be obtained from the additive nature of the individual microstructure levels. There are several options for achieving miniaturized features with slanted walls. It is possible to modulate the exposure/development times of the resist, fabricate an inclined absorber, angle the radiation, or, move the mask during exposure in so-called moving mask deep x- ray lithography.

To make a slanted absorber, a slab of material can be etched into a wedge by pulling it at a linear rate out of an etchant bath. Changing the angle at which synchrotron radiation is incident upon the resist, usually 90 degrees, also enables the fabrication of microstructures with inclined sidewalls. This way, slanted microstructures may be produced by a single oblique irradiation or by a swivel irradiation. One potentially very important application of microstructures incorporating inclined sidewalls is the vertical coupling of light into waveguide structures using a 45 degree prism. Such optical devices must have a wall roughness of less than 50 nm, making x- ray lithography a preferred technique for this application. The sharp decrease of the dose in the resist underneath the edge of the inclined absorber, and the resulting sharp decrease of the dissolution of the resist as a function of the molecular weight in the developer, results in little or no deviation of the inclination of the resist sidewall over the total height of the microstructure.

2.6.4 Master Micromold Fabrication Methods

The high cost of x- ray lithography has required that engineers search for alternative means of fabricating high-aspect ratio metal or polymer micromasters. Micromold inserts (or micromasters) can be fabricated by a variety of alternate techniques such as CNC machining, silicon wet bulk micromachining, precision EDM, thick deep UV resists, DRIE, excimer layer ablation, and electron beam writing. In Table 2.6, x- ray lithography metal molds are compared with metal masters fabricated by other means.

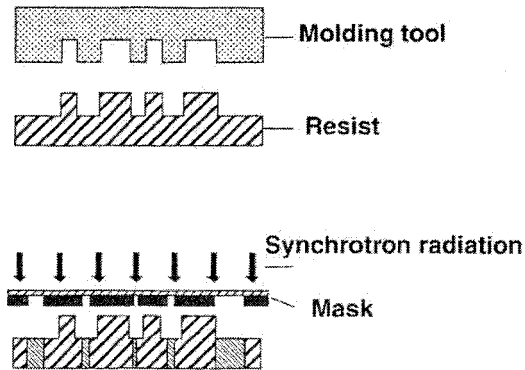


Fig. 2.12. Stepped microstructures made in the x- ray lithography process (From W. Menz and P. Bley, "Microsystems for Engineers", VCH Publishers, Germany, 1993)

For example, comparing metal mold inserts made by spark erosive cutting and x- ray lithography, the latter proves far superior. X- ray lithographic PMMA features as small as $0.1 \mu\text{m}$ are replicated in the metal shape with almost no defects. The electroformed structures have a superior surface quality with a surface roughness, R_a , of less than $0.02 \mu\text{m}$.

DRIE and thick deep UV-sensitive resists such as polyimides, are recent contenders for micromaster mold fabrication. With respect to dry etching, higher and higher aspect ratio features are being achieved, especially when using highly anisotropic etching conditions as in cryogenic DRIE. Wall roughness, causing form locking,

remains a problem with DRIE; the dry etching process was optimized for speed, not for demolding. For small-quantity production, where the lifetime of mold inserts is not crucial, a silicon wafer etched by DRIE can be utilized directly as a mold insert for anywhere from 5 to 30 molding cycles.

For longer-lasting molds, metallizing the Si structure and using the metal as the mold is preferred. Photoresist structures on a silicon substrate have also been tested as a mold insert in plastic molding because of the simplicity and low cost of the process. In low-pressure molding processes, such mold inserts do work for a limited number of production processes (applying a thin metal layer over the top of the resist may further extend the lifetime of the mold), but their applicability in high-pressure processes needs to be further verified.

Table 2.6. Comparison of micromolds manufactured using a variety of techniques.

Parameter	Laser	CNC machining	Electro discharge machining	X-ray lithography	Deep ultra violet	Deep reactive ion etching
Aspect Ratio	<10	14	<100	100	22	10-25
Roughness	100nm - 1 μ m	3-5 μ m	0.3 - 1 μ m	<20 nm	1 μ m	2 μ m
Accuracy	3-5 μ m	3-5 μ m	1-3 μ m	<1 μ m	2-3 μ m	<1 μ m
Maximum Height	300 μ m	Unlimited	3-5 mm	<10mm	300 μ m	300 μ m
Mask Required?	No	No	No	Yes	Yes	Yes

Both DUV and DRIE are more accessible than x-ray lithography and will continue to improve, taking more opportunities away from x-ray lithography. Like x-ray lithography, both alternative techniques can be coupled with plating, but neither technique can yet achieve the extreme low surface roughness and vertical walls of x-

ray lithography. Other competing technologies for making metal masters are laser ablation methods and ultra-precision CNC machining. The latter three methods are serial processes and rather slow, but since we are considering the production of a master only, these technologies might well be competitive for certain applications.

Laser microablation produces minimum features of about 10 μm width and aspect ratios of 1:10. Challenges include taper and surface finish control. Recast layers around the laser-drilled features cause form locking and infidelity in the replication. Femtosecond pulse layers promise thinner or even the absence of recast layers and excellent resolution. For large features ($>50\ \mu\text{m}$) with tolerances and repeatability in the range of about 10 μm , traditional CNC-machining of materials like tool steel and stainless steel is often accurate enough for making metal mold inserts. The advantage of this technique is that the tool materials used are the same as those in conventional polymer molding, so their design, strength, and service life are well established. Complicated 3D structures can also be machined easily. The main disadvantages are that it is difficult to make sharp corners or right angles, and the surface quality is usually poor (surface roughness is around several micrometers). In contrast, lithographic methods can produce molds with excellent surface quality (surface quality $< 0.1\ \mu\text{m}$) and sharp corners or right angles. However, they cannot be used on conventional tool materials such as steel. Diamond-based micromilling and microdrilling reduce the surface roughness to 1 μm or less. While diamond-based methods can achieve features smaller than 10 μm , they are applicable only to “soft” metals such as nickel, aluminum, and copper.

As shown in Table 2.6, a significant potential application of x-ray lithography remains the fabrication of those metal molds that cannot be accomplished with other techniques because of the tight wall roughness tolerances, small size, and high aspect ratios. From the table, it is obvious that x-ray lithography micromolds are extremely well suited at very low surface roughness levels and in terms of accuracy.

Summarizing, the requirements for an optimal mold insert fabrication technique are as follows:

- The master has to be removed from the molded structure, so the ease of release through wall inclination control is crucial;
- The most important parameters, including master life and achievable aspect ratios, depend very strongly on the surface quality of the master;
- The interface chemistry between master and polymer is a critical factor and must be controlled.

2.6.5 Future Directions

The full potential of microfabrication using x- ray lithography and the LIGA technique has yet to be realized. Advances in process technology, a greater understanding of the physics of x- ray interactions in resist materials and the availability of more intense, higher energy beams from synchrotrons provide some solutions to earlier problems and new opportunities for industrial and commercial exploitation. The future value of the technique resides in its ability to mass-produce at low cost, precision microcomponents that cannot be made using other processes. This requires design rules and agreed standards in processing and manufacturing.

Most of the technical and process knowledge exists in research centers that have links or access to synchrotron sources. The limitation in the range of materials that can be electroformed preclude many application areas. This is, however, offset by the growth in polymer and ceramic components required in almost all sectors of industry and, in particular, medical diagnostics, chemical analysis, environmental sensors, optical displays, and communications. The technology fits into the tool-making industry as basically precision molds and parts are used in the production process. The tool-making industry has an annual turnover of \$90 billion, and with a rapid growth rate predicted over the next 5 years it provides an ideal market sector for the technology.

Unfortunately there has been very little technology transfer into industry with only a few spin-off companies providing services and a limited number of products. In common with many non-IC-based

technologies, industry has not been convinced that LIGA has reached a level of maturity and a potential to mass-produce components that are free of defects and have total reliability. The high cost and accessibility to synchrotrons, the only suitable source of x- rays, is one of the barriers to wider use of the technique. Germany saw future opportunities and in 1997 built and opened ANKA, 2.5 GeV Synchrotron facility with three dedicated lithography beam lines. It provides, through a marketing subsidiary ANKA GmbH, a full range of analytical and manufacturing services on a commercial basis.

Many countries in the Asia-Pacific rim are now looking at non-silicon-based microfabrication technologies and have large growing markets for products. China, Taiwan, Korea, Singapore, have synchrotrons and microfabrication manufacturing facilities. They all are members of the global MEMS community and are adding to the research and development targeted toward the realization of commercial products. It is therefore likely that many of the problems mentioned above will be solved in the foreseeable future.

The recent establishment of an international LIGA Interest Group to bring together groups around the world and to act as a driver for commercialization is supported by Germany's FZK and the Sandia National Laboratories at Livermore, and the Center for Advanced Microstructures and Devices (CAMD) at the Louisiana State University at Baton Rouge, in the United States. This is a step towards making sure that all the work that has been carried out during the last sixteen years will be directed towards providing useful products.

2.7 Problems

1. What is x- ray lithography?
2. Explain the principles associated with synchrotron radiation.
3. Explain how synchrotron radiation is used to manufacture micro components and systems.
4. Describe the spectral characteristics of deep x- ray lithography.
5. Describe the LiGA process.

6. What are x- ray masks?
7. Compare masks used in x- ray lithography and the semi-conductors industry.
8. Describe the materials used for masks.
9. Explain how masks are made for use when machining high aspect ratio microlithographic components.
10. How do you choose a suitable resist for the substrate material?
11. What are the requirements of a resist material?
12. Explain how resists are applied to substrates.
13. Explain the many ways to manufacture master molds.
14. Show how gears, mechanisms, metering devices, and comb drives are produced using deep x- ray lithography.

References

1. Ehrfeld W, Becker EW, Hagmann P, Maner P and Munchmeyer P, *Microelectron. Engin.*, 1986, **4**, pp 35-56.
2. Bacher W et al., *IEE Transac. Industrial Electron*, **42** (5), 1995.
3. Hruby, J (Ed), Goetttert, J. *Proceedings HARMST 2003*, Monterey, June 2003.
4. Tolfree DWL, *Proceedings of COMS2003*, Amsterdam, Netherlands, Sept 2003.
5. Goetttert, J., *Proceedings of COMS2004*, Edmonton, Canada, Sept 2004.
6. NEXUS 'Market Analysis for Microsystems 2000-2005, Feb 2002.
7. Madou M, 'Fundamentals of Microfabrication', 2nd Edition, 2002, CRC Press).
8. Tolfree DWL, *Microfabrication using Synchrotron Radiation*, *Progress Reports in Physics*, **61**, 4, 1998.
9. Cerrina F, *Handbook on Lithography*, SPIE edition, 1996
10. Becker E, Betz H, Ehrfeld W, Glashauser W, Michael H, Munchmeyer D, Pongratz S and Von Siemens R, 1982, *Naturwissenschaften*, **69**, 520-523.
11. Ehrfeld W, Becker E W, Hagmann P, Maner P and Munchmeyer P, *Microelectron. Engin.*, 1986, **4**, 35-56.
12. Ehrfeld W, Bley P, Gotz F, Hagmann P, Mane A, Mohr J and Herbert O, 1987, *Proc IEEE Micro robots and Teleoperators Workshop (Fabrication of Microstructures using the LIGA process)*, **87**, 1-11.

13. Ehrfeld W, Bley P, Gotz J, Munchmeyer D, Mohr J, Schulb W, 1988, *J Vac. Sci.* **B6**.
14. Ehrfeld W and Lehr H, 1994, *Journal de Physique*, **4**, p C9-229-236.
15. Ehrfeld W and Lehr H, 1995, *Rad. Phys & Chem.*, **45**, pp 349-365.
16. Bley P, Gottert, Haemening M, Himmelhaus M, Menz W, Mohr J, Muller C and Wallrabe U, 1991, *Microsystem Technologies 1991* (ed H Reichl), 302-314, Heidelberg, Springer-Verlag.
17. Bley P, 1993, *Interdisciplinary Science Reviews*, **18**, 3, p. 267.
18. Harmening M, Bacher W, Bley P, El-Kholi, Kalb H, Kowanz, Menz, Michel A and Mohr J., 1992, *MEMS*, No. 0-7803-0497-7/92. 202-207, New York IEEE.
19. Tolfree D and Ehrfeld W, 1994, *Proc. Tech. Trans.Conf.*, Published by TCD.
20. Bacher W, Menz W and Mohr J, 1995, *IEE Trans. on Industrial Elect.* Vol. 42.
21. Guckel H, Skrobis K, Christenson T, Klein J, Han, Choi B, Loverell E and Chapman T, 1991, *Proc. Transducers (San Francisco)* (New York : IEEE).
22. Guckel H, 1993, N. I. M. in *Physics Res*, Section B, **B79**, 1-4, pp 247-8.
23. Guckel H, Skrobis K, Christenson T and Klein J, 1994, *SPIE's Symposium on Microlithography*, p.p. 2194-09.
24. Guckel H and Christenson T R, 1995, *SPIE Meeting*, Oct. 1995, Austin, Texas.
25. Tombouliau DH and Hatman, 1956, *Phys. Rev.* **102**, 1423-47.
26. Sokolov AA and Ternov IM, 1957, *Sov. Phys., JETP*, **4**, 396-400.
27. Sokolov AA and Ternov IM, 1968, *Synchrotron Radiation*, (Berlin : Akademie- Verlag).
28. Godwin RP 1969, *Synchrotron Radiation as a Light Source*, (Springer Tracts in Modern Physics 51, ed. J. Hohler.
29. Rowe EM, 1979, *Synchrotron Radiation* (topics in Current Physics 10), ed. C. Kunz, (Berlin Springer), pp 25-54.
30. Winick H, 1980, *Synchrotron Radiation Research*, ed. Winick and Doniach (New York: Plenum), p.p. 11-60.
31. Grobman W, 1985, *Synchrotron Radiation Research*, Winick H ed. Pergamon, N.Y.
32. Ternov IM, Mikhailin VV and Khalilov VR, 1985, *Synchrotron Radiation and its Applications* (New York: Harwood).
33. Marks N, 1995, *Radiat. Phys. Chem.*, **45**, 3, pp 315-331.

34. Turner S, 1989, Synchrotron Radiation and Free Electron Lasers, CERN Acc. School, Chester, Cern 90-30.
35. Krinsky S, Perlman M L and Watson R E, 1993, Handbook on Synchrotron Radiation, E Koch ed., North Holland, pp. 65-172.
36. Tombouliau D H and Hatman, 1956, Phys. Rev., **102**, 1423-47.
37. Timothy JG and Madden R P, 1983, Handbook on Synchrotron Radiation, Vol 1A, editor E E Koch (Amersterdam: North-Holland), pp325-66.
38. Elleaume P, 1990, Phys. Scripta, **T31**, 67-71.
39. Yamamoto S, Shio T, Sasaki S and Kitamura H, 1989, Rev Sci. Instrum., **60**, 1834-7.
40. Galhotra V, Marques C, Desta Y, Kelly K, Despa M, Pendse A, and Collier A., in Proceedings of the SPIE: Micromachining and Microfabrication Process Technology II, Austin, TX, 1996, p.p. 168-173.

3. Manufacturing High Aspect Ratio Microstructures

3.1 Introduction

Creating micro- and nanoscale structures in silicon is important for the semiconductor industry, which is worth billions of dollars each year. Geometrical specifications are so stringent that manufacturing methods used to create these structures must be precise. Dry etching is a technique capable of removing small quantities of substrate at specific locations. When creating micro- and nanoscale features with high aspect ratios in silicon, processes such as etching are extremely slow. Therefore, a much faster technique is required not only to machine silicon, but also to machine engineering materials such as alloys of iron, aluminum, and copper. For these materials, mechanical micromachining is the appropriate process to use. In this chapter, the etching process is discussed and compared to mechanical micromachining for producing customized products in small lot sizes. In order to produce thousands and millions of micro- and nanostructured, masters are produced for the mass production of molds. The need for micromolding products with nanoscale features on the mass production scale is discussed in this chapter.

3.2 Dry Etching

The process works because highly reactive particles called radicals react with the substrate (in this case silicon), resulting in a new molecule that is energetically more favorable than the original bond; subsequently, the new molecule is removed from the surface and

etching is achieved. Radicals are isotropic in nature and etch in all directions; if a square-sided trench is needed vertical etching is required, whereas lateral etching is unwanted. To prevent lateral etching an inhibiting layer is used.

An inhibiting layer is created when the substrate reacts with the gas and forms a barrier so that radicals cannot penetrate; this protects the substrate from being etched. However, the substrate must be exposed to radicals if etching is to take place, therefore the inhibitor must be removed and this is achieved by ion bombardment. The ions have only enough energy to remove the inhibitor and do not interact with the substrate. Etching occurs in locations where ions remove the inhibitor, and because the direction and location of ions can be controlled, material removal is highly accurate. A mask blocks incoming ions from pre-determined areas to create the outline required. Owing to the fact that etch rates are known, specific depths at these locations can be achieved. This is how a three-dimensional structure is created from a two-dimensional silicon substrate.

An attractive characteristic of plasma etching is the ability to create high aspect ratio trenches, a necessary requirement for many micro-and nanoscale applications. For example a typical requirement for transistor trench isolation would be a 0.25 micron in width and 3 microns in depth. This condition often limits which process method can be used to create the structure, making dry plasma etching the choice for creating high aspect ratio structures.

3.3 Plasma Etching Processes

Dry plasma etching was initially used because it was highly selective and cleaner compared to competing technologies of the time, namely, wet etching, which requires additional post-processing steps. Selectivity is the ratio-of-etch rates between two materials, in this case the inhibitor and the substrate. A high selectivity number means that the difference in etch rates is greater, which leads to more accurate control over the minimum resolution and accuracy the

process can achieve. As demand grew for the production of smaller and smaller feature sizes, the requirements for etching substrates moved from isotropic to anisotropic; thus ion beam etching (IBE) was developed. IBE, however, had its own problems such as poor selectivity between mask and substrate leading to the production of components that did not meet specifications. Hence, chemical assisted ion beam etching (CAIBE) was developed to counteract this particular problem. The latest technique in the evolution of this process is called ion beam assisted radical etching (IBARE). This process has both high selectivity and high anisotropy, making it an ideal way of creating high aspect ratio trenches with parallel sides and square faces.

3.3.1 Ion Beam Assisted Radical Etching

In this process, the plasma is ignited by applying a radio frequency voltage between two electrodes in a dielectric gas. Electrons have enough energy to jump from their ground state and escape the atomic bond, making the atom ionized. This results in a large number of charged particles in the chamber, namely, free electrons and ions. The electrodes are positive (anode) and negative (cathode), so the electrons (negatively charged) migrate rapidly towards the anode and ions (positively charged) move towards the cathode. During these motions collisions with the gas occur generating neutrals, radicals, electrons, ions, and photons. Ions generated from the plasma are strongly attracted toward the cathode. They can travel with enough energy so that on impact with the cathode electrons from the surface of the electrode they are released; this is a secondary generation of free electrons. Subsequently, newly created free electrons are attracted toward the anode, as they pass through the chamber they collide with neutrals and other particles in the gas creating further ionization; thus secondary generation of free electrons and subsequent collisions sustain the plasma. Electrons usually acquire energies between 1eV and 10eV before colliding with other particles, which are dependent on the gas pressure of the system.

Electrons can be involved in collisions where they carry insufficient energy to cause ionization. The energy they have acquired is used up in collisions within the gas, specifically by making orbiting electrons jump energy shells. Because this energy is not enough to cause ionization the electron decays back to its original energy level prior to impact. Decay occurs because the electron cannot exist at its new orbit for long, and the extra energy is released in the form of a photon. Release of these photons is the source of the glow of the plasma; the color of the plasma depends on the type of atom and the magnitude of the decaying process.

3.4 Characteristics Of The Plasma

3.4.1 The Sheath Region

Above the cathode, the region is dense with electrons that have just been liberated. They have low energy and there are few gas particles available for collision. Hence, there is little opportunity for photon release. Therefore no light is being emitted from this region and it is known as dark space. Similarly the anode has many electrons around it and there are few chances for collision to cause light emission; and this region is also known as dark space. The width of the dark space depends on the chamber pressure; at low pressures the mean free path of the electrons increases and the width of the dark space increases. By controlling gas pressure within the chamber, the energy with which the ions strike the surface can be controlled.

Substrates are placed on the cathode to take advantage of the incident ions. These substrates can be insulating, ion bombardment ejects electrons and a charge builds up on the insulator to the point at which the plasma can no longer be sustained. Hence an alternating current at a radio frequency is used to drive and sustain the process. The reversal of current maintains a charge balance, but if one electrode is to be used then it must be energetically favored in some way. The potential difference between electrodes is important be-

cause this field accelerates ions providing them with more impact energy. If the electrodes have equal area then they have the same potential, increasing the area of one electrode changes the potential of that electrode and overall the potential difference is increased. If the area of the anode is increased, which is usually achieved by connecting the chamber walls to the anode, the potential is at a maximum thus favoring ion bombardment of the cathode.

3.4.2 Boundary Region

When moving from the plasma glow to the sheath there is a distinct dividing line called the boundary region, or boundary layer. It can be considered as a surface emitting particles from the plasma. Ions are directed by the field lines existing between the electrodes, this causes particles to leave the boundary layer perpendicular to the substrate. The ions can now be considered as a collimated stream of particles. As ions leave the boundary layer they pass through the sheath on their way to the substrate. The sheath region contains particles so that ion collisions are possible; if they occur it will cause ions to deflect and they will no longer travel perpendicular to the boundary layer or substrate. In addition, the collision has made ions lose energy and therefore reduced the effectiveness of impact when it reaches the cathode or substrate. These are two important effects known as the ion angular distribution function (IADF), which is a measure of how collimated the particles are before they reach the substrate, and the ion energy distribution function (IEDF), which is a measure of how much energy the ions have remaining. Radical collisions in this region are unimportant because their initial direction is isotropic so that further collisions producing random motions have no effect on the overall direction.

3.5 Etching of Microstructures

Etching can occur if a chemical reaction producing a gaseous, or high vapor liquid, or solid, is energetically favored. In other words,

if a reaction can lower the overall energy of the system, then it is possible for it to be energetically favorable to cause etching. In high-pressure plasma reactors etching of Silicon, Si, is achieved using Chlorine, C, and Fluorine F. After the reactions have taken place the system must be at a lower energy; this is achieved because the radicals (in this case F) are freely available and the bond energy between Si and F is less than the bonding energy between Si and Si. In other words it is energetically more favorable for the reaction to take place. The reaction produces a SiF molecule resulting in an overall net loss of Si; this is etching. A typical gas used would be CF₄, which will not etch silicon directly. F radicals are produced by ionization in the plasma. Other bonding groups in the system are Si₂, SiF₂, and SiF₄. The Si substrate surface is coated with F, a bulk Si atom is bonded to an Si surface atom which is itself bonded to two F atoms, making SiF₂. However, because it is bonded to the wafer it is not free to move. An incoming F atom can replace the Si-Si bond with SiF₂, because Si already shares another surface F. The SiF₂ then leaves the surface and a small portion of Si has been removed. Alternatively the incoming F atom could attach itself to SiF₂, embedded on the surface making SiF₃, subsequently another F will join the system producing SiF₄, which will then leave the surface.

In the case of reactive ion etching a physical process for modeling the etching mechanism has been proposed. Chlorine gas in the forms, Cl or Cl₂, can etch undoped silicon but only very slowly. N-type doped silicon is etched spontaneously by Cl, only. In the case of undoped silicon, chlorine atoms migrate toward the surface and chemisorbs. However, this does not break the Si-Si bond. Once a layer of chlorine builds on the surface further absorption is prevented by steric hindrance. After a short time this surface becomes negatively charged, in this case ionic bonding between the Si and Cl can occur. When this happens chemisorption sites are freed, thus increasing the chances that Cl atoms will penetrate the bulk and produce volatile SiCl. This process is dramatically enhanced by ion bombardment, so areas subjected to ion bombardment etch much faster than other regions and this produces anisotropic etch profiles. However, the more heavily doped the substrate the more pronounced the charging effect is. If reasonable etch rates are to be achieved then

high doping means that undercut of the sidewalls is increased and etching characteristics are no longer anisotropic.

3.5.1 Etching Phenomena

For IBARE techniques regardless of plasma chemistry, smaller width trenches are etched more slowly than wider trenches, the controlling factor being the aspect ratio of the trench rather than its depth or width. One method of reducing this effect is to change the geometry of the shape and control the aspect ratio.

3.5.2 Inhibitor Depletion in a Trench

In small trenches the supply of inhibitors is reduced partly due to the narrow opening. The resulting depletion of inhibitors can lead to a higher etch rate, and inverse reactive ion etching (RIE) lag should be the result (i.e., the smaller trench is etched more quickly due to radical ion etching lag).

3.5.3 Radical Depletion in a Trench

Radicals can etch a surface only if they are close by when it is exposed to ions. Radicals can arrive at this site either by gas transport or by surface flow. Radicals will attack any available site, in this case the whole surface. Therefore, surface transport is not possible because the path of each radical is blocked by its surrounding neighbors. If this is the case the only way for radicals to enter the trench is by transport in the bulk gas. This is called microloading; the etch rate decreases and is inversely proportional to the amount of substrate exposed to the plasma. Generally this effect is present when radical density is exposed to an unusually high substrate area, and gives rise to inverse RIE lag.

Now consider a masked wafer with a hole in the center. Surface transport is now possible because there is no surface silicon to consume the radicals. This is the so-called micro-loading effect, which

occurs when the reactant density is depleted as a result of an excessive substrate load. Etch rate will decrease inversely to the silicon area which is exposed to the plasma glow, giving inverse RIE lag. However, etch rate seems to be influenced by the geometry of the mask shape. For a long, small silicon structure etching is faster than the square of the same area. Hence, it is important to know the transport mechanism so that RIE lag can be predicted. It is therefore important to know how the radicals reach the trench because this determines whether there will be any RIE lag.

3.5.4 Volume Transport

The gas flow within the system is one of three types: viscous, molecular, or a combination of both called transitional. The Knudsen number is defined as the ratio of the mean free path of a molecule, λ , to a characteristic dimension, d , of the channel through which the gas is flowing. (a) *Viscous flow* – is characterized by a small Knudsen number (high pressure) because the high-pressure particle density is very high and particles are most likely to collide with each other rather than the wall. Therefore, most collisions in this flow type are intermolecular and characterize the gas as $\lambda/d < 0.01$. (b) *Molecular flow* – is characterized by large Knudsen numbers (low pressure) because particles are more likely to collide with the walls rather than each other because low pressure reduces the density. Upon collision with a wall the particle or molecule is often absorbed. After a short time the molecule desorbs from the wall in a random direction, these collisions characterize the nature of the gas. Molecular flow restrictions result from the geometry being $\lambda/d > 1$. (c) *Transitional flow* – characterized by median Knudsen numbers (mid-pressures). Collisions with the wall and molecules are equally as likely in this range. $0.01 < \lambda/d < 1$.

In a realistic situation where a substrate is covered by a mask it is possible for radicals to move on the mask; therefore surface geometry determines radical supply to the bottom of the trench. Ions in a trench can become depleted for a number of different reasons, the most important is ion deflection. There are different forces that contribute to the final force that is deflecting the ions. It is possible for

the mask to become charged and the charge established on this surface can deflect ions. Charged particles are attracted towards solid bodies with a force inversely proportional to the square of their distance. In the case where a particle enters a trench the particle is subjected to two forces, one from each wall. Any ions that are captured by the walls due to image forces are unable to assist in etching at the base of the trench. This effect is usually observed in small trenches and can be reduced by increasing ion velocity; this is because the ions have less time to become captured although that in turn can lead to increased sidewall etching (Fig. 3.1).

The forces between charged particles (known as Coulomb and Lorentz forces) are not considered to be significant because the chances of two ions existing in a trench together are small, however the significance increases as the density increases. Initially when the material is placed on the cathode the distance between the boundary layer and substrate is constant and the associated electric field is constant; therefore etching ions have equal properties along the substrate length. However, when trenches form the distance from the boundary layer to substrate changes locally, and in turn the electric field also changes. It becomes distorted by an amount related to the trench size. This is yet another cause of RIE lag, although insignificant at the microscale. In this case RIE lag is initiated by the distortion that intensifies the electric field around it. Therefore, a concentrated number of ions build up to attack the inhibitor. After a short time the charge builds up and incoming ions are repelled to the point where they spread out and widen the trench producing inverse RIE lag.

Not only is it possible for ions to be depleted by forces attracting them to sidewalls, it is possible accidental collisions with other ions in the plasma glow and plasma sheath region (ion dispersion) can send ions to the sidewalls causing ion depletion. Of course these collisions alter the ion energy as well. Finite element models have been constructed to simulate the etching process, thus reducing time spent on optimizing the process. The substrate is divided into elements and these elements are subjected to incident energies simulating ion impact. When the energy exceeds a certain level the element disappears, it is assumed that immediately after an ion has removed the inhibitor a radical etches the substrate. It is possible to alter the ion

input angles and energies to simulate different etching conditions. These simulations quite accurately predict the evolution of a trench and RIE lag. The flowchart showing a typical etching simulation is shown in Fig. 3.2.

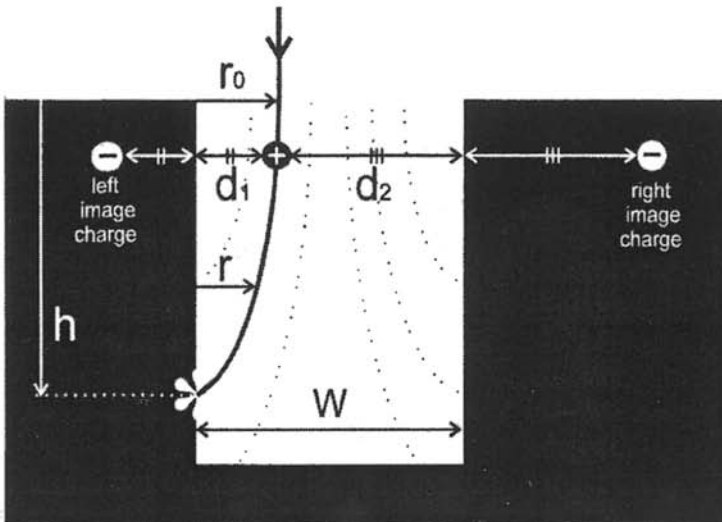


Fig. 3.1. Ion transport during the etching of a high aspect ratio trench [1]

Figure 3.3 shows the simulation of the formation of trenches by changing the ion energy flux distribution. It is possible for the image forces at the wall to give extra energy to the incoming ions, in this case they have enough energy to remove the sidewall inhibitor and etching can occur. When deciding what factors cause RIE lag there are three possible causes, inhibitor depletion, radical depletion and ion depletion. Inhibitor depletion can be eliminated from experimental evidence. Radical depletion can be tested in such a way that the effects of ions, and inhibitors are eliminated. In these experiments RIE lag is not observed, therefore this mechanism is also eliminated. Therefore, ion depletion must be the mechanism responsible, since ion depletion is reliant on contributions from the ion distribution and image force. A simulation has been developed that examines ion depletion due to sidewall capturing. It was found that the average ion energy decreases with increasing incident angle. The

particular ion angular distribution (IAD) associated with this effect usually results in bottling, and also predicts RIE lag. Simulated results are backed up by experiment. Etch rates can be predicted if the aspect ratio rather than the feature size is scaled. The aspect ratio is time dependent because the trench becomes deeper as time increases. As the trench deepens radical supply become restricted therefore it can be observed that etch rates reduce as the aspect ratio increases. The image force mechanism predicts RIE lag will increase as feature size decreases; it is thought RIE lag is significant only in high aspect ratio sub-quarter microscale trenches. Figure 3.4 illustrates the etching mechanisms associated with ion and radical etching of silicon.

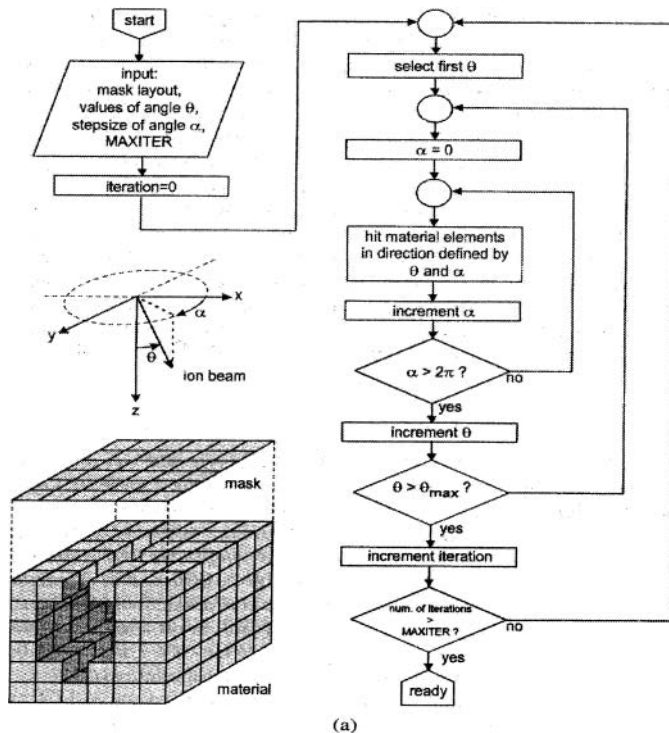


Fig. 3.2. Flowchart showing incremental steps in determining the etching characteristics of a trench [1]

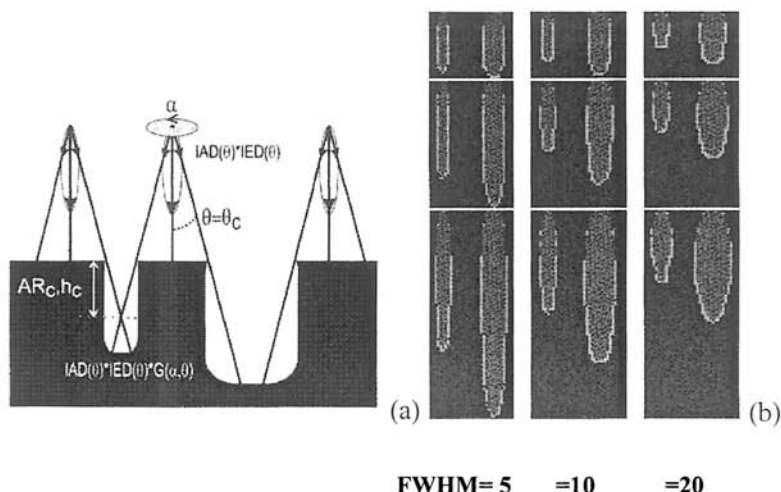


Fig. 3.3. Simulation of the formation of trenches is controlled by changing parameters such as the ion energy flux distribution that is varied by changing α and θ [1], (a) the effect of IAD on RIE lag, and (b) simulated output for different vertical etch times and the FWHM of triangular shaped IAD

3.5.5 Etching Disruption Mechanisms

The following is a summary of effects that can reduce the effectiveness of the ions and radicals entering the trench. (1) *Boundary distortion* – occurs when the distance between the boundary layer and substrate changes along the length of the substrate that can be caused by trenches. The effect causes distortion of the electric field, which changes the concentration and direction of incoming ions, they no longer impact the substrate at 90 degrees. (2) *Sidewall passivation* – results from the protective inhibiting layer formed over the substrate. However, in the case of a high aspect ratio trenches inhibitor build can vary with depth, specifically it is thicker at the trench top than at the bottom allowing the potential for undercutting.

(3) *Sidewall charging* – if the inhibitor is an insulator it can gain a charge, this causes problems because successive charges can be repelled disrupting the etching process, and incident ions can leave their charge on the wall. (4) *Ion deflection* – occurs when ions enter the trench (due to the image force) and additional deflection is caused by the negative potential of the trench walls (a result of sidewall charging), which is believed to be one of the main sources of undercuts. (5) *Ion etching* – ions should impact the inhibitor with just enough energy to cause removal and expose the substrate to radical attack. However, if the ions have too much energy they themselves can etch the substrate. (6) *Ion reflection* – if ions collide with a surface at a small angle the impact energy is not enough to trigger an event and the ion is reflected away from the wall. This usually leads to a widening of the trench because the ion is reflected into the opposing wall where it removes the inhibitor allowing radicals to attack the substrate. (7) *Ion shadowing* – the top of the trench blocks ions that are not perpendicular with the substrate, in this case part of the trench, is no longer subjected to ion bombardment that results in different etch rates. (8) *Ion depletion* – occurs in conjunction with ion capture. As a trench grows deeper there is more sidewall available for ion capture hence ion depletion increases with trench depth. Ions captured by the trench can no longer participate in inhibitor removal.

(9) *Radical capturing* – radicals impacting trench walls can either bond with it or be reflected. It is possible that before bonding radicals can be transported on the surface, higher surface temperatures gives the radicals greater surface mobility. Radical reflection occurs when a radical reaches an uninhibited trench section and there is no convenient substrate to etch, in this case the radical will leave the surface in a random direction. These two methods can help radicals to be transported towards the bottom of the trench. (10) *Radical etching* – if the inhibiting layer is too thin it is possible for radicals to reach the substrate and etching will occur in unwanted places. (11) *Radical shadowing* – occurs in the same way as ion shadowing, however radicals are isotropic. (12) *Radical depletion* – similar to ion depletion, radicals can be captured and this becomes more likely as the trench deepens. Radical deflection and high surface mobility made possible by higher temperatures are the main

mechanisms radicals can reach the bottom of high aspect ratio trenches.

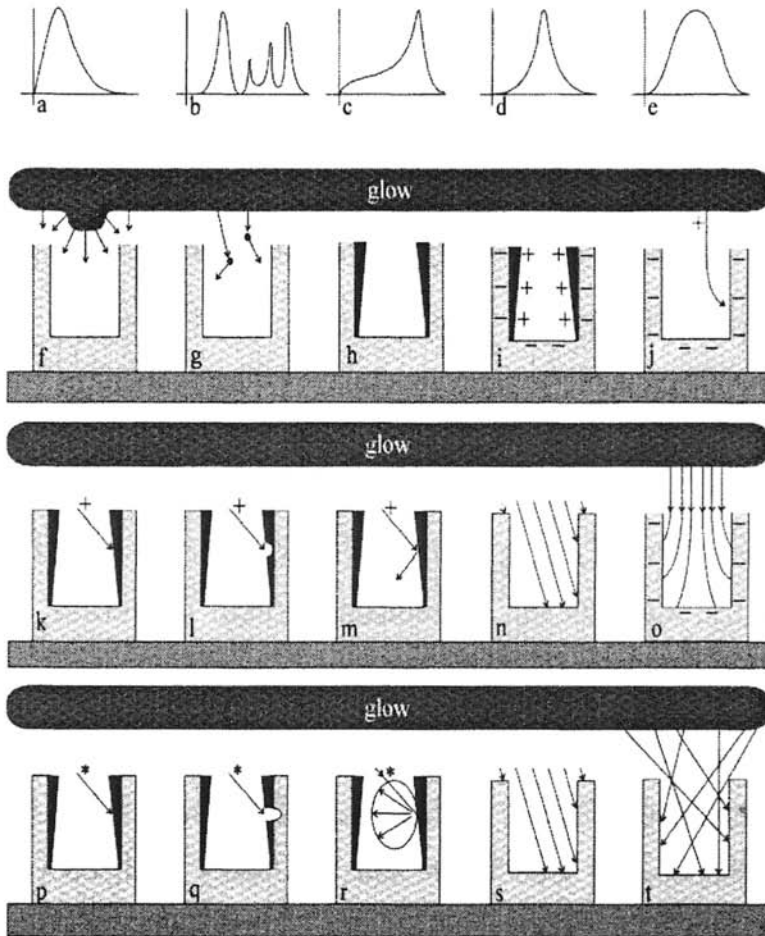


Fig. 3.4. Ion and radical etching mechanisms shown when creating a microscale trench in the substrate material [1]: (a) EEDF; (b) PEDF; (c) IEDF; (d) IADF; (e) RADF; (f) boundary distortion; (g) particle collision; (h) sidewall passivation; (i) sidewall charging; (j) ion deflection; (k) ion capturing; (l) ion etching; (m) ion reflection; (n) ion shadowing; (o) ion depletion; (p) radical capturing; (q) radical etching; (r) radical deflection; (s) radical shadowing; and (t) radical depletion

When creating microstructures the process is not always perfect, depending on the particular process parameters, different results are obtained. These effects can usually be eliminated or reduced to an acceptable level by optimizing the process for etching of a specific geometry. The variables that are changed are: gas concentration (etchant gas in the plasma), gas pressure, electric current, electrode distance, and sheath thickness.

3.5.6 Effects of Etching

Ions ideally impact the substrate at a normal angle. However, as discussed there are effects that cause the trench to grow in shapes different to the ones required. The following is a discussion of effects observed.

3.5.7 Tilting

Tilting can occur for a number of reasons (Fig. 3.5). If the cathode is inert to the particular etching chemistry radicals tend to home toward the center of the wafer. Radicals have now gained direction and are no longer isotropic. Ions still remove the inhibiting layer anisotropically, but radicals now enter a trench and etch in a preferred direction related to the center of the substrate. This problem is usually amplified by using unusual mask shapes. As previously discussed, ion impact can be abnormal compared to the substrate, which is usually due to boundary distortion. It occurs when trenches are present or because geometrical features are incorrectly spaced between the boundary of the plasma and the cathode. These problems usually occur when the sheath region is between features. Increasing the thickness of the sheath reduces the severity of tilting.

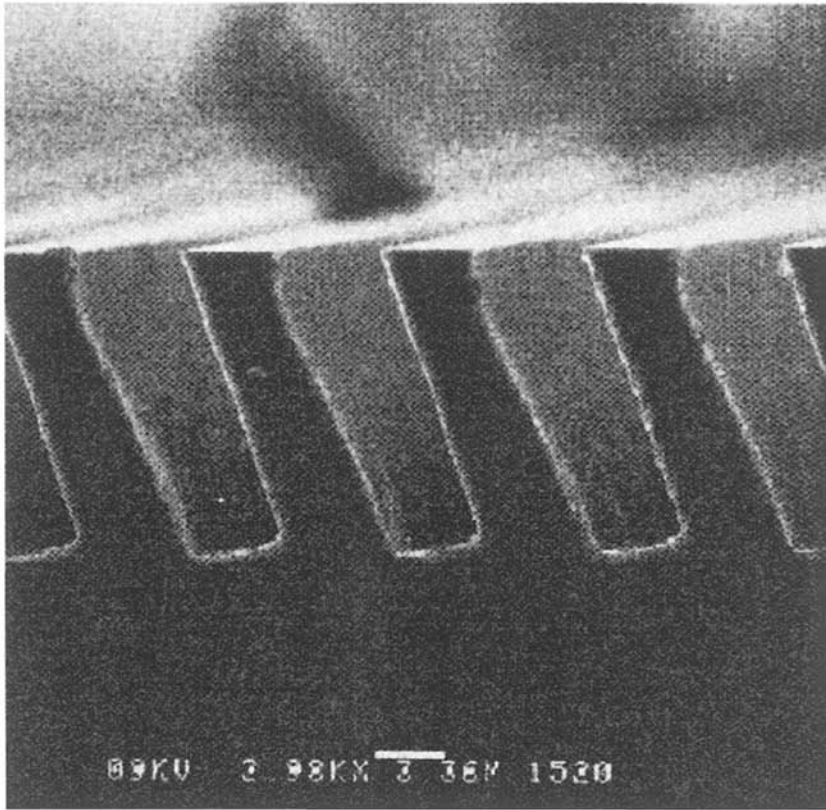


Fig. 3.5. Effects of tilting on the resultant trench [1]

3.5.8 Bowing

Bowing describes excessive undercutting of the mask to form a nearly oval trench where a square trench was originally intended; it is usually found only when the substrate is conducting. If the sidewall inhibitor is not strong enough sidewall passivation may not be efficient and unwanted etching will occur. The primary mechanism contributing to this unwanted etching is ion deflection, and its effect can be reduced by increasing sidewall passivation, wall charging, ion energy, and by reducing the image force. Cooling the sample can also decrease bowing effects by decreasing the energy of the

substrate, which can be done cryogenically. In addition, it does not follow that as inhibitor thickness increases its protection increases.

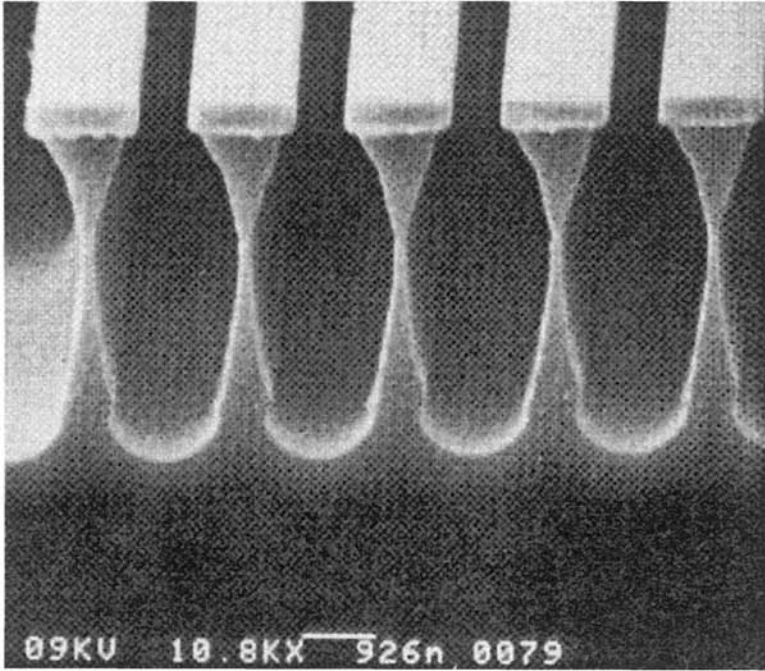


Fig. 3.6. Effects of bowing on the resultant trench [1]

3.5.9 Bottling

Bottling is a three-phase phenomenon. First, initial ions that remove the inhibitor are off normal angles, usually because of unusually high operating pressures, which causes significant undercut of the trench (Fig. 3.7). After a period of etching the trench deepens and undercut continues until a critical point is reached when the opposite sidewall begins to shadow some of the off-angle ions. At this point, the sidewall angle is such that incident ions are either captured or reflected and undercut ceases. Reflected ions then travel to the bottom of the trench where they can remove the inhibitor and cause etching. As there is no sidewall etching from this point on, the

trench cross section begins to approach the width of the mask, thus creating a “bottle” shape. To decrease the effect of bottling it is important to reduce the number of off-angle ions, which can be achieved by reducing the gas pressure or the direct current self bias. Reducing the sheath thickness may also aid this effect because there are fewer opportunities for collisions to take place, and the beam will retain its collimated profile longer.

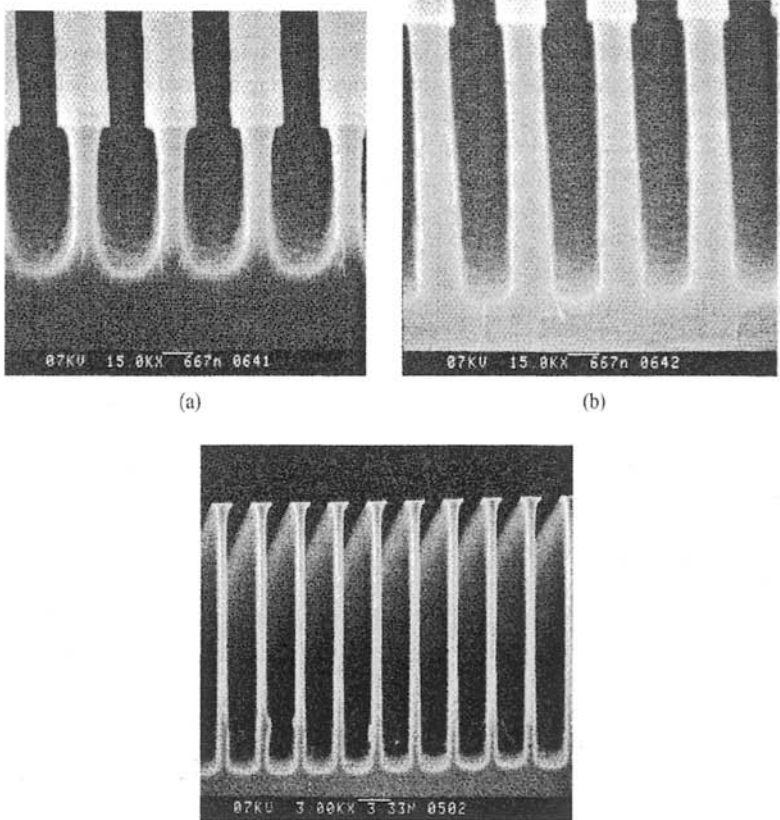


Fig. 3.7. The effects of bottling on the resultant trench [1]: (a) effect of broad-shaped ion beam; (b) effect of decreased sheath thickness; and (c) effect of using a conventional IBARE system

3.5.10 TADTOP

An interesting etch characteristic is TADTOP, or trench area dependent tapering of profiles (Fig. 3.8). Different trench widths have different cross-sectional profiles because etch rates are different for wide and small trenches. Ion deflection is the mechanism responsible for creating TADTOP, hence in wide trenches ions become attracted to a sidewall. Ions traveling toward the center of the trench are usually unaffected, but ions near a sidewall are subjected to a negative charge; hence the ion is attracted toward the sidewall and can remove the passivating layer. In narrow trenches, the ions experience a negative attraction from either sidewall and these forces tend to cancel each other out. Counteracting this effect means counteracting ion deflection, which can be achieved by the same method as counteracting bowing.

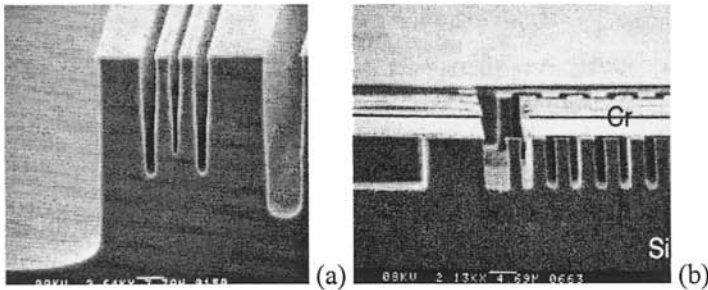


Fig. 3.8. Effects of TADTOP on the resultant trench [1]: (a) decreasing the ARDE effect due to stronger passivation; and (b) TADTOP creates wider openings as the trench gets deeper

3.5.11 RIE Lag Due to Ions

Smaller trenches can etch either faster (negative lag), or slower (positive lag) than wide trenches; this is called RIE lag (Fig. 3.9). Positive lag is accounted for by ion deflection, ions are attracted to the negatively charged walls of a trench, if the ion supply is low and

the trench is deep then all the ions can be captured by the wall and etching ceases as there are no more ions to remove the inhibitor at the base of the trench. However, a certain point is reached where the wall contains many ions and it becomes positively charged; then incoming ions experience an opposite force and are repelled. The cross section should remain unaltered because if ion deflection begins it is soon negated by ion reflection.

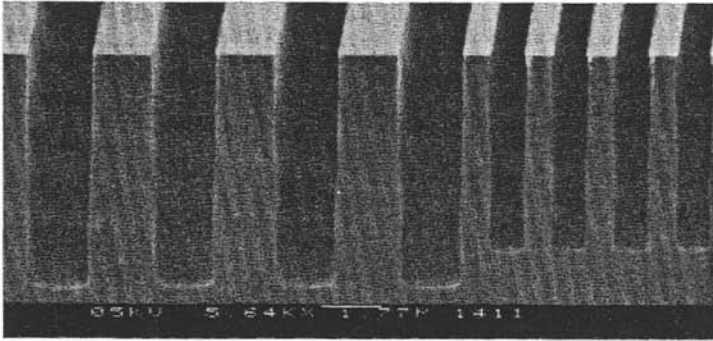


Fig. 3.9. The effect of RIE lag due to ions on the formation of a trench [1]

3.5.12 RIE Lag Due to Radical Depletion or Reflection

RIE lag due to radical depletion or reflection can cause the trench to bow slightly, thus making the sidewalls unparallel. Figure 3.10 shows the effects of RIE lag on trenches with different aspect ratios.

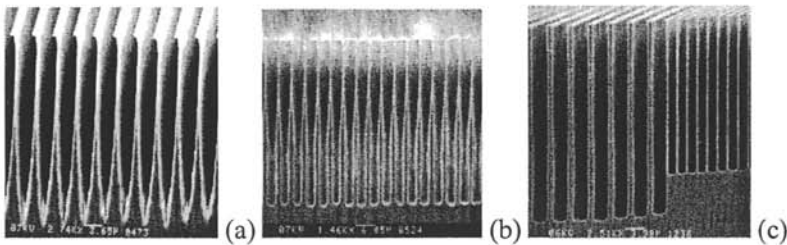


Fig. 3.10. Effects of RIE lag due to radical depletion and reflection on the formation of a trench [1]: (a) at center of silicon wafer under high pressure; (b) at the edge of the wafer under high gas pressure, and (c) at the center of the wafer under low gas pressure

3.5.13 Micrograss

Micrograss is the formation of many small spikes at the bottom of a trench (Fig. 3.11). The main formation mechanism for micrograss is unwanted particles on the surface of the substrate. These particles act as a mask and prevent ions from removing the inhibitor. There are two primary sources for these particles: (1) contamination from foreign bodies, which is why cleaning of the substrate and operating in a clean environment are important; and (2) etched particles can fall on the surface and will have reacted with the surface so that they are no longer reactive in the environment. Of course, if there is ion reflection from the sidewalls then the incoming ions no longer act normal to the substrate surface, thereby undercutting micrograss that essentially eliminates it. Hence, if incoming ions are perfectly collimated then this can increase the likelihood of micrograss formation.

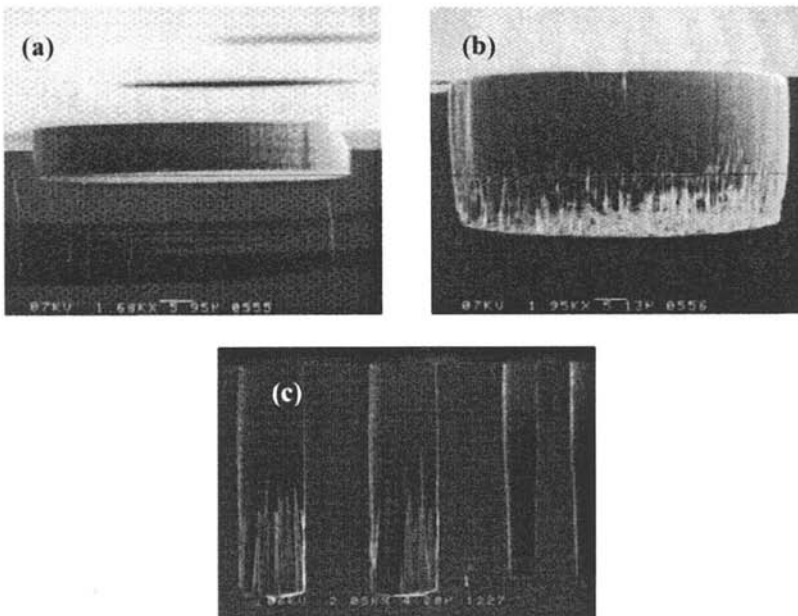


Fig. 3.11. Effect of micrograss formation after (a) 10 minutes, (b) 20 minutes, and (c) 30 minutes of etching time on the formation of a trench [1]

3.6 Micromachining High Aspect Ratio Microstructures

A method of machining high aspect ratio microstructures is via mechanical methods of micromachining using diamond coated cutting tools with bespoke profiles so that trenches can be milled in materials such as silicon, silicon-based materials, and engineering materials such as copper, aluminum, and iron-based alloys. This type of process is currently used to machine die steels to produce mold inserts and injection molds for the mass production of polymeric-based micro- and nanostructures. Microfluidic devices are machined using mechanical-based machining processes that use milling cutters and diamond profiled cutting wheels. Mold inserts are also machined using mechanical micromachining techniques. When compared with lithographic or etching processes, mold inserts are easily manufactured with three-dimensional features and curved surfaces with mechanical micromachining processes.

3.7 Micromolding

Micromolding of thermoplastic polymers is one of the most promising fabrication techniques for non-electronic micro-devices. Therefore, parts fabricated by micromolding, even from high-end materials, are suitable for applications requiring low-cost and disposable components. Moreover, thermoplastic materials are a very large material class, which allows one to find a suitable polymer for nearly every application (see Table 3.1). Molded microstructures can be either soft and elastic such as polyoxymethylene (POM) or hard and brittle such as polysulfone (PSU). They are available from optically transparent materials such as cyclo-olefin copolymer (COC) and opaque ones such as polyamide (PA) filled with graphite.

3.8 Micromolding Processes

There are four processes that are employed for micromolding of thermoplastic polymers: Injection molding, reaction injection molding, hot embossing, and injection compressing molding.

3.8.1 Injection Molding

The well-known macroscopic injection molding process can be adapted to the micro-scale by employing a variotherm process [2]. It comprises the following process steps: The mold cavity equipped with a micro-structured tool (mold insert) is closed, evacuated, and heated above the glass transition temperature of the polymer, an injection unit heats the polymer and presses the viscous polymer into the mold, and the polymer (and the tool) is cooled down below its glass transition temperature and de-molded from the tool. This cycle temperature control is called variotherm (variothermal).

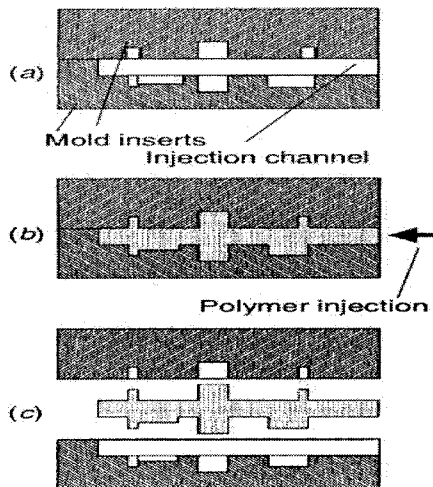


Fig. 3.12. Process procedure for the micro-injection molding process: (a) the mold is closed, evacuated, and heated to above the glass transition temperature; (b) polymer material is injected into mold; and (c) mold and polymer product are cooled down and the polymer de-molded

Table 3.1. Thermoplastic polymers used for micromolding

Acro- nym	Full name	Temperature stability [°C]	Properties	Structure
COC	Cyclo-olefin copolymer	140	High transparency	Amorphous
PMMA	Polymethyl- methacrylate	80	High transparency	Amorphous
PC	Polycarbonate	130	High transparency	Amorphous
PS	Polystyrene	80	Transparent	Amorphous
POM	Polyoxymethyl- ene	90	Low friction	Semi Crystalline
PFA	Perfluoralkoxy copolymer	260	High chemi- cal resistivity	Semi crystalline
PVC	Polyvinylchlo- ride	60	Low cost	Amorphous
PP	Polypropylene	110	Mechanical properities	Semi crystalline
PET	Polyethylene terephthalate	110	Transparent, low friction	Amorphous/ Semi crystalline
PEEK	Polyethere- therketone	250	High tem- perature resistivity	Semi crystalline
PA	Polyamide	80-120	Chemical and temperature resistivity	Semi crystalline
PSU	Polysulfone	150	Chemical and temperature resistivity	Amorphous
PVDF	Polyvinylidene- fluoride	150	Chemically inert, piezo-electric	Semi crystalline

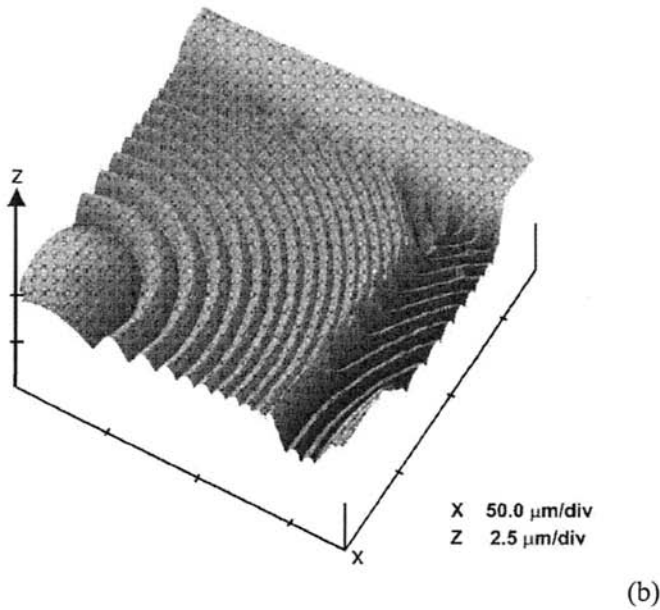
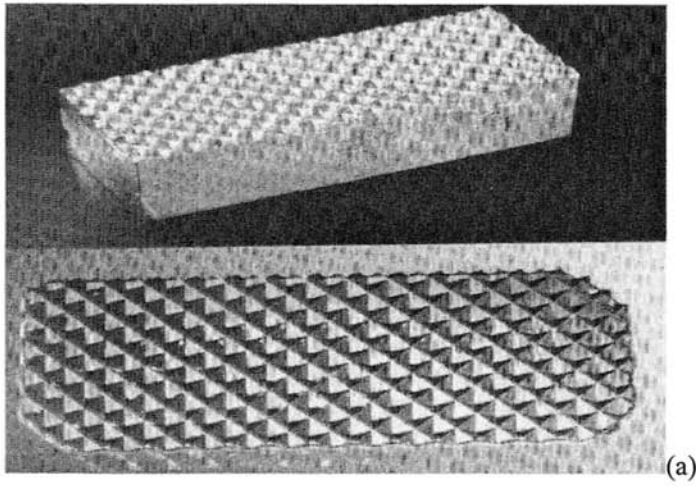


Fig. 3.13. Injection molded continuous relief micro-lens showing AFM structure of the micro-lens in three dimensions: (a) microlens; and (b) AFM image of the surface of the microlens

In general, cycle times are shortest (on the order of minutes) when producing micro-parts from polymers by injection molding. Figure 3.12 demonstrates the basic principle of micro-injection molding. Figures 3.13 and 3.14 show an array of microscale products manufactured using the injection molding technique.

3.8.2 Reaction Injection Molding

Reaction injection molding is similar to injection molding, but instead of one type of plastic, two components are injected into the closed molding tool. This technique allows fabrication of parts from polymers that are not thermoplastic, such as thermosetting materials and elastomers. The manufacture of micro-parts by reaction injection molding was investigated in the mid-1980s [3, 4] but turned out to be difficult to perform because a good mixture of the components needs to be achieved on the micro-scale and a chemical reaction has to take place in micro-structures of the molding tool, which requires a comparatively long time and results in long cycle times. Now, with the possibility of UV-curing instead of thermal initiation of the polymerization stage, reaction injection molding has again appeared.

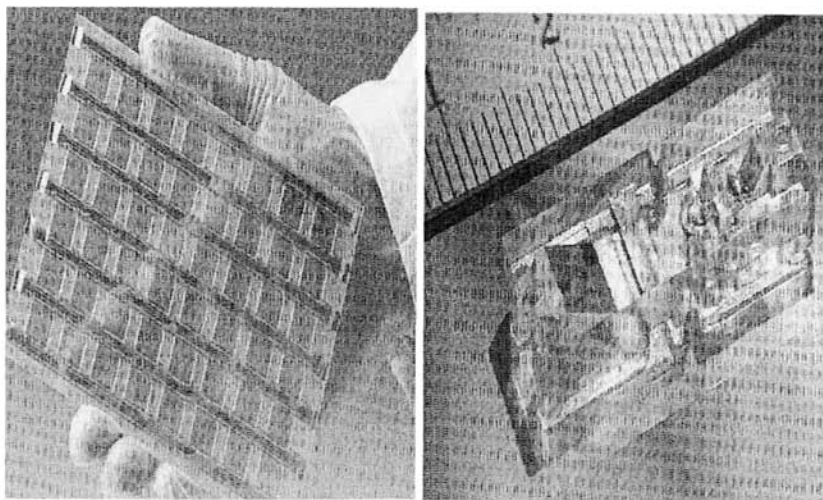


Fig. 3.14. Reaction injection molded sensor chips and optical modules

3.8.3 Hot Embossing

The principal process steps of hot embossing are [5]: A thermoplastic film is inserted into the molding machine, a micro-structured tool (mold insert) in an evacuated chamber is pressed into the film, which has been heated above its softening temperature, and the mold insert is filled by the plastic material which replicates the micro-structures in detail. Then the set-up is cooled and the mold insert is withdrawn from the plastic.

In contrast to injection molding, during hot embossing the polymer flows a very short way from the foil into the micro-structure only. As a result, very little stress is produced in the polymer and the molded parts are well suited as optical components, such as wave-guides and lenses. Hot embossing is particularly suited for forming plane plates or foils, as a small amount of plastic has to be molded. Figure 3.15 shows an outline of the process of hot embossing and a sample microscale product. Figure 3.16 shows a variety of applications and commercial equipment available for hot embossing.

Originally designed for the LiGA standard format of 26 x 66 mm² area, the embossing area has been extended considerably in the past few years, and molding machines for samples with a diameter of up to 200 mm are being introduced onto the market. With increasing area, shrinkage of the plastic component is significant. A sophisticated execution of the process is required to prevent deformation, such as overdrawn edges of the components or even damage to the mold insert. Shrinkage of hot embossed samples is smaller, and therefore, it is especially suited for a further extension of the format [6,7].

A hybrid process developed for increasing productivity in the manufacture of microscale products is laser-assisted hot embossing, or infra-red assisted hot embossing. Figure 3.17 shows the general outline of the process. Here, two variations are shown, transparent mold embossing in which the embossing process can be viewed by an observer to ensure that mold filling takes place, and transparent substrate embossing. This method is currently in development and demonstrates the advances currently being made in the manufacture and fabrication of polymeric micro-and nanostructures.

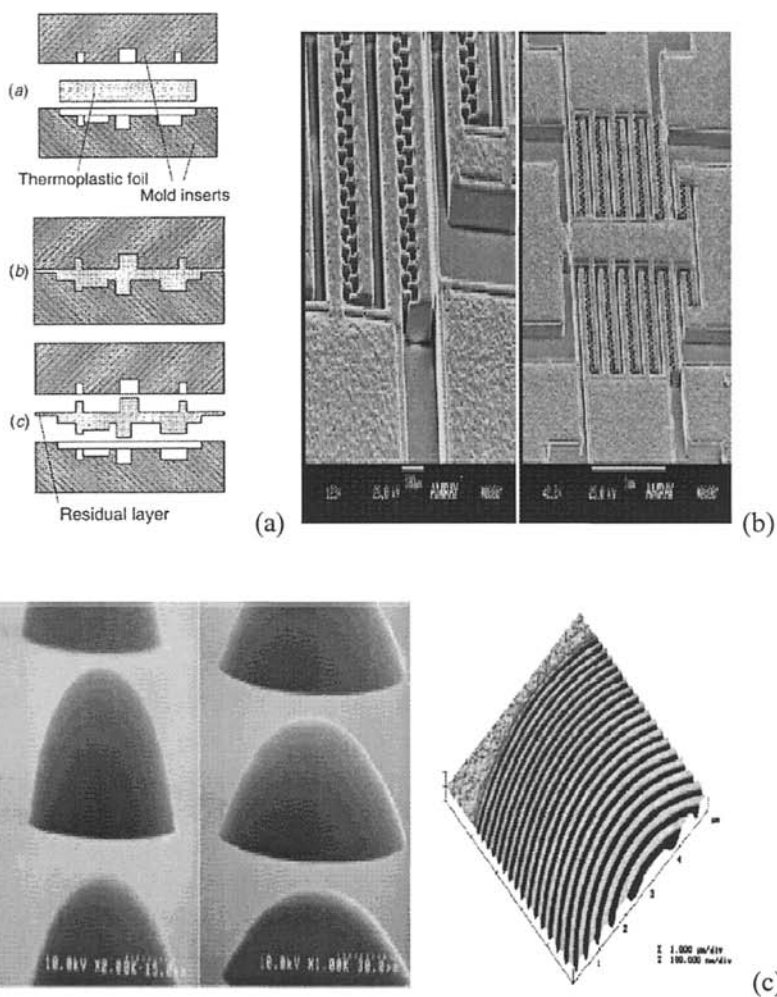


Fig. 3.15. Process steps for hot embossing: (a) thermoplastic film is inserted into the mold; (b) mold is evacuated and heated above the glass transition temperature; and (c) the polymer is cooled down and de-molded to reveal a typical microscale product such as an electrostatic comb drive, micro-lens, and a Fresnel zone plate

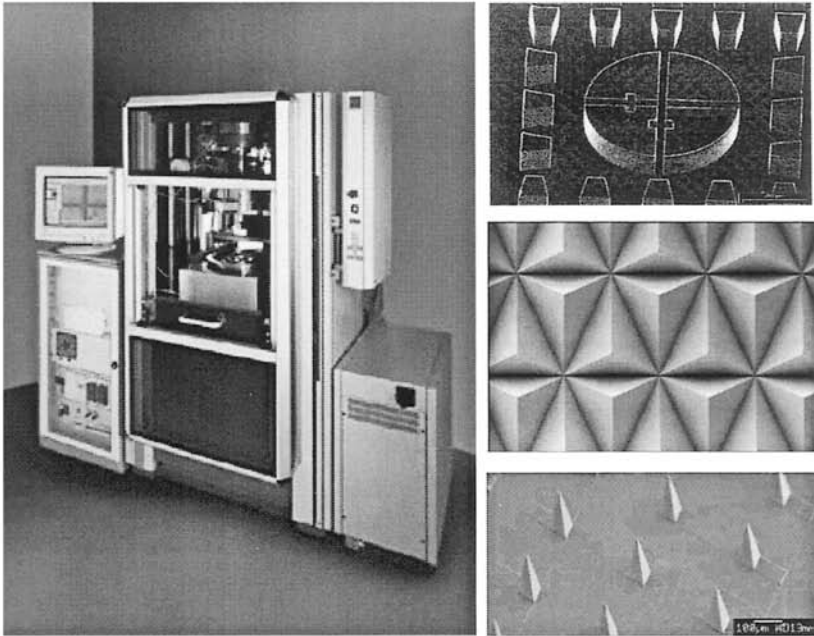


Fig. 3.16. Commercial hot embossing system manufactured by JENOPTIK Mikrotechnik GmbH (Germany). Spec: press force: $< 200\text{kN}$, temperature inside chamber: $< 500^\circ\text{C}$, max substrate size: $f=150\text{mm}$, with vacuum and cooling system. Samples of microformed structures include reflective surfaces and surfaces with needles standing proud of the surface

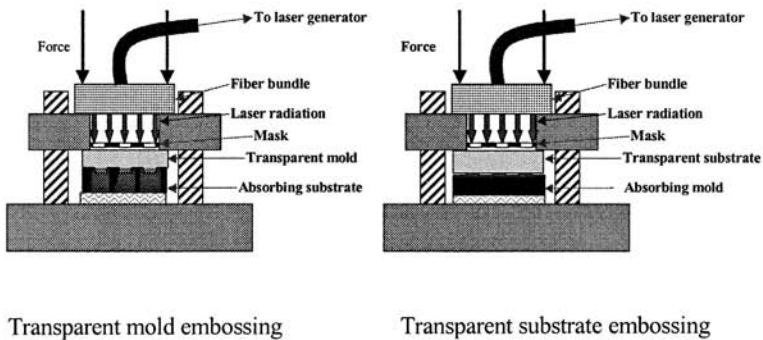


Fig. 3.17. Laser/infra-red assisted embossing

3.8.4 Injection Compression Molding

Injection compression molding is a combination of injection molding and embossing to overcome the problem of heating the polymer by the tool. The polymer is injected from a screw into the semi-closed molding tool and then pressed into the microstructure by closing the tool. In this way, the problem of injection through a small gap is avoided when producing a microstructure on a thin carrier layer. Injection compression molding is widely used to produce CDs and DVDs. CDs possess critical dimensions of less than 1 micrometer, but the aspect ratio is small and, therefore, de-molding is not a problem.

3.9 Micromolding Tools

Molding tools used in micro-engineering generally consist of a micro-structured mold insert and the tool. The requirements, which need to be fulfilled by the mold insert, are very different. The mold insert has to provide for the primary microstructure and, therefore, is manufactured with techniques appropriate for this. The microstructure should exhibit smooth sidewalls to avoid friction during de-molding and a small inclination angle, if this can be tolerated by the application of the microstructures to be molded.

While the tool and the ejection systems are manufactured by classical metal processing, various methods are applied for micro-structuring the mold insert. There are methods of direct structuring, including mechanical micro-machining, laser structuring, and electric discharge machining (EDM), and indirect processes such as lithographic processes that use x-rays or UV radiation combined with electroplating.

Electroplating allows fabrication of a metal mold insert from microstructures made of plastics, silicon, and other materials not suitable for use as a mold insert [8-10]. It may be advantageous to transform a metal microstructure worked from a solid soft metal into a hard alloy (e.g., Fe-Ni or Co-Ni) or hard metal by electroplating. Another reason for employing electroplating is that some critical mi-

crostructures such as narrow grooves or sharp concave corners cannot be milled while their inverted forms (narrow rib or sharp convex corner) can easily be manufactured by mechanical means. Even structures in the nanometer range can be replicated by electroplating and, therefore, this is an important technique for tool manufacturing. For very high aspect ratio microstructures, mold inserts need a substantial backing in order to provide the necessary mechanical stability.

Mechanical micro-machining is closest to traditional tool technology. Techniques such as turning, drilling, or milling are employed for fabricating mold inserts. Mold inserts fabricated by mechanical micro-machining with CNC machines are offered by many companies and are available from research institutes. The smoothest sidewalls of microstructures are obtained with diamond tools but these are not suitable for work in steel, which is a favored material for mold inserts. Moreover, the smallest diameter of diamond tools is approximately 200 μm . When narrower grooves need to be fabricated on a mold insert or the mold insert needs to be made of tool steel, milling and drilling tools made of hard metals can be used, with the requirements regarding the smoothness of sidewalls being reduced. Compared to lithographic processes it is easy to fabricate mold inserts with three-dimensional micro-structures even with curved surfaces by mechanical micro-machining, and sloped sidewalls of the micro-structures can be achieved by simply using milling tools with the required profile.

Another technique initially developed for macroscopic use is electric discharge machining (EDM). Today, it also allows micro-structured mold inserts to be produced. This is achieved by using wires as thin as 30 μm for wire erosion or by sinking erosion with electrodes produced by electroplating. In this way, microstructures made from nickel or other metals can be transformed into mold inserts made of steel. A disadvantage of this technique is that the sidewalls of microstructures fabricated in this way are rough compared to mechanical micromilling processes.

Lithographic processes are particularly suited for minute structures. A resist is patterned with a microstructure that is electroplated to build up a mold insert. LiGA technology is characterized by possessing extremely high structural tolerances, small lateral dimen-

sions, and sidewalls with a roughness of less than 50 nm [11,12]. UV lithography is less complex and less expensive alternative to x-ray technology, which is able to meet less demanding specifications. Both methods are based on the lithographic generation of non-conductive plastic microstructures that are filled by electroplating. Mold inserts made by both methods are available from companies and research institutes [13].

Another possibility for structuring metal is to use laser technology [11]. This development is still at its beginning, but promises to have enormous potential in terms of aspect ratios and minimum structural dimensions. This technology is of particular interest, as it allows processing of materials such as stainless steel or tungsten carbide. Figure 3.18 shows an array of micro-products using molds manufactured via a number of processes.

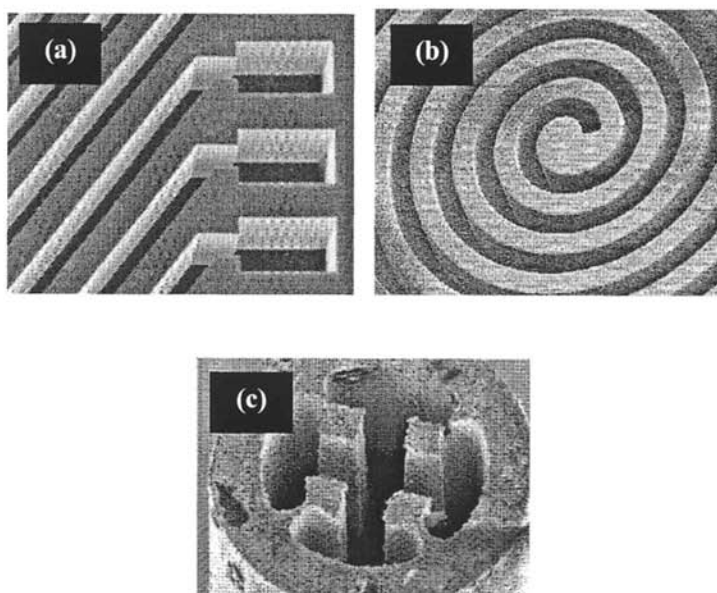


Fig. 3.18. Molds manufactured via different processes: (a) deep x-ray lithography and electroplating; (b) photolithography with SU8 resin; and (c) electro-discharge machining

3.10 Micromold Design

Most problems in micro-molding are not caused by the filling of the mold, but by de-molding. During de-molding, microstructures may be torn apart, deformed, or destroyed. De-molding affects the wear of mold inserts and delicate parts of the mold insert may even be destroyed after a single molding process, the microstructure is not designed properly or unsuitable molding parameters are chosen. It is possible to de-mold microstructures with vertical sidewalls, but an inclination angle of 2° reduces de-molding forces and is even more important than the roughness of the sidewalls. An important factor in de-molding is the shrinkage of the polymer, which occurs when cooling down the polymer between the filling of the mold and de-molding. Therefore, de-molding forces also are a function of the orientation of microstructures relative to the direction of shrinkage and the placement of critical microstructures relative to the center of shrinkage. This is why the path of the polymer into the mold has to be chosen with care for injection molding. Delicate microstructures, such as pins with high aspect ratios, can be protected against shearing forces resulting from shrinkage and mold filling by neighboring auxiliary structures that are stable enough to withstand these forces. If a mold insert is covered with areas microstructures of different height, or varying density, then these areas should be arranged symmetrically on the mold insert. In this way, tilting of the mold insert during molding is avoided.

3.11 Micromolding Applications

Micromolding has been employed to fabricate a variety of polymer components. Most applications are in the field of micro-optics and micro-fluidics, but there are also some examples of micro-(and nano) electrical and mechanical devices. The most widely sold micromolding product probably is the well known CD and DVD for data storage, music, and videos. Another application is the hologram that is attached to a credit card [14]. Other molded micro-optical components include spectrometers [15], optical switches [16,17], optical fiber components [2], waveguides [18,19], anti-

reflective surfaces [20], optical gratings [9, 21], and photonic structures [22]. There is a variety of molded microfluidic devices, such as pumps [23-25], valves [26-28], nebulizers [29], ink jets [29], degassers for HPLC systems [30], capillary analysis systems [29, 31-34], devices for investigations of living cells [29,35], pressure sensors [36], and flow sensors [37]. Prospective applications of thermoplastic molding also lie in electronics. One of them is nano imprinting [38-43] which may allow for the low-cost replication of electronic circuits with critical dimensions as small as 10 nanometers. Other future electronic applications may be electronic and optical circuit boards [19], acceleration sensors [44,45], and simple devices, such as electrical switches.

3.12 Limitations of Micromolding

What are limitations of micromolding of thermoplastic polymers? Nanoimprinting processes show that structures of only a few tens of nanometers in size are replicated very well. However, there is a limitation regarding the achievable aspect ratio of columns, grooves, and walls. This limit is a function of the geometry of the microstructure, its position on the sample, the polymer type, and the process parameters. Finite element calculations could help solve molding problems of high-aspect-ratio microstructures, but FEM codes are available for mold filling only and the limiting process step is de-molding of the microstructures. Development of FEM calculations of de-molding operations has recently become available [46].

3.13 Fabrication of Moving Microstructures

When silicon-based microstructures have been produced they have to be separated from the base that holds them. This is usually a glass substrate that can be sacrificially etched away using wet and vapor etchants. Owing to surface tension effects, the glass material usually sticks to the machined silicon. Techniques have been designed to prevent sticking and are known as SCREAM, SIMPLE, and BSM processes. These techniques are self-aligned and are suit-

able for batch fabrication. The release of the structure takes place in the gaseous phase, so that there is no problem associated with stiction by fluids. This section of the chapter describes the study of plasma release techniques for bulk and surface micromachining of silicon based materials used for the fabrication of movable micro-mechanical structures. Here, we discuss SCREAM and SIMPLE processes.

3.13.1 Single Crystal Reactive Etching and Metallization (SCREAM)

Single crystal reactive etching and metallization, or SCREAM, is a process that consists of five basic steps (Fig. 3.19):

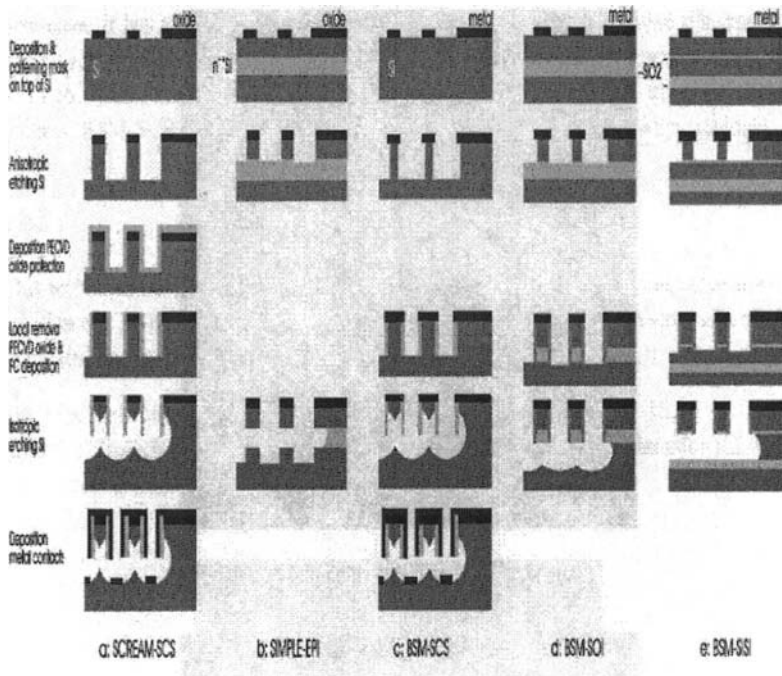


Fig. 3.19. Dry plasma processes for manufacturing movable features: (a) SCREAM; (b) SIMPLE; (c) BSM-SCS; (d) BSM-SOI; and (e) BSM-SISI [1]

- (1) Directional chlorine-based etching of silicon using the oxide as a mask material;
- (2) Trenches are passivated with the PECVD oxide;
- (3) The oxide is then removed at the bottom of the trench using a CHF_3 plasma;
- (4) An isotropic fluorine-based etch (SF_6) will release the structure; and
- (5) For electrical contacting, a deposited metal layer is required.

There are some disadvantages with the process, such as:

- (1) The deposited PECVD layer should be tensile to avoid buckling (Figure 3.20);
- (2) The mask layer should be tensile to avoid bending after release (Figure 3.21);
- (3) The released structures are hollowed out during the isotropic etch process (Figure 3.22); and
- (4) RIE lag while etching Si directions may cause problems during the isotropic etch because the etch depth may be variable along the beam (Figure 3.22).

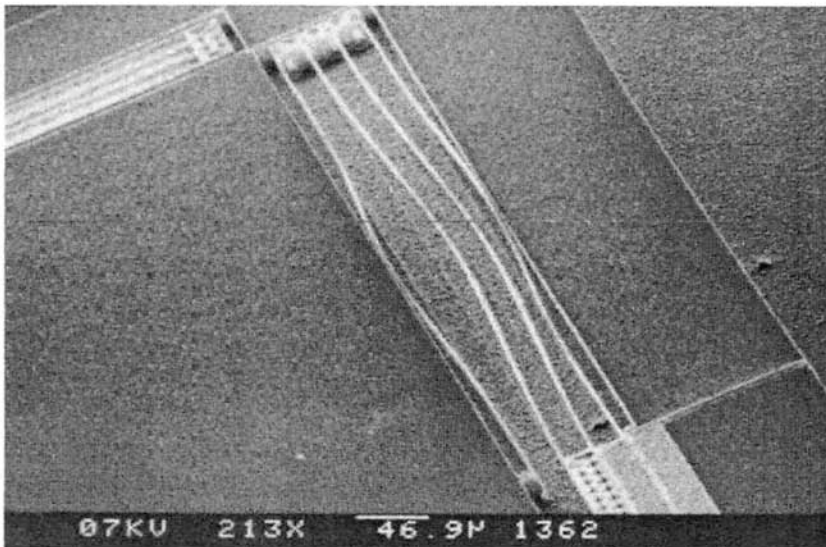


Fig. 3.20. Buckling of movable beam due to compressive stress [1]

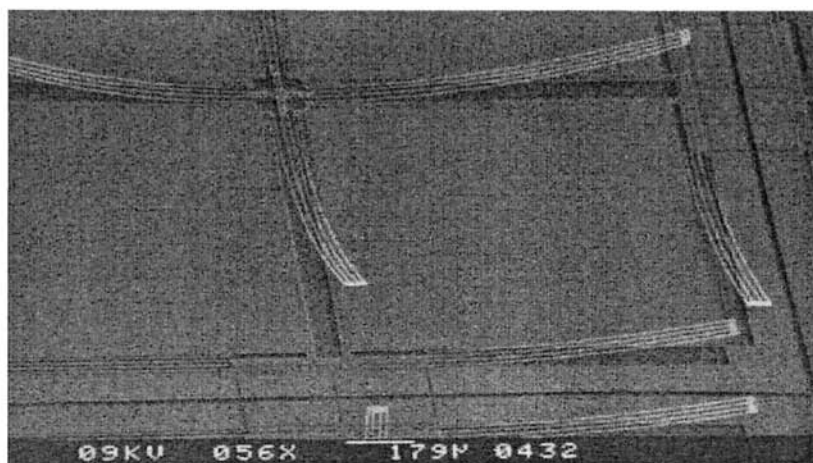


Fig. 3.21. Bending of the movable microstructure due to stress in the mask material [1]

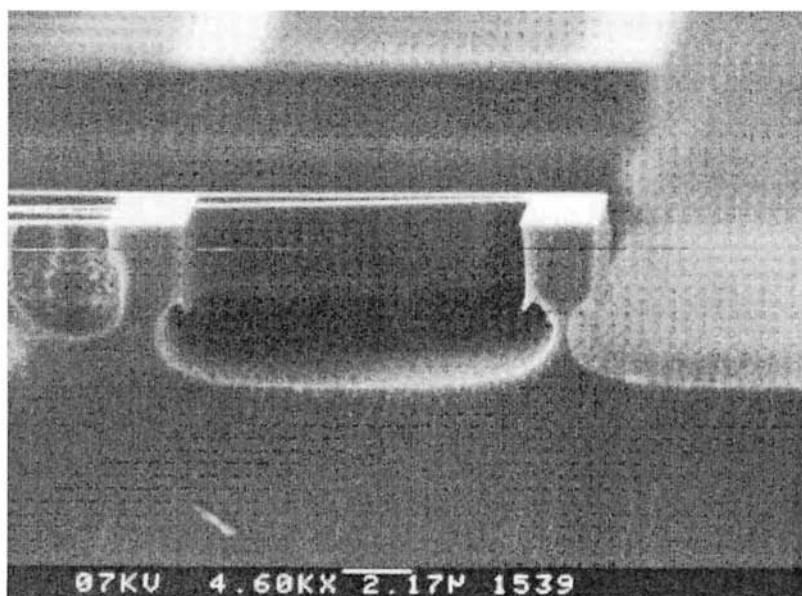


Fig. 3.22. Hollowing of beams and asymmetrical releasing due to RIE lag [1]

3.13.2 Silicon Micromachining by Single-Step Plasma Etching (SIMPLE)

Silicon micromachining by single-step plasma etching, or SIMPLE, is a process that uses Cl_2 -based plasma chemistry to remove material in silicon microstructures. The manufactured articles can be removed from the substrate as shown in Figure 3.19, but have the following disadvantages:

- (1) A thick PECVD oxide mask is needed as a mask material because the Si/SiO_2 selectivity is low in a Cl_2 plasma;
- (2) The underetch rate is low, about 50 nm/min, and is a function of doses of the buried layer and the spacing between microbeams; and
- (3) After etching, the trenches are deep that may harm the movement of free-hanging structures.

3.13.3 Black Silicon Method (BSM)

The black silicon method solves some of the problems associated with SCREAM and SIMPLE, but creates new ones. It has the ability to etch, passivate, and release silicon microstructures in one setting. The processes are described in great detail in reference [1], and are dealt with briefly in this section. There are three main processes: BSM-SCS for bulk micromachining and BSM-SOI and BSM-SISI for surface micromachining.

The BSM-SCS process uses a single crystal silicon wafer and after pattern definition has occurred, a movable microstructure can be produced in one IBARE run. Although bending and buckling problems are solved, hollowing out of beams is still a problem.

The BSM-SOI process uses a silicon-on-insulator wafer that requires the IBARE process to etch and passivate the surface of the wafer (Figure 3.23). The hollow beam problem is solved, but free hanging structures are not possible.

The BSM-SISI process uses silicon-on-insulator on silicon-on-insulator wafers to eliminate the problems of deep trenches (Figure 3.24). Here, sacrificial layers are used to prevent buckling and bending and the hollowing of beams by using small loadings af-

forded by the insulating layers and high lateral etch rates ($>1 \mu\text{m}/\text{min}$).

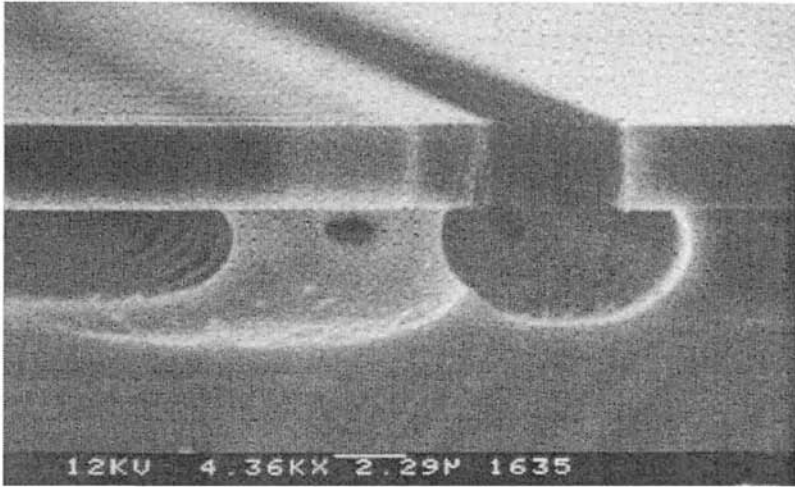


Fig. 3.23. Isotropic etch with SF_6 plasma as used in the BSM-SOI process

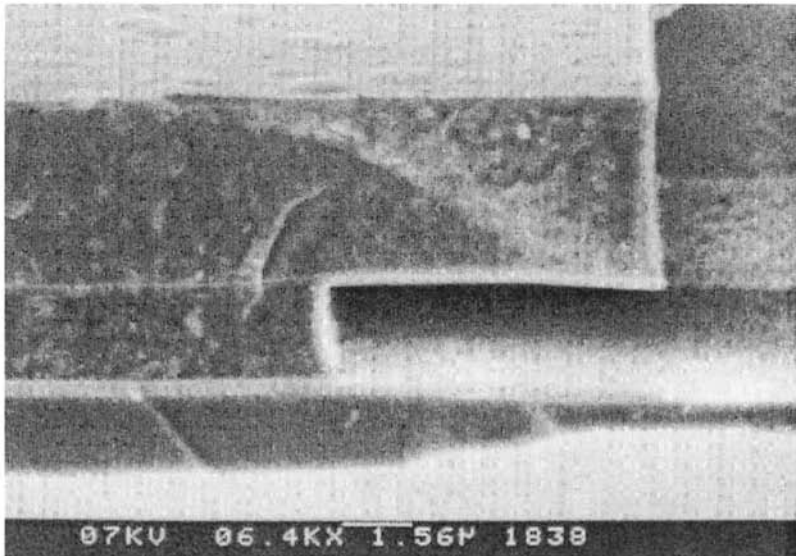


Fig. 3.24. Etched profile of movable microstructure as used in the BSM-SISI process

3.14 Conclusions

Etching of microstructures made from silicon-based materials is a well-established process. However, it has limitations in terms of being too slow for mass production and is limited to the type of substrate being etched. Therefore, etching of silicon-based materials can be considered a microfabrication process. Micro-manufacturing of microstructures can be achieved by mechanically machining substrates from engineering materials, or by mechanically machining molds for use in the mass production of microstructures made from polymeric materials.

Micro-molding of thermoplastic polymers today is a well-established process. Several micro-molding machines are sold on the market and mold inserts fabricated with various techniques suitable for most applications are available. Micro-molding can be classified as a micro-manufacturing process. Further research work will focus on achieving higher aspect ratios on larger scales and on developing special functionalities of molded parts, such as through holes and electrical paths.

3.15 Problems

1. Explain the process of dry etching.
2. Describe the ion-beam assisted radical etching technique.
3. Explain the characteristics of the plasma, especially the behavior of the sheath, and explain what happens at the region of the boundary.
4. How are radicals depleted in a trench?
5. Describe the process of volume transport in a trench.
6. Describe the numerous etching disruption mechanisms.
7. Explain and illustrate the following effects of etching: (a) tilting; (b) bowing; (c) bottling; (d) TADTOP; (e) RIE lag due to ions; (f) RIE lag due to radical depletion or deflection; (g) micrograss formation.
8. How are high aspect ratio microstructures machined?
9. Describe the material used for micromolding;
10. Characterize micromolding processes.
11. What are micromolding tools?

12. How are micromolds designed?

References

1. Elwenspoek J and Jansen H, *Silicon Micromachining*, Cambridge University Press, 1998, Cambridge, U.K.
2. Hanemann T, Hecke M and Piotter V, 2000, Current status of micromolding technology, *Polym. News*, **25**, 224-9.
3. Wallrabe U, Dittrich H, Friedsam G, Hanemann Th, Mohr J, Müller K, Piotter V, Ruther P, Schaller Th and Zißler W, 2002, Micro-molded easy-assembly multi fiber connector: RibCon, *Microsyst. Technol.*, **8**, 83-7.
4. Ehrfeld W, Bley P, Götz F, Hagmann P, Maner A, Mohr J, Moser H O, Münchmeyer D, Schelb W, Schmidt D and Becker E W 1987 Fabrication of microstructure using the LIGA process *Proc. IEEE Micro-Robots and Teleoperators Workshop (Hyannis, Cape Cod, MA, 9-11 Nov. 1987)*, ed. K J Gabriel and W S N Trimmer, IEEE Catalogue Number 87TH0204-8.
5. Hagmann P, Ehrfeld W and Vollmer H, 1987, Fabrication of microstructures with extreme structural heights by reaction injection molding, *First Meeting of the European Polymer Federation European Symp. On Polymeric Materials*, (Lyon, France, 14-18 Sept.), paper EPD05.
6. Hecke M, Bacher W and Müller K D, 1998, Hot embossing-the molding technique for plastic microstructures, *Microsyst. Technol.*, **4**, 122-4.
7. Rogge T, Rummeler Z and Schomburg W K, 2002, Piezo-driven polymer microvalve manufactured by the AMANDA process, *Proc. of Eurosensors XVI*, (Prague, 15-18 Sept. 2002), pp 214-7.
8. Niggemann M, Blaesi B, Boerner V, Gombert A, Klicker M, Kuebler V, Lalanne P and Wittwer V, 2001, Periodic microstructures for large area applications generated by holography, *Conf. Physics. Theory, and Applications of Periodic Structures in Optics*, (San Diego, CA, 1-2 Aug. 2001), *Proc. SPIE* 4438, 108-15.
9. Jian L, Desta Y M and Goettert J, 2001, Multilevel microstructures and mold inserts fabricated with planar and oblique x-ray lithography of SU-8 negative photoresist, *Conf. Micromachining and Microfabrication Process Technology VII*, (San Francisco, CA, 22-24 Oct. 2001), *Proc. SPIE* 4557, 69-76.
10. O'Donnell T, McCloskey P, Brunet M, Winfield R, Mathuna S C O, Stephen A and Metev S, 2000, High aspect ratio RF coils fabricated us-

ing laser processing and micro-molding techniques, Proc. European Microelectronics Packaging and Interconnection Symposium, (Prague, Czech Republic, 18-20 June 2000), pp 169-74, ISBN: 80-238-5509-3.

11. Mohr J, 1998, LIGA-A technology for fabricating microstructures and microsystems, *Sensors Mater.*, 10, 363-7.

12. Chung S, Hein H, Mohr J, Pantenburg J-J and Wallrabe U, 2000, LIGA technology today and its industrial applications, Proc. SPIEs Int. Conf. on Microrobotics and Microassembly II, (Boston, 5-6 Nov. 2000), Proc. SPIE 4184, 44-55.

13. Martynova L, Locascio L E, Gaitan M, Kramer G W, Christensen R G and MacCrehan W A, 1997, Fabrication of plastic microfluid channels by imprinting methods, *Ann. Chem.*, 69, 4783-9.

14. Haines K, 1996, Development of embossed holograms, Proc. SPIE 2652, 45-52.

15. Hecke M, 1997, Aufbau und Betrieb einer Kleinserienfertigung von LIGA-Spektrometern, *Swiss Plastics*, 19, 5-9.

16. Shan X C and Maeda R, 2002, Development of a low-cost 8 x 8 optical switch using micro-hot embossing 2002 IEEE/LEOS Int. Conf. Optical MEMS (Lugano, Switzerland, 20-23 Aug. 2002, IEEE (2002)), pp 21-2 (Catalogue no 02EX610), ISBN: 0-7803-7595-5.

17. Hashiura Y, Ikehara T, Kitajima A, Goto H and Maeda R, 2001, Optical switch array based on microforming process, Conf. Device and Process Technologies for MEMS and Microelectronics (Adelaide, SA, Australia, 17-19 Dec. 2001), Proc. SPIE, 4592, 414-21.

18. Ulrich R, Weber H P, Chandross E A, Tomlinson W J and Franke E A, 1972, Embossed optical waveguides, *Appl. Phys. Lett.*, 20, 213-5.

19. Krabe D and Scheel W, 1999, Optical interconnects by hot embossing for module and PCB technology-the EOB approach, Proc. 49th Electronic Components and Technology Conference (San Diego, CA, USA, 1-4 June 1999) (Catalogue no 99CH36299), ISBN: 0-7803-5231-9, pp 1164-6.

20. David C, Haberling P, Schnieper M, Sochtig J and Zschokke C, 2002, Nano-structured anti-reflective surfaces replicated by hot embossing, *Microelectron. Eng.*, 61-62, 435-40.

21. Knop K 1976, Color pictures using the zero diffraction order of phase grating structures, *Opt. Commun.*, 18, 298-303.

22. Grigaliunas V, Kopustinskias V, Meskinis S, Margelevicius M, Mikulskas I and Tomasiunas R, 2001, Replication technology for photonic band gap applications, Conf. Optoelectronics I, Materials and Technologies for Optoelectronics Devices, Symposium G of the 2000 E-MRS-IUMRS-ICEM Spring Conf., (Strasbourg, France, 20 May-2 June 2000), *Opt. Mater.*, 17, 15-8.

23. Olsson A, Larsson O, Hom J, Lundbladh L, Öhman O and Stemme G, 1997, Valve-less diffuser micropumps fabricated using thermoplastic replication, *Proc. IEEE Tenth Annu. Int. Workshop on Micro-Electro Mechanical Systems, MEMS'97* (Nagoya, Japan, 26-30 Jan. 1997), pp 305-10.
24. Schomburg W K, Ahrens R, Bacher W, Martin J and Saile V, 1999, AMANDA-Surface micromachining, molding, and diaphragm transfer, *Sensors Actuators A*, 76, 343-8.
25. Döpfer J, Clemens M, Ehrfeld W, Kämper K-P and Lehr H, 1996, Development of low-cost injection molded micropumps, *Actuator'96: Proc. Fifth Int. Conf. on New Actuators*, pp 37-40.
26. Fahrenberg J, Bier W, Maas D, Menz W, Ruprecht R and Schomburg W K, 1995, Microvalve system fabricated by thermoplastic molding, *J. Micromech. Microeng.*, 5, 169-71.
27. Goll C, Bacher W, Büstgens B, Maas D, Menz W and Schomburg W K, 1996, Microvalves with bistable buckled polymer diaphragms, *J. Micromech. Microeng.*, 6, 77-9.
28. Goll C, Bacher W, Büstgens B, Maas D, Ruprecht R and Schomburg W K, 1997, Electrostatically actuated polymer microvalve equipped with a movable membrane electrode, *J. Micromech. Microeng.*, 7, 224-6.
29. Gerlach A, Knebel G, Guber A, Hecke M, Herrmann D, Muslija A and Schaller T, 2002, Microfabrication of single-use plastic microfluidic devices for high-throughput screening and DNA analysis, *Microsyst. Technol.*, 7, 265-8.
30. Rummeler Z, Berndt M, Härtl H-G, Hempel M, Peters R and Schomburg W K, 2000, Micro-degasser made of inert polymers for HPLC devices, *ASME Winter Annual Meeting* (Orlando, FL, 5-10 Nov. 2000).
31. Lee G-B, Chen S-H, Huang G-R, Lin Y-H, Sung W-C and Lin Y-H, 2001, Microfabricated plastic chips by hot embossing methods and their applications for DNA separation and detection, *Sensors Actuators B*, 75, 142-8.
32. Blankenstein G, 2000, Microfluidic devices for biomedical applications, *MST News* (Sept. 2000), 14-15, published by: VDI/VDE-Technologiezentrum Informationstechnik.
33. Grass B, Neyer A, Johnck M, Siepe D, Eisenbeiss F, Weber G and Hergenroder R, 2001, A new PMMA-microchip device for isotachopheresis with integrated conductivity detector, *Sensors Actuators B*, 72, 249-58.
34. Weston DF, Smekal T, Rhine D B and Blackwell J, 2001, Fabrication of microfluidic devices in silicon and plastic using plasma etching, *J. Vac. Sci. Technol. B*, 19, 2846-51.
35. Kashanim D, Williams V, Shvets I V, Volkov Y and Kelleher D, 2000, Microfluidic biochips for cell guidance and separation, *Proc. First*

Annu. Int. IEEE-EMBS Special Topic Conference on Microtechnologies in Medicine and Biology (Lyon, France, 12-14 Oct. 2000), pp 279-82, (Catalogue no. 00EX451).

36. Martin J, Bacher W, Hagena O F and Schomburg W K, 1998, Strain gauge pressure and volume-flow transducers made by thermoplastic molding and membrane transfer, Proc. Int. Workshop on Micro-Electro Mechanical Systems, MEMS'98 (Heidelberg, Germany, 25-29 Jan. 1998), pp 361-6.

37. Dittman D, Ahrens R, Rummeler Z, Schlote-Holubek K and Schomburg W K, 2001, Low-cost flow transducer fabricated with the AMANDA process, 11th Int. Conf. On Solid-State Sensors and Actuators, Transducers'01 (Munich, Germany, 10-14 June 2001), paper 4B2.10P.

38. Chou SY, Krauss PR and Renstrom PJ, 1995, Imprint of sub-25 nm vias and trenches in polymers, Appl. Phys. Lett., 67, 3114-6.

39. Roos N, Luxbacher T, Glinsner T, Pfeiffer K, Schulz H and Scheer H-C, 2001, Nanoimprint lithography with a commercial 4 inch bond system for hot embossing, Conf. Emerging Lithographic Technologies V, (Santa Clara, CA, 27 Feb.-1 Mar. 2001), Proc. SPIE 4343, 427-35.

40. Lebib A, Chen Y, Cambril E, Youinou P, Studer V, Natali M, Pépin A, Janssen H M and Sijbesma R P, 2002, Room-temperature and low-pressure nanoimprint lithography, Microelectron. Eng., 61-62, 371-7.

41. Malaquin L, Carcenac F, Vieu C and Mauzac M, 2002, Using polydimethylsiloxane as a thermocurable resist for a soft imprint lithography process, Microelectron. Eng., 61-62, 379-84.

42. Roos N, Schulz H, Bendfeldt L, Fink M, Pfeiffer K and Scheer H-C, 2002, First and second generation purely thermoset stamps for hot embossing, Microelectron. Eng., 61-62, 399-405.

43. Schiff H, Heydermann LJ, Padeste C and Gobrecht J, 2002, Chemical nano-patterning using hot embossing lithography, Microelectron. Eng., 61-62, 423-8.

44. Both A, Bacher W, Hecke M, Müller KD, Ruprecht R and Strohm M, 1995, Molding process with high alignment precision for the LIGA technology, Proc. Micro-Electro Mechanical Systems (Amsterdam, The Netherlands, 29 Jan-2 Feb.), pp 186-90, (IEEE Catalogue Number 95 CH35754).

45. Ehrhardt E, Gehäuser T, Giousouf M, Kück H, Mohr R and Warkentin D, 2002, Innovative concept for the fabrication of micromechanical sensor and actuator device using selectively metallized polymers, Sensors Actuators A, 97-98, 473-7.

46. Worgull M and Hecke M, 2003, New aspects of simulation in hot-embossing, Proc. DTIP (Cannes Madelieu, 5-7 May 2003).

4. Meso-Micromachining

4.1 Introduction

When metal is removed by machining there is a substantial increase in the specific energy required with decrease in chip size. It is generally believed this is due to the fact that all metals contain defects (grain boundaries, missing and impurity atoms, etc.), and when the size of the material removed decreases the probability of encountering a stress-reducing defect decreases. Since the shear stress and strain in metal cutting is unusually high discontinuous microcracks usually form on the metal cutting shear plane. If the material being cut is very brittle, or the compressive stress on the shear plane is relatively low, microcracks will grow into gross cracks giving rise to discontinuous chip formation. When discontinuous microcracks form on the shear plane they will weld and reform as strain proceeds, thus joining the transport of dislocations in accounting for the total slip of the shear plane. In the presence of a contaminant, such as CCl_4 vapor at a low cutting speed, the re-welding of microcracks will decrease, resulting in a decrease in the cutting force required for chip formation. A number of special experiments that support the transport of microcracks across the shear plane, and the important role compressive stress plays on the shear plane are presented. Relatively recently an alternative explanation for the size effect in cutting is based on the premise that shear stress increases with increase in strain rate. When an attempt is made to apply this to metal cutting, it is assumed in the analysis that the von Mises criterion pertains to the shear plane. This is inconsistent with the experimental findings by Merchant that are discussed in great detail in this chapter. Until this difficulty is taken care of together with the premised experimental verification of the strain rate approach, it should be assumed that the

strain rate effect may be responsible for some portion of the size effect in metal cutting.

4.2 Size Effects in Machining Processes

It has been known for a very long time that a size effect exists in metal cutting, where the specific energy increases with decrease in deformation size. Backer et al. [1] performed a special series of experiments in which the shear energy per unit volume deformed (u_s) was determined as a function of specimen size for a ductile metal (SAE 1112 steel). The deformation processes involved were as follows, listed from top to bottom with increasing size of specimen deformed:

- surface grinding
- micromilling
- turning
- tensile test

The surface grinding experiments were performed under relatively mild conditions involving plunge type experiments in which an 8-inch (20.3 cm) diameter wheel was directed radially downward against a square specimen of length and width 0.5 in (1.27 cm), as shown in Fig. 4.1. The width of the wheel was sufficient to grind the entire surface of the work at different downfeed rates (t). The vertical and horizontal forces were measured by a dynamometer supporting the workpiece. This enabled the specific energy (u_s) and the shear stress on the shear plane (τ) to be obtained for different values of undeformed chip thickness (t) as shown in Fig. 4.2. The points corresponding to a constant specific energy below a value of down feed of about 28 μ inch (0.7 μ m) are on a horizontal line due to a constant theoretical strength of the material being reached when the value of t goes below approximately 28 μ inch (0.7 μ m). The reasoning in support of this conclusion is presented in Backer et al [1].

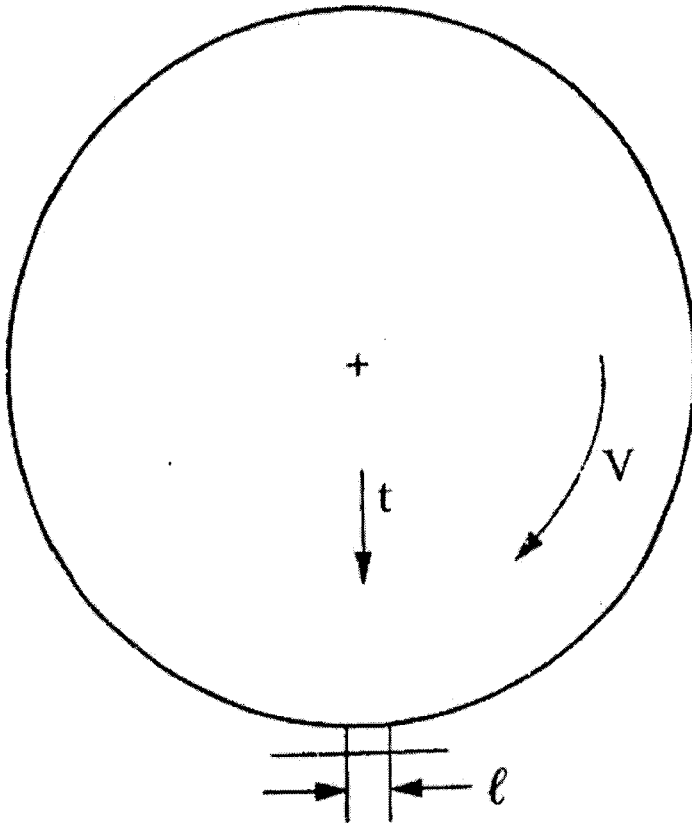


Fig. 4.1. Plunge grinding cut with wheel engaging complete area of work with downfeed t and wheel speed V [1]

In the micromilling experiments a carefully balanced 6-inch (152 cm) carbide tipped milling cutter was used with all but one of the teeth relieved so that it operated as a fly milling cutter. Horizontal and vertical forces were measured for a number of depths of cut (t) when machining the same sized surface as in grinding.

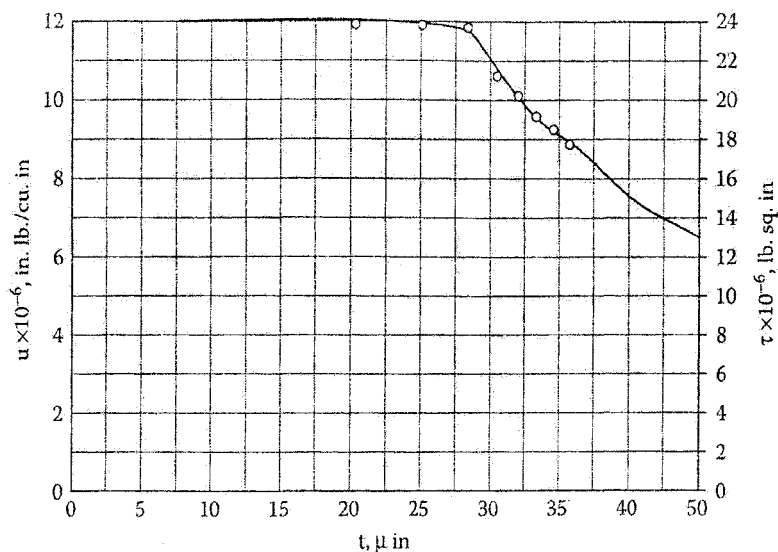


Fig. 4.2. Specific energy-depth of cut curve for grinding experiments [1]

The shear stress on the shear plane (τ) was estimated by a rather detailed method presented in Backer et al [1]. Turning experiments were performed on a 2.25-inch (5.72 cm) diameter SAE 1112 steel bar pre-machined in the form of a thin-walled tube having a wall thickness of 0.2 inch (5 mm). A zero degree rake angle carbide tool was operated in a steady-state two-dimensional orthogonal cutting mode as it machined the end of the tube. Values of shear stress on the shear plane (τ) versus undeformed chip thickness were determined for experiments at a constant cutting speed and different values of axial infeed rate and for variable cutting speeds and a constant axial infeed rate. The grinding, micromilling, and turning results are shown in Fig. 4.3.

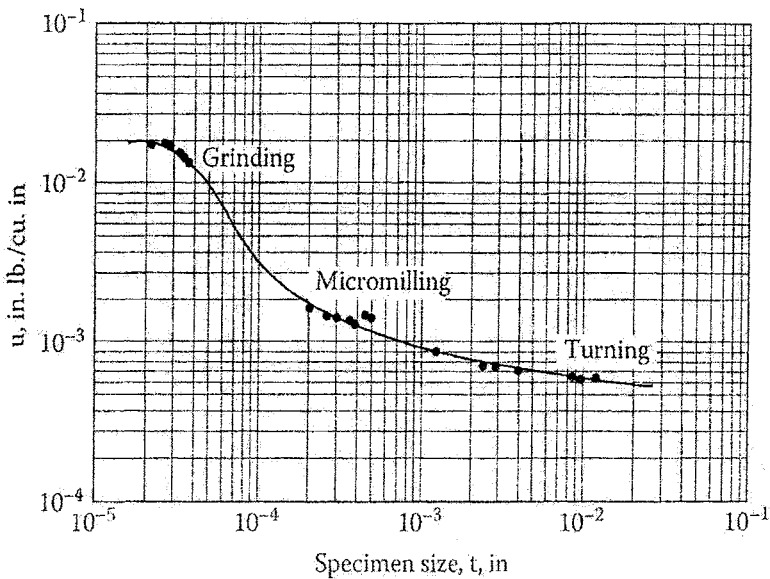


Fig. 4.3. Variation of shear stress on shear plane when cutting SAE 1112 steel [1]

A true stress-strain tensile test was performed on a 0.505-inch (1.28 cm) diameter by 2-inch (5.08 cm) gage length specimen of the same SAE 1112 steel. The mean shear stress at fracture was 22,000 psi (151.7 MPa). This value is not shown in Fig. 4.3 since it falls too far to the right.

In 1993 Dr. Nono Taniguchi was the American Society of Precision Engineers' distinguished lecturer in Seattle, WA. For his lecture, discussing the art of nanotechnology [2], Dr. Taniguchi discussed the size effect in cutting and forming and presented his version of Fig. 4.3 in Fig. 4.4, which is more complete since it includes the tensile test.

Shaw [3] discusses the origin of the size effect in metal cutting, which is believed to be primarily due to short-range inhomogeneities present in all commercial engineering metals.

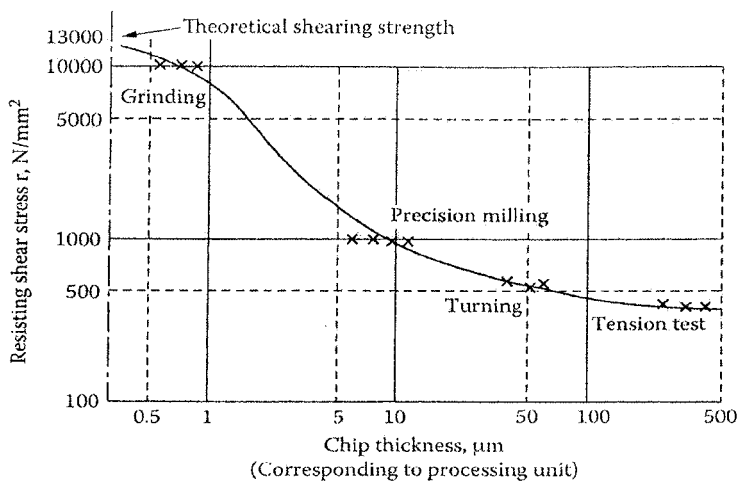


Fig. 4.4. Relationship between chip thickness and resisting shear stress for Fig. 4.3 as modified by Taniguchi [2]

When the back of a metal cutting chip is examined at very high magnification by means of an electron microscope individual slip lines are evident as shown in Fig. 4.5. In deformation studies, Heidenreich and Shockley [4] found that slip does not occur on all atomic planes but only on certain discrete planes. In experiments on deformed aluminum single crystals the minimum spacing of adjacent slip planes was found to be approximately 50 atomic spaces while the mean slip distance along the active slip planes was found to be about 500 atomic spaces as shown in Fig. 4.6. These experiments further support the observation that metals are not homogeneous and suggest that the planes along which slip occurs are associated with inhomogeneities in the metal.

Strain is not uniformly distributed in many cases. For example, the size effect in a tensile test is usually observed only for specimens less than 0.1 inch (2.5 mm) in diameter. On the other hand, a size effect in a torsion test occurs for considerably larger samples due to the greater stress gradient present in a torsion test than in a tensile test. This effect and several other related ones are discussed in detail in Shaw [3].

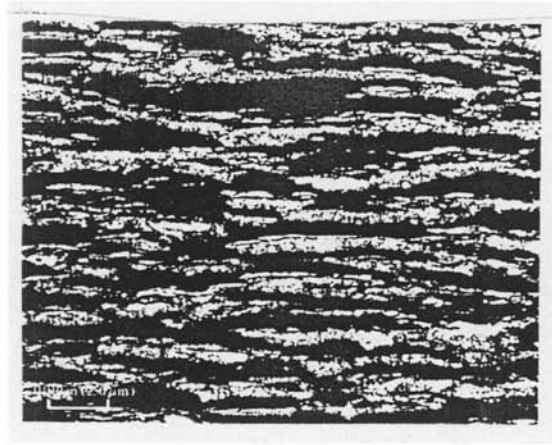


Fig. 4.5. Back free surface of chip showing regions of discontinuous strain or microfracture

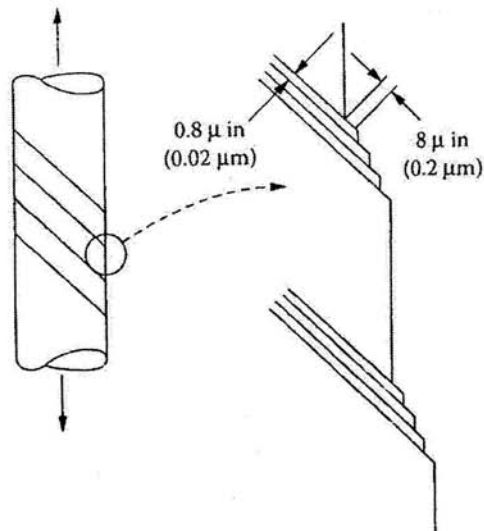


Fig. 4.6. Spacing of adjacent slip planes for pure aluminum single crystal [4]

4.2.1 Shear angle prediction

There have been many notable attempts to derive an equation for the shear angle (ϕ) shown in Fig. 4.7 for steady-state orthogonal cutting. Ernst and Merchant [5] presented the first quantitative analysis. Figure 4.8 shows forces acting on a chip at the tool point where: R = the resultant force on the tool face, R' = the resultant force in the shear plane, N_C and F_C are the components of R normal to and parallel to the tool face, N_S and F_S are the components of R' normal to and parallel to the cutting direction, F_Q and F_P are the components of R normal to and parallel to the cutting direction, and $\beta = \tan^{-1} F_C/N_C$ (is called the friction angle).

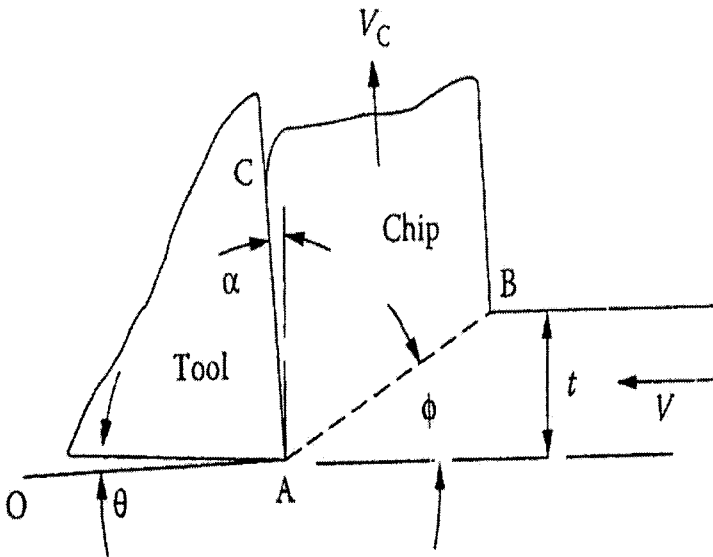


Fig. 4.7. Nomenclature for two-dimensional steady-state orthogonal cutting process

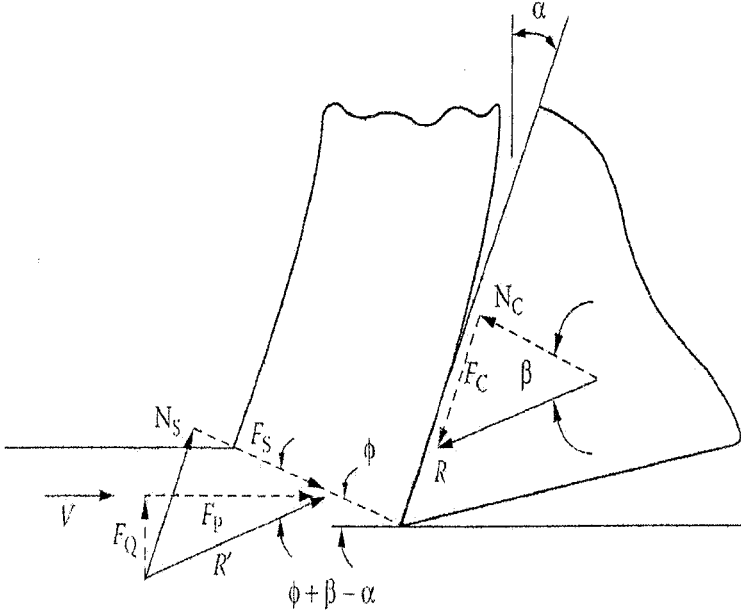


Fig. 4.8. Cutting forces at the tool tip for the cutting operation shown in Fig. 4.7

Assuming the shear stress on the shear plane (τ) to be uniformly distributed it is evident that:

$$\tau = \frac{F_s}{A_s} = \frac{R' \cos(\phi + \beta - \alpha) \sin \phi}{A} \quad (4.1)$$

Where A_s and A are the areas of the shear plane and that corresponding to the width of cut (b), times the depth of cut (t). Ernst and Merchant [5] reasoned that τ should be an angle such that τ would be a maximum and a relationship for ϕ was obtained by differentiating Eq. 4.1 with respect to ϕ and equating the resulting expression to zero. This led to:

$$\phi = 45 - \frac{\beta}{2} + \frac{\alpha}{2} \quad (4.2)$$

However, it is to be noted that in differentiating, both R' and β were considered independent of ϕ .

Merchant [6] presented a different derivation that also led to Eq. 4.2. This time an expression for the total power consumed in the cutting process was first written

$$P = F_p V = (\tau A V) \frac{\cos(\beta - \alpha)}{\sin \phi \cos(\phi + \beta - \alpha)} \quad (4.3)$$

It was then reasoned that ϕ would be such that the total power would be a minimum. An expression identical to Eq. 4.2 was obtained when P was differentiated with respect to ϕ , this time considering τ and β to be independent of ϕ . Piispanen [7] had done this previously in a graphical way. However, he immediately carried his line of reasoning one step further and assumed that the shear stress τ would be influenced directly by normal stress on the shear plane as follows:

$$\tau = \tau_0 + K_\sigma \quad (4.4)$$

Where K is a material constant. Piispanen then incorporated this into his graphical solution for the shear angle.

Upon finding Eq. 4.2 to be in poor agreement with experimental data Merchant also independently (without knowledge of Piispanen's work at the time) assumed the relationship given in Eq. 4.4, and proceeded to work this into his second analysis as follows:

From Fig. 4.8 it may be seen that

$$\sigma = \tau \tan(\phi + \beta - \alpha) \quad (4.5)$$

Or, from Eq. 4.4

$$\tau_0 = \tau + K \tau \tan(\phi + \beta - \alpha) \quad (4.6)$$

Hence

$$\tau = \frac{\tau_0}{1 - K \tan(\phi + \beta - \alpha)} \quad (4.7)$$

When this is substituted into Eq. 4.3 we have:

$$P = \frac{\tau_0 A V \cos(\beta - \alpha)}{[1 - K \tan(\phi + \beta - \alpha)] \sin \phi \cos(\phi + \beta - \alpha)} \quad (4.8)$$

Now, when P is differentiated with respect to ϕ and equated to zero (with τ_0 and p considered independent of ϕ we obtain:

$$\phi = \frac{\cot^{-1}(K)}{2} - \frac{\beta}{2} + \frac{\alpha}{2} = \frac{C - \beta + \alpha}{2} \quad (4.9)$$

Merchant called the quantity, $\cot^{-1} K$, the machining “constant” C . In Fig. 4.9 the quantity C is seen to be the angle the assumed line relating τ and ϕ makes with the τ axis.

Figure 4.10a shows the variation of shear stress on the shear plane versus compressive stress on the shear plane for a range of cutting conditions when SAE 9445 steel is turned with a carbide tool. The value of C in Eq. 4.9 is seen to be 77° to a good approximation. Fig. 4.10b shows a comparison of the experimental data based on Eqs. 4.2 and 4.9. Figure 4.11 shows similar results for SAE 4340 steel where the value of C is seen to be 80° to a good approximation. Merchant [8] has determined the values of C given in Table 4.1 for materials of different chemistry and structure being turned under finishing conditions with different tool materials. From this table it is evident that C is not a constant. Figures 4.10 and 4.11 illustrate how use of the Merchant empirical machining “constant” C

that gives rise to Eq. 4.9 with values of ϕ is in reasonably good agreement with experimentally measured values.

Table 4.1. Values of C in Eq. 4.9 for a variety of work and tool materials in finish turning without a cutting fluid

Work material	Tool material	C (Degrees)
SAE 1035 Steel	HSS*	70
SAE 1035 Steel	Carbide	73
SAE 1035 Steel	Diamond	86
AISI 1022 (lead)	HSS*	77
AISI 1022 (lead)	Carbide	75
AISI 1113 (sul.)	HSS*	76
AISI 1113 (sul.)	Carbide	75
AISI 1019 (plain)	HSS*	75
AISI 1019 (plain)	Carbide	79
Aluminum	HSS*	83
Aluminum	Carbide	84
Aluminum	Diamond	90
Copper	HSS*	49
Copper	Carbide	47
Copper	Diamond	64
Brass	Diamond	74

*HSS = High-speed steel

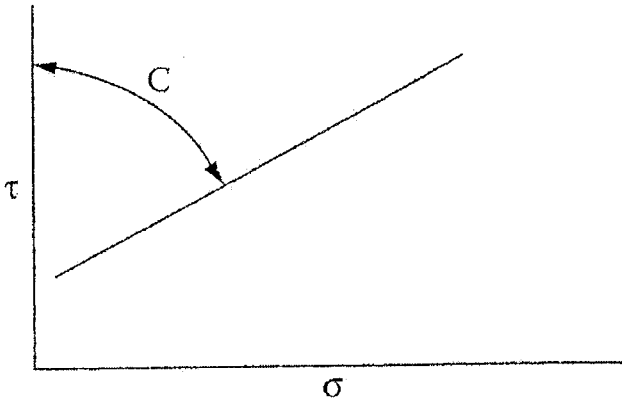


Fig. 4.9. Relationship between shear stress and normal stress on the shear plane assumed by Piispanen [7] and by Merchant independently [6,9]

While it is well established that the rupture stress of both brittle and ductile materials is increased significantly by the presence of compressive stress (known as the Mohr Effect), it is generally believed that a similar relationship for flow stress does not hold. However an explanation for this paradox with considerable supporting experimental data is presented below. The fact that this discussion is limited to steady-state chip formation rules out the possibility of periodic gross cracks being involved. However, the role of micro-cracks is a possibility consistent with steady-state chip formation and the influence of compressive stress on the flow stress in shear. A discussion of the role micro-cracks can play in steady-state chip formation is presented in the next section.

Hydrostatic stress plays no role in the plastic flow of metals if they have no porosity. Yielding then occurs when the von Mises criterion reaches a critical value. Merchant [9] has indicated that Barrett [10] found that for single crystal metals τ_s is independent of τ_s when plastics such as celluloid are cut. In general, if a small amount of compressibility is involved yielding will occur when the von Mises criterion reaches a certain value.

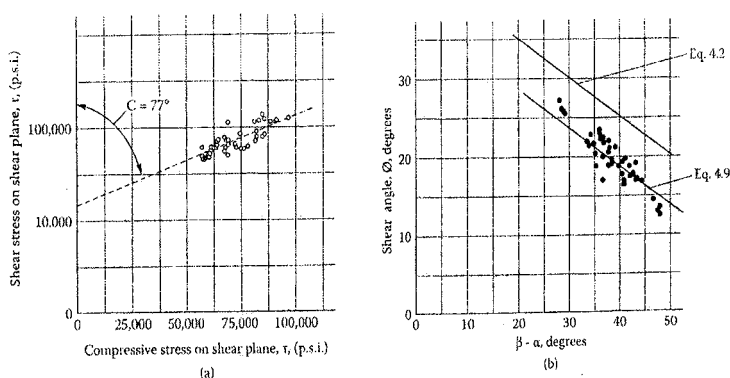


Fig. 4.10. (a) Shear stress on shear plane versus compressive stress on shear plane for SAE 9445 steel machined with carbide tool (b) Observed shear angle ϕ vs. $\beta - \alpha$ (Merchant [9])

Legend

Open points, $\alpha = +10^\circ$

Solid points, $\alpha = -10^\circ$

◦ $V = 542$ fpm (165 m min^{-1}), variable t

□ $t = 0.0018$ in. ($45.7 \mu\text{m}$), variable V

Δ $t = 0.0037$ in. ($94 \mu\text{m}$), variable V

▽ $t = 0.0062$ in. ($157 \mu\text{m}$), variable V

However, based on the results of Figs. 4.10 and 4.11 and Table 4.1 the role of compressive stress on shear stress on the shear plane in steady-state metal cutting is substantial. The fact there is no outward sign of voids or porosity in steady-state chip formation of a ductile metal during cutting and yet there is a substantial influence of normal stress on shear stress on the shear plane represents an interesting paradox. It is interesting to note that Piispanen [7] had assumed that shear stress on the shear plane would increase with normal stress and had incorporated this into his graphical treatment. This was unknown to Merchant in writing his 1942 papers since a translation of Piispanen's paper from Finnish into English became available only between the time Merchant's paper was written and when it was published.

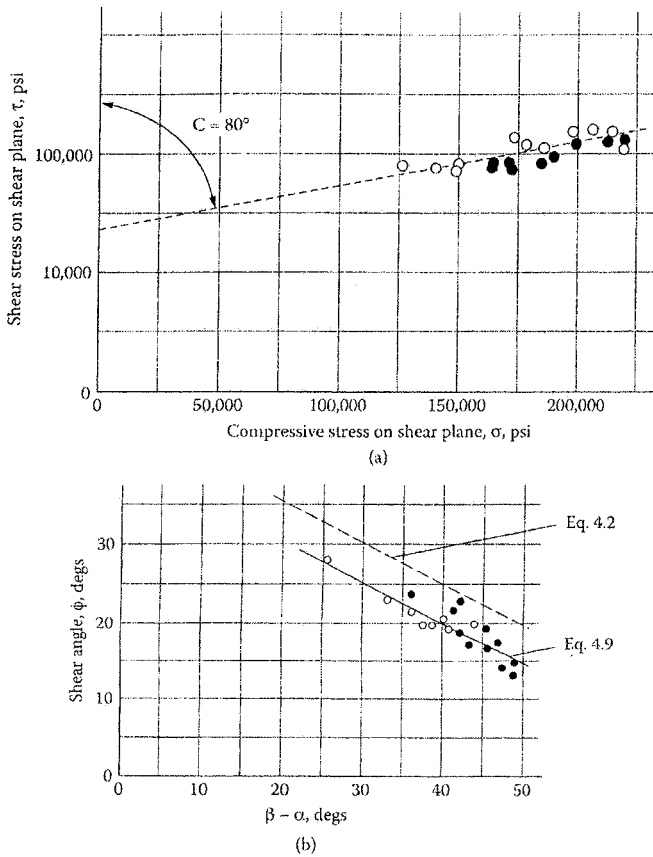


Fig. 4.11. (a) Shear stress on shear plane versus compressive stress on shear plane for SAE 4340 steel machined with tungsten carbide tool, (b) Observed shear angle ϕ vs. $\beta - \alpha$ (after Merchant [9]).

Legend

Open points, $\alpha = +10^\circ$

Solid points, $\alpha = -10^\circ$

$\phi V = 542 \text{ fpm } (165 \text{ m min}^{-1})$, variable t

$t = 0.0011 \text{ in. } (27.9 \text{ } \mu\text{m})$, variable V

4.2.2 Plastic Behavior at Large Strains

There has been remarkably little work done in the region of large plastic strains. Nobel Laureate Bridgman [11] using the hollow tubular notched specimen shown in Fig. 4.12 performed experiments under combined axial compression and torsion. The specimen was loaded axially in compression as the center section was rotated relative to the ends. Strain was concentrated in the reduced sections and it was possible to crudely estimate and plot shear stress vs. shear strain with different amounts of compressive stress on the shear plane. From these experiments Bridgman concluded that the flow curve for a given material was the same for all values of compressive stress on the shear plane, a result consistent with other materials experiments involving much lower plastic strains. However, the strain at gross fracture was found to be strongly influenced by compressive stress. A number of related results are considered in the following subsections.

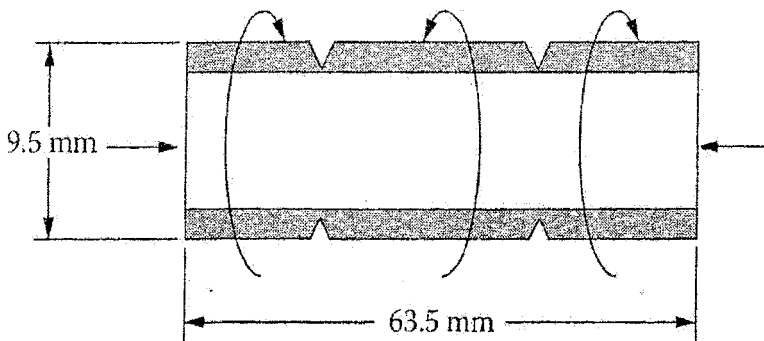


Fig. 4.12. Bridgman's 1952 specimen for combined axial load and torsion

4.2.3 Langford and Cohen's Model

Langford and Cohen [12] were interested in the behaviour of dislocations at very large plastic strains and whether there was saturation relative to the strain hardening effect with strain, or whether strain hardening continued to occur with strain to the point of fracture.

Their experimental approach was an interesting and fortunate one. They performed wire drawing on iron specimens using a large number of progressively smaller dies with remarkably low semi die angle (1.5°) and a relatively low (10%) reduction in area per die pass. After each die pass, a specimen was tested in uniaxial tension and a true stress-strain curve obtained. The drawing and tensile experiments were performed at room temperature and low speeds to avoid heating and specimens were stored in liquid nitrogen between experiments to avoid strain aging effects. All tensile results were then plotted in a single diagram, the strain used being that introduced in drawing (0.13 per die pass) plus the plastic strain in the tensile test. The result is shown in Fig. 4.13a. The general overlap of the tensile stress-strain curves gives an overall strain-hardening envelope, which indicates that the wire drawing and tensile deformations are approximately equivalent relative to strain hardening. Figure 4.13b shows similar results on the same iron wire tested in uniaxial compression following drawing [13].

Figure 4.13c shows somewhat similar results obtained earlier by Blazynski and Cole [14] for AISI 1012 steel carried to much lower values of total strain. Blazynski and Cole were interested in strain hardening in tube drawing and tube sinking. Drawn tubes were sectioned as shown in Fig. 4.13d and tested in plane strain compression as shown in Fig. 4.13e. Fig. 4.13c shows the flow stress in compression plotted against the total strain. The curves in Fig. 4.13c were obtained using graphite grease as a lubricant in the plane strain experiments while the data points were obtained in similar experiments using a more effective molybdenum disulfide lubricant. The smooth curve drawn through the molybdenum disulfide data points constitutes the flow curve essentially in the absence of friction.

Up to a strain of about 1 (Fig. 4.13 (a), (b) and (c)) the usual strain-hardening curve was obtained that is in good agreement with the generally accepted equation

$$\sigma = \sigma_1 \varepsilon^n \quad (4.10)$$

However, beyond a strain of 1, the curve was linear corresponding to the equation

$$\sigma = A + B\varepsilon, (\varepsilon > 1) \quad (4.11)$$

Where A and B are constants. It may be shown that

$$A = (1 - n) \sigma_1 \quad (4.12)$$

$$B = n \sigma_1 \quad (4.13)$$

In order that the curves of Eqs. 4.10 and 4.11 have the same slope and ordinate at $\varepsilon = 1$.

While Eq. 4.10 is well known and widely applied there is relatively little data in the literature for plastic strains greater than 1 and hence Eq. 4.11 is relatively unknown. From transmission electron micrographs of deformed specimens, Langford and Cohen found that cell walls representing concentrations of dislocations began to form at strains below 0.2 and became ribbon shaped with decreasing mean linear intercept cell size as the strain progressed. Dynamic recovery and cell wall migration resulted in only about 7 percent of the original cells remaining after a strain of 6. The flow stress of the cold-worked wires was found to vary linearly with the reciprocal of the mean transverse cell size.

Data that make one question the wisdom of extrapolating ordinary materials test data into the larger strain regime of metal cutting are given in Fig. 4.14.

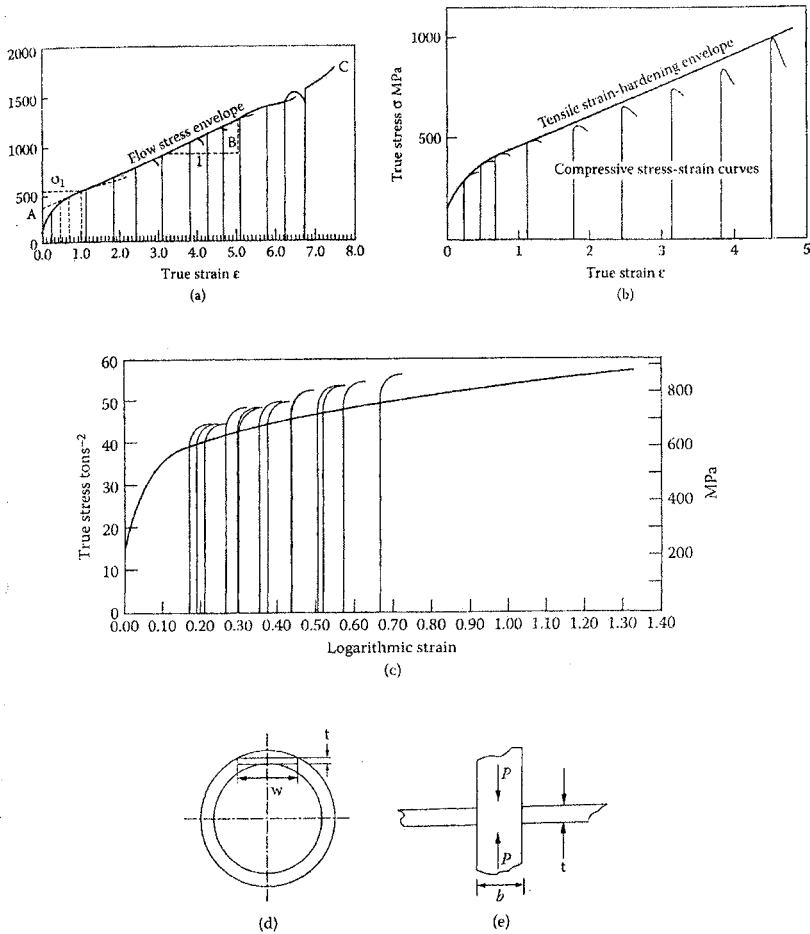


Fig. 4.13. (a) Effect of wire drawing strain on uniaxial stress-strain curve (corrected for necking) of furnace cooled iron (0.007 w/o C) drawn and tested at room temperature. (after Langford and Cohen [12]). (b) Uniaxial compression test data following wire drawing of same materials (tested in tension following drawing) shown in a). (c) Plane strain compression experiments following tube drawing of AISI 1012 steel. Curves with hooks at top are with graphite lubricant while data points are for a more effective molybdenum disulfide lubricant [14]. (d) How plane strain specimen was removed from drawn tube by Blazynski et al [14] tube diameter was approximately 55 mm, wall thickness 4.8 mm. (e) Plane strain compression test used by Blazynski et al [14] following tube drawing. $t = 0.045$ in. (1.14 mm); $b = 0.115$ in. (2.92 mm), w (perpendicular to paper = 0.690 in. (17.53 mm))

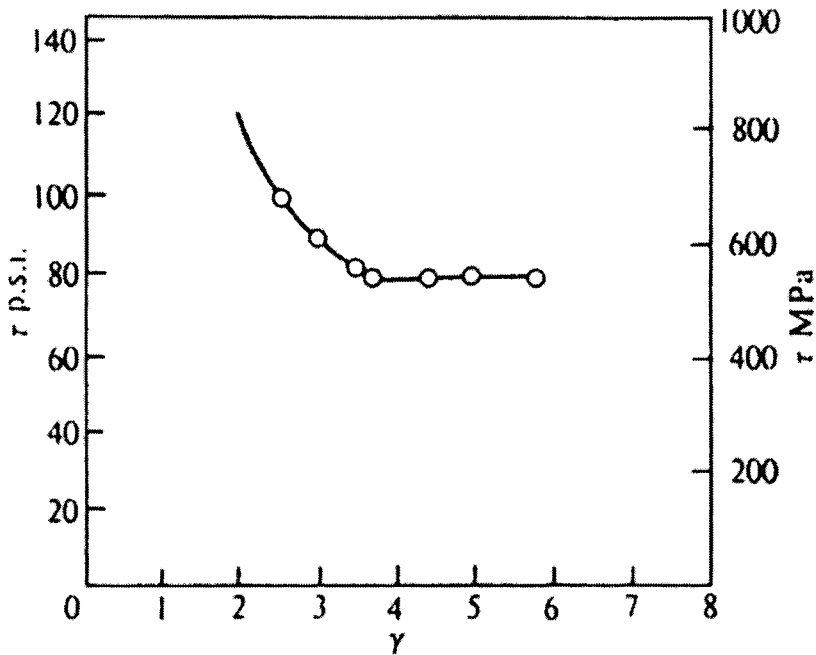


Fig. 4.14. Values of shear stress on shear plane versus shear strain in chip when cutting the same material with tools of different rake angle [15]

These are data for the same material cut under the same conditions except for rake angle (α). The shear stress on the shear plane is obviously not constant but appears to decrease with increase in shear strain (negative strain hardening).

4.2.4 Walker and Shaw's Model

Toward the end of the 1960s Professor M. C. Shaw decided to conduct an acoustical emission study of concentrated shear at Carnegie-Mellon University. The initial acoustical studies were on specimens of the Bridgman type but fortunately, lower levels of axial compressive stress than Bridgman had used were employed in order to more closely simulate the concentrated shear process of metal cutting. The apparatus used that was capable of measuring stresses and strains as

well as acoustic signals arising from plastic flow is described in the dissertation of T. J. Walker [16]. Two important results were obtained:

1. A region of rather intense acoustical activity occurred at the yield point followed by a quieter region until a shear strain of about 1.5 was reached. At this point there was a rather abrupt increase in acoustical activity that continued to the strain at fracture which was appreciably greater than 1.5.

2. The shear stress appeared to reach a maximum at strain corresponding to the beginning of the second acoustical activity ($\gamma \approx 1.5$)

The presence of the notches in the Bridgman specimen (Fig. 4.12) made interpretation of stress-strain results somewhat uncertain. Therefore, a new specimen was designed (Fig. 4.15) which substitutes simple shear for torsion with normal stress on the shear plane. By empirically adjusting distance Δx (Fig. 4.15) to a value of 0.25 mm it was possible to confine all the plastic shear strain to the reduced area, thus making it possible to readily determine the shear strain ($\gamma \approx \Delta y / \Delta x$). When the width of minimum section was greater or less than 0.25 mm, the extent of plastic strain observed in a transverse micrograph at the minimum section either did not extend completely across the 0.25 mm dimension or beyond this width.

A representative set of curves is shown in Fig. 4.16 for re-sulfurised low carbon steel. Similar results were obtained for non-re-sulfurised steels and other ductile metals. There is little difference in the curves for different values of normal stress on the shear plane (σ) to a shear strain of about 1.5.

This is in agreement with Bridgman. However, beyond this strain the curves differ substantially with compressive stress on the shear plane. At large strains (τ) was found to decrease with increase in (γ), a result that does not agree with Bridgman [11]. When the results of Fig. 4.13a and 4.16 are compared they are seen to be very different. In the case of Fig. 4.13a strain hardening is positive to normal strains as high as 7. In the case of Fig. 4.16 strain hardening becomes negative above a particular shear strain that increases with normal stress on the shear plane.

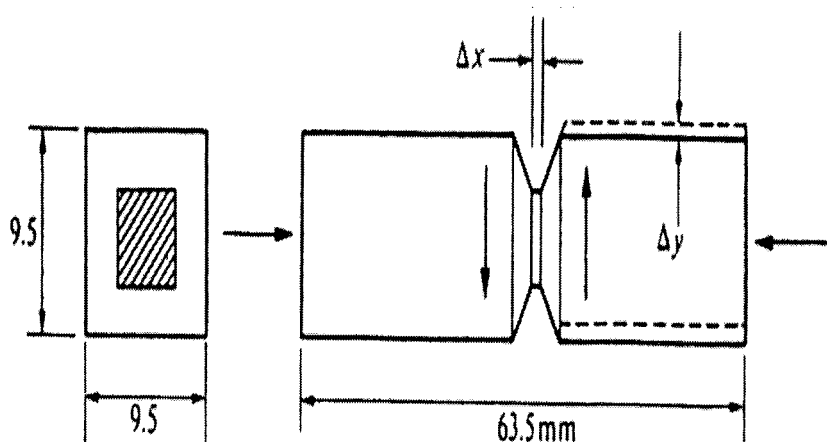


Fig. 4.15. Plane strain simple shear-compression specimen of Walker and Shaw [17]

From Fig. 4.16 it is seen that for a low value of normal stress on the shear plane of 40 MPa strain hardening appears to be negative at a shear strain of about 1.5; that is, when the normal stress on the shear plane is about 10% of the maximum shear stress reached, negative strain hardening sets in at a shear strain of about 1.5. On the other hand, strain hardening remains positive to a normal strain of about 8 when the normal stress on the shear plane is about equal to the maximum shear stress (note curve for $\sigma = 497$ MPa in Fig. 4.16).

4.2.5 Usui's Model

In Usui et al [18] an experiment is described designed to determine why CCl_4 is such an effective cutting fluid at low cutting speeds. Since this also has a bearing on the role of microcracks in large strain deformation, it is considered here.

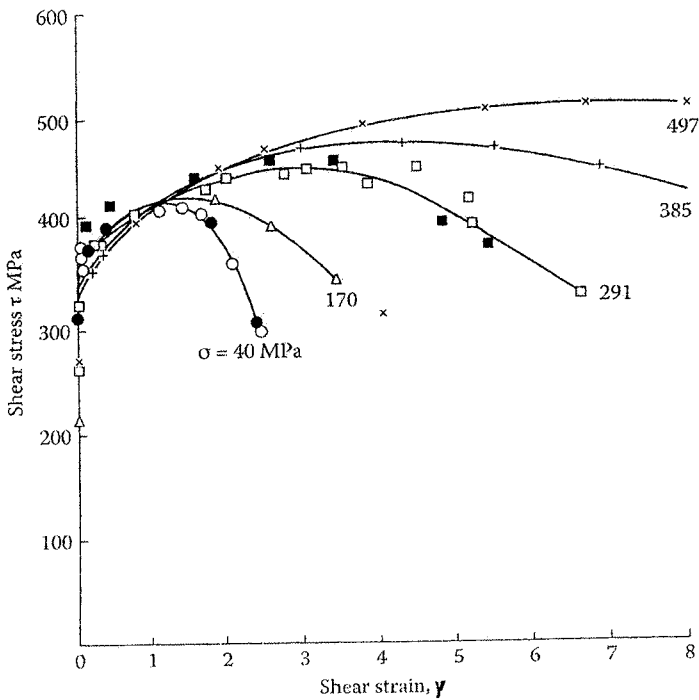


Fig. 4.16. Shear stress-shear strain results for resulfurized low carbon steel for specimen of Fig. 4.15 [17]

A piece of copper was prepared as shown in Fig. 4.17. The piece that extends upward and appears to be a chip is not a chip but a piece of undeformed material left there when the specimen was prepared. A vertical flat tool was then placed precisely opposite the free surface as shown in Fig. 4.17 and fed horizontally. Horizontal F_P and vertical F_Q forces were recorded as the shear test proceeded. It was expected that the vertical piece would fall free from the lower material after the vertical region had been displaced a small percentage of its length. However, it went well beyond the original extent of the shear plane and was still firmly attached to the base. This represents a huge shear strain since the shear deformation was confined to a narrow band. When a single drop of CCl_4 was placed at A in Fig.

4.17 before the shear test was conducted the protrusion could be moved only a fraction of the displacement in air before gross fracture occurred on the shear plane. Figure 4.18 shows photomicrographs of experiments without and with CCl_4 . It is apparent that CCl_4 is much more effective than air in preventing microcracks from re-welding.

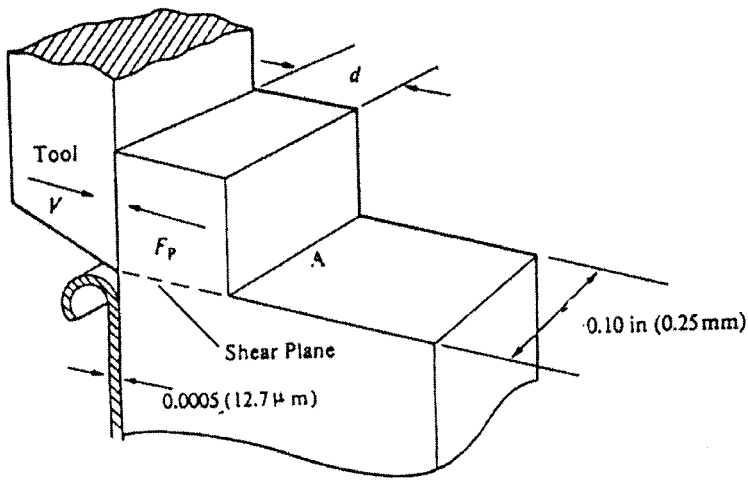


Fig. 4.17. Special shear test arrangement [18]

4.2.6 Saw Tooth Chip Formation in Hard Turning

Saw tooth chip formation for hard steel discussed in Vyas and Shaw [19] is another example of the role microcracks play. In this case gross cracks periodically form at the free surface and run down along the shear plane until sufficient compressive stress is encountered to cause the gross crack to change to a collection of isolated microcracks.

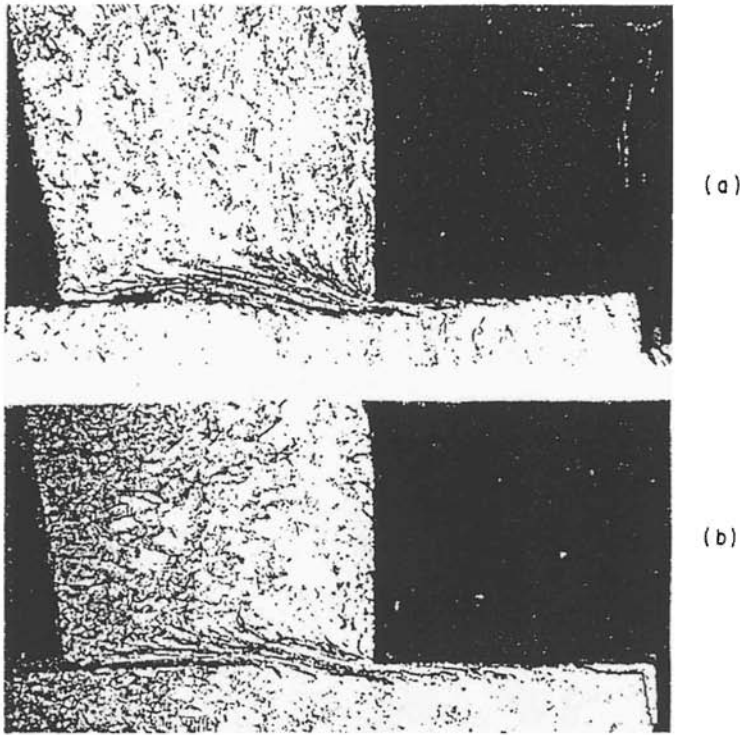


Fig. 4.18. Photomicrographs of specimens that have been sheared a distance approximately equal to the shear plane length: (a) in air; and (b) with a drop of CCl_4 applied at point A shown in Fig. 4.17

4.2.7 Fluid-Like Flow in Chip Formation

At the General Assembly of the International Institution for Production Engineering Research (CIRP) in 1952, an interesting paper was presented by Eugene [20]. Figure 4.19 shows the apparatus he used. Water was pumped into baffled chamber A that removed eddy currents and then caused flow under gravity past a simulated tool at B.

Powdered bakelite was introduced at C to make the streamlines visible as the fluid flowed past the tool. The photographs taken by the camera at D were remarkably similar to quick stop photomicrographs of actual chips. It was thought by this author at the time that any similarity between fluid flow and plastic flow of a solid was not to be expected. That was long before it was clear that the only logical explanation for the results of Bridgman and Merchant involve microfracture [21].

At the General Assembly of CIRP 47 years later, a paper was presented that again suggests that metal cutting might be modeled by a fluid [22]. However, this paper was concerned with ultraprecision machining (depths of cut $< 4\text{ }\mu\text{m}$) and potential flow analysis was employed instead of the experimental approach taken by Eugene.

It is interesting to note that chemists relate the flow of liquids to the migration of vacancies (voids) just as physicists relate ordinary plastic flow of solid metals to the migration of dislocations. Henry Eyring and co-workers [24-26] have studied the marked changes in volume, entropy and fluidity that occur when a solid melts. For example, a 12% increase in volume accompanies melting of Argon, suggesting the removal of every eighth molecule as a vacancy upon melting. This is consistent with X-ray diffraction of liquid argon that showed good short-range order but poor long-range order. The relative ease of diffusion of these vacancies accounts for the increased fluidity that accompanies melting. A random distribution of vacancies is also consistent with the increase in entropy observed on melting. Eyring's theory of fluid flow was initially termed the "*hole theory of fluid flow*" but later "*The Significant Structure Theory*" which is the title of the Eyring-Jhon book [25].

According to this theory the vacancies in a liquid move through a sea of molecules. Eyring's theory of liquid flow is mentioned here since it explains why the flow of a liquid approximates the flow of metal passed a tool in chip formation. In this case microcracks (voids) move through a sea of crystalline solid.

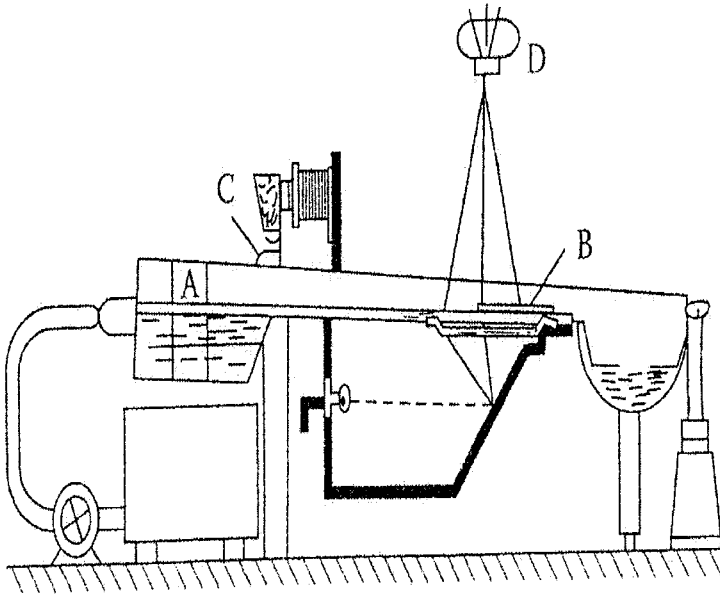


Fig. 4.19. Apparatus used by Eugene [20] to photograph flow paths passed tools having different rake angles

4.2.8 Kececioglu's Models

Kececioglu has presented several papers that illustrate the difficulty of predicting the mean shear stress on the shear plane in steady-state chip formation [26-28]. The last of these builds on the others and is most important relative to modeling being discussed here. Based on a large number of dry cutting experiments on AISI 1015 steel tubing having a hardness of 118 Brinell and using a steel cutting grade of carbide, Kececioglu concluded that the mean shear stress on the shear plane depends upon the following variables:

- mean normal stress on the shear plane (σ_s)
- the shear volume of the shear zone (e)
- the mean strain rate in the shear plane ($\dot{\gamma}$)
- the mean temperature of the shear plane (θ_s)
- the degree of strain hardening in the work before cutting

If this were not complicated enough it is clear from Kececioglu's experimental results that these items do not act independently (i.e., the influence of a high normal stress on the shear plane on shear stress on the shear plane depends upon the combination of other variables pertaining). This is an important result since it means that in general it is not possible to extrapolate materials test values of shear stress to vastly different cutting conditions.

It is interesting to note that Kececioglu suggests that the specific energy should be related to the shear plane area (e) instead of (t) as in most treatments of metal cutting mechanics. The shear plane area is

$$e = b(t/\sin\phi) \Delta y \text{ (in}^3 \text{ or mm}^3\text{)} \quad (4.14)$$

This appears to be a useful suggestion. In both cases the inverse relation between u and t or e is due to the greater chance of encountering a stress-reducing defect as t or e increases. The use of e instead of t is a more general although more complex way of expressing the "size effect". The range of values covered by Kececioglu in his orthogonal experiments on AISI 1015 steel were as follows:

- rake angle: -10 to +37 degrees
- undeformed chip thickness (t): 0.004 to 0.012 in (0.2 to 0.3 mm)
- cutting speed (V): 126 to 746 fpm (38.4 to 227.4 m/min)
- inclination angle (i): 0 to 35 degrees

This resulted in the following wide range of dependent variables:

- width of shear zone : 0.002 to 0.007 inch (0.10 to 0.18 mm)

- rate of strain : 20,000 to 40,000 s⁻¹
- mean shear stress on shear plane (τ_s) 62,000 to 84,000 psi (427.5 to 579.2 MPa)
- mean normal stress on shear plane: 1,000 to 12,000 psi (6.9 to 83 MPa)
- mean shear plane temperature : 410 to 840 F (210 to 449°C)

Figure 4.20a shows considerable scatter of the variation of shear stress with normal stress due to the fact that the effect of changing one independent variable on shear stress depends upon a combination of the other variables as well. Figure 4.20b shows the variation of the mean value of shear stress for a group of points in Fig. 4.20a in the vicinity of the value of normal stress plotted in Fig. 4.20b. This indicates, on average, that shear stress increases with an increase in normal stress. This is consistent with the view that under the very high strains involved in metal cutting (a mean value of about 3.5 in Kececioglu's experiments) localized microcracks are likely to form on the shear plane and an increase in normal stress should decrease their number and give rise to an increase in shear stress on the shear plane.

Figures 4.21a and b show similar results for the mean shear stress on the shear plane versus the volume of the shear zone (e). This shows clearly that in general a decrease in the shear zone volume causes an increase in the shear stress on the shear plane, particularly for shear volumes below 10^{-5} in³. Figure 4.22 shows results for the mean shear stress on the shear plane versus the shear strain for the experiments of Figs. 4.20 and 4.21. This yields the unusual result that the shear stress decreases with increase in strain, which is not consistent with ordinary materials test results that involve strain hardening. The reason for this paradox is due to the fact that in addition to strain several other variables are involved and the net effect is a decrease in shear stress with shear strain.

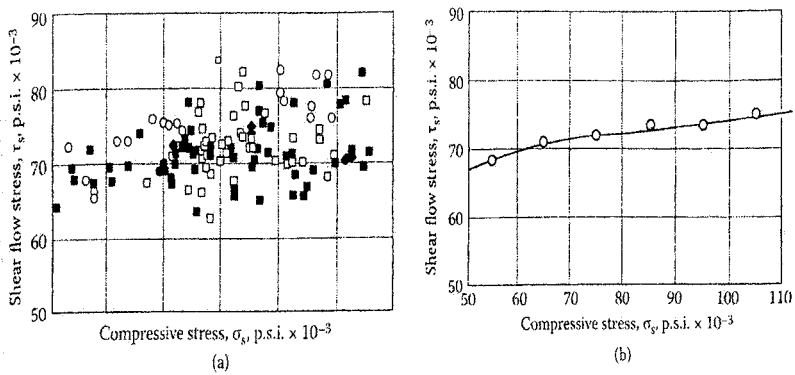


Fig. 4.20. Variation of shear stress on the shear plane with normal stress on the shear plane. (a) for 43 experiments involving a wide range of rake angle, cutting speed, undeformed chip thickness, and inclination angle, (b) mean values of shear stress on the shear plane for values of normal stress indicated [28]

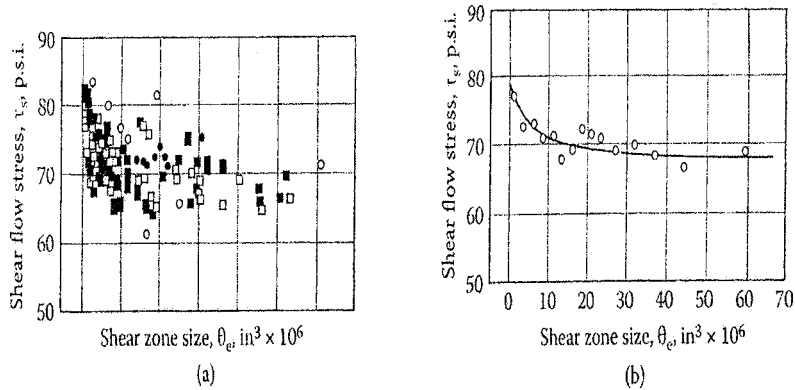


Fig. 4.21. Variation of shear stress on shear plane with shear zone volume (a) for 43 experiments involving a wide range of rake angle, cutting speed, undeformed chip thickness, and inclination angle, (b) mean values of shear stress on the shear plane for values of shear volume close to the values of e indicated [28]

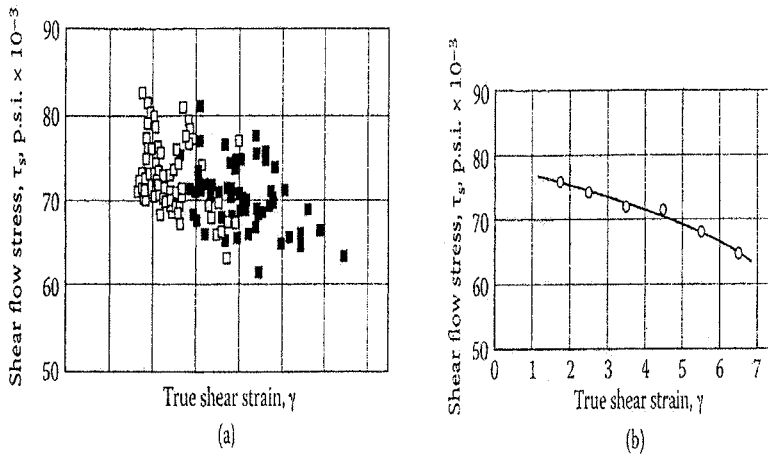


Fig. 4.22. Variation of shear stress on the shear plane with shear strain on a shear plane, (a) for 43 experiments involving a wide range of rake angle, cutting speed, undeformed chip thickness, and inclination angle, (b) mean values of shear stress on the shear plane for values of shear strain (γ) close to the values of shear strain (γ) indicated [28]

4.2.9 Zhang and Bagchi's Model

Zhang and Bagchi have presented a valuable analysis of the chip separation problem in FEM in terms of microfracture mechanics. This is based on the fact that ductile metals fail in three steps: nucleation, growth, and coalescence of microvoids that initiate at points of stress concentration [29]. Figure 4.23 illustrates how the three steps lead to gross fracture in shear. Figure 4.24 shows a random distribution of defects (points of stress concentration) in a ductile metal chip. As the work material approaches a stationary tool defects along the x -axis in the cutting direction are subjected to an increasing stress. This leads to nucleation of a void at A in Fig. 4.24a, growth as the void moves to B in Fig. 4.24b and coalescence with the tool as shown in Fig. 4.24c.

Zhang and Bagchi [30] suggest that voids approaching the tool tip grow but do not coalesce before reaching the tool tip. This is im-

portant since coalescence would lead to a gross crack extending in front of the tool tip and this is never observed experimentally even when hard materials are machined. Zhang and Bagchi [30] have applied the continuum model for void nucleation of Argon et al. [31]. It is assumed that separation occurs when the leading void reaches its maximum size.

The theory presented by Zhang and Bagchi based on the presence of points of stress concentration, formation of microvoids, void growth and void coalescence within the tool tip offers a very reasonable explanation for the flow separation problem involved when FEM is applied to metal cutting chip formation. Figure 4.25 shows a diagram equivalent to Fig. 4.24 including action along the shear plane. Here the material in the shear plane is subjected to very large strains and any points of stress concentration should be expected to give rise to microcracks instead of microvoids. In the presence of relatively high normal stress on the shear plane and the absence of a contaminating film such as CCl_4 vapor, these microcracks will reweld after moving a relatively short distance. Also, because of the very high strains associated with the shear plane a very much higher density of microcracks will be involved than the density of microvoids involved in the un-deformed work material of Fig. 4.24.

Based on the discussion presented it is concluded that microcracks usually play an important role in steady-state metal cutting chip formation because of the unusually large strains involved. Also, there is considerable experimental evidence that normal stress on the shear plane has a substantial influence on shear stress on the shear plane. Both of these rule out use of the von Mises criterion in metal cutting modeling except as a very rough approximation.

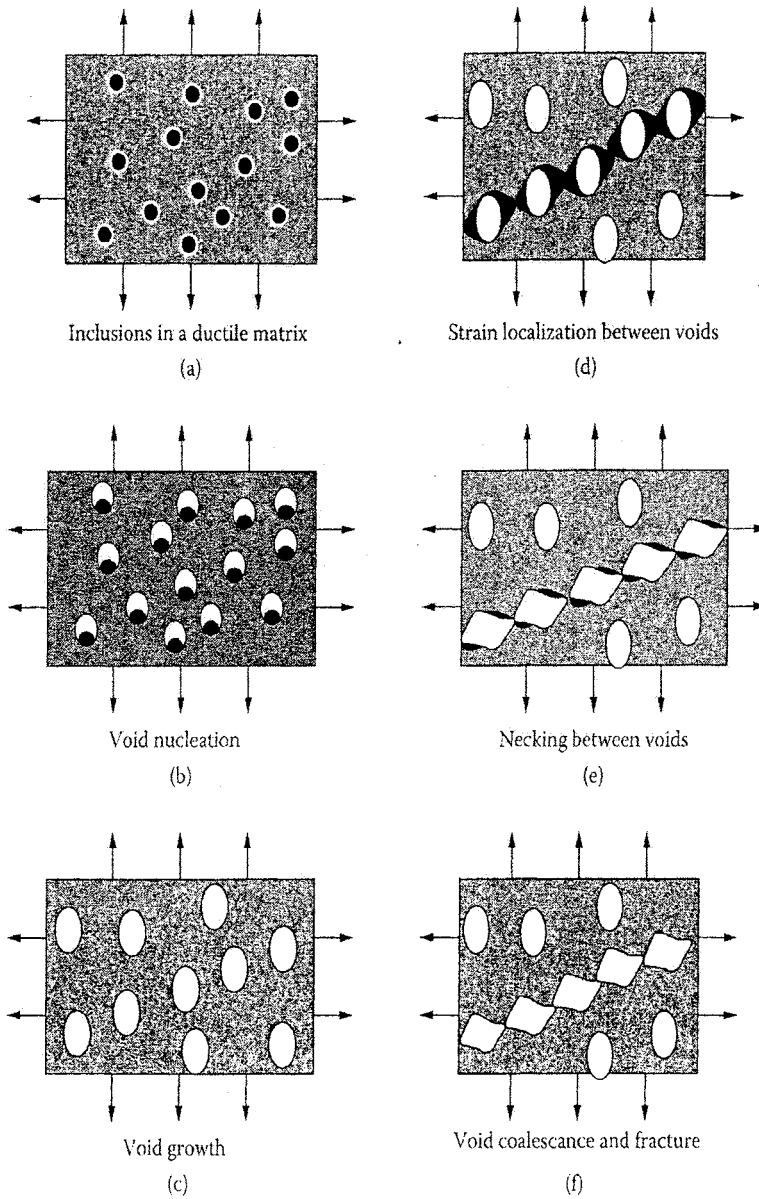


Fig. 4.23. Void nucleation, growth, and coalescence in ductile metals [29]

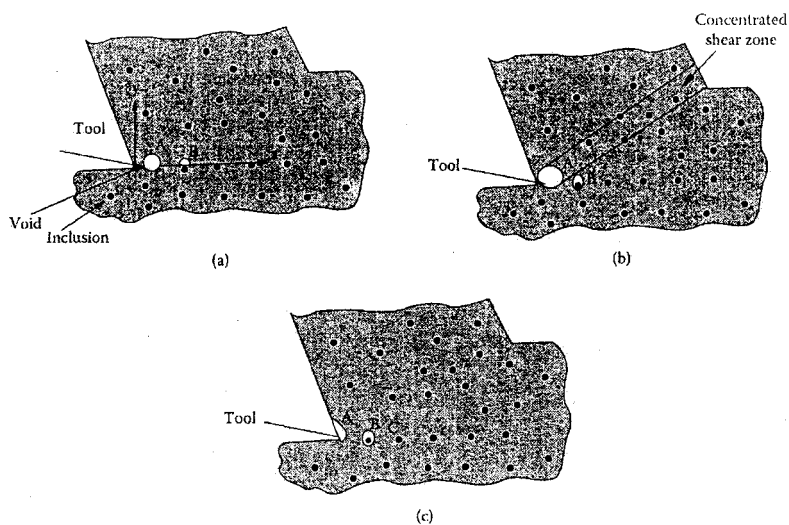


Fig. 4.24. Chip separation based on microstructure mechanics [30]

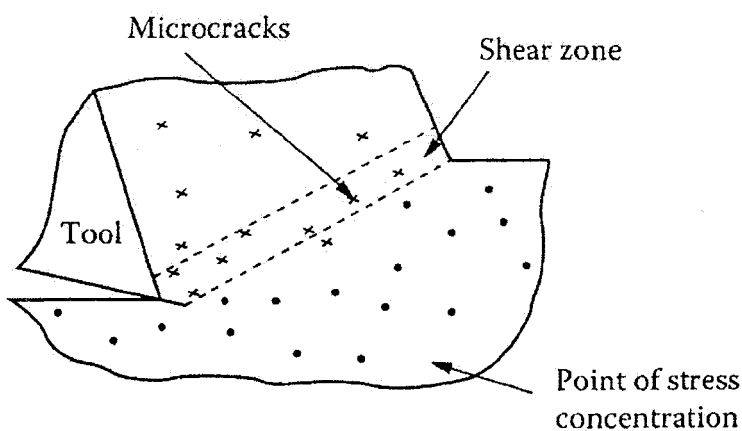


Fig. 4.25. Chip formation involving transport of microcracks across the shear plane by formation, displacement and re-welding.

4.3 Mechanism for Large Plastic Flow

It is seen that whereas the Bridgman and Langford and Cohen results are in agreement, these results are completely different from those of Walker and Shaw [17]. A proposed mechanism of large strain plastic flow [21] suggests that at moderate values of normal stress on the shear plane discontinuous microcracks begin to appear in a plane of concentrated shear at a shear strain of about 1.5. As strain proceeds beyond this point the first microcracks are sheared shut as new ones take their place. The sound area on the shear plane gradually decreases until it becomes insufficient to resist the shear load without gross fracture. What seems to be negative strain hardening in Fig. 4.16 is due to what might be described as “internal necking” (i.e., a gradual decrease in sound internal area with load just as the area in the neck of a tensile specimen decreases with load to give the appearance of negative strain-hardening in an engineering stress-strain curve).

The reason such “negative strain hardening” was not observed by Bridgman [11], or by Langford and Cohen [12], appears to be due to the normal compressive stress on the shear plane in their experiments being high enough to prevent the formation of microcracks. The choice of a die angle (only 1.5 degree half angle) and a reduction per pass (0.22) in the Langford and Cohen drawing experiments provides essentially homogeneous compressive strain in the deformation zone and under such conditions, one would not expect microcracks to develop. There is considerable indirect evidence to support the formation of microcracks in metal cutting. While it has been reported [32] that microcracks have been observed on the shear plane of quick-stop chip roots, one should not expect to find many. Such cracks will be very small and most of them would be expected to coalesce as the specimen is suddenly unloaded.

The new theory of plastic flow discussed here is an addition to dislocation theory. As long as microcracks do not occur in appreciable number, a material may be deformed to very large strains with a continuous increase in dislocation density and strain hardening. This is consistent with the experimental results of Bridgman [11] and Langford and Cohen [12]. However, at a particular value of shear

strain, depending upon the ductility of the material and the normal stress on the shear plane, microcracks will begin to form. If the normal stress on the shear plane is tensile, these cracks will spread rapidly over the shear surface leading to gross fracture. If, however, a moderate compressive stress (for example $\frac{1}{2}$ the shear flow stress for a ductile metal) is present on the shear plane, the new mechanism will pertain. When this occurs there will be an extended stress-strain region exhibiting a decrease in flow stress with strain as the ratio of real to apparent area on the shear plane (A_R/A) decreases from one to the critical value at which gross fracture occurs.

It is suggested that in metal cutting the shear stress on the shear plane is not independent of normal stress on the shear plane. That part of the shear plane that involves microcracks should show an increase in shear stress with normal stress, as Piispanen and Merchant suggested. However, the part that does not involve microcracks should have a shear stress that is independent of normal stress in keeping with the experimental results of Bridgman and Langford and Cohen.

It should not be inferred that the foregoing discussion has brought us any nearer to the solution of the shear angle problem. It should, however, serve to further explain why it is unlikely that a simple solution to this persistent problem is to be found.

4.4 Inhomogeneous Microstrains

When metallic single crystals are plastically deformed as previously stated it is found that slip does not occur uniformly on every atomic plane but that the active slip planes are relatively far apart (Fig. 4.6). It is further found that polycrystalline metals also strain blockwise rather than uniformly. Crystal imperfections are responsible for this inhomogeneous behaviour.

When the volume of material deformed at one time is relatively large, there will be a uniform density of imperfections and for all practical purposes, strain (and strain hardening) may be considered to be uniform. However, as the volume deformed approaches the

small volume associated with an imperfection, the material will show obvious signs of the basic inhomogeneous character of strain. The mean flow stress will rise and the ends of the active shear planes will be evident in a free surface as in Fig. 4.5. This is called the size effect.

In metal cutting, the undeformed chip thickness (t) is small, the width of shear zone (Δy) is very small but the width of cut (b) is relatively large. It would thus appear that the volume deformed at one time would be $(bt \Delta y / \sin \phi)$. However, when the back of a continuous chip is observed under the microscope it is found (Fig. 4.5) that the edges of the slip bands that are observed are not continuous across the width of the chip but have an extent characteristic of the imperfection spacing (a). Thus, the volume deformed at any one time should be taken to be $(bt \Delta y / \sin \phi)$ where $a \ll b$. In metal cutting this volume will approach a^3 (mean imperfection volume) and there will be a size effect. This is the main reason specific energy (u) increases with decrease in undeformed chip thickness (t).

Under ordinary conditions, the shear planes will be very closely spaced corresponding to the closeness of spacing of the weak spots in the metal. It may be assumed that slip planes are so spaced that a single weak spot is present on each plane. Drucker [33] has employed a random array of weak points to qualitatively demonstrate the increase in unit cutting energy with decrease in depth of cut. However, in much as the spacing of weak points is very small compared with the usual depths of cut, an orderly array of weak spots seems justified. The dots shown in Fig. 4.26 represent such an orderly arrangement of weak points to an exaggerated scale. These points have a uniform spacing of a unit in each direction.

Let P_1 and P_2 be two shear planes making an angle ϕ with the direction of cut and passing through adjacent points in the first row below the surface. If the depth of cut is t , then t/a planes may be placed between those at P_1 and P_2 such that a single plane passes through each weak spot in the layer in the process of being cut. The number of planes per unit distance in a direction perpendicular to the shear plane will be:

$$n = \frac{t}{a(a \sin \phi)} \quad (4.15)$$

Or the spacing of successive planes is

$$\Delta y = \frac{a^2 \sin \phi}{t} \quad (4.16)$$

The total slip on a given shear plane will be:

$$x = \frac{z^2 \sin \phi}{t} \gamma \quad (4.17)$$

Where y is the unit uniform strain. Assuming a normal stress on the shear plane that is sufficient to suppress microcrack formation as in the Langford and Cohen experiments [12], the flow stress should vary with strain as given by Eq. 4.10. However, beyond this strain Eq. 4.11 will pertain giving rise to a source of displacement due to the formation, transport, and re-welding of microcracks in addition to strain due to dislocations.

4.5 Origins of the Size Effect

It is appropriate at this point to mention that an alternative explanation for the increase in hardness that occurs when the indentation size is reduced in metals has recently been introduced [34-38]. This is based on the fact that there is an increase in the strain gradient with reduction in indentation size. This has been extended by Dinesh et al [39] to explain the size effect in machining. In the Dinesh et al [39] analysis the size effect in hardness is related to that in cutting by assuming the von Mises criterion is applicable. Based on the experiments of Merchant, it is evident that this is not applicable in steady-state chip formation.

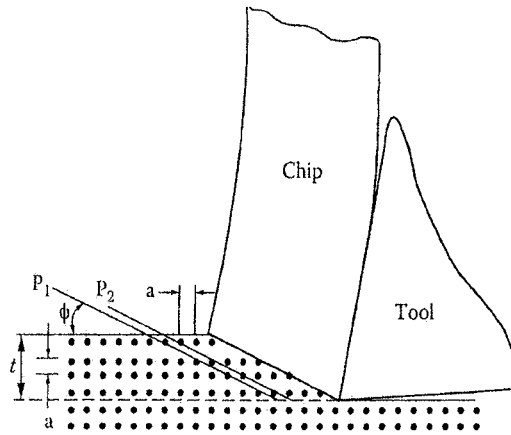


Fig. 4.26. A specimen with uniform distribution of points of stress concentration [15]

In this strain gradient theory two types of dislocations are proposed: geometrically necessary dislocations (ρ_g) that are responsible for work hardening and statistically stored dislocations (ρ_s) that are affected by a strain gradient. When $\rho_g \gg \rho_s$ conventional plasticity pertains (strain rate unimportant) but when $\rho_g \ll \rho_s$ a constitutive equation including strain rate should be included.

The impression one obtains in reading Dinesh et al [39] is that the strain gradient approach is uniquely responsible for the size effect in cutting. In their concluding remarks it is suggested that it should be possible to verify the validity of the strain rate formulation by experiments designed to test predictions of this approach. This has not yet been done and until it is it will not be possible to determine whether the influence of strain rate is significant in the chip formation application. In any case, it is believed the explanation presented here based on the influence of defects and normal stress on the shear plane is sufficiently well supported by the experiments described that it should not be considered insignificant.

4.6 Meso-Micromachining Processes

There is already a growing trend to develop microcutting processes whose effectiveness may be curtailed because of the size effect. At present, these processes are in an embryonic phase of development. These processes offer the ability to machine engineering materials other than silicon for use in MEMS components. The overall development of these miniature machine tools will clearly be affected by the nature of machining at the microscale and the size effect. The physical processes that are of secondary importance at the conventional scale dominate at the microscale. Examples include the size of the cutting tool being smaller than the individual grains in the material being machined, the resulting large cutting tool edge radius producing very large plowing forces, and the reduced stiffness of the tool rendering very pronounced dynamic effects at the microscale. These effects will result in the development of: (a) mechanistic models for multi-phase materials; (b) molecular dynamic models of chip formation in milling; and (c) micro drilling dynamic models.

4.6.1 Mechanistic Model Development for Multi-Phase Materials

A mechanistic force model for the micro milling of multi-phase materials has been developed [40]. The model considers the various phases in a material, for instance, ductile iron is composed of ferrite, graphite, and pearlite. Secondary and tertiary phases are modeled as spheres in determining the magnitude and size of cutting force (Fig. 4.27). These spheres are randomly generated and are located near to grid points in the model matrix.

The grid point spacing and the radii of the spheres are chosen to approximate the volumetric composition of the workpiece being machined. Through simulations it was shown that frequency of the variation in machining is attributed to the spacing of the second phase. The second phase clearly has an impact at the microscale and at the mesoscale. The model was validated by constructing workpieces made from the constituents of ductile iron. It was found that up to 35% of the energy consumed was due to cutting.

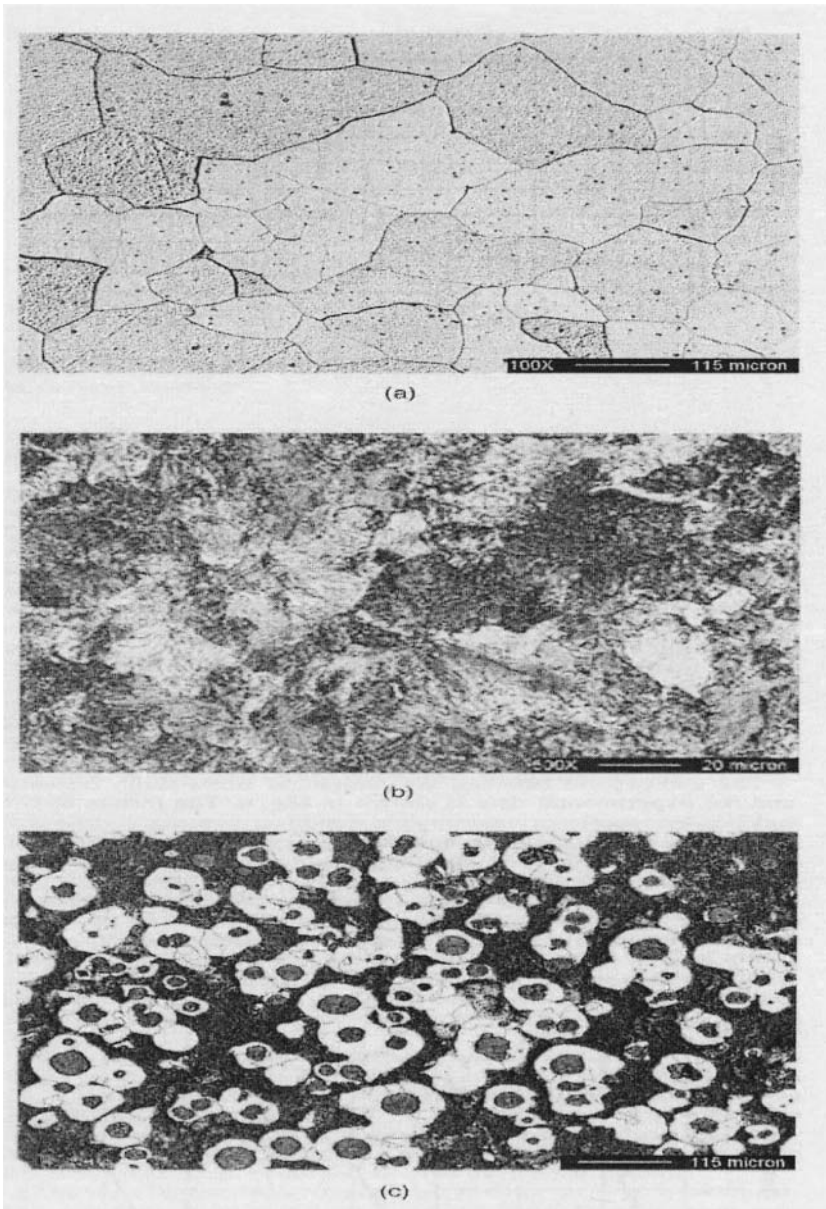


Fig. 4.27. Microstructure of ductile iron: (a) ferrite; (b) pearlite; and (c) pearlitic-ferritic ductile iron

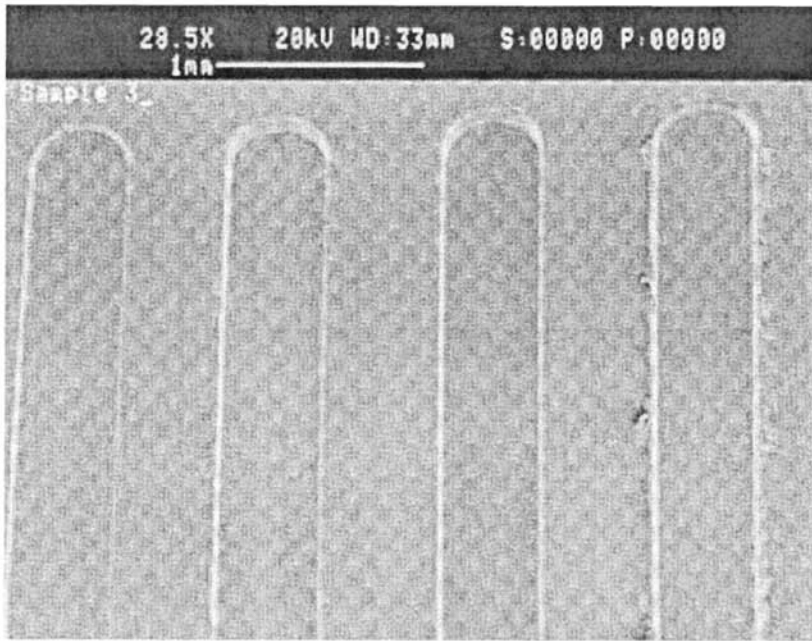


Fig. 4.28. Machined ferrite workpiece

Slots were machined in ferrite and are shown in Figure 4.28. Initial experiments on aluminum created burrs and the edge condition of the tool confirmed the generation of burrs. Peak cutting forces ranged from 300 mN to 3N when the tool rotated at 120,000 rpm with a feedrate of 2 microns per tooth and a depth of cut of 50 to 100 microns. The measured waviness had a wavelength of 20 microns with feed marks with a period of 4 microns.

4.6.2 Molecular Dynamics Models for Micromilling

Numerical simulations have been carried out that determine the mechanisms of chip formation when the uncut chip thickness is much smaller than the edge radius of the cutting tool [41]. When cutting aluminum, material is removed when the depth of cut is about one half of the radius of the cutting edge (Figure 4.29). The size of the cutting tool and the geometry is shown in Figure 4.30.

The surface roughness shown on the surface of aluminum is shown in Figure 4.31.

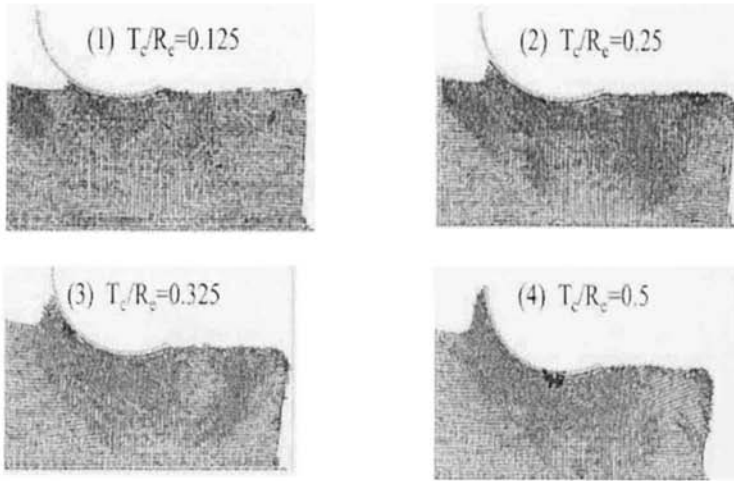


Fig. 4.29. Molecular dynamic simulations of chip formation in meso-micromachining

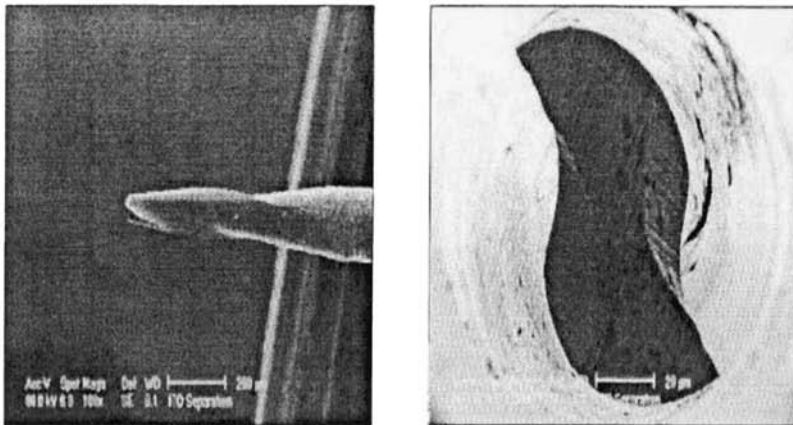


Fig. 4.30. Scanning electron micrograph of micromilling tools

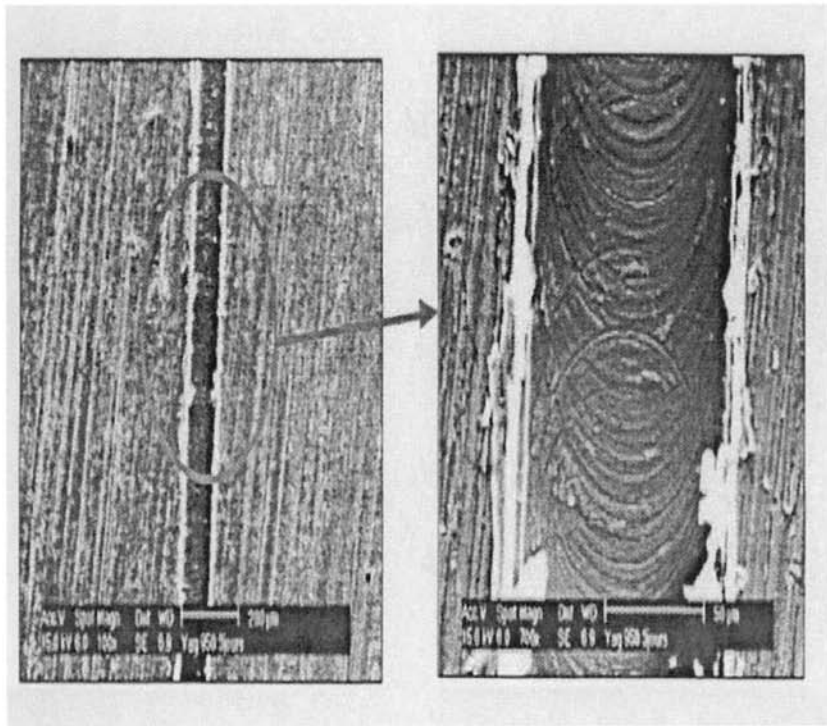


Fig. 4.31. Micrographs of the milled slot in aluminum

4.6.3 Micro Drilling Dynamic Model

A mechanistic force model for micro drilling has been developed that considers the influence of tool grinding errors [42], errors in torque, and the dynamic characteristic of cutting force components. The model considers the skidding or wandering of the tool with respect to the center of the cut at the initial contact. The ability to predict this behavior is critical in assuring the ability to machine holes at the microscale. A comprehensive set of experiments has been conducted that verify the accuracy of the models [42]. A set of experimental values of the predicted behavior is shown in Figure 4.32.

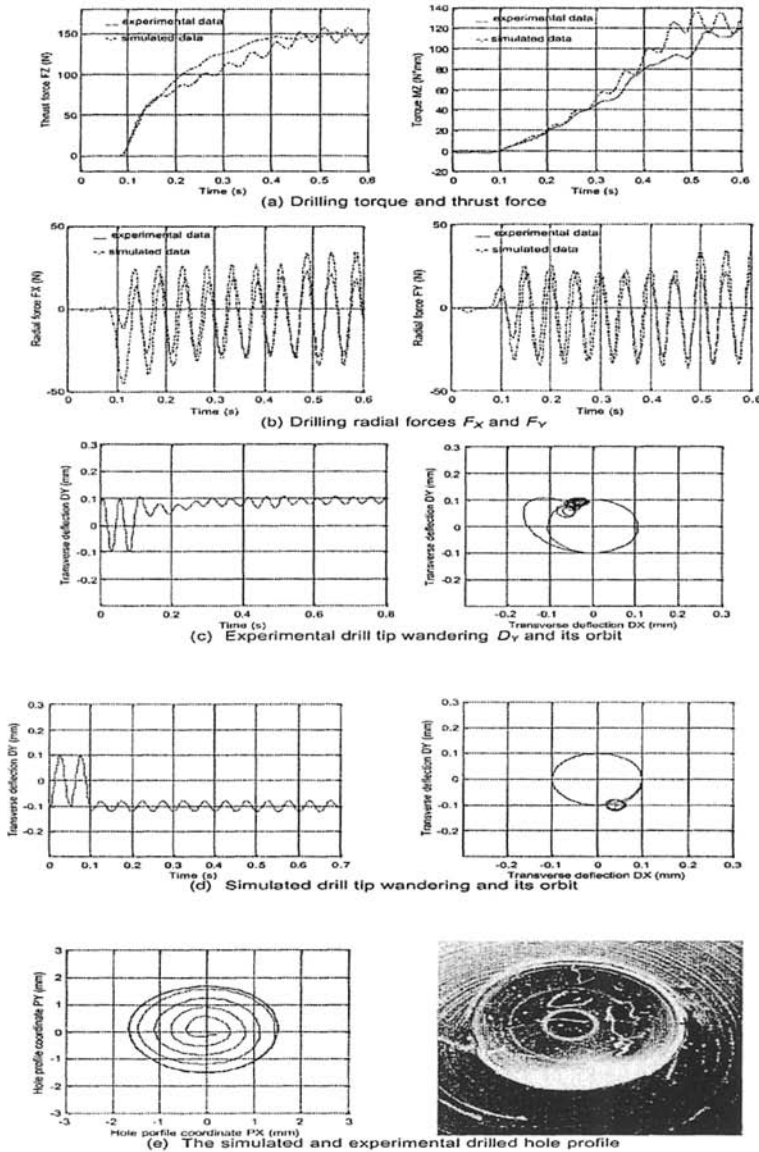


Fig. 4.32. Comparison of predicted and measured micro-drilling process variables in the presence of initial drill contact errors

4.7 Problems

1. What are size effects in micromachining processes?
2. Explain the variation in specific energy required to grind small chips of material.
3. What is the shear stress required to micromill SAE 1112 steel at a depth of cut of 0.001 inches?
4. Explain the mechanism of slip in polycrystalline metals.
5. Explain the mechanism of slip in single crystal metals.
6. Calculate how shear plane angles can be predicted.
7. Does a shear plane zone occur in micromilling?
8. Describe Langford's and Cohen's model of plastic behavior at large strains.
9. Explain saw-tooth chip formation in hard turning.
10. What effect does CCl_4 lubricant have on chip formation?
11. Describe Eugene's experimental apparatus to describe fluid-like flow in metal cutting.
12. Describe the mechanism of large plastic flow and how it may affect burr formation at the microscale.
13. What is inhomogeneous strain?
14. Briefly describe the origins of the size effect.
15. What special problems does the size effect have on micromilling?

References

1. Backer WR, Marshall ER, and Shaw MC, 1952, Trans. ASME, **74**, p.61
2. Taniguchi N, 1994, Precision Engineering, **16**, 5-24.
3. Shaw MC, 1952, J. Franklin Inst., **254**, 2, 109.
4. Heidenreich RO, Shockley W, 1948, Report on Strength of Solids, Phys. Soc. of London, 57.
5. Ernst HJ, Merchant ME, 1941, Trans. Am. Soc. for Metals, **29**, 299.
6. Merchant ME, 1945, J. Appl. Phys., **16**, 267-275.
7. Piispanen V, 1937, Teknillinen Aikakaushehti (Finland), **27**, 315.
8. Merchant ME, 1950, Machining Theory and Practice, Am Soc. for Metals, 5-44.

9. Merchant ME, 1945, J. Appl. Phys., **16**, 318-324.
10. Barrett CS, 1943, Structure of Metals, McGraw Hill Co., NY, 295.
11. Bridgman PW, 1952, Studies in Large Plastic Flow and Fracture, McGraw Hill Co., NY.
12. Langford G, Cohen M, 1969, Trans. ASM, **62**, 623.
13. V. Piispanen, 1948, J. Appl. Phys., **19**, p.876.
14. Blazynski TZ, Cole J M, 1960, Proc. Instn. of Mech. Engrs., **1**, 74, 757.
15. Shaw MC, 1950, J. Appl. Phys., **21**, 599.
16. Walker TJ, 1967, PhD Dissertation, Carnegie-Mellon University, PA.
17. Walker TJ, Shaw M C, 1969, Advances in Machine Tool Design and Research, Pergamon Press, 241-252.
18. Usui E, Gujral A, Shaw MC 1960, Int. J. Mach Tools and Res., **1**, 187-197.
19. Vyas A, Shaw MC, 1999, Trans. ASME-J. Mech. Sc., **21**, 1, 63-72.
20. Eugene F, 1952, Annals of CIRP, **52**, 11, 13-17.
21. Shaw MC, 1980, Int. Jour. Mech. Sc., **22**, 673-686.
22. Kwon KB, Cho DW, Lee SJ, Chu CN, 1999, Annals of CIRP, **47**/1, 43-46.
23. Eyring H, Ree T, and Harai N, 1958, Proc. Nat. Acad. Scs., **44**, 683.
24. Eyring H, Ree T, 1961, Proc. Nat. Acad. Scs., **47**, 526-537.
25. Eyring H, Jhon MS, 1969, Significant Theory of Liquids, J. Wiley and Sons, NY.
26. Kececioglu D, 1958, Trans. ASME, **80**, 149-168.
27. Kececioglu D, 1958, Trans. ASME, **80**, 541-546.
28. Kececioglu D, 1960, Trans. ASME-J. Eng for Industry, **82**, 79-86.
29. Anderson TL, 1991, Fracture Mechanics, CRC Press, Florida.
30. Zhang B, Bagchi A, 1994, Trans. ASME- J. of Eng for Industry, **116**, 289.
31. Argon AS, Im J, Safoglu R, 1975, Metallurgical Transactions, **6A**, 825.
32. Komanduri R, Brown RH, 1967, Metals and Materials, **95**, 308.
33. Drucker DC, 1949, J. Appl. Phys., **20**, 1.
34. Fleck NA, Muller GM, Ashby M F, Hutchinson J M, 1994, Acta Metallurgica et Materialia, **41**, 10, 2855.
35. Stelmashenko NA, Walls M G, Brown L M, Milman Y V, 1993, Acta Metallurgica et Materialia, **41**, 10:, 2855.
36. Ma Q, Clarke D R, 1995, J. Materials Research, **46**, 3, 477.
37. Nix WD, Gao H, 1998, J. Mech. and Physics of Solids, **1**, 4, 853.
38. Gao H, Huang Y, Nix W D, Hutchinson J W, 1999, Jour. of Mechanics and Physics of Solids, **47**, 1239.
39. Dinesh D, Swaminathan S, Chandrasekar S, and Farris T N, 2001, Proc ASME-IMECE, NY: 1-8.

40. Vogler M, DeVor R, Kapoor SG, 2001, Symposium on Modeling, Sensing and Controlling Micro Machining Processes, IMECE 2001, New York, USA.
41. Kim, CJ, 2001, Cutting Mechanics and Surface Generation in Micro Milling Processes, Ph. D. Thesis, University of Michigan.
42. Gong Y and Ehmann K, Symposium on Modeling, Sensing and Controlling Micro Machining Processes, IMECE 2001, New York, USA.

5. Mechanical Micromachining

5.1 Introduction

The development of microfluidic devices in recent years such as “lab-on-a-chip” has created a need to machine microscale features that do not negatively interfere with fluid flow at that scale. Microfluidic devices are classified as active or passive devices. Passive microfluidics is a control topology in which the physical configuration of the microfabricated system determines the functional characteristics of the system with and without an external power source. Passive microfluidics exploit various physical properties such as shape, contact angle, and flow characteristics that achieve desired functions. These devices function as pumps, valves, filters and reactors. They are classified as “BioMEMS devices” and include fluidic sensors, micro-reactors, dispensers, valves, micro-pumps, flow channels, filters, and separators, and biosensors. A review of microfluidic principles is provided by Gravesen, Branebjerg, and Jensen [1]. Owing to the principle of operation of BioMEMS devices, geometric construction of microchannels requires micromachining techniques to be highly accurate and to be able to machine engineering materials in addition to traditional materials currently used in BioMEMS devices.

5.2 Microfluidic Systems

Microfluidic devices require microscale channels to be machined such that the dominant effects of passive microfluidic devices can be

exploited. These effects are classified as: surface tension effects; capillary force effects; Hagen-Poiseuille pressure drop effects; and surface roughness effects to produce hydrophobic and hydrophilic flows. Passive micro-valves are traditionally made from a Si/Poly-silicon based material in the form of check valves that are easy to fabricate and can be integrated into a microfluidic system. The most important dimension to be machined accurately is the diameter of the microchannel because it determines the pressure drop across the channel, and the pressure required to push fluid across an abrupt restriction. Conventional valves consist of valves with 45° taper geometry, 30° taper geometry, rounded valves and valves with restrictor channels. These valves are very easily machined but the pressure drop across the valve requires external power sources to make the fluid flow, or by using capillary suction so that an external power source is no longer required. Novel types of mixing valves are based on exploiting the “Coanda effect” that uses Taylor dispersion of fluids to agitate and combine liquid flows by combinations of diffusion and convection mixing. These valves require a more sophisticated way of machining in order to achieve the correct mixing of the fluid. The construction of such valves is shown in Fig. 5.1 and shows a complex set of channels that is used to mix fluids prior to being dispensed using a fixed volume microdispenser that is composed of fluid inlets and outlets, fixed volume reservoirs, passive valves, and mixing chambers.

The development of mixing devices and their subsequent micromachining is only one part of the microfluidic device. Microfluidic devices are multiplexed with integrated microdispensers that are systems that form “lab-on-chip” products. By definition these require a reservoir for holding fluids such that a dispersed volume is dispensed using an air driving force that can be dispensed in a programmed ratio in the nanoliter range by using passive valves. The challenges to machining these features are the generation of roughness features on the microchannel that supports hydrophilic or hydrophobic effects. Control of microsurface roughness is best achieved by mechanically machining using a high-speed milling machine tool.

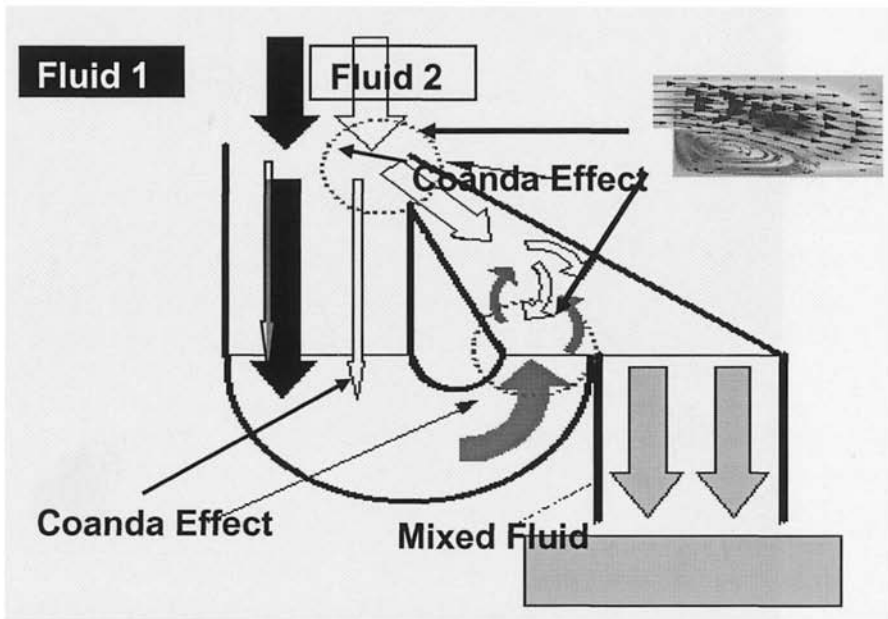


Fig. 5.1a. Mixing cell in a microfluidic channel incorporating a Coanda mixing chamber and diffuser. The inset shows a simulation of the Coanda effect and its mixing effect

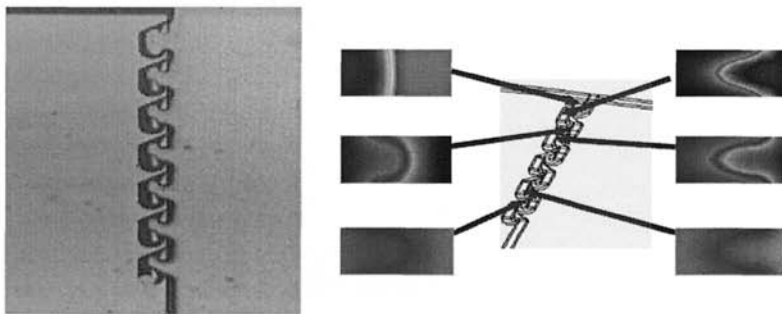


Fig. 5.1b. The micromachined channel on the left shows the difficulties associated with micromachining this type of microfluidic chamber. The CFD simulation to the right shows the mixing effect of this type of microfluidic channel

The development of soft lithography has generated interest in the manufacture of micro- and nanofluidic systems in which a “rubbery” solid can be attached to a solid substrate to perform operations such as controlling liquid flows, pumping fluids to act like syringes, and controlling flows using a combination of valves, mixers, and separators. The substrates can be silicon, but more robust materials such as engineering materials require mechanical micromachining techniques to generate the required profiles. Figure 5.2 shows the nature of some complex shaped microfluidic systems. The figure shows a stepped profile in the substrate so that liquid can flow on two levels. A soft material such as polydimethylsiloxane (PDMS) is placed on top of this network so that the fluid can be controlled and manipulated to produce the right type of flow and concentration of chemicals. The nature of the complex topography of these channels is also shown and can be machined from a variety of materials using micromilling tools.

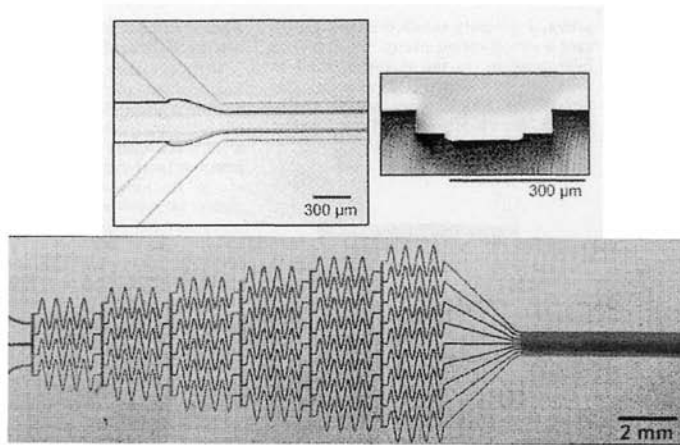


Fig. 5.2. Microfluidic channel showing three-dimensional topographic profile that is machined using micromilling tools. The branched network is also shown that combines flows and mixes them as performed by adding colored dyes to a liquid that produces a graded output of fluid

The following section shows how micromilling can be used to produce these features and to create microscale debris that can be recycled by pressing in a mold to create powdered metal products with extremely good engineering properties. The machining debris contains nanocrystals produced during high strain rate machining of the microfluidic channel.

5.3 Theory of Micromachining

5.3.1 Micromilling

As micro-and nanotechnology becomes increasingly important to the needs of society, the need to create microfluidic devices in engineering materials becomes more apparent. High-speed milling has been shown to provide a great deal of promise in creating microstructures and in nanotexturing surfaces in engineering materials. Cutting tool rotation is expected to reach 1,000,000 revolutions per minute (rpm) compared with conventional cutting speeds of around 30,000 rpm. Rotating the tool this quickly reduces cutting forces which produces a higher quality of cut so that post-processing is not required. Clearly, strain rates imparted to the workpiece at these speeds are very high and this influences initial chip formation and chip removal mechanisms. High strain rates imparted cause distinct chip formations in engineering materials to occur which are similarly observed in other materials, most notably biological materials such as cancellous bone. Certain soft metals such as aluminum do not machine very well because the material adheres to the cutting tool. However, high strain rates tend to overcome these limitations. During the last five years MEMS and nanotechnology have promised to make available small-scale devices with the potential to improve our daily lives. To a certain extent this has been achieved but the market has not realized its potential. Most products available are based on products used in the semiconductor industry, or in the form of sensors. Manufacturing processes used in the production of these components are limited by the material used. Hence, there are few produc-

tion processes available for products requiring metals and other engineering materials. One technique that shows much promise is ultra high-speed milling, which has been shown to produce micro-and nanoscale structures in the same way as a conventional machine tool produces macroscale features. A special requirement of machining at such small scales is the need to increase the rotational speed of the cutting tool. The cutting speed of the cutting tool is given by the following equation assuming that the mass of the tool is concentrated at radius, r :

$$V = r\omega \quad (5.1)$$

Where V is the cutting velocity (m/s), r is the cutting tool radius (m) and ω is the rotational speed in (radians/s). From this relationship it can be seen that as the cutter diameter reduces in size to create micro-and nanoscale features the rotational speed must dramatically increase to compensate for the loss of cutting speed at the micro-and nanoscale. At the present time, the fastest spindle commercially available rotates around 360,000 rpm under load conditions.

Research is being conducted to improve the performance of these spindles where the initial aim is to reach 1,000,000 rpm [2]. Strain rates induced at these high speeds cause chip formation mechanisms to be significantly different than at low speeds. Additionally, it is now possible to experiment at the extreme limits of the fundamental principles of metal cutting at ultra high speed and at the micro-and nanoscales using the conventional theories of metal cutting.

Following the development of equations proposed by Shaw [3], these expressions will be applied to a 6 flute end milling cutter with a shank of diameter 1.59 mm, cutting diameter 700 μm , rotated at a speed of 250,000 rpm or 26180 rad/s. The rake angle was $\alpha = 7^\circ$, clearance angle $\theta = 10^\circ$ and the shear plane angle $\phi = 24^\circ$. To illustrate the application of the established theories of metal cutting at these scales, the metal used as an example was a hypoeutectoid AISI 4340 steel, and the horizontal force F_h was calculated using the equation:

$$F_h = mr\omega^2 \quad (5.2)$$

Where m is the tool mass (kg), and r is the tool radius (m). Coefficients of friction between different materials have been investigated by Bowden and Tabor [4]. They discovered that when a curved tungsten-carbide tool (WC) slides against a steel substrate the coefficient of friction is in the range $\mu = 0.4 - 0.6$ under dry cutting conditions, and between 0.1 and 0.2 under lubricated conditions. Here, dry cutting conditions are used at high cutting speeds in order to remove chips in an environmentally conscious manner that does not use a lubricant that is harmful to the environment. Using the following equation,

$$\beta = \tan^{-1} \mu \quad (5.3)$$

The friction angle β can then be determined under these conditions. It was found to be 30.96° . This is in excellent agreement with Merchant and Zlatin's nomograph [3]. The vertical force F_v can be found using the relationship:

$$F_v = \frac{\mu F_h - F_h \tan \alpha}{1 + \mu \tan \alpha} \quad (5.4)$$

This was found to be 5.25 N. Again, referring to the Merchant and Zlatin's [3] nomograph for the coefficient of friction, the value of F_h can be independently predicted to be 5.33 N. The force perpendicular to the tool plane F is found to be:

$$F = F_h \sin \alpha + F_v \cos \alpha \quad (5.5)$$

F was determined as 6.66 N. The force normal to the tool plane N is provided using the equation:

$$N = F_h \cos \alpha - F_v \sin \alpha \quad (5.6)$$

Where N was found to be 11.1 N. The force perpendicular to the shear plane F_s can now be determined by,

$$F_s = F_h \cos \phi - F_v \sin \phi \quad (5.7)$$

And was estimated to be 8.76 N. The force normal to the shear plane N_s is given by the equation:

$$N_s = F_v \cos \phi + F_h \sin \phi \quad (5.8)$$

Where N_s is 9.61 N. Now the frictional force F_f is:

$$F_f = F_v \cos \alpha + F_h \sin \alpha \quad (5.9)$$

F_f is approximately 6.66 N. It is possible to check this value with Merchant and Zlatin's [3] nomograph for frictional force. However, the values for F_h and F_v are so small that the extreme limits of the nomograph are reached so it is difficult to give an accurate value for F_f , it is certain this value is below 10 N which is in close agreement with the calculated answer. The shear stress τ is found using the following quotient:

$$\tau = \frac{F_s}{A_s} \quad (5.10)$$

Which has a value of 1.8 GN/m². The direct stress ρ is found by applying the relationship,

$$\sigma = \frac{N_s}{A_s} \quad (5.11)$$

σ is found to be 1.95 GN/m^2 . The chip thickness ratio, r , is given by:

$$r = \frac{t}{t_c} \quad (5.12)$$

Where t is the un-deformed chip thickness (or depth of cut) and t_c is the measured chip thickness. The milling experiment was conducted at such a small scale that it was difficult to measure, t . Therefore r was calculated using the equation:

$$r = \frac{\tan \phi}{\cos \alpha + \sin \alpha \tan \phi} \quad (5.13)$$

Which yields $r = 0.425$ and therefore $t = 4.25 \text{ } \mu\text{m}$. This is in excellent agreement with Merchant and Zlatin's [3] nomograph for shear angles and the calculation can be made in confidence. Shear strain γ is found from

$$\gamma = \frac{\cos \alpha}{\sin \phi \cos(\phi - \alpha)} \quad (5.14)$$

γ was found to be 2.55, this can be independently verified from Merchant and Zlatin's nomograph [3] for shear strain which yields a value of 2.51. The cutting velocity V is found using:

$$V = r\omega \quad (5.15)$$

Where V is 9.1 m/s. The chip velocity is found from applying the following equation:

$$V_c = \frac{\sin \phi}{\cos(\phi - \alpha)} \quad (5.16)$$

Where V_c is equal to 3.9 m/s, this can also be found from

$$V_c = rV \quad (5.17)$$

The two results are in agreement with each other. The shear velocity V_s is given by:

$$V_s = \frac{V \cos \alpha}{\cos(\phi - \alpha)} \quad (5.18)$$

Where V_s is calculated to be 9.5 m/s. V_s can also be found from:

$$V_s = \gamma V \sin \phi \quad (5.19)$$

Again, the two results are in agreement with each other. The strain rate $\dot{\gamma}$ is given by:

$$\dot{\gamma} = \frac{V \cos \alpha}{\Delta y \cos(\phi - \alpha)} \quad (5.20)$$

Where Δy is the shear plane spacing and $\dot{\gamma}$ is found to be $8333 \times 10^6 \text{ s}^{-1}$. The feed rate is 1 mm/min under experimental conditions and the feed per tooth δ is given by,

$$\delta = \frac{F_r}{N\omega} \quad (5.21)$$

Where N is the number of teeth. Therefore, Δ is $6.66 \mu\text{m}$ and the scallop height is found by using the following:

$$h = \frac{\delta}{\left(\frac{4T_{td}}{\delta}\right) + \left(\frac{8N}{\pi}\right)} \quad (5.22)$$

Therefore h is calculated to be $1.59 \times 10^{-11} \text{ m}$ under the experimental conditions. The scallop height is so small that microscale channels can be machined with such low surface roughness levels that the effects of wall friction on fluid flow in the microfluidic channel are negligible. This allows microfluidic flows to be determined by geometry of the channel rather than by surface roughness effects in microfluidic channels. However, surface roughness effects are significant in nanofluidic channels that can control whether the liquid flowing in the channel is hydrophilic, or hydrophobic.

5.3.2 Initial Chip Curl Modeling

Chip curvature is a highly significant parameter in micromachining operations from which a continuous chip is produced. There is a great deal of uncertainty regarding the mechanism of curly chip formation and the factors determining the chip radius. Observations are made on initial chip curl in the simplified case of orthogonal cutting at the micro- and nanoscale. The cutting process may be modeled using a simple primary shear plane and frictional sliding of the chip along the rake face. When the region of chip and tool interaction at the rake face is treated as a secondary shear zone and the shear zones are analyzed by means of slip-line field theory, it is predicted that the chip will curl. Thus chip curvature may be interpreted as the consequence of secondary shear. Tight chip curl is usually associated with conditions of good rake face lubrication [5]. At the beginning of the cut, a transient tight curl is often observed, the chip radius increasing as the contact area on the rake face grows to

an equilibrium value. Thus it might be suggested that tight curl is an integral part of the initial deformation.

It has been suggested that the process of continuous chip formation is not uniquely defined by the boundary conditions in the steady state and that the radius of curl may depend on the build-up of deformation at the beginning of the cut [5]. A treatment of initial chip curl at the micro-scale curl is now presented, which considers chip curl as a series of heterogeneous elements in continuous chip formation at the micro-scale. The free surface of the chip always displays fine striations, or “lamellae”, parallel to the cutting edge. The chip is usually considered to form by a regular series of discrete shear events giving a straight chip made up of small parallel segments. However, no account is taken of the workpiece material that moves passed the tool between shear events. The following observations follow on from Doyle, Horne, and Tabor’s [5] analysis of initial chip formation.

Figure 5.3 shows the instabilities during chip formation that gives rise to initial chip curl. The shaded range of Fig. 5.3b is the consequence of a built-up edge that very quickly becomes part of the segmented chips shown in Fig. 5.3d. This “material” provides the means to curl the chip and as a consequence of this event, the following model is presented. Previous treatments of chip curl analysis [6] have focused on chip formation with a perfectly stiff cutting tool. However, during micromachining the cutting tool bends as it machines the workpiece material [7]. This means that primary chip curl models must account for deflection of the cutting tool by bending during an orthogonal micromachining operation. Computational approaches to modeling chip formation at the micro-and nanoscales have been attempted in recent years by a number of researchers [8,9], who have used a molecular dynamics simulation approach using stiff cutting tools.

The generation of a transient built-up edge ahead of the cutting tool between shearing events in a bulging-type of motion generates the shape of the segment of the metal chip. This is shown in Fig. 5.3c, with the built-up edge forming the “shaded triangle” above the shear plane. If it is assumed that the built-up edge does not “escape” under the tool edge, then the areas of the shaded triangles in Figs. 5.3b and 5.3c will be equal. The chip moves away from the rake

force in a manner shown in Fig. 5.3d. The radius of chip curl can be calculated by assuming that the built-up edge in transient and that the element of the “bulged” material contains a small angle relative to the tool and workpiece.

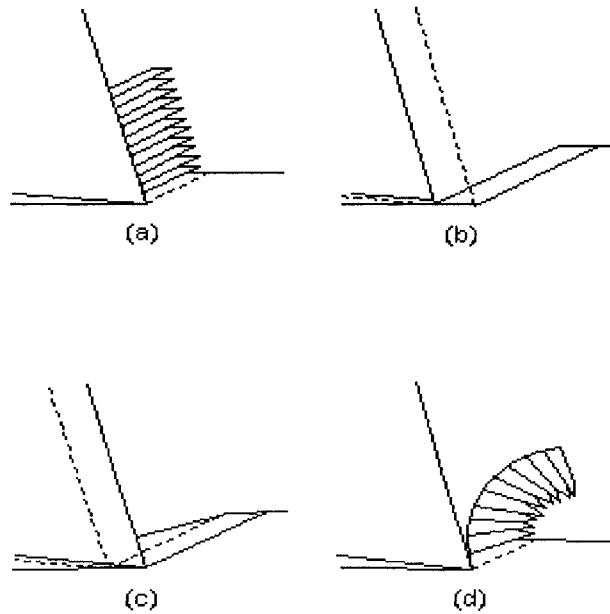


Fig. 5.3. Instability during the formation of a chip during micromachining: (a) segmented, continuous chip; (b) chip forming instability due to built-up edge; (c) movement of a built-up edge to form a chip; (d) serrated, continuous chip curl

This angle will inevitably change during the bending action of the cutting tool. With reference to Fig. 5.4, if we assume that the cutting tool moves from point A to point D then the shear plane AC rotates to position HC as the built-up edge from triangle ABD is pushed into the segment of the chip. At point D, the shear along DF begins and segment DHCF is completed. HC and DF meet at R, the center of the circle of the chip segment. Since the angle HRD is small, RD may be referred to as the radius of the chip. The clearance angle is θ .

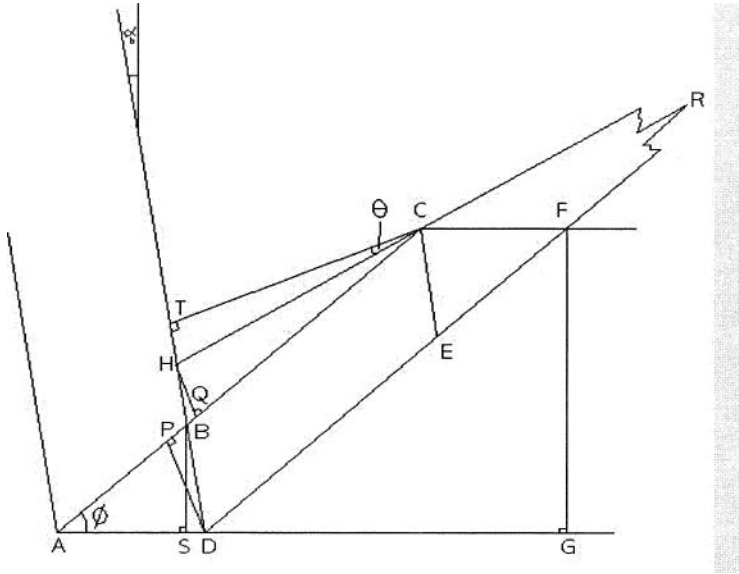


Fig. 5.4. Schematic diagram of the geometry of the primary chip that forms a curled chip

Triangles ABD and HBC are equal in area and the depth of cut FG is equal to d . The spacing between the segments, i.e., the lamellae, is CE, which is equal to BD, which is equal to s . The chip thickness between lamellae, TC, is equal to t , while the rake angle SBD is equal to α . The cutting tool bends when machining at the microscale, which reduces the effective rake angle to α_b . We know that the chip radius r can be taken as RD, whilst the shear angle subtended is $\hat{B}AD$, or ϕ . The calculation of the chip radius is provided by the following analysis:

$$DP = s \cdot \cos(\phi - \alpha_b) \quad (5.23)$$

$$AB = \frac{B \cdot S}{\sin \phi} \quad (5.24)$$

Where,

$$BS = s.\cos\alpha_b \quad (5.25)$$

Thus,

$$DF = AC = \frac{d}{\sin\phi} \quad (5.26)$$

And,

$$AB = \frac{s.\cos\alpha_b}{\sin\phi} \quad (5.27)$$

Now,

$$BC = AC - AB = \frac{d}{\sin\phi} - \frac{s.\cos\alpha_b}{\sin\phi} \quad (5.28)$$

Therefore,

$$BC = \frac{(d - s.\cos\alpha_b)}{\sin\phi} \quad (5.29)$$

The areas of $\triangle ABD$ and $\triangle HBC$ are equal, such that,

$$AB.DP = HQ.BC \quad (5.30)$$

Hence,

$$HQ = \frac{DP.AB}{BC} = \frac{s.\cos\alpha_b.s.\cos(\phi - \alpha_b).\sin\phi}{\sin\phi.(d - s.\cos\alpha_b)} \quad (5.31)$$

And thus,

$$HQ = \frac{s^2 \cdot \cos \alpha_b \cdot \cos(\phi - \alpha_b)}{(d - s \cdot \cos \alpha_b)} \quad (5.32)$$

Also,

$$BH = \frac{HQ}{\cos(\phi - \alpha_b)} = \frac{s^2 \cdot \cos \alpha_b}{(d - s \cdot \cos \alpha_b)} \quad (5.33)$$

And,

$$DH = BH + BD = s + \frac{s^2 \cdot \cos \alpha_b}{(d - s \cdot \cos \alpha_b)} \quad (5.34)$$

Such that,

$$DH = \frac{s \cdot d}{(d - s \cdot \cos \alpha_b)} \quad (5.35)$$

Hence,

$$CH = \frac{TC}{\cos \theta} = \frac{t}{\cos \theta} \quad (5.36)$$

Therefore,

$$\sin \hat{HRD} = \sin \hat{HCB} = \frac{HQ}{HC} = \frac{s^2 \cdot \cos \alpha_b \cdot \cos(\phi - \alpha_b) \cdot \cos \theta}{t \cdot (d - s \cdot \cos \alpha_b)} \quad (5.37)$$

And,

$$\sin \hat{DHR} = \sin \hat{THC} = \cos \theta \quad (5.38)$$

In triangle HRD,

$$\frac{RD}{\sin \hat{DHR}} = \frac{DH}{\sin \hat{HRD}} \quad (5.39)$$

Therefore,

$$RD = r = DH \cdot \frac{\sin D\hat{H}R}{\sin H\hat{R}D} = \frac{s \cdot d}{(d - s \cdot \cos \alpha_b)} \cdot \frac{\cos \theta \cdot t \cdot (d - s \cdot \cos \alpha_b)}{s^2 \cdot \cos \alpha_b \cdot \cos(\phi - \alpha_b) \cdot \cos \theta} \quad (5.40)$$

Thus,

$$r = \frac{d \cdot t}{s \cdot \cos \alpha_b \cdot \cos(\phi - \alpha_b)} \quad (5.41)$$

If the width of the lamellae, s , is small compared to the chip thickness, then for continuous machining with a single shear plane,

$$\frac{d}{t} = \frac{\sin \phi}{\cos(\phi - \alpha_b)} \quad (5.42)$$

Hence,

$$\frac{t}{\cos(\phi - \alpha_b)} = \frac{d}{\sin \phi} \quad (5.43)$$

And so,

$$r = \frac{d^2}{s \cdot \cos \alpha_b \cdot \sin \phi} \quad (5.44)$$

Equation 5.44 predicts a positive chip radius at negative rake angles. The approximations considered in this model are appropriate when one considers that the model assumes that a secondary shear plane exists. These models applied at the microscale are highly appropriate because they account for acute bending of the cutting tool that is not significant at the macroscale. The formation of highly strained metal chips provides a raw material for the manufacture of nanocrystalline metal products. This ensures that no waste is generated during dry milling of microfluidic channels, leading to the development of environmentally benign micro-manufacturing processes.

5.4 Experimental Micromachining

5.4.1 Micromachining Apparatus

To validate or refute the model described for machining micro-fluidic channels and to provide the material required to manufacture nanostructured metals pressings, machining experiments were conducted at the microscale. The machine tool was constructed to incorporate a high-speed air turbine spindle rated to operate at 360,000 rpm under no-load conditions. When operating at relatively deep depths of cut, the speed of the spindle decreases to approximately 250,000 rpm. The table of the machine tool was configured to move in x-y-z co-ordinates by attaching a cross-slide powered by a d.c. motor, in all three principal axes. Each motor was controlled by a MotionmasterTM controller with a resolution as low as 500 nm. The cutting tools used were uncoated. The high strain rate micromachining center is shown in Fig. 5.5.

The cutting tools were inspected at the end of all machining experiments using an environmental scanning electron microscope. The measured spindle speed was 250,000 rpm during the machining experiments. The depth of cut was 100 μm for all machining experiments. The machining feed rate was conducted at 5 mm/s (0.3 m/min). The microscale cutting tool used was 700 μm in diameter and was associated with a cutting speed of 117 m/min and a machining feed rate of 0.3 m/min. The experimental results are shown in Table 5.1. Machining experiments consisted of machining several materials including steel using the micromachining center. The machined chips were examined in an environmental scanning electron microscope where the lamellar spacing on each chip was determined. The curl radii were then compared with the calculated value derived using the idealized model, taking into account the degree of bending of the cutting tool.

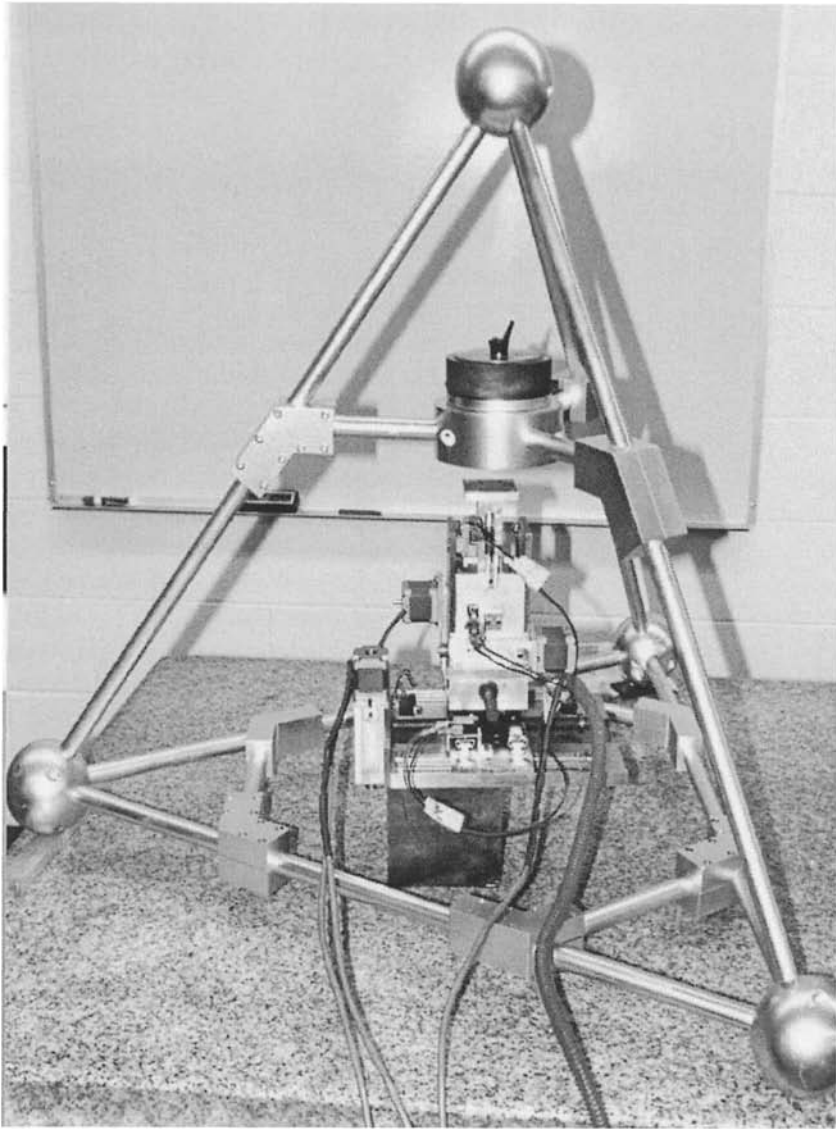


Fig. 5.5. High strain rate micromachining center equipped with a high-speed air turbine spindle for rotating coated micro-milling tools

Table 5.1. Experimental data comparing initial chip curl during micromachining and initial chip curl predicted by the model

Type of metal	Rake angle after bend (°)	Shear plane angle (°)	Depth of cut (μm)	Mean lamellar spacing (μm)	Observed chip curl (mm)	Calculated chip curl (mm)
Lead	23°	37°	100	1.0	17.6	18.05
“	16°	26°	100	1.6	14.4	14.8
“	8°	18°	100	1.9	16.6	17.2
“	3°	12°	100	3.0	15.8	16.0
Pure aluminum	24°	28°	100	1.2	21.2	19.5
“	4°	15°	100	2.4	15.7	16.1
Pure copper	25°	27°	100	1.3	20.4	18.7
“	5°	17°	100	2.5	12.4	13.7
4340 Steel	22°	45°	100	2.0	6.5	7.62
4340 Steel	18°	35°	100	2.9	6.1	6.32
4340 Steel	6°	21°	100	3.3	8.0	8.5

5.4.2 Observations on Chip Formation

When comparing chip forms at low and high speed, significant differences in chip shape are observed. Figures 5.6 and 5.7 illustrate the differences between typical chip collections at low speed and high speed, respectively. It is seen in Fig. 5.6a that many of the particles are in fact chunks of material rather than nicely formed chips. It is possible that the chunks were formerly parts of larger chips that have since broken down and that chip thickness values should be recalculated based on the larger chip size. It can also be seen that the high-speed chips in Fig. 5.6b are more consistent in terms of length, width, and depth. Their lamellar spacing is also regular in period,

which would indicate that cutting conditions at high speed are stable. Single chip formations are shown in Fig. 5.7. While the width observed is similar to that for low-speed cutting, Fig. 5.7a is compared to the high-speed chip form in Fig. 5.7b. The chip length of high-speed chips is much shorter than of low-speed chips. This could be because at low speed the chip has a greater time in contact with the workpiece thereby removing more material, which is reflected in the increased chip length.

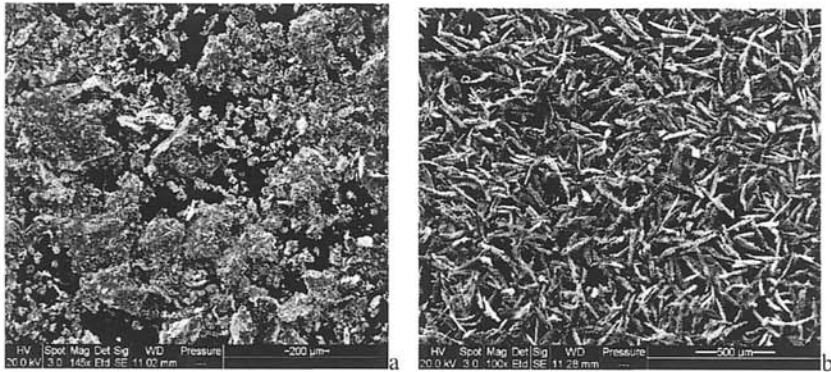


Fig. 5.6. Characteristic chip shape at (a) low and (b) high cutting speeds

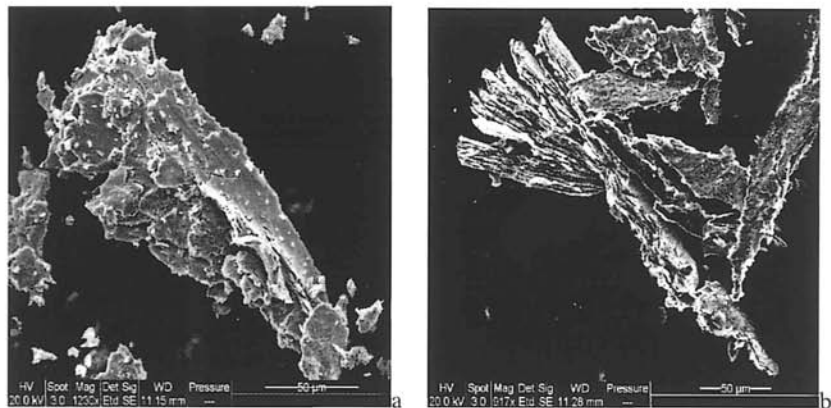


Fig. 5.7. Individual chip forms at (a) low and (b) high cutting speeds

One of the major differences observed between low- and high-speed milling is in the spacing of the lamellae. In low speed cutting, the chip spacing varies by a significant amount. However, at high cutting speeds the spacing is regular in period. Part of the mechanism of chip removal is the forced alignment of dislocations resulting from the impact of the cutting tool against the workpiece. At high speeds this process is accelerated to an extremely high level as the strain rate calculations have shown. In fact experiments show that chip types are similar in different materials such as copper, brass, and most notably cancellous bone. This suggests that high strain rates induce a material removal mechanism independent of the material itself. Figure 5.8 shows cancellous bovine femur machined at high speed. The closely spaced lamellae seen in metallic chips are exhibited here and the spacing is at a similar value, around $10\text{ }\mu\text{m}$. This is a most unexpected result when one considers how structurally different these materials are.

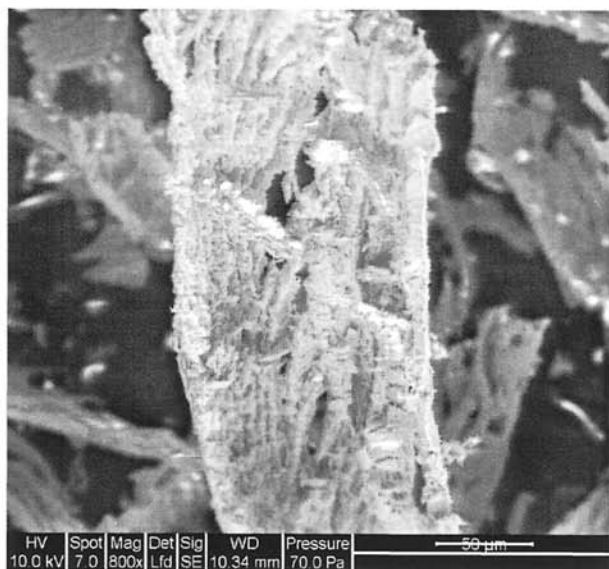


Fig. 5.8. Cancellous bovine femur that has been machined at high speed (250,000 rpm)

5.4.3 Micromachining Results

The results of machining certain metals at the microscale are compared to the model described for primary chip curl during the primary stages of metal cutting. It should be noted that all results presented in Table 5.1 are for metals machined in an oxidizing environment. Table 5.1 shows the results for micromachining using a variety of rake angles. It should be noted that bending of the cutting tool produces a less acute rake angle when machining takes place. However, the shear plane angle is increased and larger chips are produced.

Under the conditions specified, material removal rates were measured for three important engineering materials. The removal rates were $30 \text{ mm}^3/\text{min}$ for aluminum, $36 \text{ mm}^3/\text{min}$ for copper, and $48 \text{ mm}^3/\text{min}$ for steel. Removal rates of this magnitude can also be used for machining molds and dies for use in micro-molding processes such as injection molding and hot embossing. Unfortunately, at certain speeds and depth of cut there is a problem with burr formation.

5.4.4 Burr Formation in Micromachining

Burrs in micromachining occur because the chip that is formed is not removed at the end of the machining path. Burrs are hazardous and can interfere with the assembly of parts of components and products. In conventional machining, burrs are simple to remove but not so at the microscale. Unlike macroscale processes, there are no handbooks on cutting at the microscale in order to determine optimal machining conditions. Tool run-out is also a problem at the microscale because of the way that the tool bends when machining. In initial experiments by Lee, Stirn, and Essel, machining 6061 aluminum alloy indicate that the cutting edge to workpiece interaction is approximately $D < R$, where D is the radial feed and R is the radius of curvature at the cutting edge. The initial burr is shown in Figure 5.9.

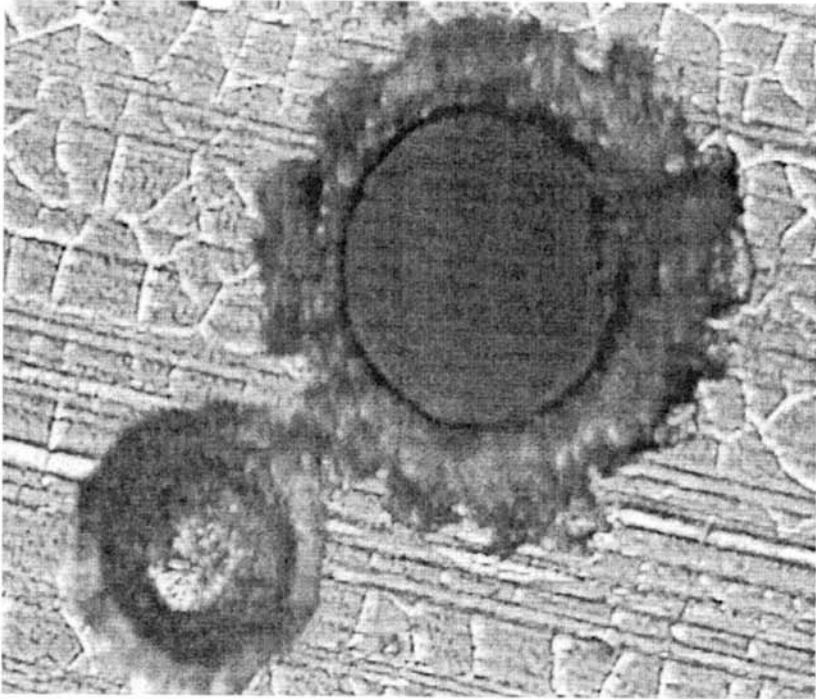


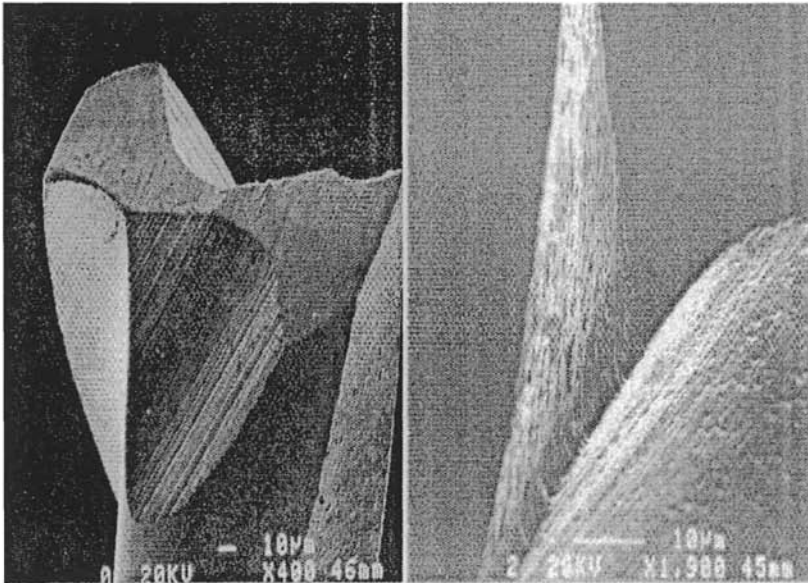
Fig. 5.9. Microdrilling burr with inner cap fragment attached. Microdrill diameter is 100 μm

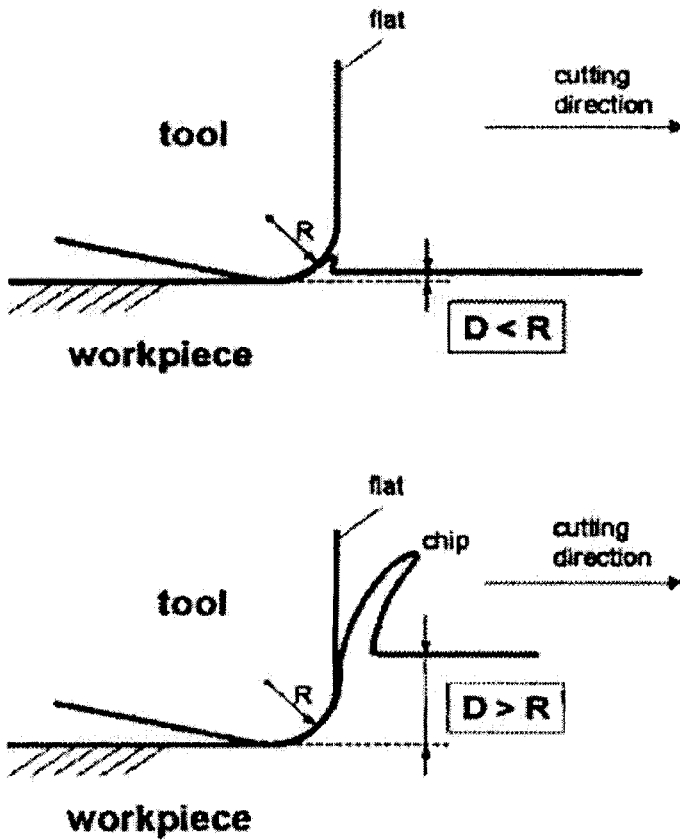
Two different tools were used to machine at this scale, 254 μm and 508 μm . Because smaller tools are used, a much higher spindle speed is required. Tools are shown in Figure 5.10 and the cutting parameters are shown in Table 5.2.

Figure 5.11 shows the effect of cutting edge and workpiece interaction for a given curvature of radius of the cutting edge. Milled channels resulting from the experiments conducted by Lee and others are shown in Figure 5.12. The experimental observations indicated that exit burrs are larger than the entrance burrs, large tool feed marks can be seen on the surface of the milled track, with large depths of cut, chips adhered to the side of the workpiece, built-up edges are created when cutting time is large, and higher feed rates are accompanied by large burrs.

Table 5.2. Microcutting parameters compared with conventional machining parameters

	Dia.	DOC	RPM	SPM	chip load	chip load/D
	mm	mm	RPM	m/min	um/tooth	
Handbook	10		3183	100.00	50.000	0.0050
	12		2653	100.00	75.000	0.0063
	18		1768	100.00	130.000	0.0072
	32.5		979	100.00	150.000	0.0046
	0.254	0.127	7500	5.98	0.085	0.0003
	0.254	0.127	7500	5.98	0.339	0.0013
	0.254	0.254	7500	5.98	0.085	0.0003
	0.254	0.254	7500	5.98	0.339	0.0013
	0.508	0.254	7500	11.97	0.169	0.0003
	0.508	0.254	7500	11.97	0.677	0.0013
	0.508	0.508	7500	11.97	0.169	0.0003
	0.508	0.508	7500	11.97	0.677	0.0013

**Fig. 5.10.** Micrographs of microcutting tools



R: radius of curvature of the cutting edge
D: radial feed

Fig. 5.11. Cutting edge-workpiece interaction for different radial feeds at the given radius of curvature of the cutting edge

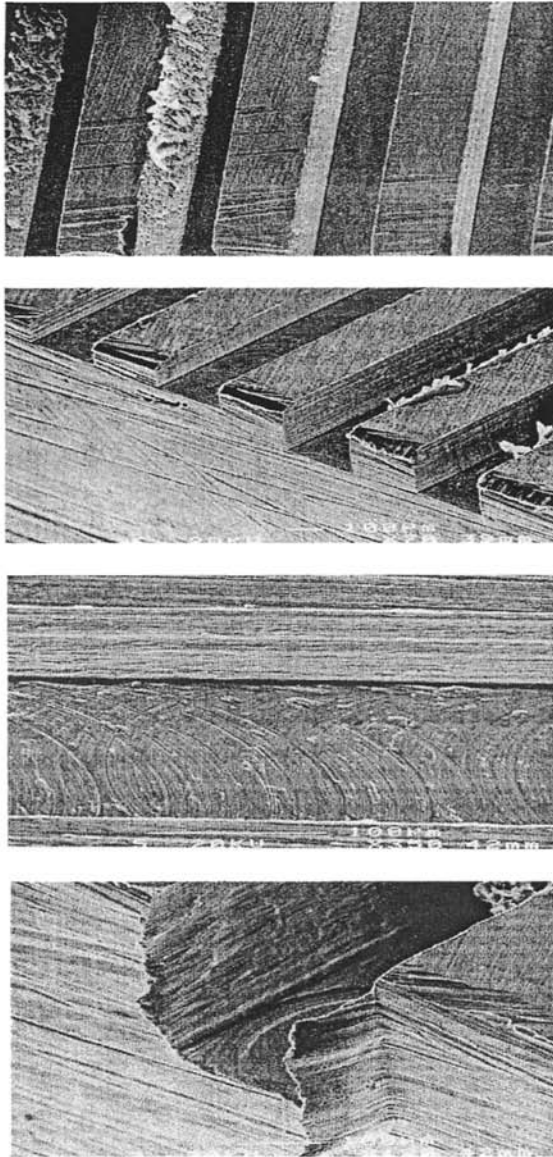


Fig. 5.12. Milled slots in 6061 aluminum alloy showing tool marks and exit burrs

Gillespie postulated that burrs are classified in the following terms: Tear burrs; rollover burrs, Poisson burrs, and cut-off burrs. A tear burr is the result of material tearing loose from the workpiece rather than shearing. The rollover burr is essentially a chip that is bent rather than sheared, resulting in a comparatively large burr. This type of burr is also known as an exit burr. The Poisson burr is one that results from the material's tendency to bulge at the sides of the machined cut when it is compressed until permanent plastic deformation takes place. Figure 5.13 shows the tear and rollover burr formations.

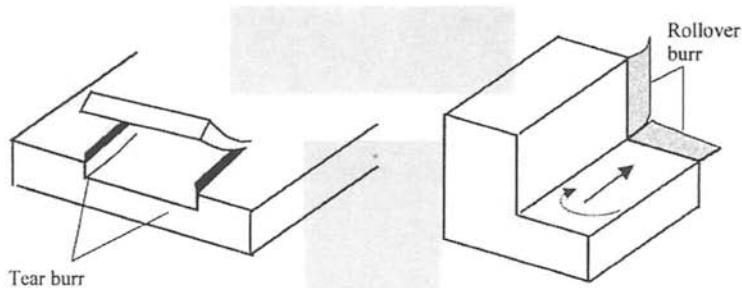


Fig. 5.13. Tear burr and rollover burr formation

A combination of the Poisson burr and the tear burr can form the so-called top burr or entrance burr along the edge of a machine slot, or around the periphery of a hole. Figure 5.14 shows such a burr.

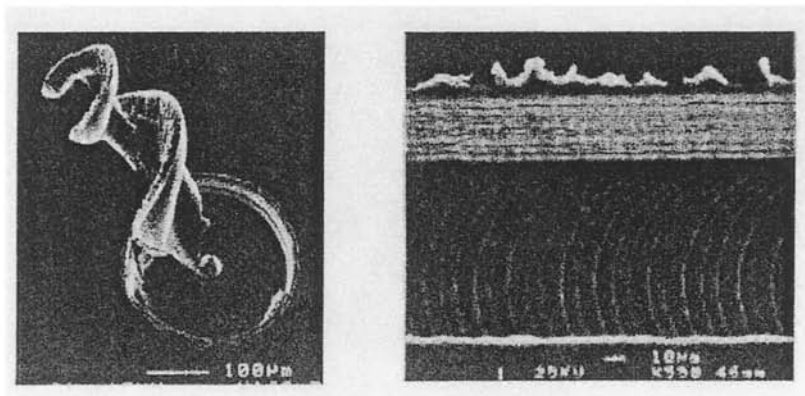


Fig. 5.14. Top burr in a micro-drilled hole and micro-machined slot

Recent results from micromachining stainless steel tended to show that burr height increases as the feed per tooth and the cutting speed increases linearly. Figure 5.15 shows the effect clearly.

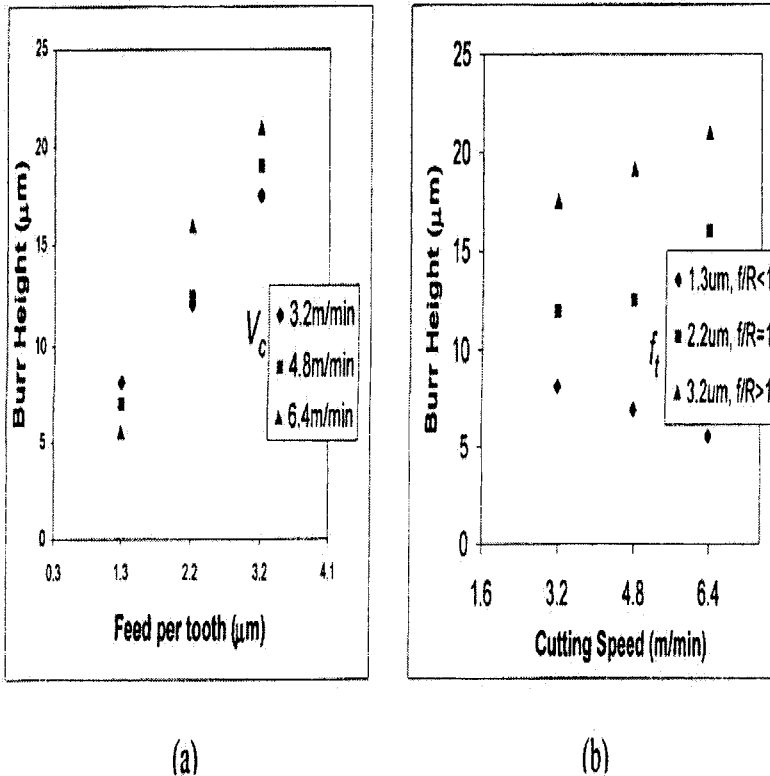


Fig. 5.15. Burr height as a function of feed per tooth and cutting speed

Tool wear also has a significant effect on burr formation. As the cutting tool wears, the ratio of chip thickness and cutting tool radius changes significantly. This changes the way that the tool removes material and consequently, burr height increases. Figure 5.16 shows the effect of tool wear on burr height.

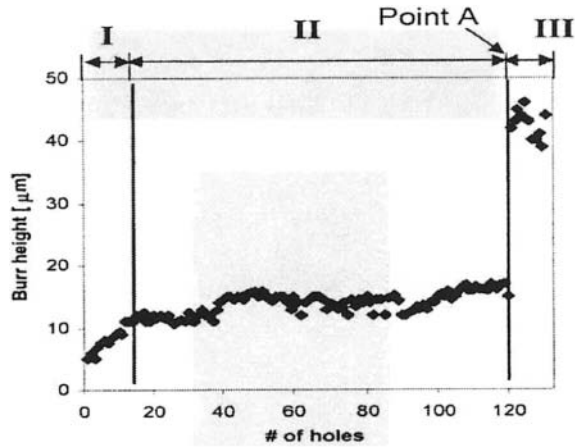


Fig. 5.16. Burr height as a function of tool wear as the number of holes drilled increases

The amount of tool wear that is experienced is measured by looking at the edge that is worn during machining. Figure 5.17 shows the magnified image of a cutting tool worn during drilling of material.

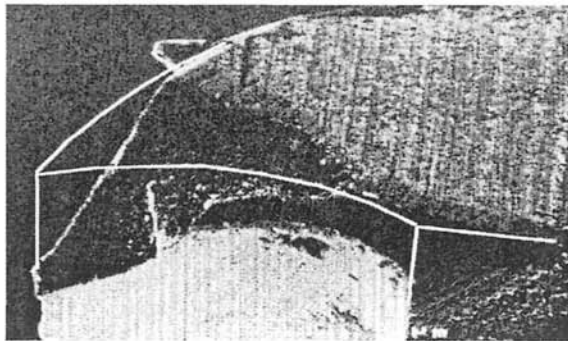


Fig. 5.17. Scanning electron micrograph of a fractured cutting tool

The coating of cutting tools to prevent burr formation has already started to form significant research efforts at different academic institutions. Machining at such small scales clearly present research engineers with significant challenges.

5.5 Micromachining Tool Design

The accurate machining of microfluidic channels has created a requirement for miniaturized machine tools referred to as meso machine tools (mMTs). The ability to machine pockets, slots, channels, and contours of MEMS based devices, is dependent upon the ability to spin a cutting tool at speeds in the range, 100-to-200 m/min. This requires spindle speeds to be in excess of 500,000 revolutions per minute using microscale cutting tools. Developments in the area of micro-cutting tools, spindle design, and vibration dampening of mMTs is being investigated by the author at Purdue University, and developments in the area of process modeling, mechanistic model development for multi-phase materials, molecular dynamics models for chip formation in micromilling, and micro-drilling dynamics are being conducted by Ehmann, DeVor, and Ni, at Northwestern University, and the Universities of Illinois and Michigan.

Conventional machine tool frames have been developed to minimize vibrations and other sources of error during machining operations. Most desktop conceptual machines are based on open-frame models that provide easy access but the structural loop is prone to Abbe errors. Figure 5.18 shows such a configuration.

Closed frame structures provide a better solution but the structure is not optimized for developing desktop machine tools. A better solution is afforded by the tetrahedral shape of structure that is composed of six legs joined at spherical nodes, where the machining zone is in the center of the frame. It has high stiffness and thermal stability, and has viscous shear damping mechanisms built into the legs of the structure. Damping of vibrations is afforded by means of sliding bearing material applied to the self-centering spherical joint (Fig. 5.19).

Several prototype mMTs have been built to explore the feasibility of using feed drives and spindle technologies. The two principal feed drive technologies used include piezoelectric actuated systems and voice-coil actuated systems. The first machines developed include those shown in Fig. 5.20 that use piezoelectric transducers that operate similar to the inch-worm principle.

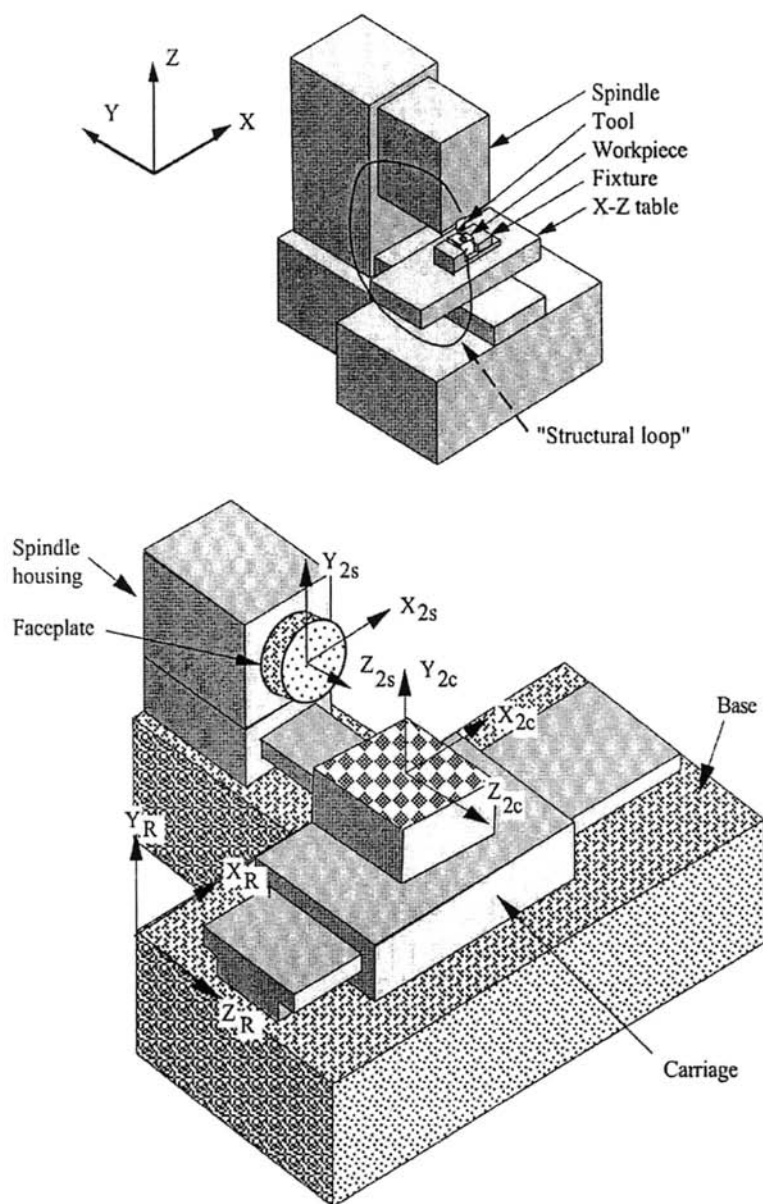


Fig. 5.18. Illustration of the open frame structure

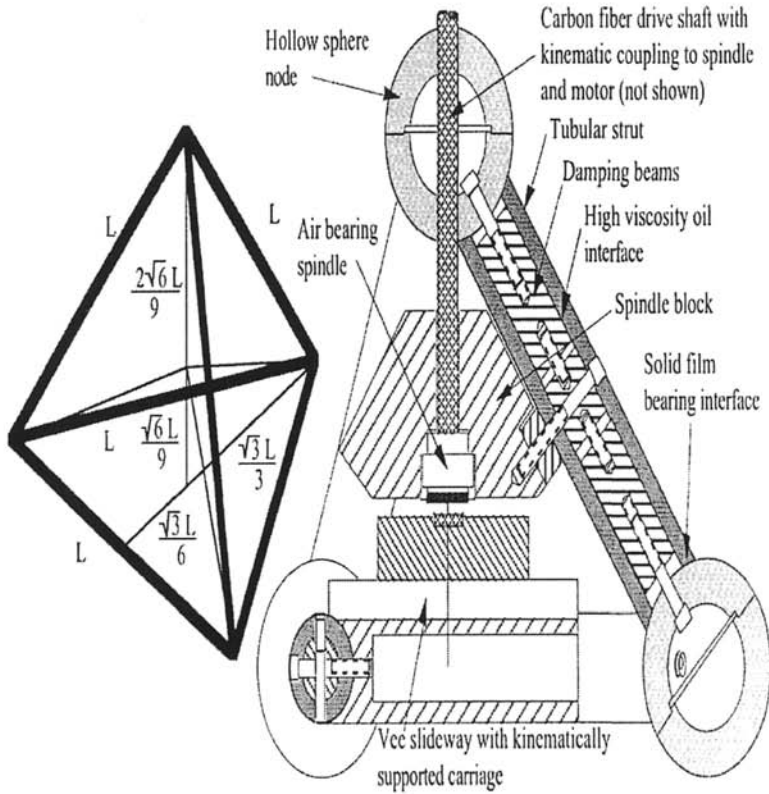


Fig. 5.19. Schematic diagram of the tetrahedral structure developed by the National Physical Laboratory, London

Open-loop machines have proven to be troublesome due to the inability to maintain a constant velocity. The amount of pre-load on the actuators produced wide variations in the velocity, and the applied loads caused velocities to change spuriously. Since actuators are operated in the on/off mode, velocity was difficult to control and adjust. Therefore, feedback control using LVDTs will provide a greater level of control.

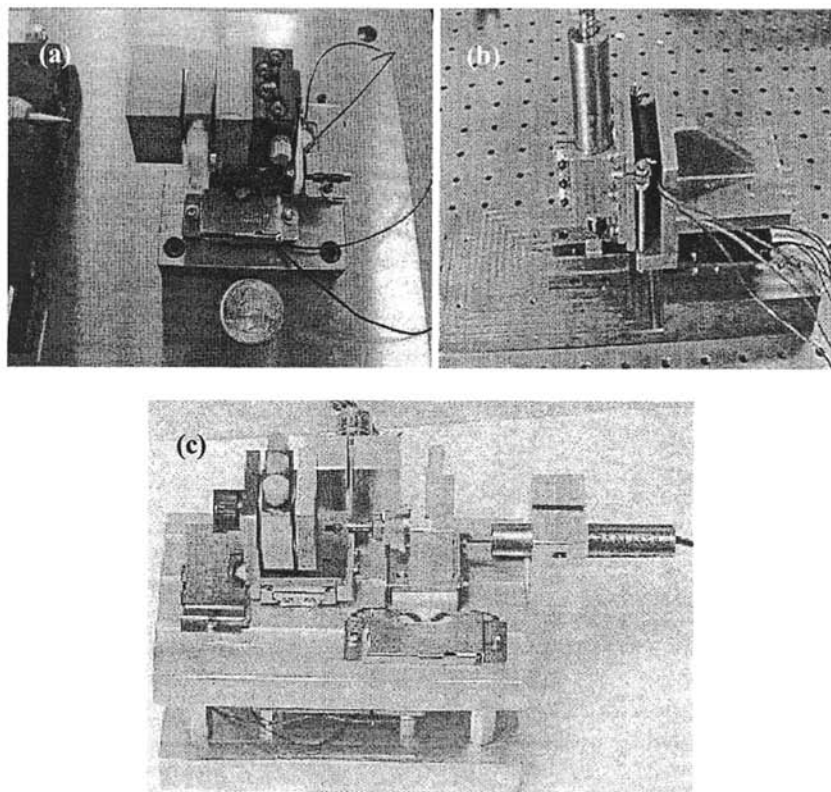


Fig. 5.20. Piezoelectric-actuated mMTs. (a) Open-loop with mounted load cell (University of Illinois at Urbana-Champaign); (b) Open-loop milling center (University of Michigan); and (c) closed-loop mMT (Northwestern University)

Voice coil actuated mMTs have been developed with a three-axis voice coil stage, triaxial load cell, and triaxial accelerometer again with a low speed air turbine spindle. Figure 5.21 shows the general arrangement. All axes have a 1 micron resolution linear encoder and actuators apply a peak force of 42 N and 80 N for x and y-axes, respectively. Feed velocities range from 1 mm/s to 4 mm/s. The principal author has developed a tetrahedral shaped mMT with an ultra high-speed spindle (Fig. 5.5).

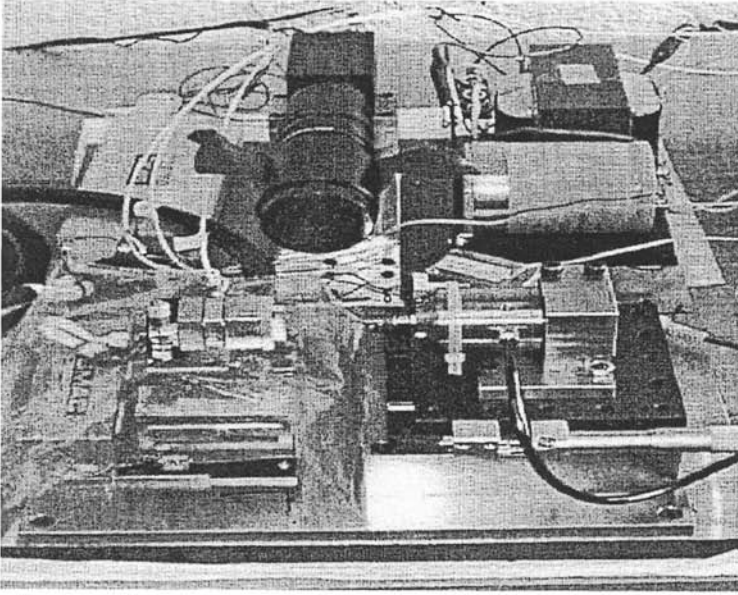


Fig. 5.21. Voice-coil-actuated mMT (University of Illinois at Urbana-Champaign)

The design of high-speed spindles is of paramount importance when one considers the size effect at the microscale. As discussed elsewhere in this book, extremely high strain rates are required to overcome the difficulties of removing material at the micro- and nanoscales. High-pressure variations on the rotor causes the rotor to fail and this severely limits the reliability and durability of the high-speed spindles to support new developments in micro- and mesoscale manufacturing technologies. Different designs of rotor are proposed and optimum designs were chosen based on the lowest amount of pressure variation on the surfaces of the rotor. Numerical simulations of different rotor designs for different rotational speeds were carried out using commercial computational fluid dynamics (CFD) software package known as CFX. The results revealed that changes in the rotor, inlet, and outlet geometries affect the pressure coefficient significantly.

5.6 High Speed Air Turbine Spindles

Figure 5.22 shows a conventional high-speed air turbine spindle. To drive a high-speed spindle a motor, or compressor, is integrated with the spindle shaft. High-pressure compressed air enters into the housing of the spindle from the compressor via a standard pneumatic connector.

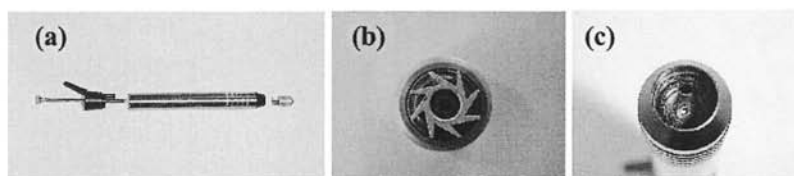


Fig. 5.22. Conventional high-speed air turbine spindle: (a) expanded view; (b) view of rotor; and (c) view of spindle where rotor body is located showing exhaust port where air is directed to vanes of the rotor in (b)

The compressed air enters the housing through the shaft and rotates the rotor of the spindle. The cutting tool, which is attached to the center of the rotor, rotates with the speed of the rotor and machines the workpiece more quickly than conventional spindles. The rotor is supported by an air bearing, which provides stability to the rotor and also transmits the necessary torque. In the present chapter, various designs of rotor for different rotational speeds are proposed and to check the validity of their performance, fluid analysis of rotors has been undertaken using a proprietary software package. Pressure coefficients on the rotors were calculated and compared for different designs of rotor to determine the optimum design of the rotor. The pressure coefficient is defined as the difference between the highest and the lowest pressure on the surface of the rotor, which is normalized by the imposed inlet pressure. The pressure coefficient determines the pressure exerted by high-speed compressed air on the rotor and for the optimum design of the rotor, the pressure coefficient should be as low as possible as large values of pressure coefficient indicate that high pressure variations may cause a severe imbalance of the load on the rotor.

5.6.1 Fluid Flow Analysis

Fluid analysis of different designs of high-speed rotor was carried out using the commercial CFD software, CFX 5.5.1. With the development and use of CFD, it is possible to examine and predict the rotor's performance and to optimize the geometry prior to the construction of a prototype. In the present section, the design of the rotor governed by its fluid domain is described by the governing equations of fluid flow. The boundary conditions for the numerical solution are described.

5.6.2 Assumptions in the CFD Approach

The following assumptions were considered for the numerical solution of high-speed spindles using the CFD approach:

- (1) The rotor's rotational speed depends on the pressure of the compressed air, entering from the compressor. But the numerical simulation was carried out by considering a decoupled system, i.e., for a given pressure (60 psi) of the air, the rotating speed of the rotor has been assumed to have a constant value such as half-a-million rpm, one million rpm, etc. This means that the current study deals only with fluids problem, not the fluid-structure problem.
- (2) Steady-state simulation was assumed for all numerical simulations.

5.6.3 CFD Geometry Model

Typical rotor geometry is shown in Fig. 5.23. The bearing component of the high-speed spindle was omitted in the CFD model, as the pressure distribution across the rotor is the key objective. The outer diameter of the rotor is 0.3 inches (7.6 mm), inner diameter of the

rotor is 0.092 inches (2.34 mm), the height along the z-direction is 0.1445 inches (3.6 mm) and the angle between the rotor blades is 90° .

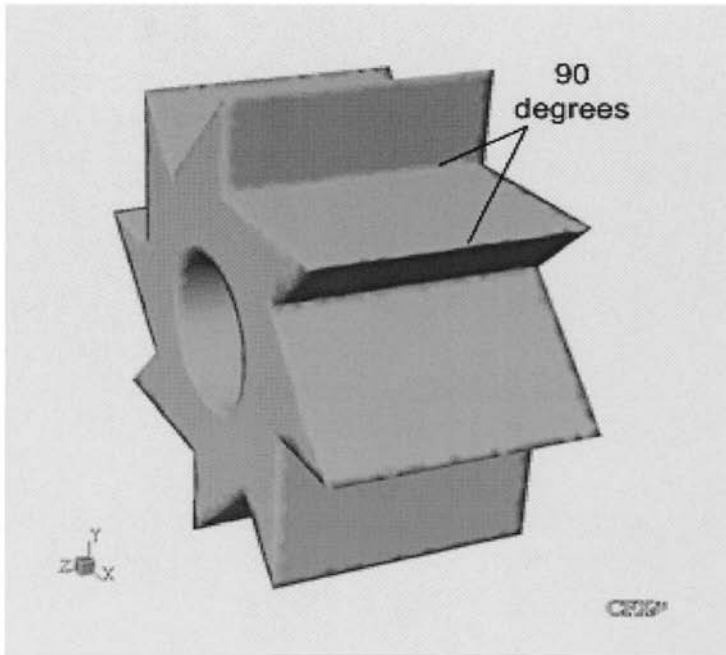


Fig. 5.23. Modeled rotor shown in Fig. 5.11 [2]

A cylindrical housing with a diameter of 0.31 inches (7.8 mm) was modeled around the rotor with a height along the z-direction of 0.1735 inches (4.4 mm) so that the rotor could rotate freely inside the housing. The spindle is driven by compressed air. Three inlets, with a diameter of 0.055 inches (1.4 mm), that make an angle of 120° with each other, were created around the housing. The inlets were created at an angle of 45° with the z-axis of the rotor, so that the air can directly impinge on the rotor blades, thus the torque and the angular speed of the rotor could be varied. An outlet for the air was created at the center of the housing. Three inlets and cylindrical housing are shown in Fig. 5.24.

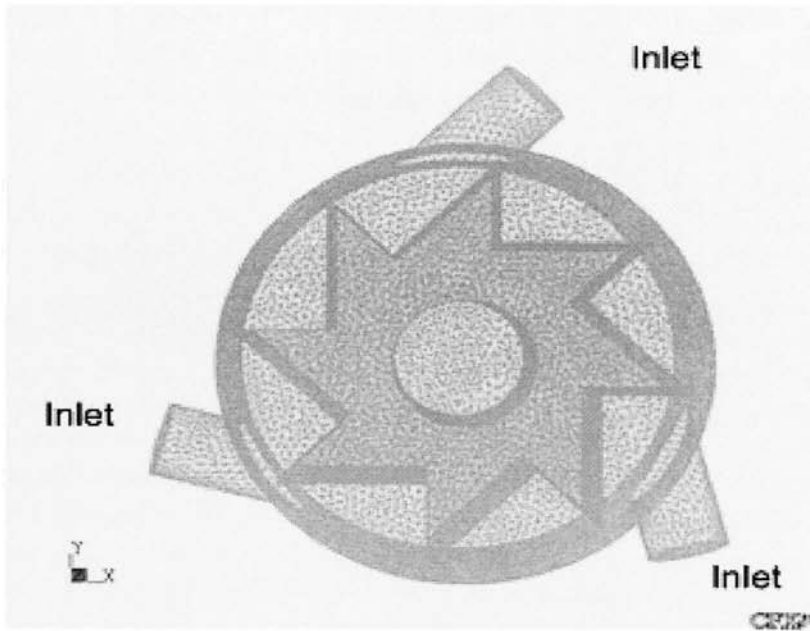


Fig. 5.24. Front view of the geometry considered for numerical solution with three inlets and housing [2]

5.6.4 Fluid Models

Air was considered to be a compressible, viscous ideal gas, with a molar mass of 0.03 kg/mol, dynamic viscosity of 1.725E-05, specific heat capacity of 1003.8 J/kg.K, and a thermal conductivity of 0.02428 W/m.K. The flow in the high-speed spindle is seen as completely turbulent. Turbulence is described by the k - ε turbulent model, in which k is the turbulent kinetic energy and ε is the turbulent eddy dissipation. A total energy heat transfer model was considered as the kinetic energy effects are important in the model.

5.6.5 Boundary Conditions

The following boundary conditions were applied to the model:

- (1) Opening boundary condition with a static pressure of 60 psi and static temperature of 293 K at three inlets;
- (2) Opening boundary condition with a static pressure of 0 (zero) and static temperature of 293 K at the outlet;
- (3) A no-slip (moving) wall boundary condition on the rotor. A constant angular speed of the rotor was also specified;
- (4) A no-slip (stationary) wall boundary condition on the housing surfaces and inlet surfaces.

5.6.6 Governing Equations

The governing equations of three-dimensional fluid flow were represented as:

Continuity Equation,

$$\frac{\partial(\rho U_i)}{\partial X_i} = 0 \quad (5.45)$$

Momentum Equation,

$$\frac{\partial(\rho U_i U_j)}{\partial x_j} = -\frac{\partial P}{\partial x_i} + \frac{\partial}{\partial x_j} (\mu_{eff} \frac{\partial U_i}{\partial x_j} + \mu_{eff} \frac{\partial U_j}{\partial x_i}) \quad (5.46)$$

Where repeated indices imply summation from 1 to 3, ρ is the density, U_i are the cartesian velocity components, P is the pressure, X_i are the coordinate axes, and μ_{eff} is the effective viscosity, which is defined as:

$$\mu_{eff} = \mu + \mu_t \quad \text{and} \quad \mu_t = C_\mu \rho \frac{k^2}{\varepsilon} \quad (5.47)$$

Where μ_t is the eddy viscosity, C_μ is a constant, and is equal to 0.09, k is the turbulent kinetic energy and ε is the turbulent eddy dissipation. The turbulence model is given by,

$$\frac{\partial \rho k}{\partial t} + \frac{\partial}{\partial x_j} (\rho U_j k) - \frac{\partial}{\partial x_j} \left(\frac{\mu_{eff}}{\sigma_k} \frac{\partial k}{\partial x_j} \right) = \mu_t \frac{\partial U_i}{\partial x_j} \left(\frac{\partial U_i}{\partial x_j} + \frac{\partial U_j}{\partial x_i} \right) - \frac{2}{3} \frac{\partial U_j}{\partial x_j} \left(\mu_t \frac{\partial U_j}{\partial x_j} + \rho k \right) - \rho \varepsilon \quad (5.48)$$

And

$$\frac{\partial \rho \varepsilon}{\partial t} + \frac{\partial}{\partial x_j} (\rho U_j \varepsilon) - \frac{\partial}{\partial x_j} \left(\frac{\mu_{eff}}{\sigma_\varepsilon} \frac{\partial \varepsilon}{\partial x_j} \right) = \frac{\varepsilon}{k} (C_{\varepsilon 1} \mu_t \frac{\partial U_i}{\partial x_j} \left(\frac{\partial U_i}{\partial x_j} + \frac{\partial U_j}{\partial x_i} \right) - \frac{2}{3} \frac{\partial U_j}{\partial x_j} \left(\mu_t \frac{\partial U_j}{\partial x_j} + \rho k \right)) - C_{\varepsilon 2} \rho \varepsilon \quad (5.49)$$

Where $\sigma_k = 1.0$, $\sigma_\varepsilon = 1.3$, $C_{\varepsilon 1} = 1.44$ and $C_{\varepsilon 2} = 1.92$ are constants from the k - ε model.

Energy Equation,

$$\frac{\partial (\rho U_j h_{tot})}{\partial x_j} = \frac{\partial (\lambda \frac{\partial T}{\partial x_j})}{\partial x_j} + S_E \quad (5.50)$$

Where h_{tot} is defined as the specific total enthalpy, which for the general case of variable properties is given in terms of the specific static enthalpy, h , by:

$$h_{tot} = h + \frac{1}{2} U^2; \quad h = h(p, T) \quad (5.51)$$

And S_E is the source term, which represents the work done by the viscous and pressure forces.

Equation of State,

For high-speed flows, the density of the fluid changes with pressure and temperature, i.e., the fluid is compressible, therefore the equation of state plays an important role. The equation of state for an ideal gas is given as:

$$p = \rho RT \quad (5.52)$$

Where p is fluid pressure, ρ is the density of the fluid, T is the temperature of the fluid and R is the gas constant and is equal to 286.9 J/kg. K for air as an ideal gas.

5.6.7 Method of Solution

The parameter “pressure coefficient” was defined to determine the pressure variation across the rotor.

$$\text{Pressure coefficient} = \frac{P_{\max} - P_{\min}}{P_{\text{inlet}}} \quad (5.53)$$

Where P_{\max} = maximum pressure exerted by air on the rotor, P_{\min} = minimum pressure exerted by air on the rotor, and P_{inlet} = air pressure at the inlet. Maximum pressure and minimum pressure exerted by air can be obtained by CFX-Post. Inlet pressure was considered for determining the pressure coefficient to non-dimensionalize the value of the pressure coefficient, as the inlet pressure (60 psi) was standard for all geometries considered for numerical simulation.

5.7 Mechanical Design of High-Speed Rotors

To estimate and to minimize the pressure distribution across the rotor, various designs of rotor have been proposed for the numerical simulation of high-speed spindles. The following section describes the different designs of the rotor:

5.7.1 Basic geometry of the rotor

The outer diameter of the rotor was 0.30 inches (7.6 mm), inner diameter was 0.092 inches (2.34 mm) and height along the z-direction was 0.1445 inches (3.6 mm). Figure 5.25 shows the three-dimensional geometry of the rotor. Housing with a diameter of 0.31 inches (7.8 mm) was built around the rotor with a height of 0.1735 (4.4 mm) inches. Three inlets, with a diameter of 0.055 inches (1.4 mm), that make an angle of 120 degrees with each other, were created around the housing. An outlet hole was created at the center of the housing with a diameter of 0.02 inches. The angle between the blades was considered as 55 degrees. Figure 5.26 shows the front view of the geometry with housing, rotor and three inlets.

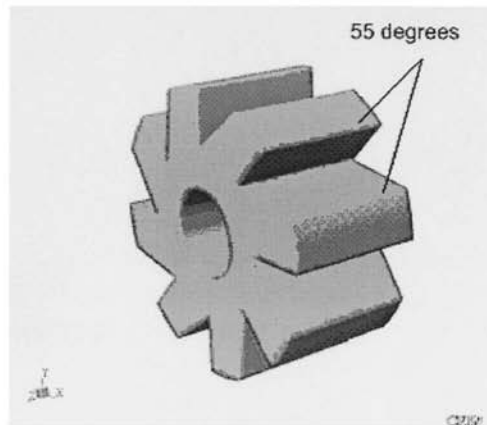


Fig. 5.25. Three-dimensional view of the rotor [2]

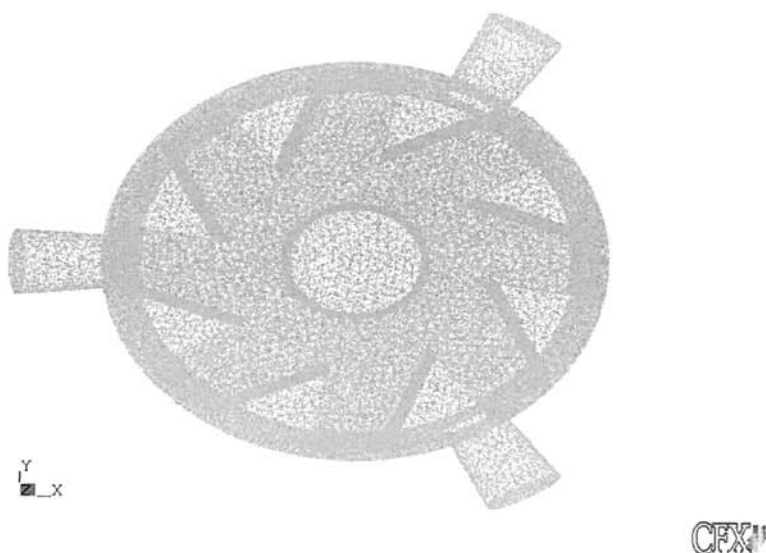


Fig. 5.26. Front view of the geometry considered for numerical simulations [2]

5.7.2 Rotor with Fillet Surfaces

The basic geometry of the rotor was modified with fillets on the blade surfaces and in between the blade surfaces of the rotor. It is observed (Fig. 5.26) that the air that is entering the housing from the inlets is impinging on the blades and in between the blades. The modified geometry allows the flow to be streamlined in order to avoid the sharp edges of the rotor. The dimensions of this geometry were considered the same as the basic geometry of the rotor. As in the basic geometry case, three inlets, which make an angle of 120 degrees to each other were considered around the housing and an outlet at the center of the housing. The geometry of the rotor with fillets is shown in Fig. 5.27 and the geometry of rotor along with housing and three inlets is shown in Fig. 5.28.

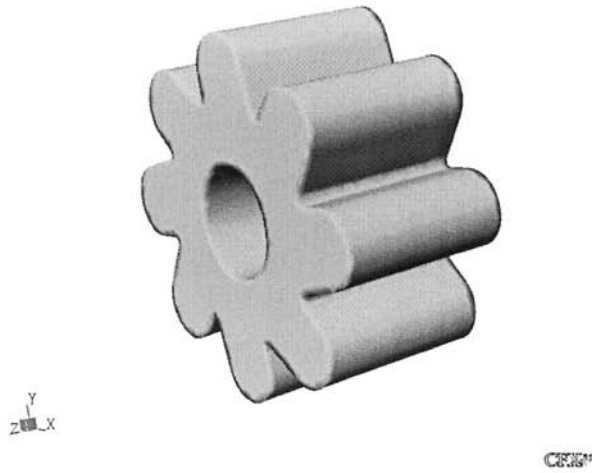


Fig. 5.27. Rotor with rounded vanes [2]

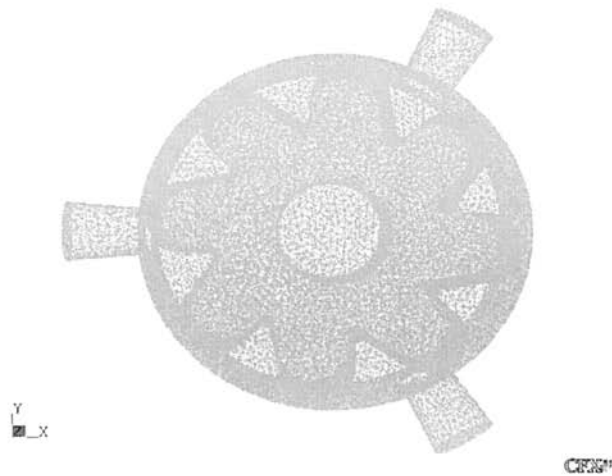


Fig. 5.28. Front view of the *rounded* vane geometry considered for numerical simulation [2]

5.7.3 Rotor with a 70-Degree Blade Tip Angle

The geometry of the rotor with 70° blade angle is shown in Fig. 5.29. The basic geometry was modified by changing the angle between the rotor blades to 70° . Three inlets and an outlet were modeled similar to the previous geometry. Figure 5.30 shows the geometry considered for the numerical simulation.

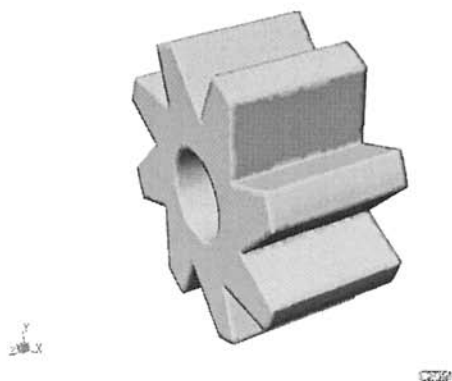


Fig. 5.29. Rotor with a 70° blade tip angle [2]

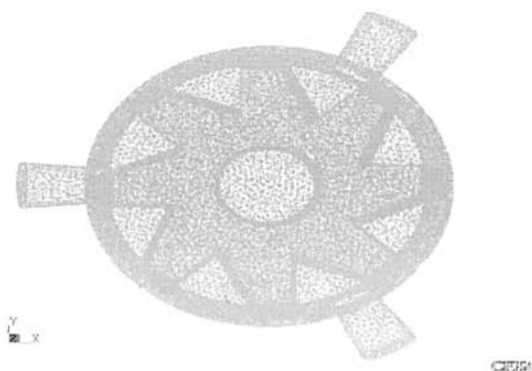


Fig. 5.30. Front view of the geometry shown a rotor with 70° blade tip angle, housing, and three outlets [2]

5.7.4 Rotor with 90-Degree Blade Tip Angle

The basic geometry of the rotor was modified by increasing the angle between the blades to 90° . The rotor geometry is shown in Fig. 5.31. The dimensions of the rotor and housing were similar to the basic rotor geometry. The geometry of the rotor and housing, along with three inlets and an outlet is shown in Fig. 5.32. CFD simulations have been carried out for the above geometries of the rotor and the pressure coefficient was found to be less for rotors with 90° blade angles. Therefore, the rotor with 90° blade angle geometry was used in all the subsequently modified cases.

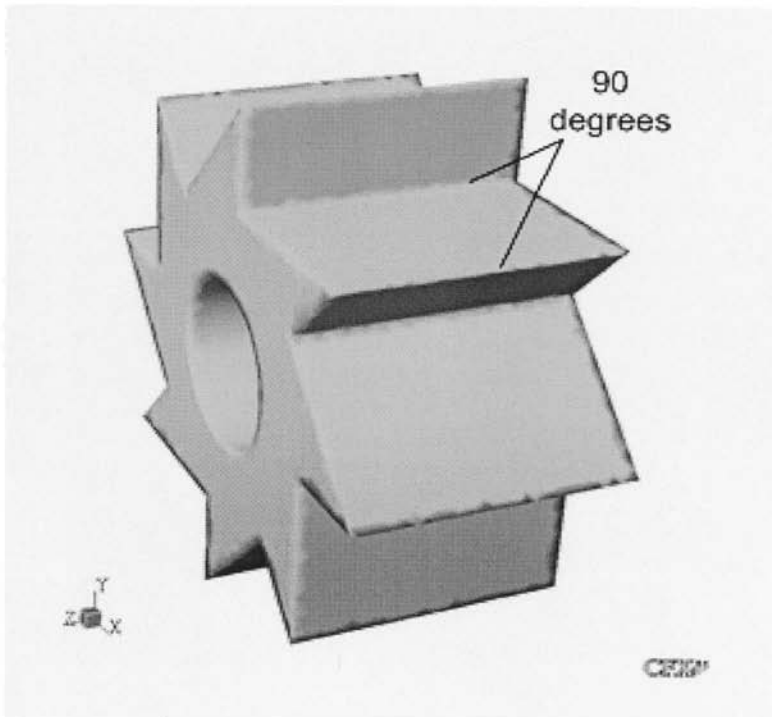


Fig. 5.31. Rotor with a 90° blade tip angle [2]

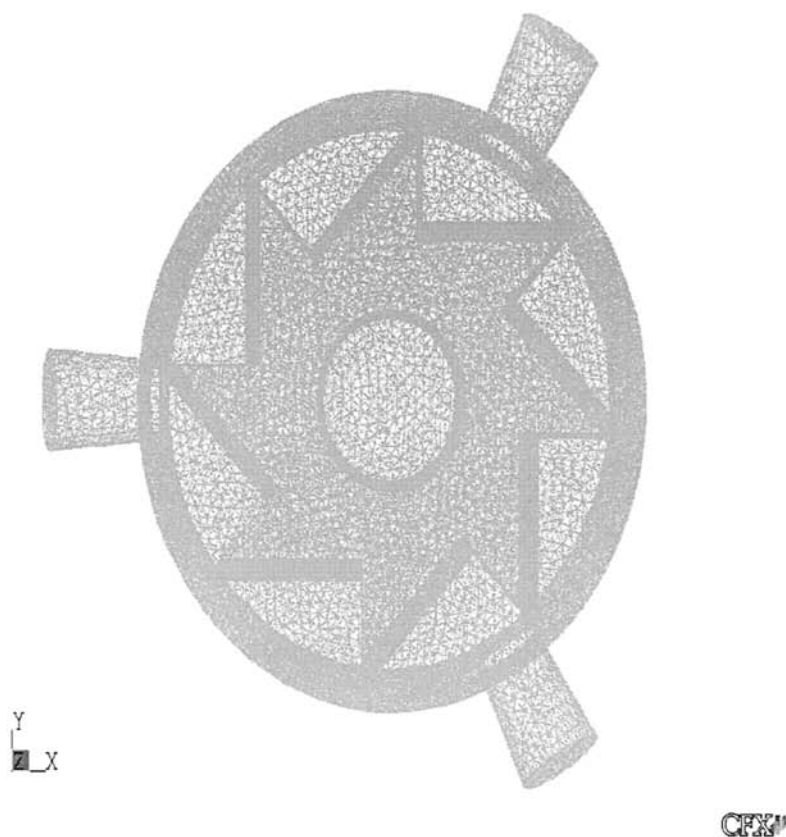


Fig. 5.32. Rotor with a 90° blade tip angle, housing, and three inlets [2]

5.7.5 Rotor with 12 Blades

In this case, the number of blades of the rotor was increased to twelve and the angle between the rotor blades was 90° . Owing to the increase of the number of blades, the surface area of the rotor increases and the pressure variation on the rotor decreases. The geometry of the rotor is shown in Fig. 5.33.

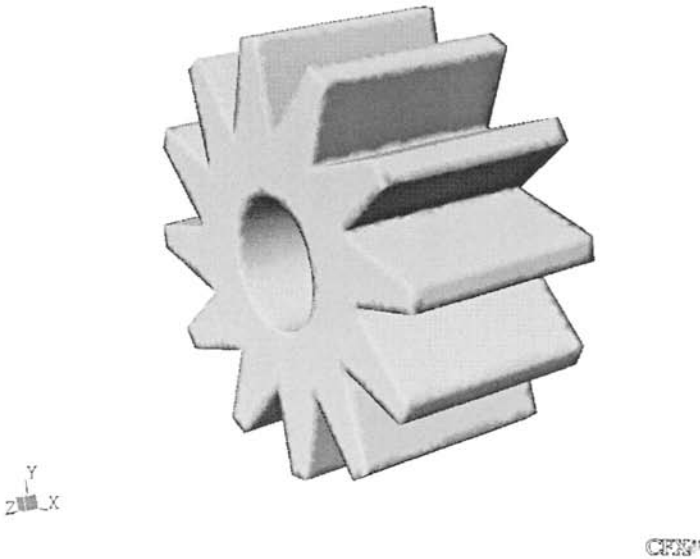


Fig. 5.33. Rotor with 12 blades [2]

5.7.6 Housing with Inclined Inlets

The dimensions of the rotor and housing were same as that of the basic geometry of the rotor. The inlets were modified such that they make an angle of 45° with the z-axis, so that the air can directly impinge on the rotor blades, thus the torque and the angular speed of the rotor could be increased. An outlet for the air was created at the center of the housing with a diameter of 0.02 inches (0.51 mm). Three inlets and a cylindrical housing are shown in Fig. 5.34. The rotor with three inlets inclined at an angle of 30° with z-axis was also considered for the numerical simulations. Figure 5.35 shows the geometry of the rotor with three inlets inclined at an angle of 30 with the z-axis.

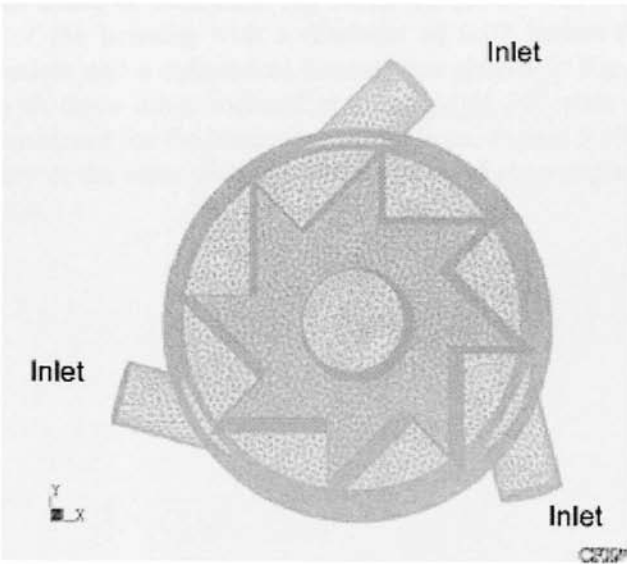


Fig. 5.34. Housing with three inclined inlets at an angle of 45° with Z-axis [2]

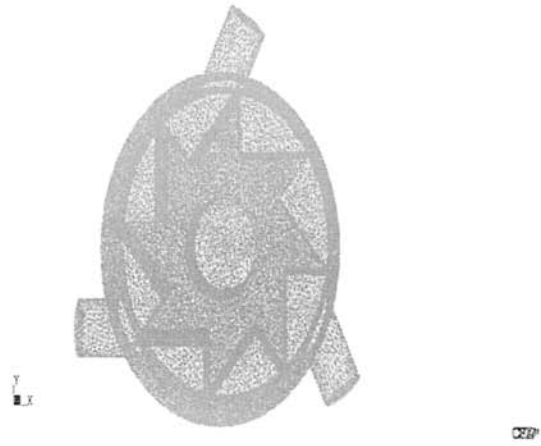


Fig. 5.35. Housing with three inclined inlets at an angle of 30° with Z-axis [2]

5.7.7 Rotor with 3 Inlets and 3 Outlets

The geometry of the rotor was modified such that the fluid entering from the inlet is expelled immediately after it crosses some part of the domain. Therefore, three outlets that make an angle of 120° with each other were created around the housing. The rotor considered for this case was the rotor with a 90° blade angle and the diameter of the inlets and outlets were considered to be 0.027 inches (0.68 mm). The dimensions of inlets, housing and the rotor were same as that of the basic geometry of the rotor. The geometry of the housing is shown in Fig. 5.36.

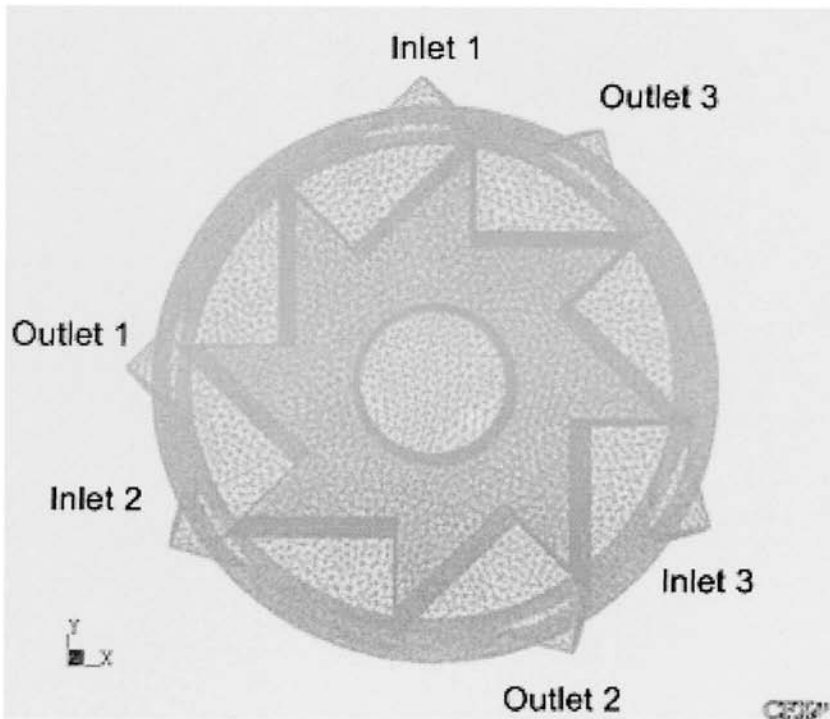


Fig. 5.36. Housing with 3 inlets and 3 outlets [2]

5.7.8 Two-Stage Rotor

The geometry of the two-stage rotor along with the housing, inlets and outlets is shown in Fig. 5.37. The diameter of the rotor is 0.27 inches (7 mm) and the diameter of the housing is 0.35 inches (9 mm). Height of the rotor along the z-direction was 0.55 inches (14 mm). Two inlets and 2 outlets were created at the upper part of the housing and 2 inlets and 2 outlets were created at the lower part of the housing. Fig. 5.38 shows an improved view of the two-stage rotor.

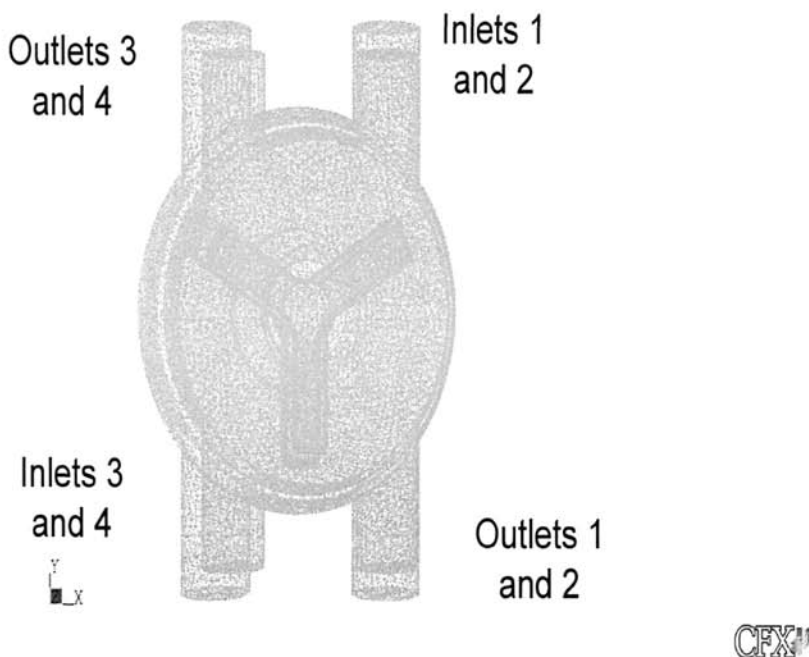


Fig. 5.37. Two-stage rotor, which contains 4 inlets and 4 outlets around the housing [2]

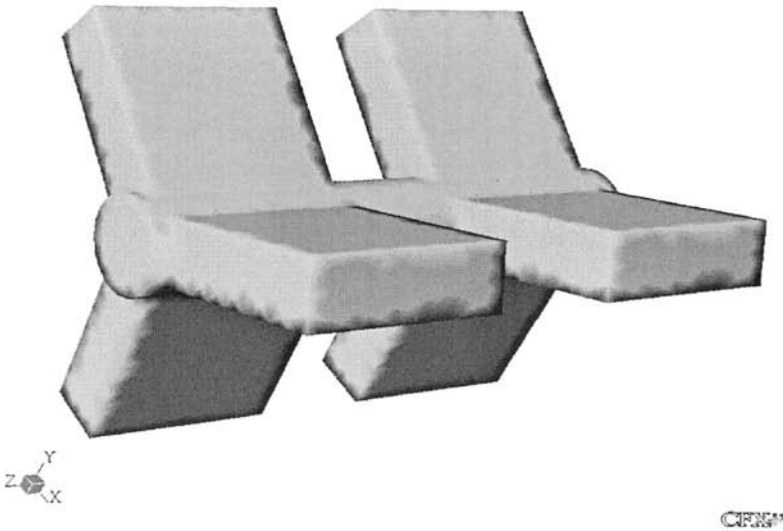


Fig. 5.38. Two-stage rotor [2]

The pressure variation and flow topology across the two-stage rotor and rotor with three inlets inclined at an angle of 45° is described. Numerical simulations of the two-stage rotors for rotational speeds of $\frac{1}{2}$ million rpm, 1 million rpm, 2 million rpm, and five million rpm were carried out using CFD simulations.

5.7.9 Flow Topology for Two-Stage Rotor

The inlet static pressure was considered to be 60 psi and outlet static pressure as 0. The rotor's speed was specified as 2 million rpm (2,000,000). In Fig. 5.39, the flow topology is illustrated. Air entering from the upper part of the housing (through inlets 1 and 2) gets diverted by rotor blades. One part builds a re-circulation area in the upper part of the housing and the other flows over the rotor blade

into the housing and exists to the atmosphere through outlets 1 and 2. Fluid entering from the lower part of the housing (through inlets 3 and 4) becomes bifurcated and most of the fluid slides through the lower part of the housing and exits to the atmosphere through outlets 1 and 2.

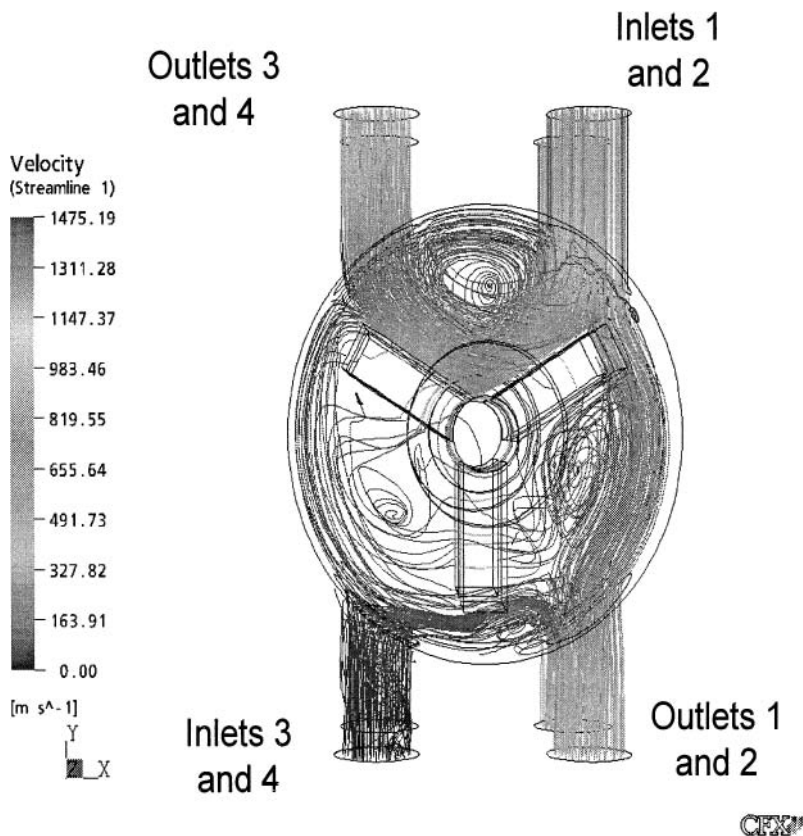


Fig. 5.39. Stream lines of the flow pattern [2]

5.7.10 Pressure Variation for the Two-Stage Rotor

In Fig. 5.40 the static pressure distribution on the two-stage rotor is shown. The fluid entering from the upper part of the housing impinges directly on the rotor blade surface and the total kinetic energy of the fluid gets converted into pressure energy due to stagnation of the fluid. Therefore, the maximum pressure is observed in the vicinity of the leading edge of the rotor blades, which bifurcates the inlet stream entering from the upper part of the housing. The pressure coefficient on the rotor can be determined from Eq.(5.53) by substituting values of maximum pressure and minimum pressure on the rotor from Fig. 5.40 and inlet pressure (60 psi).

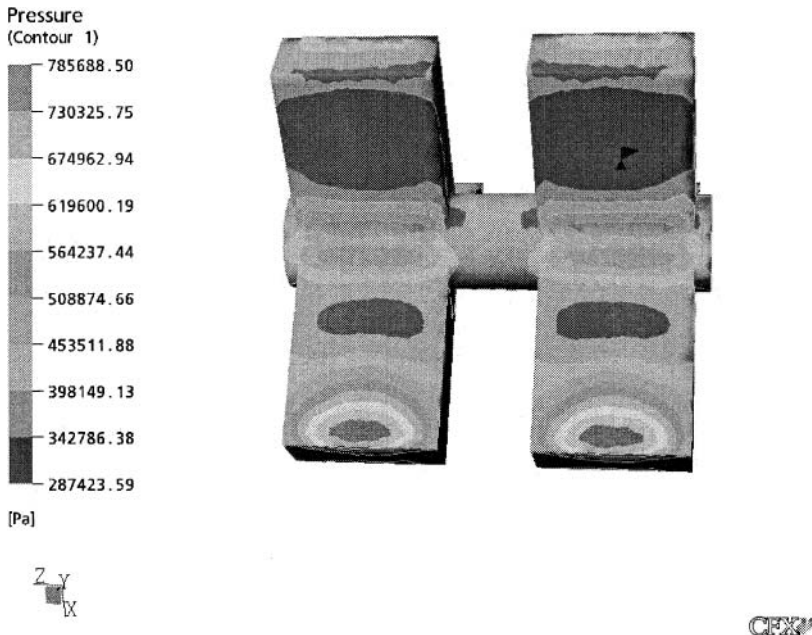
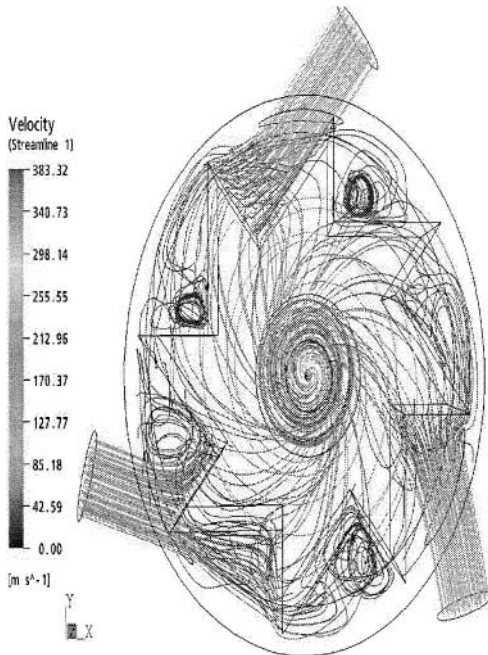


Fig. 5.40. Static pressure distribution on the rotor [2]

5.7.11 Flow Topology for Rotor with Three Inlets Inclined at 45°

Flow topology and pressure variation on the rotor with three inlets, inclined at an angle of 45° with the z-axis is described as the pressure coefficient values for this geometry was found to be minimum. The rotational speed of the rotor was specified as $\frac{1}{2}$ million (500,000) rpm.

Flow pattern in the geometry can be seen in Fig. 5.41. Fluid entering from three inlets impinges on the rotor blades. Some part of the inlet fluid gets diverted and flows into the housing. The figure clearly shows the impingement of the fluid on the rotor blades. At the hollow part of the rotor, the fluid gets swirled and at the outlet the velocity increases due to the sudden contraction of the surface area at the outlet. The outlet is located at the center of the housing.



CET

Fig. 5.41. Stream lines of the flow pattern [2]

5.7.12 Pressure Variation on the Rotor with Three Inlets, inclined at 45°

From Fig. 5.41 it can be clearly seen that the regions of the rotor, where the fluid flow directly impinges experiences maximum pressure due to stagnation of fluid when compared to other regions. Figure 5.42 shows the pressure variation on the surface of the rotor.

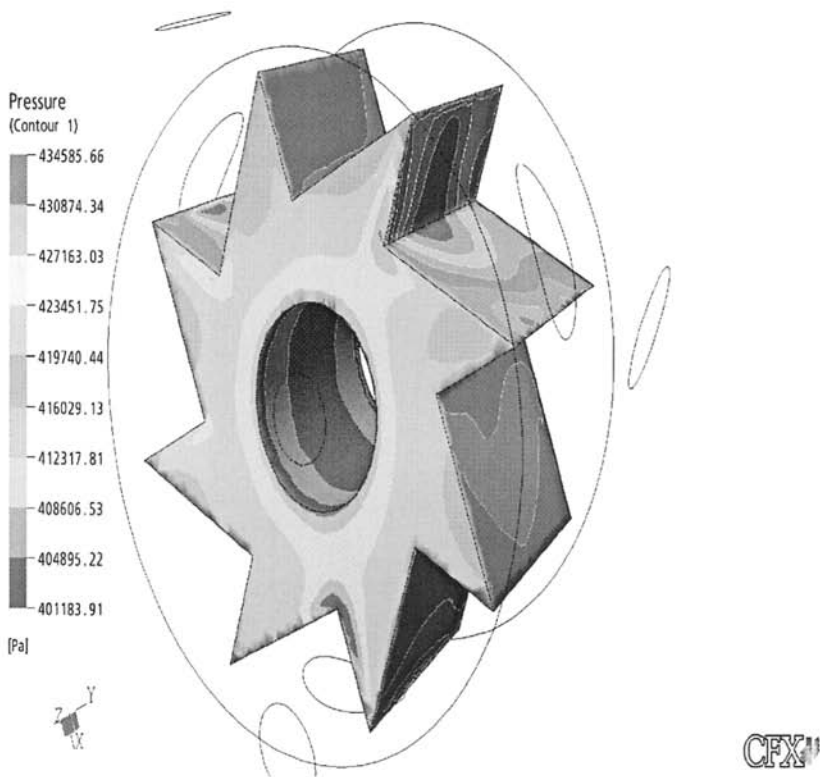


Fig. 5.42. Static pressure distribution on the rotor [2]

5.7.13 Pressure Coefficients for All Geometries

Numerical simulations of all the geometries described were carried out for different rotational speeds of rotor such as $\frac{1}{2}$ million rpm, 1 million rpm and 2 million rpm. Table 5.3 shows a non-dimensional pressure coefficient obtained for different geometries of rotor, i.e., basic geometry of rotor, rotor with fillets, rotor with 70° blade angle, and rotor with 90° blade angle.

Table 5.3. Pressure coefficients for different rotating speeds and geometry of rotor [2]

Rotational speed (rpm)	Basic geometry of rotor	Rotor with fillets	Rotor with 70° blade angle	Rotor with 90° blade angle
$\frac{1}{2}$ million	0.13	0.12	0.13	0.08
1 million	0.40	0.47	0.35	0.25
2 million	0.87	0.88	0.88	0.84

From the above table it can be observed that the rotor with a 90° blade angle has less pressure coefficient for all rotating speeds (1/2 million, 1 million and 2 million rpm) of the rotor when compared to other geometries of rotors. So, this geometry was considered for further numerical simulations. From Table 5.3 it can also be seen that as the rotating speed of the rotor increases, pressure variation on the rotor increases and the pressure coefficient is almost the same for all geometries.

Table 5.4 shows the pressure coefficients of geometries of rotor with 12 blades, rotor with inclined inlet at 30° , rotor with inclined inlet at 45° , housing with 3 outlets, and 3 inlets and two-stage rotor. As in the previous case, pressure coefficients increased with in-

creases in rotating speed of the rotor. It can be observed that the pressure coefficient values of the rotors with inlets inclined at an angle of 45° and 30° are almost the same. It can be said that for half-a-million rpm rotating speed, the rotor with three inlets inclined at an angle of 45° is the optimum design compared to other designs of rotor, and for 1 million rpm rotational speed of rotor, rotor with 3 inlets inclined at an angle of 30° is the optimum design compared to other designs of rotor. For 2 million rpm, both the designs have equal values of pressure coefficient and this value is less when compared to the other two designs of rotor.

Table 5.4. Pressure coefficients for different rotating speeds and geometry of rotor [2].

Speed (rpm)	Rotor with twelve blades	Rotor with inclined inlets at 30°	Rotor with inclined inlets at 45°	Rotor with 3 outlets and 3 inlets	Two- stage rotor
Half-a-million	0.10	0.09	0.08	0.36	0.86
One million	0.35	0.09	0.10	0.48	0.95
Two million	0.88	0.40	0.40	0.44	1.20

Experimental designs of high-speed air turbines are currently being constructed for micromachining applications such as microfluidic systems and high aspect ratio trenches in engineering materials for applications in the automotive, die and mold tool, and aerospace industries. The discussion of how high-speed air turbine spindles are used in micromachining operations are discussed elsewhere in this book.

5.8 Discussion

It can be seen from micromachining analysis that despite the extremely high strain rates imposed due to high speed cutting, macro-scale equations can be applied accurately and produce impressive results. The most significant differences, however, appear in the following categories: strain rate, scallop height, and chip type. Many of the forces are of a similar order of magnitude offering no significant difference between macro low-speed and micro-high speed machining. This is important during tool design as small tools must absorb the same impact forces as larger tools do during impact. However, when considering the strain rate it can be seen during micro-high-speed machining the strain rate is $8333 \times 10^6 \text{ s}^{-1}$ compared to the macro low-speed case of $667 \times 10^6 \text{ s}^{-1}$, a 12.5 times increase which relates directly to a 12.5 increase in speed from 20,000 rpm to 250,000 rpm. The increase in strain rate is directly related to the increase in cutting speed, this is expected as the cutter is imparting the strain and therefore a rate of strain to the material. The lamellae spacing Δy in Eq. 5.20 has a significant effect on the strain rate, comparing macro- and micro-scale chips it is found that lamellae are 10 times more closely packed in the high-speed chips than the low speed chips.

The purpose of milling is to create surfaces that are useful, hence surface quality should be an important consideration of milling, a measure of this is scallop height. An improvement is seen in the micro-high-speed case with a scallop height of $1.58 \times 10^{-11} \text{ m}$ compared to $8.9 \times 10^{-9} \text{ m}$ for macro slow speeds. Although both values seem insignificant it must be remembered at the micro-and nanoscale post process finishing is inappropriate, therefore created structures must be produced to specification without further processing. In addition, owing to the aspect ratio small imperfections become serious defects at small scales. From the calculations it can be seen that there is an improvement in the scallop height, which is not the improvement required when considering the scale order of magnitude has changed by a factor of four. This is because the current spindle speeds reached are not high enough for effective machining. If this speed is

increased to 1,000,000 rpm then the orders of magnitude are increased further still.

The experimental results and observations provide an interesting view of machining a variety of metals at the microscale. When one considers the approximations made in the derivation of the chip curl model, the experimentally measured results compare well with the calculated chip curl. This indicates that cutting tool bending contributes significantly to initial chip curl prior to any significant frictional interactions on the rake face of the cutting tool. The proposed model describes the initial stages of chip curl quite well. If the description of chip curl is accurate, then continuous chip formation at the microscale needs to be re-investigated. If one considers the movement of the cutting tool (Fig. 5.4), from point A toward point D, we expect the shear plane to oscillate between AC and HC depending on the amount of energy required to move the built-up edge into the segment of the subsequent chip. The cycle begins again when accumulated metals are deposited to the edge of the cutting tool, then to the subsequent segment of the chip produced during machining. Under the conditions specified, material removal rates were measured for three important engineering materials. The removal rates were $30 \text{ mm}^3/\text{min}$ for aluminum alloys, $36 \text{ mm}^3/\text{min}$ for copper alloys, and $48 \text{ mm}^3/\text{min}$ for steel.

The development of high-speed spindles using air turbine technology clearly plays an important role in the development of very high strain rate machining applications. These applications will have a significant impact on the automotive, mold and die tool, and aerospace sectors, in addition to the medical device industry for machining bone prior to prosthetic implantation and of course, the manufacture of micro-and nanofluidic devices.

5.9 Conclusions

The equations of metal cutting can be applied in the high-speed micro-scale environment. The nomographs of Merchant and Zlatin [3] can be applied confirming that future calculations can be compared to these well-constructed charts. High strain rates change the

mechanism of chip formation, thereby altering the shape of the chip. Also, high strain rates appear to provide less dependence on material properties in determining chip formation and shape. A model of chip curl at the microscale has been developed and agrees well with experimental data. It appears that the bending of the cutting tool contributes significantly to the primary chip prior to significant frictional interactions on the rake face of the cutting tool. It is shown that primary chip curl is initiated by the amount of material deposited onto the cutting tool that manifests itself as a wedge angle that controls the amount of material pushed into the base of the segment of the chip between oscillations of the primary shear plane. Further studies on chip formation at the atomic scale are needed to develop nanomanufacturing processing methods for metals and other engineering materials. High strain rate machining of structural steels can be achieved but only with increases in spindle speeds. The future development of this technique lies in the ability to rotate cutting tools at extremely high spindle speeds.

5.10 Future Developments

The development of micromachining processes is focused on the construction of high-speed spindles and stable machine tools. In addition to the basic construction of the machine tool itself, the development of tool coatings on tools other than milling cutters will be of paramount importance.

The construction of reconfigurable micromachining centers will also form the basis of combining a number of different micromachining processes into one unit that will reduce manufacturing costs. In this way, “top down” and “bottom up” micro-and nanomanufacturing processes could be realized. Therefore, the development of hybrid micro-and nanomachine tools may be a step forward in the right direction.

5.11 Problems

1. Explain how microfluidic devices work.
2. Why are microfluidic devices manufactured?
3. What are the challenges facing traditional silicon micro-machining processes when producing complex-shaped micro-and nanofluidic channels?
4. What is a lab-on-a-chip?
5. What is the Coanda effect?
6. How are mixing channels machined using micromilling tools?
7. Describe the method of modeling initial chip curl.
8. What effect does micro-tool bending have on initial chip curl?
9. Describe the observation on chip formation in micromachining.
10. Describe the developments in meso-micro-machine tools and what characteristics do they have compared with conventional machine tools?
11. Why are high-speed air turbine spindles useful for micro-machining?
12. Describe the different ways that machine tools are designed.
13. Why do burrs form and how can they be eliminated?
14. Explain why burr formation affects the mating of microparts.

References

1. Gravesen P, Branebjerg J, and Jensen OS, 1993, Microfluidics – A Review, *Journal of Micromechanics and Microengineering*, **3**, p.p. 168-182.
2. Kanjekar K, Cui J, and Jackson MJ, 2004, Design and Analysis of High-Speed Spindles For Nano-Machining Applications Using a Computational Fluid Dynamics Approach, *Proceedings of the ASME South Eastern Region XI Technical Journal*, **3**, 1, p.p.1.1 – 1.8.

3. Shaw MC, 1996, Metal Cutting Principles, Oxford Science Publications – Series on Advanced Manufacturing, Clarendon Press, University of Oxford, p.p. 18-46.
4. Bowden FP and Tabor D, 2001, The Friction & Lubrication Of Solids, Oxford Science Publications, Clarendon Press, University of Oxford, p.p. 168, 327.
5. Doyle ED, Horne JG, and Tabor D, 1979, Frictional interactions between chip and rake face in continuous chip formation, Proc. Roy. Soc., of London, **A366**, 173 – 183.
6. Jawahir IS, and Zhang JP, 1995, An analysis of chip formation, chip curl and development, and chip breaking in orthogonal machining, Trans. North Amer. Manuf. Res. Inst. – Soc. Manuf. Eng., **23**, 109 – 114.
7. Kim CJ, Bono M, and Ni J, 2002, Experimental Analysis of chip formation in micro-milling, Trans. North Amer. Manuf. Res. Inst.- Soc. Manuf. Eng., **30**, 247 – 254.
8. Komanduri R, Chandrasekaran N, and Raff LM, 2001, Molecular dynamics simulation of the nanometric cutting of silicon, Philosophical Magazine, **B81**, 1989-2019.
9. Luo X, Cheng K, Guo X, and Holt R, 2003, An investigation into the mechanics of nanometric cutting and the development of its test bed, Int. J. Prod. Res., **41**, 1449-1465.

6. Microgrinding

6.1 Introduction

Microgrinding is an aspect of advanced manufacturing technology that has been growing rapidly and playing an important role in manufacturing [1]. Precision levels in machining can be classified into four categories [2]:

- i. Normal machining
- ii. Precision machining
- iii. High-precision machining
- iv. Ultra-high precision machining

Figure 6.1 shows the progress of achievable machining accuracy in each category as a function of time (years). Notable events that led to a rapid surge toward high precision are [3]:

Taylor 1906 - 26	High-speed steel tools
Schroeter 1939	Tungsten/ titanium carbide tools
Merchant 1945	Mechanics of machining
Gilbert 1960	Economics of machining

For example, terms used for precision machining 30 years ago have become normal machining today. As the machining accuracy increases, energy processes become more relevant for the future machining processes to produce extremely accurate machining components. These processes include laser beam machining (LBM), elec-

tron beam machining (EBM), and focused ion (FIB) beam that do not require sharp tools to remove materials. Choice of materials and machining processes are directly affected by the machining achievable accuracy since different processes provide different range of tolerance bands. Taniguchi's Table 6.1 [2] classifies components into mechanical, electronic, and optical system according to precision levels and tolerance limits.

For instance, optical lenses and mirrors are manufactured to precise and ultraprecise machining levels. Most of these applications require a crack-free surface [5]. Generally, hard and brittle materials such as glass, silicon and germanium are commonly used for making these products [6]. Traditionally, optical glasses require grinding and finishing by a polishing process in order to remove the damage caused by the previous operation and to obtain a mirror-like surface [7]. The conventional ground surface of glass results in a matt finish due to brittle fracture during removal process and this surface needs to be polished to less than 20 nm R_{max} to reduce absorption and scattering of light on the glass surface [8]. However, advances in precision machining of brittle materials have led to the discovery of a "ductile regime" of operation in which material removal is by plastic deformation. Fracture mechanics predicts that even brittle solids can be machined by the action of plastic flow, as is the case in metal, leaving crack free surfaces when the removal process is performed at less than a critical depth of cut [9]. This means that under certain controlled conditions, it is possible to machine brittle materials such as ceramics and glass using single-point diamond tools so that material is removed by plastic flow, leaving a smooth and crack-free surface.

It has been reported that almost 100% ductile mode machining is possible when machining hard materials using a well defined geometry of single-point single-crystal diamond tools on a rigid ultraprecision turning machine [12]. Ductile regimes are realized on a machined component that exhibits a mirror-like finish with nanometric roughness, with crack free smooth surfaces and continuous ribbon chip generation during turning [5,13]. Although ductile mode cutting can be achieved through the application of this advanced technology, the rapid tool wear continues to present problems [14,15]. In order to overcome these problems, multi-point cut-

ting (grinding) therefore becomes more economical especially when machining hard and brittle materials [4,14]. Ultraprecision surface grinding with electrolytic in-process dressing (ELID) provides in-process dressing of the wheel [8,16,17], achieving almost 100% ductile regime machining with a finish surface without the need for subsequent polishing when grinding optical glasses and silicon-based materials. With conventional grinding machines, less than 90% ductile mode grinding is achievable because of lack of in-process dressing and therefore requires subsequent polishing [12].

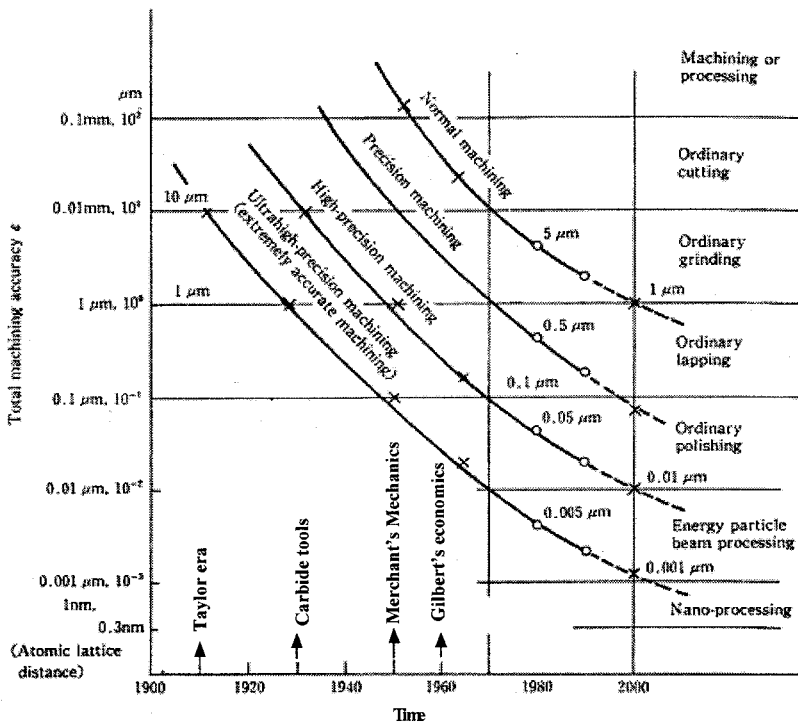


Fig. 6.1. Modified Taniguchi chart [2] of achievable machining accuracies as a function of time with insertion of landmark events that led to an upsurge in machining activities

Table 6.1. Modified Taniguchi table of various products categorized in different achievable tolerance bands with surface finish [4,10,11]

Precision levels	Tolerance band	Mechanical	Electronic	Optical	Surface finish R_a μm	ISO Tolerance
Normal machining	200 μm	Normal domestic appliances and automotive fittings etc.	General purpose electrical parts, e.g., Switches, motors and connectors.	Camera, telescope and binocular bodies.	Shaping 12.5 - 16 Milling 6.3 - 0.8 Reaming 3.2 - 0.8	IT 10 IT 9 IT 6 IT 9
	50 μm	General purpose mechanical parts for typewriters, engines etc.	Transistors, diodes, magnetic heads for tape recorders.	Camera shutters, lens holders for cameras and microscopes.	Turning 6.3 - 0.4 Drilling 6.3 - 0.8	
Precision machining	5 μm	Mechanical watch parts, machine tool bearings, gears, ball-screws, rotary compressor parts.	Electrical relays, resistors, condensers, silicon wafers, TV color masks.	Lenses, prisms, optical fibre and connectors (multi mode)	Boring 6.3 - 0.4 Laser 6.3 - 0.8 ECM 3.2 - 0.2 Grinding 3.2 - 0.1	IT 6 IT 5 IT 3 - IT 5
	0.5 μm	Ball and roller bearings, precision drawn wire, hydraulic servo-valves, aerostatic bearings, ink-jet nozzles, aerodynamic gyro bearings	Magnetic scales, CCD, Quartz oscillators, magnetic memory bubbles, magnetron, IC line width, thin film pressure transducers, thermal printer heads, thin film head discs.	Precision lenses, optical scales, IC exposure masks (photo x-ray), laser polygon mirrors, x-ray mirrors, elastic deflection mirrors, monomode optical fibre and connectors.	ELID 0.6 - 0.2 Honing 0.8 - 0.1	
Ultraprecision machining	0.05 μm	Gauge blocks, diamond indenter tip radius, microtome cutter edge radius.	IC memories, electronic video discs, LSI.	Optical flats, precision Fresnel lenses, optical diffraction gratings, optical video discs.	Super finishing 0.2 - 0.025 Lapping 0.4 - 0.05	IT 3 - IT 4 IT 1 - IT 2
	0.005 μm	Ultraprecision parts (plane, ball, roller, thread), Shape (3-D)	VLSI, super-lattice thin films.	Ultraprecision diffraction gratings.		

Several models have been put forward to explain ductile mode theory in real machining processes. Scattergood and his colleagues [18, 19, 20] proposed a critical depth of cut and a feed rate concept for ultraprecision machining as shown in Fig. 6.2.

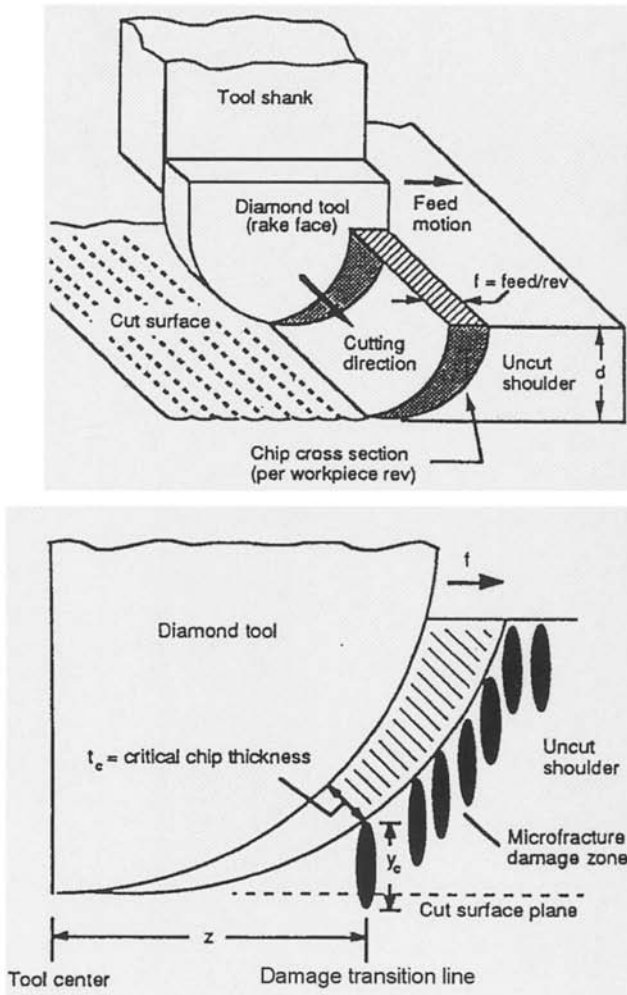


Fig. 6.2 Scattergood's model of ultraprecision machining showing 3-D view of diamond tool while cutting material and a cross-sectional view of the tool and workpiece [10]

An initial model was developed based on indentation fracture mechanics analysis [9]. According to Scattergood, fracture initiation plays a central role for ductile-regime machining. A critical penetration depth, d_c , for fracture initiation was derived by Scattergood and Blake [18] and is:

$$d_c = \beta \left[\frac{K_c}{H} \right]^2 \left[\frac{E}{H} \right] \quad (6.1)$$

Where K_c is fracture toughness, H is hardness and E is elastic modulus. β is a factor that will depend upon geometry and process conditions such as tool rake angle and coolant.

A round nosed diamond tool moves through the workpiece as shown in Fig. 6.2. Figure 6.2 shows a projection of the tool perpendicular to the cutting direction. Using the critical depth concept, fracture damage will initiate at the effective cutting depth d_c ($t_c \cong d_c$ as shown in Fig. 6.2) and will propagate to an average depth y_c as shown. If the damage does not continue below the cut surface plane, ductile regime conditions are achieved. The cross feed f determines the position of d_c along the tool nose. Larger values of f move d_c closer to the tool centerline. It is important to note that when ductile regime conditions are achieved material removal still occurs by fracture. The model proposed was verified by interrupted tests and the following relationship was obtained [10]:

$$\frac{Z_{eff}^2 - f^2}{R^2} = \frac{d_c^2}{f^2} - 2 \left[\frac{d_c + y_c}{R} \right] \quad (6.2)$$

where R is the tool nose radius and the other parameters are defined as shown in Fig. 6.2. For a typical example using [100] Ge single crystal, it was found that $d_c = 130$ nm and $y_c = 1300$ nm when using equation 6.2 with a tool having a nose radius of 3.175mm and -30° rake angle.

6.2 Grinding Wheels

Grinding wheels are made up of two materials, the abrasive grains and the bonding material (Fig. 6.3). They are produced by mixing the appropriate grain size of the abrasive with the required bond and pressed into shape. The abrasive grains do the actual cutting and the bond holds the grain together and supports them while they cut. The cutting action of a grinding wheel is dependent on bonding materials, the abrasive type, grain size (grit size), wheel grades, and wheel structure. Selection of the right combination of these features is essential for optimum solution of different grinding tasks.

6.2.1 Bond Materials

Bonds are usually made of different types of raw materials and are classified as follows [21,22]:

- i. Vitrified materials (ceramics consist of glass, feldspar and clay),
- ii. Resinoid materials (thermoset plastics – phenolformaldehyde resin),
- iii. Rubber (both natural and synthetic),
- iv. Shellac,
- v. Metal (sintered powdered metals and electroplated – bronze, nickel aluminum alloys, zinc, etc.)
- vi. Oxychloride (chemical action of magnesium chloride and manganese).
- vii. Silicate (sodium silicate NaSiO_3 or water glass)
- viii. No bond

Vitrified bonds are also called ceramic bonds [23,24], which allow porosity of up to 55%, and the rigidity of this bond makes it

possible to obtain high stock removal rates. Some cBN wheels are made from this kind of bond for grinding steel. Compared to vitrified and metal bonds, resinoid bonds furnish more flexibility while grinding and thus produce a finer surface than the two. Both resin and metal bonds are commonly used in the manufacture of diamond and cBN wheels. Because of the resiliency of rubber, it makes them excellent bond materials for polishing wheels and is used where burr and burn must be held to a minimum. Rubber bond is also used for thin flexible cut-off wheel application [21,23,25] and regulating wheel in centerless grinding [21]. Shellac-bonded wheels are good for producing high finish required in roll, camshaft, and cutlery grinding [22]. Oxychloride bonds are considered to be the weakest bond among the grinding wheel and used particularly for disc grinders. The wheels are cool cutting and seldom produce burn. Silicate bond wheel can be used in operations that generate less heat. It is not as strong as vitrified. Among all, silicate, shellac, and oxychloride have limited uses [23].

6.2.2. Abrasive Types

Abrasive grains used for grinding wheels are very hard, highly refractory materials and randomly oriented. Although brittle, these materials can withstand very high temperatures. They have the ability to fracture into smaller pieces when the cutting force increases. This phenomenon gives the abrasive its self-sharpening effect. During grinding, whenever dulling begins, the abrasive fractures thus create new cutting points. The following four types of abrasives are commonly used:

- i. Aluminum oxide, or alumina (Al_2O_3)
- ii. Silicon carbide (SiC)
- iii. Cubic boron nitride (cBN)
- iv. Diamond

Aluminum oxide and silicon carbides are known as conventional abrasives while cBN and diamond are known as superabrasives. Aluminum oxide wheel is usually used for grinding metals such as carbon steel, alloy steel, high-speed steel, annealed malleable iron, wrought iron and bronzes, and similar metals. On the other hand, silicon carbide wheel is harder but more brittle than alumina and commonly used to grind low tensile strength materials such as gray iron, chilled iron, brass, soft bronze and aluminum, as well as stone/marble, rubber, leather and other non-ferrous metals [26,27]. Diamond wheels are suitable for machining non-ferrous metal while cBN is normally good for grinding ferrous metal. However, the latter also used for grinding titanium alloys and the performance is better than SiC and Al₂O₃ wheels. Aluminum oxide wheel is often replaced by cBN for hardened steel (>45HR_c), superalloys (nickel, cobalt, or iron base with hardness greater than 35HR_c), high-speed steels and cast iron. cBN has four times the abrasion resistance of aluminum oxide. The high thermal conductivity of cBN prevents heat buildup and associated problems such as wheel glazing and workpiece metallurgical damage [27]. Some properties of these abrasives compared to hardened steel and glass are shown in Table 6.2

Table 6.2 shows that diamond has promising properties compared to the three other abrasives. One of the unique properties of diamond that stands out is its extreme hardness. The hardness of this material gave it the greatest electrical resistance and thermal conductivity of all known substances. Also, it is chemically inert. Chemical inertness normally prevents the diamond from bonding to or reacting with other substances [32]. For these reasons it is the most desirable abrasive for many applications, but there are limitations to its usefulness other than cost. The surface chemistry of diamond limits its usefulness in certain conditions. Diamond is carbon and at high enough temperatures will burn, or will react with carbide-forming metals. If either event occurs to any significant extent, the diamond is lost. The service conditions that are required to avoid such losses are low temperatures and avoidance of carbide-forming metals except at temperatures close to room temperature such as in lapping and polishing operations. The high thermal conductivity of diamond helps to relieve the problem by conducting heat away [33].

Table 6.2. Properties of some hard and brittle materials [23,28-31]

Material	Melting point (°C)	Thermal conductivity (W/m.K)	Hardness Knoop (kg/mm ²)	Density (kg/m ³)
Hardened steel	1371 - 1532	15 - 52	700 - 1300	6920 - 9130
Glass	350 - 750	0.6 - 1.7	300 - 810	2270 - 6260
Aluminum oxide	2040 2050	29	2000 - 3000	4000 - 4500
Silicon carbide	2830 2500	63 - 155	2100 - 3000	3100
Cubic boron nitride	3200	1300	4000 - 5000	3480
Diamond	3700	2000	7000 - 8000	3500

Diamond is excellent for machining non-ferrous metal (such as copper, zinc, aluminum and their alloys), plastics, ceramics, glass, fiberglass bodies, graphite, and other highly abrasive materials [34]. Though diamonds are very hard they wear out when machining steel, titanium alloys, and stainless steel because they consist of pure carbon. Carbon in diamond dissolves in γ -Fe at a high rate at a temperature higher than 900°C [3]. Diamond also is not particularly effective for machining superalloys that contain cobalt or nickel, probably for the same reason stated earlier [3,35]. A recent study on grinding wear mechanisms showed that cBN wheel is superior to Al_2O_3 and SiC wheel due to greater chemical stability of cBN at higher temperatures when grinding titanium alloy (Ti6Al4V) and nickel-based alloy (K417) [36].

6.2.3 Abrasive Grain Size

The size of an abrasive grain is identified by a number, which normally is a function of mesh width of the sieve size either in micron or mesh openings per inch. Table 6.3 shows the equivalent grain size used by FEPA (micron), ASTM 11 (inches), ISO, and DIN (micron) standard both for diamond and cBN wheels. In the metric system (micrograin size), the smaller the number the smaller the grain size. However, the coding is reversed in the imperial system in which smaller number represents coarser grain size.

6.2.4 Mechanical Grade

The grade of a grinding wheel refers to its strength in holding the abrasive grains in the wheel. This is largely dependent on the amount of bonding material used. As the amount of bonding material is increased, the linking structure between grains becomes larger, which makes the wheel act harder. A hard wheel has a stronger bond than a soft wheel. The type and the amount of bond in the wheel also influence the overall strength. In standard marking systems, the grade of the grinding wheel is labeled by A-Z (soft to hard).

6.2.5 Abrasive Structure

The structure of a grinding wheel represents the grain spacing and is a measure of the porosity of a bonded abrasive wheel. Figure 6.3 illustrates the structure of a grinding wheel, showing bigger pore areas (voids) in open structure than medium and dense structure. Porosity allows clearance space for the grinding chips to be removed for proper cutting action during grinding operations. This clearance space must not be too small or the chip will stay in the wheel, causing what is called wheel loading. A loaded cutting wheel heats up and is not efficient in its cutting action. When this happens, frequent dressing is needed to remove loaded workpiece particles off the

wheel. On the other hand, too large a space is also inefficient, as there will be too few cutting edges. A dense structure has stronger grit holding power than an open structure. Some porosity is essential in bonded wheels to provide not only clearance for the minute chips being produced but also cooling; otherwise they would interfere with the grinding process. In standard marking systems, the structure of the wheel is labeled by numbers. Smaller numbers denote open structure while dense structures are represented by higher numbers.

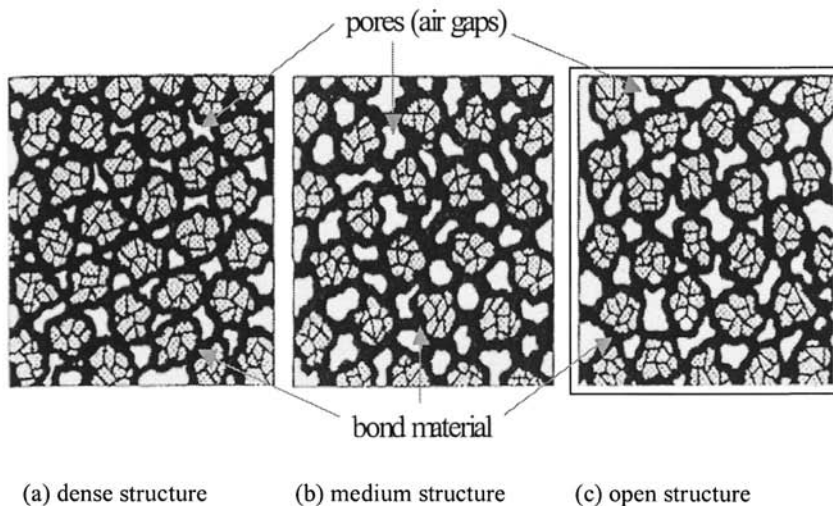


Fig. 6.3. Grinding wheel structure [38]

International efforts have been carried out to minimize variability of grit spacing and projection height of the grain in order to make the grinding process more predictable [39, 40]. As illustrated in Fig. 6.4, grain depths of cut and space between grains are higher in (a) than (b) and these are distinct advantages for effective grinding, involving less loading and heat generation.

Table 6.3. Equivalent international standard of grit sizes for diamond and cubic boron nitride used by FEPA, US, DIN, and ISO standards compared to an industrial designation [37]

International Standardization of Grit Sizes for Diamond and Cubic Boron Nitride									
Sieve Grit Designations							Micron Grit Sizes*)		
Diamond FEPA-Standard WINTER designation narrow wide		CBN FEPA-Standard WINTER designation narrow wide		Diamond + CBN US-Standard ASTM-E-11-70 narrow wide		Nominal mesh size to ISO 6106 DIN 848 Part 1, 1980 µm	Diamond WINTER design- nation	CBN WINTER design- nation	For comparison grit size µm
D 1181	D 1182	B 1181	B 1182	16/ 18	16/20	1180/1000	D 25		32-52
D 1001		B 1001		18/ 20		1000/ 850	D 20 B		30-40
D 851	D 852	B 851	B 852	20/ 25	20/30	850/ 710	D 20 A	B 30	25-30
D 711		B 711		25/ 30		710/ 600	D 15		10-25
D 601	D 602	B 601	B 602	30/ 35	30/40	600/ 500	D 15 C		20-25
D 501		B 501		35/ 40		500/ 425	D 15 B	B 15	15-20
D 426	D 427	B 426	B 427	40/ 45	40/50	425/ 355	D 15 A	B 9	10-15
D 356		B 356		45/ 50		355/ 300	D 7	B 6	5-10
D 301		B 301		50/ 60		300/ 250	D 3	B 3	2- 5
D 251	D 252	B 251	B 252	60/ 70		250/ 212	D 1	B 1	1- 2
D 213		B 213		70/ 80		212/ 180	D 0,7		0,5- 1
D 181		B 181		80/100		180/ 150	D 0,25		< 0,5
D 151		B 151		100/120		150/ 125	* - Grits recommended by WINTER *) Similar FEPA Standard exists with designations M 63...M 1.0 FEPA = Fédération Européenne des Fabricants de Produits Abrasifs.		
D 126		B 126		120/140		125/ 106			
D 107		B 107		140/170		106/ 90			
D 91		B 91		170/200		90/ 75			
D 76		B 76		200/230		75/ 63			
D 64		B 64		230/270		63/ 53			
D 54		B 54		270/325		53/ 45			
D 46		B 46		325/400		45/ 38			

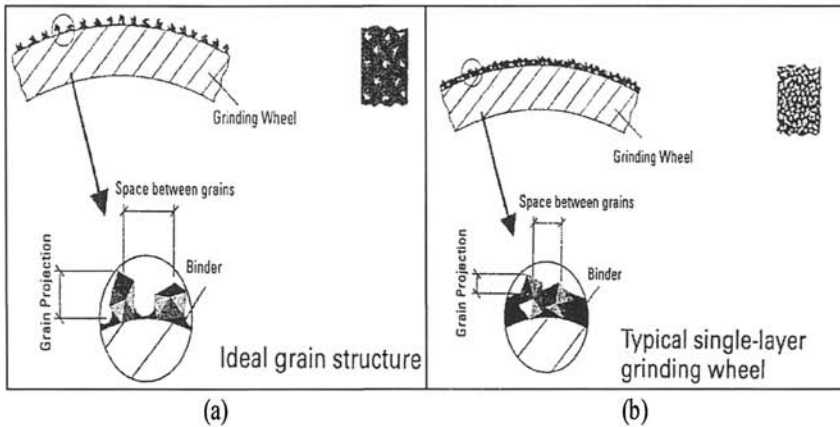


Fig. 6.4. Schematic diagrams show (a) ideal grain structure with controlled grain spacing and projection height, (b) typical single-layer grinding wheel with random grain spacing and projection height [41]

6.2.6 Abrasive Grain Concentration

While the percentages of grain, bond, and their spacing in the wheel determine the wheel's structure, the concentration indicates the volume of diamond or cBN in the grinding layer. It is defined by the percentage weight of the abrasive grit per cubic unit of the grinding layer. For diamond, the basic value of C100 means that every cm^3 of layer volume contains 4.4 carats of diamond (1 ct = 0.2 g, diamond density = 3.53 g/cm^3), which is equivalent to 25% by volume of diamond content in the grinding layer. As a general rule for selection of the desired concentration, high concentrations are suitable for small contact areas and low concentrations for large contact areas to minimize wheel breakdown [37].

6.2.7 Grinding Wheel Design and Selection

Wheels used for grinding operations can range widely in their shape, size and configuration. The successful application of grinding wheels will depend both on a thorough understanding of the grinding process and the wheel configurations.

Figure 6.5 shows some of available shapes for conventional (left side) and superabrasive (right side) wheels, respectively. It is clearly seen that in this figure the entire shape of conventional wheels is often made of abrasives, whereas in contrast, only small sections of the superabrasive wheel contain abrasives.

Since superabrasive wheels are very expensive compared to conventional abrasive grains, it is not economical to make entire wheels with abrasives, as is common for conventional wheels. Hence, superabrasive wheels are often designed with a core section that does not carry the abrasive. The abrasive forms a layer of a few millimeters thick, and the outer section of the core and their shape is partly regarded as a standard wheel configuration. Extra care should be taken when deciding the grinding face during grinding operations for different wheel configurations as it may damage/break the wheel if the wrong side is engaged to the workpiece and thus subject the operator to unsafe conditions. Apart from the wheel shape and configurations, users must also take account of outside diameter, height, width of abrasive, bore size, and other dimensions as necessary.

Bonded abrasives are marked with a standardized system of letters and numbers, indicating the type of abrasive, grain size, grade, structure, concentration, bond type and layer thickness of abrasive. Table 6.4. shows one type of marking order in a block diagram that is generally used for wheel marking system.

Table 6.4. Standard method of wheel marking order [42]

	X	X	X	X	X	X
Marking order	Grain/ abrasive type	Grain size	Grade	Structure	Bond type	Manufacturer's no.(optional)

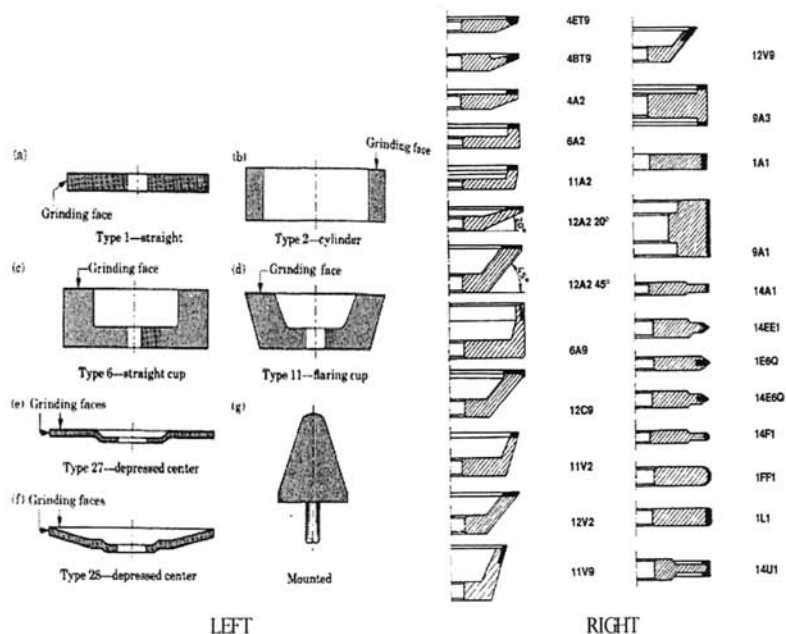


Fig. 6.5. Pictures on the left show some common types of grinding wheels made with conventional abrasives [23] while on the right are typical shapes of standard metallic rim configurations for superabrasive wheels [37]

This coding system simplifies all technical specifications of the bonded abrasive required for the wheel and normally it is designed slightly different for conventional and superabrasive wheels as indicated in Figs. 6.6 and 6.7. In the superabrasive wheel coding system, the diamond/CBN concentrations replace structure and the thickness of the abrasive layer is added at the end. Usually wheel coding systems use the letters A, C, B, and D to represent abrasive types for aluminum oxide, silicon carbide, cubic boron nitride, and diamond, respectively. However, manufacturers also often use their own acronym to distinguish variety of specific abrasive types available within the same group. Table 6.5 lists some examples of these.

Table 6.5. Some examples of specific abrasive types and their acronyms used in standard wheel marking system [43, 44].

Abrasive group	Abrasive type	Acronym
Aluminum oxide	Brown fused alumina	A
	White fused alumina	WA
Silicon carbide	Black silicon carbide	C
	Green silicon carbide	GC
Cubic boron nitride	Cubic boron nitride metal coated	CBC
	Cubic boron nitride microcrystalline	CBM
Diamond	Natural diamond	D
	Synthetic diamond	SD
	Synthetic diamond metal coated	SDC

Boothroyd [45] suggested that the following general guidelines be used for selection of a grinding wheel:

1. Choose aluminum oxide for steels and silicon carbide for carbides and non-ferrous metals.
2. Choose a hard-grade wheel for soft materials and a soft-grade wheel for hard materials.
3. Choose a large grit for soft and ductile materials and a small grit for hard and brittle materials
4. Choose a small grit for a good finish and a large grit for maximum metal removal rate.
5. Choose a resinoid, rubber, or shellac bond for a good finish and a vitrified bond for a maximum metal removal rate.

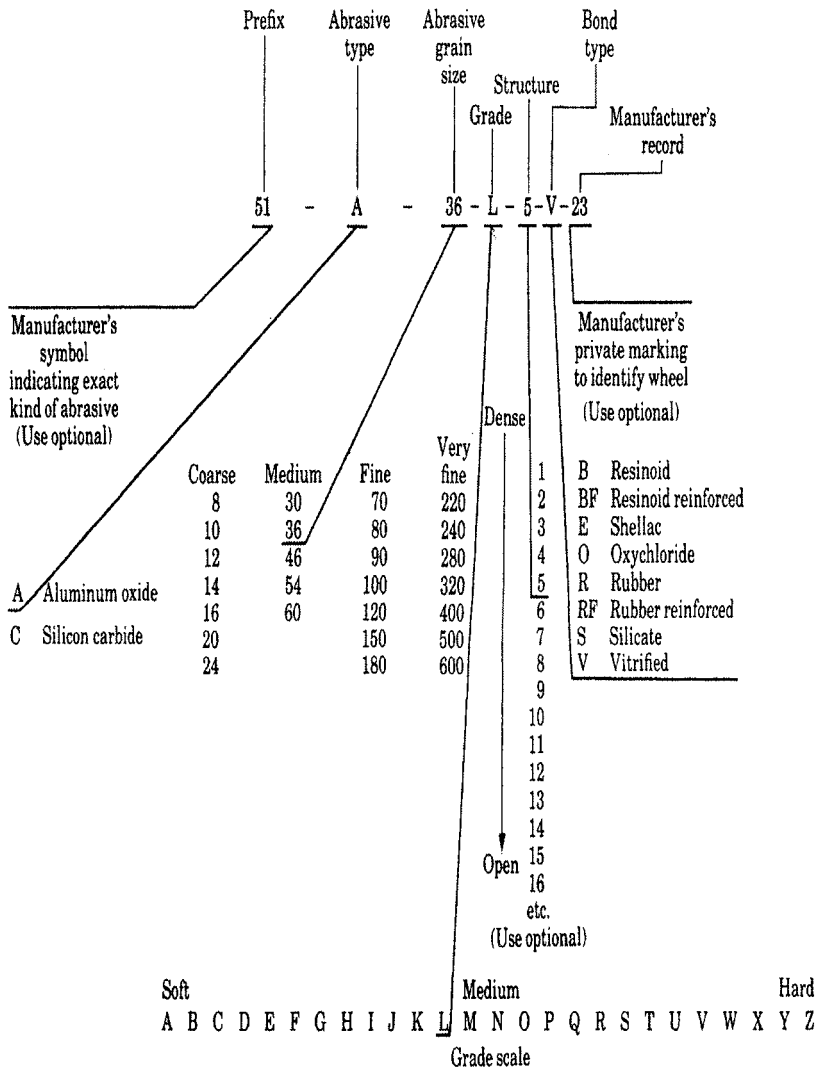


Fig. 6.6. Standard marking system for conventional bonded abrasives wheels [44]

Prefix	Abrasive type	Grit size	Grade	Diamond concentration	Bond	Bond modification	Diamond depth (in.)
Manufacturer's symbol to indicate type of diamond	B Cubic boron nitride	20	A (soft)	25 (low)	B Resinoid		1/16
		24					
	D Diamond	30		50	M Metal		1/8
		36	to	75	V Vitrified		1/4
		46					
		54		100 (high)			Absence of depth symbol indicates solid diamond
		60	Z (hard)				
		80					
		90					
		100					
		120					
		150					
		180					
		220					
		240					
		280					
		320					
		400					
		500					
		600					
		800					
		1000					

Fig. 6.7. Standard marking system for superabrasive bonded wheels [44]

6.2.8 Mounted Grinding Wheels

Mounted points, sometimes known as mounted wheels or grinding pins, are commonly used as grinding tools for internal grinding operations. Apart from the above applications, these wheels can be used as a deburring tool to remove excess material after machining processes, smoothing out casting risers, fins, and repair welds. They have various types and shapes to suit different applications (Fig. 6.8(a-c)). Materials used for the tool can be in the form of tungsten carbide and abrasive. Mounted tools made from tungsten carbide (Fig. 6.8(b)) are commonly used for smoothing die cavities, chamfering corners and forming fillets [44], [46]. Abrasive type mounted tools include aluminum oxide, silicon carbide, and diamond.

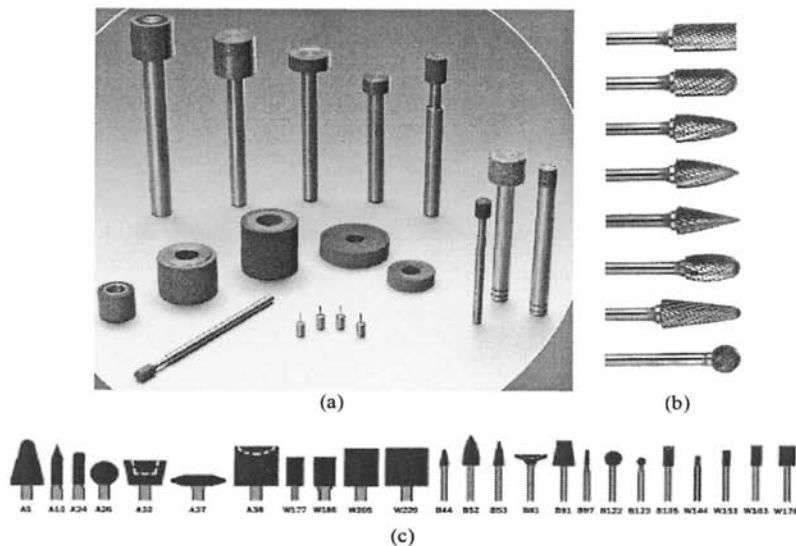


Fig.6.8. (a) Different sizes of diamond-grinding pins that are usually used for internal grinding operations available both in resinoid and metal bond [47], (b) Tungsten carbide deburring tools in various shapes ideally suited for fast stock removal on hard materials [48], (c) Various shapes of aluminum oxide/silicon carbide mounted points used together with portable hand grinder for general purpose grinding and deburring on most ferrous and non-ferrous materials [49, 50]

Figure 6.8 is interesting as it indicates the use of tungsten carbide (WC) as an abrasive for deburring. WC abrasives are also

used for grinding rubber such as fax machine rollers. This figure also suggests a use of disc shape grinding wheels.

6.3 Conventional Grinding Processes

One machining process that developed as a precision process (fixed abrasive) ahead of turning is grinding, which was followed by lapping and polishing which may be considered as a high precision loose abrasive grinding process. There are various types of conventional grinding operations available today and some of them are summarized in Fig. 6.9 In general, grinding operations are carried out on the external and internal surfaces of workpieces by using vertical or horizontal spindle grinding machines.

The development of hardened steel in the latter part of the nineteenth century created a need for a machine that was capable of finishing workpieces, which were as hard as cutting tools. This led to the development of grinding machines, which over the years were improved and modified to become the high-precision grinders of today [52].

Surface grinding operations are commonly used for grinding flat surfaces depending on the workpiece size and shape. Reciprocating and rotating tables that have an electromagnetic holding surface are usually employed for holding the workpiece (Fig. 6.10). Cylindrical and centerless grinding operations are used to grind the outside diameters of round surfaces (Fig. 6.11). These surfaces may be straight, stepped or tapered. In cylindrical grinding, the work is held between centers that are rotated at a much lower speed in a direction opposite to that of the grinding wheel. However, in centerless grinding operations, the workpiece is held between the grinding wheel and a regulating wheel and a work rest blade. By tilting the rotational axis of the regulating wheel with respect to the grinding wheel, the workpiece is given a longitudinal force, creating movement or through-feed that is helpful for automation.

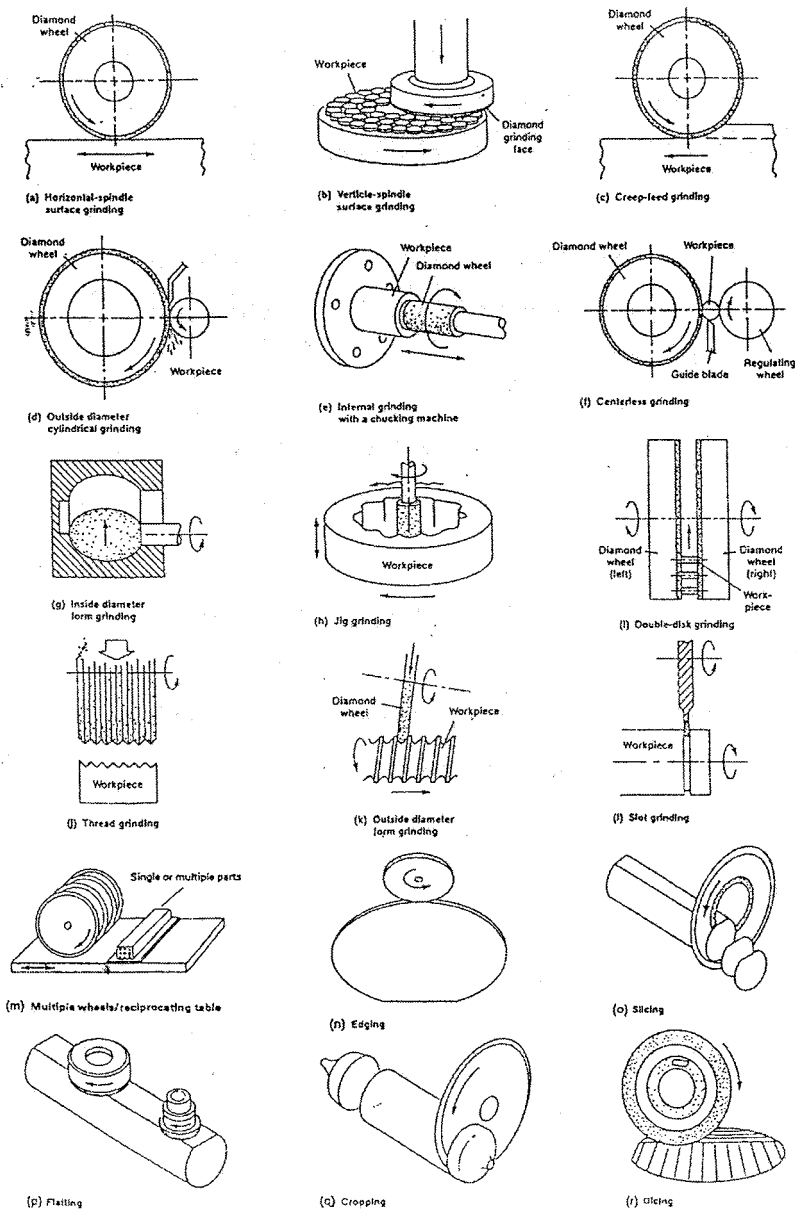
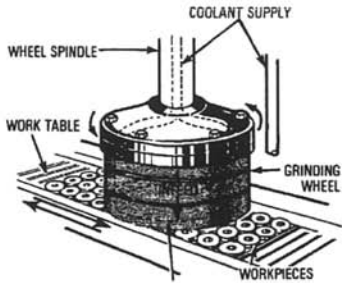


Fig. 6.9. Examples of manufacturing processes using specific grinding operations [51]



The vertical spindle surface grinder with a reciprocating table grinds on the face of the wheel and is capable of taking heavy cuts. This is good example of full immersion grinding in which grinding wheel is grinding 16 workpiece surfaces at a time. The main advantage of full immersion grinding are improved surface roughness and dimensional accuracy.

Fig. 6.10. Vertical surface grinder [52]

The fundamental difference between centerless grinding and most other forms of grinding is the fact that the workpiece is not firmly held either on a magnetic chuck or between centers or in a vice, but rather moves across the rim under the combined action of the grinding wheel, the regulating wheel and the blade. The grinding pressure is generated dynamically by the difference in velocity between regulating and grinding wheel.

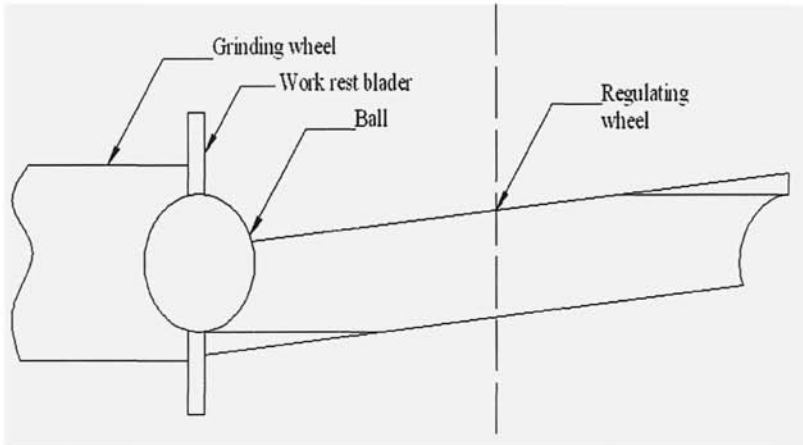


Fig. 6.11. One of the special external centerless grinding operations performed is the grinding of bearing balls. In this process, the grinding wheel is fed against the roughing wheel. Balls tend to rest on the work rest blade [53]

Internal workpiece surfaces can be fine finished by internal grinding operations. Typical examples of internal grinding are enlarging a hole or bore size similar to that by boring operations (Fig. 6.9 (e and h)) and form grinding of inside diameters (Fig. 6.9 (g)). To machine a bore, the grinding rim attached to the periphery of a supporting core of appropriate dimensions must be at the extremity of a shaft, and thin enough to permit easy entry into the bore and long enough to allow machining of the bore over its full depth. The overhang, which results in the underlying cause of a host of problems characteristic of internal grinding, leads to an inherent lack of stability and rigidity.

Slotting, slicing, cropping, and dicing operations can be called as cut off operations illustrated in Fig. 6.9 (l, o, q, r), respectively, are also recognized as conventional grinding operations. In these grinding operations, single or multiple-disks are arranged vertically on a horizontal spindle to perform simultaneous cutting operations on the workpiece that are held on a reciprocating table (Fig. 6.9m). The use of superabrasive cut-off grinding (slicing) wheels has been increasing substantially over the last 10 years, as harder and more expensive materials come on the market. These require, in a first machining step, to be cut rapidly and cheaply to dimensions commensurate with the end product. One high growth area has been, for instance, the cutting off to shape of synthetic quartz ingots, which constitute the raw material required for electronic watches.

A cut-off grinding wheel is essentially a very thin grinding wheel, whose width usually lies in the vicinity of 1 mm (0.04 in) or less. The rim is mounted on the periphery of a metal disc, usually made of steel. The primary requirement for such a cut-off wheel is sufficient freeness of cut. The workpiece should be cut-off without any substantial pressure build-up at the grinding interface [54].

Creep-feed grinding (Fig. 6.9 (c)) is a new form of grinding operation different from other conventional grinding processes. In creep-feed grinding, the entire depth of cut (infeed) is completed in one pass by using a very small feed rate. It is a technique used to grind a form into a workpiece in a single pass of the grinding wheel. The workpiece is fed into the revolving grinding wheel, opposite to the wheel rotation, at a slow, steady table feed rate. The wheel height is set to the final size and the desired form is generally completed to

size, tolerance, and surface finish in one pass. It is possible to grind profiles with depths of cut of 1.0 to 30 mm in one pass using work speeds from 1.0 to 0.025 m/min [38].

Creep-feed grinding can be competitive with surface grinding, milling, gear cutting, broaching, and other processes where heavy stock removal is required. It is very effective where a precise, accurate form is required, and profile accuracy is critical. The key advantages to creep-feed grinding are increased productivity, better dimensional part accuracy, and less metallurgical damage to the workpiece [52].

Double disk grinding (Fig. 6.9 (i)), edging operations on silicon wafer periphery (Fig. 6.10 (n)) and flattening of silicon ingots (Fig. 6.9 (p)) are also considered as surface grinding operations but here they involve different types of workpieces, size, and orientation. Grinding operations are also often being used for removing burrs and fine finishing of machined threads, and form grinding operations of grooves on ball screws as shown in (Fig. 6.9 (j) and Fig. 6.9 (k)), respectively.

Cubic boron nitride grinding wheels were first tested in 1957 on difficult-to-grind (DTG) hardened tool and die steel cutting tools. These steels are so hard and abrasion-resistant that they cause rapid dulling of the conventional aluminum oxide abrasive. Because of the exceptional hardness of cBN wheels, in tool grinding, tool dimensions are accurately maintained with minimum downtime for wheel maintenance. Grinding with cBN wheels improves the fatigue strength and extends the useful life of the cutting tool by removing heat from the surface of the workpiece.

6.4 Precision Grinding Processes

6.4.1 Upgrading of a Machining Center into Jig Grinding for IC Chip Manufacturing

Jig grinding is basically vertical surface grinding process, which can be considered to one of the elite precision grinding processes (Fig. 6.12). The need for accurate hole locations in hardened work led to

the development of the jig grinder. The name Jig grinding is given to the process, which was used for grinding jig holes. The final accuracy of the drilled hole is largely dependent on the accuracy of the jig used. This machine was specially designed for finishing the holes with a high degree of accuracy on drill jig plates.

This precision grinding machine is equipped with a precision hole grinding facility used to grind hard metals or ceramic workpieces. It uses aluminum oxide, diamond, or cubic boron nitride grinding wheels to grind holes in hardened steels to precise location and tolerances. It supplements other hole producing machinery. A typical product is shown in Fig. 6.9 (h)

Often the clamping, the machining, or the hardening operation would distort the workpiece and alter the hole locations so that they were no longer accurate. Although the jig grinder was designed primarily for accurately locating holes in hardened workpieces, it has found wide use for the grinding of contour forms such as radii, tangents, angles, and flats. The machine's operation centers around a high-speed air turbine with auxiliary electric rotating head with reciprocating quill. [52]

The performance of any grinding wheel depends on the capacity and working condition of the jig grinding machine. Jig grinding wheels are available in various bond types and a wide variety of styles to suit various jig grinding operations. It is important that the proper wheel be selected to suit the workpiece material so that the most efficient grinding can occur. The most important factors to consider when selecting CBN wheels for jig grinding operations are the abrasive type, bond, and grit size [45,52].

Continuous-path numerical control (NC) jig grinding requires grinding abrasives that last a long time, retain their shape, produce good surface finishes, and maintain size and form without thermal damage to the workpiece. One factor that is impossible to program is wheel wear. If the wheel loses shape, size, or stock-removal capability while making a pass, an inaccurate form will be produced.

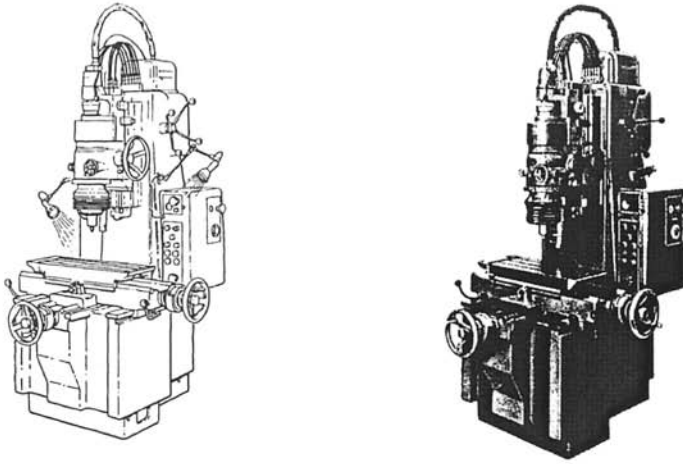


Fig. 6.12. Moore Jig boring machine: (a) line diagram [55] (b) picture of the same machine [56]

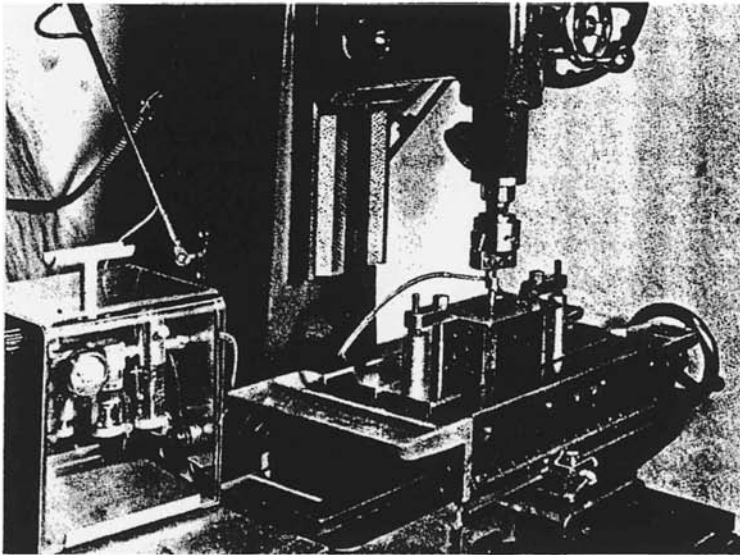


Fig. 6.13. A milling machine converted into a jig grinder with an air turbine attachment [21]. This idea was used for grinding of an IC chip [57]

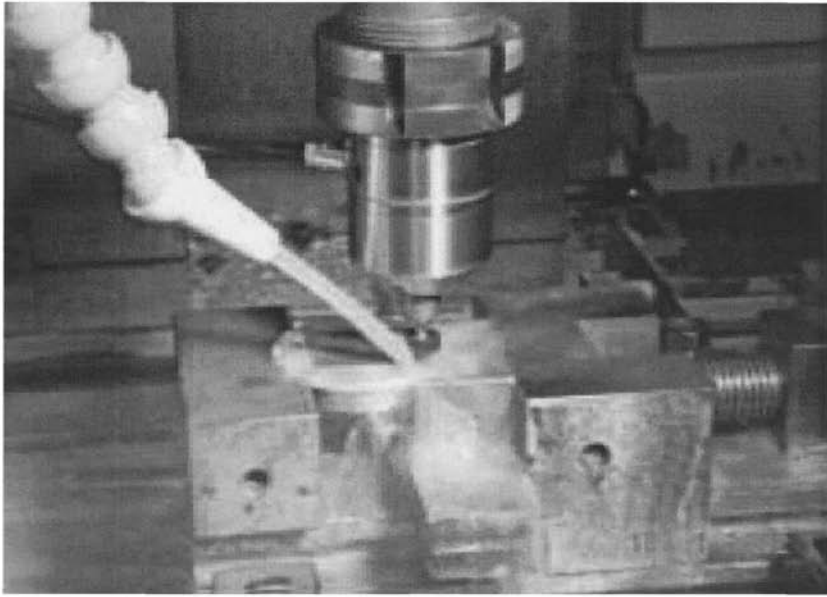


Fig. 6.14. MAHO CNC machining center upgraded for high-speed through the use of an air turbine [57]

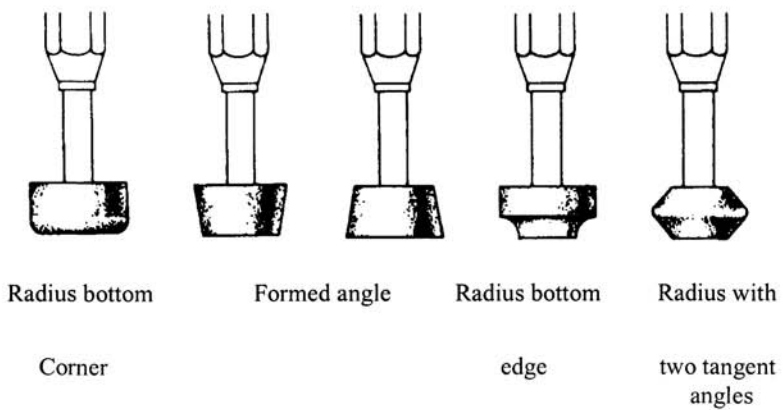


Fig. 6.15. Various types of pins available for jig grinding operations

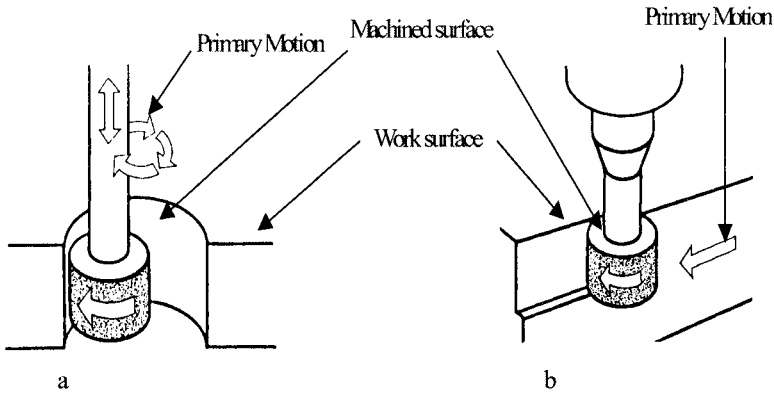


Fig. 6.16. Description of various jig grinding operations [45]: (a) hole or plunge grinding is the most common method of grinding holes where grinding pin grinds hole bottom or side surface. Pin movement is controlled by CNC machine; (b) the wipe grinding mode is generally used for form grinding. The work is fed past the revolving wheel, which is in a stationary position

Novel techniques were developed by Venkatesh et al. [58-61] to study formation of ductile streaks during the Jig (Plano) grinding of glass and Si surface using high-speed air turbine spindle (Figures 6.13 and 6.14). It was found that resinoid diamond wheels gave more ductile streaks than metal-bonded wheels but better form accuracy was obtained with the latter (Figs. 6.15 and 6.16). Ductile streaks were obtained more easily with Pyrex rather than with BK 7 glass thus necessitating very little time for polishing. Table 6.6 shows the time required to polish Pyrex glass when using a variety of polishing reagents.

Results indicate that the surface roughness of precision-ground Si sample improves with lower feed except at finest depth of cut of 5 μm where higher feed rates improves the finish. Ductile streaks also appear at higher feed rates (Fig. 6.17).

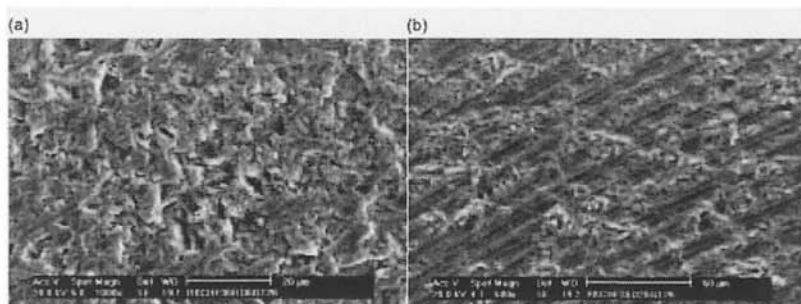


Fig. 6.17. SEM pictures of ground Si the surface consist of (a) microfractures and (b) grinding streaks [62]

6.4.2 Critical Depth of Cut

As can be seen in the Fig. 6.18, there are also various shapes of wheel end faces such as pointed, round, flat, slight conical, etc. The advantage here is that using a mounted wheel whose end face is in slight conical shape, critical depth of cut in grinding can be determined. Figure 6.15 indicates a diamond pin of 5 mm diameter that was used to grind Pyrex glass. The tapered diamond pin resulted in circular areas having fractured and partial ductile surfaces (Fig. 6.18(b)). From diamond pin and grinding geometry, the wheel depth of cut can be seen as the highest at the center of the track and gradually decreased to the shoulder. As a result, one grinding pass constitutes at least two tracks, one with fracture and the other with partial ductility. In fact, Fig. 6.18 indicates the experimental observation on grinding of Pyrex glass with 64 μm grit diamond pin. Actual cone angle of end surface was approximated to be 179.4° . Grinding conditions were 39 m/s cutting speed, 2.5 mm/min feed rate, and 10 μm maximum depth of cut. In Fig. 6.18(a), y' represents the depth of cut at which transition from brittle to ductile grinding occurs and thus the corresponding depth of cut will be critical value. With the aid of optical microscope and integrated image analysis software, the width of the tracks can be measured Fig. 6.18(c) whereas y' was found to be 7 μm .

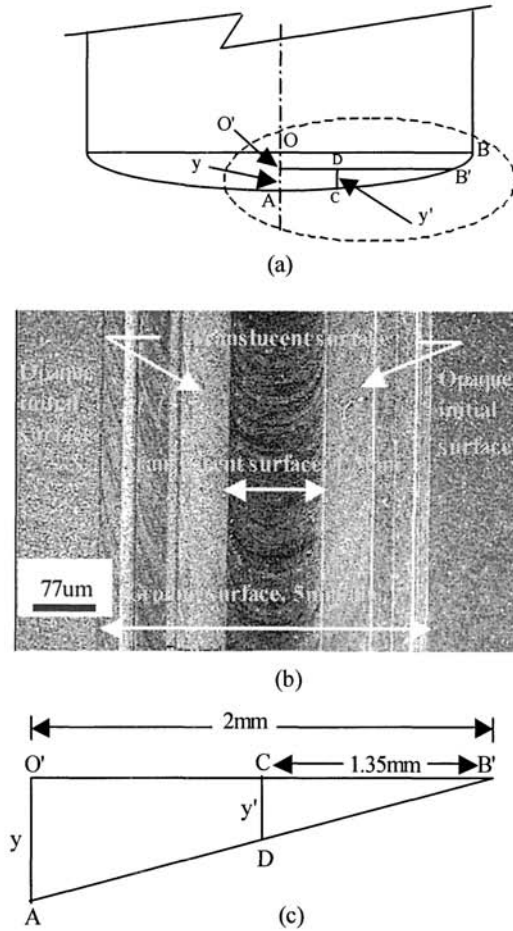


Fig. 6.18. (a) Exaggerated conicity of grinding wheel (actual cone angle will be about 179.4°). (b) Plan view of ground surface whose diameter is less than wheel diameter, because depth of cut is less than y . The central part despite being fractured is transparent and the outer part is translucent despite the occurrence of partial ductile streaks. (c) Enlargement of triangular area $O'B'A$ in (a) enables estimation of critical depth of cut (y') [62]

6.4.3 Precision Grinding with Electrolytic in-Process Dressing (ELID)

Grinding with superabrasive wheels is an excellent way to produce a precise surface finish on hard and brittle materials. To achieve this, superabrasive diamond grits need higher bonding strengths than metal bonded and resinoid bonded wheels can offer. However, truing and dressing of the wheels are a major problem as they tend to glaze because of wheel loading. These problems can be avoided by dressing periodically but this interrupted action makes the grinding process very tedious and time consuming. A Japanese research group has introduced an effective technique to overcome the poor self-dressing properties of metal bonds, especially cast iron bonds, in the presence of aqueous lubricants. Ohmori and Nakagawa [63] called the method electrolytic in-process dressing (ELID). The basic concept of grinding with ELID is illustrated in Fig 6.19. It uses an electro-chemical method to remove the metal bonds and properly expose the diamond particles, thereby maintaining the high efficiency of the grinding operation. The basic ELID system consists of a metal or cast iron bonded diamond grinding wheel, an electrode (copper or graphite), a power supply, and an electrolyte as shown in Fig. 6.19.

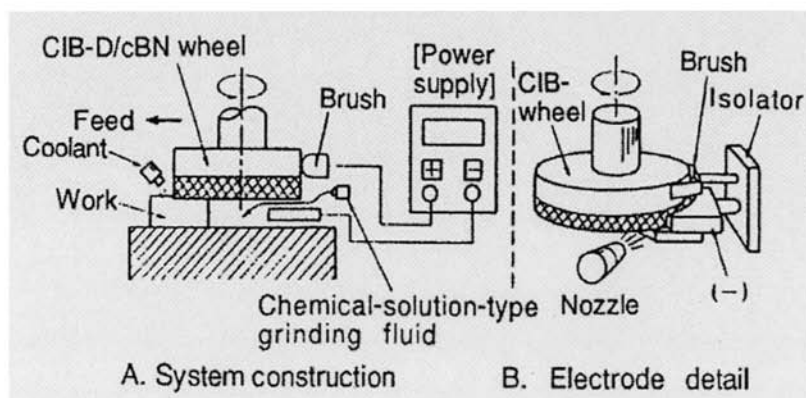


Fig. 6.19. Basic ELID system shows the essential requirement of a cast iron bond for the grinding wheel to function using the grinding fluid as an electrolyte [63]

The power supply for ELID is used to control the dressing current, voltage, and pulse width of the dressing process. The metal bonded wheel is made into the positive pole through the application of a brush smoothly contacting the wheel shaft and the electrode is made into negative pole. In the small clearance between the positive and negative pole (0.1 to 0.3 mm), electrolysis occurs through the supply of the grinding fluid and an electrical current.

There is an important feature on ELID grinding that ELID grinding makes oxide hydroxide (insulation) layer on surface of ELID wheel by electrolysis. The oxide hydroxide layer has a lower electrolytic conductivity.

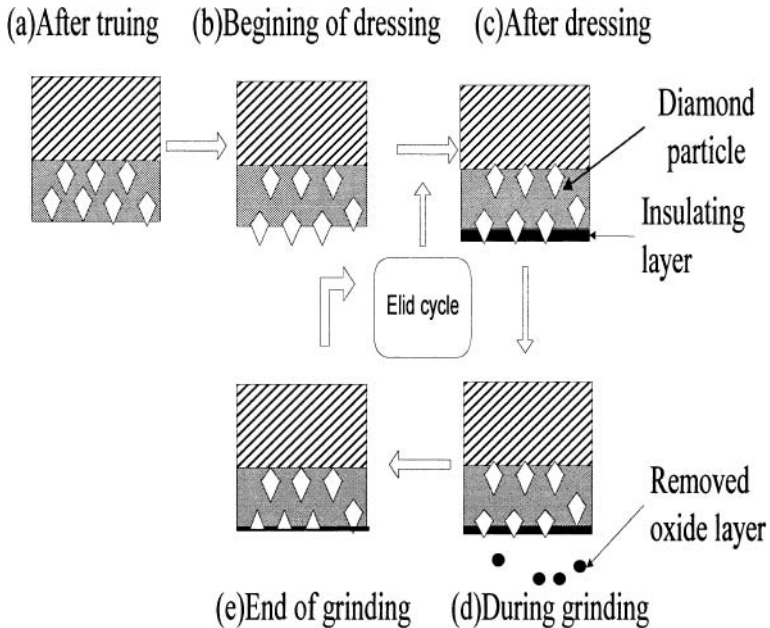


Fig. 6.20. Schematic illustration of ELID grinding principle [64]

Figure 6.20 describes the mechanism of ELID grinding of metal bonded diamond wheel. After truing (a), the grains and bonding material of the wheel surface are flattened. The trued wheel needs to be

electrically pre-dressed to protrude the grains on the wheel surface. When pre-dressing starts (b), the bonding material breaks away from the grinding wheel and an insulating layer composed of the oxidized bonding material is formed on the wheel surface (c). This insulating layer reduces the electrical conductivity of the wheel surface and prevents excessive breakdown of the bonding material from the wheel. As grinding begins, (d), diamond grains wear out and the layer also become worn, (e). As a result, the electrical conductivity of the wheel surface increases and the electrolytic dressing restarts with the breakdown of bonding material from grinding wheel. This cycle is repeated during the grinding process to achieve stable grinding [63,65,66]. ELID now becomes the most efficient method for dressing metal bonded grinding wheels continuously that eliminates the wheel loading and glazing problems during the grinding process [67]. It has been reported that surface roughness (R_a) with the ELID process can be achieved as low as 0.33 nm on BK7 glass and silicon when using ultrafine #3000000 grit metallic bond wheel [63].

The applications of ELID are numerous. It has been successfully used for processes such as surface grinding, cylindrical grinding, internal grinding, and centerless grinding. Some others are in abrasive cut-off of ceramics [68], mirror surface grinding of silicon wafers [63], small-hole machining of ceramic materials [69], sawing of steel, polymer, sapphire and glass [70], precision machining of CVC-SiC reflection mirrors [69] and mirror internal cylindrical grinding on steels and alumina components [67].

6.4.4 Partial Ductile Mode Grinding

To transform a rough piece of glass into a crystal-clear optical component, opticians grind and then polish the piece. Traditionally, opticians use small abrasive particles such as aluminum oxide mixed in water-based slurry to gradually remove imperfections and shape a rough piece of glass into the optical shape that is needed to precisely direct light rays from a distant point. The grinding process leaves tiny cracks just below the surface as well as small crater-like imperfections that make the glass piece opaque and prone to fracture. To remove the damaged layer and produce a clean optic, the piece goes

through extensive finishing or polishing. "Polishing is the most time-consuming and expensive part of the optics process", states Ruckmann [71].

Research performed by Venkatesh and Van Ligten to generate aspheric surfaces by a novel technique is described in detail. In this technique, an aspheric surface was generated on a 4 axis CNC machining center initially for glass, and subsequently for silicon and germanium [72 - 74]. Preformed blanks were obtained from the supplier and aspherics were generated using a diamond cup. When the grit size was changed from 63 μm to 20 μm , an increase in grinding streaks was observed with Si and Ge materials (Fig.6.21).

To reduce tool costs, resinoid bonded wheels were tried out with remarkable success. With Ge in particular almost 90% ductile grinding was observed (Fig. 6.22) with a wheel that was partly worn out to flatten the diamond grains.

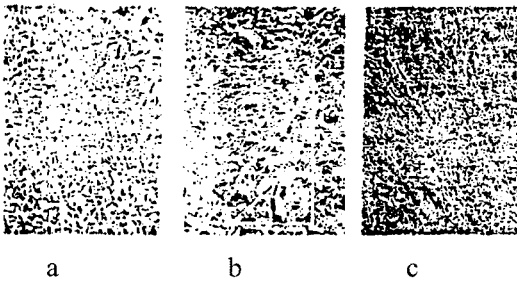


Fig.. 6.21. (a) and (b) Grinding streaks on Si and Ge. (c) Almost 90% ductile grinding on Ge [75]

Grinding and polishing of industrial aspheric lenses was carried out by Venkatesh and Zhong [75] on an aspheric profile generator. The results indicate that semi-ductile grinding works well for ophthalmic industries. Polishing time was reduced by almost 50%. (Fig. 6.23), which give maximum ductile streaks for both spherical and aspheric lenses.

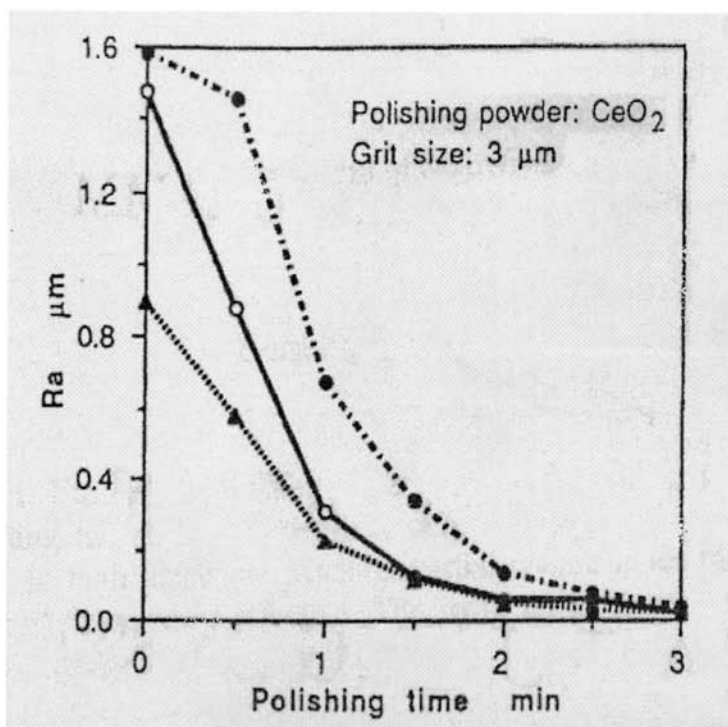


Fig. 6.22 Roughness values of polished aspheric glass moulds versus polishing time [75]

Inspired by Konig and Sinhoff's model referred to in reference [12], the following explanation is stated:

The resinoid wheel by virtue of its design is slightly elastic and with a compliant bond causes nascent diamond grits to protrude slightly and cut with a fine depth of cut that results in large amount of grinding streaks. These streaks are much more abundant in Ge than in Si and glass. Though all are brittle materials, their brittleness varies. Si and Ge become increasing ductile above 60% of the absolute melting temperature, i.e., about 450°C for Ge and 750°C for Si. An explanation of formation of ductile bands, along with fractured bands, is shown in a modified form of Konig and Sinhoff's model in Fig. 6.23.

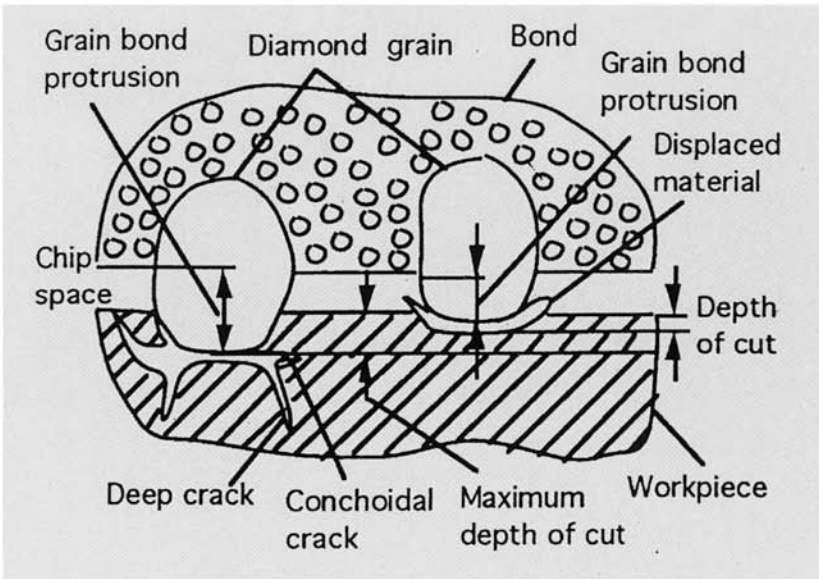


Fig. 6.23 Konig's model shows uneven protrusions out of the bond represent grain depth of cut. Abrasive grain on the right side that protrudes slightly within critical depth of cut region produces ductile streaks while on the left side grain protrudes more than critical depth of cut region produces fracture and deep crack [75]

6.4.5 Aspheric Surface Generation

In recent years, there has been a dramatic advancement in the field of optics, astronomy, and infrared applications. This led to an ever-increasing demand for simple and complex aspheric surfaces which produce better image quality when compared to that produced by spherical lenses. An aspheric surface is generally defined as a surface with a basic conic section form. To this basic conic section a symmetrical deviation can also be superimposed and is given by a symmetrical polynomial expression as follows [12]:

$$Z = \frac{\text{shapefactor} \times X^2}{R + \sqrt{R^2 - (1+k)X^2}} + A_1X + A_2X^2 + \text{etc.} \quad (6.3)$$

Where X is the horizontal distance from the aspheric axis, Z is the corresponding vertical distance or the vertical sag, shape = -1 for convex; and = +1 for concave, where

R = radius of curvature, and

k = conic constant as given below:

$k < -1$ Hyperboloid

$k = -1$ Paraboloid

$-1 < k < 0$ Ellipsoid

$k = 0$ Sphere

$k > 0$ oblate ellipsoid.

The remaining terms in the above equation are the symmetrical deviations from the basic conic form. The vertical sag of a spherical surface and an aspheric surface with their basic equations and symmetrical deviation is shown in Fig. 6.24.

Manufacture of such aspherics has always been a challenge, especially on infrared window materials and metals. Therefore, manufacturers and researchers have put in a great deal of effort to systematically apply measurement science to design, manufacture, and fabrication of highly precise devices to achieve low tolerances, better surface finish, and low subsurface damage at reduced cost.

Currently, with the development of ultraprecision machine tools, there have been reports of achieving all three desired aspects of precision aspheric. Single-point diamond turning is the principal machining method being used to machine extremely brittle materials like silicon and germanium. However, efforts are in progress to obtain the desired aspects of precision aspheric by diamond grinding. The present work also explores the feasibility of obtaining subsurface damage free aspheric surface on single crystal silicon surfaces [76].

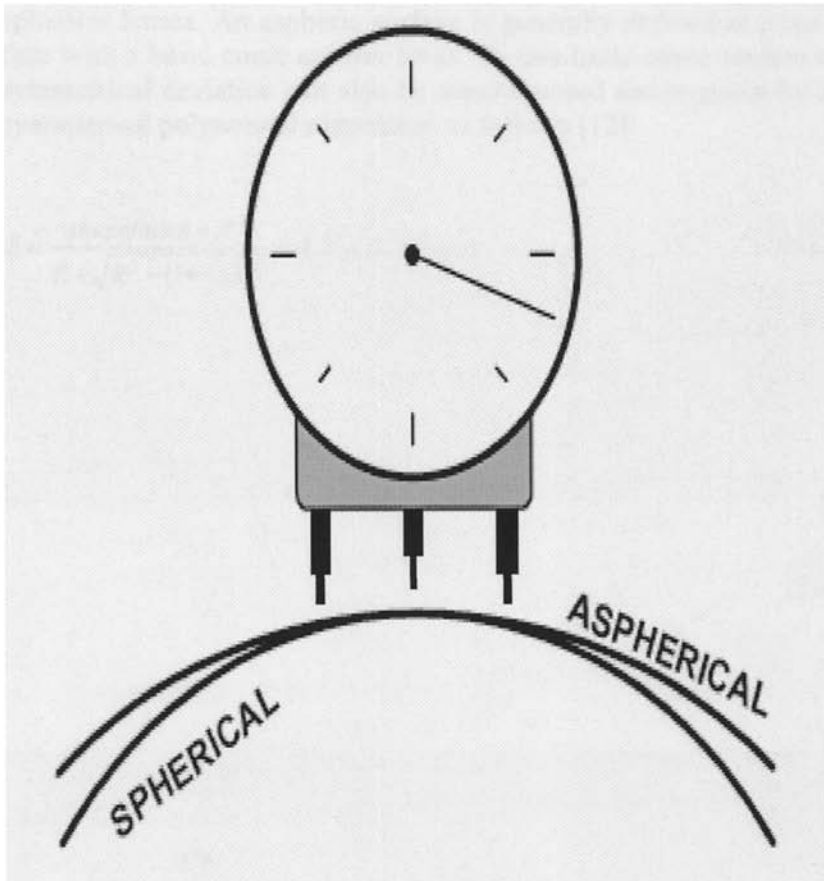


Fig. 6.24. Effects of sag creates a difference between aspheric and spherical surfaces as demonstrated by the use of a dial test indicator [76]

The principal use of aspheric lens designs is the reduction or elimination of optical aberrations produced by looking through an ophthalmic lens obliquely. We will begin our discussion of aspherics by exploring some of these optical aberrations and their effects. For ophthalmic lenses, a lens aberration occurs when rays of light fail to come to a point focus at the ideal image position of the eye (called the far point) as it rotates about its center.

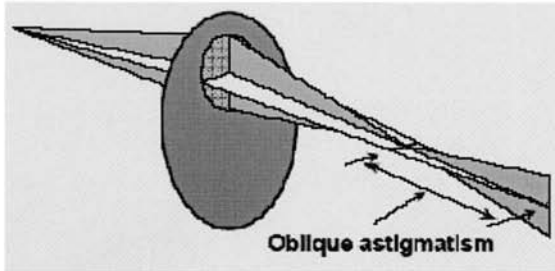


Fig. 6.25. Rays of light from an object point strike the lens obliquely and are focused into two separate focal lines, instead of a single-point focus, resulting in oblique astigmatism [76]

Astigmatic focusing error, which is illustrated in Fig. 6.25, results when rays of light from an object in the periphery strike the lens obliquely. Two focal lines are produced from each single object point. The dioptric difference between these two focal lines is known as the astigmatic error of the lens.

Rays of light striking the tangential, or radial, plane of the lens come to a line focus at the tangential focus. The resultant focal line is perpendicular to the actual tangential plane. Rays striking the sagittal, or equatorial, plane of the lens come to a line focus at the sagittal focus. This focal line is perpendicular to the sagittal plane. Both of these planes are shown in Fig. 6.26.

Coma is a distortion in image, wherein the focus and the magnification are different for rays passing through various zones of the optical system. It usually occurs when the incident rays are not parallel to optical axis and a ring shaped blur image is formed.

In refractive optics, chromatic aberration (lateral and longitudinal) alters the image quality when the optical system has to operate in a wide range of wavelengths. This is caused by the phenomenon of dispersion (change of refractive index with wavelength), producing a variation in focal length with wavelength. Chromatic aberration increases the size of the blur in the image in direct proportion to spectral range.

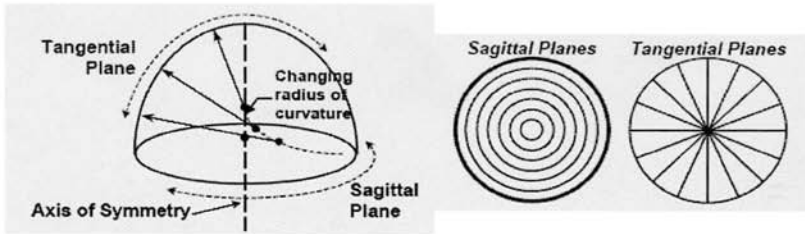


Fig. 6.26. The sagittal (equatorial) and tangential (radial) planes of a lens [76]

The three types of aberrations cannot be eliminated simultaneously. Therefore any optical system needs a combination of several lenses to get a better quality image. On the other hand, limitations on system weight and overall manufacture costs demands a lesser number of lenses. Thus, a parabolic surface on silicon proves to be a better choice for infrared application.

Traditional methods of generating aspheric surfaces on glass have been time consuming [77]. A novel technique was developed by Kapoor and Venkatesh that brought about heavy material removal without affecting surface finish and profile [72]. This technique was extended to germanium and silicon using both metal bonded and resinoid bonded wheels.

To remove material quickly and end up with the desired surface, the contact area between the grinding tool and the workpiece should be as large as possible. Since only spheres and toroids permit the condition of full area contact, partial area contact, or line contact will be the best alternative. The use of a machine with a rotating tool suggests that the contact surface must be symmetrically rotational. In general, the shape of the workpiece is not predictable. Hence, the condition of the large contact area is put in jeopardy. Thus, the method was chosen based on a long line contact between the tool and the workpiece during the first step of rough grinding. During the subsequent steps of polishing, the use of a flexible tool allows conformity between the workpiece and the tool, approaching the original condition of a contact area.

Two cup-shaped identical size diamond-grinding wheels with metallic (D20/30 MICL50M-1/4) and resinoid (SD240-R100 B69-6 mm) bonding were used. The profile of the grinding edge is circular in this case, but not restricted to this shape, thus, forming a toroid.

The important feature is that the grinding surface shape is axially symmetrical. It is now possible to program the tool path of this tool on the CNC-machine such that it is in line (or arc) contact with the workpiece as it cuts the desired shape on the glass [78].

To illustrate this, the grinding of a paraboloid is shown. The cup tool can be thought of as consisting of a collection of circles whose planes are perpendicular to the axis of rotation of the tool. When the paraboloid is intersected by a plane, as shown in Fig. 6.27, the common line is called an ellipse. When the task is to cut a concave paraboloid, the tool must fit inside the paraboloid. Hence, the tool must have a diameter smaller than the shortest radius found on the ellipse of intersection of any plane intersecting the paraboloid. In the case of a paraboloid, the shortest radius of curvature on the eclipse of intersection is found when the plane contains the axis of symmetry of the paraboloid.

Any circle at the outer side of the tool can be contained in one of the planes intersecting the paraboloid. The angle that this plane makes with the axis of the paraboloid can be adjusted such that the arc of the circle and that of the ellipse (Fig. 6.27) at d , differs in sag height no more than a preset tolerance. This condition sets a certain common arc length over which the difference in sag does not exceed a certain value, say $0.5\text{ }\mu\text{m}$. Subsequently the tool axis can be programmed to take a slightly different position relative to the axis of rotation of the workpiece, as well as relative to the apex P , of the paraboloid. The sequence is then repeated to form a neighbouring zone of the one indicated in Fig. 6.27.

Two 5-axis vertical CNC machining centers (Fadal and Deckel) are programmed to perform these sequences continuously, until the paraboloid is completed. In this manner, a zone is ground during one revolution. While in cutting with a point tool, in principle one line of the paraboloid is cut it is, thus, clear that this method of grinding with the nearest arc-contact can complete the same surface faster than in the case of cutting with a point-tool.

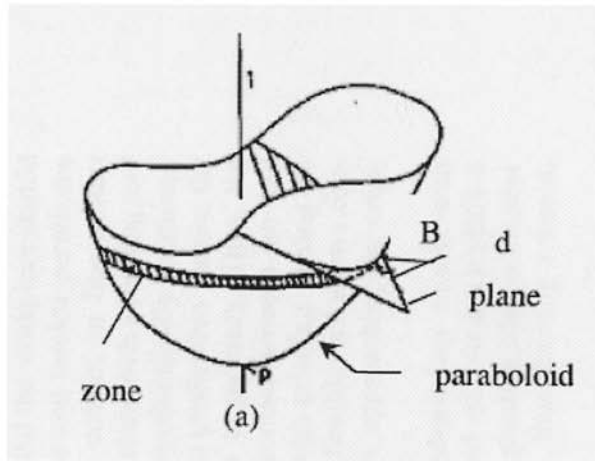


Fig. 6.27. Basic principle of grinding by zone [72]

The thermal imaging materials used were monocrystalline germanium and silicon. Both blanks were polished after grinding. A special aluminum tool was developed. A felt cloth was glued to the spherical surface of this tool and a polishing paste of one-micron alpha alumina was applied to it during polishing. The same set-up was used for polishing on the CNC machine.

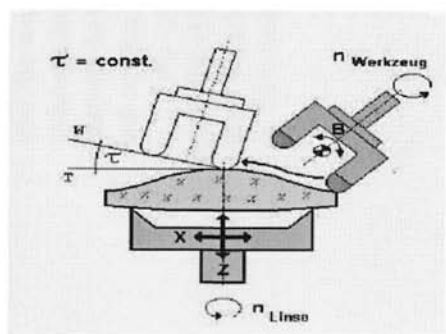


Fig 6.28. Aspheric surface generation process and schematic diagram showing speed of the workpiece and the tool [79]

The resinoid-bonded wheel was recommended by Tan [73] for grinding both Ge and Si (Figure 6.28). Better surface roughness values were obtained with both wheels for Si. Si, however, was more difficult to polish and a lighter pressure had to be applied to prevent the felt from coming off. Thus, for the same time interval, Ge had a much better surface finish. Polishing improved the form accuracy with Ge, but not with Si. Both ductile and fracture modes of material removal were observed with both Si and Ge[72]

Figure 6.29 shows some amount of ductile streaks on silicon and Fig. 6.30 a massive amount of ductile streak on Ge. Better surface roughness, form accuracy, and smoothness can be obtained with a 5-axis CNC jig grinder, and also by dressing the grinding wheel for ductile mode as suggested by Russell [74]. The same type of work has been conducted by Kapoor [72] who suggested that resinoid bonded wheels give more ductile streaks than metal bonded wheels.

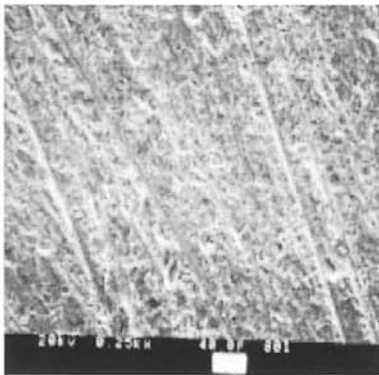


Fig. 6.29. Ductile streaks obtained on Si during aspheric generation [60].

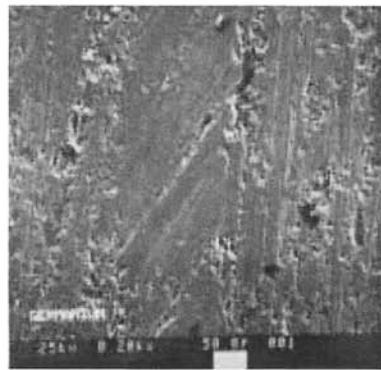


Fig. 6.30. Formation of ductile streaks on Ge during aspheric generation with a resinoid-bonded diamond wheel. [60]

6.5 Ultraprecision Grinding

6.5.1 Ultraprecision Machines and Development

Advancements in technology now make it possible for hard and brittle materials to be machined to a very close tolerance. Ultraprecision machining has been developed and a new machining concept called ductile mode machining has been introduced. Using this machine coupled with ductile mode theory, mirror finishes can be achieved on the workpiece without the intervention of polishing [80,81]. In ductile mode machining, feeds and depth of cut have to be very small in the order of 10 nm and 1 μm , respectively [82]. With the ultraprecision machine set-up, full ductile mode machining can be achieved, and surface finish is mirror-like without subsequent process like polishing [80,81].

Most of the ultraprecision machines available in the market are equipped with machining systems that adopt either single-point diamond tools or multi-point abrasive (grinding) wheels. However, in some cases both machining systems can be incorporated into one machine on customer request for enabling both single and multi-point abrasive machining operations. Figure 6.31 shows a typical construction of both ultraprecision machines. According to Schulz and Moriwaki [84], an ultraprecision machine is defined as a machine that has machining systems with the following movement accuracies:

- i. slide geometric accuracy of less than 1 μm
- ii. spindle error motions of less than 50 nm
- iii. control and feedback resolutions of less than 10 nm

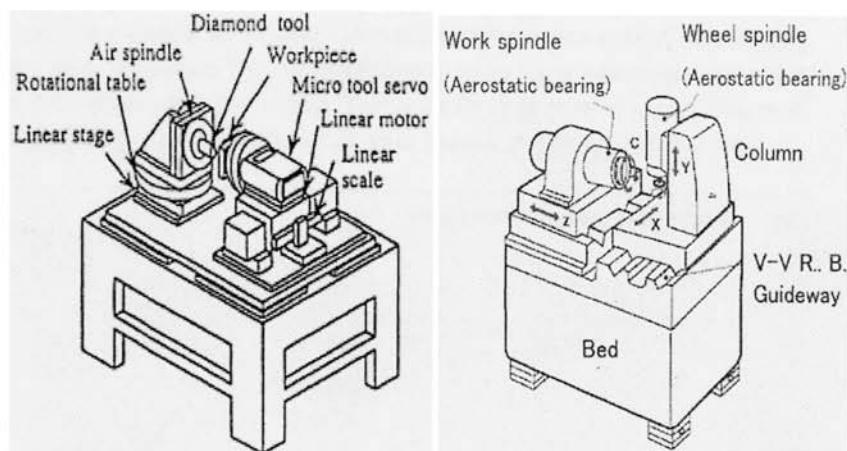


Fig. 6.31. A typical construction of (a) 2-axis an ultraprecision single-point diamond turning machine [46], (b) 4-axis an ultraprecision diamond grinding machine (Courtesy Toshiba Machine Co, Ltd.)

With the above movement accuracies, it is expected that the ultraprecision machine will be able to generate the following work-piece accuracies:

- i. dimensional accuracy in the range of a few micrometers
- ii. surface form accuracy in the range of 100nm or better
- iii. surface texture in the range of 5nm, or better

In order to satisfy the above requirements, the machine must exhibit high degrees of thermal stability, stiffness, damping, and smoothness of motion and must also be integrated with an ultraprecision metrology system in the machine tool but isolated from the response of the machine tool during machining [85]. There are at

least five main players that develop such machines in the world market, i.e., Moore Nanotechnology Systems, Precitech, Toyoda, Nachi Fujikoshi, and Toshiba [83]. These machines are available in 2 to 5 axes configurations as shown in Fig. 6.32. Usually, grinding wheel is attached on a vertical spindle, y-axis, to perform grinding operation on the workpiece where it is vacuum chucked on the main horizontal spindle. Depending on the number of axes, this kind of machine can produce various types of surfaces such as plano, cylinders, spheres, aspheres and conic sections, Fresnel and diffractives, freeform and microstructures (Figure 6.33). Applications of these surfaces include hard disks, photocopier drum, night vision devices (Figure 6.34), lenses (for camera, charged-couple-device (CCD), CD and DVD pick up, freeform optics (for laser printers, scanners and conformal military optics radar system (Figure 6.35) and display for notebooks/mobile phone, street sign reflectors [83].

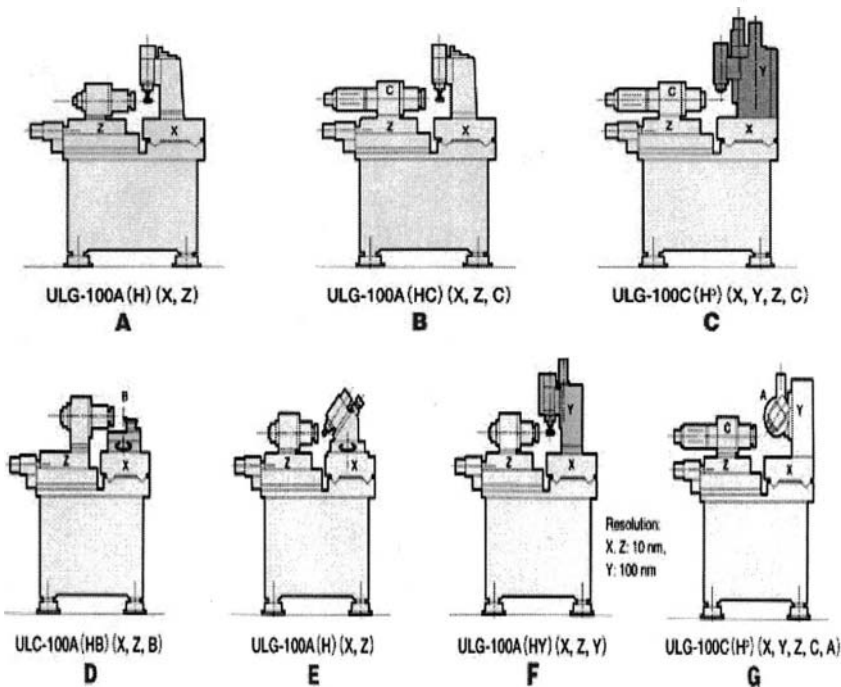


Fig. 6.32. A wide range of Toshiba models from 2 to 5 axes ultraprecision turning and grinding machines [86]

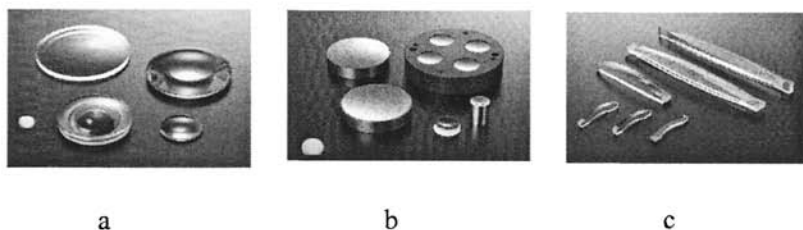


Fig. 6.33. A variety of optical products made on Toshiba machine (a) spheric and aspheric lenses (plastic and glass) (b) turning and grinding of molds for spheric and aspheric lenses (c) toric and free form lens machine [86]

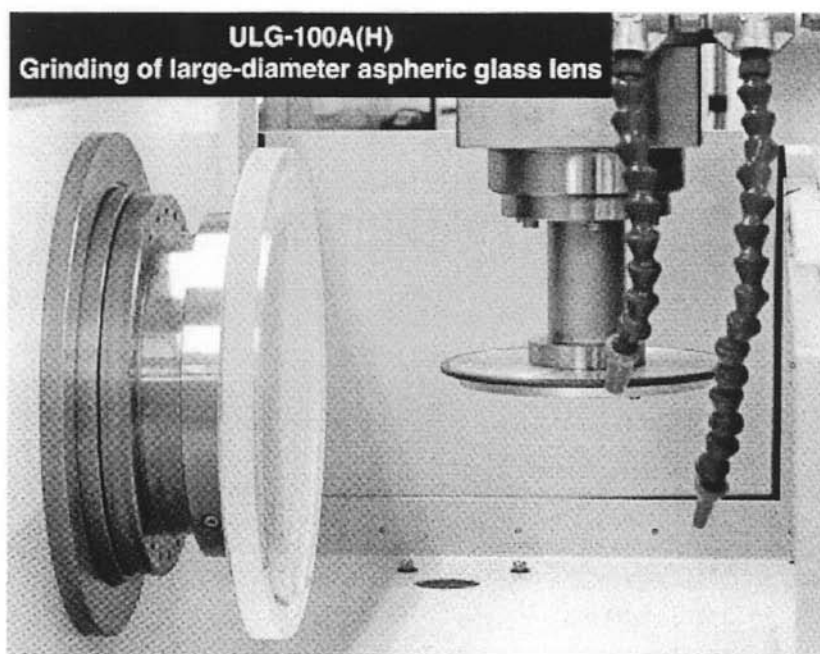


Fig. 6.34. Grinding of a large diameter aspheric lens glass on a Toshiba ULG 100A, 2 axis ultraprecision turning and grinding machine

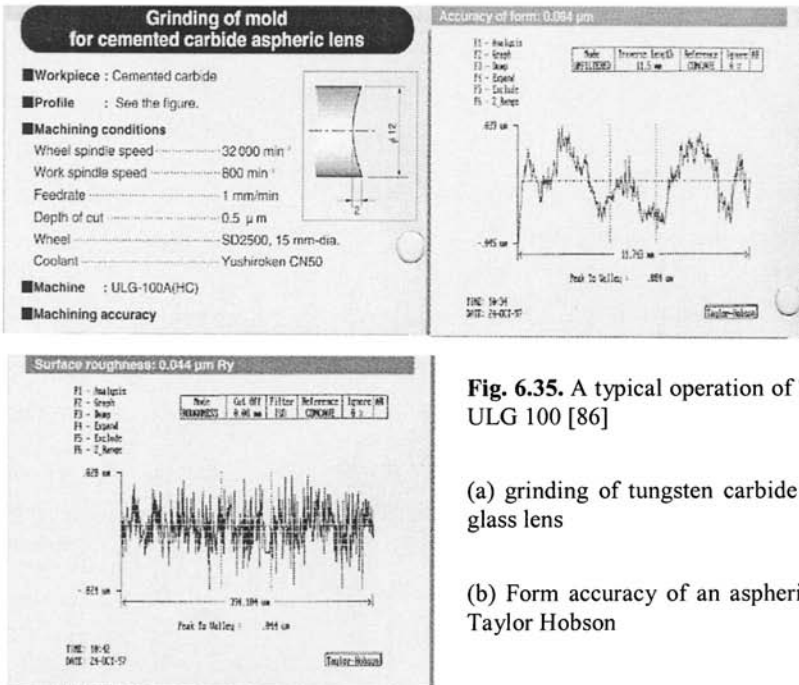


Fig. 6.35. A typical operation of Toshiba's ULG 100 [86]

(a) grinding of tungsten carbide mold for glass lens

(b) Form accuracy of an aspheric lens on Taylor Hobson

Precitech's OPTIMUM 2800 (Fig. 6.36) is a high performance, 2-axis, computer controlled, ultra-precision, contouring machine specifically designed for single-point diamond turning and grinding of ultraprecision optical components. The machine is built on a natural granite base and utilizes a pneumatic vibration isolation system. The hydrostatic oil bearing slideways are constructed in an offset "T" configuration where the x-axis (spindle) slide represents the cross-arm of the "T", and the z-axis (tool holding) slide represents the stem of the "T". Both the x- and z-axes have 200mm of travel. The work holding spindle is a pneumostatic air bearing design. The spindle is powered through the use of a brushless DC motor and will run up to a maximum speed of 3,000 rpm.

The high-speed aspheric grinding system is designed and manufactured for use on Precitech OPTIMUM machining systems. This compact aspheric grinding system utilizes a high-speed, turbine driven, air-bearing spindle. The air-bearing spindle is mounted on a

manually positioned mechanical slide assembly. The slide is mounted on a fabricated steel column such that the grinding spindle is positioned in the vertical direction.

The grinding spindle operates over a speed range of 10,000 - 70,000 rpm. The turbine drive provides extremely smooth friction free spindle rotation. The grinding system accommodates grinding wheels from 3 mm – 15 mm in diameter. The system has been designed primarily for small aspheric components, particularly lenses and lens molds up to 30 mm in diameter [87].

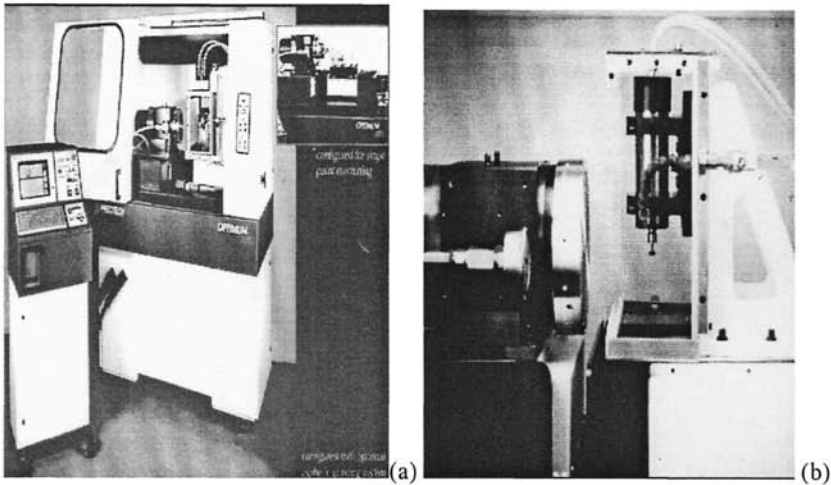


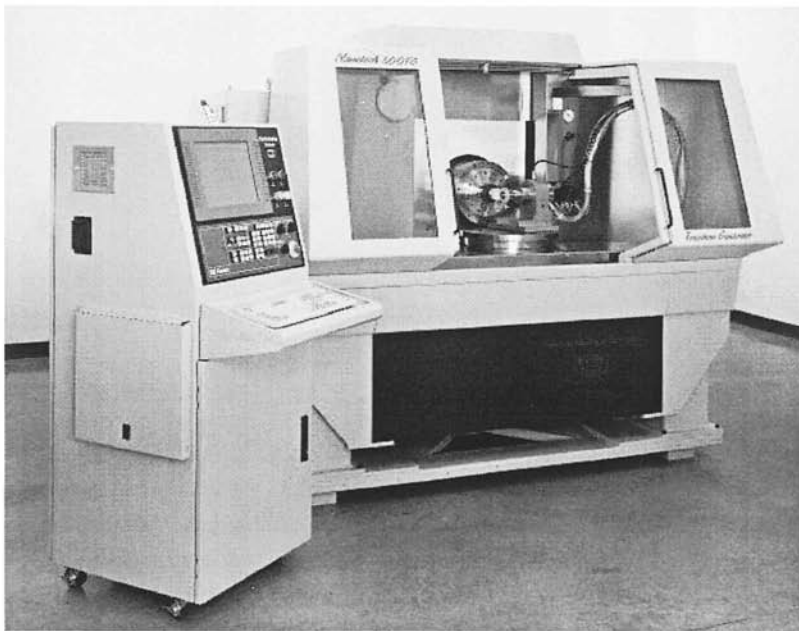
Fig. 6.36. (a) Precitech's OPTIMUM 2800 ultraprecision turning and grinding machine (b) Close view of grinding machine used to study ductile streak formation [88].

Semi-ductile grinding followed by simple mechanical polishing is an economical process for producing a mirror-like surface for hard and brittle aluminoborosilicate glass. A fine grit resinoid-bond grinding wheel was used by Ong and Venkatesh [88] to generate large amounts of ductile streaks to improve surface finish and to reduce polishing time. The ground samples were polished with different slurries on Precitech's OPTIMUM 2800.

Table 6.6. Polishing parameters for polishing aluminoborosilicate glass [88]

Preston's coefficient for plano Pyrex glass and the lightness index of each polished sample

Polishing reagent (1 μm grit size)	Thickness removed during polishing, dT (μm)	Polishing pressure, P (kPa)	Polishing time, dt (min)	Relative speed, ds/dt (m s^{-1})	Preston coefficient, k ($\text{m}^2 \text{N}^{-1}$)	Lightness index, λ
Polycrystalline diamond	39.500	55.06327	4.5	2.82743	9.397×10^{-13}	25.82
Monocrystalline diamond	3.700	33.17041	6.5	2.82743	1.012×10^{-13}	24.31
Cerium oxide	1.623	19.25292	3.0	1.41371	3.313×10^{-13}	25.91

**Fig. 6.37.** Moore's Nanotech 500FG ultraprecision machine

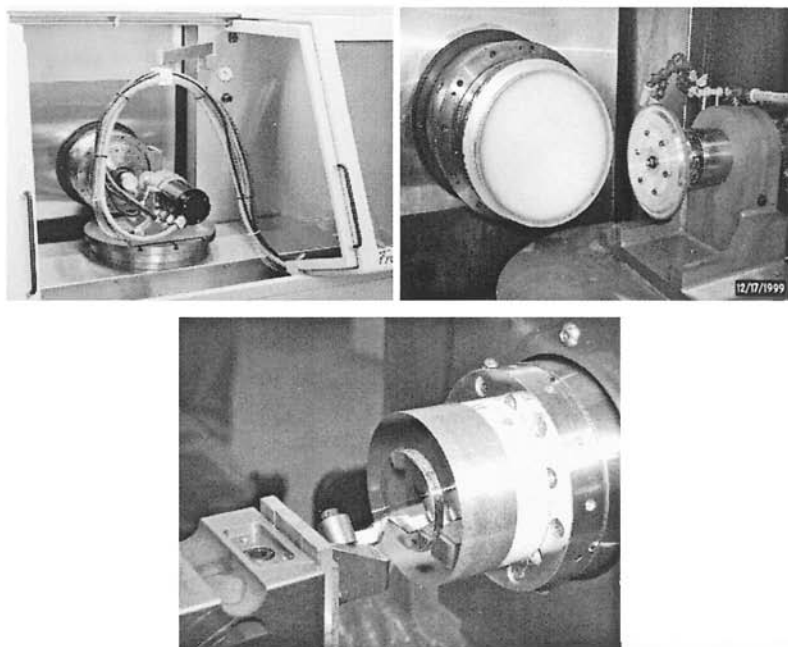


Fig. 6.38. Close-up of grinding and turning of aspheric lens glass on Moore's nanotech 500FG ultraprecision turning and grinding machine [89]

Nanotech 500FG (Fig. 6.37), developed by Moore Nanotechnology Systems adopts the microgrinding technique. The machine is capable of generating arbitrary confocal shapes on materials ranging from optical glass and infrared materials to non-ferrous metals, crystals, polymers, and ceramics. The microground surface typically requires little or no post polishing. The machine temperature is maintained stable to less than $\pm 0.5^{\circ}\text{C}$. Grinding is done in a flood-cooled environment.

Namba et al. [8] developed an ultraprecision surface grinder and succeeded in stabilizing their grinding process by using a spindle rotor made from a low-thermal expansion material. This machine has two vertical spindles with hydrostatic bearing of high precision and rigidity. It can machine at extremely fine depth of cut ($0.1\text{ }\mu\text{m}$) and capable of producing at submicron flatness and nanometer surface

roughness (5 nm R_{max}) on optical glass (NbF), Mn-Zn ferrite and electronic materials using diamond abrasive grinding wheels.

McKeown et al. [90] of Cranfield Unit for Precision Engineering (CUPE) also developed a 3-axis ultraprecision grinding machine (Nanocenter) which can perform diamond turning, grinding, polishing, and capable of measuring complex machined profiles through 1.25 nm resolution interferometry. They also suggested that as a rule of thumb, the machine must have static “loop-stiffness” between tool and workpiece of at least 300 N/ μm in order to establish safe conditions for ductile grinding.

Another example of an ultraprecision grinding machine was developed by Suzuki and Murakami of Toyoda Machine Works (1995) for machining non-axisymmetric aspheric mirrors. This is a 5-axis machine having feedback resolution of 10 nm, and the rotational positioning is controlled by a laser rotary encoder with resolution of 0.00002°. It is clearly seen that machine rigidity, high dynamic stiffness, high thermal stability, precise and smooth feedback resolution control, ability to achieve fine depth of cut, and the use of special tooling play a vital role in producing very smooth surfaces under sub-nanometric level in ultraprecision machining.

6.5.2 Tetrahedral Desktop Machine Tool

The dynamic characteristics of a revolutionary machine tool structure used for machining engineering components at the micro and nanoscales are of paramount importance. Minimizing the effects of vibrations at the micro- and nanoscale is vital because if a machined workpiece oscillates during the machining process then an increase in the depth of cut will occur that will reduce the quality of surface finish and the dimensional accuracy of the machined component. The stacking of atoms inspired the design of a new platform structure in order to improve on existing technology, since the goal of the machine is to allow the manipulation of molecules at the nanoscale. The idea for the structure comes from the structural stability afforded by the tetrahedron. The tetrahedral structure is an extremely stable structure and it is hypothesized that the shape could minimize vibrations better than conventional machine tool structures. Vibrations travel through a tetrahedral structure; they are concealed out or

minimized due to the interference between the vibrating waves as they travel through the loops of the structure. The ability to minimize vibrations is needed because if the spindle oscillates during machining, an increase in the depth of cut will occur, thus reducing the quality of surface finish, or dimensional accuracy of the machined part will be reduced significantly. Figure 5.39 shows the tetrahedral structure of the machine tool [91].

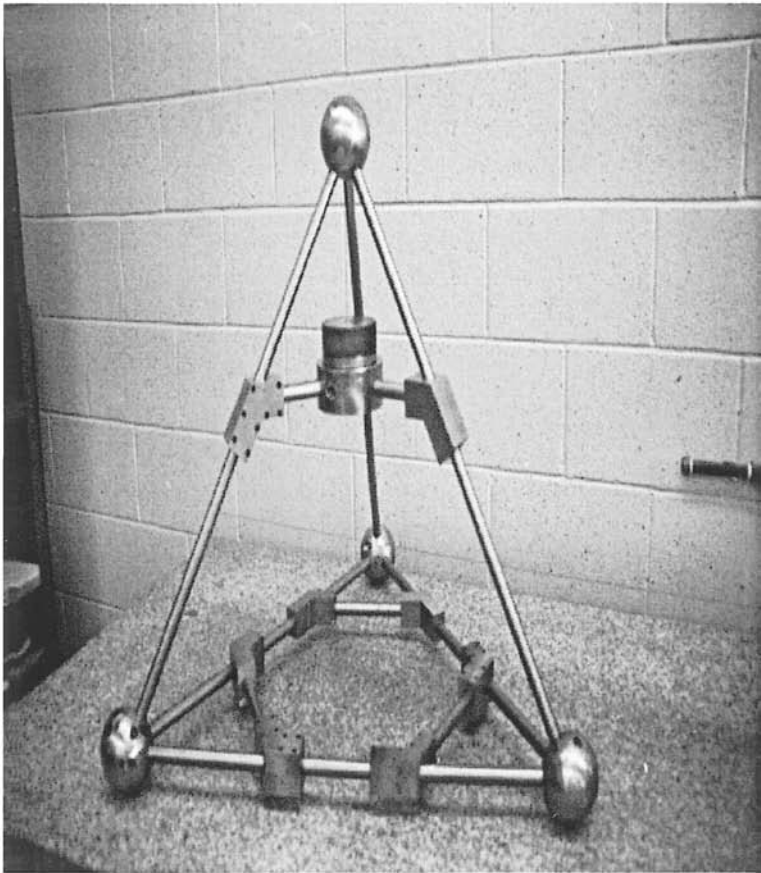


Fig. 6.39. Tetrahedral machine tool frame [91, 92]

6.5.3 Binderless Wheel

Figure 6.40a indicates the wheel shape, and nominal size of the wheel. When the wheel is in use it is fitted to a shank as shown in Fig. 6.40b [57].

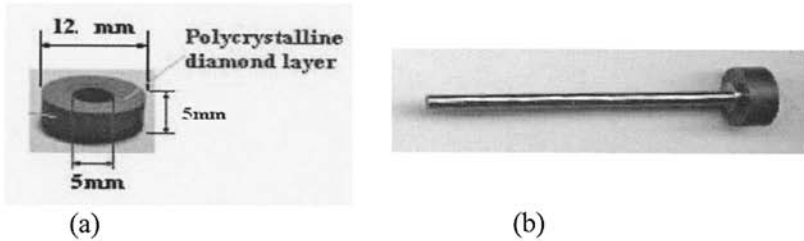


Fig. 6.40. Binderless diamond grinding wheel shown in (a) wheel shape without shank and (b) wheel with shank.

The wheel is produced by depositing diamond on a metal, commonly carbide substrate. Three types of wheel can be found based on the type of deposition method applied. Figure (6.41) shows diamond grain structure of each type of wheel. Unlike a bonded wheel, the diamond layer is only on the top of the substrate surface and can be very fine grain size whereas the smallest grain in bonded wheel must be larger than that of bond. The maximum grain size can go to 10 μm . However, it has a higher density of diamond grains.

The binderless diamond wheel was tested to machine Pyrex glass, the silicon die, and packaging chips. Pyrex glass and silicon die were machined changing feed and depth of cut to investigate machining mode and surface finish. Ductile streaks were observed on both surfaces (Fig. 6.42). The achievable surface finish was found to be 0.1 μm . The packaging chip was machined in order to examine all the six Cu trace layers. Chip packaging machined quite easily with a binderless wheel revealing Cu layers.

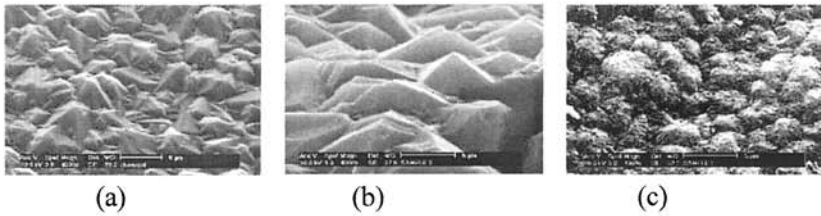


Fig. 6.41. SEM micrographs of diamond wheel surface: (a) thermally treated wheel, (b) chemically treated wheel, (c) chemically treated wheel with diamond facets [92].

Flatness of the binderless wheel helps planar delayering of the chip packaging, as seen in Fig. 6.43, without the need for polishing. Minor defects in horizontal copper traces and major ones in vertical viaducts that link the Cu traces are evident in these micrographs.

The invention of the binderless diamond-grinding wheel has made the machining of the silicon die and the chip packing much easier and more economical (Fig. 6.44). It has the potential of grinding glass and infrared optical materials such as Si and Ge.

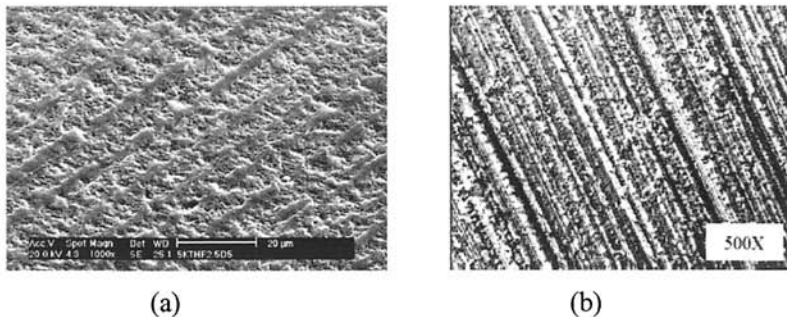


Fig. 6.42. (a) SEM picture shows elevated partial ductile streaks on optical Pyrex glass [62], (b) optical micrograph shows abundant ductile streaks on silicon die [93]

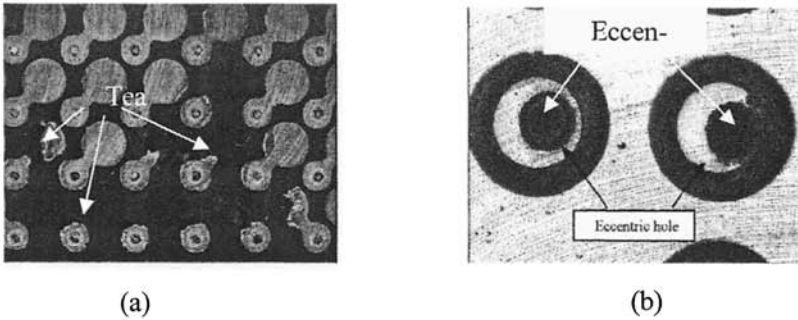


Fig. 6.43. Binderless diamond grinding of chip packaging reveals defects such as (a) tear of Cu pads and (b) eccentric via ducts [94].

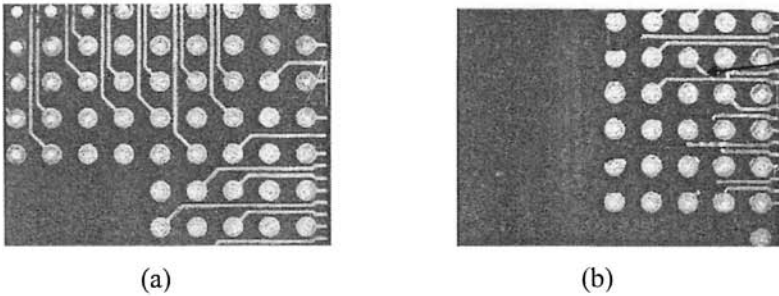


Fig. 6.4. Binderless diamond grinding of chip packaging shows (a) a near perfect 5th layer with (b) an open circuit at one end [94]

6.5.4 Freeform Optics

Free-form surfaces are not new to mankind, and sculptured idols and monuments bear testimony to human skills. They have been pervasive in manufacturing owing to their exceptional performance and properties. A novel optical system with free-form optical surfaces was developed for Polaroid's X-70 instant camera. They have found applications in eyewear, electro-optics, defense and automotive industries. Mirrors for surveillance, LTV lenses for lithography, x-ray mirrors for x-ray lithography, laser rods, and windows are some of

the important defense and commercial applications of free-form optics. The advantages afforded by free-form surfaces are numerous. Other benefits offered by free-form surfaces to optical systems are: improving aerospace designs such as improvements in field of view, aerodynamics, detectability, and cost. They could also improve semiconductors, lithography, and imaging.

Free-form optics are unsymmetric about any axis of revolution. They are sometimes categorized as one kind of asphere with non-rotational symmetry. They are also referred to as conformal optics - combination of aspheric, spherical, cylindrical, conical, diffractive, plano, or ogive (pointed) shapes. Despite the particularity in the definition and the design of these surfaces, the manufacturing systems treat them as free-form surfaces. Some examples of free-form optical surfaces are shown in Fig. 6.45.

Fabrication of free-form optical surfaces requires multi-axis machining centers and metrology system. The machining precision needed to meet the system performance requirements for free-form optics, non-traditional military optics, for example, exceeds the capabilities of commercially available machine tools and processes by two to three orders of magnitude. These free-form optics, machines, and metrology devices represent the next frontier in ultraprecision machining technology. Table 6.7 compares accuracy obtainable by the two methods of manufacturing.

Table 6.7. Comparison of free-form surface finish by different processes.

Process	Surface finish RMS (nm)	Form accuracy (μm) 0.204
Diamond turning	3	0.057
Diamond grinding	4.4	0.214

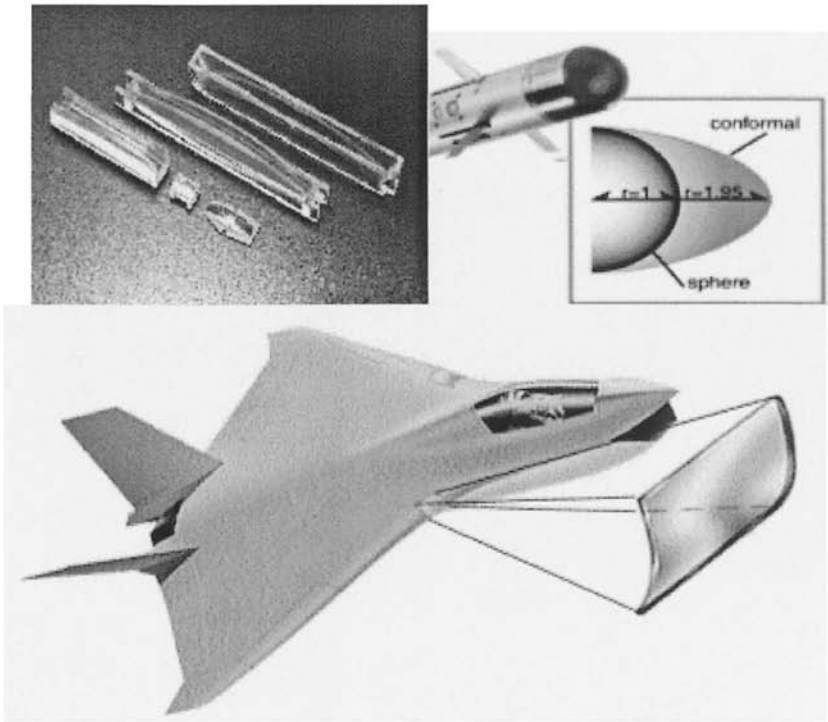


Fig. 6.45 Various shapes of free form optics and their application [89]

6.5.5 Material Removal Rates

Ductile mode machining is generally used when mirror finishes are required in hard and brittle materials. To avoid cracking, depths of cut are between 1% and 10% of those when producing a mirror finish on a metal.

Diamond Turning

Diamond turning has been used to turn germanium with roughness values of the order of 5-6 μm when machining 50 mm diameter samples. Optics made from germanium, zinc sulfide, and silicon

have been successfully turned using diamond. Typical diamond turning parameters are shown in Table 6.8.

Table 6.8 Typical diamond turning parameters

Work-piece Material	Spindle speed (rpm)	Coolant	Roughing depth of cut (mm)	Roughing feedrate (mm/min)	Finishing depth of cut (mm)	Finishing feedrate (mm/min)
Aluminum	800	Oil	0.05	12 - 25	0.0025	2.5
Copper	800	Oil	0.05	12 - 25	0.0025	2.5
Electroless nickel	400	Oil	0.007	5	0.0012	2.5
PMMA	1000	Air/oil	0.25	15	0.012	3.5

Diamond Grinding

When diamond grinding, diamond cutting points can be expected to remove material in the ductile machining mode. Typical grinding parameters are:

Grinding wheel speed: 30 – 60 m/s;
 Workpiece speed: 0.1 – 1.0 m/min;
 Depth of cut: 0.001 – 0.01 mm;
 Specific removal rate: 0.05 – 0.2 mm³/mm.s;
 Total power: <1 kW.

Polishing rates are even more critical and are shown in previous sections of this chapter.

6.6 Conclusions

Among machining processes such as turning, milling, drilling, and grinding, the latter started as a precision process, achieved high precision status with superabrasives, and became an ultraprecision technique with development of rigid machine tools. It competes with

ultraprecision diamond turning and is no longer labeled as random processes at the ultraprecision level.

6.7 Problems

1. What is precision machining and grinding?
2. Describe Taniguchi's classification of precision machining processes.
3. Describe Scattergood's model of ultraprecision machining.
4. How are grinding wheels structured?
5. Describe and explain how bonds are selected for grinding wheels.
6. Describe the many types of abrasive grain.
7. Describe the properties of hard and brittle materials.
8. How does grade and concentration affect the grinding process?
9. What is creep feed grinding and how are wheels specified for such processes?
10. What is a precision grinding process and how would you achieve it?
11. Describe the use of a binderless wheel for grinding silicon chips.
12. What is partial ductile mode grinding?
13. Explain and illustrate how aspheric surfaces are generated.
14. What are the requirements of a machine tool for producing surface roughness levels in the nanometer range?

References

1. McKeown PA, (1987), The Role of Precision Engineering in Manufacturing of the Future, *Annals of the CIRP*, **36**(2), 495-501.
2. Taniguchi N, (1994), The State of the Art of Nanotechnology for Processing of Ultraprecision and Ultrafine Products, *Precision Engineering*, **16**(1), 5-24.
3. Venkatesh VC, Chandrasekaran, H., (1987), *Experimental Techniques in Metal Cutting*, New Delhi: Prentice-Hall of India Ltd.

4. McKeown PA, (1995a), High Precision Manufacturing in an Advanced Industrial Economy, Nanyang Technological University, Singapore.
5. Yan J, Syoji K, Kuriyagawaa, T. and Suzuki, H., (2002a), Ductile Regime Turning At Large Tool Feed, *Journal of Materials Processing Technology*, **121**, 363–372.
6. Schinker MG, (1991), Subsurface Damage Mechanisms at High-Speed Ductile Machining of Optical Glasses, *Precision Engineering*, **13**(3), 208-218.
7. Komanduri R, (1996), On Material Removal Mechanisms in Finishing of Advanced Ceramics and Glasses, *Annals of the CIRP*, **45**(1), 509-513.
8. Namba Y and Abe M, (1993) Ultraprecision Grinding of Optical Glasses to Produce Super-Smooth Surfaces, *Annals of the CIRP*, **42**(1), 417-420.
9. Puttick KE, Rudman MR, Smith KJ, Franks A and Lindsay K, (1989), Single-point Diamond Machining of Glasses, *Proc. Royal. Society. London.*, **A426**, 19-30.
10. Anon.(1998). [On-line] Available at <http://www.predev.com/smg/specification.htm>
11. Anon.(1998). [On-line] Available at http://www.roytech.co.uk/Useful_Tables/ISO_Tolerances/ISO_LIMITS.htm
12. Zhong Z and Venkatesh VC, (1995), Semi-Ductile Grinding and Polishing of Ophthalmic Aspherics and Spherics, *Annals of the CIRP*, **44**(1), 339-342.
13. Morris JC, Callahan DL, Kulik J, Patten JA and Scattergood RO (1995). Origins of the Ductile Regime in Single-Point Diamond Turning of Semiconductors. *Journal of the American Ceramic Society*. 78(8): 2015-2020.
14. Ikawa N, Donaldson RR, Komanduri R, Konig W, Aachen TH, McKeown PA, Moriwaki T and Stowers IF, (1991), Ultraprecision Metal Cutting – The Past, the Present and the Future, *Annals of the CIRP*, **40**(2), 587-594.
15. Fang FZ, Liu XD and Lee LC, (2003), Micro-Machining of Optical Glasses – A Review of Diamond-Cutting Glasses, *SADHANA*, **28**(5), 945-955.
16. Namba T, Kobayashi H, Suzuki H and Yamashita K, (1999), Ultraprecision Surface Grinding of Chemical Vapor Deposited Silicon Carbide for X-Ray Mirrors using Resinoid-Bonded Diamond Wheels, *Annals of the CIRP*, **48**(1), 277-280.

17. Ohmori H and Nakagawa T, (1995), Analysis of Mirror Surface Generation of Hard and Brittle Materials by ELID Grinding with Superfine Grain Metallic Bond Wheels, *Annals of the CIRP*. **44**(1): 287-290.
18. Blake PN and Scattergood RO, (1990), Ductile Regime Machining of Germanium and Silicon, *Journal of the American Ceramic Society*. **73**(4): 949-957.
19. Blackley WS and Scattergood RO (1991). Ductile-Regime Machining Model for Diamond Turning of Brittle Materials. *Precision Engineering*. **13**(2): 95-103.
20. Bifano TG, Dow TA and Scattergood RO (1991). Ductile-Regime Grinding: A New Technology for Machining Brittle Materials. *Trans. ASME. Journal of Engineering for Industry*. **113**: 184-189.
21. Lindberg RA (1970). *Processes and Materials of Manufacture*. New Delhi: Prentice Hall of India Ltd.
22. HMT Rao, (1980). *Production Technology*. New Delhi: Tata McGraw Hill Publishing Company Limited.
23. Kalpakjian S, Schmid S (2001). *Manufacturing Engineering and Technology*. 4th edition, by Prentice Hall Inc, Upper Saddle River, NJ.
24. Rao PN (2000). *Manufacturing Technology: Metal Cutting & Machine Tools*. Tata New Delhi: McGraw-Hill Publishing Company Limited.
25. Cook NH (1966). *Manufacturing Analysis*. Addison-Wesley Publishing Co. Inc.
26. Pearce CA (1972). *Silicon Chemistry and Applications*. London: The Chemical Society.
27. Stephenson DA and Agapiou JS (1997). *Metal Cutting Theory and Practice*. New York : Marcel Dekker, Inc.
28. Anon. (1996a). *Schott Optical Glass Properties*. Pocket Catalogue.
29. Malkin S (1989). *Grinding Technology : Theory and Application of Machining with Abrasives*. England: Ellis Horwood Limited.
30. Savington D (2001). Maximizing the Grinding Process. SME technical paper. **MR01-140**: 1-12.
31. Subramaniam K and Ramanath P. (1991). Principles of Abrasive Machining. *Ceramics and Glasses*. Engineered Materials Handbook, **4**, ASM International, The Materials Information Society, 316.
32. Hensz RR (1969). *Glass Grinding and Polishing*. SME Technical paper. **MR69-230**: 1-11.
33. Dunnington BW (1978). *Diamonds for Abrasive Machining, Lapping, Polishing and Finishing*. SME Technical Paper. **MR78- 955**:1-8.
34. Bhateja C, Lindsay R, *Grinding theory and techniques and troubleshooting*, published by Society of Manufacturing Engineers, 1982 Dearborn, MI.

35. Kibbe RR, Neely JE, Meyer RO and White WT (1987). Machine Tool Practices. 3rd edition. John Wiley & Sons.
36. Xu X, Yu Y and Huang, H (2003). Mechanisms of Abrasive Wear in the Grinding of Titanium (TC4) and Nickel (K417) Alloys. *Wear*. **255**: 1421–1426.
37. Holz R and Sauren J (1988). Grinding with Diamond and CBN. WINTER Diamond and CBN Tools Catalogue. Ernst Winter & Sohn Diamantwerkzeuge GmbH & Co.
38. Lindberg RA (1990). Processes and Materials of Manufacture. 4th edition, Prentice Hall, Inc. NJ.
39. Inasaki I, Tonshoff HK and Howes TD (1993). Abrasive Machining in the Future. *Annals of the CIRP*. **42**(2): 723-732.
40. Aurich JC, Braun O and Wernecke G (2003). Development of a Superabrasive Grinding Wheel with Defined Grain Structure using Kinematic Simulation. *Annals of the CIRP*. **52**(1): 275-280.
41. Anon. (2002). Tech Front: Defining Grinding Grains. *Manufacturing Engineering*. **6**:24.
42. Shaw MC (1984). Metal Cutting Principles. Oxford University Press, NY, 1984.
43. Anon (2002a). Noritake diamond grinding catalogue.
44. Anon.(2005). [On-line] Available at <http://www.zsmec.net/product3-1.htm>
45. Boothroyd G (1981). Fundamentals of Metal Machining and Machine Tools. International Student Edition. Tokyo: McGraw-Hill International Book Company.
46. Donaldson C, LeCain GH and Goold VC (1973). Tool Design. 3rd edition. McGraw-Hill Book Company, NY.
47. Anon. (1995a). Diamond Tools and CBN Tools for Internal Grinding Catalogue. Ernst Winter & Sohn Diamantwerkzeuge GmbH & Co., Germany.
48. Anon. (1995b). Material Removal, Industrial Tooling Catalogue. Greenfield Industries, USA.
49. Anon. (2004). <http://www.schott.com/english/news/pictures.html>.
50. Anon. (2001). Tools & Industrial Supplies. Cromwell-Tools Catalogue.
51. Subramanian K and Tricard M (1995). Future Directions for the Grinding of Ceramics. Supergrind'95 - Grinding and Polishing with Superabrasives, CT: 5-31.
52. Krar, Ratterman (1990) Superabrasives: Grinding and machining with CBN and Diamond, Glencoe/McGraw-Hill, USA

53. DeGarmo PE, Black JT, Kohser RA, (2002), Materials and processes in manufacturing, 9th Edition, Macmillan Publishing Company, New York
54. Metzger JL, Superabrasive grinding, Butterworth and Co. Ltd., 1986
55. Dallas DB, (2000) Tools and Manufacturing Engineering Handbook, SME, USA
56. Moore WR, Foundations of Mechanical Accuracy, 800 Union Avenue, Bridgeport CT 06607, 1974.
57. Venkatesh VC, and Izman S, 2003, Application for Malaysian Patent for invention of novel diamond wheel filed on 30th January 2003. No. PI 20030326.
58. Lindburg RA Processes and materials of manufacture, Allyn and Bacow Inc, Boston, 1964, p859
59. Venkatesh VC, S Izman 2003. Ductile streaks in precision grinding of hard and brittle materials, Sadhana, **28**, 5, October 2003, 915–924.
60. Lindburg RA, Lecture at Ford Foundation Summer School, PSG college of Technology, Coimbatore, India, June 1965.
61. Venkatesh VC, and Izman S, Konneh M, Ultraprecision and high precision turning and grinding of brittle materials. Universiti Teknologi Malaysia
62. Mon TT, 2003, Chemical mechanical polishing of optical glass subjected to partial ductile grinding, M.Eng. Thesis, Universiti Teknologi Malaysia.
63. Ohmori H and Nakagawa T (1990). Mirror Surface Grinding of Silicon Wafers with Electrolytic In-Process Dressing. *Annals of the CIRP*. **39**(1): 329-332.
64. Rahman M, Senthil Kumar S, Lim HS, Fatima K (2003) Nano finish grinding of brittle materials using electrolytic in-process dressing (ELID) technique, Sadhana, **28**, (5) 957-974
65. Bandyopadhyay BP, Ohmori H and Takahashi I. (1997). Efficient and Stable Grinding of Ceramics by Electrolytic In-Dressing (ELID). *Journal of Materials Processing Technology*. **66**: 18-24.
66. Itoh N and Ohmori H (1996). Grinding Characteristics of Hard and Brittle Materials by Fine Grain Lapping Wheels with ELID. *Journal of Materials Processing Technology*. **62**: 315-320.
67. Qian J, Ohmori, H and Lin W (2001). Internal Mirror Grinding with a Metal/Metal-Resin Bonded Abrasive Wheel. *International Journal of Machine Tools & Manufacture*. **41**:193-208.
68. Murata R, Okano K and Tsutsumi C (1985). Grinding of Structural Ceramics. Milton C. Shaw ASME Grinding Symposium PED. **16**:261-272.

69. Zhang C, Ohmori H and Li W (2000). Small-Hole Machining of Ceramic Material with Electrolytic Interval-Dressing (ELID-II) Grinding. *Journal of Material Processing Technology*. **105**: 284-293.
70. Chen H, Li J, Spence J and Li JCM (2000). An ELID-cutting saw. *Journal of Materials Processing Technology*. **102**: 208-214.
71. Jeff Ruckman, A Tutorial on Deterministic Microgrinding News letter of Center for Optics Manufacturing Convergence Vol 7 number 6, Nov/Dec 1999.
72. Kapoor A (1993). A Study on Mechanism of Aspheric Grinding of Silicon. Tennessee Technological University, USA: M.Sc. Thesis.
73. Tan CP (1990). Aspheric Surface Grinding and Polishing of Thermal Imaging Materials. Tennessee Technological University, Cookeville, USA: M.Sc. Thesis.
74. Russell RG (1993) Comparison of metal and resinoid bonded grinding wheels with various grit sizes in the aspheric surface generation of silicon lenses. Tennessee Technological University, USA: M.Sc. Thesis.
75. Zhong Z and Venkatesh VC (1995). Semi-Ductile Grinding and Polishing of Ophthalmic Aspherics and Spherics. *Annals of the CIRP*. **44**(1): 339-342.
76. Darryl Meister July 1998, Lens Talk, Sola technical marketing Vol 26 No 25.
77. Horne DF (1983). *Optical Production Technology*. 2nd edition. Bristol: Adam Hilger Ltd.
78. Van Ligten RF and Venkatesh VC (1985). Diamond Grinding of Aspheric Surfaces on a CNC 4-Axis Machining Center. *Annals of the CIRP*. **34**(1): 295-298.
79. Anon.(2005). [On-line] Available at http://www.hkpc.org/optics/polishing.html#advanced_grinding
80. Fang FZ and Chen LJ (2000). Ultra-Precision Cutting of ZKN7 Glass. *Annals of the CIRP*. **49**(1): 17-20.
81. Namba Y, Wada R, Unno K, Tsuboi A (1989). Ultra-precision Surface Grinder Having a Glass-Ceramic Spindle of Zero-Thermal Expansion. *Annals of the CIRP*. **38**(1):331-334.
82. Venkatesh VC (1999). Diamonds in Manufacturing, SME Student Chapter (UTM) Year Book 1999.
83. Chapman G (2003). Enabling Technologies for Ultra-Precision Manufacturing & Metrology. Presented on 18 January 2003 at the Faculty of Mechanical Engineering, Universiti Teknologi Malaysia.
84. Schulz H, and Moriwaki T (1992). High-speed Machining. *Annals of the CIRP*. **41**(2): 637-643.
85. Komanduri R, Lucca DA and Tani Y (1997). Technological Advances in Fine Abrasive Processes. *Annals of the CIRP*. **46**(2): 545-596.

86. Momochi T, Masahide K, Limura Y, One day Toshiba seminar, Kolej Universiti Teknologi Kebangsaan Malaysia, High-Speed High precision machining 2002.
87. Precitech catalogue (2000).
88. Ong NS, Venkatesh VC Semi ductile grinding and polishing of Pyrex glass, *Journal of Materials Processing Technology* **83** (1996) 261-266.
89. Moore catalogue (2000).
90. McKeown PA, Carlisle K, Shore P and Read, R.F.J. (1990). Ultra-precision, High Stiffness, CNC Grinding Machines for Ductile Mode Grinding of Brittle Materials, *Infrared Technology and Applications*. SPIE 1320: 301-313.
91. Jackson MJ, Hyde LJ, Modal analysis of tetrahedral machine tool structure, ICAMT 2004, Kuala Lumpur 11-13 May 2004 pp. 394-400.
92. Venkatesh VC, Izman S, Bauer E, Oles E, Mon TT, M. Konneh, Failure analysis of IC chip using novel technique, ICAMT 2004, Kuala Lumpur 11-13 May 2004 pp. 294-299.
93. Woon KS, 2003, Binderless grinding wheel for failure analysis of silicon die on IC chips, B.Eng Thesis, Universiti Teknologi Malaysia.
94. Tang KF, 2003, Novel grinding process for failure analysis of IC chip packaging, B.Eng Thesis, Universiti Teknologi Malaysia.

7. Diamond Microcutting Tools

7.1 Introduction

Deposition technology has played a major part in the creation of today's scientific devices. Computers, electronic equipment, bio-medical implants, cutting tools, optical components, and automotive parts are all based on material structures created by thin film deposition processes. There are many coating processing ranging from the traditional electroplating to the more advanced laser or ion-assisted deposition. However, the choice of deposition technology depends upon many factors including substrates properties, component dimensions and geometry, production requirements, and the exact coating specification needed for the application of interest. For complex geometry components, small feature sizes, good reproducibility and high product throughput chemical vapor deposition (CVD) is a highly effective technology. For example, low-pressure and plasma assisted CVD is a well-established technology for semiconductor devices, which has very small feature sizes and complex geometrical arrangements on the surface.

In order to understand both physical vapor deposition (PVD) and CVD processes, one has to model them in terms of several steps. These processes can be divided into the following stages:

- **Generation of Vapor Phase Species**

The precursor materials are converted into a convenient form so that transport to the substrates is efficient. A vapor is generated in the reactor. Hot filaments, lasers, microwave, ion beams, electrons guns, etc., can be used to activate the source materials, enabling deposition to be carried out.

- **Transport of Source Materials to the Substrate Region**

The vapor species are transported from the source to the substrate with or without collisions between the atoms and molecules. During transport, some of the species can be ionized by creating plasma in this space. This is normally carried out in a vacuum system; however, atmospheric CVD systems are also employed.

- **Adsorption of Active Species on the Substrate Surface**

For deposition to take place the active species must first be adsorbed onto the active sites on the surfaces. Initially this occurs via physisorption where the species adhere to the surface with weak van der Waals forces and then strong covalent bonds are formed between the species and the surface known as chemisorption.

- *Decomposition Adsorbed Species on the Substrate Surface*

Once the gaseous species are adsorbed onto surface site and the energy of the species is sufficient then decomposition of the precursors can take place resulting in the creation of nucleation center.

- **Nucleation and Film Formation**

The process involves the subsequent formation of the film via nucleation and growth processes. These can be strongly influenced by process parameters resulting in a change in the microstructure, composition, impurities, and residual stress of the films. The final film properties are highly dependent on the microstructural and interfacial characteristics of the deposited coating.

Independent control of these stages is critical and determines the versatility or flexibility of deposition process. For example, PVD process parameters can be independently and precisely monitored

and controlled. Thus allowing microstructure, properties, and deposition rates to be tailored specifically to the performance requirements of the product. Generally, CVD processes have the advantage of good throwing power enabling complex geometry substrates to be coated, while the deposition rates in PVD processes are much higher than those in CVD processes at lower deposition temperatures.

Although CVD and PVD processes are simple in principle, one must be well versed in vacuum technology, physics, chemistry, materials science, mechanical and electrical engineering as well as in elements of thermodynamics, chemical kinetics, surface mobility and condensation phenomena in order to obtain a detailed fundamental understanding of these processes. In this chapter we restrict our attention to the deposition of diamond thin films for use in cutting tools.

7.2 Properties of Diamond

Diamond is an advanced material with an excellent combination of physical and chemical properties. If high-quality diamond films with comparable properties to natural diamond can be formed with low surface roughness numeral potential applications will emerge in the near future particularly in the emerging field of nanotechnology.

Diamond as a material possesses a remarkable range of physical attributes, which make it a promising material for a large range of applications. Selections of these are given in Table 7.1. However, owing to the cost and availability of large natural diamonds, most of these applications have not been developed to their full potential.

7.3 History of Diamond

7.3.1 Early History of Diamond Synthesis

Diamond is one of the most technologically and scientifically valuable crystalline solids found in nature. Their unique blends of properties are effectively incomparable to any other known material. Sir Isaac Newton was the first to characterize diamond and determine it to be of organic origin while in 1772, the French chemist Antoine L. Lavoisier established that the product of diamond combustion was limited to carbon dioxide.

Table 7.1. Properties of diamond

Properties	Applications
High wear resistance	Cutting tools
Chemical inertness	Electrochemical Sensors
High thermal conductivity	Heat spreaders
Biological inertness	In vitro applications
Semiconducting when doped	Electronic devices
High resistivity (insulator)	Electronic devices
Negative electron affinity	Cold cathode electron sources

English chemist Smithson Tennant showed that diamond combustion products were no different than those of coal or graphite and resulted in “bound air”. Later, the discovery of x-rays enabled Sir William Henry Bragg and his son Sir William Lawrence Bragg to determine that carbon allotropes were cubic (diamond), hexagonal (graphite) and amorphous. With this information, early attempts to synthesize diamond began in France in 1832 with C.C. de la Tour and later in England by J.B. Hanney and H. Moisson. The results of their work are disputed to this day.

Synthesis of diamond has attracted widespread attention ever since it was established that diamond is a crystalline form of carbon. Since diamond is the densest carbon phase, it became immediately plausible that pressure, which produces a smaller volume and therefore a higher density, may convert other forms of carbon into dia-

mond. As understanding of chemical thermodynamics developed throughout the 19th and 20th centuries, the pressure-temperature range of diamond stability was explored. In 1955, these efforts culminated in the development of a high pressure-high temperature (HPHT) process of diamond synthesis with a molten transition metal solvent-catalyst at pressures where diamond is the thermodynamically stable phase [1]. Three major problems can be isolated for emphasizing the difficulty of making diamond in the laboratory. First, there is difficulty in achieving the compact, strongly bonded structure of diamond, which requires extreme pressure. Secondly, even when such a high pressure has been achieved, a very high temperature is required to make the conversion from other forms of carbon to diamond proceed at a useful rate. Finally, when diamond is thus obtained, it is in the form of very small grains and to achieve large single crystal diamond requires yet another set of constraints. However, less well known has been a parallel effort directed toward the growth of diamond at low pressures where it is metastable. Metastable phases can form from precursors with high chemical potential if the activation barriers to more stable phases are sufficiently high. As the precursors fall in energy, they can be trapped in a metastable configuration. Formation of a metastable phase depends on selecting conditions in which rates of competing processes to undesired products are low [2]. In the case of diamond, achieving the appropriate conditions has taken decades of research [3]. The processes competing with diamond growth are spontaneous graphitization of the diamond surface as well as nucleation and growth of graphitic deposits.

The most successful process for low-pressure growth of diamond has been chemical vapor deposition (CVD) from energetically activated hydrocarbon/hydrogen gas mixtures. CVD is a process whereby a thin solid film, by definition, is synthesized from the gaseous phase via a chemical reaction. The development of CVD in common with many technologies, has been closely linked to the practical needs of society. The oldest example of a material deposited by CVD is probably that of pyrolytic carbon, since as Ashfold et al. [4] pointed out, some prehistoric art was done on cave walls with soot condensed from the incomplete oxidation of firewood. A similar procedure formed the basis of one of the earliest patents and commercial exploitation of a CVD process, which was issued for the

preparation of carbon black as a pigment. The emerging electric lamp industry provided the next major application of CVD with a patent issued for improvements to fragile carbon filaments [4]. Since these improved filaments were far from robust, the future for a pyrolytic carbon CVD industry was limited and a few years later, processes for the deposition of metals to improve the quality of lamp filaments were described [5]. From the turn of the century through to the late 1930s a variety of techniques appeared for the preparation of refractory metals for a number of applications. It was also during this period that silicon was first deposited by hydrogen reduction of silicon tetrachloride [5] and the use of that material for electronic applications was foreseen by the development of silicon-based photo cells [6] in 1946 as well as rectifiers [7]. The preparation of high-purity metals, various coatings, and electronic materials has developed significantly in the last 45 years or so, but it is undoubtedly the demands and requirements of the semiconductor and microelectronic industries that have been the main driving force in the development of CVD techniques as well as the greater efforts for understanding the basics of CVD processes. Consequently, a large body of literature and reviews now exists on CVD.

Indeed, it was the chemical vapor deposition from carbon-containing gases that enabled W.G. Eversole, referred to in reference [8], at the Union Carbide Corporation to be the first to grow diamond successfully at low pressures in 1952, after which conclusive proof and repetition of the experiments took place. In the initial experiments, carbon monoxide was used as a source gas to precipitate diamond on a diamond seed crystal. However, in subsequent experiments, methane and other carbon-containing gases were used as well as a cyclic growth etches procedure to remove co-deposited graphite. In all of his studies, it was necessary to use diamond seeds in order to initiate diamond growth. The deposits were identified as diamond by density measurements, chemical analysis, and diffraction techniques. The synthesis by Eversole preceded the successful diamond synthesis at high pressure by workers at the General Electric Company [1], which was accomplished in 1954. However, the important difference was that Eversole grew diamond on pre-existing diamond nuclei whereas the General Electric syntheses did not initiate growth on diamond seed crystals. Deryagin [9,10] in the

former Soviet Union began work on low-pressure diamond synthesis in 1956, in which many approaches were taken, which started with the growth of diamond whiskers by a metal-catalyzed vapor-liquid-solid process. Subsequently, epitaxial growth from hydrocarbons and hydrocarbon/hydrogen mixtures was investigated as well as different forms of vapor transport reactions. In addition, theoretical investigations of the relative nucleation rates of diamond and graphite were also performed. Angus and co-workers at Case Western Reserve University concentrated primarily on diamond CVD on diamond seed crystals from hydrocarbons and hydrocarbon/hydrogen mixtures [11,12]. They grew *p*-type semiconducting diamond from methane/diborane gas mixtures and studied the rates of diamond and graphite growth in methane/hydrogen gas mixtures and ethylene. They were the first to report on the preferential etching of graphite compared to diamond by atomic hydrogen and noted that boron had an unusual catalytic effect on metastable diamond growth.

The role of hydrogen in permitting metastable diamond growth was also recognised by some early workers. The low energy electron diffraction (LEED) study of Lander and Morrison [13,14] showed that a {111}-diamond surface saturated with hydrogen gave an unreconstructed (1×1) LEED pattern. The unsatisfied dangling bonds normal to the surface are terminated with hydrogen atoms, which maintain the bulk terminated diamond lattice to the outermost surface layer of carbon atoms. When hydrogen is absent, the surface reconstructs into more complex structures. They also showed that carbon atoms are very mobile on the diamond surface at temperatures above 1200 K and stated that these conditions should permit epitaxial growth. Other work [15,16] suggested that the presence of hydrogen enhanced diamond growth. Chauhan et al. [17,18] as well as Deryagin et al. [19] showed that addition of hydrogen to the hydrocarbon gas-phase suppressed the growth-rate of graphite relative to diamond thus resulting in higher diamond yields. Eventually, however, graphitic carbons nucleated on the surface and suppressed further diamond growth. It was then necessary to remove the graphitic deposits preferentially with atomic hydrogen [20] or oxygen [21], and to repeat the sequence. By the mid-1970s diamond growth at low pressures had been achieved by several groups. The beneficial role of hydrogen was known to some extent and growth rates of 0.1

$\mu\text{m hr}^{-1}$ had been achieved. Although the growth-rates were too low to be of any commercial importance, the results provided the experimental foundation for much of the work that followed.

7.3.2 Modern Era of Metastable Diamond Growth

Japanese researchers associated with the National Institute for Research in Inorganic Materials (NIRIM) made the first disclosures of methods for rapid diamond growth at low pressures. Research on metastable diamond growth was initiated at NIRIM in 1974. In 1982, they described techniques for synthesizing diamond at rates of several microns per hour from gases decomposed by a hot filament as well as microwave or DC discharges [22-25]. These processes produced individual faceted crystals without the use of a diamond seed crystal. The current worldwide interest in new diamond technology can in fact be directly traced to the NIRIM effort. Although Deryagin, as reported in reference [26], had reported high rate diamond growth earlier, process details were not disclosed [26]. All of the techniques are based on the generation of atomic hydrogen in the vicinity of the growth surface during deposition. Although the chemical vapor deposition of diamond from hydrogen rich/hydrocarbon-containing gases has been the most successful method of diamond synthesis, numerous other methods have been attempted with varying degrees of success, with ion beam methods being the most successful [27]. In 1971 hard carbon films were first deposited using a beam of carbon ions. As the films had many of the properties of diamond, they were called diamond-like carbon because definitive diffraction identification was not possible. In 1976, Spencer et al. [28] formed finely divided polycrystalline diamond using a beam of carbon ions with energies between 50 and 100 eV, and subsequently Freeman [29] grew diamond via ion implantation.

With further research and additional technological progress in improving and devising new methods for synthesis and fabrication, it becomes increasingly likely that new applications will be discovered. In order to be able to take full advantage of the unique characteristics of diamond as a material for the construction of solid-state devices, basic scientific understanding of the various experimental process techniques and in particular the introduction and activation

of dopants must be obtained. Attention also needs to be paid to proper design of devices incorporating novel features utilizing concepts and practices established in silicon and gallium arsenide device technology. The potential of diamond as a material for solid-state devices has been the subject of a few reviews [30-36] that have discussed the electronic material parameters of diamond and the simulated characteristics that can be obtained. Simple devices incorporating diamond have been demonstrated primarily incorporating natural or HPHT diamond. Photodetectors, light-emitting diodes, nuclear radiation detectors, thermistors, varistors, and negative resistance devices in synthetic crystals have been demonstrated. Several groups [37-41] have also demonstrated basic field effect transistor device operation in epitaxial diamond films and boron-doped layers on single crystal diamond substrates. However, for wide application of diamond solid-state devices, high-quality films on more commonly available substrates are essential as well as studies on the device potential of polycrystalline films. So far only thermistors [42] and Schottky diodes [43] have been produced and characterized in the polycrystalline material. This is due to material problems, in that the polycrystalline nature of the films results in grain boundaries, twins, stacking faults, and other defects, which have restricted exploitation in the electronic industries. To date there has been no confirmed observations of a means of achieving heteroepitaxy, that is, single-crystal diamond grown on a non-diamond substrate, and therefore no means of achieving diamond devices for practical applications. Indeed, achieving heteroepitaxy stands as the single most prominent technological hurdle for diamond-based electronics. However, CVD synthesis is a very active area that is improving with experience. In the near future, *in situ* probes may be used to optimize various diamond CVD processes by providing a maximization of the flow of diamond precursors to the surface while simultaneously minimizing the competing deposition of non-diamond carbon forms. The wide variety of means by which diamond is being routinely formed as a film will enhance its deployment and the potential for active electronic exploitation. Indeed, diamond coatings in general are expected to make so large an impact in the future that many people believe that the future age will be known as the diamond age,

going chronologically from the stone age, bronze age, to the iron age of the past and the silicon age of the present.

7.4 CVD Diamond Technology

The reactor system (comprising the reaction chamber and all associated equipment) for carrying out CVD processes must provide several basic functions common to all type of systems (Fig. 7.1). It must allow transport of the reactant and diluents gases to the reaction site, provide activation energy to the reactants (heat, radiation, plasma), maintain a specific system pressure and temperature, allow the chemical processes for film deposition to proceed optimally, and remove the by-product gases and vapors. These functions must be implemented with adequate control, maximal effectiveness, and complete safety.

Chemical vapor deposition is a crystal growth process used not only for diamond but also for a range of different semiconductor and other crystalline materials such as silicon or gallium arsenide. These industrial fields are diverse and range from gas turbines to gas cookers and from coinage to nuclear power plants.

The CVD process relies first on the generation of a species that is produced by the reaction of the element that is to be deposited with another element that results in the substantial increase in the depositing elements vapor pressure. Second, this volatile species is then passed over or allowed to come into contact with the substrate being coated. This substrate is held at an elevated temperature, typically from 800 - 1150°C. Finally, the deposition reaction usually occurs in the presence of a reducing atmosphere, such as hydrogen. The film properties can be controlled and modified by varying the problem parameters associated with the substrate, the reactor, and gas composition.

7.5 CVD Diamond Processes

Several different approaches to the deposition of diamond have been investigated and these include the ones described in the following sections.

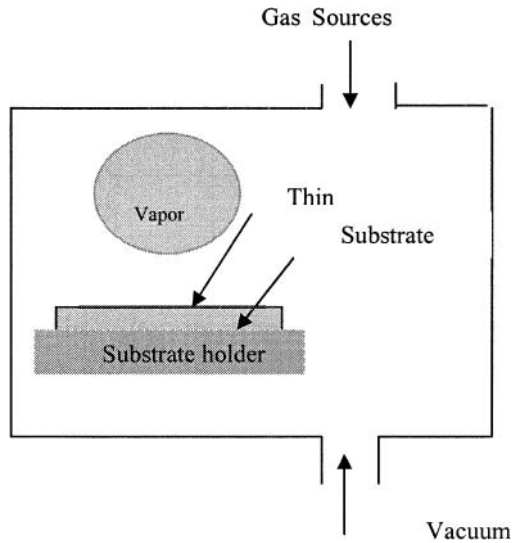


Fig. 7.1. A simple schematic of a vapor deposition process

7.5.1 Plasma-Enhanced CVD

Plasmas generated by various forms of electrical discharges or induction heating have been employed in the growth of diamond. The role of the plasma is to generate atomic hydrogen and to produce the necessary carbon precursors for diamond growth. The efficiencies of the different plasma processes vary from method to method. Three plasma frequency regimes will be discussed. These are microwave plasma CVD, which typically uses excitation frequencies of 2.45 GHz; Radio-frequency (RF) plasma excitation, which employs frequencies of usually 13.56 MHz, and direct-current (DC) plasmas,

which can be run at low electric powers (a “cold” plasma) or at high electric powers (which create an *arc* or a *thermal* plasma).

RF Plasma-Enhanced CVD

Generally, radio-frequency power can be applied to create plasma in two electrode configurations, namely, in an inductively coupled or a capacitively coupled parallel plate arrangement. A number of workers have reported the growth of diamond crystals and thin films using inductively coupled RF plasma methods [21-24] as well as capacitively coupled methods [25-26]. A high power in the discharge leading to greater electron densities was found to be necessary for efficient diamond growth. However, the use of higher power results in physical and chemical sputtering from the reactor walls, leading to contamination of the diamond films [21]. The advantage of RF plasmas is that they can easily be generated over much larger areas than microwave plasmas but the method is not routinely applied for the deposition of diamond films.

DC Plasma-Enhanced CVD

In this method, plasma in a H₂-hydrocarbon mixture is excited by applying a DC bias across two parallel plates, one of which is the substrate [27-29]. DC plasma-enhanced CVD has the advantage of being able to coat large areas as the diamond deposition area is limited by the electrodes and the DC power supply. In addition, the technique has the potential for very high growth rates. However, diamond films produced by DC plasmas were reported to be under high stress and to contain high concentrations of hydrogen as well as impurities resulting from plasma erosion of the electrodes.

Microwave Plasma-Enhanced CVD

Microwave-plasma assisted CVD has been used more extensively than any other method for the growth of diamond films [14-20]. Microwave plasmas are different from other plasmas in that the microwave frequency can oscillate electrons. Collision of electrons with gaseous atoms and molecules generates high ionization fractions. This method of diamond film growth has a number of distinct advantages over the other methods of diamond film growth. Micro-

wave deposition, being an electrodeless process, avoids contamination of the films due to electrode erosion. Furthermore, the microwave discharge at 2.45 GHz, being a higher frequency process than the RF discharges at typically 13.56 MHz, produces a higher plasma density with higher energy electrons, which effectively results in higher concentrations of atomic hydrogen and hydrocarbon radicals leading to efficient diamond growth. In addition, as the plasma is confined to the center of the deposition chamber as a ball, carbon deposition onto the walls of the chamber is prevented.

7.5.2 Hot Filament CVD (HFCVD)

In the early 1970s it was suggested that the simultaneous production of atomic hydrogen during hydrocarbon pyrolysis may enhance the deposition of diamond. Soviet researchers who generated H by dissociating H_2 using an electric discharge or a hot filament tested this suggestion [8]. It was observed that atomic hydrogen could easily be produced by the passage of H_2 over a refractory metal filament, such as tungsten, heated to temperatures between 2000 and 2500 K. When atomic hydrogen was added to the hydrocarbon typically with a C/H ratio of ~ 0.01 , it was observed that diamond could be deposited while graphite formation was suppressed. The generation of atomic hydrogen during diamond CVD enabled (a) a dramatic increase in the diamond deposition rate to approximately $1 \mu\text{m hr}^{-1}$ and (b) the nucleation and growth of diamond on non-diamond substrates [8-13]. Because of its inherent simplicity and comparatively low operating cost, HFCVD has become very popular in industry. Table 7.2 outlines typical deposition parameters used in the growth of diamond films by this technique.

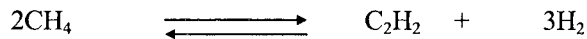
A wide variety of refractory materials have been used as filaments including tungsten, tantalum, and rhenium due to their high electron emissivity. Refractory metals, which form carbides (*e.g.*, tungsten and tantalum) typically must carburize their surface before supporting the deposition of diamond films. The process of filament carburization results in the consumption of carbon from the CH_4 , and thus a specific incubation time is needed for the nucleation of diamond films. Therefore, this process may affect the early stages of film growth, although it is insignificant over longer periods. Fur-

thermore, the volume expansion due to carbon incorporation leads to cracks along the length of the wire. The development of these cracks is undesirable, as it reduces the lifetime of the filament.

Table 7.2. Typical deposition parameters used in the growth of diamond films by HFCVD

Gas mixture	Total pressure (Torr)	Substrate tem- perature (K)	Filament tem- perature (K)
CH ₄ (0.5 - 2.0%)/H ₂	10 - 50	1000 - 1400	2200 - 2500

It is believed that thermodynamic near-equilibrium is established in the gas phase at the filament surface. At temperatures around 2300 K, molecular hydrogen dissociates into atomic hydrogen and methane transforms into methyl radicals, acetylene species, and other hydrocarbons stable at these elevated temperatures. Atomic hydrogen and the high-temperature hydrocarbons then diffuse from the filament to the substrate surface. Although the gaseous species generated at the filament are in equilibrium at the filament temperature, the species are at a super equilibrium concentration when they arrive at the much cooler substrate. The reactions that generate these high-temperature species (e.g., C₂H₂) at the surface of the filament or anywhere where there are hydrogen atoms, proceed faster than any reactions that decompose these species during the transit time from the filament to the substrate. Consider the equilibrium between methane and acetylene:



At the filament surface, the reaction is immediately driven to the right, creating acetylene. After acetylene diffuses to the substrate, thermodynamic equilibrium at a substrate temperature of ~1100 K calls for the formation of methane, but the reverse reaction proceeds much slower. Solid carbon precipitates on the substrate in order to reduce the superequilibrium concentration of species such as acetylene in the gas phase. The diamond allotrope of carbon is “stabi-

lised” by a concurrent super equilibrium concentration of atomic hydrogen. This simple explanation emphasizes the importance of reaction kinetics in diamond synthesis by HFCVD.

Advantages of the CVD Process

The process is gas phase in nature, and therefore given a uniform temperature within the coating retort and likewise uniform concentrations of the depositing species the deposition rate will be similar on all surfaces. Therefore, variable and complex shaped surfaces, given reasonable access to the coating powders or gases, such as screw threads, blind holes, or channels or recesses, can be coated evenly without build-up on edges.

Disadvantages of the CVD Process

The CVD process is carried out at relatively high temperatures and therefore limitations due to dimensional tolerances are an important consideration. Components that have tight dimensional tolerances will not be amenable to CVD. However, the reduction of distortion during coating can sometimes be controlled by careful stress relieving after rough machining of the component during fabrication.

7.6 Treatment of Substrate

7.6.1 Selection of Substrate Material

Deposition of adherent high-quality diamond films onto substrates such as cemented carbides, stainless steel, and various metal alloys containing transition element has proved to be problematic. In general, the adhesion of the diamond films to the substrates is poor and the nucleation density is very low [44-51]. Mainly refractory materials such as W (WC-Co), Mo, and Si have been used as substrate materials. Materials that form carbide, are found to support diamond growth. However, materials such as Fe and steel possess a high mu-

tual solubility with carbon, and only graphitic deposits or iron carbide result during CVD growth on these materials. For applications in which the substrate needs to remain attached to the CVD diamond film, it is necessary to choose a substrate that has a similar thermal expansion coefficient to that of diamond. If this is not done the stress caused by the different rates of contraction on cooling after deposition will cause the film to delaminate from the substrate. The influence of different metallic substrates on the diamond deposition process has been examined. Interactions between substrate materials and carbon species in the gas phase are found to be particularly important and lead to either carbide formation or carbon dissolution. Carbides are formed in the presence of carbon-containing gases on metals such as molybdenum, tungsten, niobium, hafnium, tantalum, and titanium. The carbide layer formed allows diamond to form on it since the minimum carbon surface concentration required for diamond nucleation cannot be reached on pure metals. As the carbide layer increases in thickness, the carbon transport rate to the substrate decreases until a critical level is reached where diamond is formed [52-58]. Substrates made from metals of the first transition group such as iron, cobalt, and nickel, are characterized by high dissolution and diffusion rates of carbon into those substrates (Table 7.3) [59]. Owing to the absence of a stable carbide layer, the incubation time required to form diamond is higher and depends on substrate thickness. In addition, these metals catalyze the formation of graphitic phases, which is reflected in the graphite-diamond ratio of during the deposition process, yielding a low diamond. The importance of this mechanism in relation to diamond deposition decreases from iron to nickel, corresponding to a gradual filling of the 3d-orbital [59]. This effect occurs whenever the metal atoms come into contact with the carbon species, which can take place on the substrate or in the gas phase [60].

7.6.2 Substrate Pre-Treatment

In order for continuous film growth to occur, a sufficient density of crystallites must be formed during the early stages of growth. In general, the substrate must undergo a nucleation enhancing pre-treatment to allow this.

Table 7.3. Solubility and diffusion rates of carbon atoms in different metals at 900°C

	α-Fe	γ-Fe	Co	Ni
Solubility of carbon (wt.%)	1.3	1.3	0.1	0.2
Carbon diffusion rate (cm/s)	2.35×10^{-6}	1.75×10^{-8}	2.46×10^{-8}	1.4×10^{-8}

This is particularly true for Si wafer substrates that have been specially polished to be smooth enough for micro-electronic applications. Substrates may be pre-treated by a variety of methods including:

- Abrasion with small (\sim nm/ μ m size) hard grits (e.g., diamond, silicon carbide).
- Ultrasonication of samples in slurry of hard grit (e.g., diamond).
- Chemical treatment (acid etching and Murakami agent)
- Bias enhanced nucleation (BEN) (negative/positive substrate biasing)
- Deposition of hydrocarbon/oil coatings

The basis for most of these methods is to produce scratches, which provide many sites for nucleation diamond of crystallites. It is also possible that small (\sim nm size) flakes of diamond, produced during abrasion with diamond grit, become embedded in the substrate, and that CVD diamond grows on this material [61].

It could be desirable to produce nucleation sites without damage to the underlying substrate. This is particularly important for some applications such as diamond electronics and optical components. One method for encouraging nucleation without damaging the substrate material has been developed: bias enhanced nucleation (BEN).

(a) Pre-Treatment on Mo/Si Substrate

Prior to pre-treatment Si/Mo substrate are ultrasonically cleaned in acetone for 10 minutes to remove any unwanted residue on the surface. Abrasion with 1 μm sizes of diamond powder is performed for 5 minutes. Alternatively, substrate was immersed in diamond solution containing 1-3 μm of diamond particles and water for 1 hr in ultrasonic bath. These methods produce scratches on the surface, which create many nucleation sites. The substrates are then washed with acetone in the ultrasonic bath for 10 minutes. SEM and energy-dispersive x-ray spectroscopy (EDX), characterized abraded surface of substrates.

(b) Pre-Treatment on WC-Co Substrate

The application of diamond coatings on cemented tungsten carbide (WC-Co) tools has attracted much attention in recent years in order to improve cutting performance and tool life. However, deposition of adherent high-quality diamond films onto substrates such as cemented carbides, stainless steel, and various metal alloys containing transition element has proved to be problematic. In general, the adhesion of the diamond films to the substrates is poor and the nucleation density is very low [44-50]. WC-Co tools contain 6% Co and 94% WC substrate with grain size 1-3 micron is desirable for diamond coatings.

In order to improve the adhesion between diamond and WC substrates it is necessary to etch away the surface Co and prepare the surface for subsequent diamond growth. In particular, the cobalt (Co) binder, which provides additional toughness to the tool but is hostile to the diamond adhesion. The adhesion strength to diamond films is relatively poor, and can lead to catastrophic failure of coating in metal cutting [59]. The Co binder can also suppress diamond growth, favoring the formation of non-diamond carbon phases resulting in poor adhesion between the diamond coating and the substrate [62]. Most importantly, it is difficult to deposit adherent diamond onto untreated WC-Co substrates. Figure 7.2 (a) shows sub-micron size Co crystals on diamond films that were deposited on an untreated substrate (without removal of surface Co). EDX spectra

show that trace amount of Co elements on the surface. It also appeared poor adhesion of diamond film and shows delaminated film on the surface (Fig. 7.2 (b)).

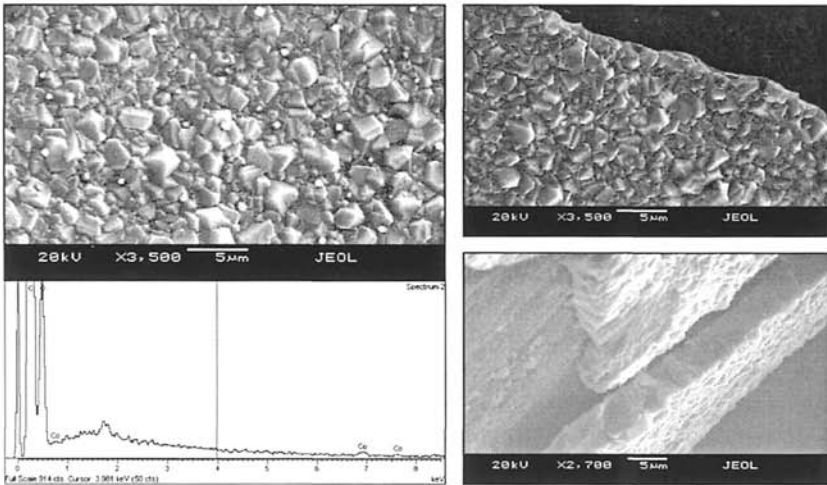


Fig. 7.2. (a) Co trace on diamond film, (b) delaminated diamond film

Poor adhesion can be related to the cobalt binder that is present to increase the toughness of the tool; however, it suppresses diamond nucleation and causes deterioration of diamond film adhesion. To eliminate this problem, it is usual to pre-treat the WC-Co surface prior to CVD diamond deposition. Various approaches have been used to suppress the influence of Co and to improve adhesion. Therefore, a substrate pre-treatment, for reducing the surface Co concentration and achieving a proper interface roughness, will enhance the surface readily available for coating process [62]. For example, chemical treatment using Murakami agent and acid etching has been used successfully for removal of the Co binder from the substrate surface [63].

The WC-Co substrates (Flat) used were 10 x 10 mm by 3 mm in thickness. The hard metal substrates used were WC-6wt% Co with WC average grain size of 0.5 μm (fine grain) and 6 μm (coarse

grain). Table 7.4 show that the data for substrate, which consist of the chemical composition, density, and hardness of samples, used for diamond deposition. Figure 7.3 (a) and (b) show that coarse and fine grain of etched WC-Co insert surface.

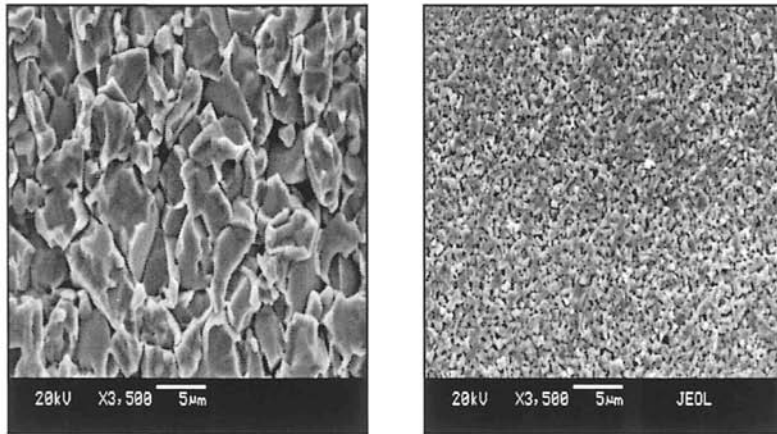


Fig. 7.3. (a) Etched coarse grain; (b) etched fine grain

The Co cemented tungsten carbide (WC-Co) rotary tools (micro-tools, microdrills), 20 mm in length including the bur head (WC-Co) & shaft (Fe/Cr) and ~1 mm in diameter, were also used. Prior to pre-treatment both set of substrates are ultrasonically cleaned in acetone for 10 mins to remove any loose residues. The following two-step chemical pre-treatment procedure is used. A first step etching, using Murakami's reagent [10 g $K_3Fe(CN)_6$ + 10 g KOH + 100 ml water] is carried out for 10 min in ultrasonic bath to etch WC substrate, followed by a rinse with distilled water. The second step etching is performed using an acid solution of hydrogen peroxide [3 ml (96% wt.) H_2SO_4 + 88 ml (30% w/v) H_2O_2], for 10 s, to remove Co from the surface. The substrates are then washed again with distilled water in an ultrasonic bath. After wet treatment the micro-tool is abraded with synthetic diamond powder (1 μ m grain size) for 5 mins and followed by ultrasonic treatment with acetone for 20 mins.

Etched surface of substrates can be characterised by SEM and energy-dispersive x-ray spectroscopy (EDX).

Table 7.4. WC-Co insert chemical composition

WC grain size (μm)	WC	Co	TaC	Density (g/cm^3)	Hardness (HRA)
WC fine grain 0.5 μm	94.2	5.8	0.2	14.92	93.40
WC coarse grain 6 μm	94.0	6.0		14.95	88.50

7.7 Modification of HFCVD Process

7.7.1 Modification of Filament Assembly

The filament material and its geometrical arrangement are important factors to consider in order to have improved coatings using the CVD method. Therefore, in order to optimize both the filament wire diameter and the filament assembly/geometry it is necessary to understand the temperature distributions of the filament. Research by the author indicated that the best thermal distribution and diamond growth uniformity is obtained using tantalum wires of 0.5 mm in diameter. To ensure uniform coating around the cylindrical shape samples (microdrills or micro-tools), tools were positioned centrally and coaxially within the coils of the filament, the six-spiral (coil) filament was made with 1.5 mm spacing between the coils (Fig. 7.4 a and b).

Tantalum wire of 0.5 mm in diameter and 12-14 cm in length is used as the hot filament. The filament is mounted vertically with the micro-tool held in between the filament coils, as opposed to the horizontal position used in the conventional HFCVD system. To ensure uniform coating the micro-tool is positioned centrally and coaxially within the coils of the filament. A schematic diagram of the modified HFCVD system is presented in Fig. 7.5 and has been de-

signed for microdrill or wire or micro-tool with similar diameter. The new vertical filament arrangement used in the modified HFCVD system enhances the thermal distribution, ensuring uniform coating, increased growth rates, and higher nucleation densities.

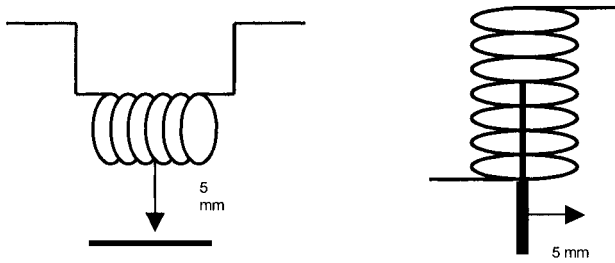


Fig. 7.4. (a) Conventional filament arrangement, (b) modified filament arrangement.

7.7.2 Process Conditions

The CVD reactor is a cylindrical stainless steel chamber measuring 20 cm in diameter and 30 cm in length. Diamond films were deposited onto the cutting edge of the tools at 5 mm distances from the filament. The gas source used during the deposition process is composed of a mixture containing 1% methane with an excess of hydrogen; the volume flow rate for hydrogen is 100 sccm, while the volume flow rate for methane is 1 sccm. The deposition time and pressure in the vacuum chamber were 5-15 hours and 20 Torr (2.66 k Pa) employed. The substrate temperature was measured by a K-type thermocouple mounted on a molybdenum substrate holder. The depositions are carried out between 800 and 1000°C. The filament temperature is measured using an optical pyrometer and found to be between 1800 and 2100°C depending upon the filament position. A summary of the process conditions is shown in Table 7.5.

7.8 Nucleation and Growth

The growth of diamond thin films at low pressures, at which diamond is metastable, is one of the most exciting developments in materials science of the last two decades. However, low growth rates and poor quality currently limit applications. Diamond growth is achieved by a variety of processes using very different means of gas activation and transport. Generalized models coupled with experiments show how process variables, such as gas activation temperature, pressure, characteristic diffusion length, and source gas composition, influence diamond growth rates and diamond quality. The modeling is sufficiently general to permit comparison between growth methods. The models indicate that typical processes, e.g., hot-filament, microwave and thermal plasma reactors, operate at pressures where concentrations of atomic hydrogen, $[H]$, and methyl radicals, $[CH_3]$, reach maxima. The results strongly suggest that the growth rate maxima with pressure arise from changes in the gas phase concentrations rather than changes in substrate temperature.

Table 7.5. Process conditions used for diamond film deposition on micro-tools

Process variables	Operating parameters
Tantalum filament diameter (mm)	0.5
Deposition time (hours)	5-15
Gas mixture	1% CH_4 in excess H_2
Gas pressure (Torr)	20 (2.66 k Pa)
Substrate temperature ($^{\circ}C$)	800-1000
Filament temperature ($^{\circ}C$)	1800-2100
Substrate (WC-Co/Mo/Ti) diameter (mm)	Wire/drill/micro-tool (approx. 1 mm)
Distance between filament and substrate (mm)	5
Pre-treatment (Murakami etching and acid etching)	20 minutes plus 10 seconds

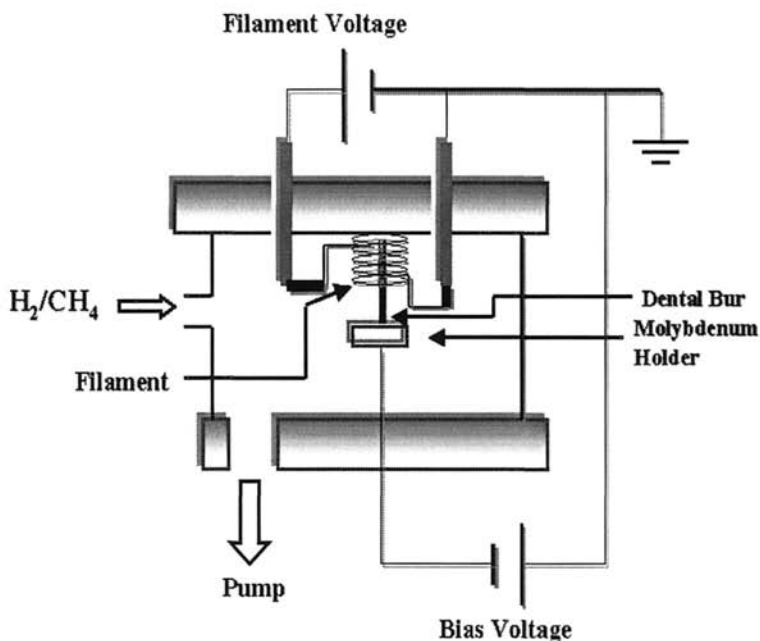


Fig. 7.5. Schematic diagram of HFCVD apparatus.

The results also suggest that, at 1 atmosphere pressure using only hydrocarbon chemistry, growth rates saturate at gas activation temperatures above 4000 K. Models of defect incorporation indicate that the amount of sp^2 , non-diamond material incorporated in the diamond is proportional to $[CH_3]/[H]$ and therefore can be correlated with the controllable process parameters. The unusual and interesting connection between diamond nucleation and growth with the process of the vapor synthesis of diamond is essentially quite simple. Carbon containing precursor molecules (like CH_4) are excited and/or dissociated and subsequently condensing via a free dangling bond of the radical in diamond configuration on a surface [64-65] (Fig. 7.6).

A nucleation pathway occurs through a stepwise process including the formation of extrinsic (pre-treatment) or intrinsic (in situ) nucleation sites, followed by formation of carbon-based precursors. It is believed that nucleation sites could be either grooves of scratching lines or protrusions produced by etching-re-deposition.

The gas activation is done either by hot filaments, microwave, or radio frequency plasmas. The most crucial parameter in all this processes is besides a carbon source the presence of large amounts of atomic hydrogen. The role of atomic hydrogen in the process is:

- Creation of active growth sites on the surface
- Creation of reactive growth species in the gas-phase
- Etching of non-diamond carbon (like graphite) graphitic, sp^2 , precursors will be explored.

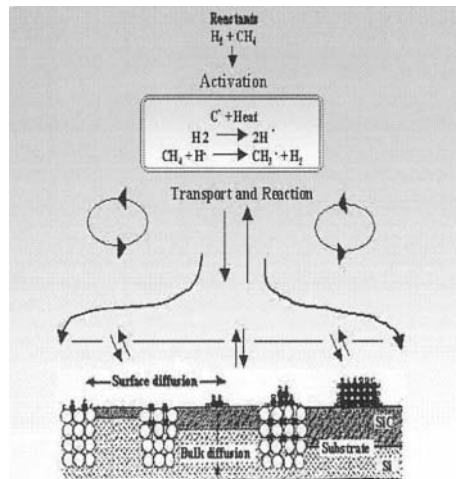


Fig. 7.6. Schematic diagram of diamond nucleation and growth

7.8.1 Nucleation Stage

Nucleation of diamond is a critical and necessary step in the growth of diamond thin films, because it strongly influences diamond growth, film quality and morphology [66]. Growth of diamond begins when individual carbon atoms nucleate onto the surface to initiate the beginnings of an sp^3 tetrahedral lattice. There are two types of diamond growth:

Homo-epitaxial growth: It is an application of diamond substrates, the template for the required tetrahedral structure is already there, and the diamond lattice is just extended atom-by-atom as deposition proceeds.

Hetero-epitaxial growth: It uses the non-diamond substrates, there is no such template for the C atoms to follow, and those C atoms that deposit in non-diamond forms are immediately etched back to the gas phase by reaction with atomic [H].

To deal with the problem of the initial induction period before which diamond starts to grow, the substrate surface often undergoes pre-treatment prior to deposition in order to reduce the induction time for nucleation and to increase the density of nucleation sites. There are two main methods to apply this pre-treatment:

Generally, seeding or manual abrading with diamond powder or immersing in diamond paste containing small crystallites processed in an ultrasonic bath enhances nucleation. The major consideration is the nucleation mechanism of diamond on non-diamond substrates. It has been shown that the pre-abrasion of non-diamond substrates reduces the induction time for nucleation by increasing the density of nucleation sites. The abrasion process can be carried out by mechanically polishing the substrate with abrasive grit, usually diamond power of 0.1-10 μm particle size, although other nucleation methods do exist such as bias-enhanced nucleation which is used in heteroepitaxial growth. The most promising in-situ method for diamond nucleation enhancement is substrate biasing. In recent years, more controlled techniques, such as bias-enhanced nucleation and nano-particle seeding, have been used to deposit smoother films [67-68]. In this method, the substrate is biased negatively during the initial stage of deposition [69]. Before CVD diamond deposition the filament was pre-carburised for 30 minutes in 3% methane with ex-

cess hydrogen to enhance the formation of tantalum carbide layer on the filament surface in order to reduce the tantalum evaporation during diamond deposition [70].

7.8.2 Bias-Enhanced Nucleation (BEN)

The substrate can be biased both negatively and positively; however, there is much research work and a large volume of literature on negative biasing. Negative substrate biasing is attractive because it can be controlled precisely; it is carried out in-situ, gives good homogeneity, and results in improved adhesion. On flat substrates, such as copper and silicon, biasing has been shown to give better adhesion, improved crystallinity and smooth surfaces.

A negative bias voltage up to -300 V has been applied to the substrate relative to the filament. This produced emission currents up to 200 mA. The nucleation times used were between 10 and 30 minutes. In the activated deposition chamber CH_4 and H_2 were decomposed into various chemical radicals species CH_3 , C_2H_2 , CH_2 , CH , C and atomic hydrogen H by the hot tantalum filament. The methyl radicals and atomic hydrogen are known to play important roles in diamond growth. In the biasing process electrons were emitted from the diamond-coated molybdenum substrate holder and moved to the filament after they gained energy from the electrical field. When the negative bias was applied to the anode the voltage was gradually increased until a stable emission current was established and a luminous glow discharge was formed near the substrate [71]. The nucleation density of diamond has been calculated from the SEM micrographs. Figure 7.7 (a) and (b) shows the effects of bias time on the nucleation density at bias voltage of -300 V. As bias time is increased the nucleation density also increases. The highest nucleation density was calculated to be $0.9 \times 10^{10} \text{ cm}^{-2}$ for a bias time of 30 minutes. At a bias time of 10 minutes the nucleation density obtained was $2.7 \times 10^8 \text{ cm}^{-2}$.

Wang et al. [72] also reported that an increase in the emission current produced higher nucleation densities [73]. Since the bias voltage and emission current are related, the enhancement of the nucleation density cannot be attributed to solely ion bombardment or electron emission of the diamond-coated molybdenum substrate

holder, but may be a combination of these mechanisms [74]. Results were based on negatively bias enhanced nucleation related to the grounded filament. However, it was reported that very low electric biasing current values (μA) were detected for applied substrate biases voltages either positive or negative. Furthermore, when increasing negative biases of up to -200 V resulted in a value of nucleation density similar to that obtained with positively bias enhanced nucleation related to the filament. In contrast, an application of negative bias applied to the substrate at -250 V resulted in (10^{10} cm^{-2}) maximum values of nucleation density. The enhancement in the nucleation density can be attributed to the electron current from the filament by increasing the decomposition of H_2 and CH_4 . The increase in the nucleation density is expected since negatively biasing the substrate increases the rate of ion bombardment into the surface creating greater numbers and density of nucleation sites. Therefore, the greater the density of nucleation sites the higher the nucleation density. Kamiya et al. reported that reproducibility of the experiment was poor and that no definite trend in the nucleation density could be found with respect to different bias conditions [74].

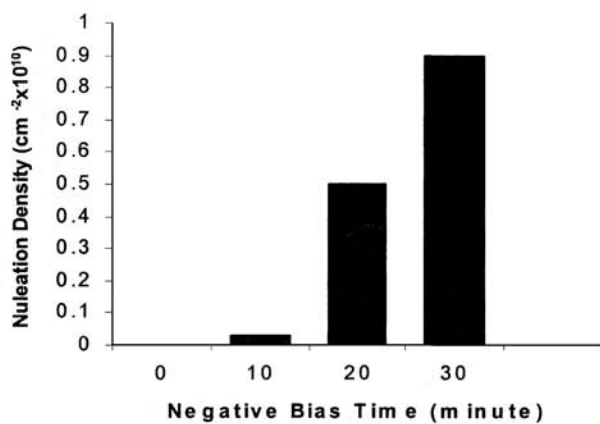
7.8.3 Influence of Temperature

The temperature is a major factor in influencing the deposition rate, crystallite size, and controlling the surface roughness. Variation in the average crystallite size of diamond along the length of the substrate (micro-tool) can be attributed to the variation in the variation in the substrate temperature. The substrate temperature from the end to the center of the filament is more accentuated for molybdenum wire with a smaller diameter [9]. Figure 7.8 demonstrates the ability of this CVD process to coat 3-D shaped components, illustrating that the process is in the kinetic control regime rather than transport control regime. Most physical vapor deposition type of processes operates at conditions where the rate-determining step of the deposition process is the diffusion of precursor gases to the substrate surface. Generally, this results in poor film uniformity in grooves and at the sharp edges. By operating under kinetic control regime film uniformity is much enhanced.

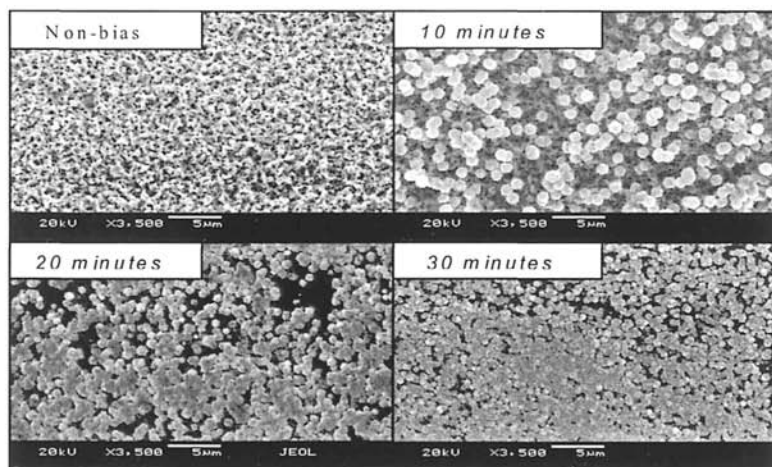
Deposition temperature can also influence the diamond film thickness in terms of substrate and filament position. Analysis of temperature distribution along the coiled filament showed that the temperature is highest at the center of the filament with a rapid decrease toward the edges (Fig. 7.8). This suggests that position A is the hottest followed by position B and C on the bur. Generally, higher substrate temperatures increase diamond film growth rate and the crystallite size. At the bottom of the filament coil temperature is lower; therefore, the part of the bur parallel to the coil at this temperature will be coated with the diamond film at a lower growth rate. Therefore, it can be expected that at these regions the film will be thinner. The thermal gradient gives variations in the film thickness and crystal sizes as evident from figure. Generally, with columnar growth, the average crystallite size increases as the films become thicker. The films were thicker and the crystallite size was larger at position A compared to position C.

Analysis of temperature distribution along the coiled filament showed that the temperature is highest at the center of the filament with a rapid decrease toward the edges. The bur substrate and filament temperature have been measured parallel to the positions A, B, and C respectively (Fig. 7.9). This suggests that position A is the hottest followed by position B and C on the bur. Variations in the film thickness and crystal sizes are mainly due to thermal gradients at various positions on the bur.

Figure 7.10 indicates that the coated micro-tool was cut in order to study the cross section of the tool. It was found that the coating is thicker at the cutting teeth with average thickness of about 43 μm due to the slightly higher temperature at the bur tip because cutting teeth is closer to the filament coil. At the base of the bur the heat is carried away faster and therefore it is at a lower temperature giving rise to lower growth rates and hence thinner films, at about 23 μm in thickness. Thicker coating at the tip is expected to give the tool longer life. Further work is required to study the effects of film thickness at the tooth tip and at the base on tool performance and lifetime.



(a)



(b)

Fig. 7.7. (a) nucleation density of diamond by BEN; (b) SEM of nucleation density on substrate

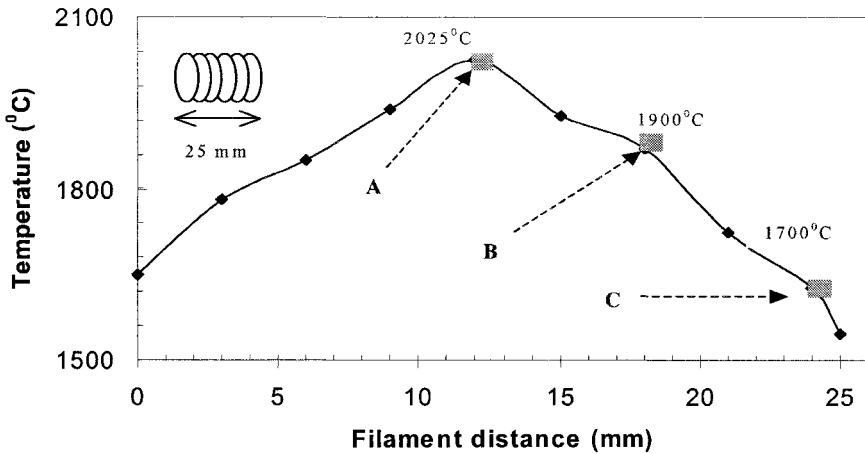


Fig. 7.8. Deposition temperature against filament position

Deposition temperature can also influence the diamond film thickness in terms of substrate and filament position. Analysis of temperature distribution along the coiled filament showed that the temperature is highest at the center of the filament with a rapid decrease toward the edges (Fig. 7.8). This suggests that position A is the hottest followed by position B and C on the bur. Generally, higher substrate temperatures increase diamond film growth rate and the crystallite size. At the bottom of the filament coil temperature is lower; therefore, the part of the bur parallel to the coil at this temperature will be coated with the diamond film at a lower growth rate. Therefore, it can be expected that at these regions the film will be thinner. The thermal gradient gives variations in the film thickness and crystal sizes as evident from figure. Generally, with columnar growth, the average crystallite size increases as the films become thicker. The films were thicker and the crystallite size was larger at position A compared to position C.

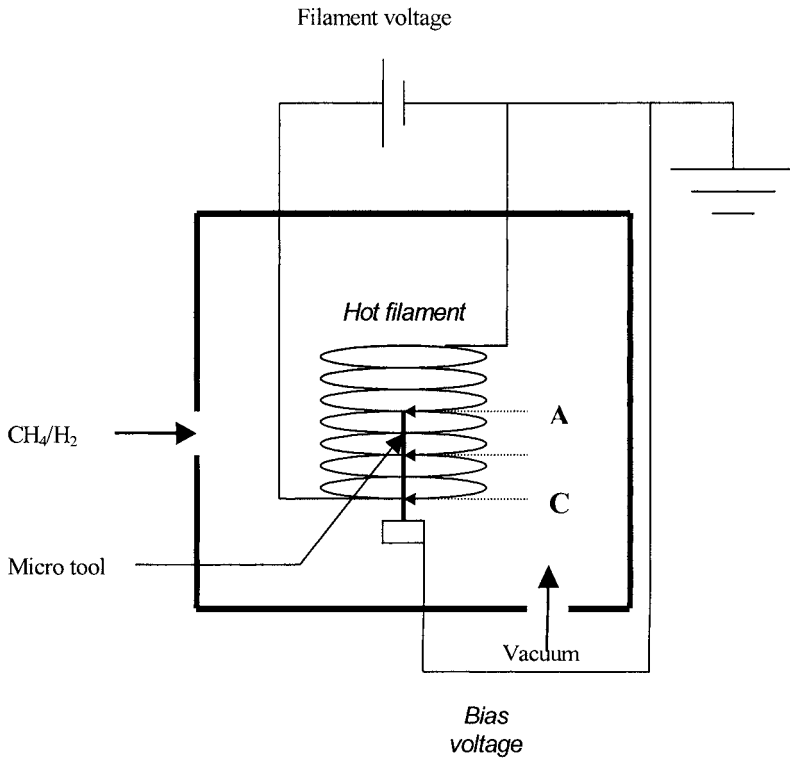


Fig. 7.9. Schematic diagram of a micro-tool assembled with filament

Analysis of temperature distribution along the coiled filament showed that the temperature is highest at the center of the filament with a rapid decrease toward the edges. The bur substrate and filament temperature have been measured parallel to the positions A, B, and C respectively (Fig. 7.9). This suggests that position A is the hottest followed by position B and C on the bur. Variations in the film thickness and crystal sizes are mainly due to thermal gradients at various positions on the bur.

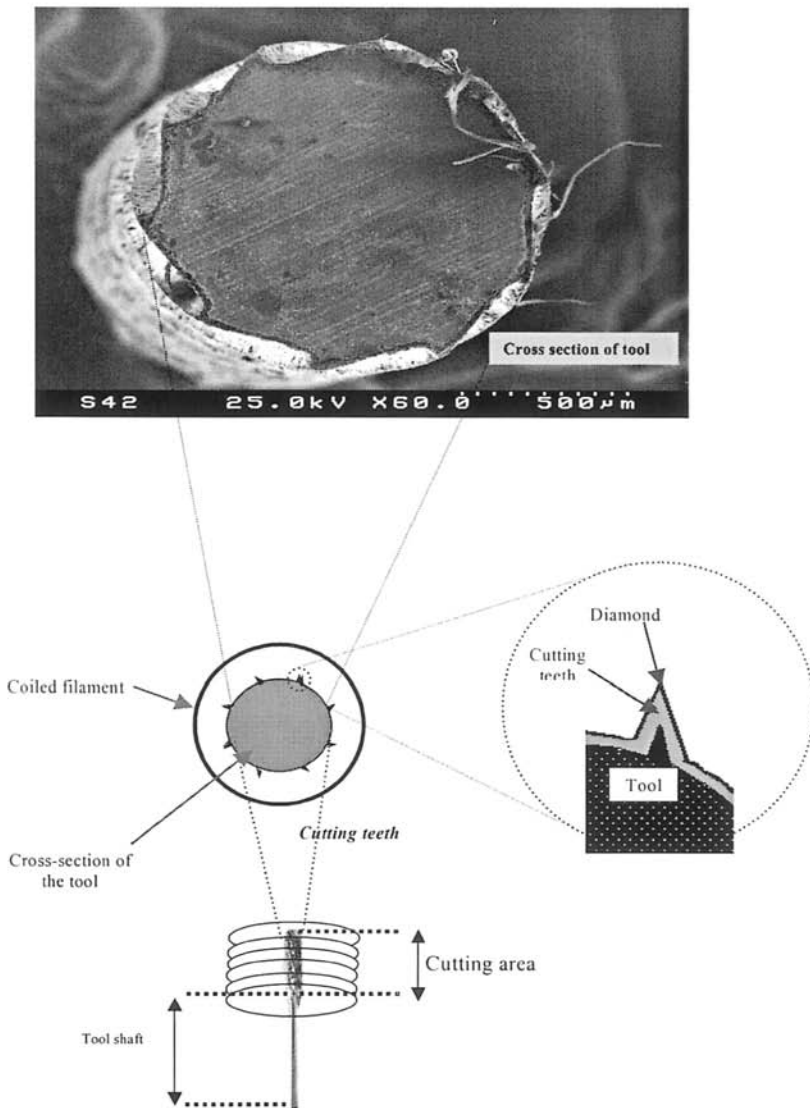
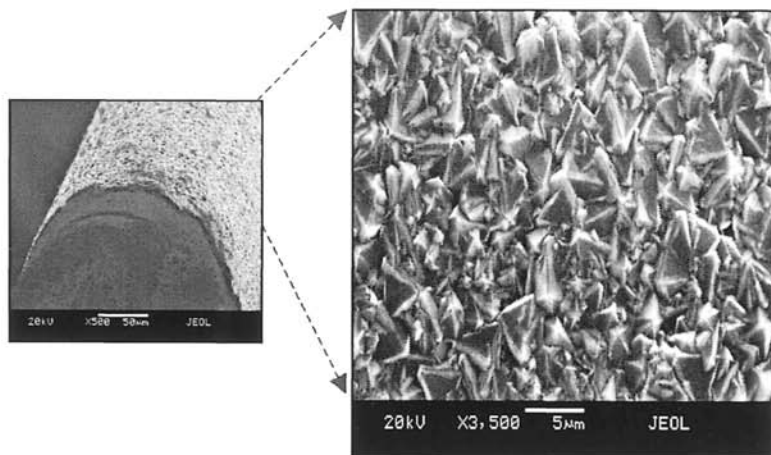


Fig. 7.10. Schematic diagram of micro-tool cutting edges

7.9 Deposition on Three-Dimensional Substrates

7.9.1 Diamond Deposition on Metallic (Molybdenum) Wire

It is difficult to deposit CVD diamond onto cutting tools, which generally have a 3-D shape and possess complex geometry and sharp edges, using a single step growth process [76]. The cylindrical shape wire, which has complex geometry, can be used as a model application for deposition of diamond on cutting tools such as microdrills and micro-tools. The molybdenum (Mo) wires are deposited with CVD diamond by modified vertical filament approach. After deposition time of 5 hours is continuous films of 5 μm thick CVD diamond were obtained (Fig. 7.11). The film morphology showed that it has good uniformity and high purity of diamond. The Raman spectroscopy confirmed that sp^3 diamond peak at wave number 1332.6 cm^{-1} as shown on Fig. 7.12.



Uniform growth of (111) faceted octahedral diamond film on

Fig. 7.11. Diamond film on molybdenum

7.9.2 Deposition on WC-Co Micro-Drill

Deposition of diamond on wires can be readily extended to microdrill used for machining tool, NEMS, and MEMS devices. The uniform and adherent coating are essential in order to obtain an improved performance. Figure 7.13 (a) shows an SEM micrograph of an uncoated microdrill. The WC-Co cutting edges are welded onto the steel shaft (Fe-Cr). The cutting tip is 4 mm in length and 0.8 mm in diameter. The microdrill has six sharp cutting edges, which is clearly visible in Fig. 7.13 (b).

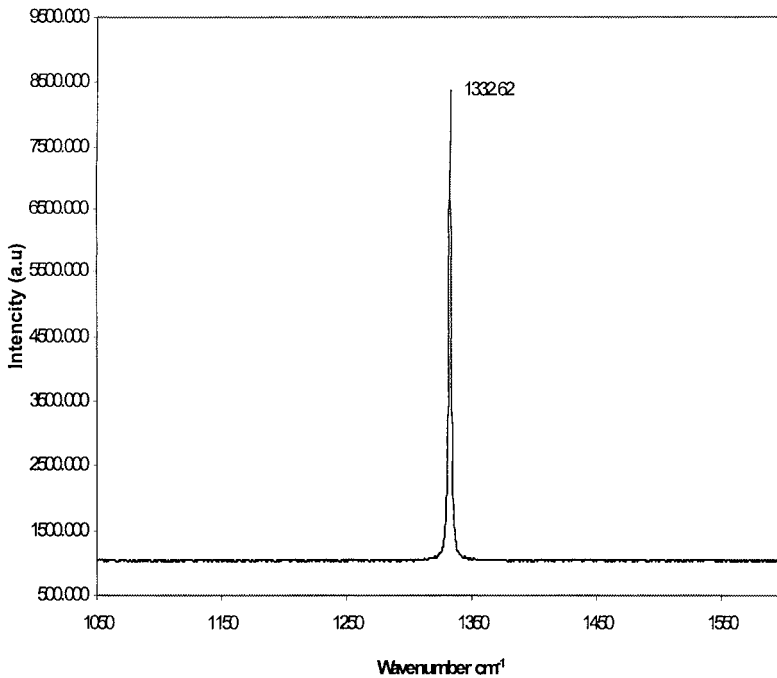


Fig. 7.12. Raman spectra of CVD diamond on molybdenum wire

Figure 7.14 shows the SEM micrographs and the corresponding EDX spectra of the WC-Co microdrill before and after the chemical etching process. Before etching, the EDS spectrum (Figure 7.14 (a)) show the peaks for cobalt (Co), carbon (C), and tungsten (W). High cobalt content inhibits diamond deposition, resulting generally in graphitic phases, which degrade the coating adhesion. The Co diffuses to the surface regions, preventing effective bonding between the substrate surface and the film coating. To improve the coating adhesion of diamond on WC-Co tools, several approaches can be employed. For example, first, the use of interlayer material such as chromium can act as a barrier against cobalt diffusion during diamond CVD. Second, the cobalt from the tool surface can be etched using either chemical or plasma methods. Third, the cobalt can be converted into stable intermediate interlayer cobalt compounds. These can act as a barrier to cobalt diffusion from the substrate during film growth [77]. Murakami solution followed by $\text{H}_2\text{SO}_4/\text{H}_2\text{O}_2$ etch can be used to chemically remove the cobalt from the bur surface. The EDX spectrum shows that the Co peak has disappeared after etching. This will prove to be beneficial in enhancing the coating adhesion. Comparison of the SEM micrograph in Figs. 7.14 (a) and (b) shows that the surface topography is significantly altered after etching in Murakami and $\text{H}_2\text{SO}_4/\text{H}_2\text{O}_2$ solutions. The etching process makes the surface much rougher with a significant amount of etch pits, which act as low-energy nucleation sites for diamond crystal growth.

An SEM micrograph of a diamond-coated WC microdrill is shown in Fig. 7.15. Six cutting edges of the microdrill tip were coated with a polycrystalline diamond film using the modified vertical HFCVD method. Analysis of the SEM picture shows that the coating uniformly covered the cutting edges as well as the nearby regions in which the placement of the microdrill within the coils of the filament, ensuring uniform deposition. The diamond crystal structure and morphology are uniform and adherent, as shown in Figs. 7.15 (a) and (b). It is also shows a close-up view of the diamond-coated region of the microdrill in Fig. 7.15 (c).

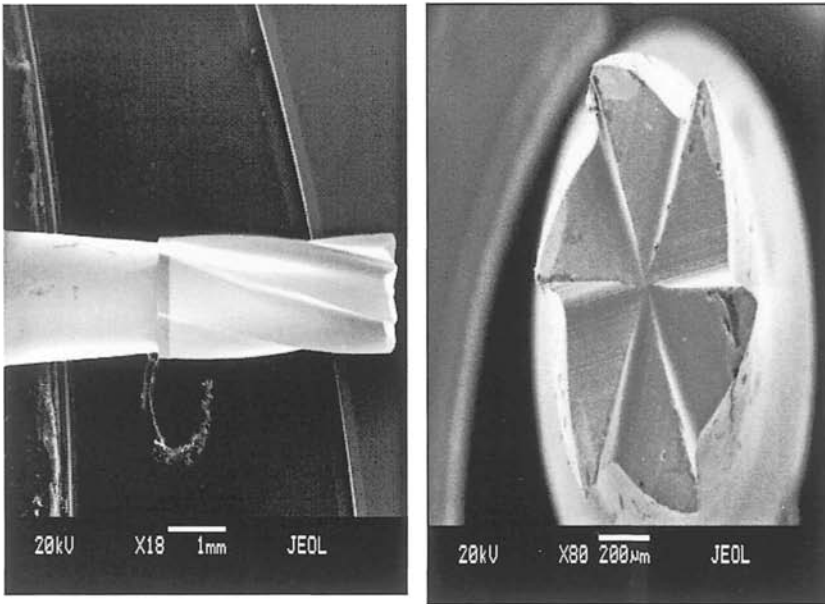


Fig. 7.13. Tip and cutting edge of micro-drill

Typically the crystallite sizes are of the order of 5–8 μm . The visibly adherent diamond coatings on the WC-Co microdrills consist of mainly (111) faceted diamond crystals. The design of the filament and substrate in the reactor offer the possibility of uniformly coating even larger diameter cylindrical substrates.

Raman analysis was performed in order to evaluate the diamond carbon-phase quality and film stress in the deposited films. The Raman spectrum in Fig. 7.16 shows a single peak at 1335 cm^{-1} for the tip of the diamond-coated microdrill. The Raman spectrum also gives information about the stress in the diamond coatings. The diamond peak is shifted to a higher wave number of 1335 cm^{-1} than that of natural diamond peak 1332 cm^{-1} indicating that stress, which is compressive in nature, exists in the resultant coatings [78].

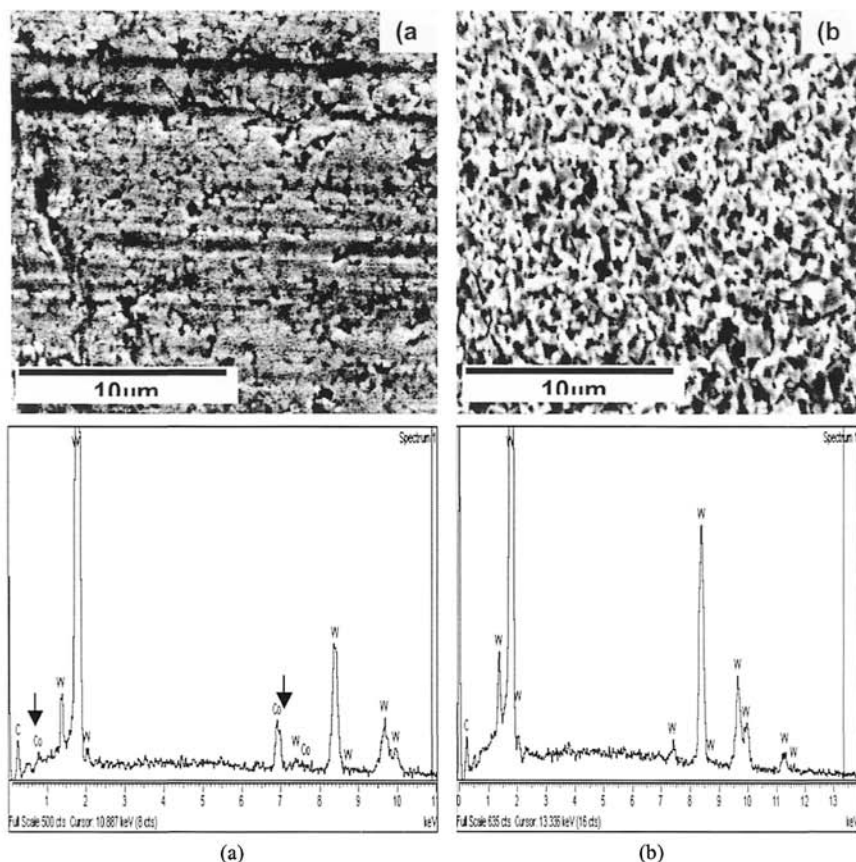


Fig. 7.14. (a) SEM and EDX of WC-Co micro-drill before etching; (b) WC-Co micro-drill after etching

7.9.3 Diamond Deposition on Tungsten Carbide (WC-Co) Micro-Tool

Laboratory grade tungsten carbide (WC-Co) micro-tools are shown in Fig. 7.17 (a) and (b) (AT23 LR) with fine WC grain sizes (1 μm) 20 -30 mm in length and 1.0 -1.5 mm in diameter [supplied by Metrodent Ltd, UK] that are used for the CVD diamond deposition process.

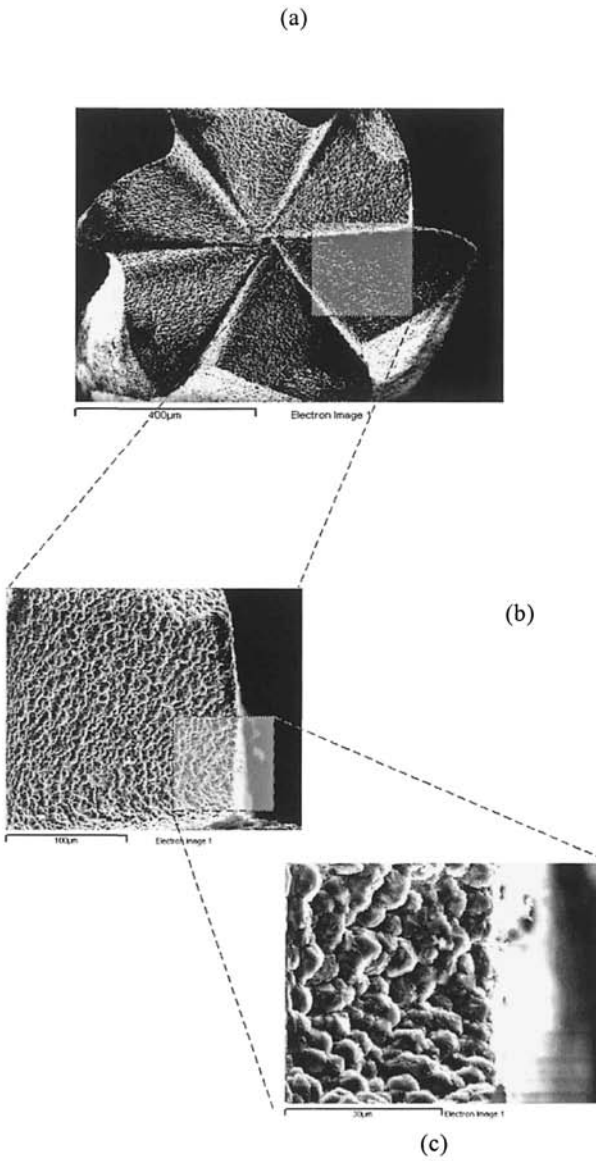


Fig. 7.15. (a) cutting edge of micro-drill after depositing with CVD diamond; (b) cutting edge of micro-drill uniformly coated with diamond; (c) SEM of micro-drill after coating with diamond

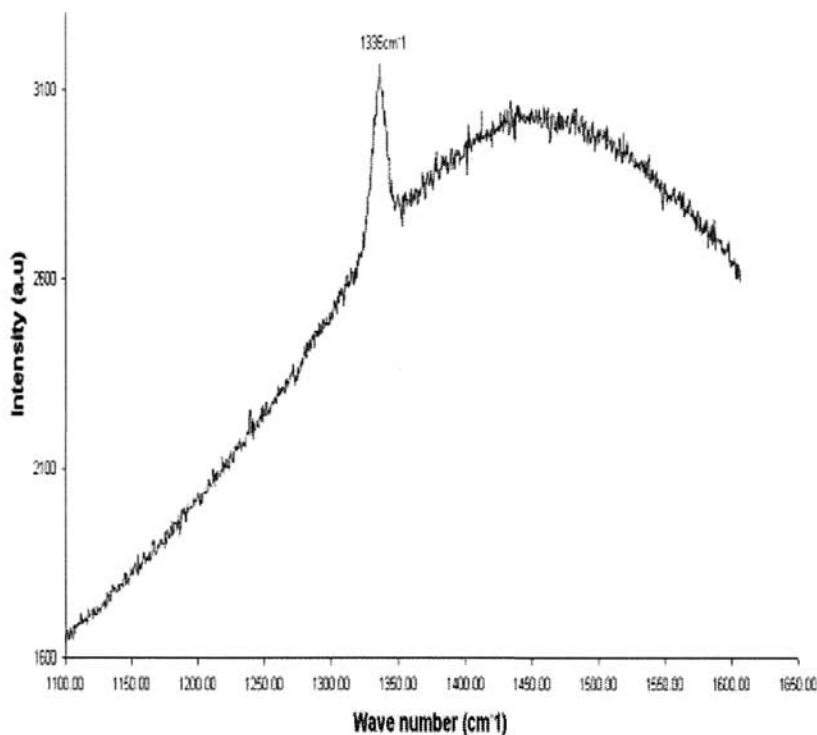


Fig. 7.16. Raman spectra of diamond-coated WC-Co micro-tool

The WC surface has etched away with Murakami solution and surface Co has been removed by acid etching followed by ultrasonically washing in distilled water. The EDX results confirmed that there is no indication of Co left on the surface of the etched micro-tool (Fig. 7.18). Diamond films have been deposited onto the cutting edge of the tools at a 5 mm distance from the tantalum wire filament.

Fig. 7.17. (a) laboratory used WC-Co micro-tool; (b) laboratory used WC-Co micro-tool before surface treatment

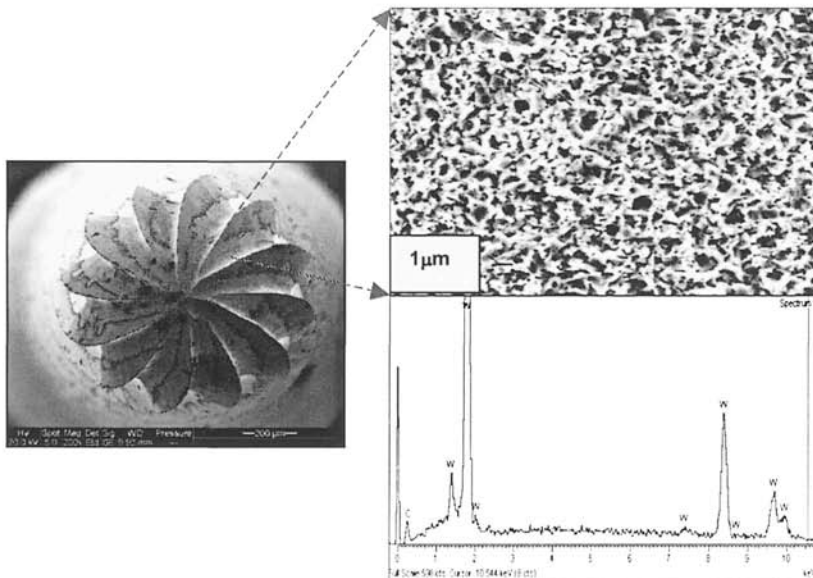
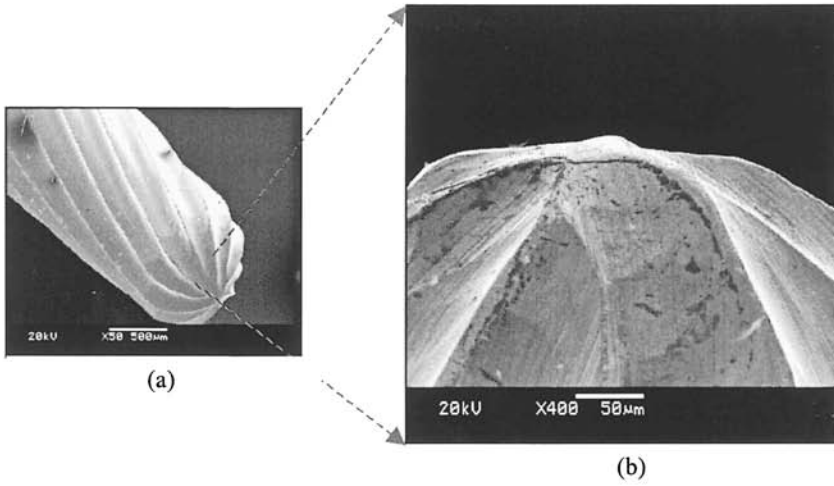


Fig. 7.18. Etched micro-tool surface after chemical treatment

Surface morphology of predominantly (111) faceted octahedral shape diamond films was obtained. The film thickness was measured to be 15-17 μm after diamond deposition for 15 hours. Figure 7.19 shows the SEM micrograph of a CVD diamond-coated micro-tool (AT 23LR) at the cutting edge. The film is homogeneous with uniform diamond crystal sizes, typically in the range of 6-10 μm . As expected the surface morphology is rough making the micro-tools extremely desirable for abrasive applications.

The Raman spectra shown show that at the tip, center, and end of cutting tool single sharp peaks at 1336, 1336 and 1337 cm^{-1} respectively were observed for different positions Fig. 7.20. The Raman spectrum also gives an indication about the stress in the diamond coating. The diamond peak is shifted to a higher wave number of magnitude such as 1336, 1337 cm^{-1} than that normally experienced in an unstressed coating where the natural diamond peak occurs at 1332 cm^{-1} thus indicating that the stress is compressive.

7.10 Wear of Diamond

The quality and economy of industrial production processes are to a great extent determined by the selection and the design of appropriate manufacturing operations. For many machining operations, especially for the technologically relevant processing of metallic materials, machining with geometrically specified cutting edge is applicable. Enhancing the performance of machining operations is therefore an economically important goal; to achieving this, coating technology can contribute in varying ways. The cutting tool is the component that is most stressed, and therefore limits the performance in NEMS and MEMS operations. Thermal and mechanical loading affects the cutting tool edges in a continuous or intermittent way. As a result, in addition to good wear resistance, high thermal stability and high mechanical strength are required for cutting materials. Opposing this objective of an ideal cutting material is the fundamental contradiction of properties hardness, strength at elevated temperature, and wear resistance on one hand, and bending strength and bending elasticity on the other hand.

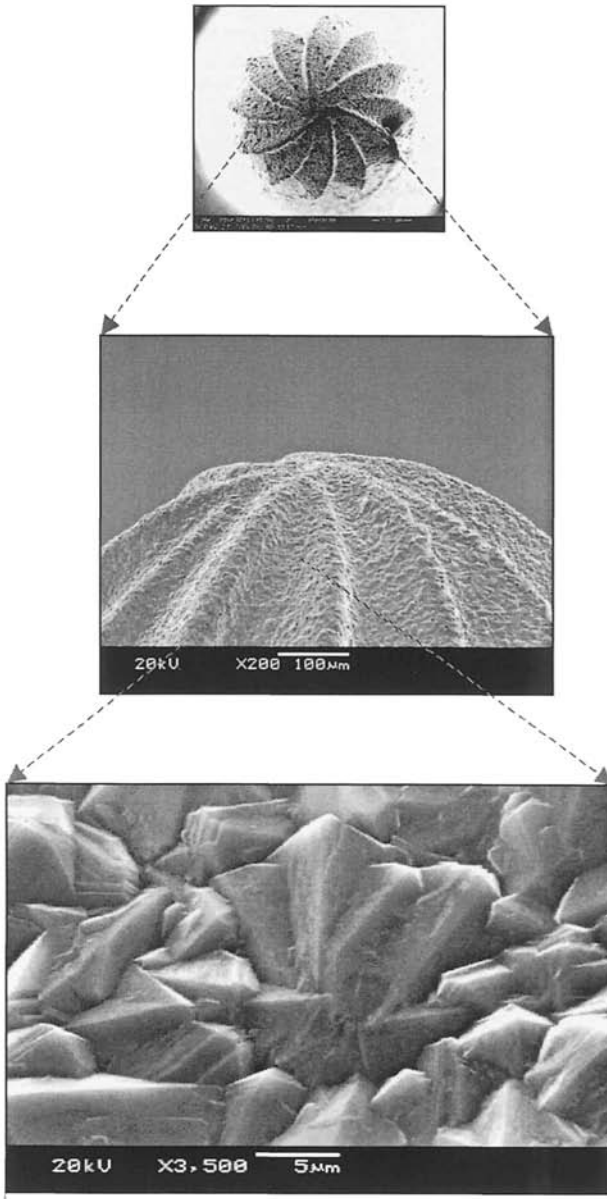


Fig. 7.19. (111) faceted octahedral shape diamond films on a micro-cutting tool

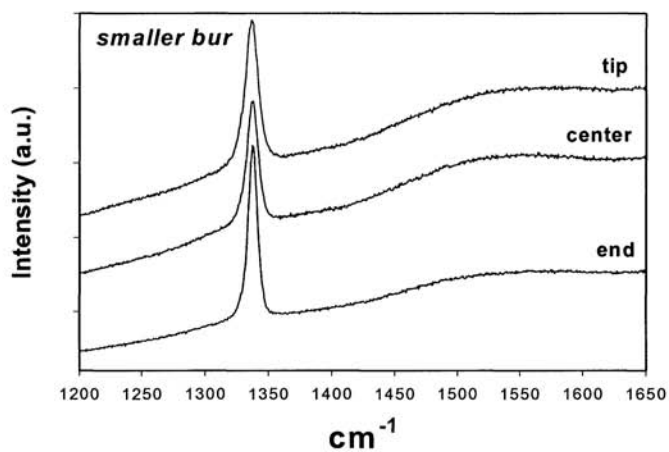


Fig. 7.20. Raman spectra of diamond film on micro-cutting tool

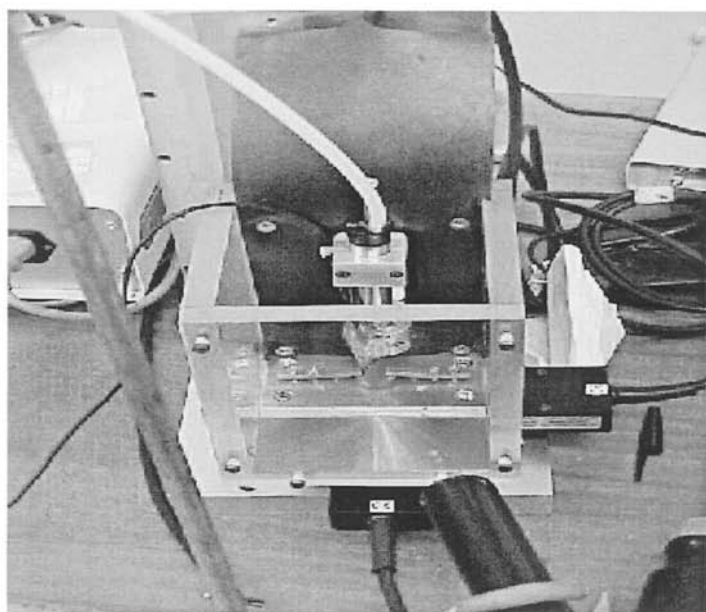


Fig. 7.21. Micro-machining center

Cutting materials for extreme requirements (for example, interrupted cuts or machining of high strength materials) consequently cannot be made from one single material, but may be realized by employing composite materials.

Surface coatings may improve the tribological properties of cutting tools in an ideal way and therefore allow the application of tough or ductile substrate materials, respectively.

The coated micro-tools have been used to machine a number of materials including copper, aluminum, and iron alloys. The coated tools were compared with uncoated micro-tools to distinguish them in terms of their machining behavior. A micro-machining unit was specifically constructed at Purdue University for such a purpose with a maximum spindle speed of 500,000 revolutions per minute, feed rates of between 5 and 20 μm per revolution, and cutting speeds in the range 100 to 200 meters per minute [79]. The micro-machining unit is shown in Fig. 7.21. The machining center is constructed using three principal axes each controlled using a D.C motor connected to a MotionmasterTM controller. A laser light source is focused onto the rotating spindle in order to measure the speed of the cutting tool during machining. Post machining analysis was performed using a scanning electron microscope to detect wear on the flanks of the cutting edges.

7.10.1 Performance of Diamond-coated Micro-Drill

After machining an aluminum alloy material, very low roughness and chipping of the diamond-coated micro-tool were detected. Figure 7.22 shows a typical machined surface in aluminum alloy. A metal chip created from this machining operation is shown in Fig. 7.23. The chip clearly shows shear fronts separated by lamellae caused by plastic instabilities within the material generated at such high speeds. Diamond-coated tools and uncoated were compared by drilling a series of holes in the aluminum alloy. The wear of each tool was determined by examining the extent of flank wear. Uncoated tools appeared to chip at the flank face, and diamond-coated tools tended to lose individual diamonds at the flank face. Uncoated tools drilled an average of 8,000 holes before breakdown occurred,

and the diamond-coated tools drilled an average of 24,000 holes [80].

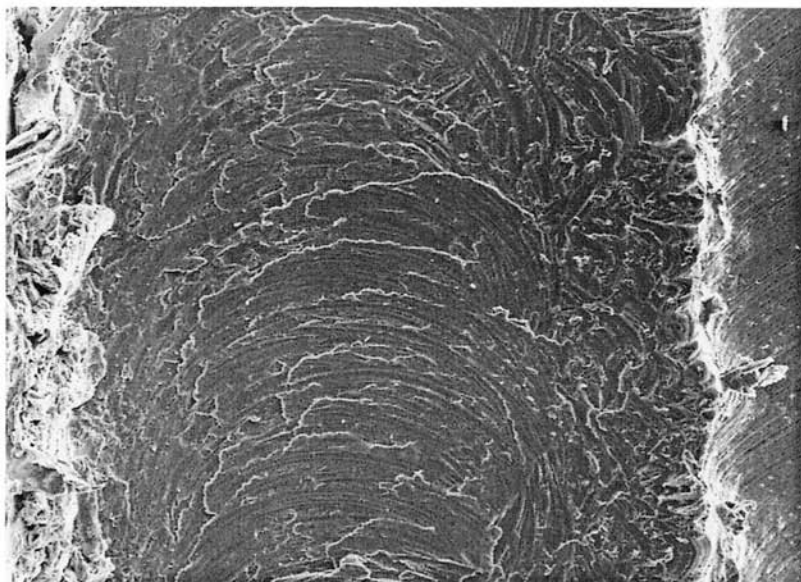


Fig. 7.22. Aluminum alloy material showing a machined track produced by a diamond-coated micro-cutting tool

7.10.2 Performance of Diamond-Coated Micro-Tool

In order to examine the cutting performance of the diamond-coated micro-tools machining materials such as borosilicate glass, acrylic teeth, and natural human teeth were used. Machining unit was set up for the laboratory bur (AT23LR supplied by Metrodent, UK), which used to operate at 20,000–30,000 rpm with a feed rate of 0.2–0.5 mm/rev without water-cooling.

The flank wear of the burs were estimated by SEM analysis at selected time interval of 1 and 3 min. Prior to SEM analysis diamond-coated burs were ultrasonically washed with 6M Sulfuric acid solution to remove any unwanted machining material, which eroded onto surface of CVD diamond-coated bur. For comparison, the commonly used conventional PCD (polycrystalline diamond) sintered burs with different geometry were also tested on the same ma-

chining materials. These burs are made by imbedding synthetic diamond particles into a nickel matrix material to bond the particles at the cutting surfaces.

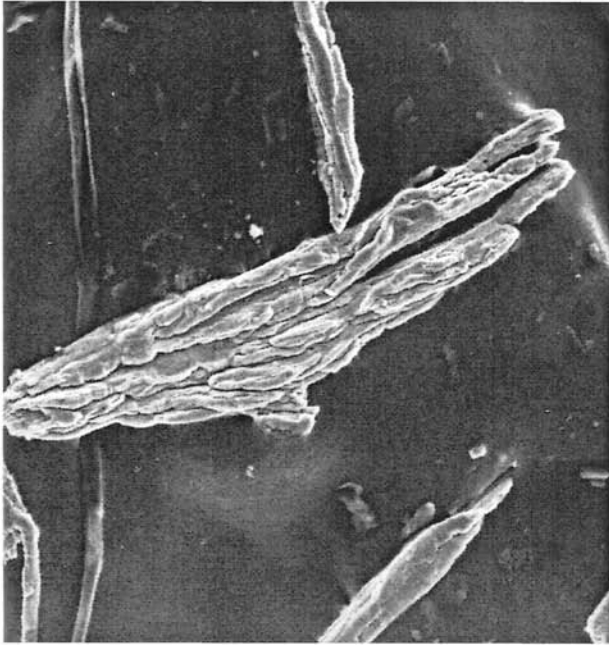


Fig. 7.23. Aluminum alloy chips generated during high-speed micro-machining operations using a diamond-coated micro-cutting tool

The morphology of a sintered diamond bur after being tested on borosilicate glass at a cutting speed of 30,000 rpm for 5 minutes with an interval at every 30 sec is shown in Fig. 7.24. It is clearly evident that there is significant removal of diamond particles from the surface of the tool after 500 holes. As expected, there is the deterioration of the abrasive performance of the PCD sintered diamond micro-tools.

SEM images of sintered diamond micro-tool tested on borosilicate glass (Fig. 7.24) and CVD diamond-coated laboratory bur after machining tests on borosilicate glass and acrylic/ porcelain teeth respectively for 5 min at a cutting speed of 30,000 rpm are shown in

Figs. 7.25 and 7.26. After machining the diamond films are still intact on the pre-treated WC substrate and diamond coating displayed good adhesion. There is no indication of diffusive wears after the initial test for 500 holes.

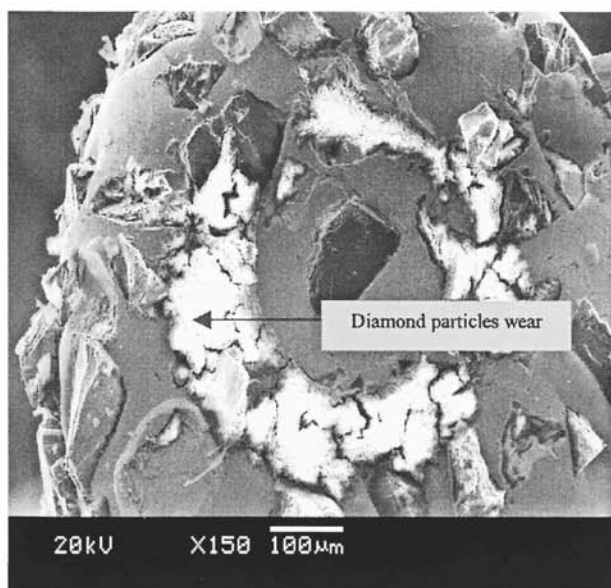


Fig. 7.24. Morphology of sintered diamond micro-cutting tool after machining glass

However, it was observed that the machining of materials such as glass pieces are eroded to cutting edge of the diamond micro-tool as adhesive wear (Fig. 7.25). After testing on acrylic teeth the mechanism of wear probably involves adhesion as well as abrasion. Figure 7.26 shows that inorganic fillers from acrylic teeth adhered to the cutting tool surface in localized areas when a higher rate of abrasion was used [81].

A micrograph of an uncoated WC-Co micro-tool tested on the borosilicate glass using the same machining conditions are shown in Fig. 7.27 (a) and (b). The uncoated WC-Co bur displayed flank wear along the cutting edge of the bur. The areas of flank wear were in-

vestigated at the cutting edge of the micro-tool. A series of machining experiments have been conducted using uncoated, diamond-coated micro-tools, and sintered diamond burs when machining extracted human tooth, acrylic tooth, and borosilicate glass. The life of the burs in the machining sense was compared by using the amount of flank wear exhibited by each type of micro-tool. The flank wear was measured at time intervals of 2, 3, 4, 5, 6, and 7 minutes' machining duration. Again, the micro-tools were examined using optical and scanning electron microscopic techniques and observed similar trends with burs that were used in drilling experiments.

Fig. 7.25. Diamond-coated micro-cutting tool after machining glass

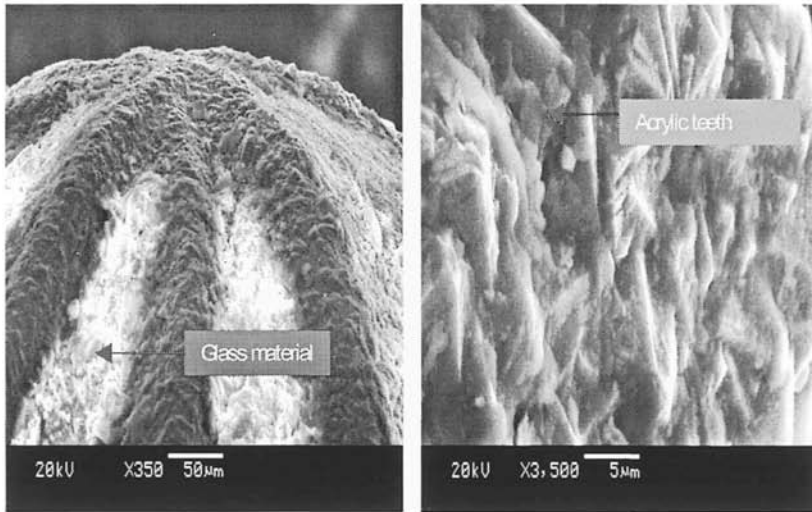


Fig. 7.26. Diamond-coated micro-cutting tool after machining acrylic

The measurements of flanks wear for each bur that machined different dental materials are shown in Figs 7.28-30. It is evident that a longer duty cycle of machining could cause higher rate of flank wear on the cutting edge of tool. Therefore, the cutting edge of WC-Co micro-tool should have significant thickness of CVD dia-

mond, which will enhance not only quality of cutting but will also prolong the tool life.

7.11 Time-Modulated CVD Diamond

In the conventional HFCVD method, using the relatively short bias-voltage pulses in bias-enhanced nucleation in which the CH_4 concentration is increased, the flow of CH_4 during film growth is kept constant. Diamond growth in a CVD vacuum reactor is conventionally performed under constant CH_4 flow, while the excess flow of hydrogen is kept constant throughout the growth process. In developing the new TMCVD process it was considered that diamond deposition using CVD consists of two stages: (1) the diamond nucleation stage and (2) crystal growth stage.

Diamond grains nucleate more efficiently at higher CH_4 concentrations. However, prolonged film growth performed under higher CH_4 concentration leads to the incorporation of non-diamond carbon phases, such as graphitic and amorphous. The TMCVD process combines the attributes of both growth stages. This technique has the potential to replicate the benefits obtained by using pulsed power supplies, which are relatively more expensive to employ.

The key feature of the new process that differentiates it from other conventional CVD processes is that it pulses CH_4 , at different concentrations, throughout the growth process, whereas in conventional CVD, the CH_4 concentration is kept constant, for the full growth process. In TMCVD, it is expected that secondary nucleation processes occur during the stages of higher CH_4 concentration pulses. This can effectively result in the formation of a diamond film involving nucleation stage, diamond growth, ad secondary nucleation and the cycle is repeated. The secondary nucleation phase can inhibit further growth of diamond crystallites. The nuclei grow to a critical level and then are inhibited when secondary nuclei form on top of the growing crystals and thus fill up any surface irregularities. This type of film growth can potentially result in the formation of a multilayer type film coating. In such coating systems, the quality and the surface roughness of the film coatings is dependent not on the overall thickness of the film but instead on the thickness of the individual layer of the film coating.

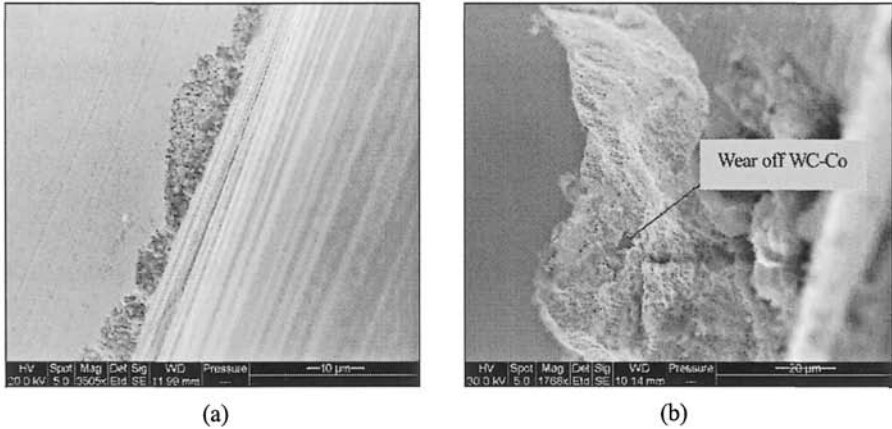
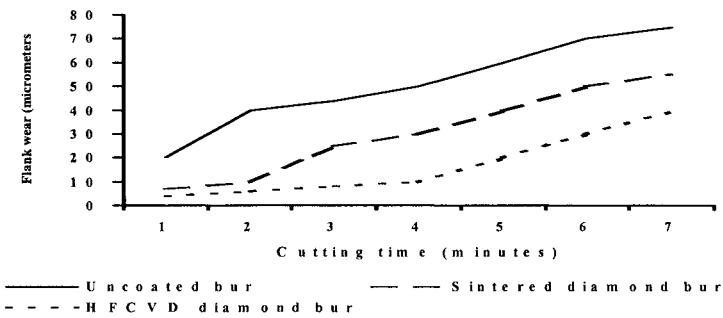
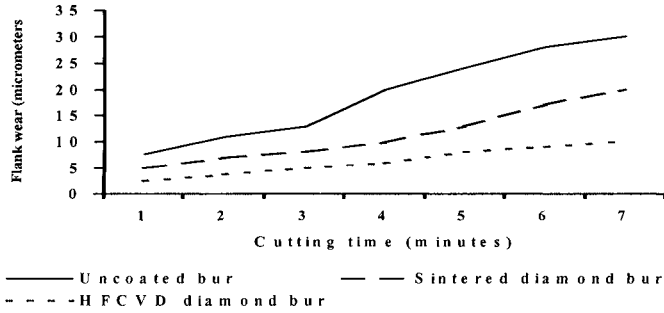
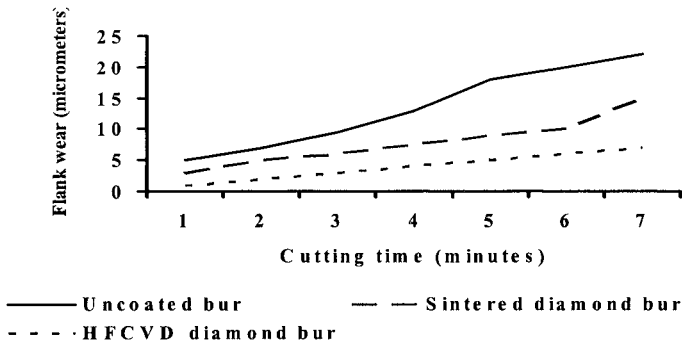


Fig. 7.27. (a) cutting edge of WC-Co micro-tool after machining glass; (b) close-up view of WC-Co surface of the micro-cutting tool.

In demonstrating the CH_4 flow regimes, typically employed in conventional diamond CVD and TMCVD processes, Fig. 7.31 shows, as an example, the variations in CH_4 flow rates during film deposition. In the CH_4 pulse cycle employed in Fig. 7.31, the CH_4 flow rate remained constant throughout the conventional CVD process at 25 sccm. It is important to note that the hydrogen flow rate remains constant under both growth modes. CH_4 modulations at 12 and 40 sccm for 15 and 2 minutes, respectively, were performed during the TMCVD process using the microwave CVD system. Since higher CH_4 content in the vacuum chamber results in the incorporation of non-diamond carbon phases in the film, such as graphitic and amorphous, and degrades the global quality of the deposited film, the higher CH_4 pulse duration was kept relatively short. The final stage of the time-modulated process ends with a lower CH_4 pulse. This implies that hydrogen ions will be present in relatively larger amount in the plasma and these will be responsible for etching the non-diamond phases to produce a good quality film. Figure 7.32 (a) and (b) displays the close-up cross-sectional SEM images of diamond films grown using TMCVD and conventional CVD processes. The conventional MCD film displays a columnar

growth structure. However, the time-modulated film displayed a somewhat different growth mode. Instead, the cross section consisted of many coarse diamond grains that were closely packed together. A pictorial model of the mechanism for the TMCVD process is depicted in Fig. 7.32 (c) as compared with the conventional CVD process (Fig. 7.32 d). Primarily, diamond nucleation occurs first in both the TMCVD and conventional CVD processes. However, in TMCVD, diamond nucleates more rapidly as a result of the high CH_4 pulse at the beginning. The high CH_4 pulse effectively ensures the diamond grains to nucleate quicker to form the first diamond layer. The second stage, in which CH_4 content is reduced to a lower concentration, the diamond crystallites are allowed to grow for a relatively longer period. This step enables the crystals to grow with columnar growth characteristics. The surface profile of the depositing film becomes rough, as expected. The third stage involves increasing the CH_4 flow back to the higher pulse. This enables further secondary nucleation of NCD to occur in between the existing diamond crystals, where the surface energy is lower. As a comparison, much less secondary nucleation occurs when the CH_4 flow is kept constant throughout the growth process. The distinctive feature of the TMCVD process is that it promotes secondary diamond-particle nucleation to occur on top of the existing grains in order to fill up any surface irregularities. Figure 7.33 displays the SEM micrograph showing secondary nucleation occurring after a high CH_4 pulse. This result justifies the proposition of the mechanism for the TMCVD process, as shown in Fig. 7.32. It can be expected that at high CH_4 bursts, carbon-containing radicals are present in the CVD reactor in greater amount, which favor the growth process by initiating diamond nucleation. The average secondary nucleation crystallite size was in the nanometer range (≤ 100 nm). It is evident that the generation of secondary nano-sized diamond crystallites has led to the successful filling of the surface irregularities found on the film profile, in between the mainly (111) crystals. Figure 7.34 shows some randomly selected SEM images of as-deposited diamond films deposited using the TMCVD process at different CH_4 pulse duty cycles.



Figs. 7.28-7.30. Flank wear of cutting tools when machining borosilicate glass, acrylic material, and dentine/enamel

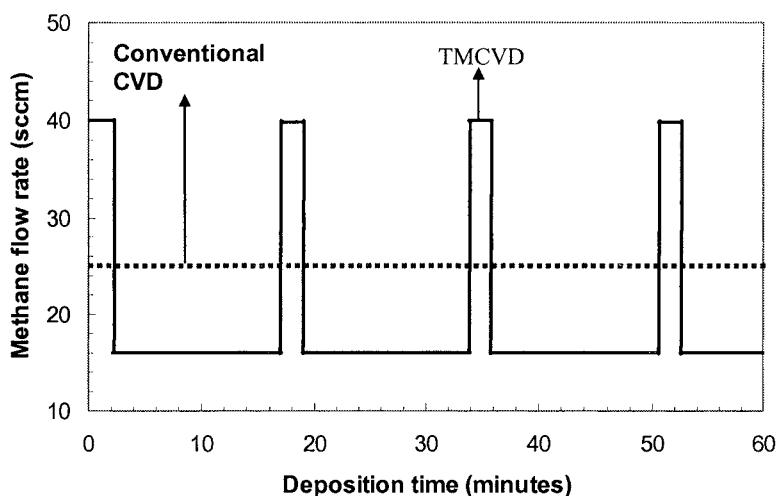


Fig. 7.31. Variations in CH_4 flow rates during film deposition in a typical time-modulated pulse cycle.

Figure 7.35 shows the graph displaying the growth rates of conventional and time modulated films grown using hot-filament CVD (HFCVD) and microwave plasma CVD (MPCVD) systems. As expected, the MPCVD system gave much higher growth rates under both growth modes, conventional and time-modulated, compared to films produced using HFCVD. A growth rate of $0.9 \mu\text{m/hr}$ was obtained using the HFCVD system under constant CH_4 flow. The time-modulated films deposited using HFCVD were grown at a rate of $0.7 \mu\text{m/hr}$, whereas with the MPCVD system, films grown using constant CH_4 flow were deposited at a rate of $2.4 \mu\text{m/hr}$ and using modulated CH_4 flow the films were grown at a rate of $3.3 \mu\text{m/hr}$. Although it is known that growth rates increase with CH_4 concentration, in the present case using the HFCVD system, the TMCVD process employs greater CH_4 flow than conventional CVD. Our results show that the growth rate of films deposited using constant CH_4 flow is slightly higher than of similar films grown using timed CH_4 modulations.

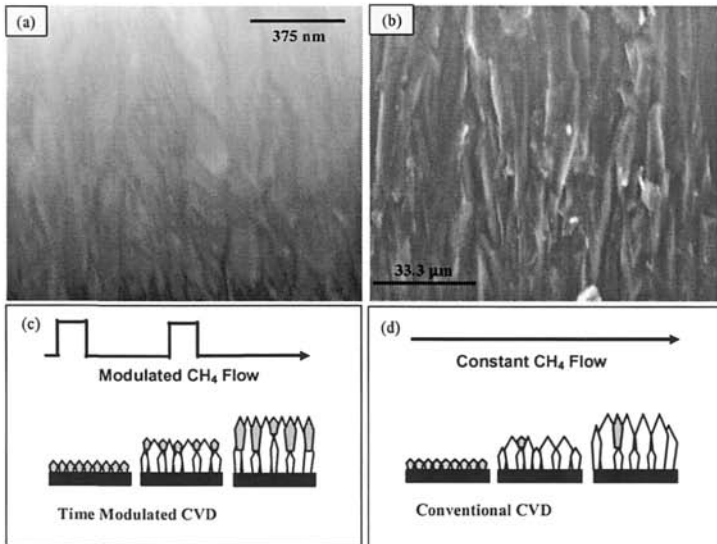


Fig. 7.32. Close-up cross-sectional SEM images of diamond films grown using (a) TMCVD and (b) conventional CVD processes. In addition, the pictorial mechanisms for film growth using TMCVD (c) and conventional CVD (d) processes are also shown

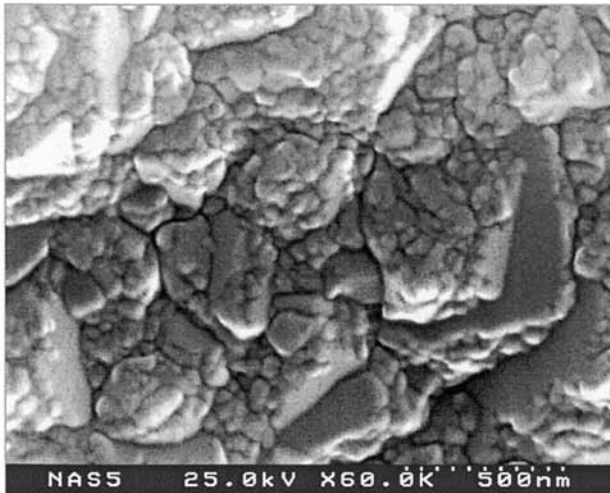


Fig. 7.33. SEM micrograph showing secondary nucleation occurring after a high CH₄ pulse

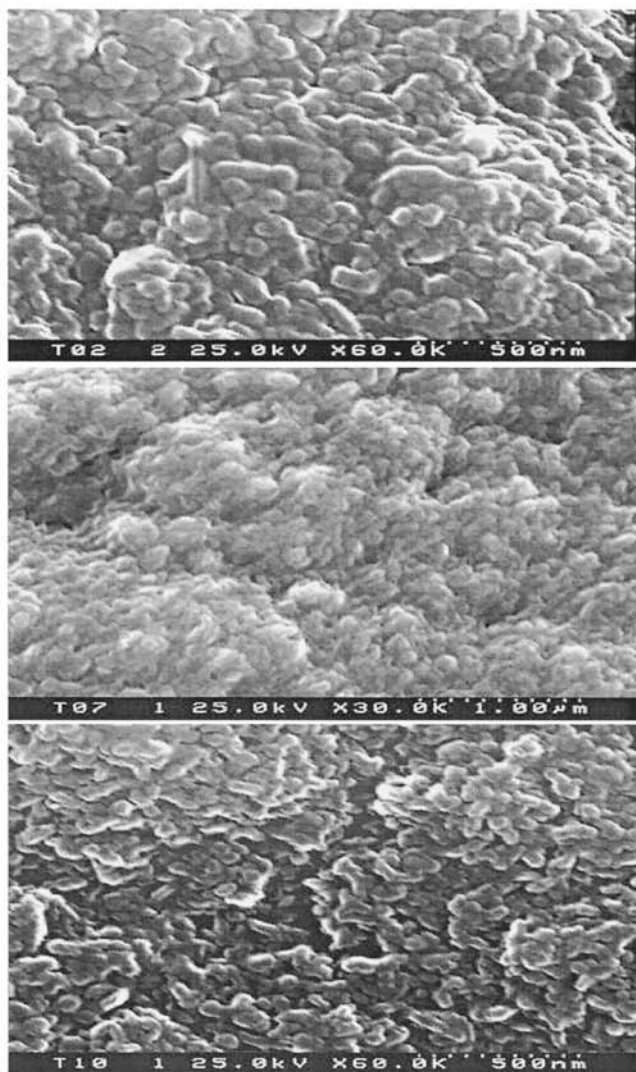


Fig. 7.34. SEM micrographs showing the morphologies of as-deposited diamond films deposited using TMCVD at different CH₄ modulation duty cycles [115]

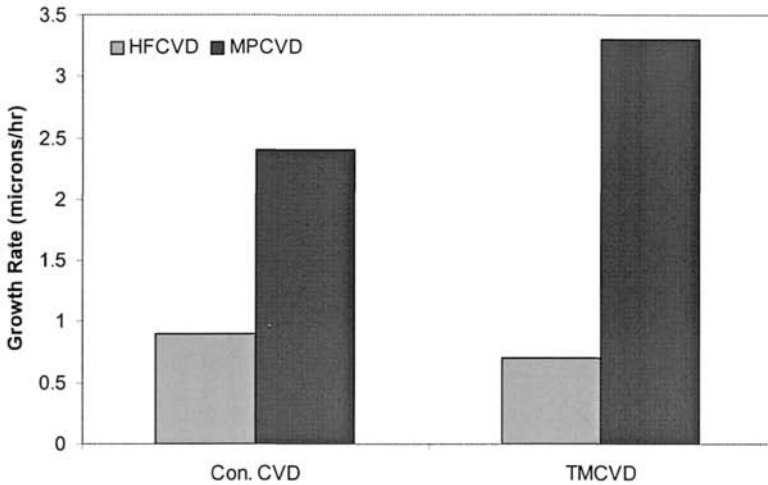


Fig. 7.35. Graph displaying the growth rates of conventional and time-modulated films grown using HFCVD and MPCVD systems

However, films grown under both modes, conventional and time modulated, using the MPCVD system produced results that were contrary to those obtained using the HFCVD system. Using the MPCVD system, the trend observed was that the films were deposited at a higher growth rate using the TMCVD process than conventional CVD. The substrate temperature is a key parameter that governs the growth rate in diamond CVD. Since the TMCVD process pulsed CH_4 during film growth, it was necessary to monitor the change in the substrate temperature during the pulse cycles. Figure 7.36 shows the graph relating substrate temperature to CH_4 concentration for both HFCVD and MPCVD systems. For the HFCVD system, it was observed that the substrate temperature decreased with CH_4 concentration. In explaining the observed trend, it needs to be considered that the dissociation of CH_4 by the hot filament absorbs energy (heat) from the filament and is considered as a cooling process. In our case the filament power was kept constant; therefore, less heat can be expected to radiate to the substrate. In addition,

only a small percentage of the thermally dissociated CH species reach the substrate and transfer kinetic energy to the substrate.

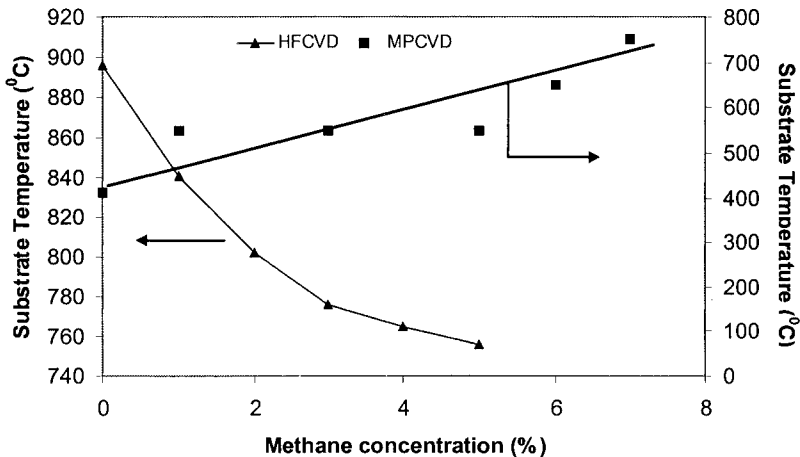


Fig. 7.36. Graph relating substrate temperature to CH_4 concentration for HFCVD and MPCVD systems

It is known that the deposition of diamond films increases with substrate temperature. During the high CH_4 pulse in TMCVD, the lower substrate temperature may be sufficient to lower the growth rate significantly. Generally, in a MPCVD reactor, the substrate temperature increases with CH_4 concentration, as shown in Fig. 7.36.

As a comparison, H_2 is dissociated more extensively in a MPCVD reactor than in a HFCVD reactor to produce atomic hydrogen. Furthermore, in a MPCVD reactor, the plasma power is much greater, 3400 W, than the plasma power in the HFCVD reactor. In fact, the plasma power used in MPCVD for growing diamond films was approximately 10 times greater than the power used in the HFCVD reactor. Therefore, the dissociation of CH_4 absorbs a lower percentage of the energy/heat from the plasma in a MPCVD compared to the HFCVD reactor. It is also understood that the reaction between atomic hydrogen and CH species at close proximity to the

substrate releases heat. Since in a MPCVD reactor there is a greater intensity of atomic H and CH species, there will be a greater number of reactions between atomic H and CH species. This means that more heat will be released in a MPCVD reactor than in a HFCVD reactor because of such reactions.

This effect contributes to the heating of the substrate. In a HFCVD reactor, the hot filament displays much lower ability to dissociate H_2 . Since atomic hydrogen is a critical species that plays an important role in producing a good quality diamond film during CVD, the quality of the films grown using HFCVD is generally lower than of similar films grown using MPCVD. In addition, the hydrogen atoms are required for the effective deposition of diamond onto the substrates. As mentioned earlier, atomic H radicals are present in greater concentration in a MPCVD reactor than in a HFCVD reactor, the MPCVD process gives higher growth rates than the HFCVD process. It is also known that by controlling the temperature during the high/low CH_4 pulse cycles, a greater number of secondary diamond grains were generated and the resultant films displayed (1) smoother surfaces and (2) higher growth rates.

7.12 Conclusions

Thin film deposition technologies, particularly CVD and PVD, have become critical for the manufacture of a wide range of industrial and consumer products. Trends in historical developments in the CVD diamond suggest that the technology is highly likely to yield substantial benefits in emerging technological products in fields of nanotechnology, biomedical engineering, NEMS, and MEMS devices. Several methods including plasma CVD, low pressure CVD, and atmospheric pressure CVD have matured into processes that are routinely used in industry. Microwave and hot filament CVD methods are now commonly used to grow diamond and these can be modified to coat uniformly for tools, NEMS, MEMS and biomedical applications. Diamond coatings examined on tools and biomedical tools showed much enhanced performance compared to uncoated tools.

7.13 Problems

1. Describe the chemical vapor deposition process for producing micro-cutting tools.
2. What are the properties of diamond?
3. Describe the synthesis of diamond.
4. Characterize the growth of CVD diamond technology.
5. Describe plasma-enhanced CVDD deposition.
6. Describe RF plasma-enhanced CVDD deposition.
7. Describe DC enhanced CVD.
8. Describe microwave plasma enhanced CVD.
9. What is hot filament CVD?
10. How can hot filament CVD be used to coat micro-cutting tools?
11. How are substrates selected and pre-treated?
12. Describe filaments are modified to produce micro-cutting tools.
13. Explain how diamond is nucleated and grown.
14. How is diamond deposited to molybdenum?

References

1. Spear KE and Dismukes JP, in *Synthetic Diamond: Emerging CVD Science and Technology*, The Electrochemical Society, John Wiley and Sons Inc., New York, 1994.
2. Wentorf RH, *J. Phys. Chem.*, **69** (1965) 3063.
3. Butler JE and Woodin RL, *Phil. Trans. R. Soc. Lond.*, **A342** (1993) 209.
4. Ashfold MNR, May PW, Rego CA and Everitt NM, *Chem. Soc. Rev.*, **23** (1994) 21.
5. Bachmann PK and Messier R, *Chem. Eng. News*, **67** (1989) 24.
6. Spear KE, *J. Am. Ceram. Sci.*, **72** (1989) 171.
7. Joffreau PO, Haubner R and Lux B, *Mater. Res. Soc. Proc.*, **EA-15** (1988) 15.
8. Spitsyn BV, Bouilov LL and Deryagin BV, *J. Cryst. Growth*, **52** (1981) 219.

9. Angus JC, *Electrochem. Soc. Proc.*, **89** (1989) 1
10. Yarbrough WA and Messier R, *Science*, **247** (1996) 688.
11. Messier R, Badzian AR, Badzian T, Spear KE, Bachmann PK and Roy R, *Thin Solid Films*, **153** (1987) 1.
12. Angus JC and Hayman CC, *Science*, **241** (1988) 913.
13. Spear KE, *Am J, Ceram. Soc.*, **72** (1989) 171.
14. Kamo M, Sato U, Matsumoto S and Setaka N, *Cryst J. Growth*, **62** (1983) 642.
15. Saito Y, Matsuda S and Nagita S, *Mater J. Sci. Lett.*, **5** (1986) 565.
16. Saito Y, Sato K, Tanaka H and Miyadera H, *Mater J. Sci.*, **24** (1989) 293.
17. Williams BE, Glass JT, Davis RF, Kobashi K and Horiuchi T, *Vac J Sci. Technol. A, Vac. Surf. Films*, **6** (1988) 1819.
18. Kobashi K, Nishimura K, Kawate Y and Horiuchi T, *Vac J Sci. Technol. A, Vac. Surf. Films*, **6** (1988) 1816.
19. Liou Y, Inspector A, Weimer R and Messier R, *Appl. Phys. Lett.*, **55** (1989) 631.
20. Zhu W, Randale CA, Badzian AR and Messier R, *Vac J. Sci. Technol. A, Vac. Surface Films*, **7** (1989) 2315.
21. Matsumoto S, *Mater J. Sci. Lett.*, **4** (1985) 600.
22. Matsumoto S, Hino M and Kobayashi T, *Appl. Phys. Lett.*, **51** (1987) 737
23. Vitkayage DJ, Rudder RA, Fountain GG and Markunas RJ, *Vac J. Sci. Technol.*, **A6** (1988) 1812.
24. Meyer DE, Ianno NJ, Woolam JA, Swartzlander AB and Nelson AJ, *Mater J. Res.*, **3** (1988) 1397.
25. Wood P, Wydeyen T and Tsuji O, in *Programs and Abstracts of the First International Conference on New Diamond Science and Technology*, New Diamond Forum, Tokyo, Japan, 1988.
26. Jackman RB, Beckman J and Foord JS, *Appl. Phys. Lett.*, **66** (1995) 1018.
27. Suzuki K, Sawabe A, Yasuda H and Inuzuka T, *Appl. Phys. Lett.*, **50** (1987) 728.
28. Akatsuka F, Hirose Y and Kamaki K, *Jap. J. Appl. Phys.*, **27** (1988) L1600.

29. Suzuki K, Sawabe A and Inuzuka T, *Jap. J. Appl. Phys.*, **29** (1990) 153.
30. Niu CM, Tsagaropoulos, Baglio J, Dwight K and Wold A, *J. Solid State Chem.*, **91** (1991) 47.
31. Popovici G, Chao CH, Prelas MA, Charlson EJ and Meese JM, *Mater J. Res.*, **10** (1995) 2011.
32. Chao CH, Popovici G, Charlson EJ, Charlson EM, Meese JM and Prelas MA, *J. Cryst. Growth*, **140** (1994) 454.
33. Postek MT, Howard KS, Johnson AH and Macmichael KL, in *Scanning Electron Microscopy*, 1980.
34. Spirsyn BV, Bouilov LL and Deryagin BV, *J. Cryst. Growth*, **52** (1981) 219.
35. Kobashi K, Nishimura K, Kawate Y and Horiuchi T, *Phys. Rev. B*, **38** (1988) 4067.
36. Pickrell D, Zhu W, Badzian AR, Messier R and Newnham RE, *Mater J. Res.*, **6** (1991) 1264.
37. Oatley CW, in *Scanning Electron Microscope*, Cambridge University Press, 1972.
38. Tobin MC, in *Laser Raman Spectroscopy*, Wiley Interscience, New York, 1971.
39. Colthup NB, Daley LH and Wiberley SE, in *Introduction to Infrared and Raman Spectroscopy*, Academic Press, New York, 1975.
40. Raman CV and Krishnan KS, *Nature*, **121** (1928) 501.
41. Nemanich RJ, Glass JT, Lucovsky G and Shroder RE, *Vac J. Sci. Tech.*, **6** (1988) 1783.
42. Knight DS and White WB, *Mater J. Res.*, **4** (1989) 385.
43. Solin SA and Ramdas AK, *Phys. Rev. B*, **1** (1970) 1687.
44. Leyendecker T, Lemmer O, Jurgens A, Esser S and Ebberink J, *Surf. Coat. Technol*, **48** (1991) 253.
45. Murakawa M and Takeuchi S, *Surf. Coat. Technol*, **49** (1991) 359.
46. Yaskiki T, Nakamura T, Fujimori N and Nakai T, *Surf. Coat. Technol*, **52**(1992)81.
47. Reineck J, Soderbery S, Eckholm P and Westergren K, *Surf. Coat. Technol*, **5**(1993)47.
48. Wang HZ, Song RH and Tang SP, *Diamond and Relat. Mater*, **2** (1993) 304.

49. Inspector A, Bauer CE and Oles EJ, *Surf. Coat. Technol.*, **68/69** (1994) 359
50. Kanda K, Takehana S, Yoshida S, Watanabe R, Takano S, Ando H and Shimakura F; *Surf. Coat. Technol.*, **73** (1995) 115
51. Luz B and Haubner R, in *Diamond and Diamond-like films and coatings*, NATO-ISI Series B, Physics, **266**, Edited by R. E. Clausing, 579, L. L. Horton, J. C Angus, and P. Koidl, Plenum Press, NY, 1991.
52. Chen X and Narayan J, *Journal of Applied Physics*, **74**, (1993), 1468.
53. Klass W, Haubner R, and Lux B, *Diamond and Related Materials*, **6**, (1997), 240.
54. Zhu W, Yang PC, Glass JT, and Arezzo F, *Journal of Materials Research*, **10**, (1995), 1455.
55. Lux B and Haubner R, *Ceramics International*, **22**, (1996), 347.
56. C.R.C. Handbook of Chemistry and Physics, Edited by R. C. Weast, C.R.C. Press, FL, 1989-1990.
57. Haubner R, Lindlbauer A, and Lux B, *Diamond and Related Materials*, **2**, (1993), 1505. 72
58. Chang CP, Flamm DL, Ibbotson DE, and Mucha JA, *J. Appl. Phys.*, **63** (1988) 1744.
59. Gusev MB, Babaey VG, Khvostov VV, Lopez-Ludena GM, Yu Brebadze A, Koyashin IY, and Alexanko AE, *Diamond and Related Materials*, **6**(1997), 89-94.
60. Endler I, Barsch K, Leonhardt A, Scheibe HJ, Ziegele H, Fuchs I, and Raatz C, *Diamond and Related Materials*, **8**, (1999), 834-839.
61. Kamiya S, Takahashi H, Polini R and Traversa E, *Diamond and Relat. Mater.*, **9** (2000) 191-194.
62. Inspector A, Oles EJ and Bauer CE, *Int.J.Refract; Metal Hard Materials*, **15** (1997) 49.
63. Itoh H, Osaki T, Iwahara H and Sakamoto H, *J. Materials Science*, **26** (1991) 370.
64. Liu H and Dandy DS; *Diamond Chemical Vapor Deposition*, Noyes, 1996.

65. Nazare MH and Neves AJ: Properties, Growth and Application of Diamond, 1998.
66. Zhang GF and Buck V, *Surf. Coat. Technol*, **132** (2000) 256.
67. Haubner R, Kubelka S, Lux B, Griesser M and Grasserbauer M, *J. Physics.4th Coll*, **C5**, 5 (1995) 753.
68. May P, Rego C, Thomas R, Ashfold MN and Rosser KN, *Diamond and Related Materials*, **3** (1994) 810.
69. Gouzman I and Hoffmann A, *Diamond and Related Materials*, **7**(1998) 209.
70. Wang W, Liao K, Wang J, Fang L, Ding P, Esteve J, Polo MC and Sanchez G, *Diamond and Related Materials*, **8** (1999) 123
71. Wang BB, Wang W and Liao K, *Diamond and Related Materials*, **10** (2001) 1622.
72. Kim YK, Han YS and Lee JY. *Diamond and Related Materials*, **7** (1998) 96.
73. Wang WL, Liao KJ and Gao GC, *Surf. Coat. Technol*, **126** (2000) 195.
74. M.C Polo, W.Wang, G.Sanshez, J.Andujar and J.Esteve, *Diamond and Related Materials*, **6** (1997) 579.
75. Kamiya S, Yoshida N, Tamura Y, Saka M and Abe H, *Surf. Coat. Technol*, **142-144** (2001) 738.
76. Sein H, Ahmed W, Rego CA, Jones AN, Amar M, Jackson M J, Polini R, *J. Phys: Condes. Matter*, **15**, (2003), S2961-S2967.
77. May PW, Rego CA, Thomas RM, Ashford MNR and Rosser KN, *Diamond and Related Materials*, **3**(1994) 810-813.
78. Amirhaghi S, Reehal HS, Plappert E, Bajic Z, Wood RJK, Wheeler DW, *Diamond and Related Materials*, **8** (1999) 845-849.
79. Jackson M J, Gill MDH, Ahmed W, Sein H, *Proceedings of the Institute of Mechanical Engineers – (Part L): J. Materials*, **217**, (2003), 77-83.
80. Sein H, Jackson M J, Ahmed W, Rego CA, *New Diamond and Frontier Carbon Technology*, **12**, (6) (2000), 1-10.
81. Sein H, Ahmed W, Jackson M J, Woodward R and Polini R, *Thin Solid Films*, **447-448** (2004), 455-461.

8. Laser Micro- and Nanofabrication

8.1 Introduction

Laser micro- and nanofabrication is based on the interaction of light with solid matter. As a result of the complex interaction between light and matter, small amounts of material can be removed from the surface. Two different phenomena are operating, namely: pyrolytic processing and photolithic processing. Pyrolytic processing is composed of heating, melting, and ablating the material at the surface, and photolithic processing is based on the direct breaking of chemical bonds in a wide range of materials.

A laser is a very intense beam of light that removes material by breaking atomic bonds. Light can be described as packets of energy, or photons, that has a wavelength and a frequency. Monochromatic light is special because it is composed of only one wavelength that has the same phase, and is coherent compared to incandescent light that is composed of different wavelengths. Optical energy is transferred to the electrons by absorption, which essentially increases the energy of electrons by increasing the vibration of the electron that is sensed as heat. This chapter describes the basic principle of using lasers to fabricate features at the micro- and nanoscale.

8.2 Laser Fundamentals

8.2.1 Creation of Monochromatic Light

The laser cavity contains an active medium that is responsible for the amplification of light energy by the process of stimulated emis-

sion due to the active medium. In fact the word LASER originates from this process, Light Amplification by the Stimulated Emission of Radiation, and the laser type is often categorized by the medium, such as CO_2 or He:Ne. The cavity operates as an optical oscillator. Energy is supplied to the medium, which must be activated to begin the process of creating a laser beam. Triggering or pumping can be produced by an AC/DC or RF power supply for CO_2 or other gas lasers, or by pulses of light created by Nd-YAG laser, or by a chemical reaction, e.g., iodine laser. This triggers the release of photons that are trapped in the cavity by a mirror at each end. One of the mirrors is only partially reflecting and allows light to escape to form the beam; the totally reflecting mirror is usually curved to reduce diffraction losses (Fig. 8.1).

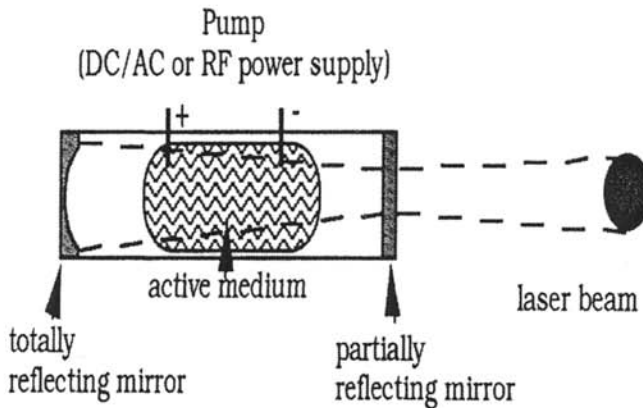


Fig. 8.1. Schematic diagram of the cavity of the laser [1]

For an example case, consider the stimulated emission in carbon dioxide lasers. The carbon dioxide molecule is naturally stable, however, it can exist at other discrete energy levels (the molecule can exist only at specific energy levels; no transition states are allowed). The allowed energy levels are quantized. Increasing the vibration of the molecule due to the high power electric field increases the energy levels; these vibrations can be either asymmetric oscilla-

tions or symmetric oscillations. The energy of CO_2 molecules is raised from the ground state to (001) by N_2 molecules that have a similar high state energy level to CO_2 . The molecule has excess energy compared to its ground state; therefore it drops an energy level from (001) to (100). This energy is lost in the form of a photon. There are further energy states the molecules must pass through (010) to get back to its preferred ground state. A high voltage is applied to the CO_2 gas. The voltage is high enough to cause some of the N_2 molecules to be raised to higher energy levels, which in turn raises the energy levels of the CO_2 molecules. High-energy molecules often lose energy through collisions with the sidewalls. However, energy can also be lost by spontaneous emission when the energy level drops from (001) to (100) and a photon is emitted. In this case the direction of the photon is random. If enough photons are produced one will have a direction that coincides with the optical axis of the cavity and will oscillate due to the reflections at each mirror. If a photon collides with a CO_2 molecule in the upper (001) energy level it causes it to lose energy and drop to the (100) level, in doing so it must emit a photon. The emitted photon will be of the same wavelength and direction as the incident photon and it will also be in phase. So each time a photon interacts with an upper energy level molecule it produces an identical photon. The mirrors at each end of the cavity have the effect of increasing the path length. This amplifies the effect of gaining more photons as the photon travels along many oscillations before exiting the cavity. Exiting is achieved by passing through one of the mirrors, which are partially reflecting. The reason for the addition of nitrogen in CO_2 lasers is that nitrogen has only one excited energy level and this upper energy level is very similar to that of CO_2 . Nitrogen is used to increase the CO_2 to its highest energy level. This leads to high efficiency but CO_2 must be kept cool for this effect to happen. To help reduce diffraction losses and aid in alignment, the mirrors are usually curved; in fact the length of the cavity and the geometry of its mirrors are important factors and define many of the laser's characteristics such as its transverse electromagnetic mode (TEM) mode, or shape of the beam. Cavities are described as stable or unstable depending on whether or not the beam converges or spreads out from the cavity (Fig. 8.2).

8.2.2 Stimulated Emission

Atoms can exist only at defined energy levels; there are no transition states. The pumping mechanism raises the energy level of an atom, and after a short time the atom tries to return to its original state of energy. To do this it ejects the energy in the form of a photon. It is the combined effect of producing many photons that produces laser light. This rise and decay of energy states to produce a photon can take place in a number of mediums, which emit different wavelength photons resulting in different laser types for different applications.

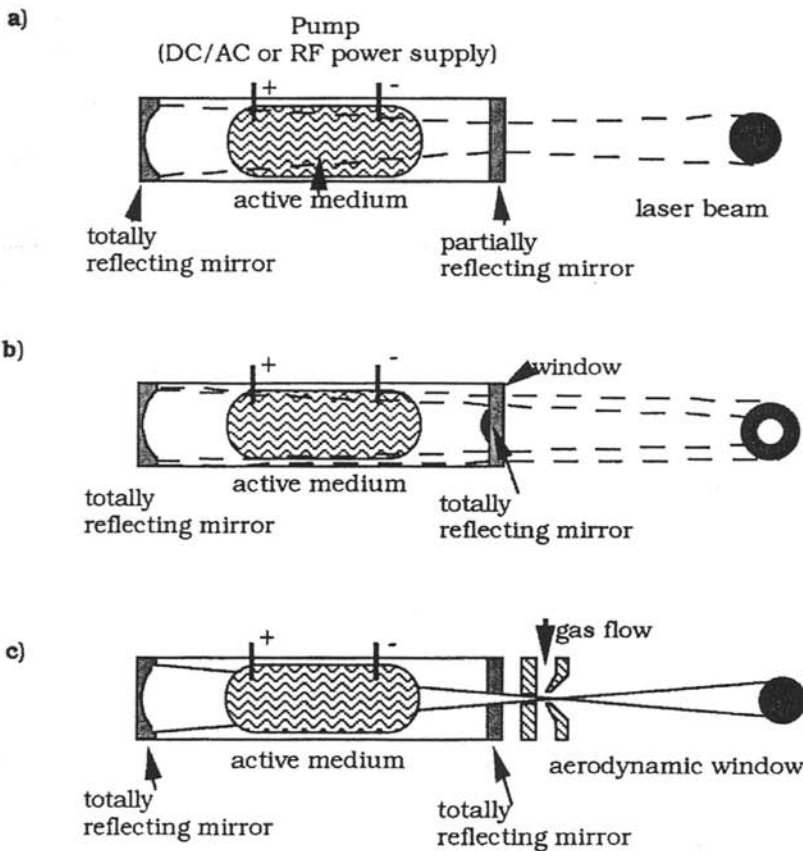


Fig. 8.2. Effect of cavity design on beam shape [1]

If the temperature of the cavity is too high the lower energy level cannot be transferred to its ground state fast enough, thus ceasing the production of laser light. Hence the maximum temperature that can be sustained by the system defines the maximum power of the laser. Carbon dioxide lasers can employ different cooling strategies. Slow flow lasers achieve cooling through the cavity walls. A uniform gain is achieved across and along the cavity giving it a good mode and making it particularly well suited for laser cutting. Fast axial flow lasers achieve cooling by convection of the gas through the discharge zone. The gas enters cold and leaves hot, usually at a speed of around 300 – 500 m/s. The configuration of the system produces a symmetric power distribution of the beam. The cavity length is such that it produces a low Fresnel number and therefore the beam has a low order and can easily be focused to a small point. The gain can be up to 500 W/m. The power these lasers produce is proportional to the cross-sectional area; therefore producing short lasers would seem like a good way to keep the design compact. However such designs produce high mode numbers making the beam difficult to focus easily. There are other types of laser that work on the same principle of gaining photons from the energy decay of various particles.

A solid crystal made up of yttrium, aluminum, and garnet with the addition of neodymium ions makes up the Nd:YAG laser. It is therefore known as a solid-state laser. It works on a similar principle to the CO₂ laser; high energy levels are achieved by the neodymium ions and their subsequent loss of energy when returning to the ground state releases a photon. Energy is supplied by a flashlamp, and the photons are emitted when the energy level drops from a high state to a low state. The decay time for each energy level is very short. After the 1.06 μm laser radiation has been emitted a terminal state is reached. In order to reach the ground state further cooling is required. Because the pumping efficiency is low, a great deal of energy has to be put into the system that requires cooling to prevent thermal distortions of the beam. A krypton lamp powers the Nd³⁺ ions in the YAG rod. The Q-switch is a way of controlling the beam, it can be a mechanical chopper, a bleachable dye, an optoelectrical shutter, or an acousto-optic switch (a piezoelectric material changes its density when an electric current is applied, which in turn changes

the refractive index of the material. Hence, the material acts as an optical grating therefore controlling the beam).

The Q-switch itself must be cooled because when it is blocking the beam it absorbs energy. Q switches can be configured to provide pulse rates between 0 and 50kHz. The idea is that while the shutter is closed, energy builds up and a high peak power is released when the shutter opens, e.g., a 20 W Nd:YAG Q-switched laser can produce 6 ns pulses of 1 mJ/pulse, which is 100 kW.

Beam output can be changed by a process known as frequency doubling. Non-linear optical devices can be swamped with photons, they can absorb two or more photons, and therefore rise to a higher energy state. This energy is released in one step; the resulting radiation has half the wavelength and twice the photon energy, e.g., A 1.06 μm Nd:YAG beam can be converted to 0.530 μm green light, this can be repeated again which would produce ultraviolet light.

A problem with the Nd:YAG laser is the poor efficiency (10-15%) of converting flash lamp energy to high Nd^{3+} energy states, which produces waste heat that can distort the YAG rod leading to poor beam quality (M^2 approximately 15-100). The flash lamp can be replaced by using a diode laser that has higher better efficiency (30-40%). This produces much better values of M^2 , as low as 1.1.

8.2.3 Diode Lasers

Diode lasers are very similar to Nd:YAG lasers where electrical energy is translated via the diode into electron excitation and eventually light is emitted. Usually they are grouped and stacked together to form high power lasers. Semiconductor materials have a bandgap such that if the electrons have enough energy (provided by an electrical field) they convert from a non-conductive state to a conductive state. Part of this change of state can release photons, similar to the laser actions already discussed. GaAs is a common type. It has a bandgap energy of 1.35 eV corresponding to a wavelength of 905 nm. Diode lasers have the advantage of being small and affordable.

Diodes tend to emit over a frequency range but they can be tuned by a grating. Low-power diode lasers have low power conversion efficiencies of around 2% whereas high power diode lasers have high power efficiencies up to 30%. A 5 μm wide strip can produce 100

mW of power, a 50 μm wide strip can produce 0.5 W, and a 500 μm wide strip can produce 4 W. Stacking such arrays can produce even more power although they usually have high divergence values that make them unsuitable for laser applications.

8.2.4 Excimer Lasers

Excited dimer molecules (hence excimer) decay and release their laser radiation. The excited dimer Kr^+F^- , lasts around 5-15 ns and the photons produced are in short pulses of 20 ns that are spread in a 0.4 nm band, which is large but the power is around 35 MW (0.2 J/Pulse).

8.2.5 Ti:Sapphire Lasers

Ti:sapphire lasers produce pulses in the femtosecond time regime. Short, low-power nanojoule femtosecond pulses are created by an erbium doped fibre laser. Amplification of these low-power pulses is required to produce a useful power output, but there are problems associated with this. These problems are overcome by using chirped pulse amplification (CPA). The pulse is stretched, amplified, and then compressed to create a high-intensity femtosecond pulse.

The problem with directly amplifying short pulses is their tendency to stretch in time, the pulse may be amplified but it will no longer be on the femtosecond timescale. Femtosecond pulses also tend to destroy the medium through which they travel. CPA avoids these problems by the basic principle of stretching short pulses to reduce the peak intensity. The pulse is then compressed back to the original time scale. The femtosecond pulse is made up of several wavelengths. The diffraction gratings or chirping mirrors separate out the different wavelengths of the pulse. This is done because the grating causes the individual frequencies to reflect at different angles. Thus light from the same pulse travels different distances, which tends to stretch the pulse and reduce the peak intensity. The stretched pulses are let into the regenerative cavity for amplification. The pulse is sent along a certain path. At a point in this path it passes through a Ti:sapphire crystal which is the gain medium, and this is

pumped by an Nd:YAG laser. Each time the stretched pulse passes through the cavity it gains a little more energy, receiving a boost from the interactions in the cavity. Along a part of this path there is a component that reflects the pulse if it is not of high enough energy. It is then sent back into the regenerative amplifier to gain more energy until it reaches some critical value. When this value is reached, the pulse encounters the device and it now has enough energy to escape from. Thus, the pulses have been amplified in terms of power but are stretched in terms of time. An exact reversal of the process that stretched the pulse is now applied to recapture the original pulse length. The pulses are now at full power and are on the femtosecond timescale. The pockel cell and polarizer perform the tasks of timing entry of pulses into the regenerative amplifier and determine how the pulses are let out of the cavity and how the gain is received.

8.2.6 Beam Characteristics

Ideally the beam is Gaussian in shape. The cross section shows the intensity of the beam. The beam is defined when 86.5% of the energy is across its diameter. Not all beams are ideal, e.g. the hot spot may be shifted slightly to the right (Fig. 8.3). This means that the laser cavity needs adjusting to correct the beam profile. The profile of the beam can be obtained by making an image in a material or by using three-dimensional beam profiling cameras that are available that describe the beam profile and intensity variations within that profile (Fig. 8.4).

The beam may be affected by the optics and apertures it travels through; for example if it passes through a small hole it could become diffracted (Fig. 8.5). Eventually the propagating beam will naturally spread out but stays parallel better than any other light source. The laser light spreads out owing to diffraction; the waist being the minimum diameter of the beam denoted W_0 . It is at this point that it becomes sensible to focus the beam on the surface. However, all is not lost if this is not achieved. Either side of W_0 is the Rayleigh length, this is a length where the beam is still highly focused and though not ideal, laser ablation can still be achieved.

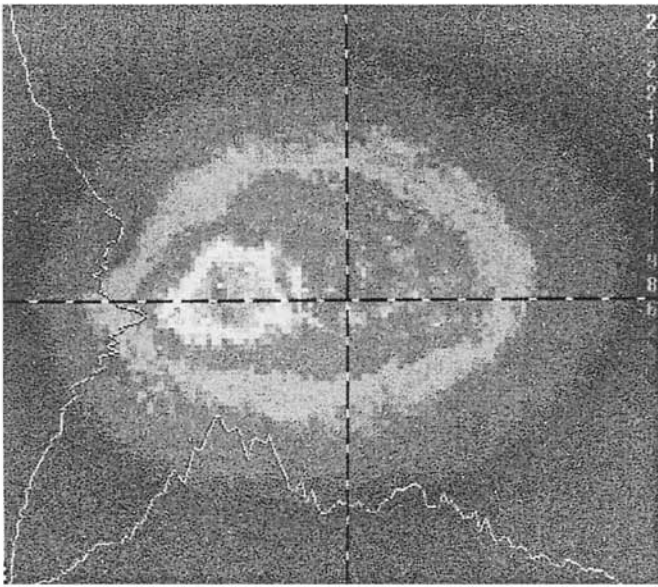


Fig. 8.3. Eccentric beam profile

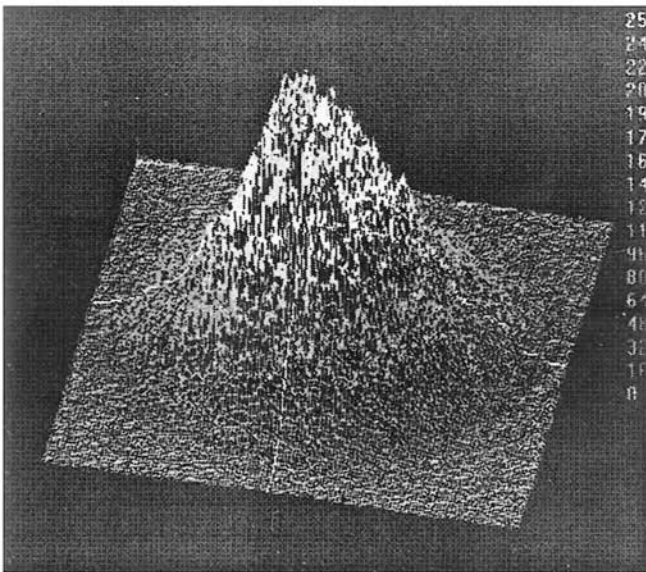


Fig. 8.4. Three-dimensional laser beam profile

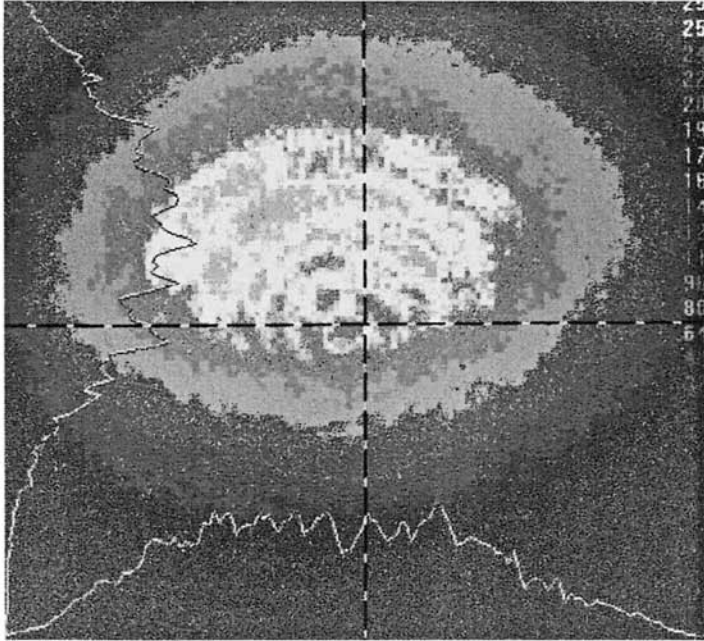


Fig. 8.5. Effects of diffraction on the laser beam

8.2.7 Laser Optics

Optics are used to change the diameter of the beam (increases the power, supplies the beam to a device with a specific inlet diameter, and changes the focal distance to the substrate), the direction of the beam, or the intensity of the beam. The conventional laws of optics apply but special care must be taken in terms of coatings and the material the optic is made from. For an ideal beam,

$$\theta W = \lambda / \pi \quad (8.1)$$

The realistic laser beam equation is:

$$\theta W = M^2 \lambda / \pi \quad (8.2)$$

Where, θ = half the divergence angle, ω = beam waist size, and λ = wavelength. As everything is ideal here this expression is true over the whole length of the beam. However, in reality perfect conditions never exist. M^2 is a beam quality number, which is one for a perfect beam. The minimum spot size can be found in the following way;

$$\theta_f = D/2f \quad (8.3)$$

Resulting in a minimum spot size,

$$\delta = \frac{4}{\pi} M^2 \lambda \frac{f}{D} \quad (8.4)$$

Where, f is the focal distance, D is the lens diameter, and δ is the minimum spot size diameter. Minimum spot size governs the minimum feature size. Remember that in conventional machining small features can be created with relatively large cutting tools. Clearly M^2 is an important parameter to control as it one of the major influences of the minimum spot size. Hence, a high-quality beam is desirable for micromachining. For micromachining, a small spot size is required. This is obtained when $M^2=1$, with a short wavelength, and a short focal lens length. Examples of beam properties are shown in Table 8.1.

8.2.8 Optical Quality

The laser cavity geometry affects the quality of the beam. Cavity length and mirror configuration cause different types of laser spot to be produced. Oscillating light between the mirrors is not forced to travel along the optical axis. It is these oscillations that create transverse electromagnetic modes (TEM). The number of off-axis modes is described by the Fresnel number, $N = a^2/\lambda L$, where N is the Fresnel number, a is the radius of output aperture, and λ is the wavelength, and L is the cavity length. Off-axis oscillations would be visible on a screen placed at mirror B when differences in wave-

lengths between on-and-off axis oscillations differs by a whole number of wavelengths n when using Pythagoras' theorem.

Table 8.1. Properties of laser beams

Laser	Wavelength, λ (μm)	Power, P (W)	w. θ (mm.mrad)	Beam quality, M^2	Spot di- ameter with f/4 lens, δ (μm)
HeNe	0.63	0.002	0.2	0.98	3
Fine drill- ing	1.06	100	6	10	50
Nd:YAG					
Nd:YAG	1.06	1000	25	80	500
Q-switched	1.06	10	2	3	15
Nd:YAG					
Q-switched	1.06	100	6	10	50
Nd:YAG					
Q-switched	1.06	1000	25	80	500
Nd:YAG					
CO ₂	10.6	1000	10	1.5	80
Copper va- por	0.51	20	0.5	3	8
Ti:Sapphire	0.78	1			
Excimer	0.193-0.351	100	20	200	

The laser cavity geometry affects the quality of the beam. Cavity length and mirror configuration cause different types of laser spot to be produced. These are known as transverse electromagnetic modes or TEM. Hence,

$$a^2 + L^2 = (L + n\lambda)^2 \quad (8.5)$$

Simplifying and ignoring the $n^2\lambda^2$ term because it is very small

$$a^2 = 2Ln\lambda \quad (8.6)$$

$$n = a^2/(2L\lambda) = (\text{Fresnel number})/2 \quad (8.7)$$

Low Fresnel numbers yield low order modes; the off-axis oscillations are lost by diffraction and cannot aid in the amplifying process. Table 8.2 shows examples of laser types, Fresnel number, and modes. Transverse electromagnetic modes of the laser beam are shown in Table 8.3.

Table 8.2. Types of industrial laser [1]

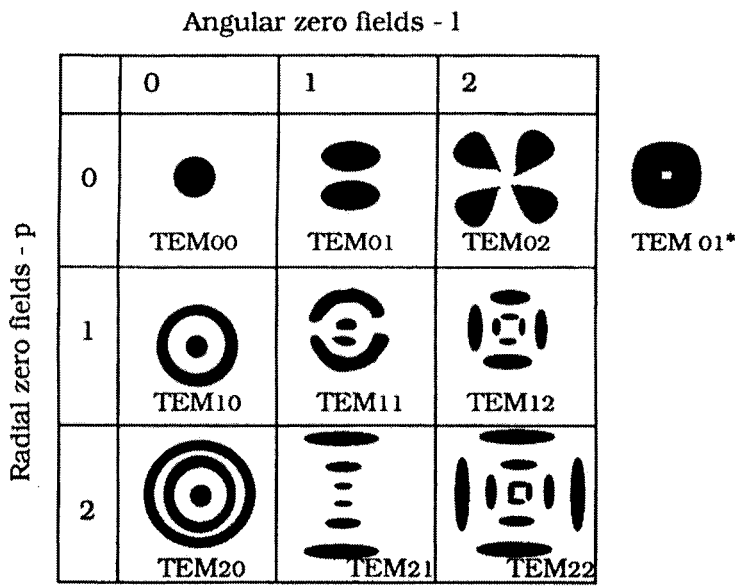
Model	Dimensions of Typical Industrial Lasers			
	Cavity radius mm	Cavity length m	Fresnel number	Mode
Laser Ecosse MF400	3.5	14.4	0.8	TEM01*/TEM00
Electrox	9	3.4	2.2	TEM01*
PRC1500	9	3.4	2.2	TEM01*
Control 2kW	17.5	6	4.8	Low
PRC3000	11	5.17	2.2	TEM01*/Low
Laser Ecosse AF5	10	15	0.6	TEM00 controllable

8.2.9 Laser Material Interactions

The principle of laser material removal is that laser light is focused on the material surface where energy is absorbed. This energy is converted to heat. The maximum depth where absorption occurs is called the penetration depth and leads to the conduction of heat into the material. The energy absorbed for a CO₂ laser is about 20%, for a Nd:YAG, or for a femtosecond laser is approximately 40 – 80; and

the rest is reflected. Special care must be taken with optics, special anti reflective coatings must be applied to prevent beams in unwanted areas of the system. Laser energy is converted to heat only as far as the penetration depth. At the penetration depth the power density is approximately $1/e$ of the original density at the surface. For a CO_2 laser this is about 15 nm, for an Nd:YAG laser this is about 5 nm. Conduction of heat into the bulk depends on the time-scale of the pulses.

Table 8.3. Transverse electromagnetic modes [1]



The mechanism that lasers use to remove material is called ablation. Ablation is achieved by melting and vaporizing the material, which is then ejected from the vicinity of the surface and is governed by power density. However, the ejected material can be deposited near to the melt region where it freezes and is known as the “re-cast” layer (Fig. 8.6).

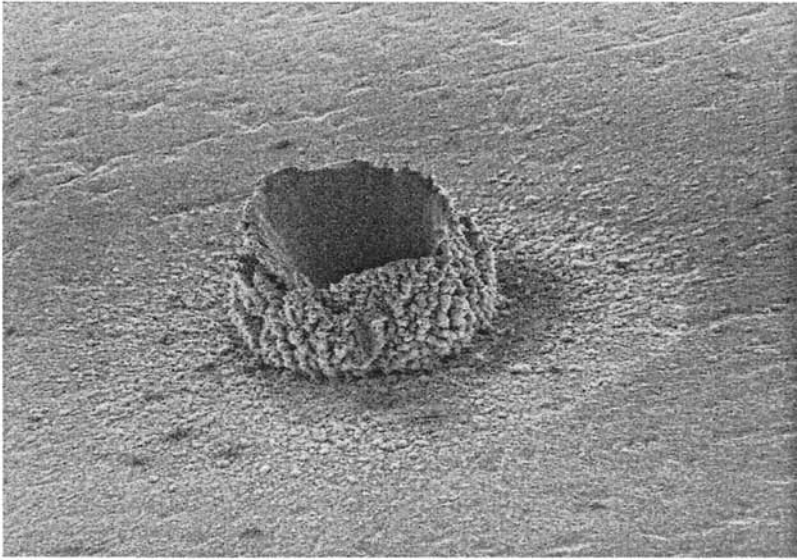


Fig. 8.6. Re-cast layer created close to the melt region

For a power density of 10^{-9} W/cm^2 the melting point is reached in 300 ns, if the power density is increased 10-fold this time is reduced 10-fold to 3 ns. The high vaporization rate then causes a shockwave that can reach speeds of 3 km/s. Expulsion of material occurs because of high pressure created in the melt and explosive-like boiling of the superheated liquid after the end of the laser pulse. This ejected material can re-form; sometimes it is not always totally vaporized, especially if it is from a deep trench that may cool quickly and reform. Nanosecond lasers produce heat flow whereas femtosecond lasers do not because no melt pool has been produced. Femtosecond laser pulses machine with minimal heat generation where the heat affected zone (HAZ) is given by the equation, $\text{HAZ} \sim (D.t)^{1/2}$, where D is the thermal diffusion coefficient and t is the pulse duration. Heat flow produces the melt pool, around which the bulk of the material heats up. If rapid heating occurs then the damage to the material is incurred at a greater depth than is desired, this

is the heat-affected zone (HAZ). Clearly the relationship, $HAZ \sim (D.t)^{1/2}$, states that shorter pulse durations will decrease the amount of HAZ. The diffusion length for a 20 ns laser is 365 times longer than a 150 fs laser. The nanosecond diffusion length is 1×10^{-4} m, and the approximate diffusion length for metals is 1×10^{-6} m. The femtosecond diffusion length is approximately 4×10^{-7} m, where a femtosecond is equal to 10^{-15} tenths of a second. Materials react to induced heat pulses in picoseconds, i.e., 10^{-12} tenths of a second. Therefore, the material can be heated and removed before the surrounding material can react; hence there can be no heat flow in the femtosecond case. Material at the top of the surface is removed by evaporation, and at the sidewalls of the hole or trench material is forced away by the plasma. Both effects cause re-deposition of material elsewhere.

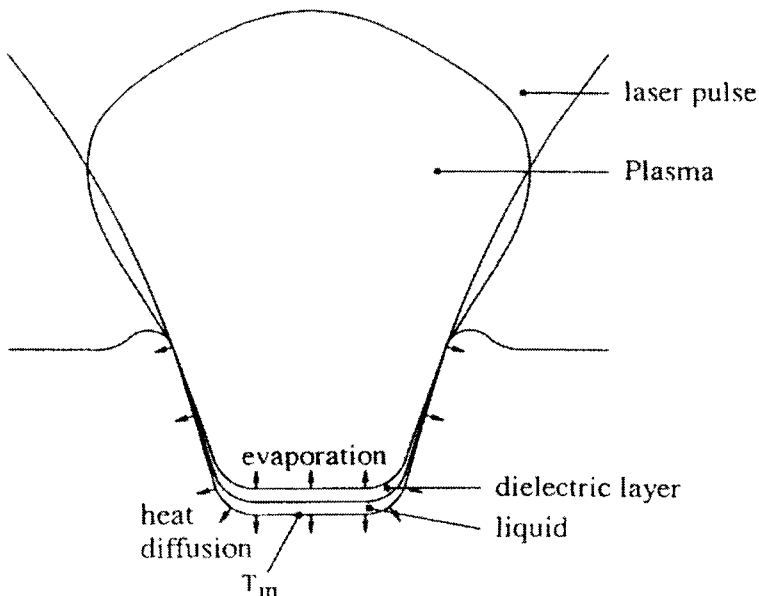


Fig. 8.7. Relationship between plasma generated during laser pulse interaction with the workpiece material and its surroundings [2]

Plasma pressure is exerted on the liquid, at the end of the pulse, the pressure suddenly drops and causes boiling of the superheated liquid to occur. Ablation occurs at the end of the pulse, and it has been discovered that for a given fluence there is a maximum ablation depth for a given pulse length. Material removal rates can be difficult to calculate due to re-deposition of molten material.

Ablation of metals is caused by the absorption of laser energy that is a three-step process: (1) Absorption of photon by electrons (10^{-15} s); (2) energy transferred to the lattice (10^{-12} s); and (3) heat transferred to the lattice (10^{-12} s). Ablation at the end of the pulse is due to the relatively thick superheated layer, which continues to evaporate as long as the surface is above the boiling temperature (Fig. 8.7). Re-deposition may occur in the path of a track, which has yet to be machined. In this case more material has to be removed. Deposition may occur elsewhere in a non-critical area. This is what makes calculating material removal rates difficult. In the case of femtosecond pulses during the solid-to-liquid transformation there is no melting because it happens so quickly that it is considered instantaneous. Owing to this effect, there is no heat transfer and there is a debate as to whether the HAZ exists or not.

If the HAZ does exist then the heat source could come from the plasma. It is expelled and extinguished rapidly, but a new one is also created just as rapidly. This means that a constant plasma heating source needs to be controlled by scan speed and power, i.e., process parameters. The types of laser discussed thus far produce pulses on the nano, pico and femtosecond scales. Each time frame has different characteristics for material removal.

8.3 Laser Microfabrication

8.3.1 Nanosecond Pulse Microfabrication

Electromagnetic waves interact with the particle on the surface of the material, the electron will re-radiate, or be constrained by the lattice; if enough energy is put into the material the lattice breaks down and the material begins to melt. Further heating causes evaporation and plasma formation to occur. When laser radiation hits a surface it is absorbed, transmitted or reflected depending on the material. The laser radiation that interacts with the particle has a magnetic and an electric component. When the radiation passes over a small elastically bound charged particle the particle is set in motion by the electric field. This induced force is so small it cannot affect the nucleus but can affect the electrons. If the electrons were left to vibrate there would be no net gain in its energy, e.g., its motion would be in the form of a sinusoidal wave, a few positive and a few negative motions resulting in zero energy change. However, if the electrons are involved in a collision, the path will be upset and they will gain some energy. If the radiation is at a lower potential than the ionization energy for the particles then no absorption occurs.

Usually there are free or conduction electrons available for this purpose, which are called seed electrons. Once the seed electron gains enough energy then further collisions will cause ionization. There are now two electrons with low kinetic energy this process is called impact ionization. This process happens repeatedly where the free electrons grow from the seed electrons exponentially.

Eventually the material is broken down until a critical plasma density is reached and the dielectric material becomes absorbing.

This is called the inverse Bremsstrahlung effect, where Bremsstrahlung is the emission of photons from excited electrons.

If the particle is constrained by the lattice by its bonding energy, vibrations will be induced that spread throughout the structure; this is registered as heat. The incoming beam may interact with the evaporated material causing plasma formation and shielding effects.

So after a period of time sufficient energy is absorbed and trans-

ferred to the electrons, which then in turn heat the material which leads to melting and evaporation. Avalanche ionization can then occur for a time where collisions further ionize the material releasing more material from the lattice.

Nanosecond ablation heats the specimen to its melting point then to its vaporization temperature. The ablation depth per pulse is;

$$Z_a \approx \sqrt{at} \ln \left(\frac{F_a}{F_{th}} \right) \quad (8.8)$$

Where Z_a is the ablation depth, F_a is the absorbed fluence, F_{th} is the threshold fluence, and (at) is the thermal diffusion depth. For $(at)^{1/2} = 0.5 \mu\text{m}$, a 20ns pulse gives a typical threshold fluence of 4J/cm^2 . Nanosecond pulses (10^{-9} s) are considered to be a long time-scale. The specimen is heated then the main energy is lost due to heat conduction into the bulk of the material. Bulk heating may cause phase transformations to occur that may be deleterious to the functioning of the material after machining.

As laser power intensity increases the interaction between substrate and laser progresses through a number of characteristic phases with subsequent changes in machining characteristics. As beam intensity is increased, the material begins to evaporate or ablate. Ablation starts when the temperature of the surface of the material exceeds its evaporation temperature. If the molten material is not sufficiently viscous to impede the ejection process, increases in laser intensity lead to material removal by melt ejection and vaporization. Rapid heating of the substrate melts, vaporizes, and then partly ionizes the vapor. The partly ionized vapor leaves the surface of the substrate at velocities up to 10^5 m/s. The net result of the production of a shock wave pushing the vapor and the melt droplets away from the substrate toward the laser beam is the creation of a recoil shock wave traveling away from the laser beam into the substrate. Several mechanisms will limit ablation rate. These include absorption and scattering of the laser beam by vapor and melt droplets being ejected

during laser-beam interaction. The properties of the material and laser parameters determine whether evaporation, melt ejection, or vaporization dominates the ablation process.

At higher intensities of the order of 10^9 W/cm² and with pulse lengths of nanosecond duration or shorter, the material is heated instantaneously beyond its vaporization temperature. Vaporization occurs within a very short time period at the start of the laser pulse. Energy dissipation of the laser pulse into the bulk of the material through thermal diffusion is slow relative to the length of the pulse. Before the surface vaporizes, the underlying material reaches its vaporization temperature. The temperature and pressure of the underlying material increase enormously leading to the explosion of the workpiece material at the surface.

Recoil pressures above the surface of the material can be up to 10^5 M Pa, leading to violent material ejection from the surface. High vaporisation and plasma pressures above the surface increases the mechanical load placed on the material owing to a recoil shock wave traveling away from the laser beam. Plasma-generated shock waves can also be responsible for material ejection. However, during an ablative interaction plasma is initiated at the surface. Plasma temperatures are in excess of 10^4 K and a plasma-material interaction, which is long in comparison to the short laser pulse, is established. This process is responsible for secondary heating of the substrate surface due to inverse Bremsstrahlung, or photoionization. The interaction of plasma with ejected molten material is responsible for deposition of the molten material at the kerf. This always leads to the formation of a re-cast layer at the side of a laser-machined trench. The vaporization of this material, when ejected from the trench, is of paramount importance in order to maintain the precision required by micro-manufacturing industries. The design of nozzles has a profound effect on the way molten material is ejected from the machined trench and, consequently, on the way the ejected molten material is deposited and subsequently vaporized.

8.3.2 Shielding Gas

Plasma is produced by laser ablation, which can shield the substrate and the plasma itself can then be ionized. Figure 8.8 shows

the action of the behavior of the plasma during the micromachining of steel using a laser wavelength of 1064 nm. The focus radius is between 100 μm and 300 μm .

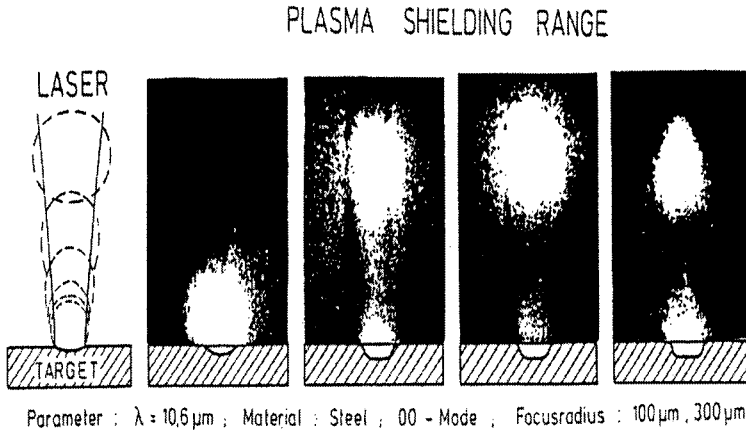


Fig. 8.8. Behavior of plasma during micromachining of steel [1]

Plasma shielding can also be beneficial. The newly exposed material is protected by the plasma from interactions with the environment, e.g., oxidization. If the plasma is ionized and the conditions are appropriate, the plasma can acquire energy from the incoming beam such that it moves away from the surface and heads toward the source of the beam. This can reduce the coupling of energy into the surface. In some cases, it blocks the path of the laser beam to the substrate and machining is halted. Various environmental gases can be used to influence this process, with the plasma being replaced with a shielding gas that requires a delivery system.

If the plasma is replaced with a gas that has a high ionization potential then ionization is made more difficult. In this way it is possible to have some control over this phenomenon. Often helium, argon, neon, and oxygen gases are used; the type of gas used depends upon the reactions that take place. Much effort has gone into the design of nozzles that have different effects on the assist gas and on the machining of materials [3-5]. Directional features include blowing a

simple gas jet that blows the re-cast layer in a particular direction, interference with the beam, which depending on the purity of the gas source, may cause the beam to reflect and become diffracted by gas contaminants, or successful removal of plasma.

8.3.3 Nozzle Designs for Laser Micromachining

Many industrial processes that use gas jets to deliver fluid pressure to a workpiece surface use simple conical nozzles. These nozzles are characterized by a minimum cross sectional area at the exit of the nozzle. Inlet pressures greater than 1.89 atmospheres for diatomic gases produce under-expanded supersonic jets that exit from the nozzle. The axial pressure distributions delivered by these jets contain significant variations in magnitude within the first few nozzle diameters along the axis of the jet. Consequently, two restrictions are imposed by the choice of such a nozzle for laser micromachining applications. First, the exit of the nozzle must be very close to the workpiece in order to utilize the maximum impact, or shear force, available in the jet. Second, the complex nature of the axial pressure distribution demands that the stand-off distance between nozzle exit and workpiece is very close in order to maintain uniform pressure at the workpiece surface. These drawbacks place limitations on the effective shear stress distribution, and hence the removal of molten material from the front of the kerf. Conventional high-speed nozzles have been used but they are associated with high shielding gas consumption and tend to generate high surface roughness features.

The alternatives to a conical nozzle are shown in Figure 8.9. The alternative designs include the use of a positive converging-diverging nozzle (de Laval) and a minimum length nozzle (M.L.N.), which can create uniform supersonic jets with specifically designed flow fields with specific properties. One such property is a highly uniform and stable pressure that extends many nozzle diameters downstream along the centerline of the jet. In order to expand an internal steady flow through a duct from a subsonic to a supersonic regime the duct has to be convergent-divergent in shape. Both nozzles exhibit uniform free jet structures especially de Laval, which if correctly designed produces a uniformly expanded jet that is free from

shock waves. Unfortunately, in laser material processing, small-scale de Laval nozzles with a very high length-to-diameter ratio, may cause problems with optical delivery. This is especially a problem for micro-laser machining applications, where the desire for a minimum laser spot size means that short focal length optics is required.

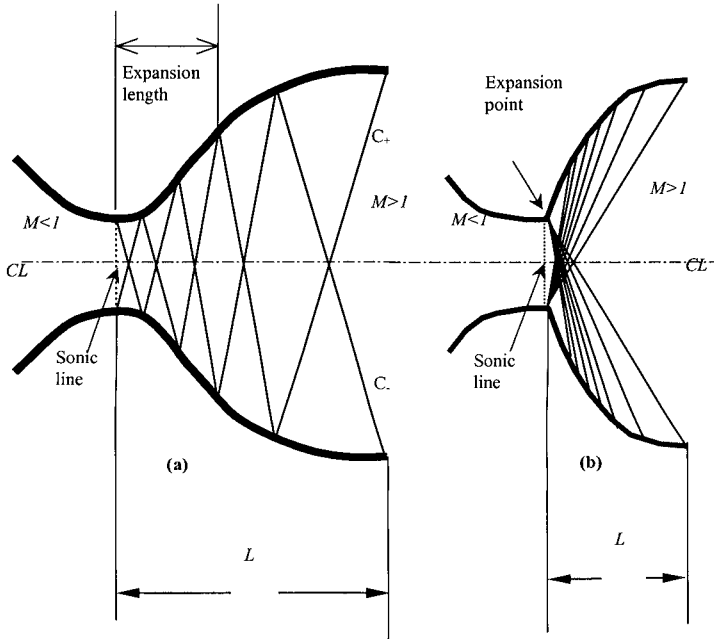


Fig. 8.9. Schematic diagram of supersonic nozzles: (a) de Laval; and (b) minimum length nozzle (M.L.N.)

Supersonic jets present significant drawbacks such as high mass flow rates and noise levels that are associated with jets of moderate size. It was shown that sound pressure levels up to 150 dB at a radius of 30 nozzle diameters for 8 mm diameter nozzle are possible.

However, miniaturized nozzles described in this study have avoided these problems by virtue of their small scale. Nozzles that have exit diameters of 1mm produce characteristic supersonic jets with low mass flow rate and low noise levels. The majority of design criteria used in micro-machining can be met by using a minimum length nozzle (M.L.N.), which were developed for use as a rocket nozzle, where minimum mass flow rates is a desirable property. This is also the case where rapid expansion is desirable, such as non-equilibrium flow in gas-dynamic lasers. Another advantage associated with minimum length nozzles is that boundary layer growth can be kept to an absolute minimum in contrast to de-Laval nozzles. This effect is noticable when nozzle dimensions are very small. A comprehensive survey of existing literature concerned with minimum length nozzles has shown that axi-symmetric and curved, sonic line M.L.N.s have been limited to gas-dynamic laser applications and rocket engines. This chapter develops techniques for the design of axi-symmetric, straight, sonic line M.L.N.s for laser micro-machining applications. A particular type of design is one in which the throat diameter is less than $300\text{ }\mu\text{m}$, which gives a fairly constant distribution of mass flow rates along the length of the nozzle between the throat and the exit region (Figure 8.10). This type of nozzle eliminates the use of exotic gas mixtures at the laser-material interaction zone.

This chapter develops computational techniques suitable for the design of an axi-symmetric, straight, sonic-line, micro-M.L.N. with a throat diameter of less than $300\text{ }\mu\text{m}$. Flow structures through the contour were modeled using FluentTM 5.4 (C.F.D.) software, and results compared with the method of characteristics (M.O.C.) algorithm. C.F.D. was also used to predict flow patterns in both laser-drilled holes and kerfs where the effects of shear stress distributions along the wall were modeled to predict flow behavior through the nozzle during laser material processing.

8.3.4 Computational Design of Nozzles

Design of M.L.N.s Using the Method of Characteristics

The design of nozzles described here is based on an inviscid flow field. The M.O.C. provides a technique for accurately designing the contour of a supersonic nozzle for shock-free, isentropic flow taking into account multidimensional flow inside the duct and assuming that the flow is non-viscous and does not form a boundary layer. In order to design a nozzle of the correct shape and to avoid the formation of a shock wave, it is necessary to examine the propagation of infinitesimally small oblique shock waves (or Mach lines) inside the nozzle.

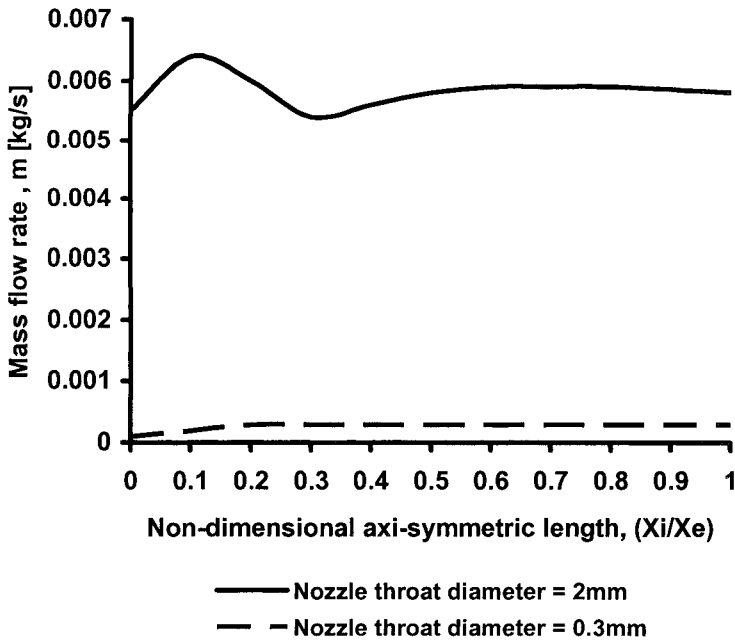


Fig. 8.10. Distribution of mass flow rates, \dot{m} , from the nozzle of the throat to the exit of the throat for a minimum length nozzle

Along the Mach lines, flow properties remain constant and they are therefore called “characteristic lines”. There are two distinct types of characteristic lines, right running and left running, which are denoted as C_+ and C_- , (Figure 8.11). The angle that the lines make with a streamline at an arbitrary angle θ to the x – axis is given by the following equations,

$$\frac{dr}{dx} = \tan(\theta - \mu) \quad \text{for } C_- \text{ characteristics} \quad (8.9)$$

$$\frac{dr}{dx} = \tan(\theta + \mu) \quad \text{for } C_+ \text{ characteristics} \quad (8.10)$$

$$\text{Where } \mu = \sin^{-1}\left(\frac{1}{M}\right) \quad (8.11)$$

Equations 8.9 and 8.10 are called the characteristic equations. When two characteristic lines meet, their directions change. For axis-symmetric flow the compatibility equations (8.12 and 8.13) describe the change in flow properties at the characteristic lines after the intersection point.

$$d(\theta + \nu) - \frac{1}{\sqrt{(M^2 - 1)} - \cot \theta} \frac{dr}{r} = 0 \quad \text{for } C_- \text{ characteristics} \quad (8.12)$$

$$d(\theta - \nu) + \frac{1}{\sqrt{(M^2 - 1)} + \cot \theta} \frac{dr}{r} = 0 \quad \text{for } C_+ \text{ characteristics} \quad (8.13)$$

The quantity $(\theta + \nu)$ is not constant along a C_- characteristic line its value depends on the spatial location in the flow field as indicated by the $\frac{dr}{r}$ term in equation 4. The same qualification is made for $(\theta - \nu)$ along the C_+ characteristic. The process of computing an axis-symmetric flow field can be achieved by replacing dif-

ferential equations 8.12 and 8.13 with a finite difference solution. Flow properties and their locations are found by a step-by-step solution of these equations, which when coupled with the characteristic equations 8.9 and 8.10, are used to construct the characteristic net.

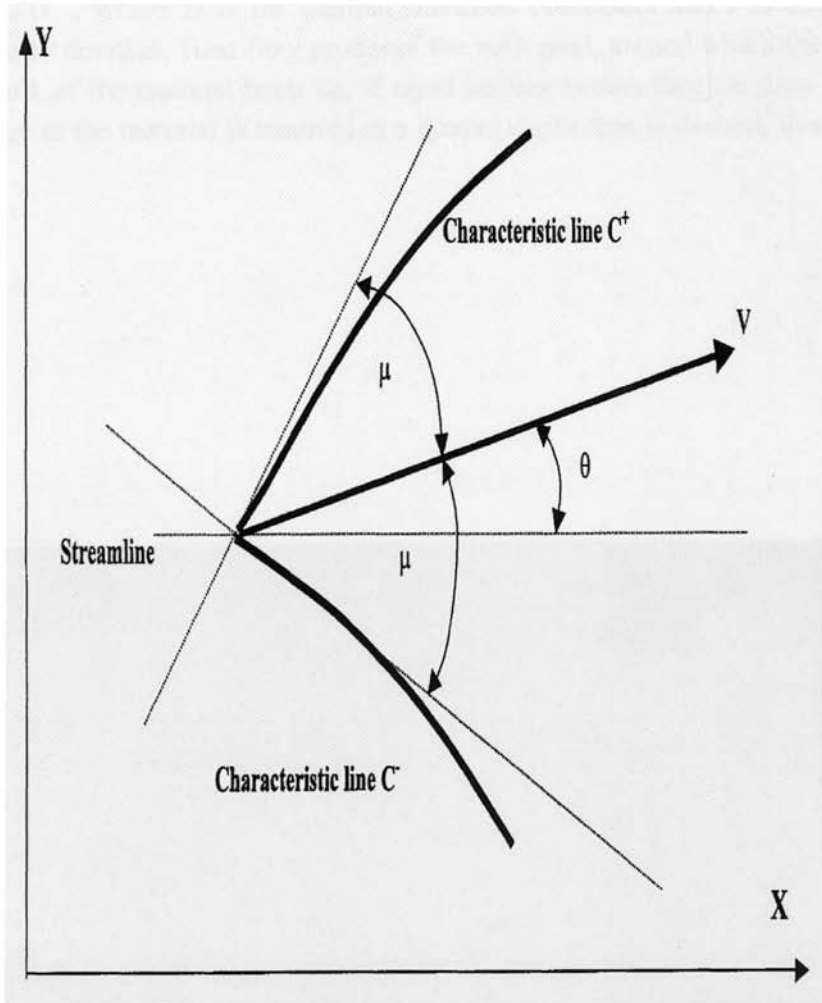


Fig. 8.11. Part of the characteristic net showing left- and right-running characteristic lines

The calculation process starts at the throat of the nozzle and is independent of flow conditions upstream to the flow. The characteristic equations are solved in the form of iterations using new values of properties at intersections, and locations obtained from compatibility equations, in the form of a finite difference. By calculating the gradients of new C_- and C_+ characteristic lines, the solution of the conditions at the nozzle contour can be obtained by propagating downstream from the initial data line. By analyzing the intersection of each Mach line in the flow regime, a nozzle shape of shock-free, isentropic flow can be predicted. The intersection point of two Mach lines are obtained with the Euler-predictor scheme, while the corrector scheme iterates the predicted property and updates the intersection point until the desired convergence criterion is obtained.

The computation process starts at the throat radius, point A (Figure 8.12), with a known value for θ_{maximum} , which is the maximum expansion angle that can be obtained using the Prandtl-Meyer function, $\nu(M)$, for a required Mach number and is given by the following equation,

$$\nu(M) = \left[\frac{\gamma + 1}{\gamma - 1} \right]^{1/2} \tan^{-1} \left[\frac{\gamma - 1}{\gamma + 1} (M^2 - 1) \right]^{1/2} - \tan^{-1} (M^2 - 1)^{1/2} \quad (8.14)$$

$$\text{Therefore, } \theta_{\text{maximum}} = \frac{\nu(M)}{2} \quad (8.15)$$

If we assume that $\Delta\theta = \Delta\nu = \frac{\theta_{\text{max}}}{N}$, then we can assume that an array, N , exists whose angular spacing decreases as the boundary, AB, is approached. The result is a highly non-uniform grid near the throat of the nozzle. Consequently, the contour of the wall downstream of point A is poorly represented. After a small duration in time during the computation, the contour is corrected by a grid compression scheme. Additional characteristics starting at point A are inserted between the sonic line and the first angular C_- characteristic.

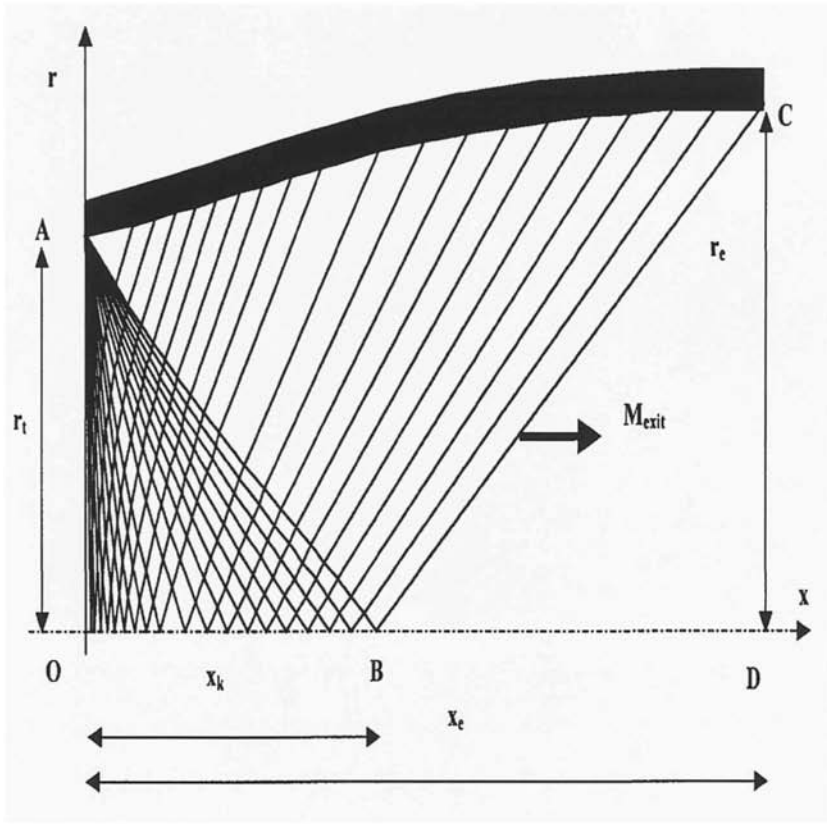


Fig. 8.12. Schematic diagram of the flow field inside the minimum length nozzle

A power law distribution is used, thus,

$$\nu_j = \theta_j = \left[\frac{j}{N_j} \right]^{M_j} \Delta \nu \quad (8.16)$$

Where, $j = 1, 2, 3, \dots, N_j$, and M_j and N_j are fixed integers that are not incremented with j . Figure 8.13 shows the effects of grid compression using the following data: specific heat ratio (γ) = 1.4; array size (N) = 10; and exit Mach number (M_{exit}) = 2.065. Figure 8.13a shows the basic grid with no compression, while Figure

8.13b has intermediate compression assuming $N_j = 5$ and $M_j = 2$. Five additional characteristics are inserted upstream of the first C -characteristic. A greater degree of compression is used in Figure 8.13c, where N_j and M_j are both five, but are positioned much closer to the sonic line and results in a satisfactory wall contour. Grid compression provides a better representation of contour location in the straight section specifically designed to cancel all the expansion waves generated by the sharp corner. The wall contour is determined by calculating the boundary streamline AC as shown in Figure 8.14. This is accomplished by solving an ordinary differential equation (Eq. 8.17) with initial conditions set as, $\theta_w = \theta_{\max}$, at the following boundary condition, $x = 0$. The following equation holds true,

$$\frac{dr_w}{dx} = \tan \theta_w \quad (8.17)$$

Where r_w is the throat radius and it should be noted that equation 8.17 is solved by iteration using Euler's predictor-corrector scheme. The iteration procedure terminates when the BC boundary characteristic is reached and when $\theta = 0$.

It should be noted that the prediction of a nozzle contour does not take into account viscosity of the fluid and hence it ignores the formation of both subsonic and supersonic boundary layers, which may adversely affect the performance of a small diameter nozzle.

The presence of a boundary layer on the nozzle wall lowers the exit Mach number, compared to inviscid flow predictions that are based on an area ratio. Four nozzle profiles with throat diameters ranging from 50 μm to 300 μm were generated using the C.F.D. computer code. To compensate for the formation of a boundary layer, the contour was displaced by the boundary layer displacement thickness δ^* . This displacement thickness was calculated using flat-plate compressible flow boundary layer theory in association with the Van Driest compressibility factor. Figure 8.15 shows both corrected and non-corrected minimum length nozzle contours for a nozzle with a throat diameter of 300 μm and inlet pressure of 8 bar.

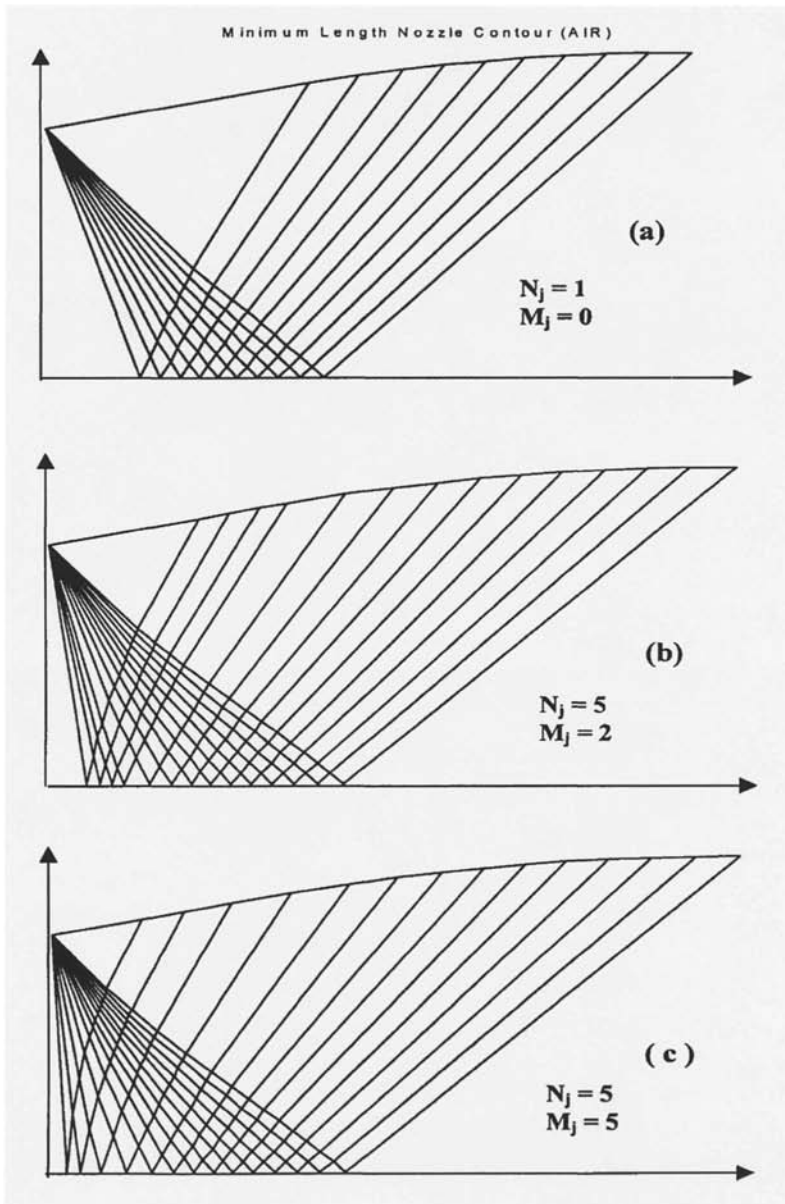


Fig. 8.13. Schematic diagram showing grid compression of the flow field in the minimum length nozzle

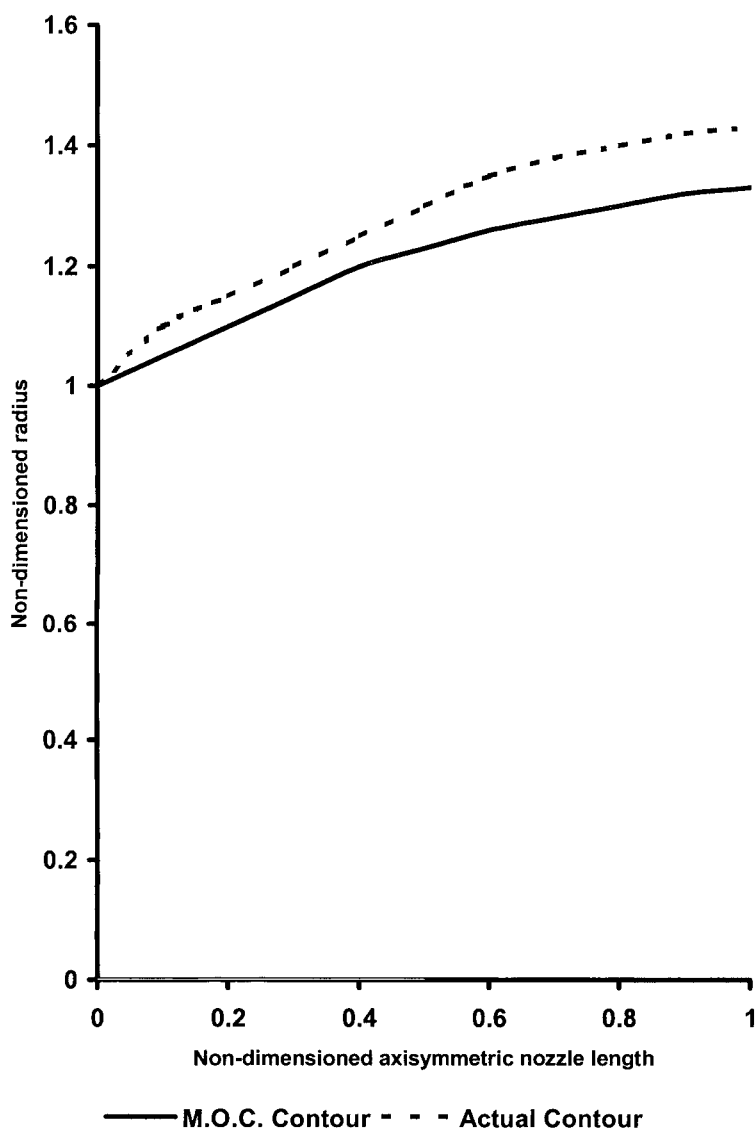


Fig. 8.14. Schematic representation of minimum length contour shown in non-dimensional parameters, r_{inner}/r_{throat} (non-dimensional nozzle radius), and x_l/x_e (non-dimensional axisymmetric nozzle length)

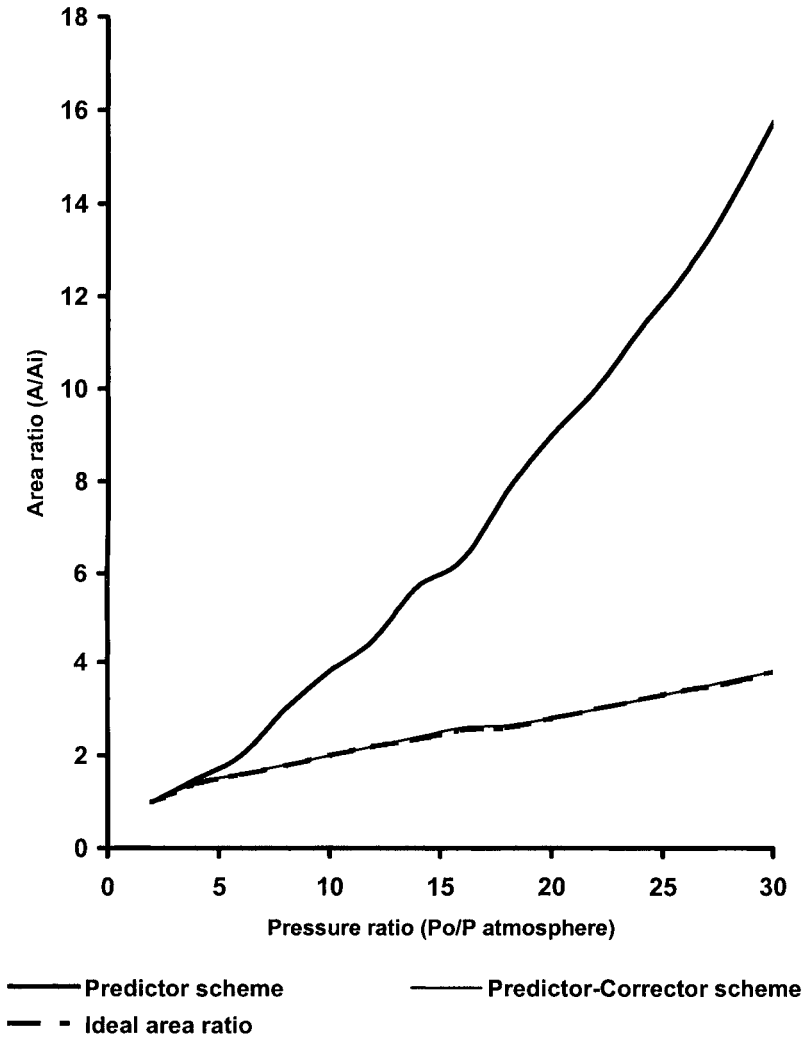


Fig. 8.15. The effect of using different computational techniques on the area ratio (A/A_i) and pressure ratio ($P_o/P_{atmosphere}$) of the minimum length nozzle

A computer program was developed using MATLABTM software for designing an axi-symmetric, straight, sonic-line M.L.N., with a

sharp throat corner. A design inlet pressure of 8 bar was used for air ($\gamma = 1.4$). Using a simple one-dimensional relationship the theoretical exit Mach number was calculated to be 2.0415. Results obtained from the computer programme gave an exit Mach number of 2.065, an error of 1.15%. It should be remembered that the exit Mach number controls the expansion ratio. Figure 8.15 shows the importance of using the predictor-corrector algorithm. It should be noted that the exit Mach number is related to the nozzle area ratio.

Description of the Flow Field Used for C.F.D. Validation

C.F.D. results show that the flow field of supersonic jets can be characterized by three distinct regions. The core region of the jet is that region where the flow has reached the desired Mach number, and where viscous effects are negligible.

In the perfectly expanded condition, a uniform maximum velocity and uniform pressure exists throughout the length of the core region. The supersonic region extends beyond the inviscid core, and flow in this region is affected by viscous forces, but remains above sonic speed. This region surrounds the core and can be characterised by the supersonic length, L_s .

The velocity profile within the supersonic mixing region is continuous and has a maximum value on the centerline. The third region shown is the subsonic mixing region that surrounds the supersonic jet. The outer radial boundary of this region is by definition, the boundary of the jet itself. It is often defined as the radial position where the axial velocity is some specific percentage of the centerline velocity. At a position beyond L_s the velocity profile is subsonic and becomes fully developed.

In order to expand the flow in a perfect manner, the contour of the nozzle has to be convergent-divergent in shape with specific curvature in the expanded section for the flow to follow the streamline. If the phenomenon does not exist then the flow will under- or over-expand depending on the inlet conditions for a similar area-nozzle ratio. C.F.D. results of three types of nozzles i.e., sonic, convergent-divergent, and minimum length nozzle, with throat diameters of 300 μ m and an inlet pressure of 8 bar are shown in Figure

8.16. The flow in the convergent-divergent nozzle is under-expanded for a given condition, whereas the sonic nozzle will always be under-expanded for inlet pressures above 1.89 bar pressure.

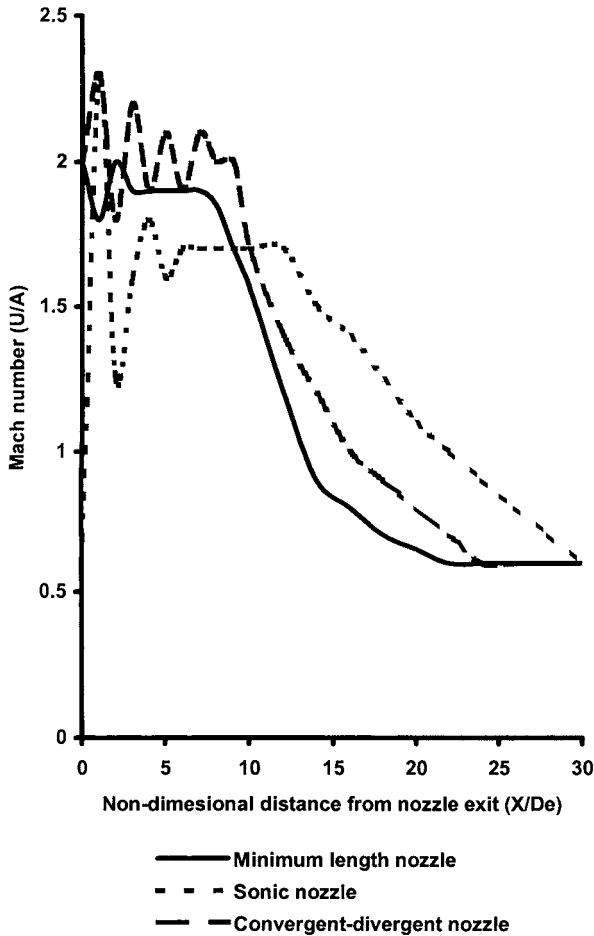


Fig. 8.16. Centreline Mach number distribution for three types of nozzles with a throat diameter of $300 \mu\text{m}$

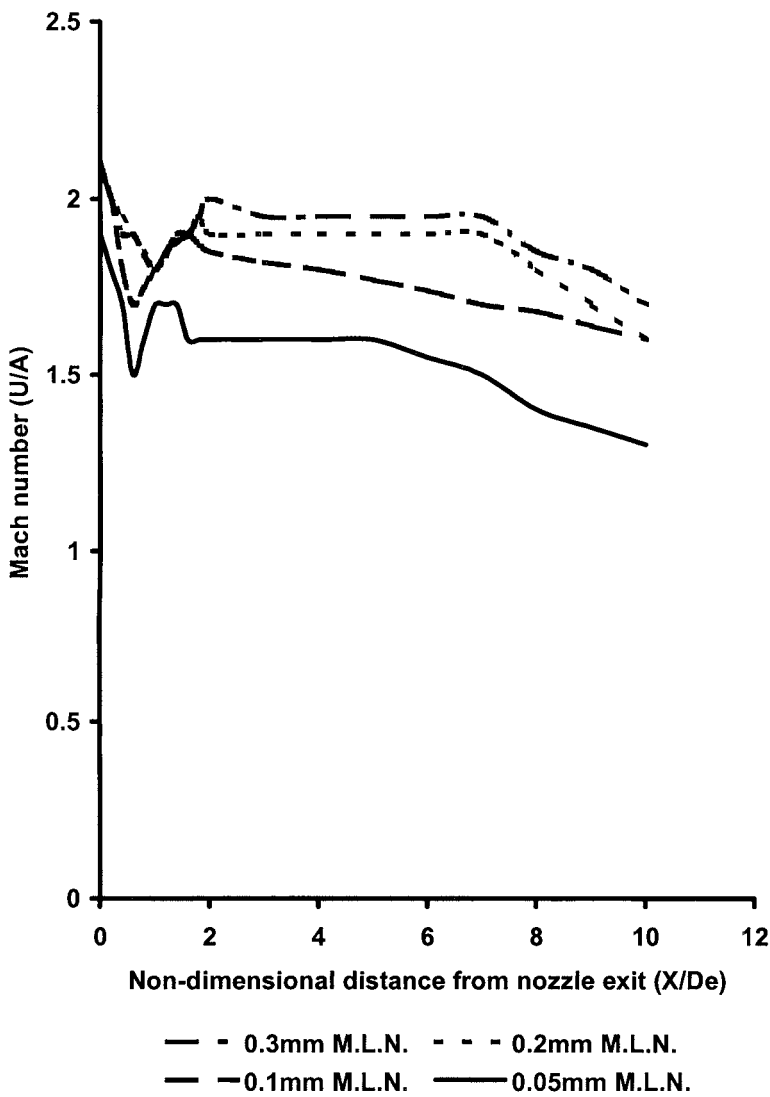


Fig. 8.17. Mach number distribution about the centreline of a minimum length micro-nozzle

When the highly under expansion condition is reached, the presence of a Mach shock disc exerts a large penalty on the centerline pressure distribution. The loss increases with increasing exit Mach number. The downstream exit Mach number distribution is not significantly increased by raising inlet pressure once the Mach shock disc forms. Sonic nozzles reach this condition very quickly with inlet pressures as low as 2.6 bar pressure. Therefore, the location of stand-off distance becomes extremely critical. Conversely, the convergent-divergent nozzle is under-expanded slightly in comparison with the sonic nozzle, but the Mach number fluctuation is still significant for laser micro-machining applications and applications where surface roughness is the governing factor. M.L.N.s provide the best possible results with uniform potential cores and very small fluctuations in Mach number distribution (Figure 8.17).

Validation of M.L.N. Contours

Predictions of supersonic nozzle flow structures using the M.O.C. inviscid contours were solved using a C.F.D. linear finite volume method. The turbulence model used was the re-normalized group-based (R.N.G.) $k - \varepsilon$ model, derived from the instantaneous Navier-Stokes equations. The near-wall treatment was in non-equilibrium. The geometry and grid were drawn in the pre-processor using non-equilibrium mesh seeds to analyze boundary formation. Figure 8.18 shows the Mach number distribution inside the nozzles along the axi-symmetric line when a viscous R.N.G. first-order diffusive model is computed through an inviscid geometry predicted by the M.O.C. theory.

As predicted by the M.O.C. theory, the exit Mach number is reduced owing to boundary layer formation. This effect is enhanced as the throat diameter of the nozzle is reduced. If a smaller diameter nozzle is used then the boundary layer is proportionally larger. Figure 8.19 shows Mach number distributions for corrected boundary layers in M.O.C. inviscid contours.

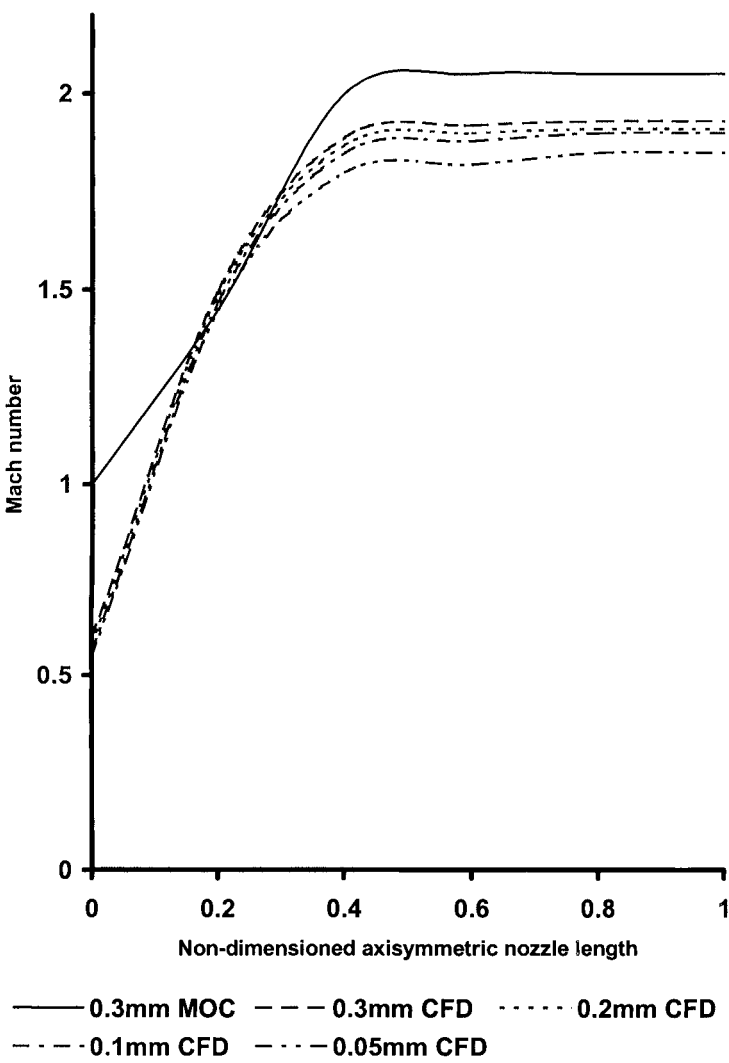


Fig. 8.18. C.F.D. generated viscid flow through a non-corrected boundary layer minimum length nozzle inviscid contour. The results are presented as Mach number (U/A) as function of non-dimensional axisymmetric nozzle length (x/x_e)

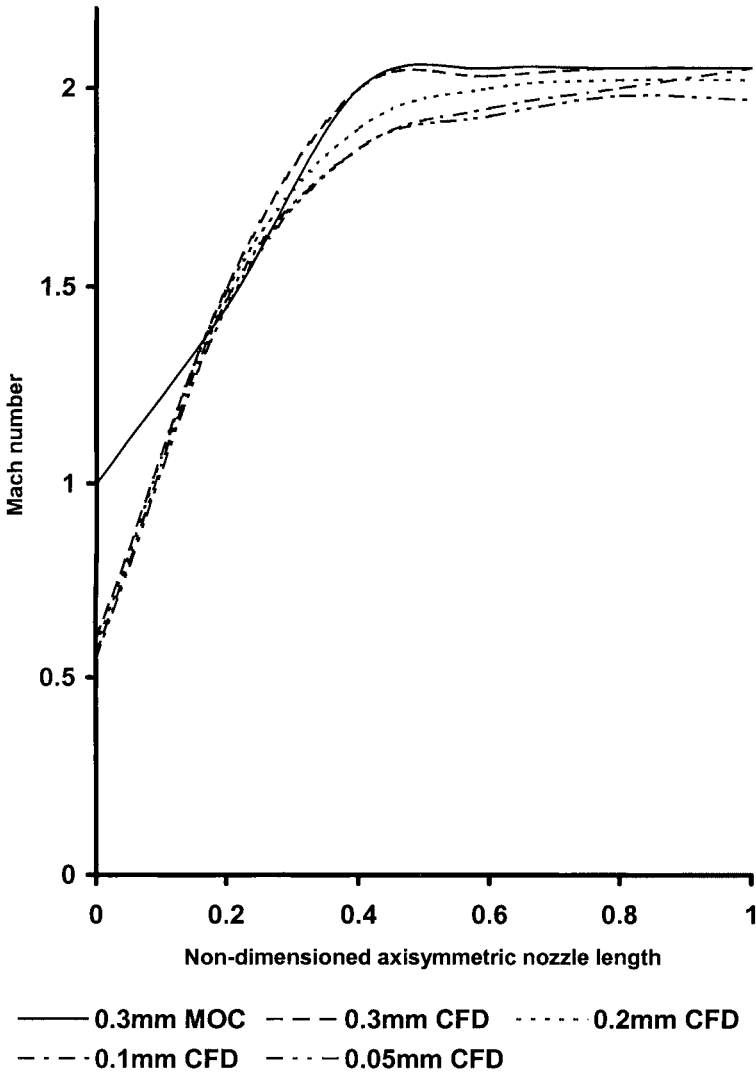


Fig. 8.19. C.F.D. generated viscid flow through a corrected boundary layer minimum length nozzle inviscid contour. The results are presented as Mach number (U/A) as function of non-dimensioned axisymmetric nozzle length (x/x_c)

When the inviscid contour is displaced by the displacement thickness, all contours from the M.O.C. are representative of C.F.D. flow propagation predictions. If the flow is supersonic, especially at high Mach numbers, a second order diffusion model must be used to highlight areas of interest, i.e., shock capturing, boundary layer information, etc. The M.O.C. has provided a very accurate method of predicting supersonic nozzle contours for both de Laval and M.L.N.s. M.L.N.s offer many advantages over de Laval, not only due to its small scale in contrast to de Laval, but because boundary layer formation in M.L.N.s is at a minimum level. This is advantageous when designing supersonic micro-nozzles allowing nozzle diameters to be as small as 50 μm .

C.F.D. models using a M.L.N. with a throat diameter of 300 μm and exit diameter of 429 μm were generated for drilled holes and kerf geometries in 1 mm thickness materials. In these circumstances the inlet pressure was set at 8 bar, and the nozzle stand-off distance was 1 mm. Figure 8.20 depicts two holes drilled to a depth of 250 μm , one with a diameter equivalent to the nozzle diameter, the second hole being eight times smaller.

Although the results represent an ideal case, in reality the hole geometry would be dependent on the pulse shape, ablation mechanism, and the dynamic characteristics of the plasma. The finding suggests that a blunt-body normal shock is present on the surface. This shock wave induces higher compressibility in the jet, producing oblique shocks upstream to the flow. Bow-like structures above the entrance to the hole represent a normal shock wave producing a diamond-shaped pattern above the normal shock in the oblique shock region. As flow properties across the shock wave change, the pressure and density increase while velocity decreases significantly. This phenomenon is further represented in Figure 8.21 as velocity vector diagrams that indicate the direction and magnitude of flow inside the processing region. The flow structures show signs of flow separation, stagnation regions, and vortex formation. The primary mechanism for removing molten and evaporated material either in the drilling or cutting process is initiated by the pressure gradient between the interaction zone and the surrounding atmosphere. Use of a supersonic assisted gas jet to remove molten material from the hole may have an adverse effect on the process mechanism.

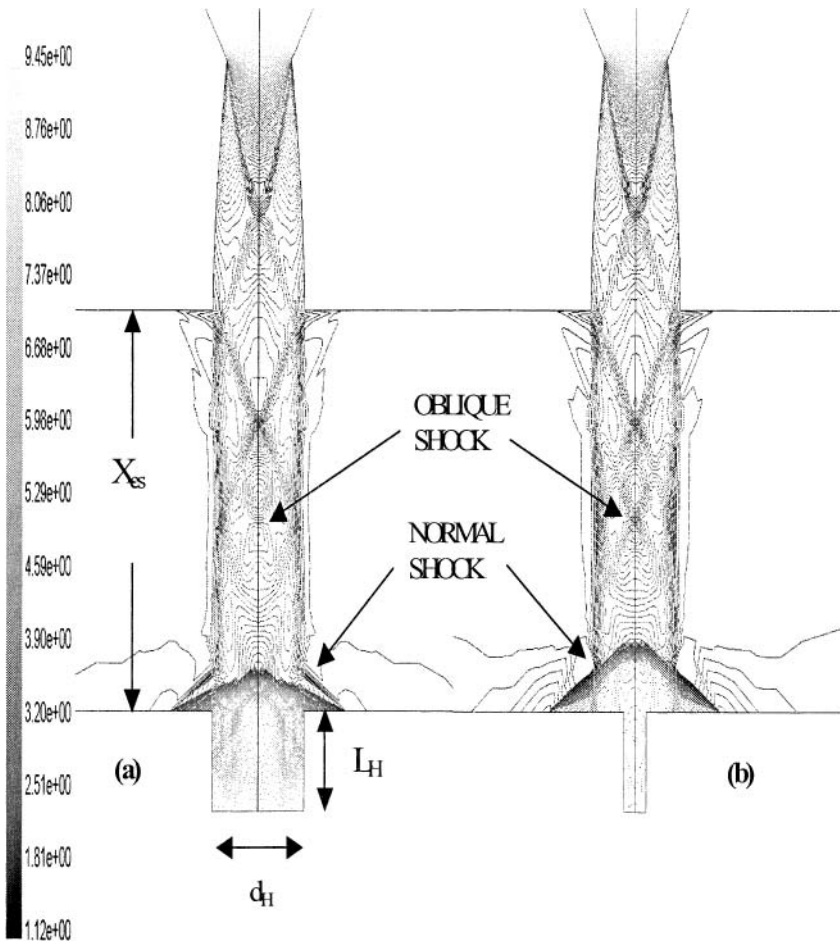


Fig. 8.20. C.F.D. generated density distribution in the jet stream that impinges onto the surface of the laser-machined surface. (a) Hole diameter, $d_H = 429 \mu\text{m}$, and length $L_H = 250 \mu\text{m}$; (b) hole diameter, $d_H = 53.6 \mu\text{m}$, and length $L_H = 250 \mu\text{m}$. Stand-off distance, X_{es} , is 1 mm. The density scale shown to the left of the density distributions is in kg m^{-3} .

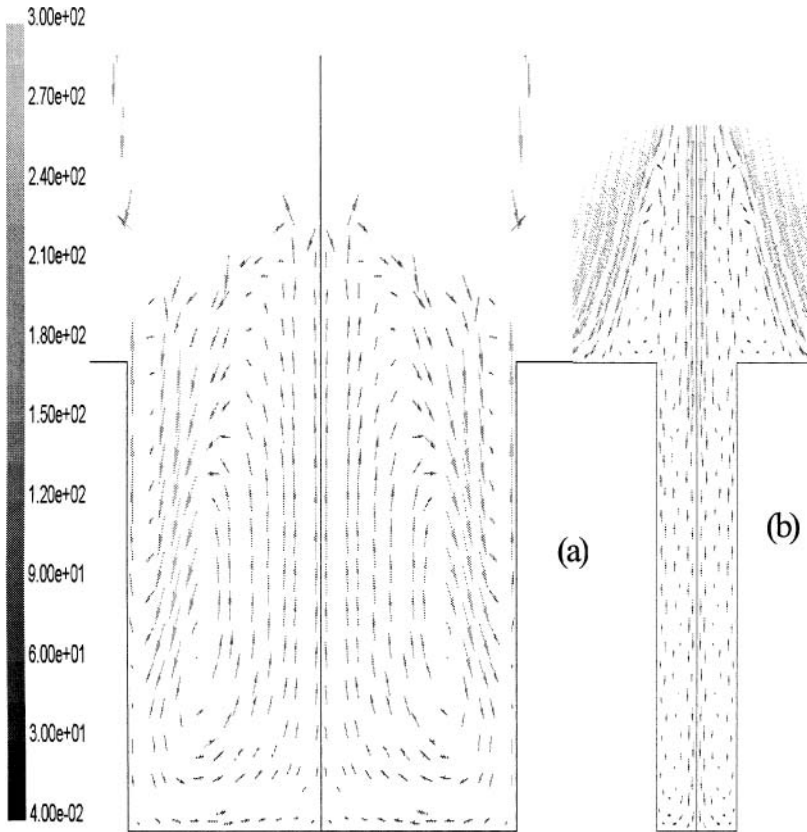


Fig. 8.21. C.F.D. generated velocity profile inside a laser-drilled hole. (a) Hole diameter, $d_H = 429 \mu\text{m}$, and length $L_H = 250 \mu\text{m}$; (b) hole diameter, $d_H = 53.6 \mu\text{m}$, and length $L_H = 250 \mu\text{m}$. The velocity scale shown to the left of the velocity profiles is in ms^{-1}

As shown in Figures 8.20 and 8.21, the supersonic jet establishes a normal shock wave at the entrance to the hole, raising the pressure just above the hole that results in a reduction of the overall pressure gradient between atmosphere and the interaction zone. Laser cutting and drilling processes are pressure-driven systems.

The difference in the pressure from the leading edge to the exit of the kerf creates viscous drag, or shear stress, on the molten film created. Ideally the pressure gradient along the kerf should exponentially decay, but in reality this may not be the case. If flow is supersonic a sudden change in the pressure gradient creates an internal shock formation. If the pressure gradient changes from positive to negative then flow separation is imminent, generating vortices, or eddies, inside the processing zone thus creating effects that are detrimental to the roughness of the processed surface.

A supersonic jet is a pressure driven system, which creates shear stresses on a molten film. The magnitude of the shear stress applied depends on the jet velocity and the surface tension of the gas-liquid-solid interface. For simplicity, walls in C.F.D. models are treated as a solid surface with no external heat source. Shear stress distributions along these walls are represented by Figures 8.22 and 8.23 for hole diameters, $d_H = 429\text{ }\mu\text{m}$ and $53.6\text{ }\mu\text{m}$, respectively. It can be seen that the shear stress distribution inside a drilled hole depends on its aspect ratio with respect to the nozzle diameter. As the aspect ratio is increased the shear stress is reduced. As long as the shear stress is positive there is no separation of flow; negative shear stresses indicate a change in velocity direction of 180° . Shear stress fluctuations indicate that there are variations in mass flow along the surface of the wall.

Very large fluctuations of shear stress are observed in the hole with the smallest aspect ratio, which leads to a turbulent flow regime. If the shock width is approximately the same size as the diameter of the hole then shock interaction with the stagnation pressure creates uneven fluid properties inside the processing zone, as shown in Figure 8.21a. At higher aspect ratios the stagnation pressure build-up is greater within the processing zone. This higher pressure decreases the velocity along the wall, hence reducing the shear stress along the wall.

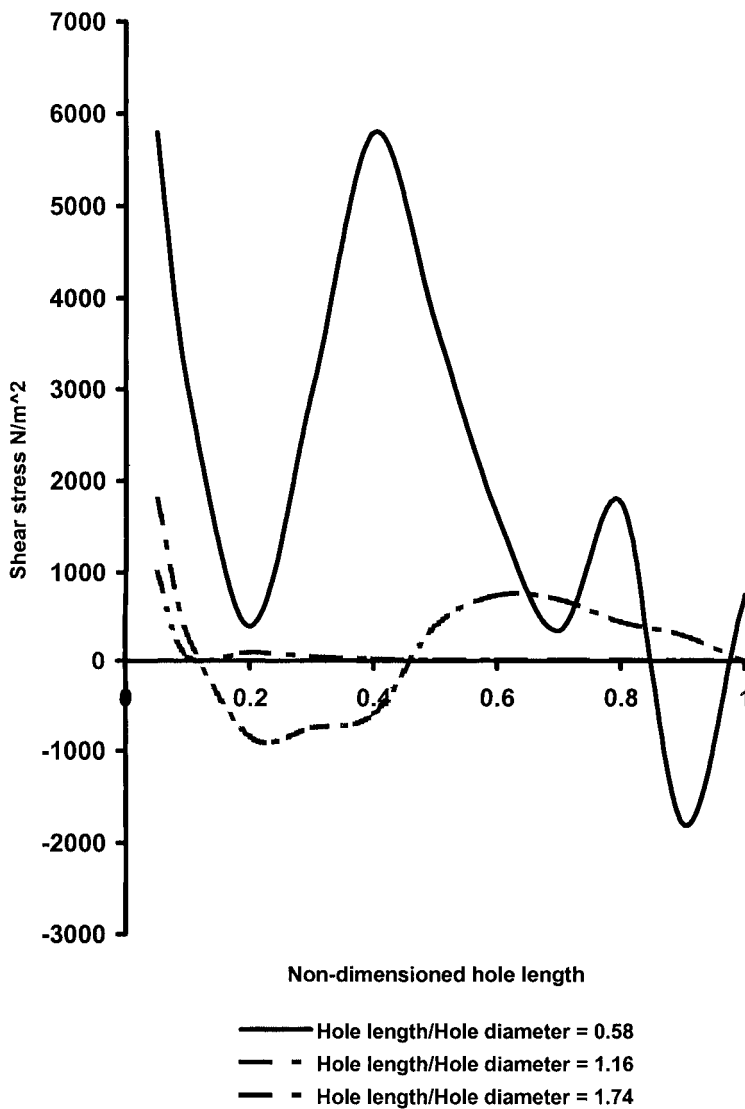


Fig. 8.22. Shear stress distribution within the melt pool inside the laser drilled hole that has a diameter of $429 \mu\text{m}$. The results are presented as function of the ratio of hole length-to-diameter, L_H/D_H . Note that the unit of shear stress is N m^{-2} .

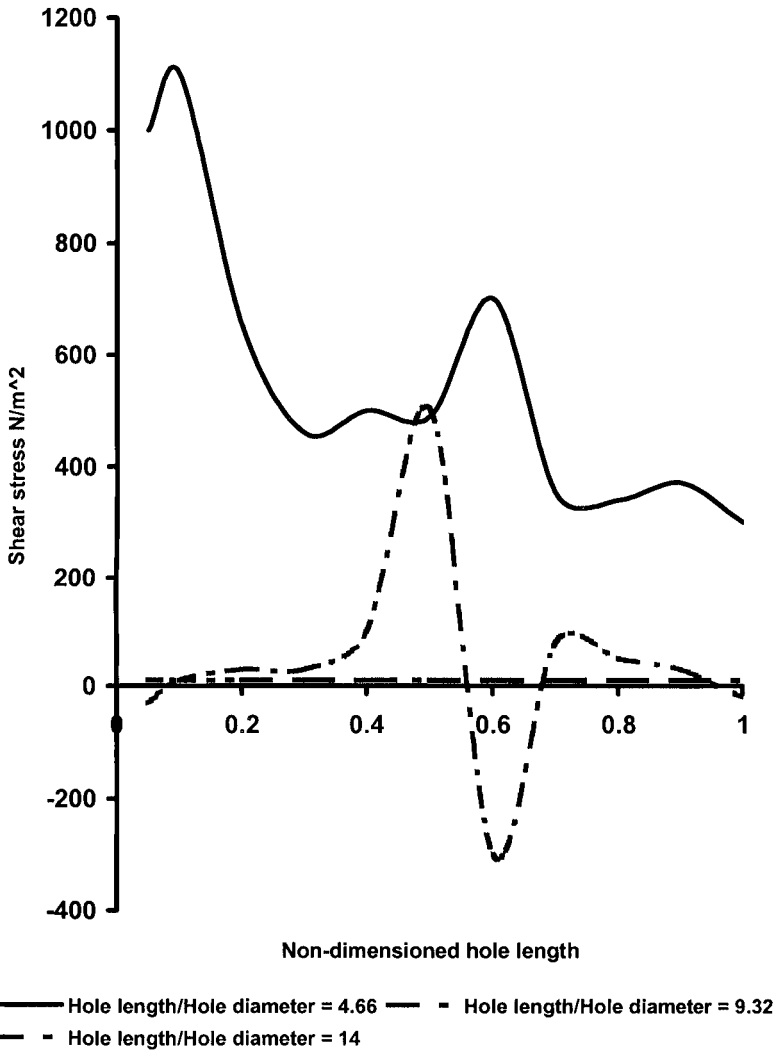


Fig. 8.23. Shear stress distribution within the melt pool inside the laser drilled hole that has a diameter of $53.6 \mu\text{m}$. The results are presented as function of the ratio of hole length-to-diameter, L_H/D_H . Note that the unit of shear stress is N m^{-2}

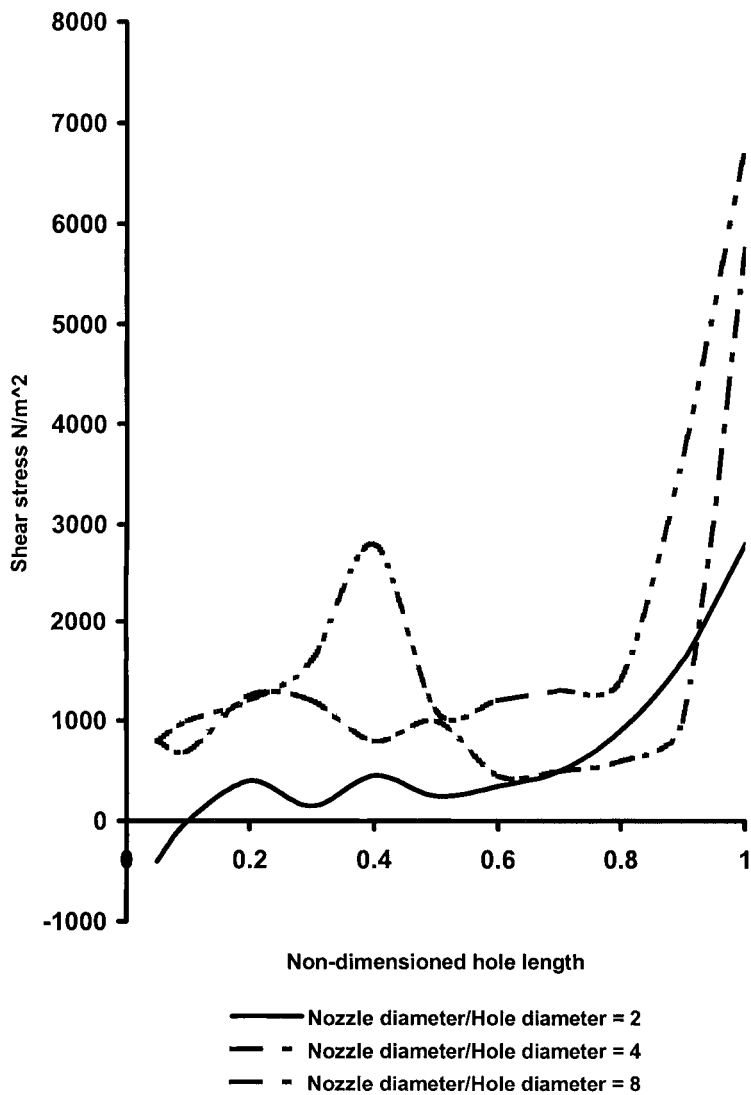


Fig. 8.24. Shear stress distribution inside a narrow channel. The results are presented as function of the ratio of nozzle diameter-to-hole diameter, D_N/D_H . Note that the unit of shear stress is $N\ m^{-2}$

Shear stress distributions in the 53.6 μm diameter hole is comparatively smaller in magnitude than that experienced in the 429 μm diameter hole. This is because the normal shock wave is larger than the diameter of the hole, thus restricting the propagation of flow downstream. The flow is forced to change direction at the entrance to the hole, hence creating a separation point at the leading edge, as shown in Figure 8.21b.

Shear stress distributions in a micro-channel behave differently in comparison to a hole. There is little or no adverse pressure gradient acting against the flow direction in a channel. Fluctuations at the channel entrance are similar to that of a hole (Figure 8.24).

The variation in pressure gradients with respect to the ratio between the nozzle and the kerf width is very important. It indicates that if the kerf width is the same size as the nozzle, and assuming that the flow is parallel, the width of the shock formed on the leading edge is approximately the same size as the kerf width (Figure 8.20a). The interaction of the shock end with the kerf edge creates an expansion wave, thus leading to secondary oblique shock formations at some angle governed by the upstream flow Mach number. If the kerf width is smaller than the shock width, then the expansion wave emanating from the kerf edge is at an increased angle. The larger the shock angle, the greater the effect on flow properties, which creates low-pressure gradients and considerably reduced shear stresses. At some distance along the kerf length the value of shear stress increases in magnitude; this is because the pressure gradient is favorable to the exit of the kerf.

8.3.5 Stages of Surface Melting

There are a number of stages associated with surface melting. First, a melt front wave forms and begins to penetrate the surface. The pulse then finishes and no more energy can be put into the process. The advancement of the wave front ceases, retracts and begins to cool the material. Finally, re-solidification occurs; the volume that was formerly melted has now solidified with the new microstructure.

However, there are problems such as different temperatures in and around the mix that causes differences in surface tension that pro-

motes mixing forces to take control within the melt. These are called Marangoni forces and produce a texture on cooling the surface that may be undesirable, thus causing residual stresses and cracking to occur. The advantages of laser surface melting means that bulk properties are unaffected, and in theory only a small surface depth is affected.

8.3.6 Effects of Nanosecond Pulsed Microfabrication

If the shielding gas is oxygen then a re-cast layer is usually produced when using nanosecond pulsed lasers. A thin oxide layer also accompanies the re-melt layer, which requires a secondary operation to remove it. The process of using assist gases is described in detail by Jackson et al. [3-5]. Figure 8.25 shows the results of machining in an oxygen-rich atmosphere.

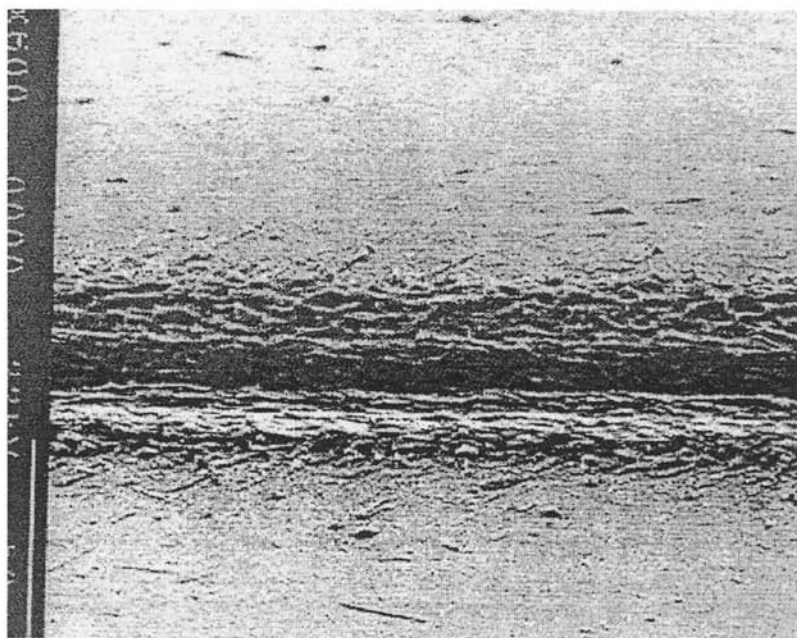


Fig. 8.25. Trench machined in steel created using a nanosecond pulsed Nd:YAG laser in an oxygen-rich gas atmosphere [5]

Helium tends to produce a highly pronounced re-cast layer that is shown in Fig. 8.26. The reasons why it is so pronounced are explained by Jackson et al [3-5]. Argon and air also tend to produce a significant re-cast layer when used in a controlled atmosphere. Figures 8.27 and 8.28 show the effects of processing in argon and air atmospheres when processing steel using a Nd:YAG nanosecond pulsed laser.

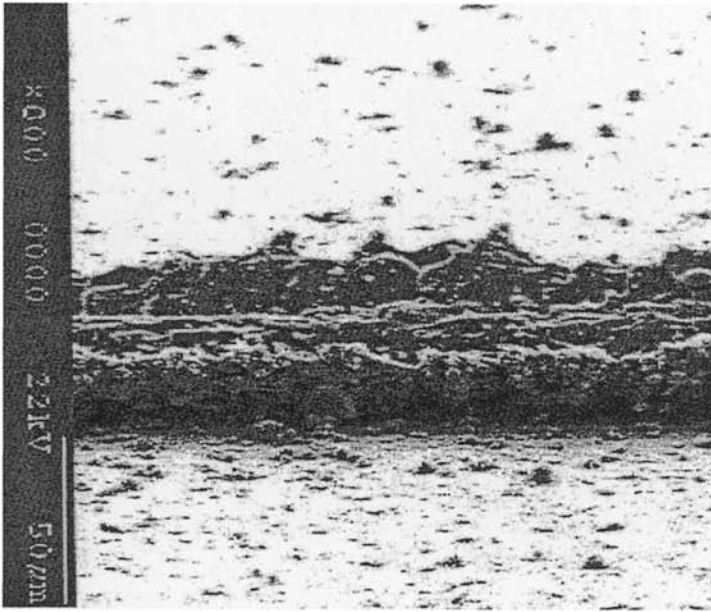


Fig. 8.26. Trench machined in steel created using a nanosecond pulsed Nd:YAG laser in a helium-rich gas atmosphere [5]

Experiments were undertaken to find out what effects the assist gas had on ablation or etch rates. It was found that adding an assist gas reduced the etch rate [3-5]. Also assist gas pressure greatly influences microfabrication using nanosecond pulsed lasers. Higher gas pressures were also found to produce a low etch rate, mainly because at high gas pressure the molten material was prevented from being expelled from the surface of the material.

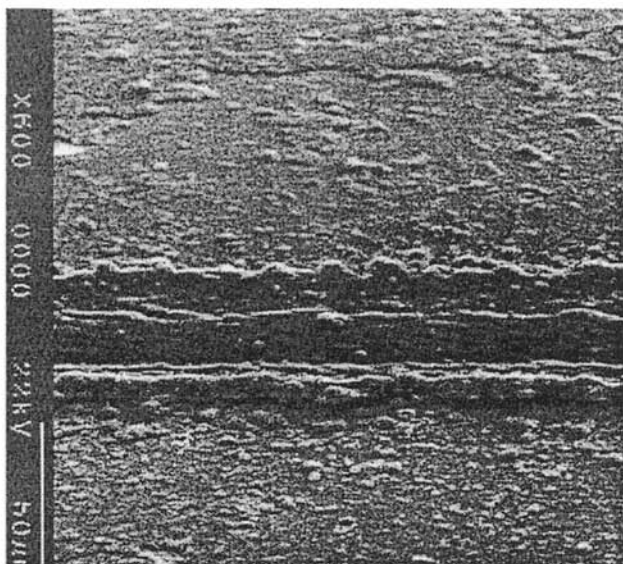


Fig. 8.27. Trench machined in steel created using a nanosecond pulsed Nd:YAG laser in an argon-rich gas atmosphere [5]

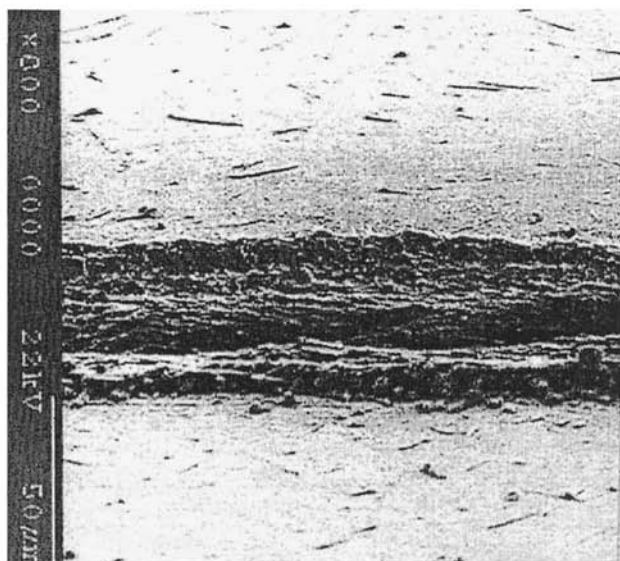


Fig. 8.28. Trench machined in steel created using a nanosecond pulsed Nd:YAG laser in an air-rich gas atmosphere [5]

The effects of varying inlet gas pressure on machining rates are shown in Figure 8.29. The Figure shows the average etch depth per pulse achieved, when drilling a 1 mm thickness M2 tool steel plate. It is evident that the etch rate achieved was considerably higher than for no process assisted gas, which relies solely upon the vaporization of molten material.

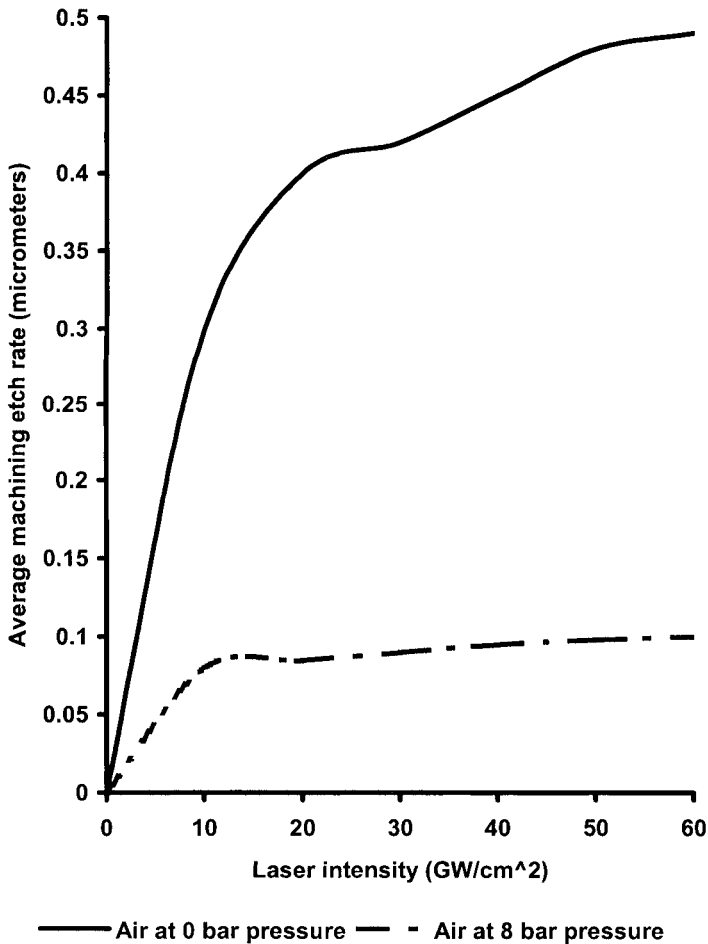


Fig. 8.29. Variation of the machining etch rate as a function of gas pressure

High-speed photography of plasma initiation was undertaken using an Imacon 468 high-speed camera (Figure 8.30). The images shown were taken 240 ns after firing the laser and are negatively exposed to show the plasma as a dark region.

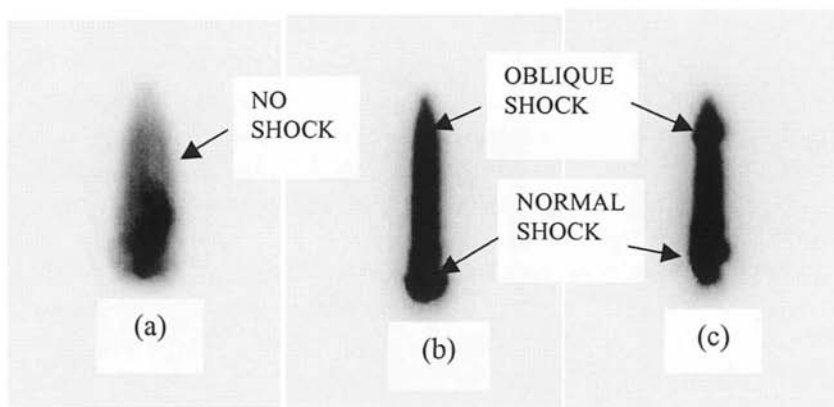


Fig. 8.30. Dynamic plasma field initiated using a 1064 nm laser wavelength at different shielding gas pressures. The plasma was initiated 240 ns after firing the laser beam at: (a) 0.5 bar gas pressure; (b) 4.0 bar gas pressure; and (c) 8.0 bar gas pressure

The complete plasma life cycle was measured to be approximately 850 ns with no shielding gas. A significant change in the plasma geometry is evident when changing the gas jet pressure. Particularly distinct regions of distortion can be seen at 4 and 8 bar pressure. The distortions manifest themselves as a diamond shape at the top of the plasma and a longitudinal expansion at the base. These regions correspond to the positions achieved by the primary (normal) and the secondary (oblique) shock waves, as shown in Figure 8.20a. Immediately after a shock, the molecular density of the jet increases significantly, thus reducing the mean free path of molecules due to compression and hence increases ionisation of the gases. This complex plasma structure will severely disturb beam propagation and affect the etch rates, as demonstrated in Figure 8.30.

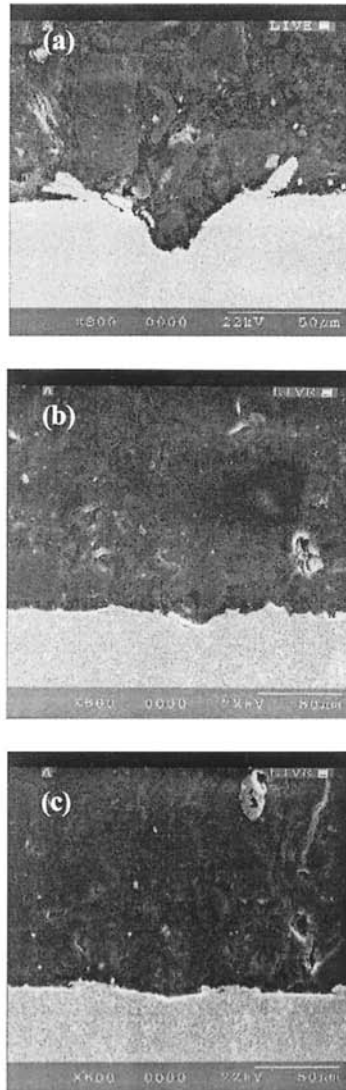


Fig. 8.31. Micrographic cross sections of laser machined M2 tool steel material showing the results of laser-material interactions at different gas pressures: (a) 2 bar shielding gas pressure; (b) 4 bar shielding gas pressure; and (c) 8 bar shielding gas pressure. The length-to-diameter ratio of the hole (L_H/D_H) was approximately equal to 9

The effect of the design of nozzles for laser micro-machining processes is shown in Figures 8.31 and 8.32. The variation in shielding gas pressure has a significant effect on the material removal rate in the form of an etch rate, as shown in Figure 8.31.

At low shielding gas pressures, there is a pronounced removal of material that results in the formation of a trench (Figure 8.31a) in the workpiece material. The micrograph shows a typical cross section of a laser-machined material with a correspondent re-cast layer. The re-cast layer is caused by the suppression of the molten material from being released into the jet stream and subsequently vaporized. This leads to the molten material being deposited at the sides of the machined trench (Figure 8.31a). On further increasing the shielding gas pressure, the formation of oblique and normal shock waves prevents the molten material from being removed from the trench and leads to the non-formation of a machined trench (Figures 8.31b and 8.31c). As a result of a reduction in the machining etch rate, the amount of material re-deposited at the sides of the depression in the center is very small compared to the low shielding gas pressure regime. In all cases, the aspect ratio (L_H/D_H) is 9.32.

The effect of the aspect ratio is shown in Figure 8.32. Low aspect ratios tend to produce the greatest amount of re-cast layers owing to the high shear stresses generated in the molten material (Figure 8.32a), while high aspect ratios tend to produce depressed re-cast layers owing to the lack of shear stresses in the molten material. Figure 8.23 shows the magnitude of shear stresses generated within the melt pool using nozzles of different length when machining a 53 μm diameter trench in M2 tool steel. Figures 8.32a, b, and, c, confirm the effect of variations in the aspect ratio of the nozzle at a shielding gas pressure of 8 bar. The latter pressure was chosen in order to illuminate the negative effects re-cast layers have on the resultant morphology of micro-machined components.

Figures 8.31 and 8.32 show an interesting trend. The increase in surface roughness as a function of nozzle length-to-diameter ratio appears to show the advantages of using a high aspect ratio nozzle with a low-pressure inlet shielding gas jet.

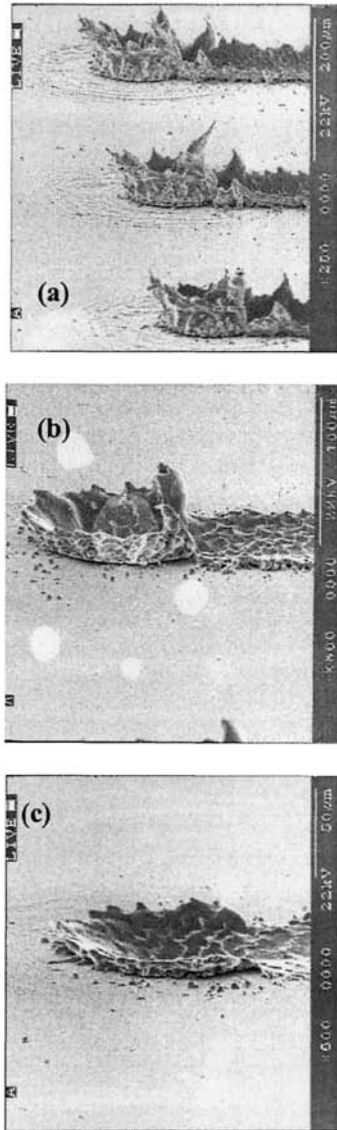


Fig. 8.32. Micrographic cross sections of laser machined M2 tool steel material showing the results of laser-material interactions at different L_H/D_H ratios: (a) $L_H/D_H = 4.6$; (b) $L_H/D_H = 9.3$; and (c) $L_H/D_H = 14$. The shielding gas pressure was equal to 8 bar

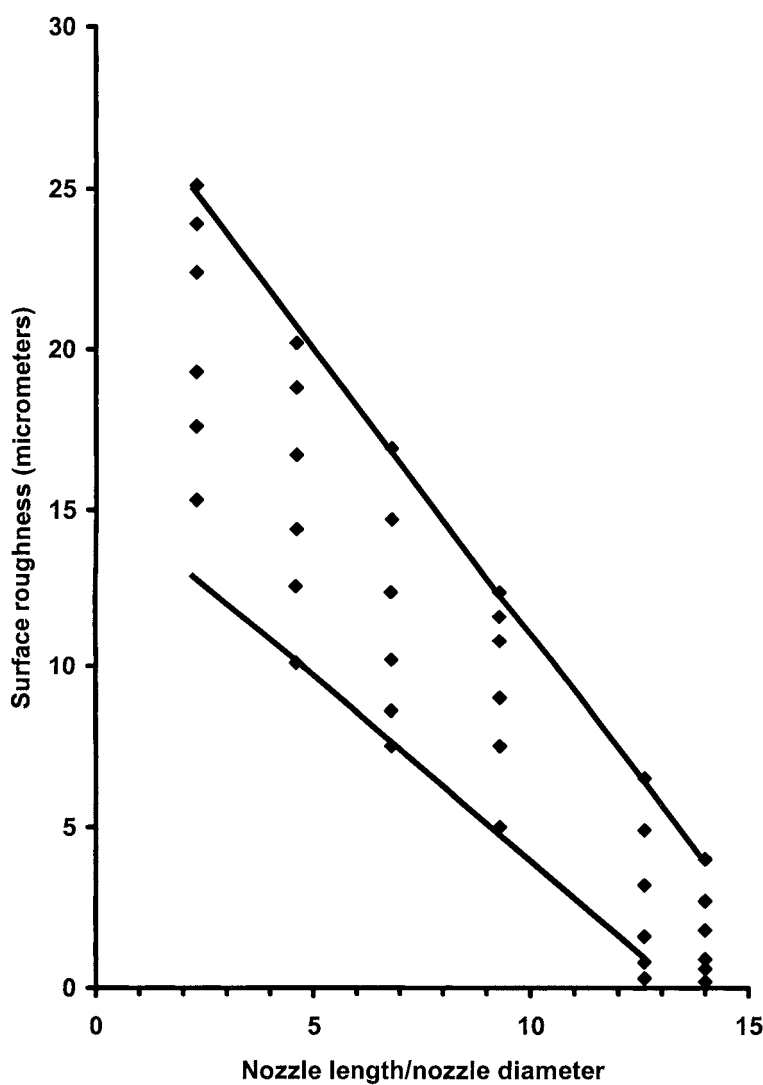


Fig. 8.33. Effect of using different nozzle length-to-diameter ratios on the surface roughness of machined trenches. Inlet gas pressure was 8 bar

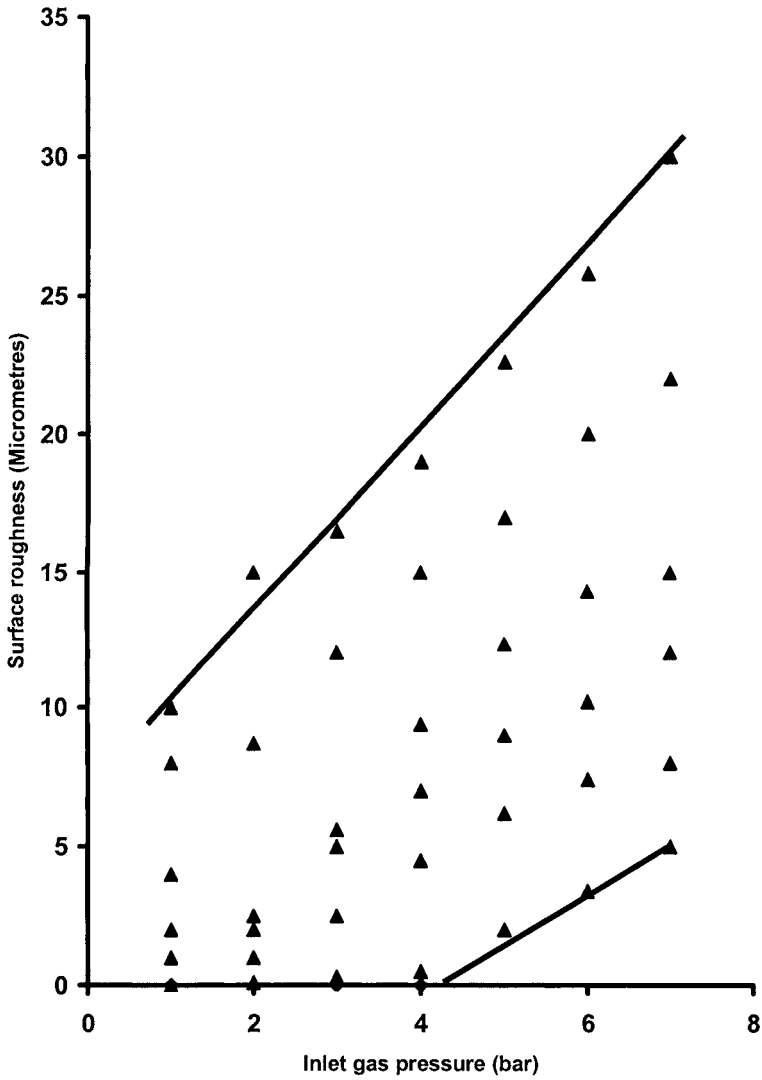


Fig. 8.34. Effect of using different inlet gas pressures on the surface roughness of machined trenches. Nozzle length-to-diameter ratio was approximately equal to 9

However, when the surface roughness of laser-processed samples was performed, the author noticed that a range of surface roughness values existed for a variety of aspect ratios and inlet gas pressures.

The range of surface roughness as a function of aspect ratio is shown in Figure 8.33, and as a function of inlet gas pressure in Figure 8.34. The variation in surface roughness is not easily explained. One explanation may be the influence of interacting shock waves that prevents molten material from entering the jet stream above the interaction zone. Here, the laser beam normally makes contact with the jet of molten material in order to vaporize it. However, this is not the case when shock waves in the gas jet interact with each other.

This explains why, in some cases, the re-cast layer is larger than in other cases. Another explanation may be attributed over a longer period of time. As the laser beam establishes contact with the work-piece material, a dynamic plasma is initiated that causes interference with the action of the laser beam, thereby allowing the laser beam to deflect about a point where expulsion of the molten material is prevented.

This means that molten material is not vaporized because the laser beam has been deflected away from the interaction zone. The material then solidifies at the side of the machined trench, which exaggerates the size of the re-cast layer. In both cases, time-dependent behavior of the laser interaction process appears to have produced a variation in the size of the re-cast layer. This has tremendous implications on the accuracy of micro-components manufactured using laser-based processing techniques.

8.3.7 Picosecond Pulse Microfabrication

In picosecond laser ablation, pulses are of the same timescale that it takes to transfer energy from electrons to the lattice of the material being machined. There is little heat conduction but a great deal of heat flow caused by free electrons. At the surface there is a solid-to-plasma phase; however there is a liquid phase “inside” the material. The ablation depth per pulse is:

$$Z_a \approx \alpha^{-1} \ln \left(\frac{F_a}{F_{th}} \right) \quad (8.18)$$

Where α is the absorption depth. This liquid phase reduces the precision of the machining process. It has been shown that for processing metals, the pulse duration should be less than the electron-phonon thermalization time. For engineering materials like steel, copper, aluminum and iron the thermalization time is around 10 ps. With shorter femtosecond pulses deformation of the high intensity beam such as astigmatism coupled with non-linear interactions with the ambient gas cause unwanted effects. Diode pumped solid-state picosecond lasers are thus suitable for laser materials processing because they operate at high average power levels and repetition rates at around 100 kHz. An incident laser beam is absorbed by collisions with energetic electrons (electron collision time is around 100 fs) and free electrons, which results in heating of the lattice. The time for the electron-phonon relaxation is greater than the electron collision time. In the case when the time is shorter than the electron-phonon relaxation time, the material dependent relaxation time is the dominant mechanism governing evaporation and solidification. For example the electron-phonon relaxation time for aluminum is around 100 ps. Ideally to minimize unwanted thermal effects the pulse duration should be less than the electron-phonon relaxation time. Therefore the electron-phonon relaxation time of the material determines the extent to which thermal damage will be incurred. Therefore, picosecond laser micromachining is suited to cutting lines or patterns, drilling holes, surface structuring, or milling. A comparison can be made with femtosecond lasers for the production of a mask. A 100 μm thick steel sheet 20 x 20mm² takes 3200 s to machine with a femtosecond system operating at 100 fs, 100 nm, 10 kHz and 0.37 W (37 $\mu\text{J}/\text{pulse}$) (Fig. 8.35). The same mask can be produced to the same specification with a picosecond system operating at 1064 nm, 50 kHz, 0.84 W (17 $\mu\text{J}/\text{pulse}$) but the machining time in this case is only 570 s (Fig. 8.36).

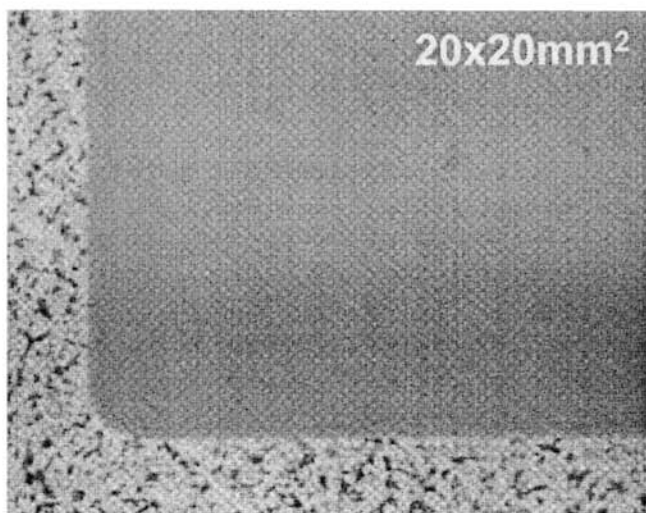


Fig. 8.35. Femtosecond pulsed laser micromachining of steel showing rough edge preparation. (Courtesy of Lumera Laser)

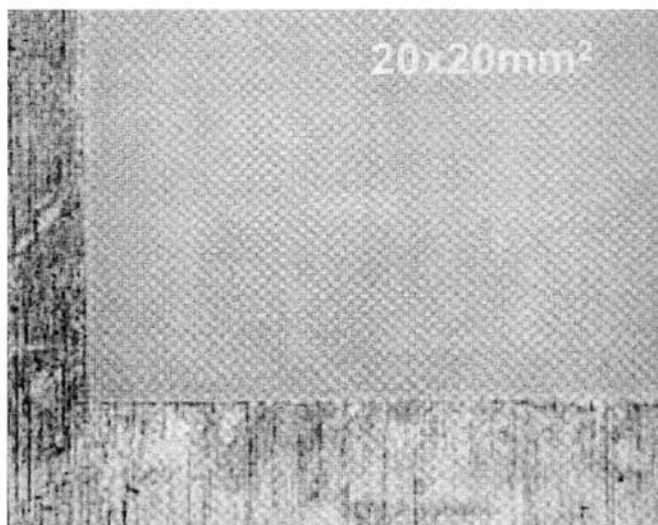


Fig. 8.36. Picosecond pulsed laser machining of steel mask show smooth edge preparation. (Courtesy of Lumera Laser)

If the repetition rate is doubled to 100 kHz the processing time can be further reduced by a factor of 12 with little sacrifice in quality when measured against parameters such as dimensional accuracy, minimal debris, minimal burr formation and a minimum heat affected zone. Figure 8.37 shows the machining of a pattern in steel using a repetition rate of 100 kHz.

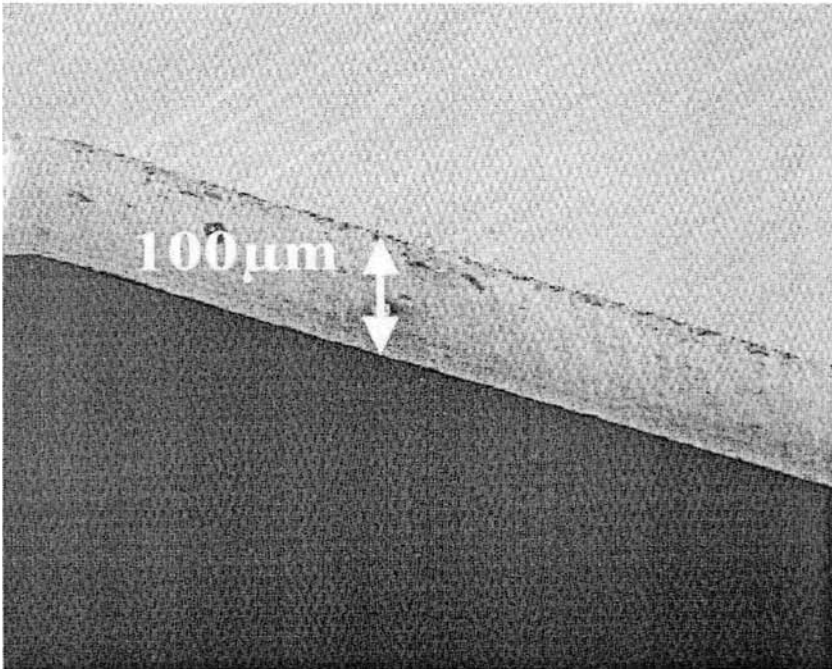


Fig. 8.37. Picosecond pulsed laser machining of a steel pattern using a repetition rate of 100 kHz. (Courtesy of Lumera Laser)

Surface structuring or surface modification is possible with picosecond systems. Figure 8.38 shows an example where 25 μm grooves have been placed in 50 μm thick stainless steel. No burr formation, or re-cast layer is observed, the power was 0.4 W (of 10 W) and the removal rate was 0.066 mm^3/min .

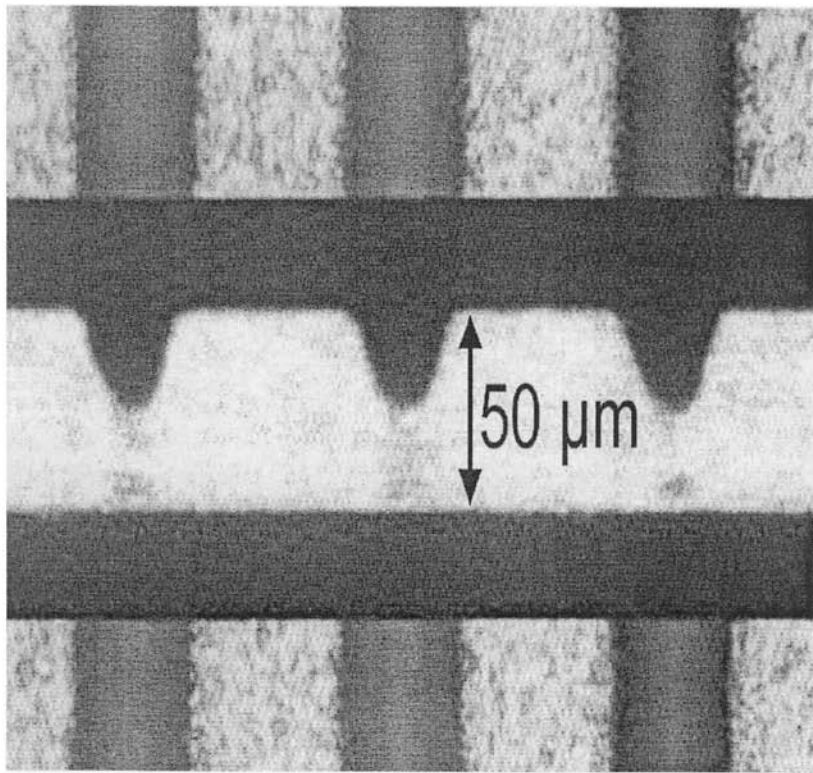


Fig. 8.38. Grooves machined in a 50 μm thickness stainless steel workpiece. Courtesy of Lumera Laser

Another application for surface structuring is the removal of thin layers (10 μm or less) that are structural features. Examples include direct delamination of metal layers, removal of thin indium tin oxide layers, and laser honing. Typical powers are around 0.5 to 1 W and material removal rates of $10^{-3} \text{ mm}^3/\text{s}$ are commonplace.

Lasers can be used to drill holes but special care must be taken. It is possible that because of reflection and diffraction effects the hole may not have the same exit and entry diameter, nor will its walls be straight or parallel. To counter this effect, techniques such as helical drilling and polarization control with trepanning optics must be employed (Fig. 8.39).

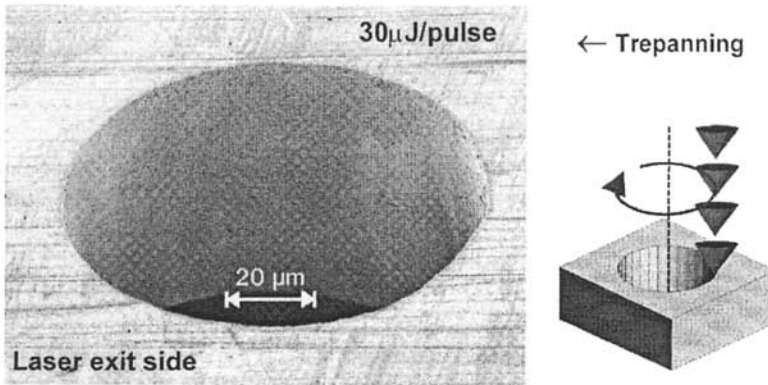


Fig. 8.39. Microdrilling of holes using a trepanning technique. (Courtesy of Lumera Laser)

Small holes around 50 μm diameter can be produced with good edge quality, no burr, or debris is observed at a power of 2 W and a rate of 3 holes/s (Fig. 8.40).

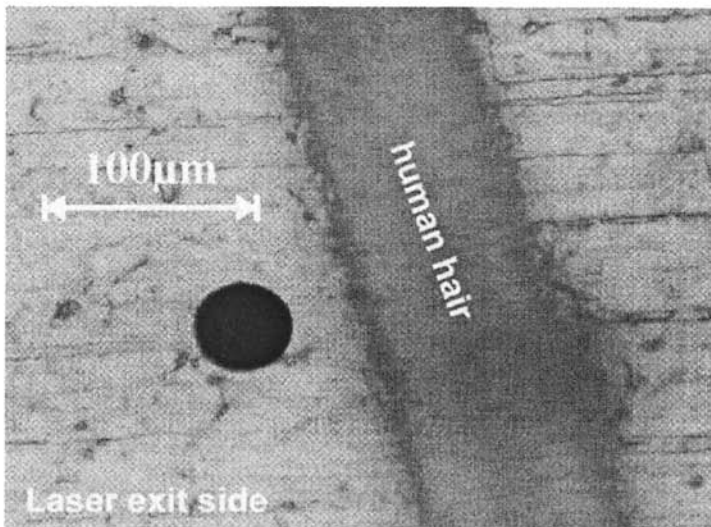


Fig. 8.40. Small holes drilled in steel with human hair for comparison of scale. (Courtesy of Lumera Laser)

Another example of laser-drilled holes is where an array of $30\text{ }\mu\text{m}$ holes are drilled in $25\text{ }\mu\text{m}$ thick steel foil at a rate of 2 holes/s at a power of 0.5 W (Fig. 8.41). The holes have good edge quality, good circularity were highly reproducible, and had minimal burr or debris formation.

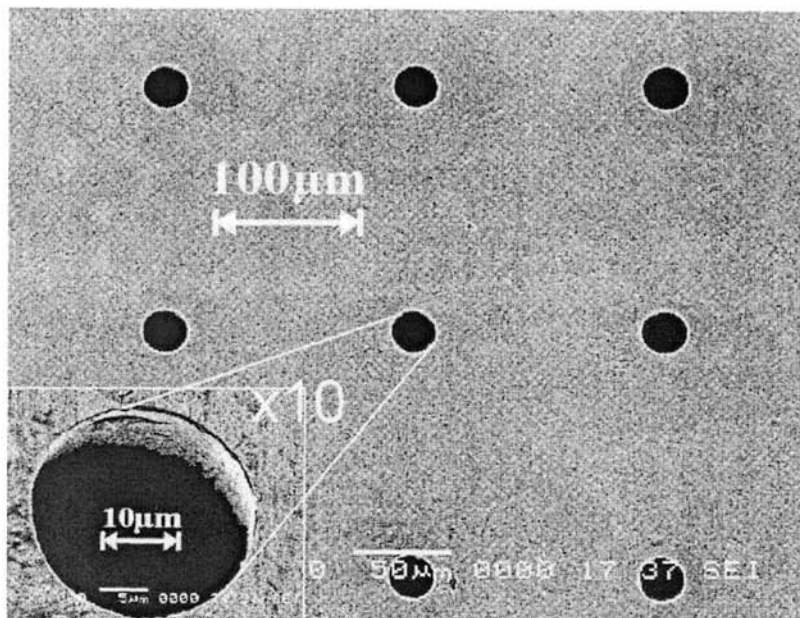


Fig. 8.41. Picosecond pulsed laser machined holes in stainless steel. (Courtesy of Lumera Laser)

Where milling is concerned with the production of smooth μm surfaces can be achieved, for aluminum this rate is $1 \times 10^{-3}\text{ mm}^3/\text{s}$; for steel it is $20 \times 10^{-3}\text{ mm}^3/\text{s}$.

An important application for lasers is the cutting of silicon wafers. The kerfs between chips must be minimal to ensure that maximum density of chips are produced from the wafer. Machining is performed at 1.2 W with a removal rate of $3 \times 10^{-3}\text{ mm}^3/\text{s}$ and the requirements are good edge quality, minimal debris, minimal recast, and no crack formation (Figures 8.42 and 8.43).

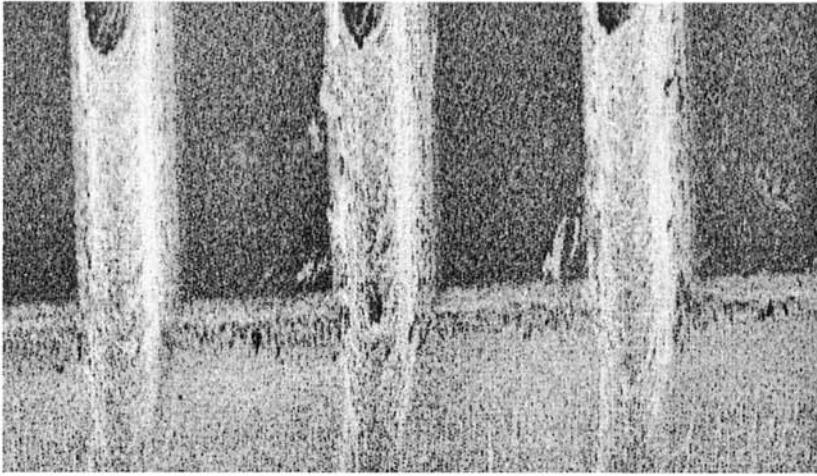


Fig. 8.42. Residual silicon bases between four machined lines using a picosecond pulsed laser. (Courtesy of Lumera Laser)

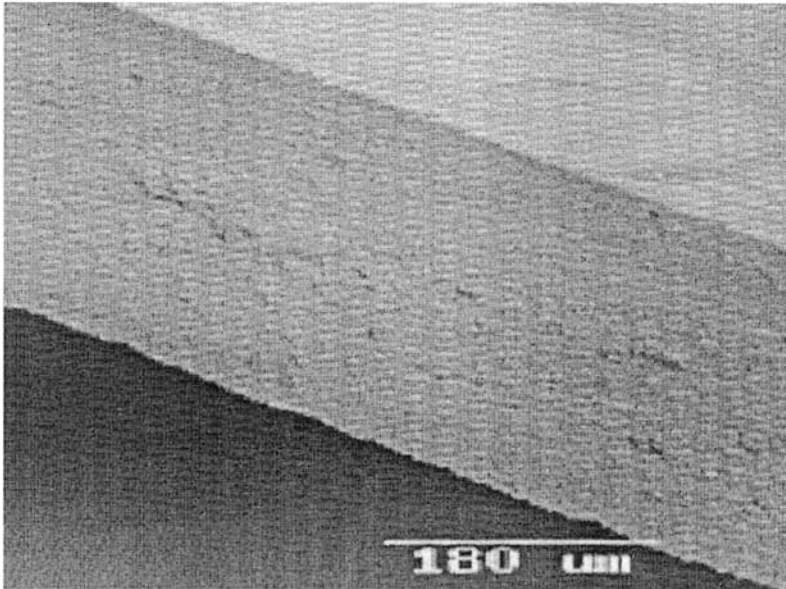


Fig. 8.43. Laser machining of silicon wafer using a 532 nm wavelength picosecond pulsed laser. (Courtesy of Lumera Laser)

Drilling holes in silicon is important for high frequency technologies where electronic components pass through holes in silicon wafers. These holes cannot be produced in a satisfactory way by etching alone. Picosecond lasers with a beam diameter of 0.5 – 2 mm using a power of 5 W and a time of 10 s are used to perform this function (Fig. 8.44).

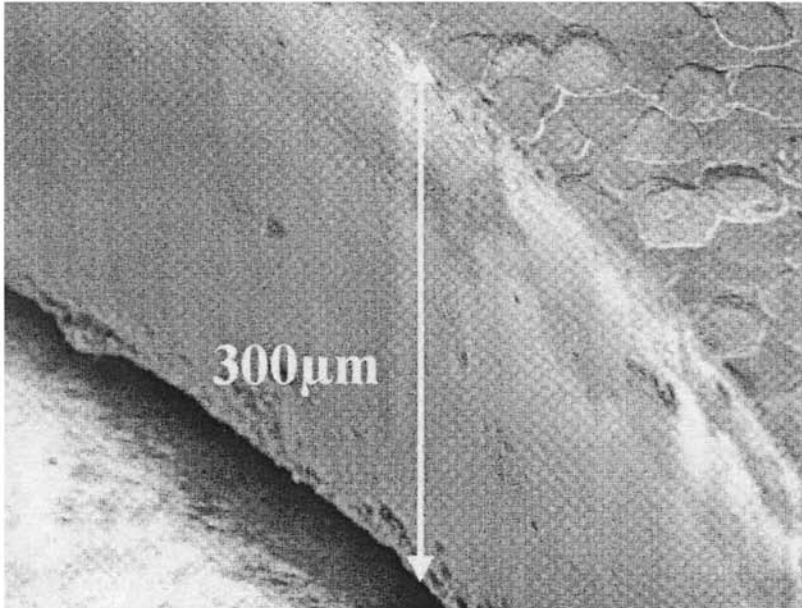


Fig. 8.44. Machining of 2 mm hole in silicon wafer using a picosecond pulsed laser. The hole depth is 300 μm . (Courtesy of Lumera Laser)

Ultrashort ps pulses have Terawatt power densities per square centimeter. Usually free electrons are involved in absorption of laser energy. However, some materials do not have free electrons but the energy of these ultrashort pulses is deposited by multiphoton absorption and electron impact absorption, or interband transitions. Hence, materials that are difficult to machine with a conventional laser such as very hard or transparent materials such as diamond or PTFE can be machined by ultrashort picosecond pulses. For example, PTFE has excellent properties for medical and electronic applications. Hence, microparts for these applications that are difficult to me-

chanically machined can now be machined using lasers. Processing of PTFE can be carried out at 10 W with a material removal rate of $0.2 \text{ mm}^3/\text{s}$ (Fig. 8.45).

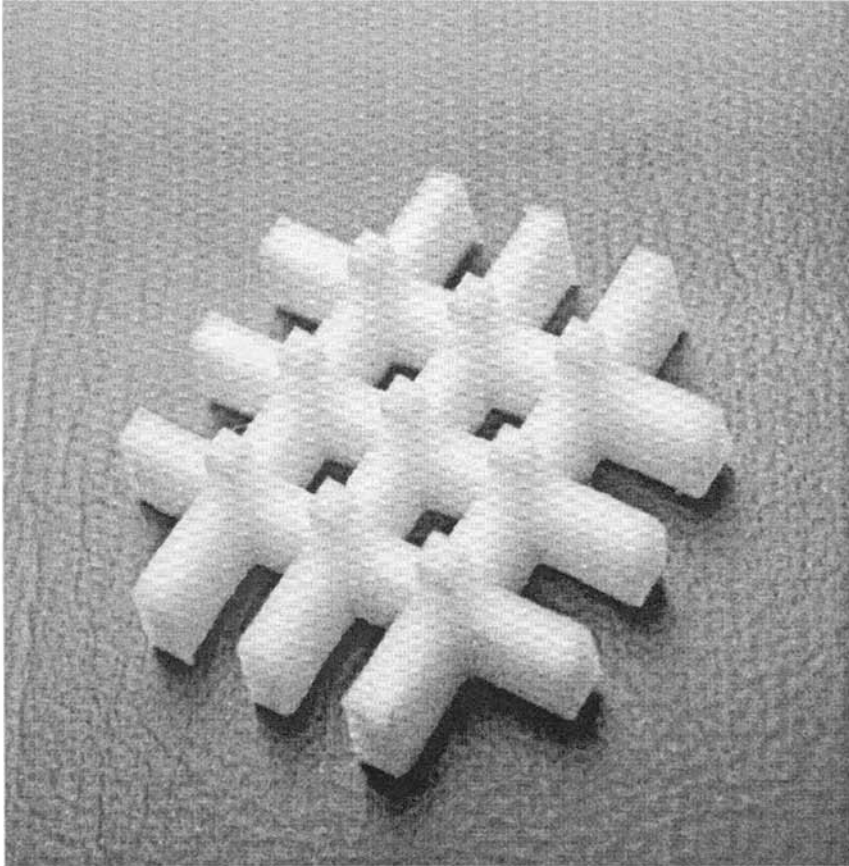


Fig. 8.45. Support structure made from PTFE processed using a picosecond pulsed laser. (Courtesy of Lumera Laser)

Laser machining of ceramics has also been shown to be successful. Ultrashort ps pulses produce good hole geometry due to non-thermal ablation with no thermal cracks present. This can be carried out at 10 W at 8 holes/min (Fig. 8.46).

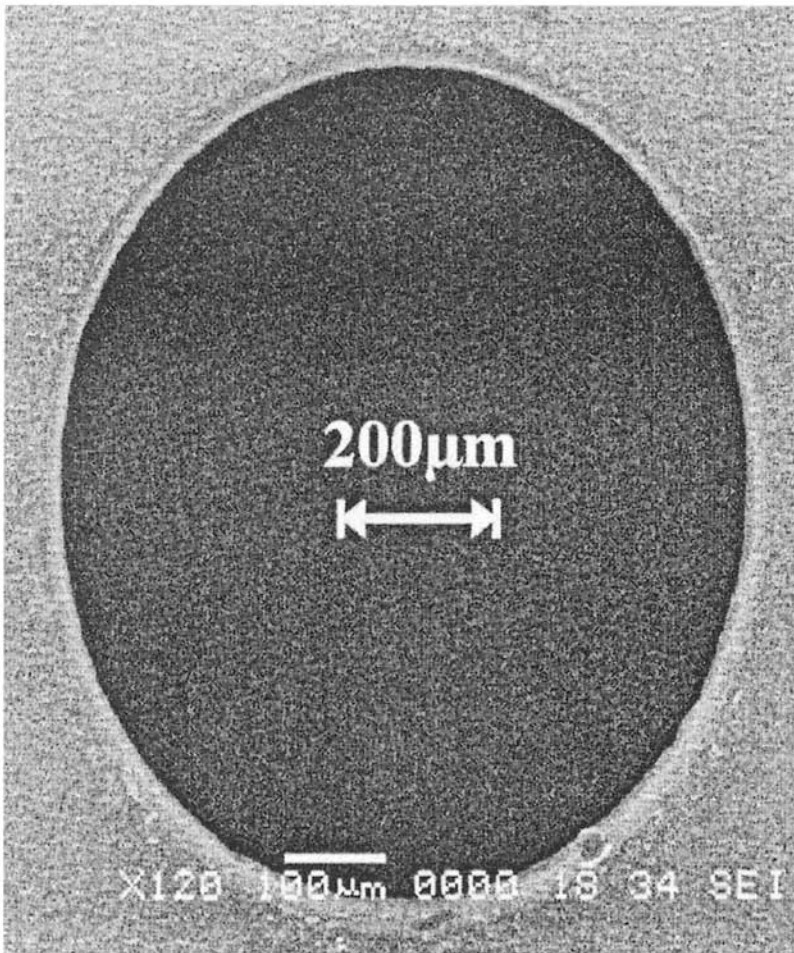


Fig. 8.46. 1mm hole drilled in 200 μm thickness ceramic using a picosecond pulsed laser. (Courtesy of Lumera Laser)

Similarly holes can be drilled in borosilicate glass. The holes have a 1 mm diameter, are 140 μm thick and the edge quality is excellent with no cracking, which was carried out at 2 W at 20 holes/min (Fig. 8.47).

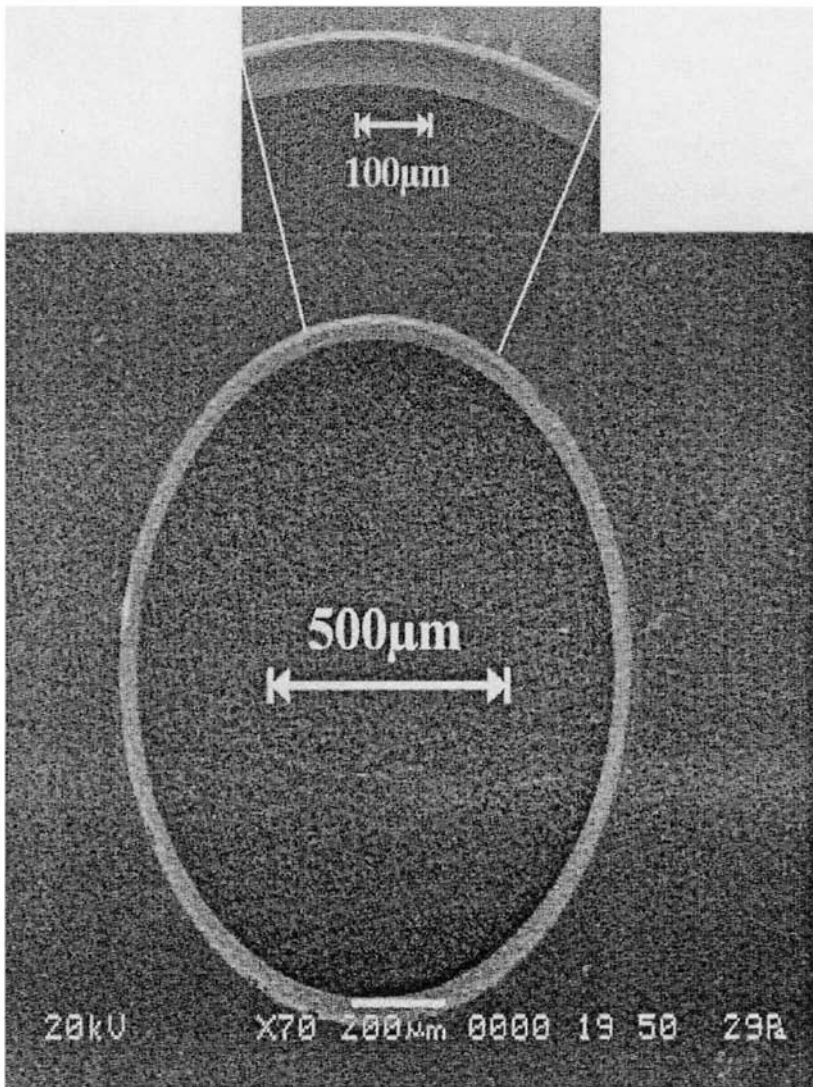


Fig. 8.47. 1 mm hole drilled in 140 μm thickness ceramic using a picosecond pulsed laser. (Courtesy of Lumera Laser)

Table 8.4. Material removal rates of materials using picosecond pulsed lasers. (Courtesy of Lumera Laser)

Material	Material removal rate (mm ³ /s)
Aluminum	0.001
Steel	0.02
Copper	0.001
Titanium	0.06
Silicon	0.005
Ceramic	0.08
Glass	0.14
WC	0.03
SiC	0.009
PTFE	0.2

Table 8.4 shows typical material removal rates for picosecond pulsed lasers machining a wide variety of engineering materials.

8.3.8 Femtosecond Pulse Microfabrication

When machining with femtosecond pulsed lasers, electromagnetic wave interact with the particle, multi-photon absorption occurs and, there is no liquid phase. In theory the pulse and the evaporation interaction occur before the next pulse impacts the material. Bounded electrons of the material can be directly ionized by multi-photon absorption. Photons with energy, $h\nu$, can be absorbed to ionize the atom, for this to happen the ionization potential or band gap must be surmounted. The electron does not have to wait for energy to be

supplied to it. The pulse is so short that the energy is supplied at a rate where direct ionization occurs. Long pulses have low breakdown field strength whereas short pulses have high breakdown field strengths. The breakdown fluence threshold can be defined as the fluence at which there is a 50% probability that a laser of this pulse width and fluence will cause breakdown to occur. The field strength is determined by the density of the field lines of the electromagnetic wave. For long pulses the field lines are spread out and for short pulses the field lines are closer together. For long pulses avalanche breakdown thresholds trigger the material removal process but are random in nature; for short pulses multiphoton absorption is the dominant breakdown trigger and occurs rapidly. For long pulses, statistical variations occur as a result of the distribution of seed electrons required for the onset of ionization, which can take some time for avalanche ionization to be triggered.

For multiphoton absorption there is no randomness as there is no reliance on seed electrons to initiate the process. Any electron, free or otherwise, can be ionized by multiphoton absorption. This is why femtosecond lasers are capable of machining any material. The ablation process is completed by avalanche ionization even if it is triggered by multiphoton absorption. Once the plasma density reaches a critical level ablation can occur. Electrons absorb energy by collisions and are heated to extremely high temperatures. Simultaneously, electrons transfer energy to the ions and the lattice that tends to heat the surface. Energy transfer depends on pulse duration and the coupling coefficient. Short pulses avoid a long wait before the critical level is reached because they do not rely on free electrons while waiting for the critical level to be reached are avoided. For long pulses the energy transfer from electrons to ions is efficient. The heat diffusion zone is larger and as the pulsewidth decreases the field strength increases and electrons reach a much higher temperature than the ions or the lattice. Vaporization occurs rapidly and the HAZ is very small. An interesting observation is that because multiphoton absorption does not depend on the presence of free electrons any material can be processed. Materials that are transparent to the wavelength such as glass can be machined.

In femtosecond ablation, no energy is transferred to the lattice, i.e. all energy is stored in a thin surface layer. The ablation depth per pulse is given by,

$$Z_a \approx \alpha^{-1} \ln \left(\frac{F_a}{F_{th}} \right) \quad (8.19)$$

Note that Eq. 8.19 shows that there is no ablation observed at the threshold fluence. For $\alpha = 10 \text{ nm}$, the threshold is typically 0.1 J/cm^2 . If the energy stored in the thin surface layer is greater than the specific heat of evaporation then vigorous evaporation will occur after the pulse. Ideally, the ablation fluence should be around three times greater than threshold to remove an irradiated layer thickness, α^{-1} . Ablation occurs from the solid to the plasma phase. The plasma expands rapidly and is expelled from the surface, and because there is no time for heat transfer to occur, it is therefore a very precise ablation process. This implies that re-cast layers should no longer form on the surface of the material being machined. Figure 8.48 shows a comparison between using a nanosecond pulsed laser and a femtosecond pulsed laser to micromachine. It is shown that the left-hand figure has a pronounced re-cast layer that is produced using a nanosecond pulsed laser. The right-hand micrograph has no re-cast layer, indicating that it has been machined using a femtosecond pulsed laser.

Nanosecond machining often produces re-cast layers resulting in a loss of dimensional accuracy. There is also a heat-affected zone and post processing is required to generate the final micropart. Femtosecond machining results in no re-cast layers being formed and clean holes and tracks, which can be produced without secondary processing. Femtosecond laser machining can produce microfluidic channels in a variety of materials. Figure 8.49 shows the machining of trenches in borosilicate glass that is used for microfluidic applications.

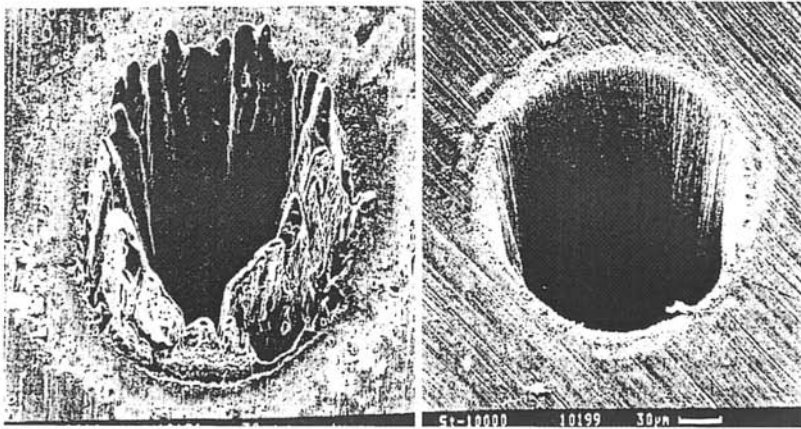


Fig. 8.48. Effects of using nanosecond and femtosecond pulsed lasers to machine an engineering material. The material in the left image is machined using a ns pulsed laser and the right image is machined using a fs laser. Note lack of re-cast layer using fs lasers [10]

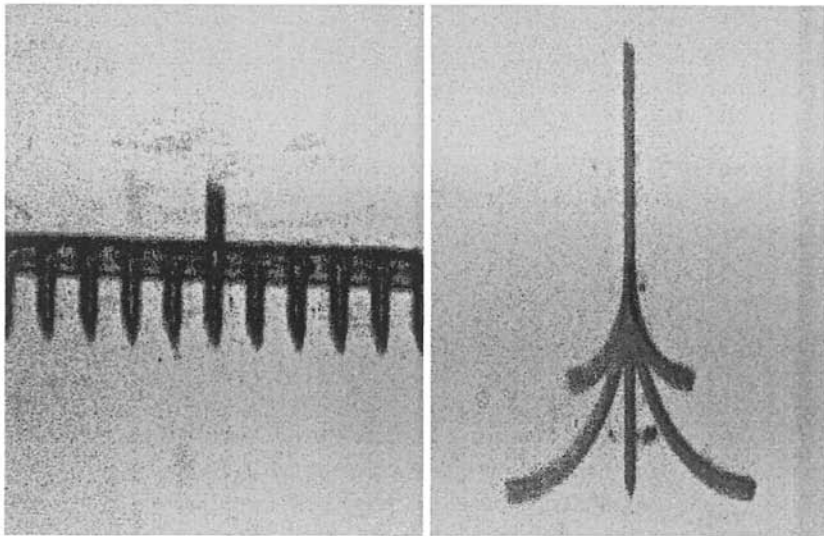


Fig. 8.49. Femtosecond laser machined trenches/channels in borosilicate glass used for microfluidic applications

Femtosecond Ablation of Aluminium

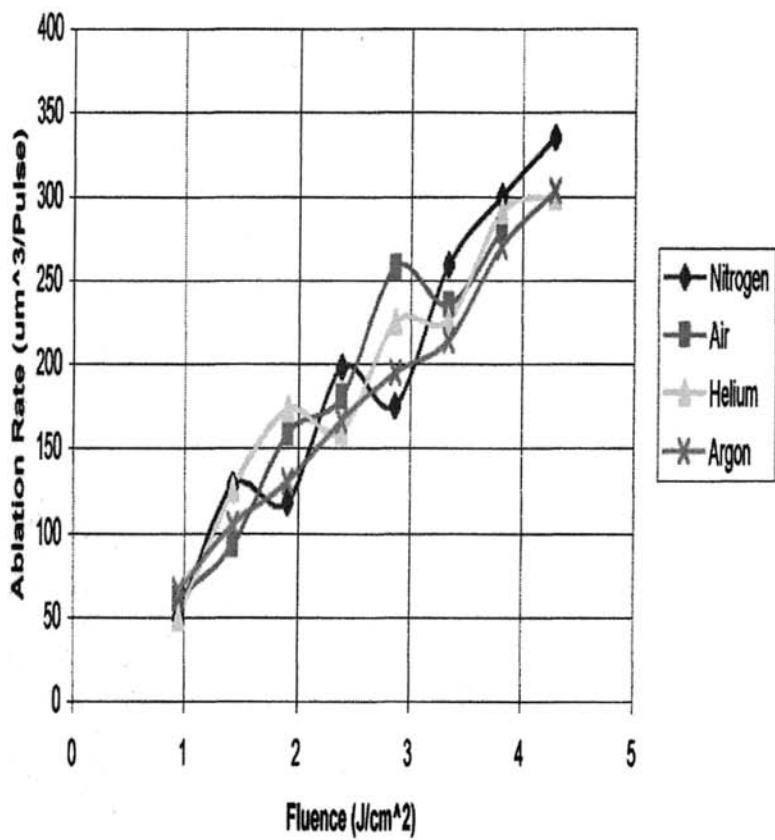


Fig. 8.50. Effect of assist gas on the ablation rate of aluminum using a femtosecond pulsed laser

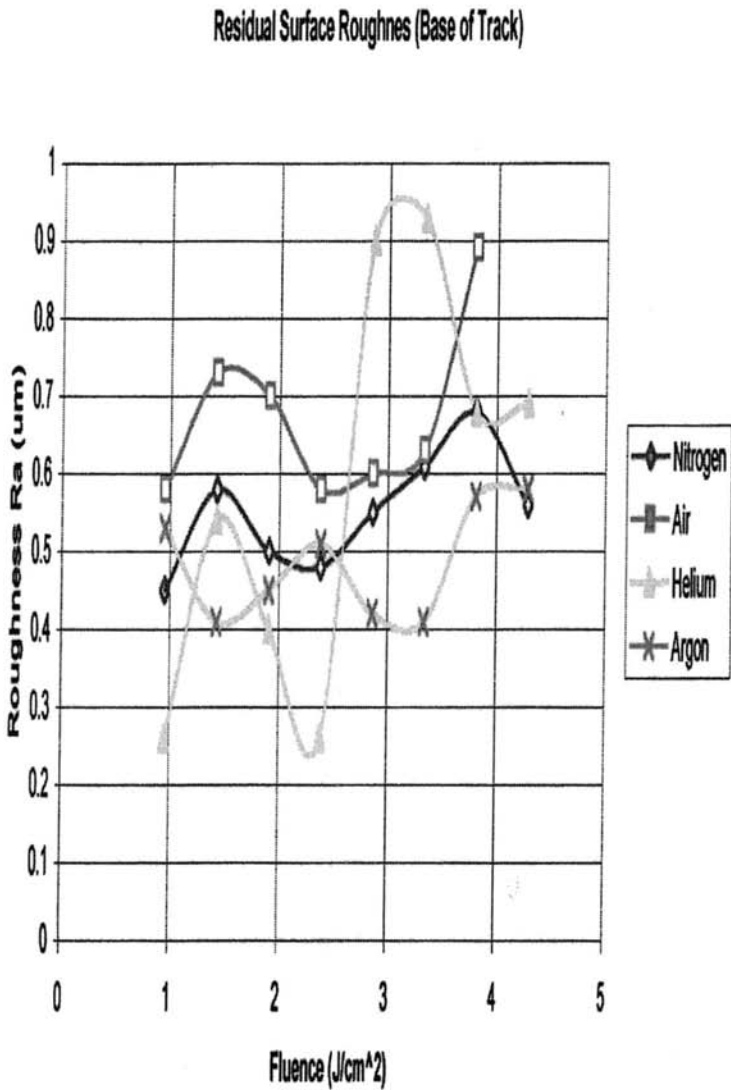


Fig. 8.51. Effect of assist gas on the surface roughness of aluminum using a femtosecond pulsed laser

The effects of using different assist gases were investigated. As is the case for nanosecond pulsed laser ablation, the ablation rate is affected by the type of assist gas used at various levels of fluence. Figures 8.50 and 8.51 show the effects of using assist gases on the ablation rate and on surface roughness. Figure 8.52 shows the physical surface roughness of microparts produced using a femtosecond pulsed laser under various gas atmospheres.

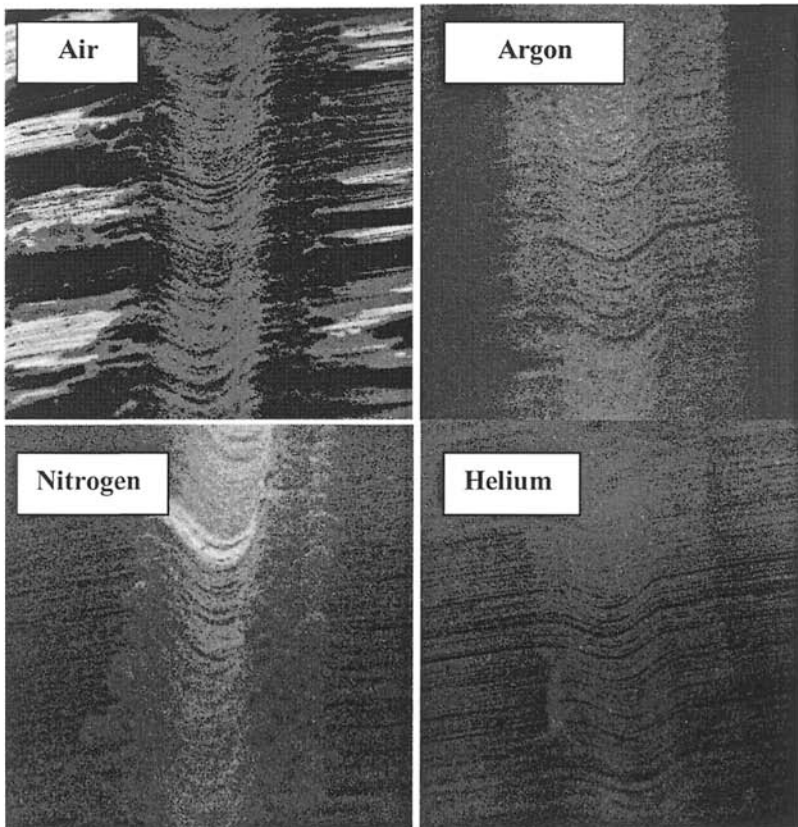


Fig. 8.52. Surface roughness of aluminum processed using a femtosecond pulsed laser in various gas atmospheres

Note that the roughness of the machined trenches is identical to the roughness of the original material. This is because the femtosecond laser removes a very small amount of material. Thus the same vertical distance is removed and an identical profile to that at the surface is created at the base and side walls of the trench. Air produces relatively good results with small amounts build-up of material around the edges. Argon produces a powdery residue around the track, while nitrogen yields poor results, causing a build-up of material around the machined trench or channel. Helium produced the cleanest results. All other gases produced a powder that was black, helium on the other hand, produced a silvery deposit. The black powder produced was thought to be a nanoscale powder with deposits so small they are below the wavelength of light and therefore no interaction is possible, resulting in the black appearance. Clearly the assist gas has some effect but this has not yet been quantified. Processing with femtosecond lasers may provide an economic way to produce nanometal powders.

8.3.9 Effects of Femtosecond Laser Machining

The following results are conducted in an ambient airflow generated at 150 $\mu\text{J}/\text{pulse}$, the spot diameter is approximately 30 μm and is slightly elliptical the overlap between lines is 10 μm . The results in Figure 8.53 show the effect of increasing the number of over-scans in aluminium while maintaining the laser power and scan speed. The textured surface produced at the base of the cube increases in variability with increasing number of scans. It can be seen, that the relief of the sidewalls, becomes more severe as the number of over-scans increases; this may be attributed to the nature and shape of the Gaussian profile of the beam.

The textured surface appears to be globules of metal left behind by ablation of the surrounding matrix. Alternatively, the structured surface could be condensed droplets of re-cast that have fallen and solidified. Alternatively, the texture could be localized solidified melt pools created by the heat from the plasma (heat from the beam directly evaporates material, therefore, if present, secondary heating effects are likely to arise from the plasma). Figure 8.54 shows that

increasing the scan speed reduces the severity of surface texturing, however, the depth of the machined surface is severely reduced.

It could be reasoned that the best quality machined surface, is machined with a combination of a fast scan speed to reduce texturing and many over-scans to achieve a reasonable depth. This was examined and is shown in Figure 8.54 where a scan speed of 10mm/s was used to scan the surface 50 times. However, even with these parameters there is still significant texturing on the base (Figure 8.54). Further experiments are required to conduct these experiments at varying power levels, where it could be reasoned that at very low power levels the formation of texture is reduced. The inherent problem with laser micromachining is the shape and nature of the Gaussian beam profile. This problem is manifest in trenches where the walls of the machined slot are not parallel.

8.4 Laser Nanofabrication

Laser nanofabrication is being used to enhance processes such as atomic force microscopy and molecular beam epitaxy by dispersing accumulated atoms that forms “islands” of atoms from randomly deposited sources. Using the forces exerted by laser light that is tuned to near atomic resolution, an array of atomic lenses is formed that concentrates atoms in an array of lines with lengths of around 30 nm. This novel form of nanofabrication can create nanostructures without the use of a resist or other pattern transfer technique. The technique has been used to focus sodium, aluminium, and chromium atoms by the force created by the nodes of the standing wave of light that touches them. Laser-focused atomic deposition has been used to create nanostructures of chromium atoms that are 60 nm in height and 28 nm in width. Figure 8.56 shows the basic principle of laser focused atomic deposition [6-8]. The figure shows that atoms pass through a near-resonant laser standing wave as they deposit to the surface. An included dipole moment on the atom interacts with the laser light to cause a force to act toward the nodes of the standing wave. The resulting nanostructures are as small as 28 nm and are spaced at half-a-wavelength.

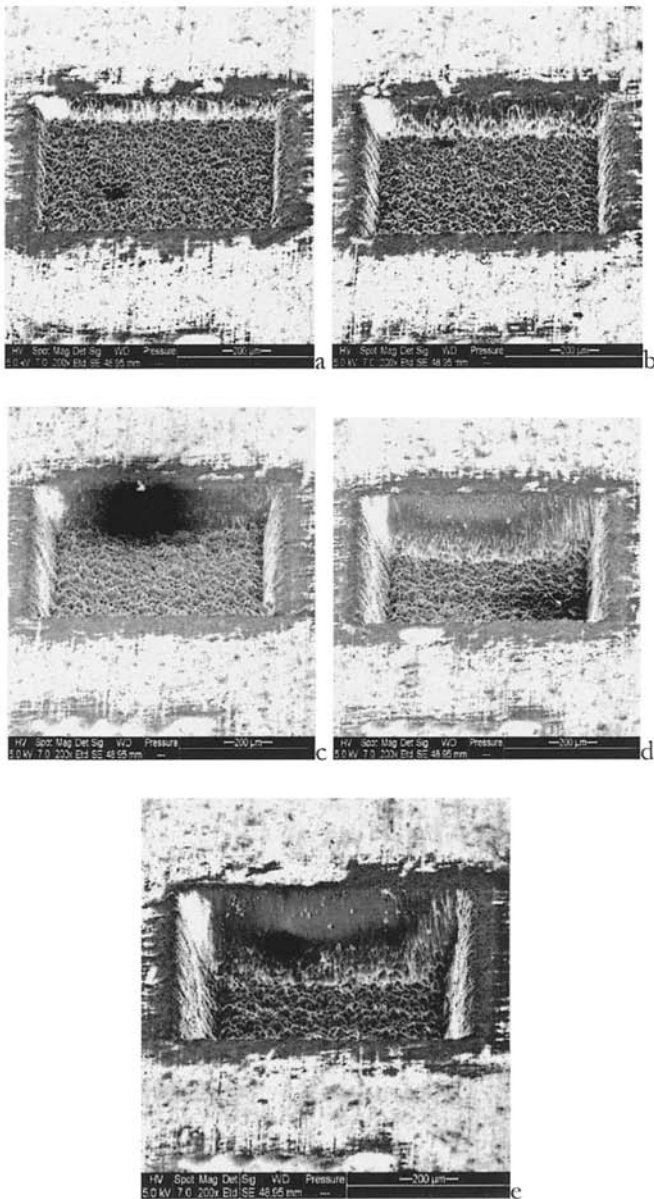


Fig. 8.53. Trench structure variation at 1 mm/s and number of over-scans: (a) 1; (b) 2; (c) 3; (d) 4; and (e) 5

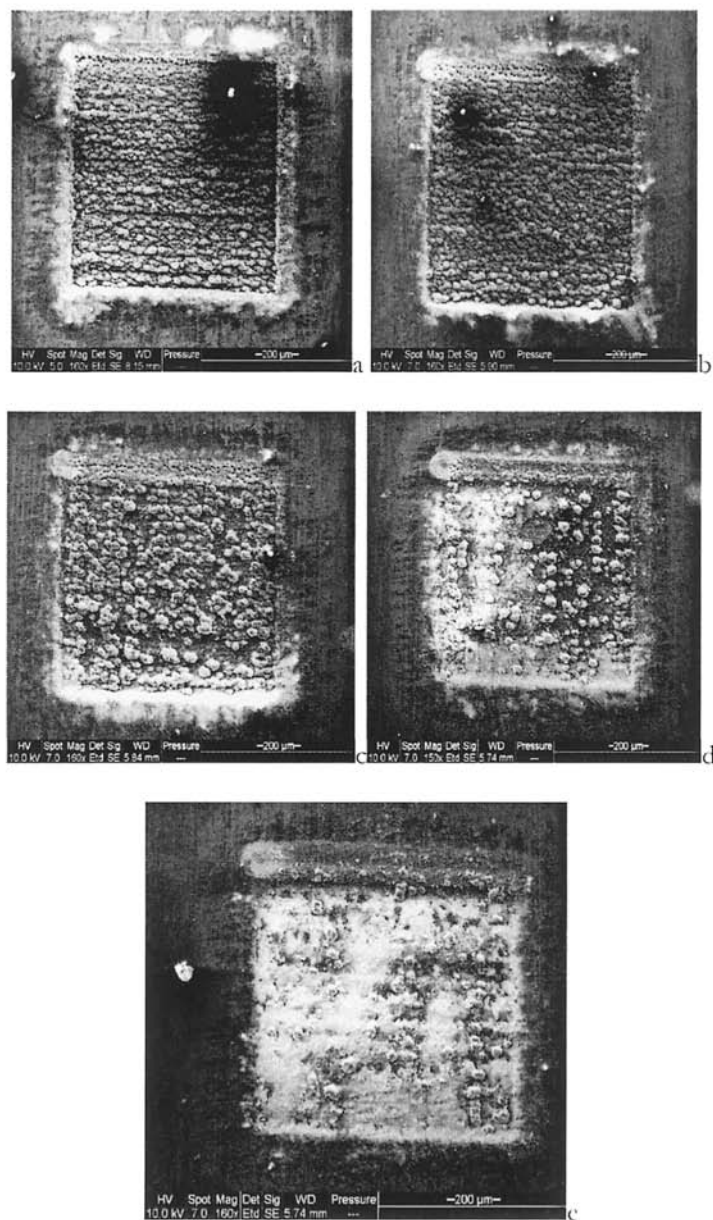


Fig. 8.54. Trench structure variation at 21 over-scans and increasing scan speed (mm/s): (a) 1; (b) 2; (c) 3; (d) 4; and (e) 5

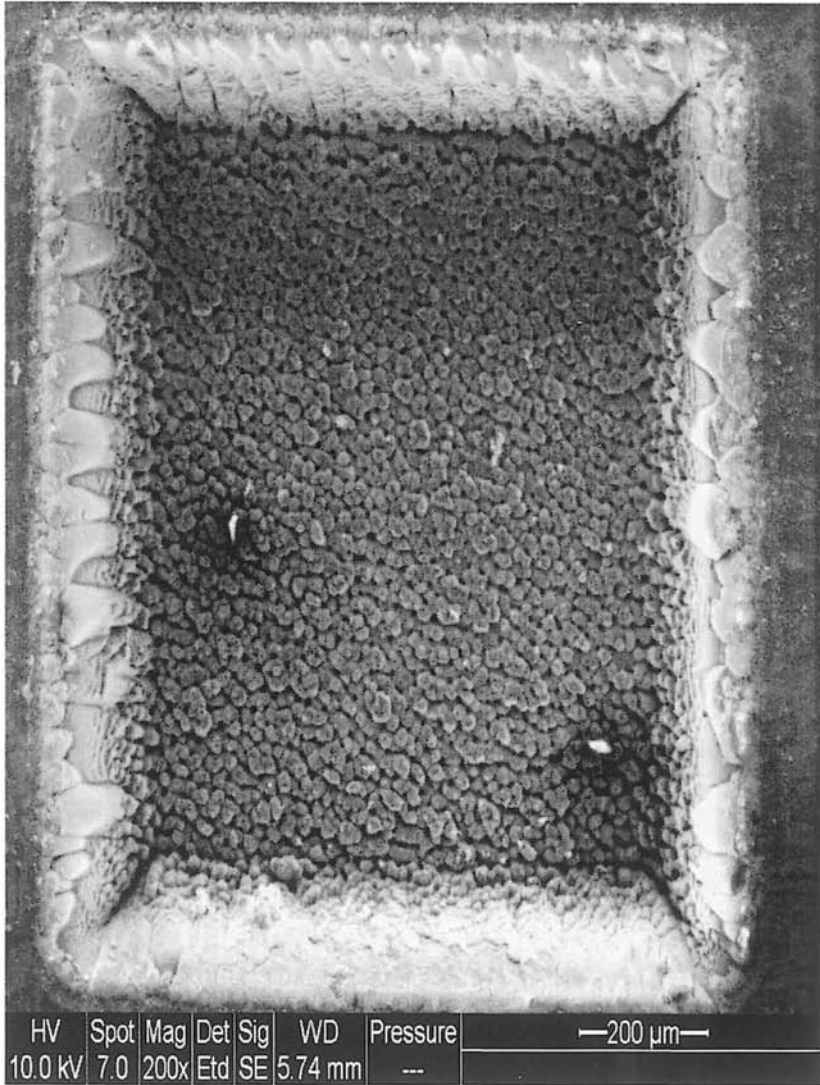


Fig. 8.55. Effects of fast scan speed and 50 over-scans (10 mm/s, 50 over-scans)

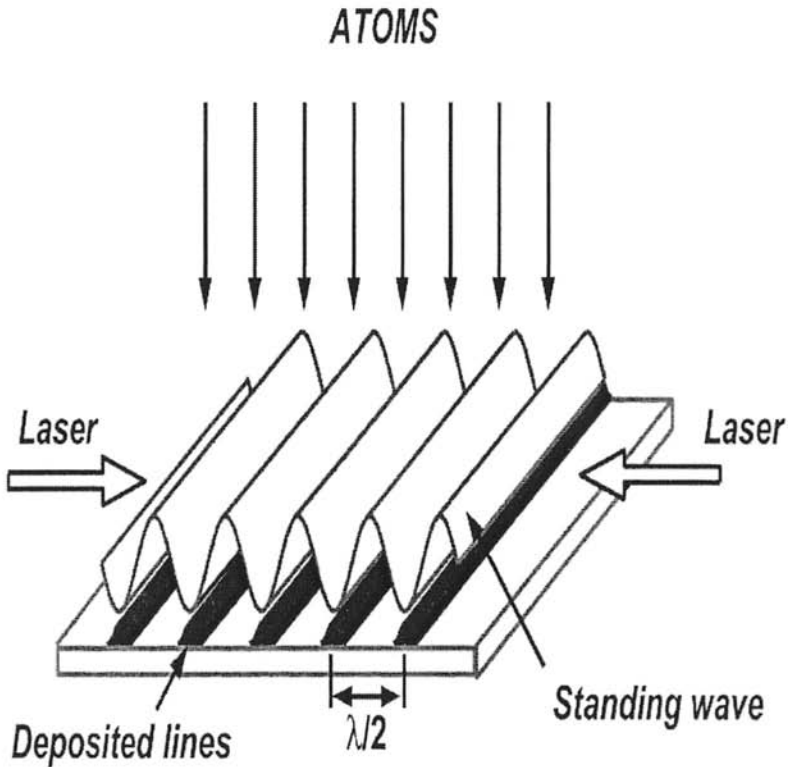


Fig. 8.56. Principle of laser-focused atomic deposition [6]

The deposited features can also be used as pattern masters that have been successfully used for polymer molding processes that make it suitable for developing into a nanomanufacturing process. In other approaches to solve nanofabrication problems, metastable rare-gas atoms have been shown to be an effective exposure tool for lithographic processes. Metastable atoms can be focused using a laser in ways similar to chromium atoms and be manipulated to produce nanofeatures. Figure 8.57 shows an array of AFM images of structures produced using laser-focused lithography.

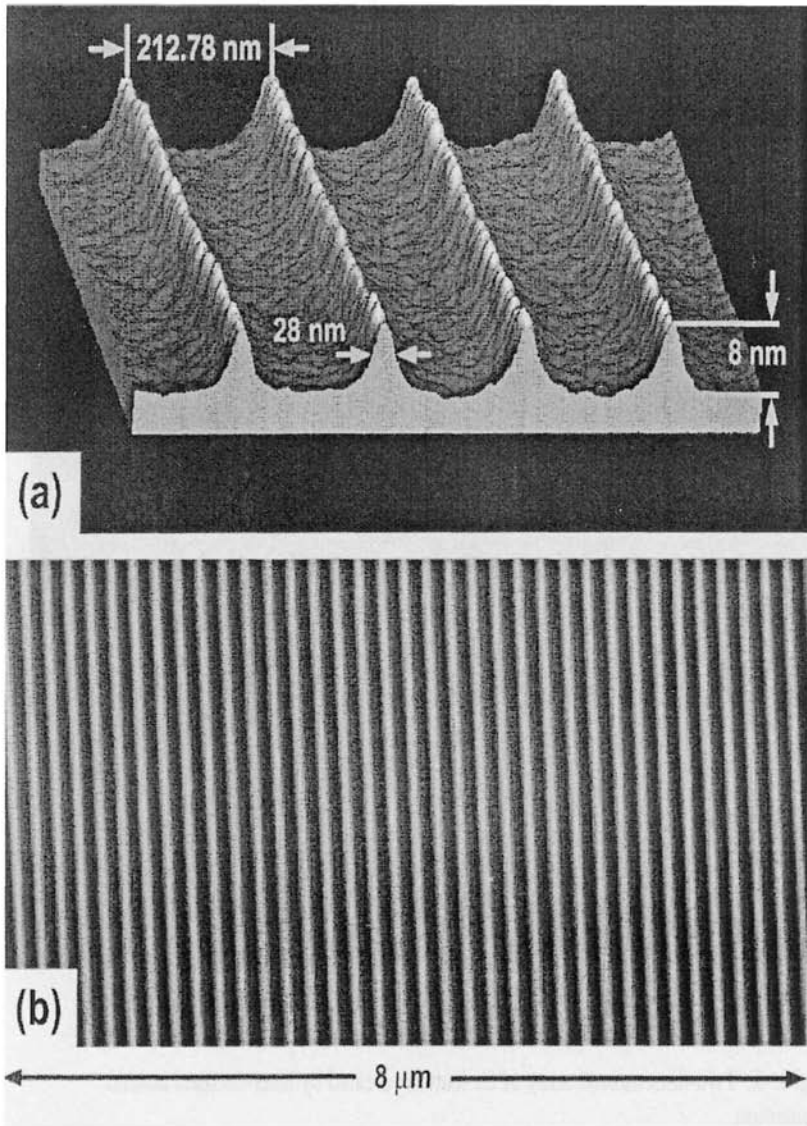


Fig. 8.57. Atomic force microscope images of laser-focused chromium nanostructures: (a) three-dimensional image of nanoscale features deposited to silicon; and (b) image of 60 nm high nanofeatures on sapphire

When coupled with reactive ion etching procedures, laser based nanofabrication of chromium nanostructures can be deposited to create trenches and channels that may prove useful for nanofluidic applications. Figure 8.58 shows the results of combining the two methods.

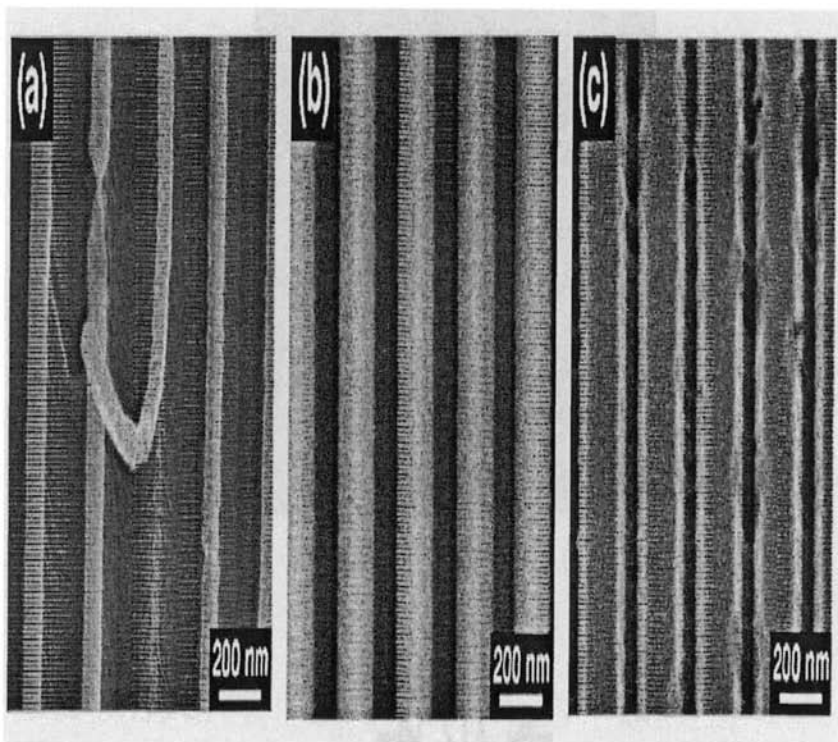


Fig. 8.58. Nanostructures formed when combining reactive ion etching with laser-assisted deposition of chromium atoms: (a) 66 nm wires formed when chromium contrast is highest; (b) uniform trenches in a silicon substrate formed at medium contrast; and (c) narrow trenches formed when contrast is low

Another interesting development in the use of lasers to fabricate products at the nanoscale was developed by Grier at the University of Chicago. Grier used a laser as an optical tweezer to move material from one place to another that was originally in the form of a suspension, or colloid. The beam of light is split up into an array of

beams so that particles become trapped in between the beams of light. Arrays of nanostructures can be manipulated in this way, which can lead to a new form of nanomanufacturing when coupled with established processes. Figure 8.59 shows an array of microscopic beads that have been manipulated using the laser beam [9].

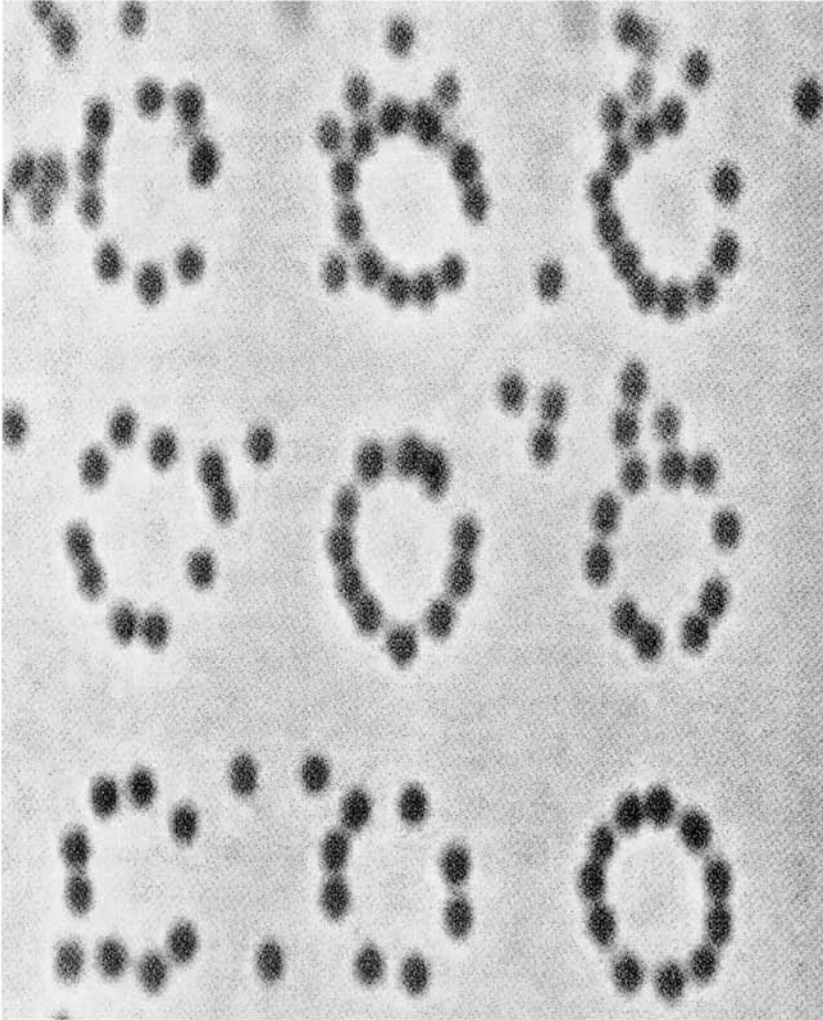


Fig. 8.59. Optical vortices generated by a laser beam to drive microscopic beads in circles [9]

Laser nanofabrication is at a very early stage of development at the moment and will probably need to be combined with other processes to form hybrid nanofabrication and nanomanufacturing processes. A large number of researchers are currently investigating the development of hybrid forms of laser nanofabrication.

8.5 Conclusions

The use of lasers to fabricate products at the microscale is well established. C.F.D. studies of supersonic jets interacting with holes of varying aspect ratio have highlighted complex shock wave structures present during laser micro-machining that enhances the shear stress distribution in the molten pool that is required to physically remove molten material and send it into the jet stream above the surface of the material. Experimental observation has revealed reduced etch rates at high gas pressures, which is coincident with dense plasma formation within the shocked gas stream above the surface of the workpiece. A reduction of gas pressure to near atmospheric pressure reduced detrimental plasma effects and reduced the height of re-cast layers once dominant at high pressure. A simple design rule used for laser micro-machining is to reduce the length-to-diameter ratio of the nozzle, and use the nozzle with shielding gas pressures in the range 0 to 0.5 bar in order to prevent the formation of shock waves in the dynamic plasma field that is responsible for the formation of re-cast layers. The development of processing at the microscale continues to be dominated by the application of femtosecond pulsed processing of engineering materials. However, the development of attosecond pulsed lasers may eliminate the problems created by the formation of a plasma that accompanies the more traditional lasers currently used for microfabrication. Nanofabrication processes that use lasers to create useful nanofeatures are still in their infancy of development. Although the rapid strides made in laser manipulation at the nanoscale may see the development of laser-based nanomanufacturing processes in the not too distant future.

8.6 Problems

1. How is light formed into a single beam of monochromatic energy?
2. What is stimulated emission?
3. Describe the construction of a laser cavity.
4. What are excimer and Ti-sapphire lasers?
5. Describe the characteristics of a laser beam.
6. What is optimal optical quality and how is it measured?
7. Describe laser interactions with various materials.
8. What is the heat-affected zone?
9. Describe the use of a shielding gas in nanosecond pulsed microfabrication.
10. Describe the stages of surface melting.
11. Describe picosecond pulsed laser microfabrication.
12. Explain and illustrate the process of femtosecond pulse microfabrication.
13. Explain how various assist gases affect the surface roughness in femtosecond laser ablated surfaces.
14. Describe recent developments in laser nanofabrication.

References

1. Steen WM, Laser Materials Processing, Second Edition, Springer, New York, 1998.
2. McGeough JA, Micromachining of Engineering Materials, Marcel Dekker, New York, 2002.
3. Jackson MJ, Gill MDH, Khan AH, and O'Neill W, Evaluation of Supersonic Nozzle Designs for Laser Micro-Machining of High Speed Steels, Transactions of S.M.E. – Journal of Manufacturing Processes, (2002), 4, 42-51.
4. Jackson MJ, Robinson GM, Khan AH, Gill MDH, Mills B, and O'Neill W, Micromachining of High Chromium Content Steel Under Controlled Gas Atmospheres,

- Transactions of S.M.E. – Journal of Manufacturing Processes (2003), **5**, 106-117.
5. Jackson MJ, Robinson GM, Mills B, and O'Neill W, Laser Micro-Machining of Chromium Rich Die Steel Under Controlled Atmospheres, Proceedings of the Institution of Mechanical Engineers (London): Part B – Journal of Engineering Manufacture (2003), **217**, 553-562.
6. McClelland JJ, et alia., Laser-focused Atomic Deposition, Science (1993), **262**, p.87.
7. Gupta R, McClelland J, Cellotta R, Nanofabrication of a Two-Dimensional Array Using Laser-focused Atomic Deposition, Appl. Phys. Lett. (1995), **67**, p.3718.
8. Meschede D and Metcalf H, Atomic Nanofabrication: Atomic Deposition and Lithography Using laser and Magnetic Forces, J. Phys. D.:Appl. Phys., (2003), **36**, R17-R38.
9. Stix G, Hands of Light, Scientific American, August 2003, p.p. 30-31.
10. Chichkov BN, Momma C, Nolte F, von Alvensleben A, and Tubbermann A, Applied Physics (1996) **A63**, 109-115.

9. Micromachining Using Pulsed Water Droplets

9.1 Introduction

Water drop machining using a continuous stream of water was developed in the 1970s as a non-traditional form of machining developed for use at the macroscale. To form a continuous drop, water is pumped to pressures in excess of 400 MPa and is expelled through a sapphire or diamond nozzle that generates a fine cutting stream. The stream of water is ejected at speeds in excess of 900 ms^{-1} and is used to cut materials such as paper, leather, plastics, cloth, fibre-glass, and composite materials. Typical applications of water stream cutting systems are provided by Hashish and Hilleke [1]. The material removal rate of continuous water drop machining processes can be increased by mixing abrasive particles with the stream of water in the form of a suspension. The suspension of abrasive particles provides a five-fold increase in material removal rates compared to the abrasive water drop technique [1]. However, the effects of a continuous drop of water creating unacceptable kerf widths and taper of cut are well documented [1]. The continuous water drop system has not been adapted for material removal at the microscale, which would encounter difficulties in maintaining shape integrity if used at this scale.

One way of eliminating these effects is to use a pulsed stream of water drops that create high pressures at the extremities of the impacting drop of water that is powerful enough to erode material more effectively at the microscale than using the abrasive suspension water drop machining technique. Pulsed water drops that contact the surface of the material can be described using the theory of liquid impact [2]. There are various important implications from the theory of liquid impact. The first is that it is the initial stage of impact, which generates the extreme pressures that, leads to damage. This explains why thin plates are easily machined using a continuous

stream of water. For thicker plates, a suspension of abrasive particles is usually mixed with a continuous stream of water. The second is that the precise geometry in the contact region is critical in determining the duration of the high-pressure stage. For example, if the radius of curvature of a drop at contact with a plane surface is double that of a sphere of equivalent volume then the release time after impact is similarly doubled. The circumferential crack pattern that is produced after impact is generated by the interaction of the Rayleigh surface wave with pre-existing cracks in the surface of the material. This chapter illustrates how pulsed water drops can be used to machine selected materials at the microscale using a specially constructed pulsed water drop machining center, and also explains how the theory of liquid impact can be used to predict the machining characteristics of elastically deformable brittle materials when subjected to pulsed water drops. The development of meso machine tools (mMTs) that are capable of delivering high-velocity water droplets on a variety of materials is also described.

9.2 Theory of Pulsed Liquid Impact

The impact of a water drop is divided into two regimes. The first is when the contact edge travels across the surface of the target at a velocity, V_c , which is greater than the shock wave velocity propagating into the water drop. The water behind the shock front, as a result of impact, is compressed as there are no free surfaces through which the pressure can be released. The shock-wave velocity into the water drop is reasonably well described, up to impact velocities of 1000 m s⁻¹ using the following equation:

$$C = C_o + kV \quad (9.1)$$

Where C_o is the acoustic velocity, V is the impact velocity and k is approximately equal to 2. Under the impact conditions considered here, the pressure exerted on the surface of a rigid target is known as

the “water-hammer pressure”, P_c , which is described by the equation:

$$P_c = \rho CV \quad (9.2)$$

Where ρ is the density of the water, 1000 kg m^{-3} . If the compressibility of the target is taken into consideration then the pressure in this initial regime is,

$$P_c = \frac{V\rho_1\rho_2C_1C_2}{\rho_1C_1 + \rho_2C_2} \quad (9.3)$$

Where ρ is the density and C is the shock wave velocity and the subscripts refer to the liquid and solid, respectively. The water-hammer pressure is not constant over the loaded region, which has high-pressure peaks, up to three times the contact pressure, at the edge of the contact zone at the point when the shock wave overtakes the contact edge. However, these edge pressures are of very short duration (usually a few nanoseconds) and can be ignored.

When the shock envelope overtakes the contact edge, a free surface is generated that allows the compressed region to release. The release waves propagate into the water drop from the free surfaces, thus reducing the pressure that is approximately the incompressible Bernoulli pressure, P_i , is given by:

$$P_i = \frac{\rho V^2}{2} \quad (9.4)$$

For velocities considered in this study, the Bernoulli pressure is very much lower than the water-hammer pressure with the precise value dependent on the velocity, since the ratio of pressures is given by $2C/V$. The radius over which high pressure acts can be calculated by examining the geometry of the impacting drop and considering the critical angle between the drop at the contact surface and the target. The radius of release, r , is the point at which the shock wave

travels faster than the velocity at the edge of contact, V_c . The release radius is:

$$r = \frac{RV}{C} \quad (9.5)$$

Where, R , is the radius of the impacting drop. For a 4mm diameter water drop impacting at 300 ms^{-1} , the radius at which release occurs is approximately $300 \text{ }\mu\text{m}$. The time at which the release occurs can also be calculated using the geometry of the impacting drop. The time, after impact, τ , at which release first commences is:

$$\tau = \frac{RV}{2C^2} \quad (9.6)$$

The release waves then propagate towards the center of the compressed region. The total time for complete decompression is:

$$\tau_{\text{rel}} = \frac{3RV}{2C^2} \quad (9.7)$$

The duration of loading is very short. For example, the time for a 4mm diameter drop to release is $0.2 \text{ }\mu\text{s}$ for a 300 m s^{-1} impact. From Eq. (9.5) and (9.7), it is clear that there are considerable changes in r and τ with changes in the drop diameter, R . There are various important implications from the theory of liquid impact. The first is that it is the initial stage of impact, which generates the extreme pressures that leads to damage.

This explains why thin plates are easily machined using a continuous stream of water. For thicker plates, an abrasive is usually mixed with a continuous stream of water. The second is that the precise geometry in the contact region is critical in determining the duration of the high-pressure stage. For example, if the radius of curvature of a drop at contact with a plane surface is double that of a sphere of equivalent volume then τ is similarly doubled. The circumferential crack pattern that is produced after impact is gener-

ated by the interaction of the Rayleigh surface wave with pre-existing cracks in the surface of the material.

Liquid impact is conveniently studied by extruding a stream of water of known volume through a nozzle or drop. It is possible to relate the damage caused by a particular size of drop to that produced by an “equivalent” spherical drop [3]. The point at which circumferential damage becomes visible at a particular velocity and is accompanied by material removal is known as the “machining threshold velocity” (M.T.V.). At velocities higher than the M. T. V., material loss is increased leading to increased machining efficiency. The dynamic criterion for crack growth, and thus strength loss, is given by Steverding and Lehnigk [4] as:

$$\sigma^2 \tau = \text{constant} \quad (9.8)$$

For liquid impact by water drops, Eq. (9.8) becomes:

$$\sigma^2 \tau = \frac{3\rho^2}{2} RV^3 \quad (9.9)$$

Where σ is the impact, or water hammer, pressure and τ is the release time (refer to Eq. 9.7) [4]. This equation can be used to predict the machining threshold velocity for different sizes of water drops, R_1 and R_2 , if the machining threshold velocity for one of the drop sizes is known. As $\sigma^2 \tau$ is constant between the two drops, Eq. (9.9) can be used to find the water-drop radius ratio,

$$\frac{R_1}{R_2} = \left(\frac{V_2}{V_1} \right)^3 \quad (9.10)$$

Where, V_1 is the machining threshold velocity for crack extension for a water drop of radius, R_1 . If a water drop is distorted in such a way that it has a profile equivalent to an effective increase in

the radius of a factor of two, then the threshold velocity, V_2 , is equal to $2^{-1/3} V_1$.

9.3 Impact by Water Drops

9.3.1 Circumferential Damage

The typical damage pattern induced on the surface of a brittle material shows an undamaged region in the center and a clearly defined point, the release radius, at which damage is initiated (Fig. 9.1). This can be explained by considering the decelerating contact edge.

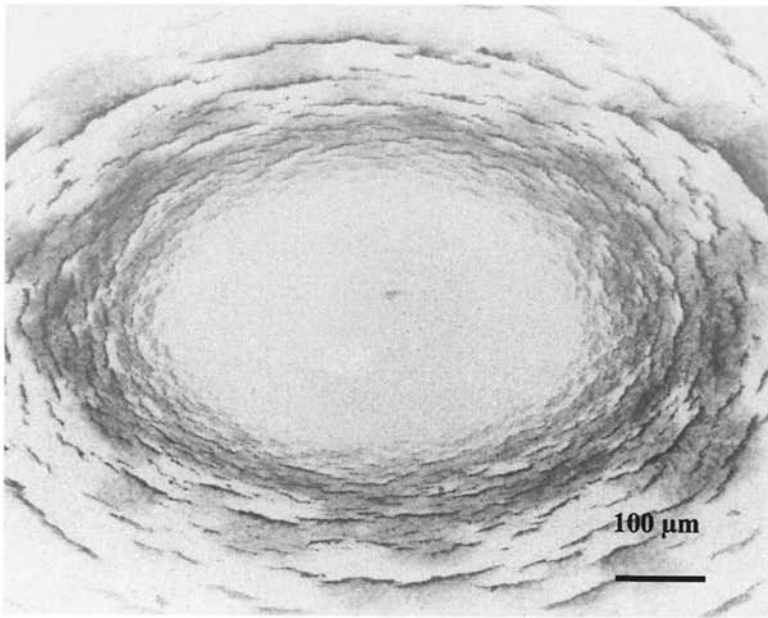


Fig. 9.1. Surface damage created by a single pulse of water impacting the surface at 300 ms^{-1} [2]

When the contact velocity drops below that of the Rayleigh wave, the surface wave emerges and interacts with surface cracks. The cracks are distorted and tend to have a raised lip away from the impact center [3]. As the Rayleigh wave moves away from the center of impact, it is dispersed by interaction with surface cracks and distorts to a broader, less intense, pulse. The very sharp intense wave at the release radius extends many surface cracks by a short amount. As the wave propagates, the width of the wave increases and the magnitude tends to decrease as a result of attenuation and interaction with cracks.

The result is, at a greater radius, only the longer cracks are extended due to the greater stress intensity at the tip of the crack. At the edge of the visible damage, the wave has become so dispersed that it can only extend very large cracks, larger than are intrinsically seen in the material. When polishing scratches are present on the surface, they may be sufficiently large enough to extend. With single-crystal materials and diamond, the damage pattern consists of the opening of cleavage planes, and in the case of chemical-vapor deposited materials, the damage consists of reinforced ring cracks [5].

9.3.2 Lateral Jetting

When the shock wave moves to the free surface of the water drop and release commences, the water drop begins to spread across the surface of the material [6,7]. The interaction of the water droplet with the target causes a high-velocity sideways drop of fluid that has a velocity, V_j , which is faster than the impact velocity, V . Lateral jetting exploits surface asperities, which arise from surface roughness or damage, introduced by the Rayleigh surface wave, resulting in material loss and further extension of cracks (Fig. 9.2). Jackson and Field [6] discuss the contribution of lateral jetting to material loss in single-crystal materials.

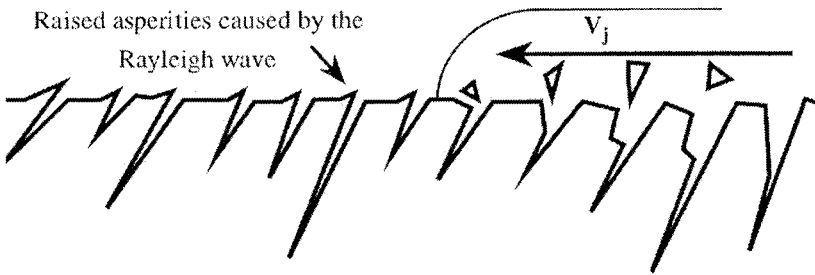


Fig. 9.2. Interaction of water pulse with surface of material exploiting asperities created by the preceding Rayleigh wave [2,6]

9.4 Modeling Machining Thresholds

Machining threshold curves generated using the specially constructed machine tool are reproducible between samples of the same material. Figure 9.1 shows a typical impact damage crater caused by the impact of a single water droplet. Small circumferential cracks surround the site and each crack is modeled as a single crack with a critical crack length that is perpendicular to the impacting drop of liquid. Figure 9.2 illustrates the depth of the crack into the material, which is modeled to represent the machining threshold limit. Again, the critical crack length is that reached when the crack becomes visible to the naked eye.

The absolute machining threshold velocity (A.M.T.V.) of the sample material is related to the logarithm of the static fracture toughness, K_{IC} , of the material. However, the single-impact threshold velocity and the remaining part of the threshold curve, although reproducible, do not seem to have a simple relationship to a single fundamental material property. A computer program was written that predicts the characteristic machining threshold velocity (M.T.V.) curve for a material with a particular crack size, fracture toughness, Young's modulus, and Poisson's ratio.

Once developed it was possible to modify various material properties (such as critical crack size), thus allowing the possibility of

investigating how the machining threshold velocity varies with changes in material properties.

9.4.1 Machining Threshold Model

The damage threshold model incorporates three sections. The first section contains a mathematical approximation of the damaging Rayleigh wave that relates to the quasi-static stress calculations and the stress intensity at the tip of the crack. The second section considers whether the crack being sampled is static, or opening, because an opening crack may have a lower fracture toughness and, therefore, be easier to extend than a static one. The third section considers the time dependency of the stress concentration at the crack tip, which can be considered as the response time to the passing wave, and relates strongly to the depth of the crack. The three components described are multiplied together, giving the dynamic stress intensity, K_{ID} . If the dynamic stress intensity is greater than the fracture toughness, K_{IC} , then the crack will extend.

In generating a threshold curve, up to 300 impacts may be directed onto a single site. If the impact velocity is greater than the A.M.T.V. of the material then the crack will extend. It is believed that the machining threshold velocity, after 300 impacts, will equate to the absolute machining threshold velocity of the material, i.e., if a crack starts to grow then it will be visible after 300 impacts. Therefore, a loop had to be generated in the computer program that simulated a sequence of impacts, extending the crack after each impact until it had grown beyond a critical length when it became visible using an optical microscope.

The damage threshold model performs a theoretical impact and repeats this until the crack is greater than its critical length. The number of impacts required to extend the crack beyond its critical length and reach a length of 100 μm was recorded. If the visible length of the crack is not reached after 300 impacts, then it is assumed that the impact velocity is lower than the A.M.T.V. of the material. The data generated are then used to produce a theoretical machining threshold curve.

9.4.2 Quasi-Static Stress Intensity

The quasi-static stress intensity is the intensity of the stress experienced at the crack tip assuming that the load is applied statically and across the whole length of the crack. However, it is not possible to provide a full stress analysis for a semi-elliptical crack in a varying stress field. The model uses the edge crack analysis by Hartranft and Sih [8], in which the quasi-static stress intensity is:

$$K_s = 2Y \left(\frac{C_L}{\pi} \right)^{1/2} \int_0^{C_L} \frac{\sigma(z)(1 + F(z/C_L))}{\sqrt{(C_L^2 - z^2)}} dz \quad (9.11)$$

Where Y is a dimensionless value which has a magnitude of approximately two for an edge crack, C_L is the crack length, and z is distance into the material, with $z = 0$ representing the impact surface. The integral was stored as a series of numerical values in an array that was interpolated depending on the impact conditions to be simulated. Hartranft and Sih [8] calculated the function $F(z/CL)$ for the geometry of an edge crack as:

$$F(z/C_L) = (1 - (z/C_L)^2) \left[\begin{aligned} &0.295 - 0.391(z/C_L)^2 + 0.769(z/C_L)^4 \\ &- 0.944(z/C_L)^6 + 0.509(z/C_L)^8 \end{aligned} \right] \quad (9.12)$$

$F(z/C_L)$ is equal to 0.295 at the surface of the sample and zero at the crack tip. The function K_s has a discontinuity at the crack tip when $z = C_L$. For the purpose of the model, the upper limit of the integral was changed to $0.99C_L$, which approximates to a real crack due to blunting. The integral was evaluated numerically by using the rectangular method with integral steps of $1/10,000$ of the total crack length.

The function, $\sigma(z)$, as expressed by Eq. (9.11), refers to the stress wave induced by the Rayleigh surface wave over the complete length of the crack. Kolsky [9] stated that the wave function is:

$$\delta_1^6 - 8\delta_1^4 + (24 - 16\alpha_1^2)\delta_1^2 + (16\alpha_1^2 - 16) = 0 \quad (9.13)$$

Where δ_1 and α_1 , are functions of Poisson's ratio such that,

$$\alpha_1^2 = \frac{1 - 2\nu}{2 - 2\nu} \quad (9.14)$$

$$\delta_1 = \frac{h}{\alpha_1} \quad (9.15)$$

Where h is a decay function of the Rayleigh wave [9]. Accounting for finite compressibility of, say, polycrystalline magnesium fluoride that has a Poisson's ratio of 0.18, Eq. (9.13) becomes,

$$\delta_1^6 - 8\delta_1^4 + (24 - 6.24)\delta_1^2 + (6.24 - 16) = 0 \quad (9.16)$$

$$4\delta_1^6 - 32\delta_1^4 + 71\delta_1^2 - 39 = 0 \quad (9.17)$$

The roots given by Eq. (9.17) are:

$$\delta_1 = \pm 0.91, \pm 1.6, \text{ and } \pm 2.15$$

Hence, $\delta_1^2 = 0.828, 2.56, \text{ and } 4.62$

Kolsky [9] stated that attenuation functions, f , q , and s , should be applied along the direction of propagation to describe the decaying nature of the passing wave. Therefore,

$$\frac{q}{f} = \sqrt{1 - \alpha_1^2 \delta_1^2} \quad (9.18)$$

$$\frac{s}{f} = \sqrt{1 - \delta_1^2} \quad (9.19)$$

Substituting the values of δ_1^2 and α_1^2 , for polycrystalline MgF_2 , gives the attenuation functions shown in Table 9.1. Lord Rayleigh [10] stated that, “the general theory of vibrations of stable systems forbids us to look for complex solutions of δ_1^2 ”. Therefore, inserting real values of δ_1^2 into the decay functions expressed by Kolsky [9] gives $\frac{q}{f} = 0.822$ and $\frac{s}{f} = 0.415$.

Table 9.1. Attenuation functions for a material with Poisson’s ratio of 0.18 [2]

α_1^2	δ_1^2	$\underline{q/f}$	$\underline{s/f}$
0.39	0.828	0.822	0.415
0.39	2.56	0.045	Complex solution
0.39	4.62	Complex solution	Complex solution

The rate at which the amplitude of the displacement along the direction of wave propagation is attenuated with depth depends on the attenuation factor,

$$e^{-qz} - 2qs(s^2 + f^2)^{-1} e^{-sz} \tag{9.20}$$

Substituting the values previously calculated for a material with a Poisson’s ratio value of 0.18, gives,

$$\exp^{(-0.822fz)} - 0.582 \exp^{(-0.415fz)} \tag{9.21}$$

Here, the attenuation function, f , is the wave number of the stress pulse when used to calculate the Rayleigh wave function. For polycrystalline magnesium fluoride, the Rayleigh stress wave function is:

$$\sigma_r(z) = \sigma_o(\exp^{-0.822 f z} - 0.582 \exp^{-0.415 f z}) \quad (9.22)$$

Where σ_o is the magnitude of surface stress at impact, and again, f , is the wave number of the stress wave which is,

$$f(\lambda) = \frac{2\pi C^2}{3C_R R V} \quad (9.23)$$

Where, C , is the over-driven shock wave speed, C_R is the Rayleigh wave speed, R is the radius of the water drop, and V is the impact velocity. Stress wave functions were calculated for the materials investigated in this paper.

The Rayleigh wave contains both a shear and a longitudinal component. The wave is tensile at the surface and becomes compressive at a depth of approximately 40 % of its wavelength, which for a 200 m s^{-1} impact on zinc sulfide, occurs at approximately $200 \mu\text{m}$. As the spatial decay of the Rayleigh wave is frequency dependent, it is necessary to determine the frequency for a given velocity.

The Rayleigh wave is a single pulse and does not have a single well-defined frequency. With the original simulation, it was decided to simply use the fundamental frequency to avoid having to perform a Fourier transform on the approximately shaped triangular pulse. Swain and Hagan [11] suggest that at the release radius, the peak height of the simplified triangular wave pulse be:

$$\sigma_{max} = \beta \rho C V \quad (9.24)$$

Where $\rho C V$ is the water-hammer pressure, and β is a function of the Poisson's ratio, ν , of the target material, being equal to,

$$\beta = \frac{1}{2}(1 - 2\nu) \quad (9.25)$$

The decay of the magnitude of the Rayleigh wave is proportional to $r^{-1/2}$. Therefore, the magnitude at any specified distance from the center of impact may be calculated from the initial impact conditions and the properties of the target material. For the purpose of the model, the crack under examination was at its most stressed point, the release radius.

9.4.3 Dynamic Stress Intensity Factor

To model the interaction of a Rayleigh surface wave with a crack it is necessary to calculate the dynamic stress intensity factor at the crack tip. Freund [12] has analysed the case of a plane wave incident on a semi-infinite crack. The dynamic stress intensity factor has the following general form:

$$K_{ID} = k(v) \cdot k(t) \cdot K_s \quad (9.26)$$

Where $k(t)$ is the time-dependent coefficient of the dynamic stress intensity factor due to the shape of the stress wave, K_s is the quasi-static stress intensity factor for a crack of length, C_L , and $k(v)$ is a modifying coefficient to account for crack speed. The velocity of the opening crack must also be considered in the model.

A crack that is opening with a low crack velocity, has high critical stress intensity than a crack with a high crack velocity (i.e., it is easier to keep the crack growing than it is to initiate growth). The damage threshold curve model relies on a crack becoming visible when it reaches 100 μm in length; therefore, it is vital to know its velocity. A modifying function is incorporated in Eq. (9.26) to take account of the possibility of the crack opening. Freund [12] calculated the modifying function ($v = 0.25$) as:

$$k(v) = \frac{1}{\left(1 + \frac{v}{C_R - v}\right) \left(1 - 0.531 \frac{v}{C_R}\right)^{1/2}} \quad (9.27)$$

Where v is the velocity of the crack. When the crack is static, $k(v)$ is equal to one, and when the crack is opening up at the maximum theoretical velocity, the value of $k(v)$ is zero, which is in agreement with the work of Broberg [13]. The current crack velocity (initially set at zero) is evaluated from the dependence of the crack velocity on the dynamic stress intensity factor and is given by:

$$v = v_{\max} \left(1 - \left(\frac{K_{IC}}{K_{ID}} \right)^2 \right) \quad (9.28)$$

Equation (9.28) is valid when the current crack velocity is greater than zero, where K_{ID} is the dynamic stress intensity, K_{IC} is the fracture toughness of the impacted material, and v_{\max} is the maximum crack velocity [14]. Dulaney and Brace [15] and Berry [16], calculated the maximum crack velocity as:

$$v_{\max} = \sqrt{\frac{2\pi E}{B\rho}} \left(1 - \frac{C_L}{a} \right) \quad (9.29)$$

Where B is a constant and C_L/a is the ratio of the crack length to sample thickness. Roberts and Wells [17] obtained a value for B , when $a \gg C_L$, giving the maximum crack velocity as,

$$v_{\max} = 0.38 \sqrt{\frac{E}{\rho}} \quad (9.30)$$

Which is approximately equal to $0.6 C_R$, where the Rayleigh wave velocity is the maximum theoretical crack velocity for fracture of brittle materials. Considering the time dependency of the dynamic stress intensity, for a time-dependent stress profile, $\sigma(t)$, the stress wave may be considered as an incremental sum such that,

$$\delta\sigma(t) = \sigma \delta t \quad (9.31)$$

The time-dependent coefficient of the dynamic stress intensity factor may then be evaluated using:

$$k(t) = \frac{2}{\pi} \int_0^t \dot{\sigma}(s)(t-s)^{1/2} ds \quad (9.32)$$

This analysis is based on the geometry of a semi-infinite crack. For a finite crack, of length C_L , the result must be modified to account for stress wave reflection from the free surface (application of Eq. (9.32) would otherwise suggest that, for a finite length crack, the dynamic stress intensity factor tends to infinity as time tends to infinity, i.e., K_{ID} approaches ∞ as t approaches ∞).

In this case the time-dependent coefficient of the dynamic stress intensity factor can be expressed in the following form:

$$k(t) = f\left(\frac{vt}{C_L}\right) \quad (9.33)$$

Where v is the velocity of the crack [18]. Sih [19] has evaluated the function shown in Eq. (9.33) numerically. The general form of a stress wave pulse implies that K_{ID} increases initially as $t^{1/2}$ reaches a maximum value that is 1.25 times greater than the quasi-static value.

It then decays in an oscillatory manner towards the quasi-static value as the time tends to infinity. This behavior has been approximated in the present study by a dynamic stress intensity factor of the form,

$$K_{ID} = \frac{k(v)K_s}{\tau^{1/2}} \int_0^t \dot{\sigma}(s)(t-s)^{1/2} ds \quad t < \tau \quad (9.34)$$

9.4.4 Simulation Of Impact Machining

Liquid impact was simulated by modeling an approximately shaped triangular wave (the Rayleigh stress wave) moving radially away from the center of impact. A computer program was written [2, 6, 20] that simulated the extension of a surface crack until it appeared visible to the naked eye and resulted in material loss. The crack was situated immediately outside the release radius where the Rayleigh wave was developed.

The program calculated the initial impact conditions such as equivalent water drop diameter based on the properties of the material, impact velocity, and the distance of the crack from the center of impact. In order to increase the speed of computation, a set of pre-generated tables of quasi-static stress intensity factors were accessed using a simple linear interpolation routine to provide input for calculating the dynamic stress intensity factor. After setting the initial crack length as the critical crack length and its velocity at zero, a crack was excited by simulating the action of a passing Rayleigh wave over the length of the crack. An iterative procedure was established to simulate the passing wave over the crack up to 300 times in order to establish the damage threshold of the target material.

Every iteration of the program calculated the length of the crack after each wave pulse. Initially, the crack tip response time was calculated. The stress wave distribution, as a function of depth, was calculated and incremented with a pre-determined series of time steps. The time dependence of the stress wave, and its effect on the dynamic stress intensity factor was established by selecting the appropriate dynamic stress intensity factor that is dependent on the response characteristics of the material subjected to liquid impact.

The program also checked to see whether the crack was moving, or not, by comparing the dynamic stress intensity factor with the static fracture toughness of the material. The current crack velocity was calculated together with the new crack length. If the crack length exceeded 100 μm , then the number of iterations was determined for that particular impact velocity. For crack lengths less than 100 μm , the program would re-iterate the routine to find the number of iterations required for the crack to grow to a length of 100 μm .

9.4.5 Machining Threshold Curves

Machining threshold curves were determined using the model described and by impacting specimens using the pulsed water drop machining apparatus. The accurate control of impact position, impact rate, and impact velocity means that a sample of material measuring approximately one-inch diameter can be used to generate a machining threshold curve. Up to twenty impacts sites are designated within the boundary of the specimen each with a different velocity assigned to it. These sites must be at least five millimetres apart from the edge so those cracks from different sites do not interact with each other. Figure 9.3 shows an illustration of the pulsed water drop machining apparatus. The firing sequence for each water drop takes approximately 5 seconds to complete. This means that twelve pulses per minute can be ejected from the apparatus.

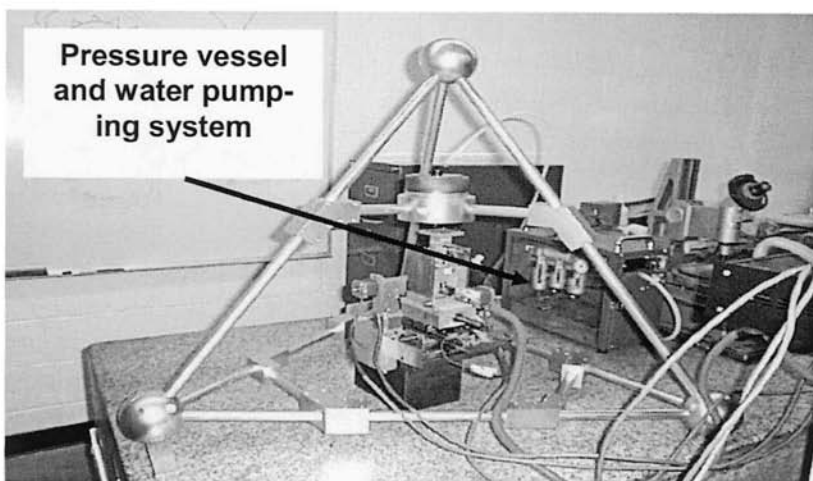


Fig. 9.3. Pulsed water drop machining center

Each site is impacted once at its assigned velocity. The specimen is examined using an optical microscope at 100 x magnification to inspect the occurrence of circumferential impact damage. Impact sites that remain undamaged are subjected to further impacts and re-

examined via the optical microscope. The impact process is repeated until each site has been impacted 300 times.

The characteristic machining threshold curve is a function of the number of impacts at particular velocities. The damage threshold point at 300 impacts is assumed to be the absolute machining threshold velocity of the target material. At velocities below this point, circumferential damage is not developed. This is because the energy provided by liquid impact is not significant enough to extend cracks up to the visible limit. The materials used in this investigation were zinc sulfide, silicon, sapphire, and magnesium fluoride. All materials were polycrystalline and are used in applications in the aerospace industry.

9.5 Comparative Results

9.5.1 Silicon

The visible difference between a silicon substrate and a zinc sulfide substrate is that silicon is opaque. Therefore, the experimental damage threshold curve was obtained by observing the damage with reflected light only. This technique is less sensitive at observing cracks than using transmitted light as surface cracks are very small. With a transparent material, extensive cone cracking allows accurate observation of the initiation of surface damage. As a result, the velocity at which damage was seen after one impact may be greater than the true velocity. Therefore, this substrate was selected to investigate the difference in velocities.

The theoretical machining threshold curve, shown in Fig. 9.4, shows good agreement with the experimental machining threshold curve after a large number of impacts.

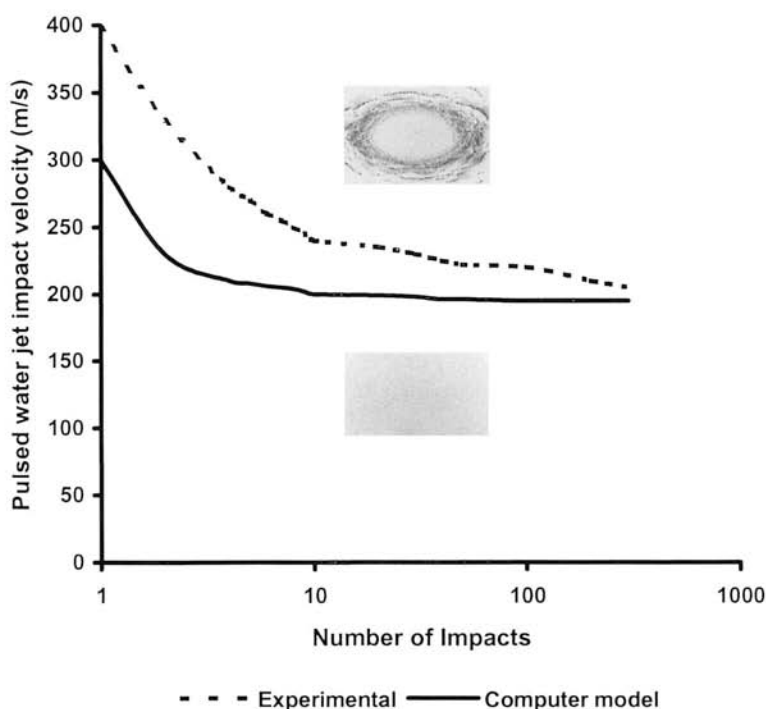


Fig. 9.4. Computer-modeled and experimental machining threshold curves for silicon

It should be noted that the fracture toughness and average crack size values used in the theoretical model were those values obtained from experiments conducted on samples used for determining threshold curve studies. However, the model became inaccurate when compared to the experimental data observed at the lower end of the damage threshold curve. This may be due to the method of observing machining threshold damage, and the fact that the first impact may excite a crack that is larger than the average crack size. The average crack size was determined to be $40\text{ }\mu\text{m}$ while the fracture toughness was found to be $0.94\text{ MPa m}^{-1/2}$.

9.5.2 Alumina

Alumina was selected to investigate whether the model could simulate a threshold curve for a tougher material than zinc sulfide and silicon, and one having a higher crack growth velocity. The fracture velocity used was 3700 m s^{-1} that ignores any crystalline orientation. As shown in Fig. 9.5, there is good agreement with the machining threshold velocity using a fracture toughness of $2.5 \text{ MPa m}^{-1/2}$ and a crack size of $30 \text{ }\mu\text{m}$. The two experimental machining threshold curves shown are for samples with different surface roughness.

In this case, the surface roughness is incorporated into the computer program by varying the crack size. However, the theoretical single-shot threshold velocity was higher than expected. The size of the minimum visible crack was investigated and was found to change the single-shot threshold velocity quite significantly with little variation in the A.M.T.V. Again, this may be explained by the fact that the first impact may excite a crack that is much greater than the crack size specified in the computer program.

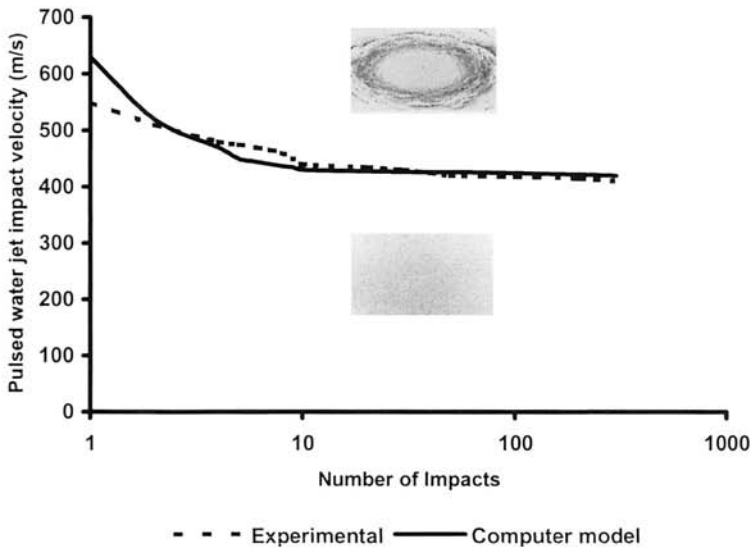


Fig. 9.5. Computer-modeled and experimental machining threshold curves for alumina

9.5.3 Magnesium Fluoride

Magnesium fluoride is a material that has a range of machining threshold velocities. A number of samples impacted suggested an average M.T.V. of 230 m s^{-1} . However, samples examined recently produced a machining threshold velocity of 190 m s^{-1} . The difference between the two samples may be due to differences in the way the materials were fabricated. If this is the case then the samples may have different fracture toughness and, as a result, different absolute machining threshold velocities (A.M.T.V.). To understand the difference a theoretical machining threshold curve was produced. The theoretical machining threshold curve produced accurate agreement with the latest samples examined. The predicted M.T.V. (300 impacts) was $185 \pm 5 \text{ m s}^{-1}$ (Fig. 9.6). The model, in this case, may be used to provide the user with a quality control tool to be used in the manufacture of such materials.

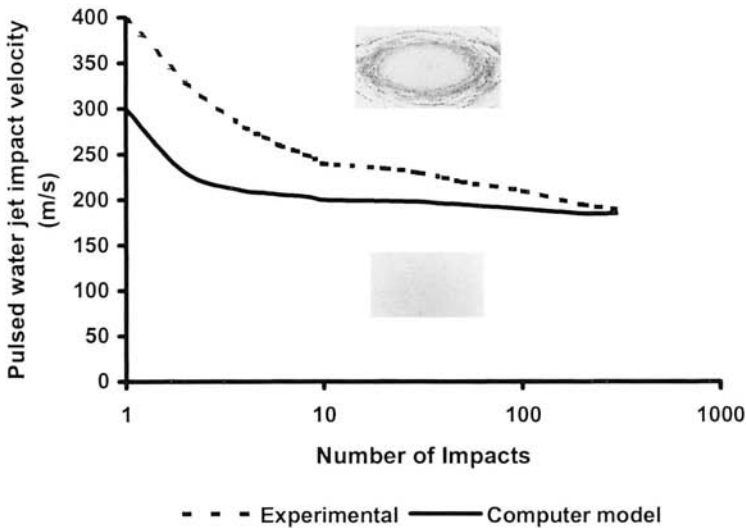


Fig. 9.6. Computer-modeled and experimental machining threshold curves for magnesium fluoride

9.6 Material Removal Rates

The area of damage caused by liquid impact on polymeric surfaces has been investigated by Hand, Field, and Townsend [20]. The measurement of impact erosion by water drops ejected from a converted air rifle was performed using a surface profilometer [20]. A model of damage was developed that incorporated an angle of impact between water drop and target. The equation derived for the area of damage was shown to be:

$$A_d = K \cdot \frac{\rho \pi r^2 V^3 \cos \theta}{C} \cdot \left(1 + \frac{V^2 \sin^2 \theta}{8C^2} \right) \quad (9.35)$$

Where K is a material constant, r is the radius of impact, C is the shock wave velocity, V is the impact velocity, ρ is the density of water, and θ is the impact angle. Multiplying the depth of impact by the area of damage provides a measure of the removal of material by one single pulse of water at a particular velocity. In the present study, the author has directly measured a series of damage sites caused by water drop impacts and has presented this as a material removal rate. The impact sites were measured by traversing a surface profilometer across the impact sites (Fig. 9.7) in a variety of different directions and depths in order to produce an impact profile of each crater. The maximum number of water pulses ejected from the pulsed water drop machining apparatus is 12 per minute, therefore, the damage per pulse is multiplied by 12 to achieve a volumetric material removal rate per minute. Table 9.2 shows the measured material removal rates for silicon, alumina, and magnesium fluoride materials at impact velocities in the range 250 to 1000 ms⁻¹. It should be noted that the lowest removal rates shown in Fig. 9.2 (at impact velocities in the range of 200 and 400 ms⁻¹) are similar to those obtained when micromachining using pulsed nanosecond and picosecond lasers. The highest removal rates obtained at impact velocities greater than 500 ms⁻¹ are comparable to micromachining methods that use traditional cutting tools.

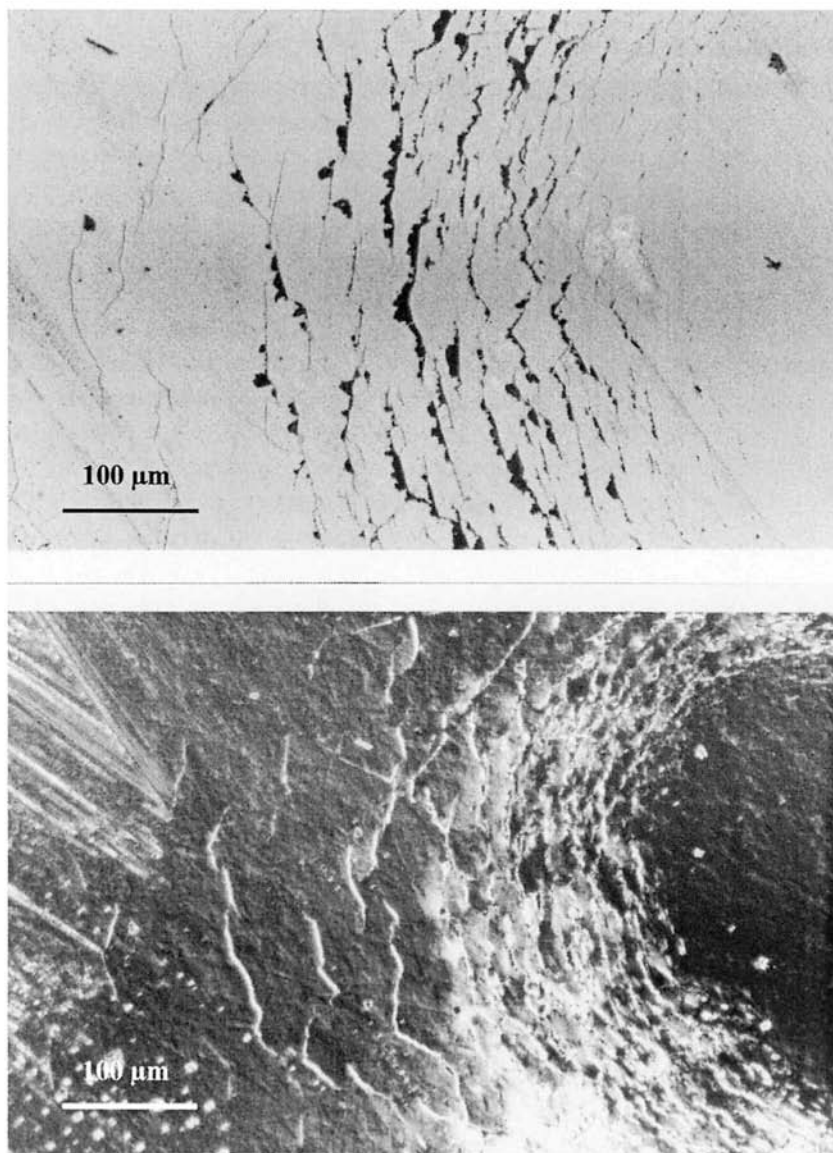


Fig. 9.7. Edge of the impact crater showing localized damage caused by the Rayleigh surface wave

Table 9.2. Material removal rates for materials machined using pulsed water drops.

Material	Impact velocity (ms^{-1})	Material removal rate ($\text{mm}^3 \text{min}^{-1}$)
Silicon	250	5
	300	8
	400	12
	500	15
	600	24
	700	31
	800	36
	450	2
	500	4
Alumina	600	6
	700	8
	800	12
	900	15
	1000	18
	250	6
	300	10
Magnesium fluoride	400	14
	500	22
	600	30
	700	36
	800	43

9.7 Design of Water-Based Machine Tools

The problem with existing machine tool structures is the amount of vibration that is transmitted through the spindle or nozzle, which affects the quality of surface finish and the dimensional accuracy imparted to the workpiece being machined. Owing to the way the spin-

dle is mounted at the end of a cantilevered structure, low resonant frequencies can occur that are easily excited.

In addition, the amplitude of oscillation is more pronounced as a result of the geometry of the spindle mounting. An alternative approach is to design a vibration suppressing machine tool structure. When vibrations travel through a tetrahedral structure, they are canceled out or minimized due to the interference between the vibrating waves as they travel through the loops of the structure. The ability to dampen out vibrations is needed because if the spindle oscillates during machining, an increase in the depth of cut, or a variation in the plane of impact, will occur, thus reducing the quality of surface finish, or dimensional accuracy of the machined part will be reduced significantly.

Figure 9.8 shows the tetrahedral space frame structure constructed for the purpose of pulsed water drop micromachining. Modal analysis experiments were performed to investigate the structural response of the structure. Modal analysis experiments consisted of measuring the natural frequencies of the structure and performing frequency response functions (F.R.F.) to determine the mode shapes of the structure. In addition, a finite element model (F.E.A.) model was constructed to compare to the experimental data, which also may be used for modeling any alterations to the design.

9.8 Analysis of Space Frame

The tetrahedral frame was initially analyzed from a numerical viewpoint using a closed-form solution and a numerical solution using finite element analysis.

9.8.1 Finite Element Model

Modal analysis of the tetrahedral structure using the finite element method was performed to obtain the natural frequencies and the mode shapes within the range of 0 - 8500 Hz, to compare to experimentally determined mode shapes. Modal analysis simulation was performed using the finite element software package ANSYS 6.1.

Model preparation was the first step in analyzing the modes of the tetrahedral structure.

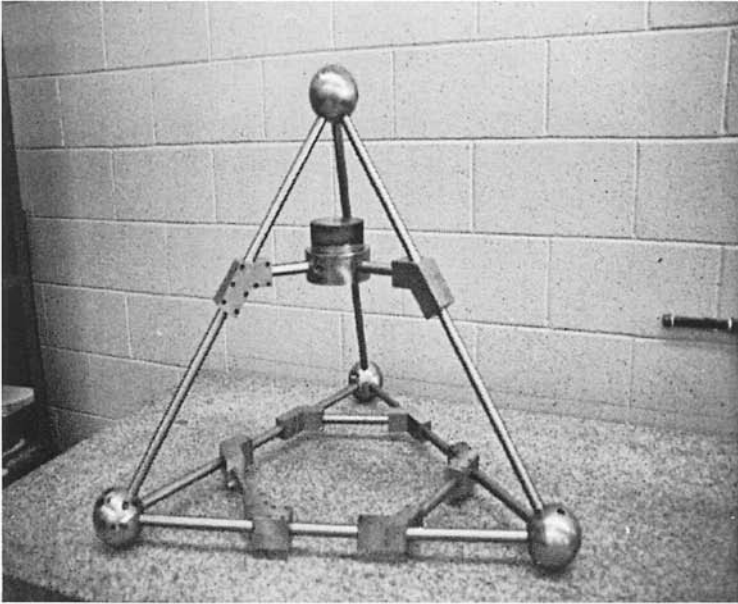


Fig. 9.8. Tetrahedral space frame

This step involved creating a beam model of the structural members. The six bars that link the spheres and the reinforcement connections, which tie together the spindle sub-frame and the reinforcement bars were modeled using (ANSYS beam 188 elements), which have three translational degrees of freedom U_x, U_y , and, U_z at each node and three rotational degrees of freedom θ_x, θ_y , and θ_z . The three rotational degrees of freedom were needed to accurately simulate the boundary conditions at the vertices of the structure. The finite element model, shown in Fig. 9.9 consists of 115 elements and 513 nodes. The material properties of cold rolled steel were used in the modal analysis.

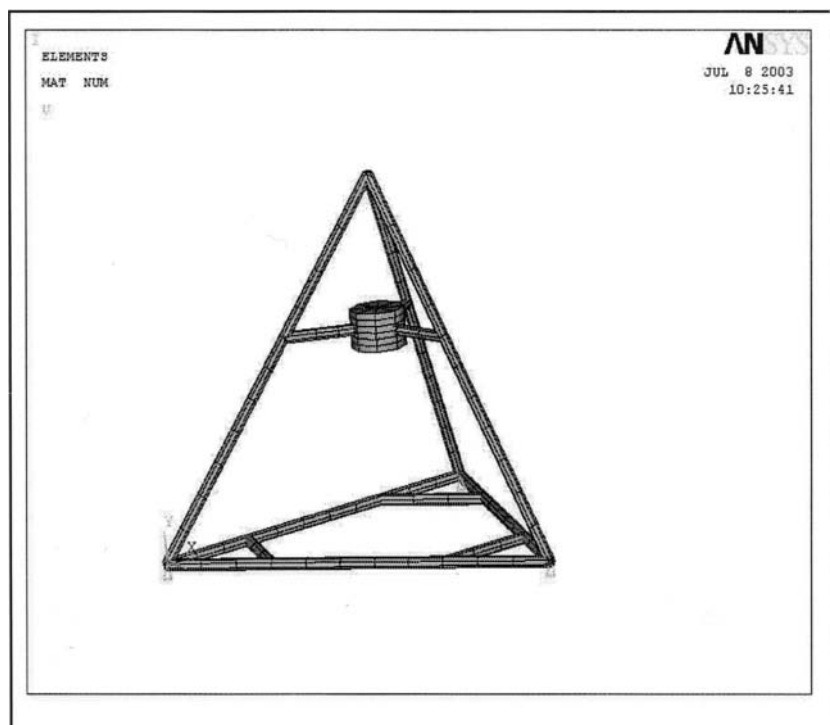


Fig. 9.9. Finite element model of the tetrahedral space frame

Each of the beam elements used enabled a geometric cross-section to be assigned. Each of the structural beams was given a circular cross-section of 0.75-inch diameter. The spindle holder was modeled by using a 3.5-inch outer diameter and a 0.70-inch inner diameter beam. This allowed the spindle holder to rotate and bend in a smooth manner. To simulate the spheres located at each of the vertices of the structure, a mass element (ANSYS mass 21) was used. The actual spheres of the structure were weighed and mass moments of inertia were calculated, and then put into the mass element model. Beam elements were chosen over solid elements to reduce the computation time required to solve the problem.

9.8.2 Closed-Form Solution Model

Sample calculations were performed to approximate the dynamic response of the tetrahedral structure. The purpose of these calculations is to obtain a continuous model of the structure instead of a finite element approximation. The structure was modeled as four spheres at each of the vertices of the tetrahedron, with springs simulating the structural links between them. Equation 9.36 was the equation used to generate a mathematical model of the structure.

$$[M] * \ddot{X} + [K] * X = 0 \quad (9.36)$$

Where, $[M]$ is the matrix of masses for each sphere, \ddot{X} is the acceleration of each sphere, $[K]$ is the stiffness matrix for all of the structural links, and X is the displacement of each sphere. Equation 9.37 was used to model the stiffness (K) of each connecting rod (axial displacements are considered in this formulation to decrease the complexity of the solution):

$$K = \frac{A * E}{L} \quad (9.37)$$

Where A is the cross-sectional area, E is Young's modulus of elasticity, and l is the length of the beam. Since this structure was modeled as a 9 degree-of-freedom (d.o.f.) system, the methods listed by Inman [21] were used. This method assumes that each of the d.o.f.'s can be modeled by the superposition of several single d.o.f. systems. The structure is a three-dimensional structure, in which each equation had to be related to a global coordinate system similar to the methods used in finite element formulations. There were 3 degrees of freedom for the top sphere and 2 degrees of freedom for the base spheres, which led to 9 possible natural frequencies. Damping was not considered in the mathematical modeling of this structure because it would create more difficulty in solving the equations.

9.9 Mode Shapes of Tetrahedral Structures

The impact hammer test has become a widely used device for determining mode shapes. The peak impact force is nearly proportional to the mass of the head of the hammer and its impact velocity. The load cell in the head of the hammer provides a measure of the impact force. This data is used to compute the frequency response function (F.R.F.). The use of an impact hammer avoids the mass-loading problem and is much faster to use than a shaker. An impact hammer consists of a hammer with a force transducer built into the head of the hammer. The hammer is used to impart an impact to the structure at designated points of the structure and excite a broad range of frequencies. The impact event is supposed to approximate to a Dirac-delta function [22].

9.9.1 Experimental Method

The tetrahedral structure was placed on a granite table in order to gain accelerometer measurements, thus the structure was allowed to freely move longitudinally and transversely across the table. The roving accelerometer approach was used for all of the measurements. The center of the spindle frame was used as the excitation point for the structure. The accelerometer was placed at various points of interest about the structure. Figure 9.10 shows the experimental structure and the impact hammer used to excite the structure.

9.9.2 Experimental Procedure

The data acquisition system was set up to take data at a sampling frequency, F_s , of 17,000 Hz for 8192 points with a delay of 100 points. The voltage range on both channels was set to ± 5 volts. Data was acquired in the time domain by averaging 8 ensembles and storing the data in binary format. This data was used to find the natural frequencies of the structure and their corresponding mode shapes.

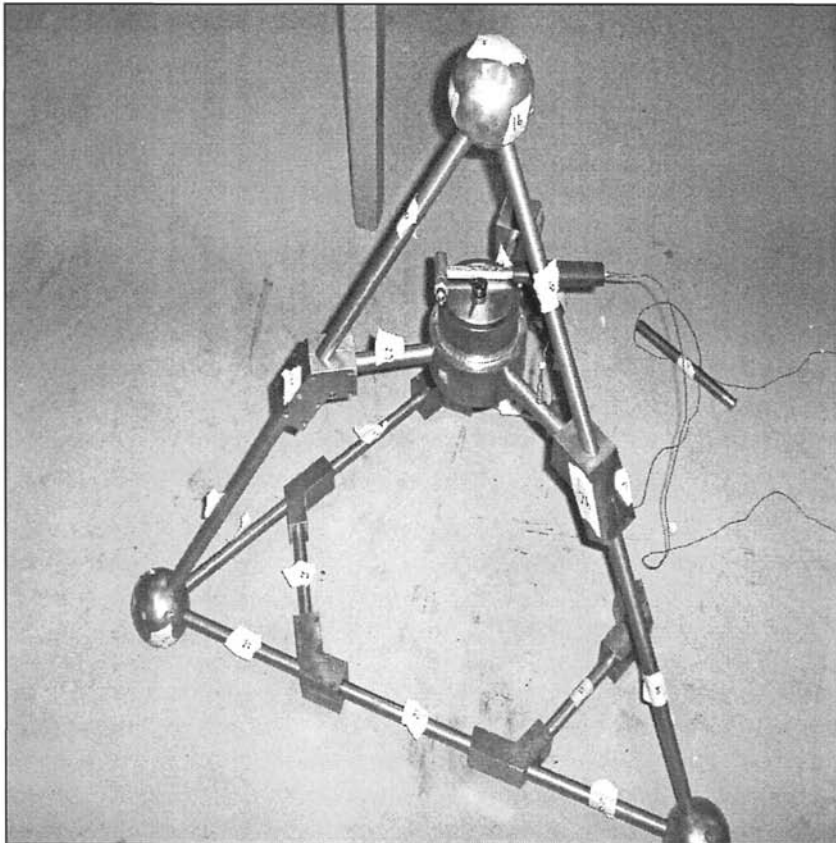


Fig. 9.10. Tetrahedral structure showing marked points of vibration measurement and the impact hammer used to excite the structure

While applying the roving accelerometer technique, the structure was excited in the center of the spindle sub-frame and data were acquired at points 1-28. Before the time domain data was stored, it was filtered to remove any aliasing that might have occurred from under-sampling. This was accomplished by installing an analog filter between the power supply and the P.C. The frequency was set at 8500 Hz, which corresponds to the Nyquist frequency of the measured data. After the data were recorded, they were translated into a binary file.

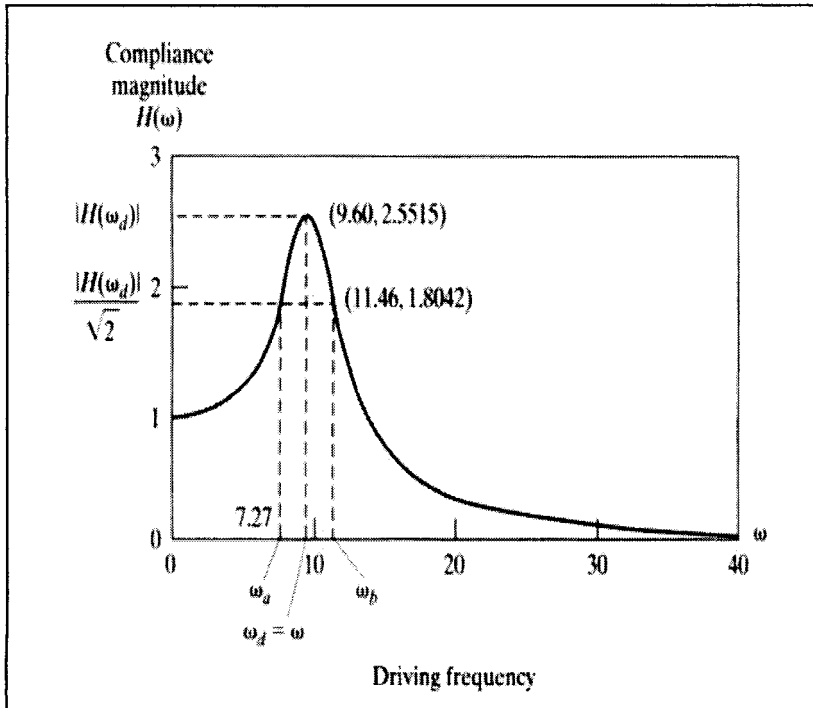


Fig. 9.11. Magnitude of the frequency response function

The method used on the F.R.F. data of a multi-degree-of-freedom structure is the single-degree-of-freedom-curve-fit (S.D.O.F.). In this method the frequency response function for the compliance is sectioned off into frequency ranges bracketing each successive peak. Each peak is analyzed by assuming that it is the F.R.F. of a single-degree-of-freedom system. This assumes that in the vicinity of resonance the F.R.F. is dominated by that single mode. Once the frequency response function (F.R.F.) is completed for the chosen data points of a structure, it is then appropriate to compute the natural frequencies, damping ratios and modal amplitudes with each resonant peak.

An example of one of the F.R.F.s is shown in Fig. 9.11. The damping ratio associated with each peak is assumed to be the modal

damping ratio, zeta (ζ). The modal damping ratio zeta is related to the frequencies corresponding to Eq. 9.38.

$$|H(\omega_a)| = |H(\omega_b)| = \frac{|H(\omega_d)|}{\sqrt{2}} \quad (9.38)$$

And $\omega_b - \omega_a = 2\zeta\omega_d$, so that

$$\zeta = \frac{\omega_b - \omega_a}{2\omega_d} \quad (9.39)$$

ω_d is the damped natural frequency at resonance such that ω_a and ω_b satisfy Eq. 9.38. The condition of Eq. 9.39 is termed the 3 dB down point. Both the natural frequency and the damping ratio Zeta may be found via this method. Once the values of ω_a and ω_b are determined, then ζ is found for the structure at the prescribed frequency (Eq. 9.39). This method was used in the software to experimentally determine the damping and mode shapes. Figure 4 gives an example of F.R.F. data set that was found from the tetrahedral structure.

9.9.3 Experimental Analysis

Using the measured data obtained from Me-Scope software, a model (Figure 9.13) was constructed and the data were used to find structural damping and mode shapes. At first it was thought that the data were too low because the operating frequencies of the spindle are above 4500 Hz. However the operating frequencies of the spindle could excite lower frequencies while machining. Therefore, these data are useful if the structure is excited at these frequencies by some other means, such as localized impacts the structure might experience during a machining operation. This is shown in the following series of illustrations at the chosen frequencies (Figs. 9.14 – 9.19).

The measured data for each node was adjusted such that the axis of orientation corresponded with the orientation of the accelerometer.

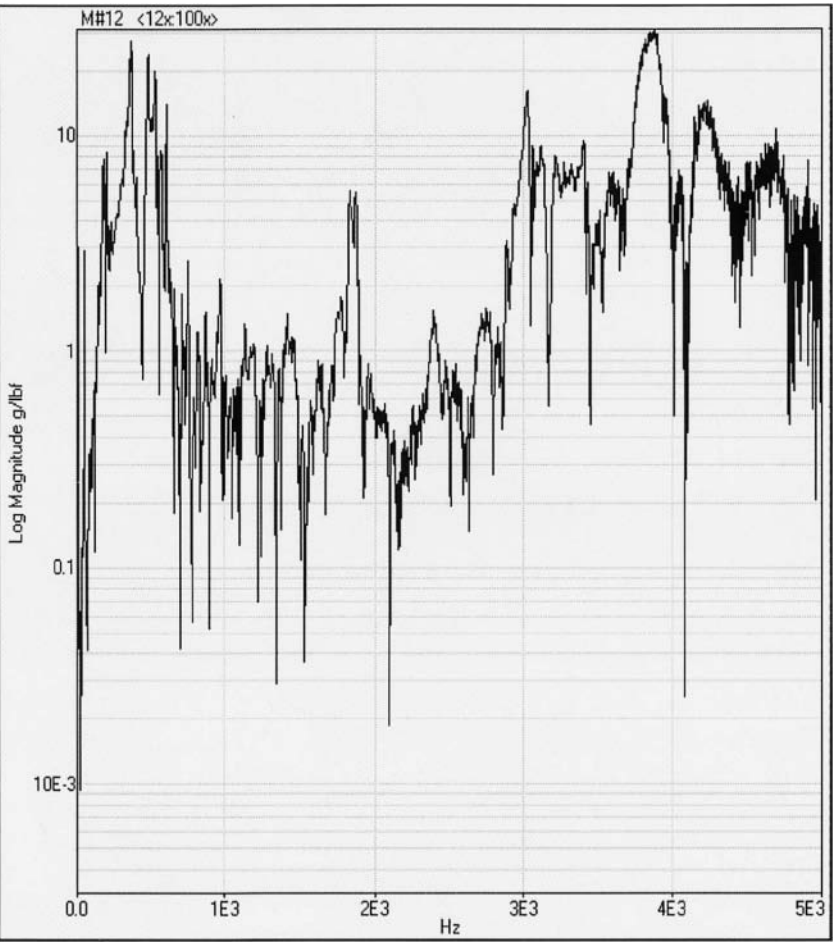


Fig. 9.12. F.R.F. data set cut off at 5000 Hz

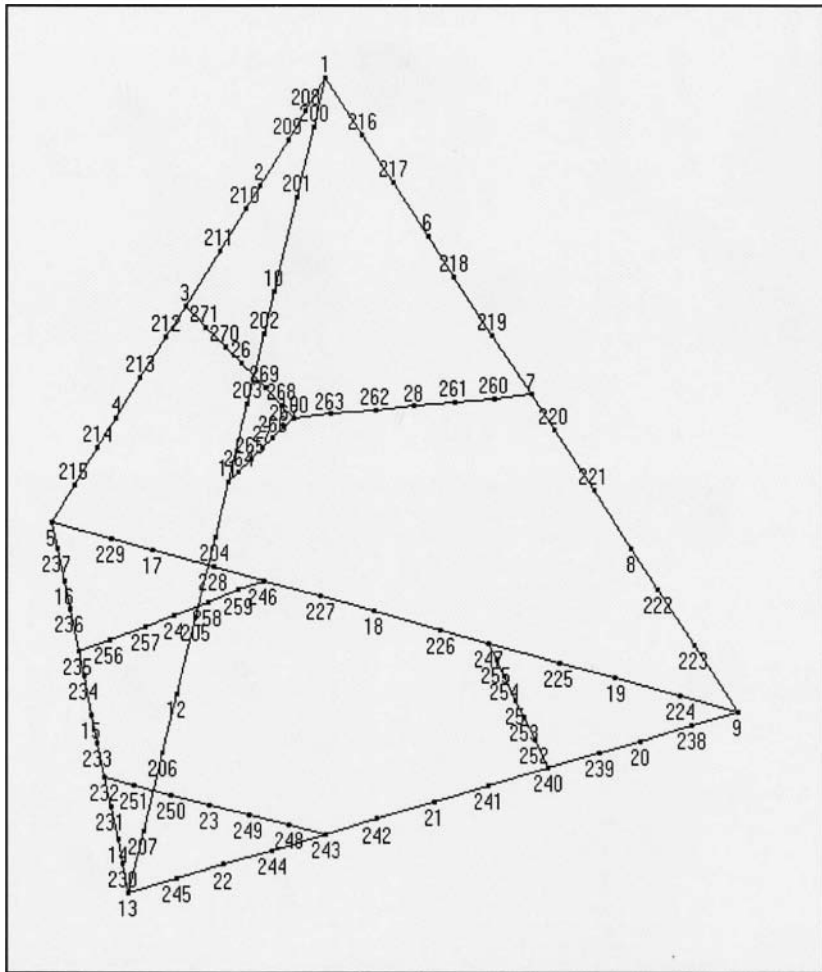


Fig. 9.13. Schematic diagram of the tetrahedral space frame showing experimental points-of-measurement for determining mode shapes

Figure 9.13 illustrates where mode shape measurements were taken during the experimental phase of this study (numbers 1-28 represent actual data points, whereas the other numbers were used for interpolation between measurement points).

The measured data compared accurately with the finite element results. It was found that the placement of the center of the spindle proved to be a point inside the structure that experienced minimal oscillations. It appeared that the structure was kinematically balanced such that different parts of the structure had oscillations that were out of phase with other parts. The results from finite element compare favorably. The tetrahedral structure was analyzed in its working orientation. The results are tabulated in Table 9.3. Not all of the results are listed, only those of interest. The first column is the measured natural frequency, followed by the finite element generated natural frequency in the second column. The observed modes of interest are shown in Figs. 9.14-9.16. The following figures illustrate how the tetrahedral structure oscillates at various frequencies. The measured data mode shape is given first, followed by a corresponding finite element generated mode shape. As the frequency is increased, the results from the finite element model seem to diverge from the measured mode shapes.

Experimental data (Me-Scope software)	Finite element results (ANSYS software)	% Difference in results
125	125	0%
203	200	1%
401	407	-1%
534	535	0%
601	600	0%
1070	1085	-1%
1820	1794	1%

Table 9.3. Comparison between experimental results and finite element calculations

It is thought that as oscillation modes increase they tend to depart from Bernoulli beam theory upon which the finite element generated results depend. For most of the natural frequencies, the amount of oscillation of the spindle is small, or approximately zero, which is preferred since the amount of spindle oscillation from equilibrium is translated directly to the machined workpiece.

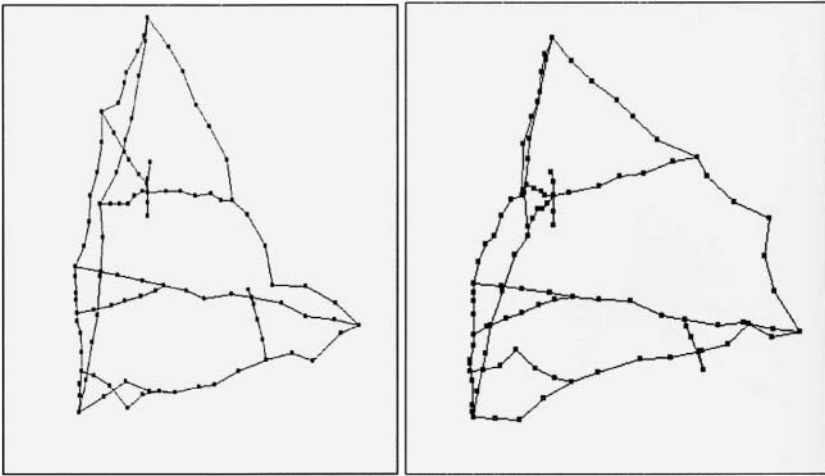


Fig. 9.14a. Me-Scope measured mode shape data at a frequency of 125 Hz

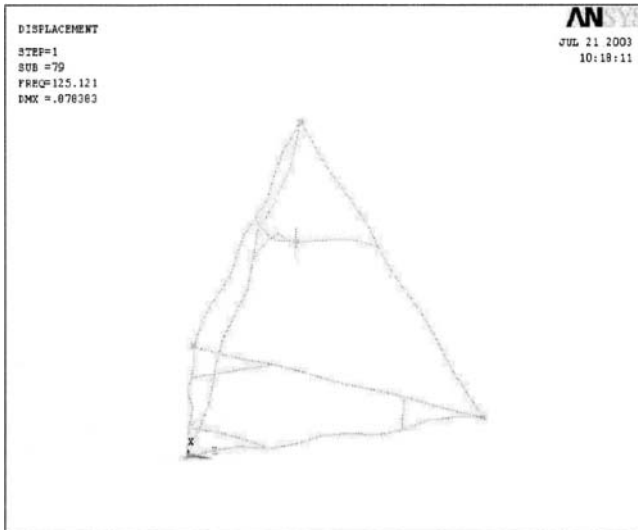


Fig. 9.14b. Finite element generated Ansys model of mode shape data at a frequency of 125 Hz

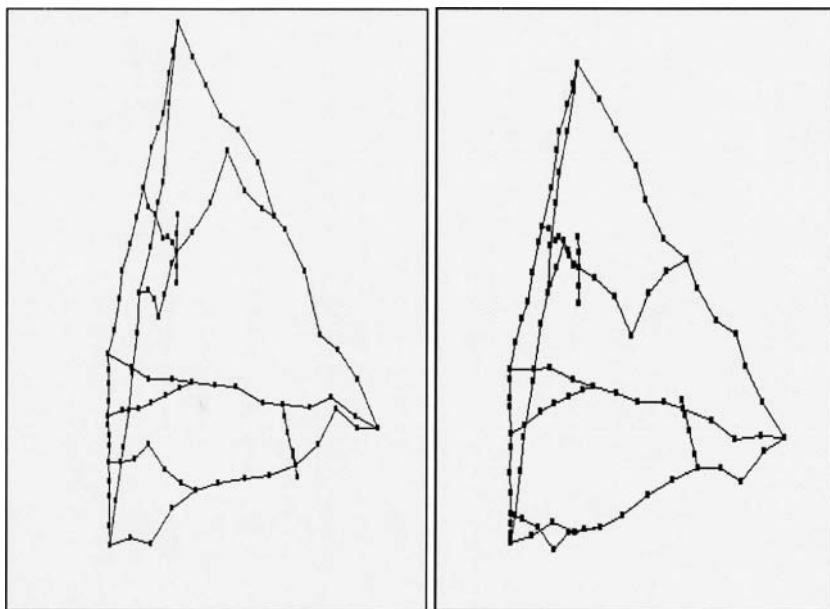


Fig. 9.15a. Me-Scope measured mode shape data at a frequency of 232 Hz

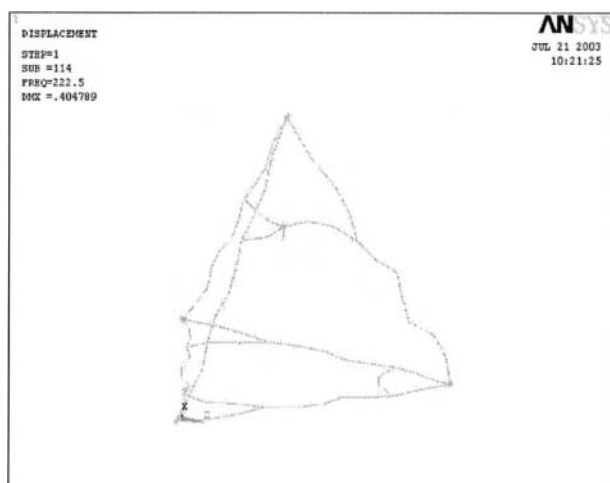


Fig. 9.15b. Finite element generated Ansys model of mode shape data at a frequency of 222 Hz

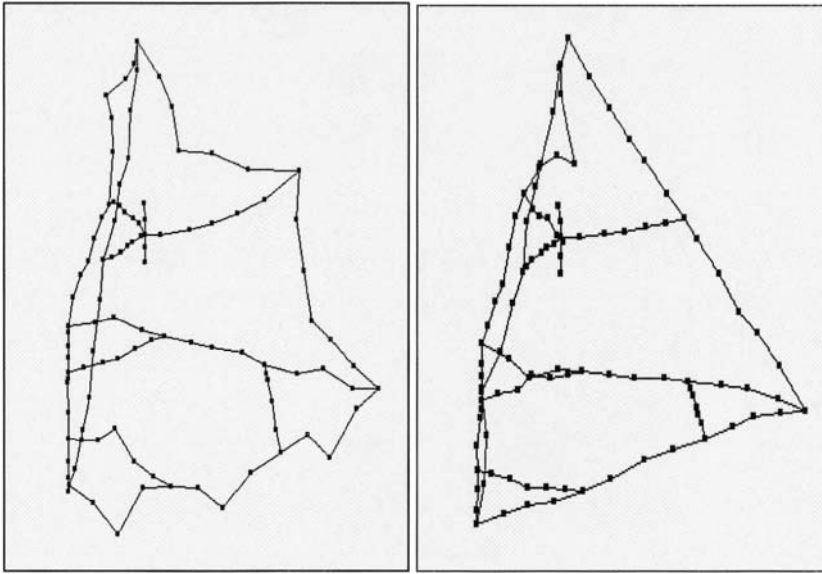


Fig. 9.16a. Me-Scope measured mode shape data at a frequency of 1820 Hz



Fig. 9.16b. Finite element generated Ansys model of mode shape data at a frequency of 1794 Hz

The results from ANSYS above 1794 Hz did not coincide with what was measured and therefore no comparison was made. However, measured frequencies above 1820 Hz are shown because they are useful for future design revisions to the structure. Axial responses, as well as transverse responses, from the measured data were used to compare to the finite element results.

Torsional data was ignored since they were not recorded using the accelerometer and the Me-Scope measurement software. It can be seen from the percent difference that the results from ANSYS have a natural frequency that resembles the measured results. However, they do not converge exactly instead the results oscillate about the measured data. The measured mode shape data using Me-Scope software at a frequency of 125 Hz shows an axial deflection for the spindle frame. However, the spindle itself remains stationary. The ANSYS model shows bending in the spindle sub-frame. The finite element models show bending modes in the structural bars.

The measured mode shape at 232 Hz illustrates how the structure cancels out oscillations that are transmitted through the spindle. It is apparent from the measured mode shape, as well as the finite element model, how various structural members are out of phase, which prevents any displacement of the spindle from its equilibrium position thus achieving a preferred effect for micromachining.

The measured data vaguely coincides with the finite element model once the frequencies reach approximately 1800 Hz, as illustrated from the images from Me-Scope at 1820 Hz and the finite element results at 1794 Hz. For this reason the finite element results have been omitted above 1820 Hz. This may be due to inadequate modeling of the structural connections, but most likely to Bernoulli beam theory not being applicable at these frequencies.

The only characteristic that is common to both of the models is the restricted oscillation of the spindle. It can readily be seen from Figures 9.17 – 9.19 that there is virtually zero oscillation in the spindle at most of the measured frequencies, which is accompanied by the finite element model as well. The reason for omitting results above 4460 Hz is because the F.R.F. from the measured data was not clear, thereby resembling noise, which is not useful for an adequate conclusion to be made. This is because the impact hammer method of exciting a structure is limited to approximately 4000 Hz.

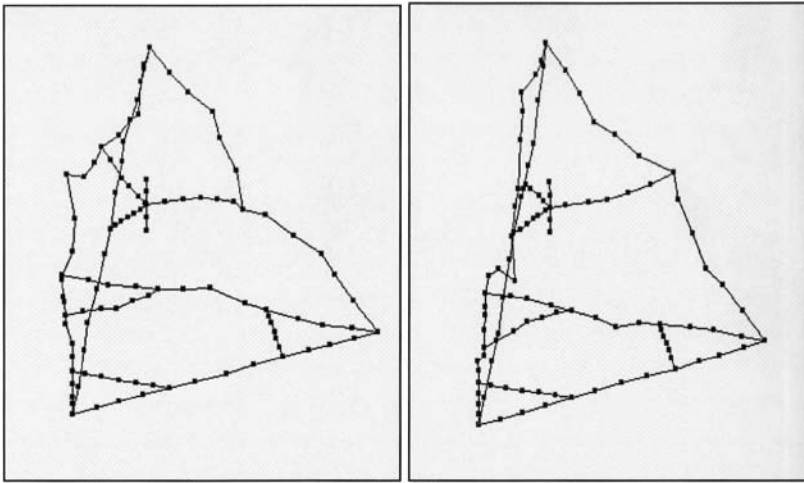


Fig. 9.17. Me-Scope measured mode shape data at a frequency of 2890 Hz

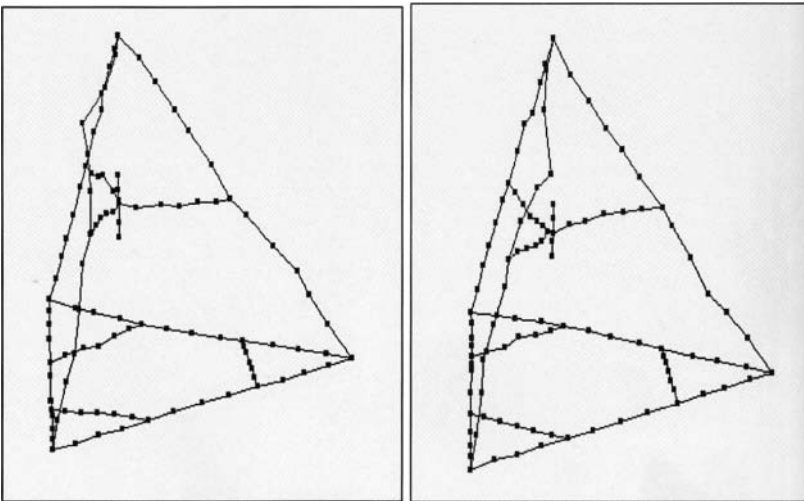


Fig. 9.18. Me-Scope measured mode shape data at a frequency of 3400 Hz

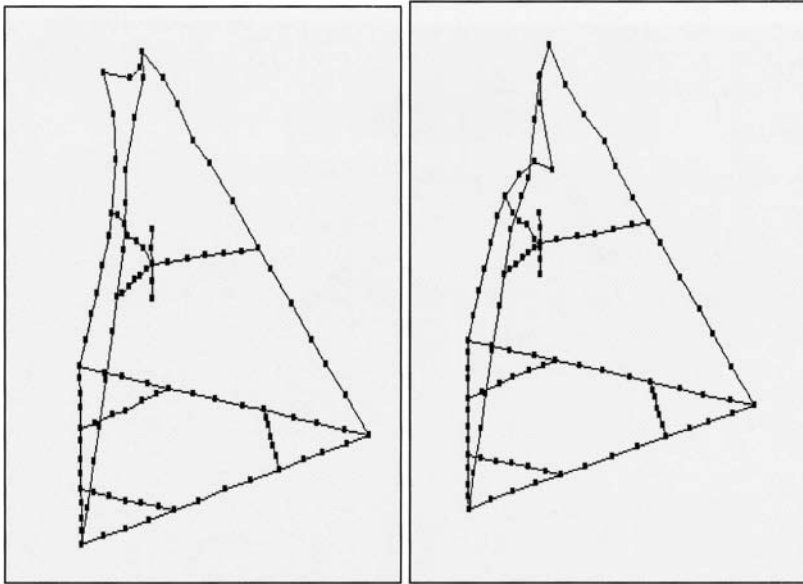


Fig. 9.19. Me-Scope measured mode shape data at a frequency of 4460 Hz

However, the frequencies used in this design exercise are those commonly encountered during micromachining processes. It appears that further improvements can be made by using passive damping systems on subsequent designs of meso machine tools (mMT) used for micromachining processes.

9.10 Conclusions

The computer model developed for pulsed water drop micromachining simulates impacts from an 0.8 mm diameter nozzle and determines the extent of crack growth. If an estimate of “visible” crack size is made, then the machining threshold velocity for a given liquid impact velocity can be predicted. The simple machining threshold model of liquid impact produced accurate M.T.V.s (300 impacts) with good agreement with experimentally obtained values. The lower impact end of the damage threshold curve was the most difficult to model as it depends on the size of the largest crack and the

minimum crack size that is detectable by eye via an optical microscope. This was apparent when an opaque material was investigated.

With silicon, the model underestimated the experimental single impact threshold velocity. The model showed that the M.T.V. (300 impacts) is a reliable estimate of the A.M.T.V. The variation in the absolute machining threshold velocity with crack size was investigated and was seen to increase when the initial crack length was reduced. When the crack became longer, the A.M.T.V. became almost independent of the length of the crack. This is an agreement with experimentally obtained data, where the change in the M.T.V. (300 impacts) with surface roughness is lower than the effect on fracture stress. This is due to the brevity of the Rayleigh wave pulse both spatially and temporally, and the fact that the damaging Rayleigh wave decreases rapidly with depth. When breaking samples, the whole piece is quasi-statically loaded and, therefore, larger cracks are exploited in reducing strength and resulting in a loss of material. Pulsed water drop micro machining appears to be a new method to add to the newly developing field of environmentally conscious manufacturing processes.

It should be pointed out that the pulsed water drop machining process has not been compared to the traditional continuous water drop machining processes. Therefore, one cannot compare the effectiveness of the new method compared to these techniques other than in terms of the quality of cut and material removal rates.

The finite element model predictions of the pulsed water drop machining center compare well with measured data at low frequencies. Owing to this fact, the finite element model may be used for future design improvements to the structure. It can be seen from the experimental and the measurement results that multiple constraints on the spindle enhance the ability of the structure to resist excitation. One possible reason for the structure's oscillation is probably due to the lack of passive damping. Therefore, it is recommended that improvements be made to improve passive damping of oscillations. The results presented show that modifications can be made to a seemingly stiff machine tool structure. Improvements made to enhance passive damping through the use of different materials that will enable the tetrahedral framework to be adapted to produce a

meso machine tool (mMT) structure that will possibly allow pulsed water drop micromachining processes to become mass manufacturing processes.

9.11 Problems

1. What is abrasive water jet machining?
2. State the problems associated with water jet machining.
3. Describe the theory of pulsed liquid impact.
4. Describe and illustrate the nature of damage caused by water drop impacts.
5. What is the machining damage threshold?
6. Explain how Rayleigh waves affect the removal of material in pulsed water drop machining.
7. What is lateral jetting and how does it affect the removal of material?
8. How are machining threshold curves generated?
9. Comment on material removal rates and how they are affected by the shape and size of water drops.
10. Explain how machine tools are designed for pulsed water drop machining of ceramic materials.

References

1. Hashish M, and Hilleke M., (1999), Water Drop Machining of Composites and Ceramics, in *Machining of Ceramics and Composites*, Chapter 13, p.p. 427-482, Marcel Dekker, New York.
2. Jackson MJ and Field JE, (2000) Modelling Liquid Impact Fracture Thresholds in Brittle Materials, *Journal of the Institute of Materials, Minerals, and Mining - British Ceramic Transactions* , **99**, 1-13.
3. Bowden FP and Brunton JH (1961), The deformation of solids by liquid impact at supersonic speeds, *Proc. Roy. Soc. Lond.*, **A263**, 433-450.
4. Steverding B, and Lehnigk SH, (1969), Dynamic thresholds for crack propagation, *Int. J. Fract. Mech.*, **5**, 369-370.

5. Miller GF, and Pursey H, (1956), On the partition of energy between elastic waves in a semi-infinite solid, *Proc. Roy. Soc. Lond.*, **A233**, 55-69.
6. Jackson MJ, and Field JE, (1999), Liquid impact erosion of single-crystal magnesium oxide, *Wear*, **233-235**, 39-50.
7. Obara T, Bourne NK, and Field JE (1995), Liquid drop impact on liquid and solid surfaces, *Wear*, **186-187**, 338-344.
8. Hartranft RJ, and Sih GC (1973): in *Methods of analysis and Solutions of crack problems* (ed. G.C. Sih), 179-238, Noordhoff International Publishing.
9. Kolsky H (1953), "Stress waves in solids", Clarendon Press, Oxford, England.
10. Lord Rayleigh (1885), On waves propagated along the plane surface of an elastic solid, *Proc. Lond. Math. Soc.*, **17**, 4-11.
11. Swain MV, and Hagan JT (1980), Rayleigh wave interaction with, and the extension of, microcracks, *J. Mat. Sci.*, **15**, 387-404.
12. Freund LB (1972), *J. Mech. Phys. Solids*, **20**, 129-140.
13. Broberg KB (1960), The propagation of a brittle crack, *Arkiv. Fur Fysik.*, **18**, 159-192.
14. Kerkhoff F, and Richter H (1969): in 2nd Int. Conf. "Fracture", 463-473, Brighton, England.
15. Dulaney EN, and Brace WF (1960), *J. Appl. Phys.*, **31**, 2233-2236.
16. Berry JP (1960), *J. Mech. Phys. Solids*, **8**, 194-216.
17. Roberts DK, and Wells AA (1954), *Engineering*, **178**, 820-821.
18. Evans AG, in "Treatise on Materials Science and Technology", Erosion (ed. C.M. Preece), 1979, 16, 1-67, Academic Press, New York.
19. Sih GC: "Handbook of stress intensity factors", 1973, Lehigh University Press, Pennsylvania, U.S.A.
20. Hand RJ, Field JE, and Townsend D, (1991), The use of liquid water drops to simulate angled drop impact, *J. Appl. Phys.*, **70**, 7111-7118.
21. Inman DJ, *Engineering Vibration*, Prentice Hall, Upper Saddle River, New Jersey, 2001.
22. Cook RD, *Finite Element Modeling For Stress Analysis*, John Wiley & Sons Inc., New York, 1995.

10. Diamond Nanogrinding

10.1 Introduction

Nanoscale fabrication requires a substrate made from an engineering material to be truly flat so that “bottom-up” nanofabrication techniques such as lithographically induced self-assembly and soft lithography can be used to deposit nanofeatures. The coating of piezoelectric materials with sub-micron size diamond particles has enabled the production of truly flat substrates so that nanofeatures can be created on engineering materials using a new manufacturing process known as “piezoelectric nanogrinding”. The principle of the process relies on applying an electric current to the diamond coated piezoelectric material that causes the material to strain. When the diamond-coated piezoelectric material is placed in close proximity to the substrate, the diamonds remove extremely small fragments of the substrate when the electric current is applied to the material. The magnitude of the applied current controls the material removal rate. The process can be used to process biomedical materials especially in the production of nanoscale ducts and channels in micro-and nanofluidic devices. To achieve the generation of truly flat surfaces, the process must be executed within a specially constructed vibration dampening space frame. The chapter describes the principle of the process of nanogrinding using coated piezoelectric materials, and correlates the wear of diamonds with stresses induced into the diamonds when an electric current is applied to the piezoelectric in order to remove very small amounts of material. The removal of material can also be performed using a porous tool with abrasive materials embedded in them such as diamonds that increases the ma-

terial removal rate as long as the porous tool is engineered in such a way that the loss of abrasive fragments is eliminated. This is achieved by laser assisted dressing, by engineering the bond of the porous tool to resist wear, and by laser assisted microstructural modification of the surface of the porous tool. The chapter describes how the bonds in porous tools are engineered to minimize abrasive grain loss and how vitrified bonding bridges can be processed using a laser to form extremely sharp nanoscale cutting wedges. The porous nanogrinding tool can be bonded to a piezoelectric material so that it can be used in the piezoelectric nanogrinding process.

10.2 Piezoelectric Nanogrinding

The piezoelectric nanogrinding process is a process that relies on using a nickel-coated ceramic material with microscale diamond particles bonded to it that are cubo-octahedral in shape to machine nanoscale features in a variety of workpiece materials. The diamonds are bonded to the piezoelectric material by gaseous deposition, laser cladding, or directly bonding a porous tool to the material via an adhesive paste. The process is executed by applying a known sinusoidal frequency to the piezoelectric crystal in order to achieve a desired oscillatory displacement. Rapid vibration of the crystal will allow material removal rates to be increased, thus making it a nanomanufacturing process. The nanogrinding process is accompanied by wear of the diamond grains, and the rate of this wear plays an important role in determining the efficiency of the nanogrinding process and the quality of the nanomachined surface. Wear mechanisms in nanogrinding processes appear to be similar to that of single-point cutting tools, the only difference being the size of swarf particles generated. Fig. 10.1 shows the arrangement of grinding swarf and abrasive grains that have been lost during the nanogrinding process.

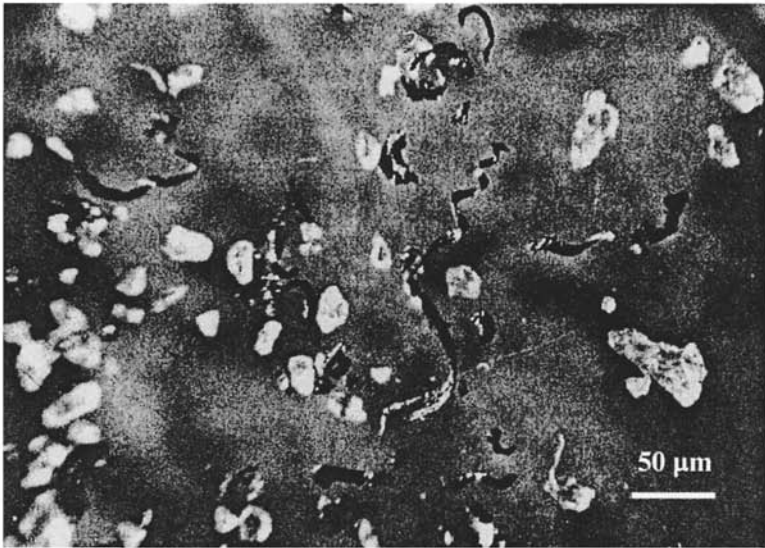


Fig. 10.1. Nanoscale grinding detritus showing blunt and sharp abrasive grains of diamond and metal chips

Figure 10.1 shows abrasive grains with blunted cutting edges (wear flats), and abrasive grains with sharp cutting edges that are released from the surface of the piezoelectric crystal before they have chance to grind nanoscale chips from the surface of the workpiece. The process suffers with a loss of diamond grains even when the interfacial adhesion between diamond and piezoelectric material is very good. A more closely related process that has been reported widely is that of the wear of probes used in atomic force microscopy [1,2]. However, these observations were purely experimental with no explanation of how to design probes that inhibit, or retard, wear.

A performance index used to characterize diamond wear resistance is the grinding ratio, or *G*-ratio, and is expressed as the ratio of the change in volume of the workpiece removed, Δv_w , to the change in the volume of the diamond abrasive grain removed, Δv_s , and is shown in Eq. (10.1),

$$G = \Delta v_w / \Delta v_s \quad (10.1)$$

Grinding ratios for processes at the nanoscale have not yet been characterized. However, the complexities of wear of abrasive materials at any scale lead us to believe that the variety of different and interacting wear mechanisms involved, namely, plastic flow of abrasive, crumbling of the abrasive, chemical wear etc., makes the wear of diamond at the nanoscale too complicated to be explained using a single theoretical model [3].

The following analysis of diamond grains represented by loaded wedges assumes that grain fracture is the dominant wear mechanism when grinding at the nanoscale using the piezoelectric nanogrinding process.

10.3 Stress Analysis in a Nanogrinding Grain

10.3.1 Nomenclature

a	Wedge half-space	[mm]
C	Constant	
F_t	Tangential force	[N]
F_Y	Equivalent tangential grinding force	[N]
F_Z	Equivalent normal grinding force	[N]
G	Grinding ratio	[mm ³ /mm ³]
n	Force multiplier, or coefficient	
P	Point load	[N]
r	Radial polar co-ordinate	
t	Thickness of wedge	[mm]
V_S	Volume of grinding wheel removed	[mm ³]
V_W	Volume of workpiece material removed	[mm ³]
β	Rake angle of wedge (abrasive grain)	
ϕ	Stress function	
θ	Angular polar co-ordinate	
σ_1	Principal stress	[N/mm ²]
σ_3	Principal stress	[N/mm ²]
σ_c	Compressive strength of abrasive	[N/mm ²]

σ_r	Radial stress	$[\text{N/mm}^2]$
σ_t	Tensile strength of the abrasive	$[\text{N/mm}^2]$
σ_θ	Circumferential, or hoop stress	$[\text{N/mm}^2]$
$\tau_{r\theta}$	Shear stress	$[\text{N/mm}^2]$
ω	Angle between point load and apex of wedge	

10.3.2 Analysis of Loaded Nanogrinding Grains

Diamond grains are blocky in nature and possess sharp cutting points prior to nanogrinding workpiece materials. Figure 10.2 shows a collection of diamond abrasive grains that have well defined cutting points that form a wedge at their apex. When bonded into a strong matrix, these grains can be considered to be representative infinite wedges.

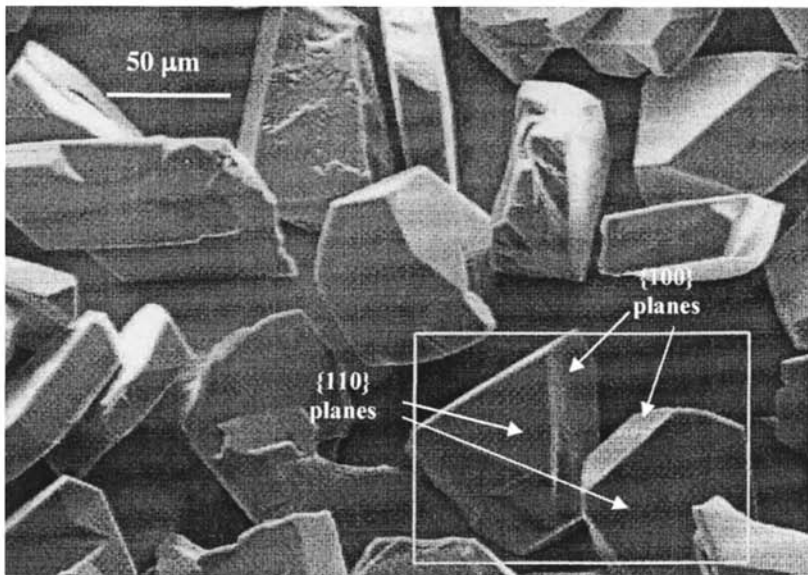


Fig. 10.2. A collection of diamond grains showing cutting points located at their apex, and locations of $\{100\}$ and $\{110\}$ planes. Diamond grains are approximately $60\ \mu\text{m}$ in diameter.

An infinite wedge represents the cutting point of an abrasive grain in contact with the workpiece material (Fig. 10.3).

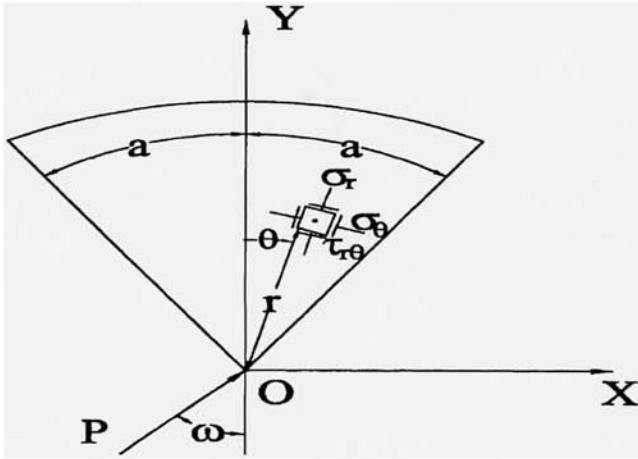


Fig 10.3. The single-point, loaded infinite wedge

The wedge is loaded at the apex by a load P in an arbitrary direction at angle ω to the axis of symmetry of the wedge. Resolving the force into components $P \cos \omega$ in the direction of the axis, and $P \sin \omega$ perpendicular to that the stresses due to each of these forces can be evaluated from two-dimensional elastic theory [4]. The state of stress in the wedge, due to force $P \cos \omega$, can be obtained from the stress function,

$$\phi = C.r.\theta.\sin \theta \quad (10.2)$$

Where r and θ are polar coordinates, or the point N in Fig. 10.4, and C is a constant.

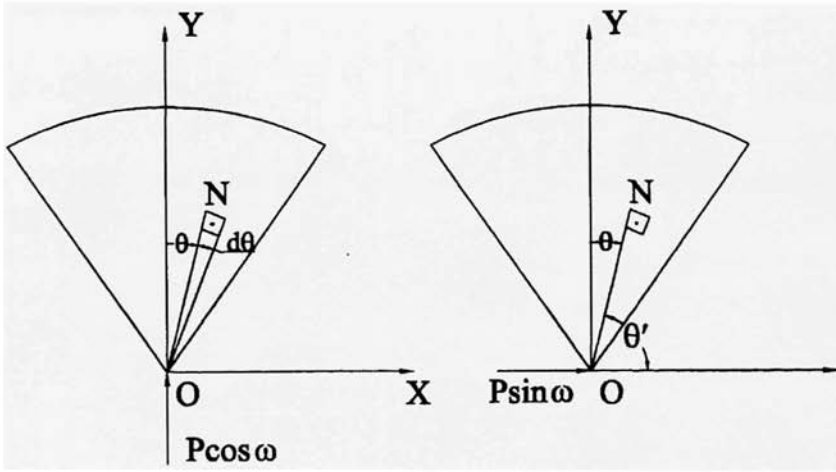


Fig. 10.4. The single-point, loaded infinite wedge showing force components, and the point N within the wedge at polar co-ordinates, r and θ

The stress function yields the following radial, tangential, and shear stress components,

$$\sigma_r = -2C \frac{\cos \theta}{r} \quad (10.3)$$

$$\sigma_\theta = 0 \quad (10.4)$$

$$\tau_{r\theta} = 0 \quad (10.5)$$

To determine the constant, C , the equilibrium of forces along the y -axis is:

$$P \cos \omega - \int_a^r \sigma_r \cos \theta dA = 0 \quad (10.6)$$

Where dA is an element of cross sectional area within the wedge. If, t , is the thickness of wedge, then,

$$\cos \omega P = \int_{-a}^a 2C \frac{\cos \theta}{r} t.r.\cos \theta d\theta = 2Ct \int_{-a}^a \cos^2 \theta d\theta =$$

$$Ct [2a + \sin 2a] \quad (10.7)$$

$$\text{Therefore, } C = \frac{P \cos \omega}{t(2a + \sin 2a)} \quad (10.8)$$

And,

$$\sigma_r = -\frac{2P \cos \theta.\cos \omega}{r.t(2a + \sin 2a)} \quad (10.9)$$

Note that the negative sign denotes that the stress is compressive. The state of stress in the wedge, due to force $P \sin \omega$, can be obtained from the stress function,

$$\phi = C'.r.\theta'.\sin \theta' \quad (10.10)$$

Therefore,

$$\sigma_r = -2C \frac{\cos \theta'}{r} \quad (10.11)$$

$$\sigma_{\theta} = 0 \quad (10.12)$$

$$\tau_{r\theta} = 0 \quad (10.13)$$

Equilibrium of forces along the x-axis (Fig. 10.4) yields the following solution for the constant, C ,

$$P \sin \omega - \int_{\pi/2-a}^{\pi/2+a} \sigma_r . t . r . \cos \theta' d\theta' = 0 \quad (10.14)$$

$$P \sin \omega = - \int_{\pi/2-a}^{\pi/2+a} 2C \frac{\cos \theta'}{r} . t . r . \cos \theta' d\theta' = 2Ct . \int_{\pi/2-a}^{\pi/2+a} \cos^2 \theta' d\theta' =$$

$$- C.t (2a - \sin 2a) \quad (10.15)$$

$$C = \frac{P \sin \omega}{t(2a - \sin 2a)} \quad (10.16)$$

Thus,

$$\sigma_r = - \frac{2P \cos \theta' . \sin \omega}{r . t (2a - \sin 2a)} \quad (10.17)$$

Expressing in terms of the angle θ (where θ' is negative), yields,

$$\sigma_r = - \frac{2P \cos \theta . \sin \omega}{r . t (2a - \sin 2a)} \quad (10.18)$$

Therefore, the combined stresses are:

$$\sigma_r = - \frac{2P}{r.t} \left[\frac{\cos \omega \cos \theta}{2a + \sin 2a} + \frac{\sin \omega \cos \theta}{2a - \sin 2a} \right] \quad (10.19)$$

It follows that σ_r vanishes for angle θ_o defined using the expression:

$$\tan \theta_o = \frac{1}{\tan \omega} \cdot \frac{2a - \sin 2a}{2a + \sin 2a} \quad (10.20)$$

This equation corresponds to a straight line through the apex as shown in Fig. 10.5. This natural axis separates the regions of

compressive and tensile stresses. It can be seen that for values of angle ω which gives, $|\theta_o| > |a|$, the neutral axis lies outside the included angle of the wedge. This means that the whole area of the wedge will be under stresses of uniform sign. Expressing Eq. (10.19) in terms of the rake angle of the abrasive grain, β , and force components F_t and nF_t (Fig. 10.6), yields,

$$\sigma_r = -\frac{2F_t}{rt} \left\{ \frac{[n \cos(a - \beta) + \sin(a - \beta)] \cos \theta}{2a + \sin 2a} + \frac{[\{\cos(a - \beta) - n \sin(a - \beta)\} \cos \theta]}{2a - \sin 2a} \right\} \quad (10.21)$$

It can be observed that:

$$\tan \omega = \frac{\cos(a - \beta) - n \sin(a - \beta)}{n \cos(a - \beta) + \sin(a - \beta)} \quad (10.22)$$

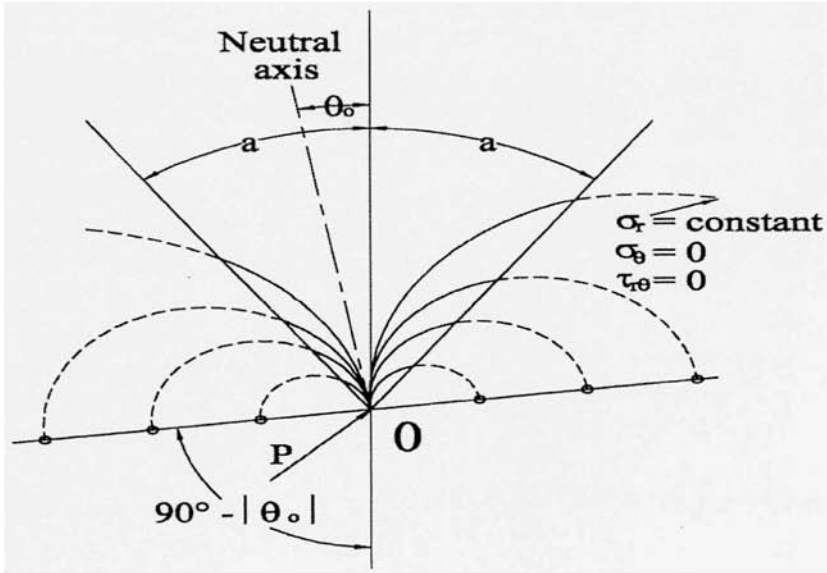


Fig. 10.5. Stress analysis of a single-point loaded wedge

In the simple case of a wedge with the normal force nF_t along the wedge axis, α is equal to β , hence,

$$\tan \omega = 1 / n \quad (10.23)$$

It is interesting to examine the radial stresses on the left-hand face of the wedge, which corresponds to the leading face of idealized wedge. Thus, for the left-hand face, θ is equal to $-\alpha$, and from Eq. (10.19),

$$\sigma_r = -\frac{2P}{r.t} \left[\frac{\cos \omega \cos \alpha}{2\alpha + \sin 2\alpha} + \frac{-\cos \alpha \cdot \sin \omega}{2\alpha - \sin 2\alpha} \right] \quad (10.24)$$

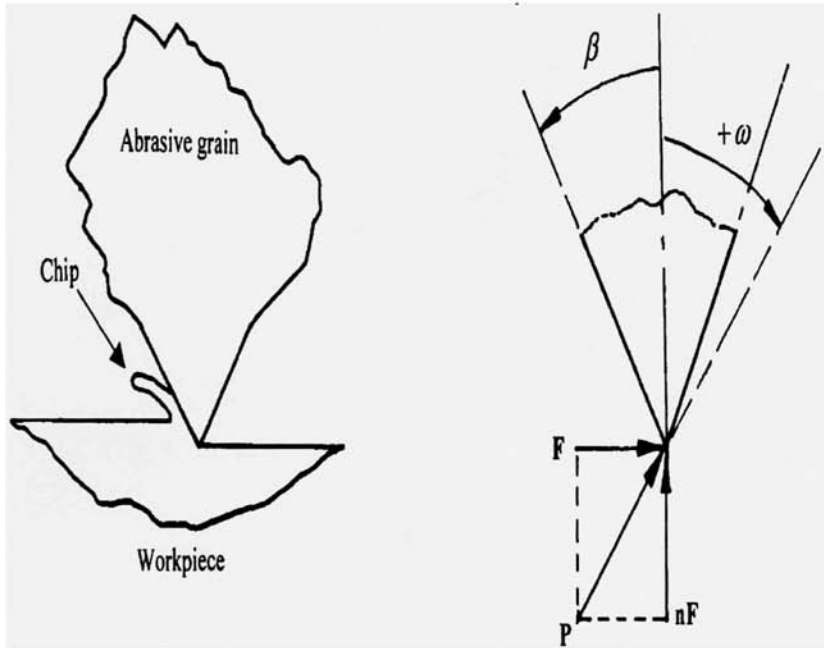


Fig. 10.6. Ideal wedge-shaped cutting point and grinding force diagram

This stress is zero, i.e., the neutral axis coincides with the left-hand limit of the wedge, when,

$$\frac{1}{\tan \omega} = \frac{\sin a(2a + \sin 2a)}{\cos a(2a - \sin 2a)} \quad (10.25)$$

Thus if,

$$(a) \quad a = \beta, \text{ then,}$$

$$n = \frac{\sin a}{\cos a} \cdot \frac{2a + \sin 2a}{2a - \sin 2a} \quad (10.26)$$

$$(b) \quad a - \beta = \frac{\pi}{2} - a$$

(as is the case when F_t is parallel to the right-hand face of the wedge). From Eq. (10.23),

$$\tan \omega = \frac{\sin a - n \cos a}{n \sin a + \cos a} = \frac{\sin a - n \cos a}{n \sin a + \cos a} \quad (10.27)$$

And substituting in (10.25), yields,

$$\frac{n \sin a + \cos a}{\sin a - n \cos a} = \frac{\sin a}{\cos a} \cdot \frac{2a + \sin 2a}{2a - \sin 2a} \quad (10.28)$$

$$\frac{\frac{1}{2} n \sin 2a + \cos^2 a}{\sin^2 a - \frac{1}{2} n \sin 2a} = \frac{2a + \sin 2a}{2a - \sin 2a} \quad (10.29)$$

$$\begin{aligned}
& \frac{1}{2} \cdot n \cdot \sin 2a (2a - \sin 2a) + 2a \cos^2 a - \cos^2 a \cdot \sin 2a = \\
& = 2a \cdot \sin^2 a + \sin^2 a \cdot \sin 2a - \frac{1}{2} \cdot n \cdot \sin 2a (2a + \sin 2a) \\
& \frac{1}{2} \cdot n \cdot \sin 2a (2a - \sin 2a + 2a \sin 2a) = 2a (\sin^2 a - \cos^2 a) + \sin 2a \\
& n \cdot 2a \cdot \sin 2a = -2a \cdot \cos 2a + \sin 2a \\
& \therefore n = \frac{1}{2a} - \cot 2a \tag{10.30}
\end{aligned}$$

Equation (10.25) expresses the condition for the whole of the wedge's cross-sectional area to be under compressive stress. It can be seen that this depends not only upon the rake angle, β , but also upon the ratio, n . In general the relative size of the region of compressive to the region of tensile stresses depends upon β and n as Eq. (10.20) and (10.22) indicate. Also, from Eq. (10.21), the magnitude of the stress on the left-hand face of the wedge is found to be dependent upon the tangential force component, F_t , and the force component ratio, n . Referring to Eq. (10.19), it can be seen that for constant stress, $\sigma_r = \text{constant}$,

$$r \cdot C_1 = C_2 \cdot \cos \theta + C_3 \cdot \sin \theta \tag{10.31}$$

Where C_1, C_2, C_3 are constants. Eq. (10.31) represents, in polar co-ordinates, the circumference of a circle tangent to the line,

$$0 = C_2 \cdot \cos \theta + C_3 \cdot \sin \theta \tag{10.32}$$

that is to the neutral axis at the point $r = 0$. However, the point $r = 0$ must be considered separately because the stress at that point approaches infinity, since by definition P is a point load. The central point of these circles are of constant radial stress, and so the point of constant maximum shear stress must lie on a line perpendicular to the neutral axis at the point where r is equal to zero. The radius of each of those circles depends upon the magnitude of the radial stress, σ_r .

10.4 Fracture Dominated Wear Model

Brittle materials exhibit high strength properties when loaded in compression than in tension. The ratio of rupture strengths is usually between 3:1 and 10:1. The existence of relatively low tensile stresses in the abrasive grains may cause failure by fracture to occur. To model the action of diamonds bonded to piezoelectric ceramics, one must consider a single active cutting grain to be classed as a wedge of constant width loaded at its inverted apex with point loads, F , and, nF , which represent the radial and tangential force components with reference to the grinding wheel in which the grain is supported, and P is the resultant force (Fig. 10.6).

The stress distributions within point-loaded wedges can be determined analytically, and the results of such an analysis indicate that if tensile stresses exist within the wedge then it will occur at its maximum along the rake face. The existence of a tensile stress depends on the magnitude of the force ratio, n . If the ratio is especially small that a tensile stress exists in the wedge, then for a specific force ratio the tensile stress is proportional to the tangential grinding force, F . Stresses of this nature would extend to and beyond the abrasive grain-bonding interface. The fracture of abrasive grain, bonding phase, or the interface between the two, depends on the particular type of piezoelectric ceramic material used and the magnitude of the tensile stress induced during nanogrinding.

Grains of diamond are 10 times stronger in compression than in tension. The probability of grain fracture is likely to increase with an increase in tensile stress exerted in the grain although the magnitude of the stress may be slightly higher than one-fifth the magnitude of the maximum compressive stress in the grain. A significant barrier to the acceptance of stress patterns evaluated for such situations arises because point loads applied to perfectly sharp wedges produce infinitely high stresses at, and about, the point of contact. Loads must be applied over a finite area.

It seems likely that higher tensile stresses are associated with higher grain fracture probability resulting in rapid loss of diamond grains and, consequently, lower grinding ratios. The wear model should incorporate the fact that the loads are spread over a finite area. This implies that point loads are applied along the rake face.

The model should allow the examination between the wear rate of a diamond coated piezoelectric ceramic material and the general nature of stresses established in active cutting grains subjected to nanogrinding forces. This means that it is necessary to estimate the force components of grinding on each active cutting grain.

10.5 Nanogrinding

10.5.1 Nanogrinding Apparatus

The experimental apparatus consisted of holding a polished specimen between the jaws of a vice so that a piezoelectric crystal oscillator traverses back-and-forth the specimen thus machining the specimen by creating a depth of cut between the diamonds adhered on the piezoelectric crystal and the workpiece material. Workpiece materials were polished with a 100 nm sized polishing compound. All samples were divided into four sections and each section was analyzed prior to machining and after machining occurred. The workpieces were mounted in a vice that was attached to a x-y-z linear slide in order to achieve accurate positioning of the workpiece. The piezoelectric crystal was mounted on a steel framework that was orthogonal to the workpiece. The whole unit was located within a tetrahedral space frame to dampen excess vibrations (Fig. 10.7).

10.5.2 Nanogrinding Procedure

When the crystal and workpiece were aligned, the depth of cut was incremented in stages of 10 nm. The motion of the diamonds attached to the piezoelectric crystal generates a machining effect that is caused by the action of diamonds grinding into the workpiece material. Tracks or trenches are created by the diamond grain gouging the surface of the material when an electric current is applied. The material is removed until the end of the oscillating motion creates the material to plow.

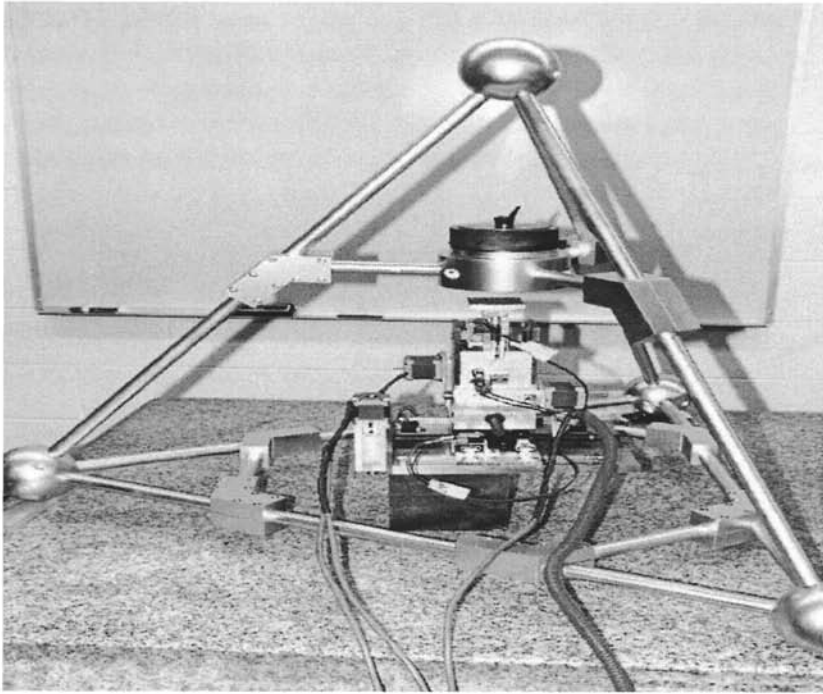


Fig. 10.7. Piezoelectric machining center capable of nanogrinding

The mechanism of oscillation can be described as a restricted bending mode that simulates a shear displacement of the crystal. At this point it is normal procedure to know how to estimate the number of grains contacting the surface of the workpiece.

The estimation of the number of active cutting grains is estimated quite simply by driving the diamond coated piezoelectric ceramic at the prescribed specific metal removal rate into a piece of lead. The impression that the grinding wheel produces in the length of lead is equal to the number of cutting points that are active during the grinding stroke at that particular depth of cut. The effect of oscillating the diamond-coated crystal is shown in Fig. 10.8.

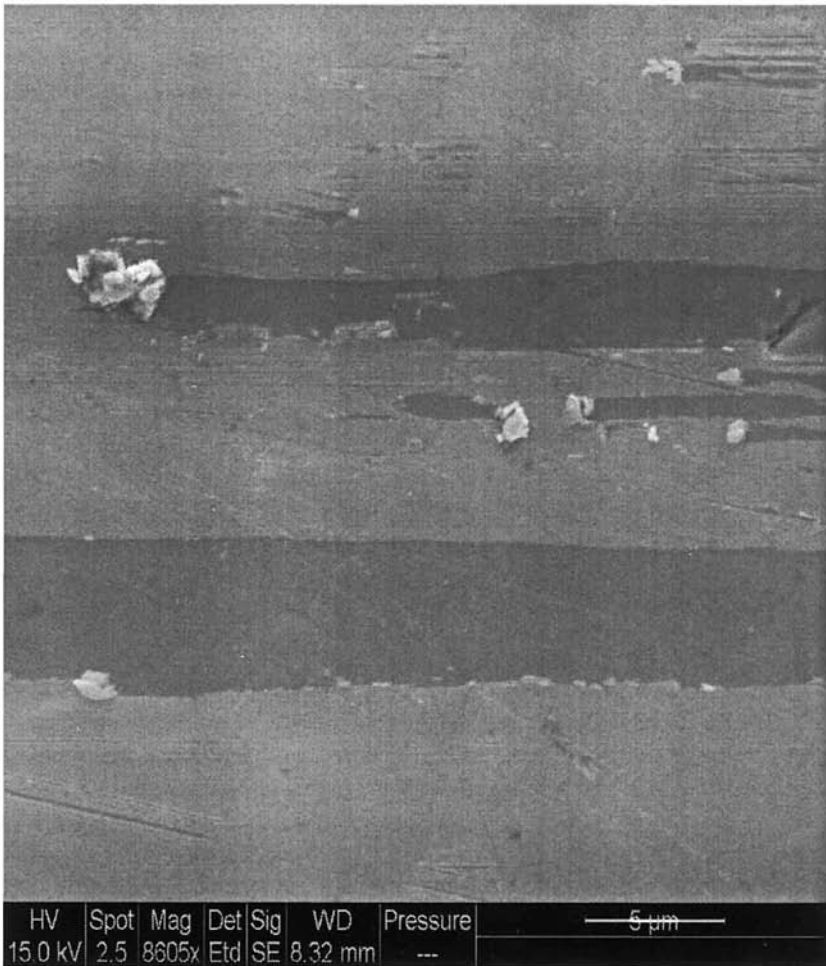


Fig. 10.8. Material removal by oscillating a diamond-coated piezoelectric ceramic crystal

The motion of the diamonds imparted by oscillating the crystal in the bending mode that causes a shear displacement to occur, which contributes to plowing of the material at the end of the nanogrinding stroke, is shown in Fig. 10.9.

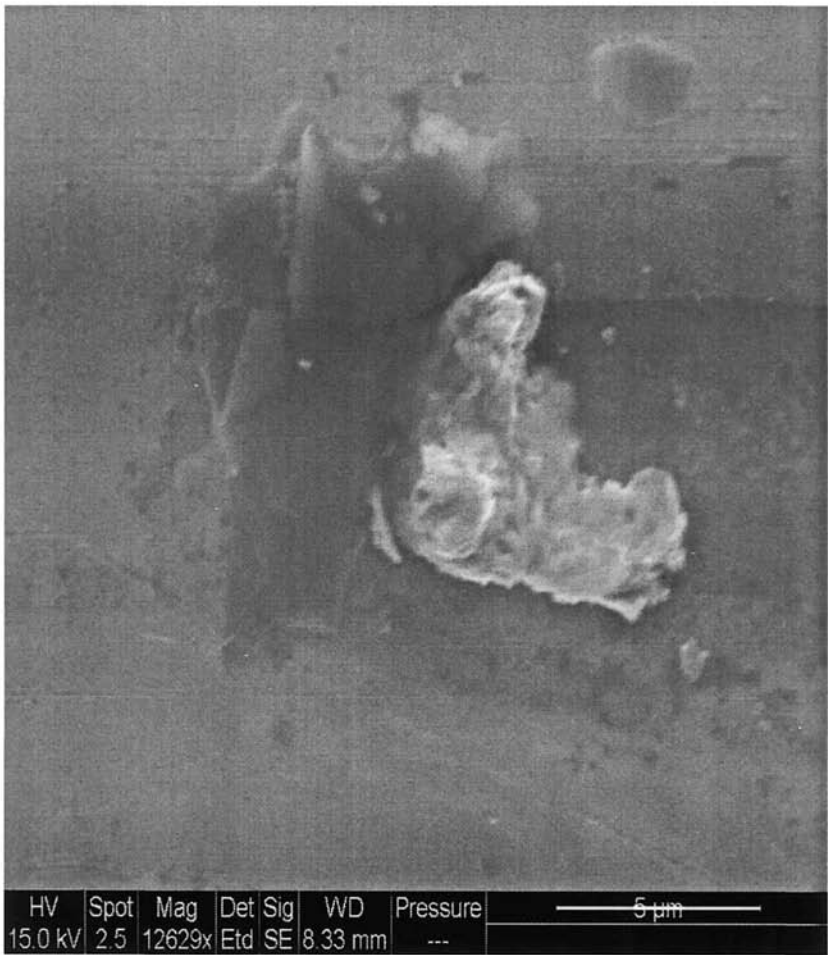


Fig. 10.9. Plowed material at the end of a nanomachined track

The effect of using the piezoelectric to machine tracks, or trenches, in engineering materials opens up the prospect of nanomanufacturing products that require geometric features such as channels so that fluids and mixed phase flows can be manipulated in devices such as micro-and nanofluidic “lab-on-a-chip” products. Figure 10.10 clearly shows such a channel produced using the piezoelectric nanogrinding process.

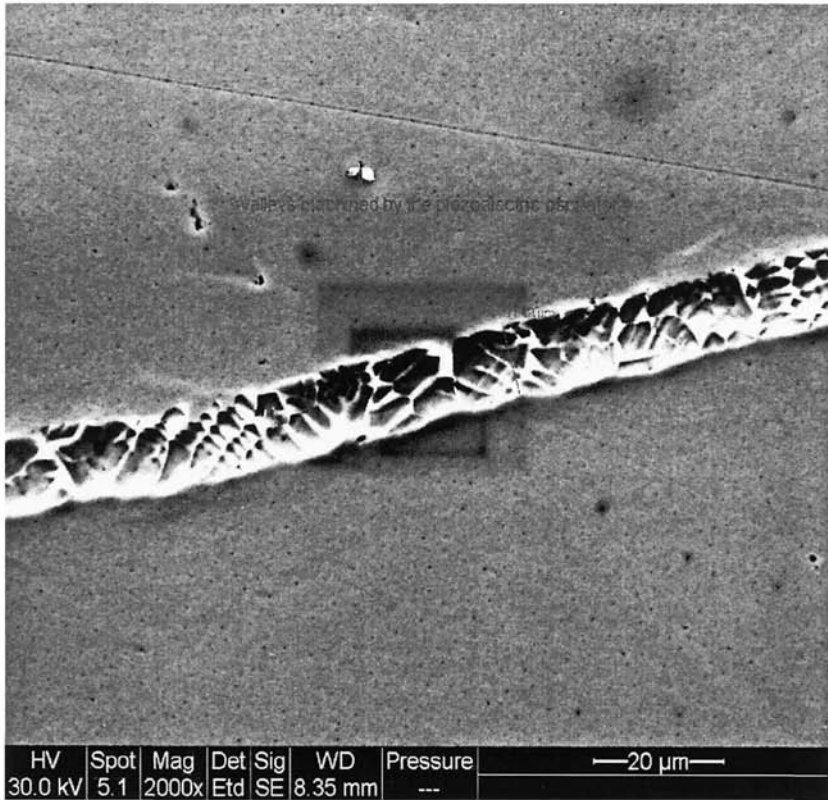


Fig. 10.10. Nanomachined tracks in steel

The measured force components of the nanogrinding operation are measured using a dynamometer. These components of force are then applied to a “model abrasive grain by dividing the grinding force data into the number of active cutting grains over an area that simulates the abrasive grain-workpiece contact area. Stresses established in this area are calculated using finite elements. The wear of the piezoelectric material by diamond loss, expressed in terms of a grinding ratio, and its relationship to the stress levels set up in the model grain is investigated using a stress analysis method.

10.5.3 Stress Analysis

The assumed geometry of an ideal grain in the vicinity of its cutting edge is a simple symmetrical wedge of constant width with an included angle of 70° that results in a rake angle of -35° . There is no wear flat on the model cutting grain. In order that a finite element method is used to evaluate stresses in the wedge, the wedge was subdivided into 210 diamond-shaped elements with a total of 251 nodes. Forty-one nodes were constrained at the boundary of the wedge and the leading five nodes on the rake face were loaded (Fig. 11.11). The tangential and normal grinding forces were replaced by equivalent forces acting perpendicular to (normal load) and along (shear load) the rake face of the wedge.

The concentrated loads at the five nodes are representative of the distributed and normal loads acting on the rake face over the abrasive grain-chip contact length. The normal force distribution on the rake face was taken to be maximum at the cutting edge and decreasing linearly to zero at the end of the abrasive grain-chip contact length. The shear force was taken to be constant over the first half of the contact length, decreasing linearly to zero over contact length.

Grinding loads were also applied directly to the rake face and at the tip of the grain without calculating equivalent forces. This was performed in order to compare and contrast the effect of different force distributions on the stresses generated within the wedge.

To measure the value of using the maximum tensile stress as a way to estimate grain fracture tendency, the correlation between the two sets of data were calculated for each set of data. The region of fracture initiation was also located using Griffith's criterion of fracture. For,

$$\frac{\sigma_c}{\sigma_t} \cdot \sigma_1 + \sigma_3 > 0 \quad (10.33)$$

Then,

$$\sigma_1 = \sigma_t \quad (10.34)$$

But for,

$$\frac{\sigma_c}{\sigma_t} \cdot \sigma_1 + \sigma_3 < 0 \quad (10.35)$$

Then,

$$(|\sigma_1| - |\sigma_3|)^2 + 8\sigma_t(|\sigma_1| - |\sigma_3|) = 0 \quad (10.36)$$

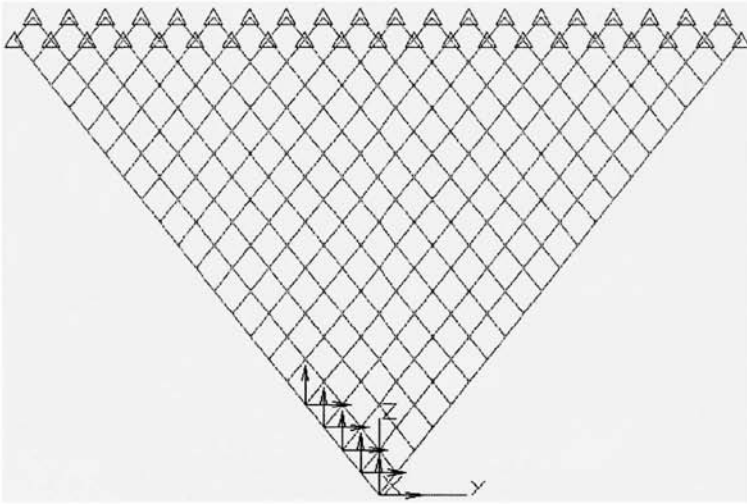


Fig. 10.11. Finite element assemblage with grinding loads applied at the rake face nodes

Where σ_1 and σ_3 are the principal stresses, assuming that $\sigma_1 > \sigma_3$, σ_t is the ultimate tensile strength of the abrasive grain, and σ_c is the ultimate compressive strength. For diamond grain material, the ratio of σ_t and σ_c is 0.1.

The results of the two-dimensional stress analyses were consistent with the experimentally determined stress distribution obtained by Loladze [5] when cutting soft metal with photoelastic tools. The maximum tensile stress always occurs at the rake face at a distance from the cutting edge ranging from 1.5 to 4 times the abrasive grain-chip contact length, the exact magnitude of the coefficient depends on the loading conditions for a particular machining event. For a given value of the tangential force component, F , the higher the force ratio, F/nF , the greater the distance the maximum tensile stress is away from the cutting edge.

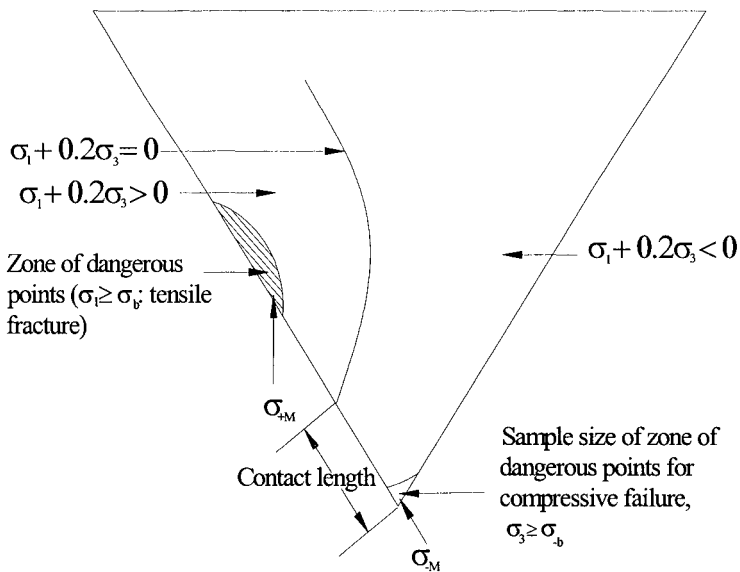


Fig. 10.12. Griffith's criterion applied to the idealized wedge showing tensile and compressive fracture initiation zones

These results indicate that mechanically induced fracture occurs at a finite distance away from the cutting edge. When using Griffith's criterion, the influence of mechanically induced stresses indicate that fracture initiation zones are established. Figure 10.12 shows the occurrence of such zones in an idealized wedge. The first zone is located around the point of maximum tensile stress and is always at the rake face.

Failure in this zone is tensile in nature and would initiate fracture at a point on the rake face of the order of two-to-three times the abrasive grain-chip contact length away from the cutting edge. This type of fracture is consistent with fracture on scale comparable with the chip thickness. The second much smaller zone is located at the immediate vicinity of the cutting edge. Failure is compressive in this region and results in small-scale crumbling of the cutting edge leading to the formation of a wear flat on the abrasive grain.

The correlation between the magnitude of the maximum tensile stress in the model abrasive grains and the appropriate grinding ratio (Table 10.1) is high and is dependent on the way the forces are applied to the grains. It would be expected that the higher the tensile stress, the greater is the rate of diamond wear and consequently the corresponding grinding ratio. Perfect linear correlation in accordance with this would result in a correlation coefficient of -1 .

The correlation coefficient between the maximum tensile stress and the grinding ratio is significant. This is to be expected as the force ratio may vary slightly. However, if the tangential component of the grinding force changes significantly without a change in force ratio, then it is expected that the maximum tensile stress will change significantly and reduce the grinding ratio.

The calculation and application of equivalent grinding loads produce a lower correlation coefficient compared to directly applied grinding loads. This implies that grinding loads are simply not point loads acting at the tip of the inverted apex and along the abrasive grain-chip contact length of the diamond grain. In fact, directly applied grinding forces produce better correlation coefficients.

This means that for perfectly sharp diamond grains, one must apply the component grinding loads directly to the rake face.

Table 10.1. Correlation coefficient between maximum tensile stress and grinding ratio for an idealized wedge using experimental data. Comparison is also made between the methods of applying loads to the idealized wedge models

Workpiece material	Exact wedge model with point loads applied to apex of wedge	Approximate finite element model: equivalent grinding forces applied to rake face of wedge	Approximate finite element model: grinding forces applied directly to the rake face of the wedge
Diamond on steel	-0.8	-0.9	-0.94
Diamond on MgO	-0.6	-0.7	-0.8
Diamond on copper alloy	-0.55	-0.65	-0.78
Diamond on aluminum alloy	-0.7	-0.85	-0.95
Diamond on silicon	-0.85	-0.87	-0.9

It can be seen from Table 10.1 that induced tensile stresses account for the loss of grain material from the diamond coated piezoelectric ceramic material. Therefore, the maximum tensile stress is the best indicator of diamond performance, in terms of grinding ratio, during a nanogrinding operation. The analysis performed on perfectly sharp diamond grains has provided a strong correlation between maximum tensile stress induced in the grain material and the wear parameter, grinding ratio, for the experimental data used in this chapter.

Correlations with other data sets have not proved so fruitful. From this, we can safely assume that the mechanism of grain fracture is not the dominant mechanism, which implies that other mechanisms are operating. The correlation coefficient demonstrates that a tougher grain material must be used in order to limit the effects of abrasive wear and the formation of wear flats, or a stronger bond, and possibly a higher volume of bond between diamond and

piezoelectric crystal, is required to nanogrind under the current experimental conditions.

Therefore, the present method of calculating the correlation coefficient between the maximum tensile stress and the grinding ratio demonstrates its potential application to the wider problem of selecting abrasive grains based on specific metal removal rates and the nature of the nanogrinding operation. When porous tools are used to embed diamonds or any other abrasive material, the same analysis can be used but account of the properties of the bonding bridge must be made. The bonding bridge can be made of a variety of different materials but the most common one used for dressable applications is the vitrified type, which is made from a mixture of clays, glasses, and minerals. The emphasis on using dressable types for nanogrinding is based on their ability to be re-sharpened by dislodging worn grains and by microstructural phase transformations by focusing optical energy on the bonding bridges that hold the grains in place.

10.6 Porous Nanogrinding Tools

Porous nanogrinding tools are composed of abrasive particles (sub micron size) embedded in a vitrified bond with porosity interspersed between grinding grains and bonding bridges. The porosity level is approximately 15 – 21%. Figure 10.13 shows the image of a nanogrinding tool prior to laser modification. The vitrified bonds are specially engineered to promote the formation of texture that creates ridges of cutting planes and nanogrinding “peaks” of α - Al_2O_3 in the preferred (012), (104), and (110) planes. The peaks created due to laser modification of the surface aid the nanogrinding process. Vitrified bonds are composed of glasses that are formed when clays, ground glass frits, mineral fluxes such as feldspars, and chemical fluxes such as borax melt when the grinding wheel is fired at temperatures in the range, 1000°C to 1200°C. With reference to raw material nomenclature, a “frit” is a pre-ground glass with a pre-determined oxide content, a “flux” is a low melting point siliceous clay that reduces surface tension at the bond bridge-abrasive grain interface, a “pre-fritted” bond is a bond that contains no clay miner-

als (i.e., clays and fluxes), and “firing” refers to vitrification heat treatment that consolidates the individual bond constituents together [6]. Considering individual bond constituents, mineral fluxes and ground glass frits have little direct effect on the ability to manufacture grinding wheels. However, most clays develop some plasticity in the presence of water (from the binder), which improves the ability to mould the mixture so that the wheel, in its green state, can be mechanically handled.

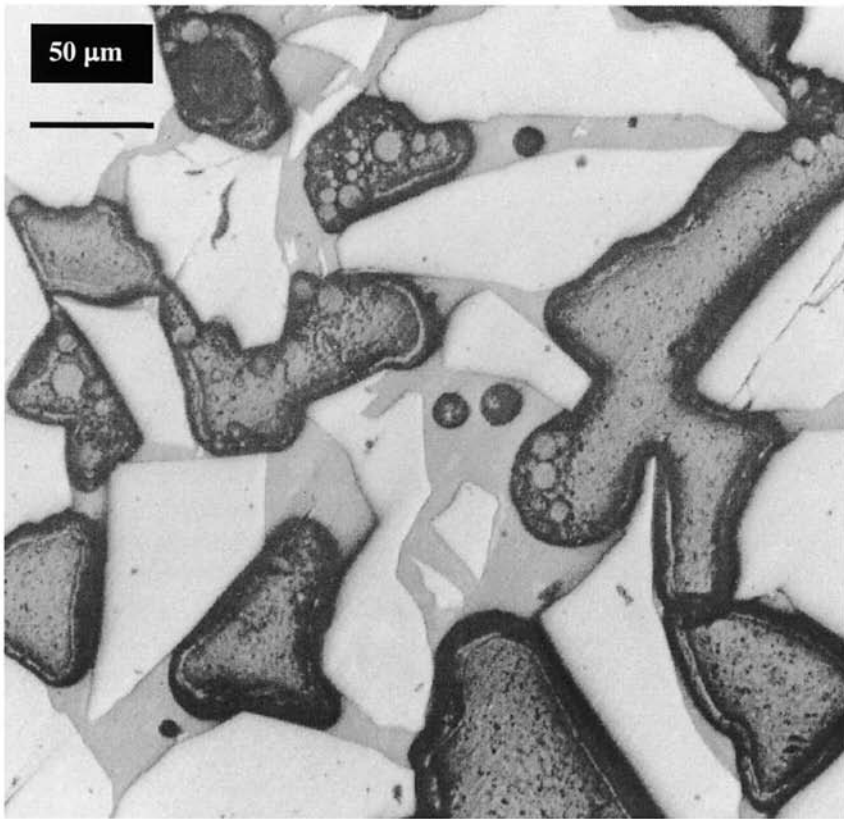


Fig. 10.13. Structure of the porous tool used for nanogrinding

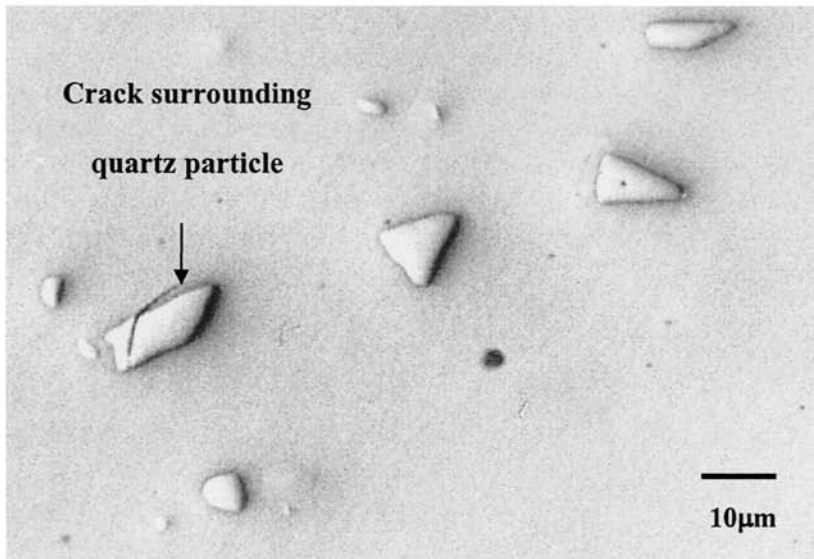


Fig. 10.14. A collection of quartz particles in a vitrified bonding system. The quartz particle on the left has a circumferential crack extending into the dissolution rim

Clays and clay-based fluxes contain an amount of free quartz that has a detrimental effect on the development of strength during vitrification heat treatment. Clays are used to provide vitrified grinding wheels with green strength during the heat treatment process. However, when the glass material solidifies around the particles of clay and quartz, the displacive transformation of quartz during the cooling stage of vitrification leads to the formation of cracks in the glass around the quartz particle (Fig. 10.14). The strength of the bonding bridge is impaired and leads to the early release of the abrasive particle during the cutting of metal.

The basic wear mechanisms that affect vitrified grinding wheels are concerned with grain fracture during metal cutting, fracture of bond bridges, mechanical fracture of abrasive grains due to spalling, and fracture at the interface between abrasive grain and bond bridge. Failure in vitrified silicon carbide grinding wheels is more probable due to the lack of a well-developed bonding layer between abrasive grain and glass bond-bridge. The bonding layer is

approximately a few micrometers in thickness, and is caused by the use of a high clay content bonding system. High glass content bonding systems tend to aggressively decompose the surface of silicon carbide abrasive grains. In vitrified corundum grinding wheels, high glass content bonding systems are used extensively and lead to bonding layers in excess of one hundred micrometers in thickness.

In addition to the formation of very thin bonding layers in vitrified silicon carbide grinding wheels, the use of high clay content bonding systems implies that there is an increase in the amount of quartz in the bond bridges between abrasive grains. Although the likelihood of decomposition of silicon carbide surfaces is reduced, the probability of bond bridge failure is increased due to the increased quartz content. Therefore, the dissolution of quartz is of paramount importance in order to compensate for thinner interfacial bonding layers.

The dissolution of quartz in a liquid phase does not require a nucleation step. One process that determines the rate of the overall reaction is the phase-boundary reaction rate that is fixed by the movement of ions across the interface. However, reaction at the phase boundary leads to an increased concentration at the interface. Ions must diffuse away from the reaction interface so that the reaction can continue. The rate of material transfer and the diffusion rate are controlled by molecular diffusion in the presence of a high-viscosity liquid phase. For a stationary solid in an unstirred liquid, or in a liquid with no fluid flow produced by hydrodynamic instabilities, the rate of dissolution is governed by molecular diffusion.

The effective diffusion length over which mass is transported is proportional to \sqrt{Dt} , where D is the diffusion coefficient and t is time, and therefore the change in thickness of the solid, which is proportional to the mass dissolved, varies with \sqrt{t} . Natural, or free, convection occurs because of hydrodynamic instabilities in the liquid which gives rise to fluid flow over the solid. This enhances the kinetics of dissolution. Generally, a partially submerged solid undergoes more dissolution near to the solid-liquid interface. Below this interface the kinetics of dissolution of the solid can be analyzed using the principles of free convection.

The boundary layer thickness is determined by the hydrodynamic conditions of fluid flow. Viscous liquids form much thicker

boundary layers that tend to impede material transfer. Higher liquid velocities promote the formation of thinner boundary layers and permit more rapid material transfer. Considering the dissolution of quartz in glass materials, the high viscosity and slow fluid flows combine to give thick boundary layers. Also, the diffusion rate is much slower in viscous silicate liquids than in aqueous solutions, thus giving a tendency for the reaction process to be controlled by material-transfer phenomena rather than by interface reactions.

Difficulties encountered when developing a dissolution model arise from the fact that the phase boundary between quartz particle and molten glass moves during the diffusion process. The problem of a fixed boundary can be solved without difficulty although this is not equivalent to the conditions associated with a moving boundary between quartz particle and a highly viscous glass melt.

The development of dissolution models is required to determine the magnitude of quartz remaining in the bonding system after a period of heat treatment. The models are then compared with experimentally determined quartz content of the bonding systems using x-ray diffraction techniques.

10.6.1 Dissolution Models for Quartz in Bonding Bridges

When densification occurs in a vitrified grinding wheel, the cooling rate is reduced to prevent thermal stress cracking in the bonding layer between abrasive particles. Cooling rates are reduced when crystalline inversions occur that involve volume changes. The inversion range for quartz and cristobalite are 550°C – 580°C and 200°C – 300°C, respectively. Since the formation of cristobalite is rare in most vitrified bonding systems used for grinding wheels, the rapid displacive transformation of quartz tends to promote the formation of cracks in bonding bridges (Fig. 10.15). Once the grinding grain is lost the remaining bonding bridges can be modified using a high power laser to create an oriented texture that forms “peaks” of α -Al₂O₃ in the preferred (012), (104), and (110) planes.

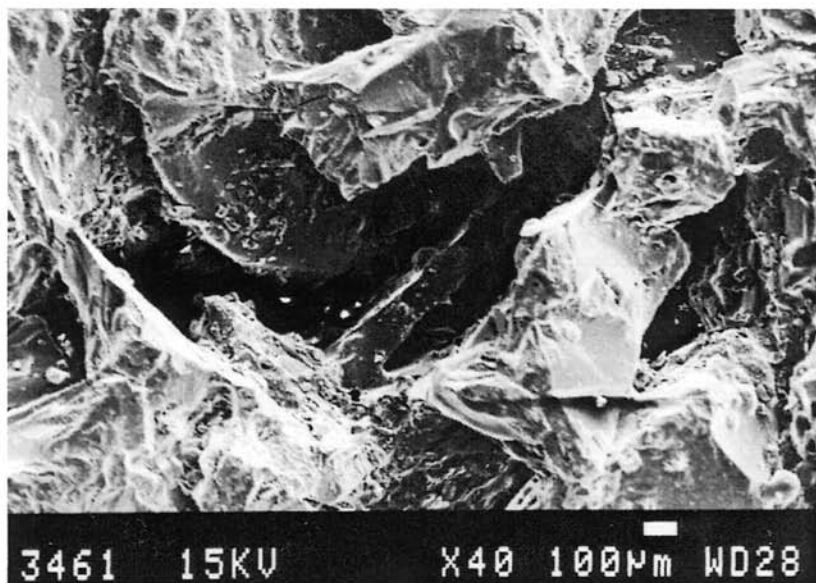


Fig. 10.15. Bonding bridge failure in a vitrified grinding wheel caused by the displacive transformation of quartz at high temperature during heat treatment

When quartz-containing bonds begin to cool from the soaking, or vitrification, temperature it is thought that the liquid phase relieves stresses resulting from thermal expansion mismatch between itself and the phases, β -quartz, β -cristobalite, and mullite, to at least 800°C . At 800°C , stresses will develop in quartz particles and the matrix that causes micro-cracking to occur. The shrinkage behaviour of quartz and the glass phase has been described by Storch et al [7]. Between the temperature range, 573°C and 800°C , the glass phase shrinks more than the quartz phase that causes tangential tensile stresses to form cracks in the matrix. At 573°C , β -quartz transforms to α -quartz that causes residual stresses to produce circumferential cracking around quartz particles (Fig. 10.14). Some of these cracks have been seen to propagate into the glass phase [8]. Similar observations occur in the cristobalite phase. Spontaneous cracking of quartz has been found to occur over a temperature range that depends on the size of the quartz particles [9]. Particles larger than 600 micrometers' diameter cracked spontaneously at 640°C ,

whereas smaller particles of less than 40 μm diameter cracked at 573°C. This observation agrees with temperature-dependent micro-cracking reported by Kirchhoff et al [10]. To maintain the integrity of the bond bridges containing coarse quartz particles, the grinding wheel must remain at the vitrification temperature until the quartz particles have dissolved.

The dissolution model assumes that at a constant absolute temperature, T , a particle of quartz melts in the surrounding viscous glass melt, and that the rate of change of the volume of quartz present in the melt at a particular instant in time is proportional to the residual volume of quartz. The above assumption is based on the fact that alkali ions diffuse from the viscous glass melt to the boundary of the quartz particle, thus producing a dissolution rim around each quartz particle. A high reaction rate will initially occur which continuously decreases as the quartz particle is converted to a viscous melt.

Jackson and Mills [11] derived a mathematical relationship that accounts for the change in density when β -quartz transforms to α -quartz on cooling from the vitrification temperature, thus,

$$m_{T,t} = M\gamma \exp\left(-At^{1/2} \exp\left[\frac{-B}{T}\right]\right) \quad (10.37)$$

Where, $m_{T,t}$ is the residual mass fraction of quartz at a constant time and temperature couple, M is the original mass fraction of quartz prior to heat treatment, γ is the ratio of densities of β -quartz and α -quartz, A and B are constants, t is time, and T is absolute temperature. The model was compared with experimental data determined using the powder x-ray diffraction method. The experimental work was divided into two parts. The first part concentrates on comparing the dissolution model with x-ray diffraction data using “sintering” bond compositions that are used in vitrified silicon carbide nanogrinding tools, while the second part focuses on comparing the model with “fusible” bond compositions that are used in high-performance vitrified corundum nanogrinding tools.

10.6.2 Preparation of Bonding Bridges for Nanogrinding Wheels

The raw materials used in the experimental study were Hymod Prima ball clay, standard porcelain China clay, potash feldspar, and synthetic quartz (supplied as silica flour). The chemical analysis of the raw materials is shown in Table 10.2. Rational analysis of the raw materials was performed to reveal the mineralogical composition of the raw materials. The rational analysis appears in Table 10.3. The characteristic x-ray diffraction spectra for ball clay and China clay are shown in Figs. 10.16 and 10.17. The bond mixture described is one typically used in vitrified silicon carbide grinding wheels where the erosion of the abrasive grain is reduced by using high clay content bonding systems.

Table 10.2. Chemical analyses of raw materials

Oxide (wt. %)	China clay	Ball clay	Potash feldspar	Quartz
Al ₂ O ₃	37	31	18.01	0.65
SiO ₂	48	52	66.6	98.4
K ₂ O	1.65	1.8	11.01	0.35
Na ₂ O	0.1	0.2	3.2	0.04
CaO	0.07	0.2	0.09	0.00
MgO	0.03	0.3	0.09	0.00
TiO ₂	0.02	0.9	0.00	0.07
Fe ₂ O ₃	0.68	1.1	0.11	0.03
Loss on ignition	12.5	16.5	0.89	0.20

Fusible bonding systems using a mixture of ball clay and potassium-rich feldspar were made to test the model developed by Jackson and Mills [11]. The ball clay used contained 12.77 wt. % quartz, and the feldspar contained 4.93 wt.% quartz. The bonding system was composed of 66 wt.% ball clay, and 34% feldspar. The initial quartz content, M, of the bond mixture was 10.1 wt.%. The

bond mixture described is one typically used in high-performance vitrified corundum grinding wheels.

Table 10.3. Mineralogical analyses of raw materials

Compound (wt. %)	China clay	Ball clay	Potash feldspar	Quartz
Quartz	4.05	12.77	4.93	98.40
Orthoclase	0.00	15.23	64.96	0.00
Kaolinite	79.70	62.71	2.17	0.00
Mica	13.94	0.00	0.00	0.00
Soda feldspar	0.8	1.69	27.07	0.00
Miscellaneous oxides/losses	1.51	7.60	0.87	1.60

The raw materials were mixed in a mortar, pressed in a mold, and fired at various temperatures. A heating rate of $2.9^{\circ}\text{C min}^{-1}$ was employed until the vitrification temperature was reached.

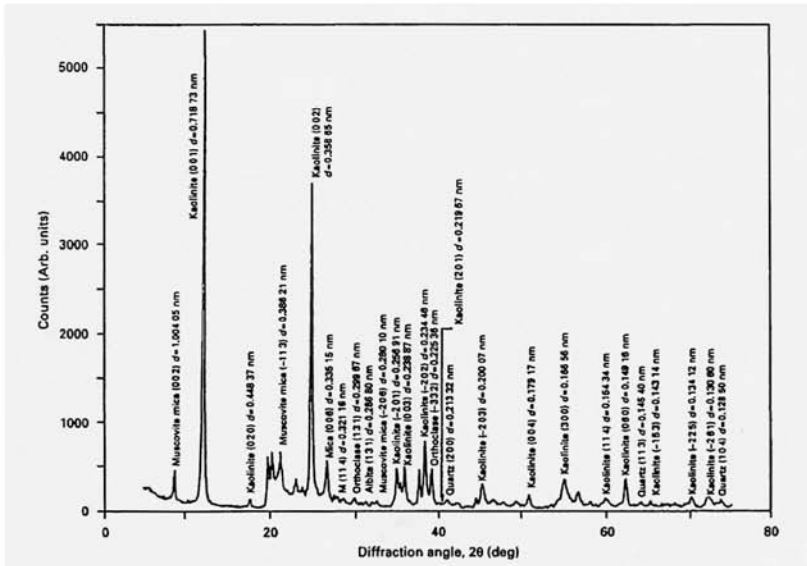


Fig. 10.16. X-ray diffraction spectrum of China clay showing crystallographic planes and interplanar distances of various mineral phases in the clay

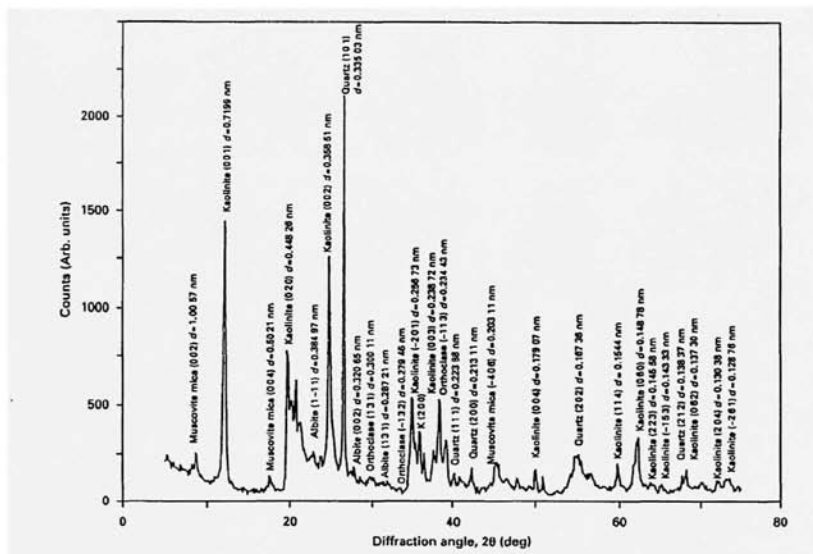


Fig. 10.17. X-ray diffraction spectrum of ball clay showing crystallographic planes and interplanar distances of various mineral phases in the clay

The typical soaking temperature was varied between 1200°C and 1400°C for “sintering” bond compositions, and 950°C and 1050°C for “fusible” bond compositions in order to simulate industrial firing conditions. The samples were cooled at a rate of 1.8°C min⁻¹ to avoid thermal stress fracture. The fired samples were crushed to form a fine powder in preparation for x-ray diffraction.

10.6.3 X-ray Diffraction of Bonding Systems

The dissolution model was compared with experimental data using the x-ray powder diffraction method. X-ray diffraction of the raw materials was performed on a Phillips 1710 x-ray generator with a 40 kV tube voltage and a 30 mA current. Monochromatic Cu $k\alpha$ radiation, $\lambda = 0.154060$ nm, was employed. A scanning speed of 2° per minute for diffraction angles of 2θ was used between 2θ angles of 10° and 80°, and the x-ray intensity was recorded using a com-

puter. The spectrum was then analyzed and compared with known spectra.

Powder specimens were prepared by crushing in a mortar and pestle in preparation for quantitative x-ray diffraction. To eliminate the requirement of knowing mass absorption coefficients of ceramic samples for quantitative x-ray diffraction, Alexander and Klug [12] introduced the use of an internal standard. First, the ceramic sample is crushed to form a powder - the sizes of particles should be small enough to make extinction and micro-absorption effects negligible. Second, the internal standard to be added should have a mass absorption coefficient at a radiation wavelength such that intensity peaks from the phase(s) being measured are not diminished or amplified. It should be noted that the powder diffraction mixture should be homogeneous on a scale of size smaller than the amount of material exposed to the x-ray beam, and should be free from preferred orientation. The powder bed that is subjected to "x-rays" should be deep enough to give maximum diffracted intensity.

The expected equilibrium phases from the fired mixtures are quartz (unreacted and partially dissolved), mullite, cristobalite and glass. However, from the samples tested, the compounds quartz, mullite and glass were successfully detected. A calibration curve was constructed using a suitable internal standard (calcium fluoride), a diluent (glass made by melting potash feldspar), and a synthetic form of the phase(s) to be measured. Synthetic mullite had a purity greater than 99.8%, whilst powdered quartz had a purity greater than 99.84% SiO_2 . The method used for quantitative analysis of ceramic powders was developed by Khandelwal and Cook [13].

The internal standard gave a fairly intense (111) reflection ($d = 0.1354\text{nm}$) lying between the (100) reflection for quartz ($d = 0.4257\text{nm}$) and the (200) reflection for mullite ($d = 0.3773\text{nm}$). Using copper $k\alpha$ radiation ($\lambda = 0.15405\text{nm}$), the corresponding values of diffraction angle 2θ are: (100) quartz = 20.82° ; (111) calcium fluoride = 28.3° ; and (200) mullite = 32.26° . Fig. 10.18 shows the calibration curve generated by varying proportions of calcium fluoride, synthetic quartz and mullite. Mass fractions of the crystalline phases in the mixture can be read from the calibration lines by measuring the intensity ratio of the phase(s) to the internal standard.

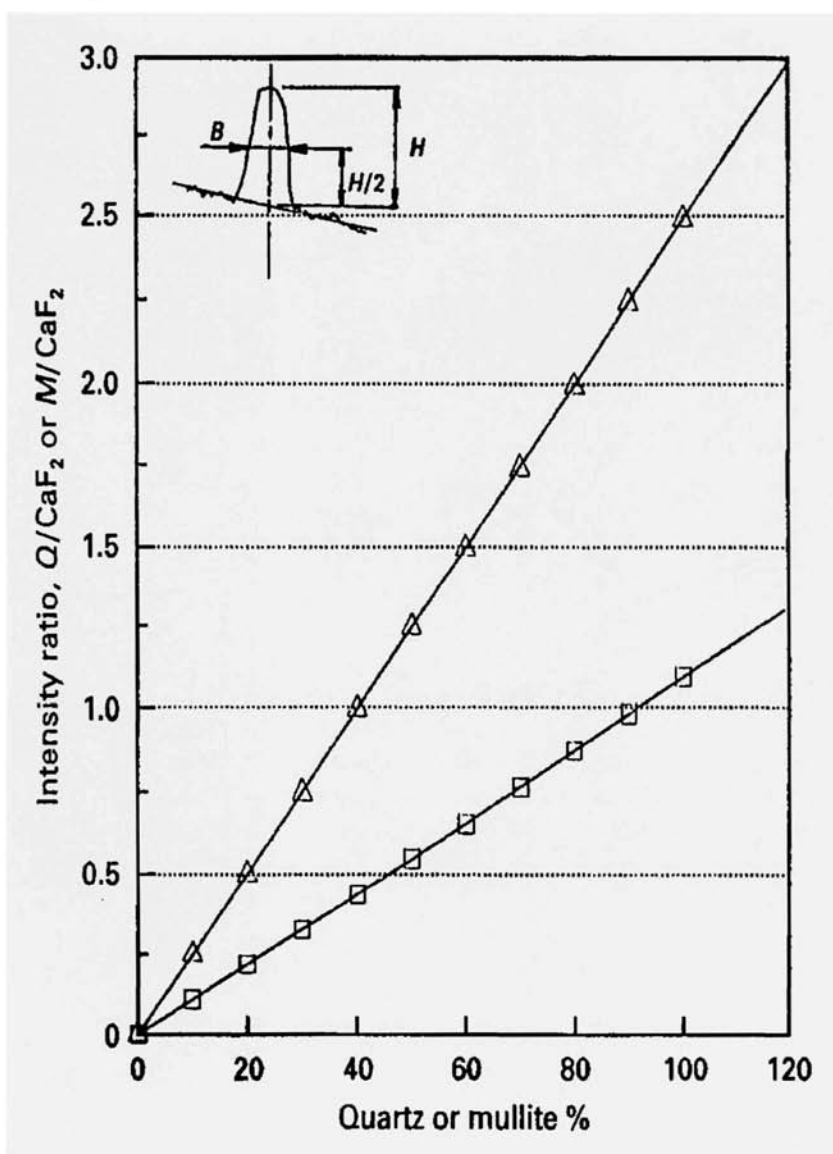


Fig. 10.18. Calibration curve for quantitative analysis of x-ray determined quartz and mullite using the CaF₂ (111) plane generated by the internal standard

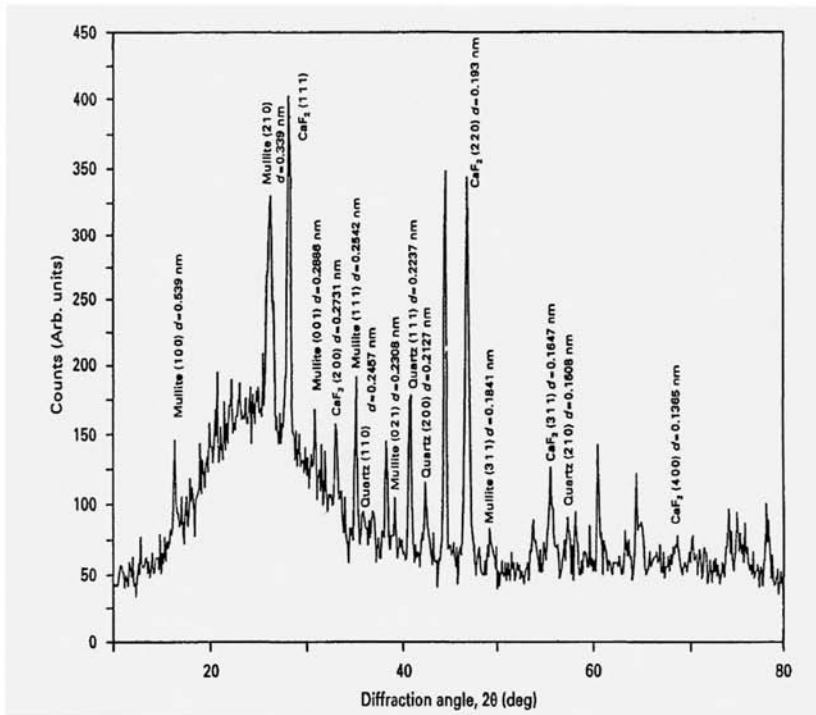


Fig. 10.19. X-ray diffraction spectrum of a vitrified bonding system showing the interplanar distances of crystallographic planes of mullite, quartz and calcium fluoride. Scan rate was 2° per minute

Figure 10.19 shows the diffraction peaks of interest for quantitative analysis lying between 15° and 40° of the diffraction angle 2θ . The figure shows the reflections of the (111) plane of calcium fluoride, (200) plane of mullite, and the (100) plane of quartz. In order to calculate the mass fractions of quartz and mullite in the mixture, the height of the chosen diffraction peak and its width at half-height were measured from the diffraction spectrum. The product of these two measures were then compared with that of the internal standard, and the resultant intensity ratio was used to find the exact mass fraction of the phase(s) measured in the glass that has been x-rayed.

10.6.4 Refractory Bonding Systems – Verification and Comparison of Dissolution Models for Quartz

In addition to comparing the experimental results to the dissolution model, results published in the literature were also used to test the accuracy of the model. The composition of the experimental mixtures was matched to those specified by Lundin [6]. Lundin's experimental mixtures were composed of 25 wt.% quartz (13.2 μm particle size), 50 wt.% clay (kaolin), and 25 wt.% flux (potassium feldspar - 25 μm particle size).

The constants A and B for the sintering bonding system were calculated,

$$A = 5.62 \times 10^8 \quad (10.38)$$

$$B = 33374 \quad (10.39)$$

From which the experimental activation energy, Q , is 132.65 kcal/mole. The residual quartz content for the sintering bonding system is,

$$m_{T,t} = 26.25 \cdot \exp \left[-5.62 \times 10^8 t^{1/2} \cdot e^{\frac{-33374}{T}} \right] \quad (10.40)$$

The data comparing Lundin's experimental results, the author's experimental results, and the dissolution model are shown in Table 10.4.

When the data are plotted as the logarithm of $(-\ln[m/M]/t^{1/2})$ versus the reciprocal of absolute temperature, $1/T$, then all data fits a straight-line relationship. The gradient was calculated to be 33374, the constant B , using two data points. Lundin's experimental gradient gave a value of 32962 using the least squares method, and 34000 for the present work. The corresponding activation energies for both systems are 131 kcal/mole for Lundin's work [6], and 135 kcal/mole for the present work, respectively. Figures 10.20 and 10.21 show the

effects of time on residual quartz content at different temperatures according to Eq. 40 together with comparative experimental data.

A comparison was made with dissolution models published in the literature. One of the earliest models was derived by Jander [14]. The equation can be expressed:

$$\left(1 - \sqrt[3]{1 - Z}\right)^2 = \left\{ \frac{C_1 \cdot D}{r^2} \right\} \cdot t \quad (10.41)$$

Where Z is the volume of quartz that has been dissolved, r is the original particle radius, and D is the diffusion coefficient for the diffusing species. This equation can be transformed into mass fractions using Archimedes' law, thus,

$$\left(1 - \sqrt[3]{\frac{m}{M}}\right)^2 = C_2 \cdot t \quad (10.42)$$

Where C is a constant dependent on soaking temperature and initial particle size of quartz. Krause and Keetman [15] expressed the dissolution of quartz as a function of isothermal firing time, viz,

$$M - m = C_3 \cdot \ln t \quad (10.43)$$

Where M is the initial quartz content, and m is the residual quartz content after time, t . The unit of time here is seconds such that after one second of firing the residual quartz content is equal to the initial quartz content. Monshi's dissolution model [16] can be transformed into the following equation assuming isothermal firing conditions:

$$\ln \left\{ \frac{m}{M} \right\} = -C_6 \sqrt{t} \quad (10.44)$$

Table 10.4. Residual quartz content of a sintering bonding system at various vitrification temperatures. Lundin's [6] experimental data are compared with the author's experimental data and the model [11]. The asterisk indicates values used for deriving the constants used in the theoretical model

Temp. (°C)	Time (hrs.)	Lundin's exp. result (wt.%)	Exp. result (wt.%)	Jackson and Mills' [11] re- sult (wt.%)
1200(1473K)	1	24.1	24.2	24.2
1200	1	24.7	24.3	24.2
1200	1	26.1	24.8	24.2
1200	2	23.7	23.8	23.4
1200	2	23.6	23.9	23.4
1200*	2	23.4	23.4	23.4
1200	4	21.3	22.2	22.3
1200	8	20.3	20.9	20.8
1200	18	19.0	18.5	18.6
1200	18	18.9	18.6	18.6
1200	48	15.2	15.1	14.9
1250(1523K)	1	22.7	22	22.1
1250*	2	20.6	20.6	20.6
1250	4	18	18.5	18.6
1250	8	15.5	16	16.2
1250	18	12.6	12.5	12.6
1250	48	8.3	7.8	8.0
1300(1573K)	0.5	22.6	20.4	20.6
1300	0.5	21	20.9	20.6
1300	1	20	18.3	18.6
1300	2	16.1	15.9	16.2
1300	4	13.4	12.8	13.2
1300	8	10	9.7	9.9
1300	18	5.9	5.8	6.1
1300	50	1.6	1.8	2.3
1300	120	0.3	0.2	0.6

Jackson and Mills' model [11] for isothermal firing conditions is transformed into:

$$\ln \left\{ \frac{m}{\gamma \cdot M} \right\} = -C_7 \sqrt{t} \quad (10.45)$$

Where γ is the ratio of densities of β - and α -quartz. Constants for all the equations presented here are calculated using quartz mass fraction data after 18 hours' firing. The constants are dimensioned in seconds. The equations shown were compared with experimental data generated by Lundin [6] for a clay-based material containing 40 wt.% kaolin, 40 wt.% quartz, and 20 wt.% feldspar. According to the transformed equations, the mass fraction of quartz can be calculated as follows,

Jander's model [14]

$$m = 41.9 \left(1 - \left\{ 1.55 \times 10^{-6} t \right\}^{3/2} \right) \quad (10.46)$$

Krause and Keetman's model [15]

$$m = 41.9 - (2.58 \cdot \ln t) \quad (10.47)$$

Monshi's model [16]

$$m = 41.9 \cdot e^{-4.5 \times 10^{-3} \sqrt{t}} \quad (10.48)$$

Jackson and Mills' model [11]

$$m = 41.73 \cdot e^{-4.5 \times 10^{-3} \sqrt{t}} \quad (10.49)$$

The transformed equations are then tested using data provided by Lundin [6]. Referring to Table 10.5, it can be shown that the mass fraction of quartz obtained using the equations derived by Jander [14] and Krause and Keetman [15] did not agree with Lundin's experimental results [6].

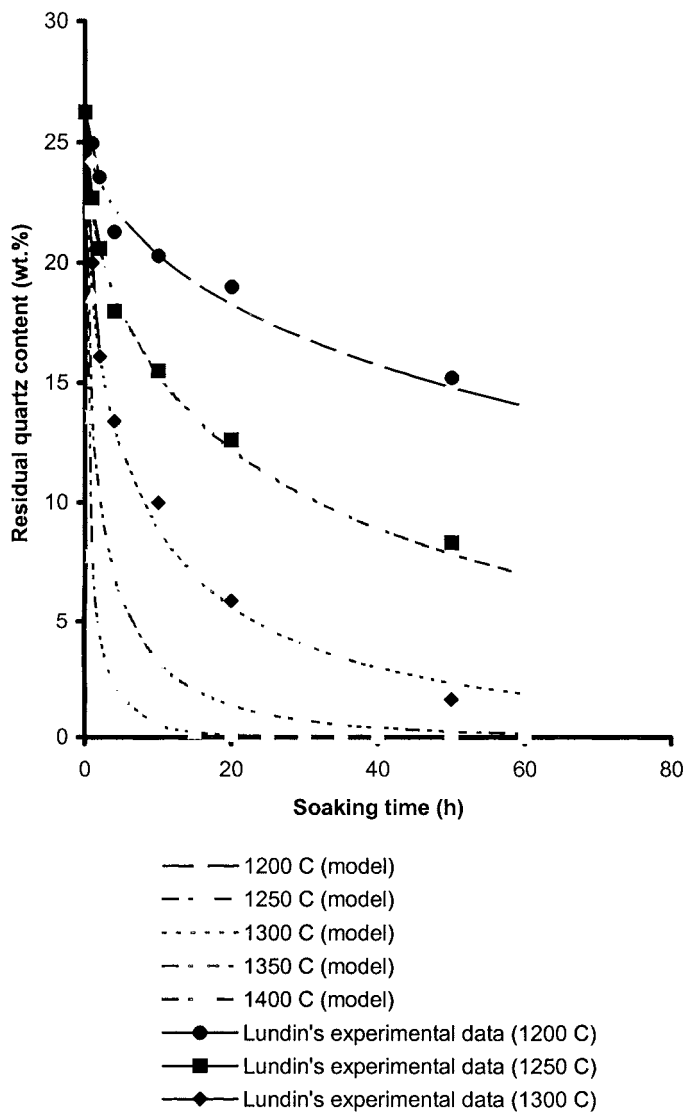


Fig. 10.20. Effect of time on residual quartz content of a sintering bonding system according to Jackson and Mills's model [11], and compared with Lundin's experimental data [6]

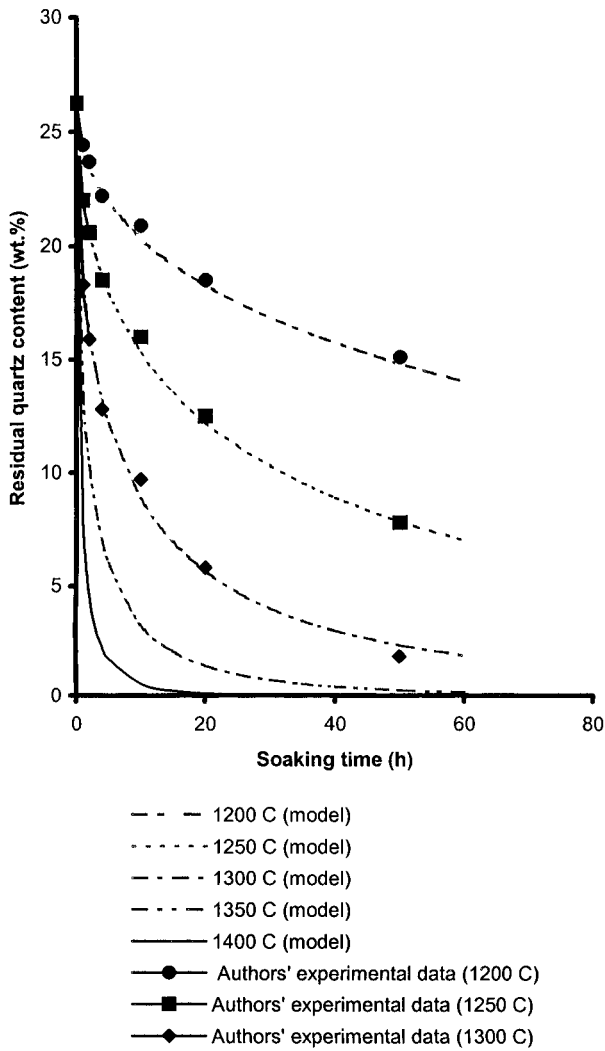


Fig. 10.21. Effect of time on residual quartz content of a sintering bonding system according to Jackson and Mills's model [11] and compared with the authors' experimental data

Table 10.5. Residual quartz content for different soaking times at 1300°C for a sintering bonding system composed of 40 wt.% kaolin, 40 wt.% quartz, and 20 wt.% feldspar (Lundin's mixture number M21 [6]) compared with other dissolution models.

Time (hours)	Lundin's exp. data [6]	Jander [14]	Krause and Keet-man [15]	Monshi [16]	Jackson and Mills [11]
0	41.9	41.9	0.00	41.9	41.9
0.5	35.9	41.72	22.55	34.61	34.76
1	32.8	41.54	20.76	31.97	32.12
2	29.2	41.19	18.97	28.58	28.72
4	23.2	40.49	17.18	24.39	24.51
8	19.5	39.11	15.39	19.49	19.59
18	13.3	35.72	13.30	13.30	13.36
24	10.7	33.74	12.56	11.13	11.19
48	6.9	26.18	10.77	6.43	6.51
120	3.6	7.85	8.96	2.17	2.17
190	2.7	0.00	7.22	1.00	1.01
258	2.0	0.00	6.43	0.54	0.55

The results obtained using Monshi's model [16] are in much better agreement compared to Lundin's data. However, the results obtained using Jackson and Mills' model [11] is more accurate at predicting the mass fraction of quartz remaining owing to the differences in the density of quartz. After long periods of heat treatment, the model predicts lower magnitudes of mass fractions of quartz when compared to Lundin's experimental results [6].

10.6.5 Fusible Bonding Systems – Verification and Comparison of Dissolution Models for Quartz

The constants, A and B , for the fusible bonding system were determined using time and temperature couples at 2 hours and 10 hours and were calculated to be, -5.2×10^8 and -33205 , respectively. The dissolution equation then becomes,

$$m_{T,t} = 10.06 \exp \left[-5.2 \times 10^8 t^{1/2} . e^{\frac{-33205}{T}} \right] \quad (10.50)$$

Equation (10.50) is used to compare the experimentally determined mass fraction of quartz remaining after heat treatment with the predicted values. The calculated mass fraction of quartz remaining after a period of heat treatment is calculated using the equation derived by Jackson and Mills [11]. The results of the dissolution model compare well with the experimental data over short periods of time.

However, over longer periods of heat treatment the model tends to become less accurate (Fig. 10.22). A comparison was made with published dissolution models. The equations shown were compared with experimental data at 1050°C.

The equations shown were compared with experimental data at 1050°C. According to the transformed equations, the mass fraction of quartz can be calculated as follows:

Jander's model [14]

$$m = 10.1 \left(1 - \left\{ 3.44 \times 10^{-6} t \right\}^{3/2} \right) \quad (10.51)$$

Krause and Keetman's model [15]

$$m = 10.1 - (0.59 \ln t) \quad (10.52)$$

Monshi's model [16]

$$m = 10.1 \cdot e^{-6.4 \times 10^{-3} \sqrt{t}} \quad (10.53)$$

Jackson and Mills' model [11]

$$m = 10.06 \cdot e^{-6.37 \times 10^{-3} \sqrt{t}} \quad (10.54)$$

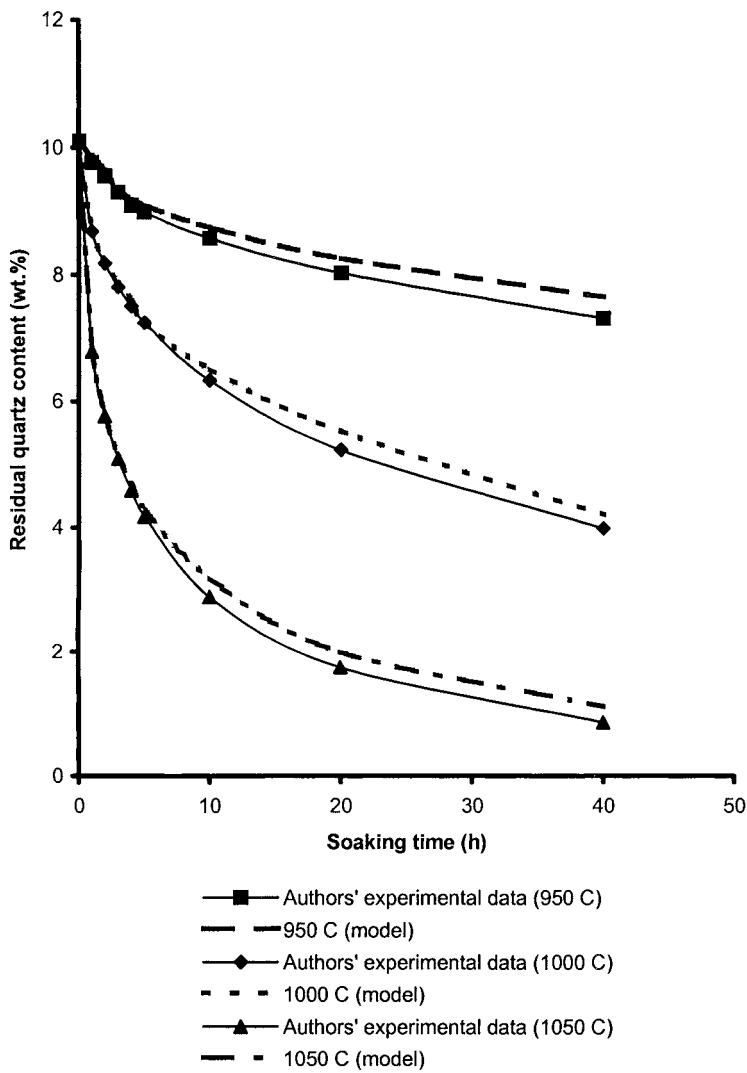


Fig. 10.22. Effect of time on residual quartz content of a fusible bonding system according to Jackson and Mills's model [11] and compared with the author's experimental data

With reference to Table 10.6, it can be shown that the mass fraction of quartz obtained using the equations derived by Jander [14] and Krause and Keetman [15], did not agree with the experimental results at 1050°C. The results obtained using Monshi's model [16] are in much better agreement compared to the experimental data. However, the results obtained from Jackson and Mills's model are more accurate at predicting the mass fraction of quartz remaining owing to the differences in the density of quartz. After long periods of heat treatment, the model predicts slightly lower magnitudes of mass fractions of quartz when compared to the experimental results.

Table 10.6. Residual quartz content for different soaking times at 1050°C for a fusible bonding system compared with other dissolution models

Time (h)	Exp. Data	Jander model [14]	Krause and Keetman model [15]	Monshi's model [16]	Jackson and Mills' model [11]
0	10.1	10.1	0	10.1	10.1
1	6.84	9.91	5.23	6.88	6.86
2	5.79	9.72	4.82	5.87	5.86
3	5.13	9.54	4.58	5.21	5.19
4	4.7	9.36	4.41	4.7	4.68
5	4.28	9.18	4.28	4.28	4.28
10	3.2	8.28	3.87	2.99	3
20	2	6.6	3.46	1.81	1.82
40	1.1	3.62	3.04	0.89	0.89

The dissolution of quartz during heat treatment has a significant effect on the wear of vitrified grinding wheels. Figure 10.23 shows the effect of using a high and a low quartz content bonding system on the wear of vitrified corundum grinding wheels grinding a large number of tool steel materials [17]. The classification of tool steels is in the form of an abrasive hardness number, which is a weighted average of the number of carbides contained within the tool material. As shown in Fig. 10.23, the grinding ratio, or G-ratio, is a measure of the efficiency of the grinding wheel. It is the quotient of the volume of workpiece material removed and the volume

of the wheel material removed. The figure demonstrates the effectiveness of reducing the quartz content of the bonding system of porous nanogrinding tools.

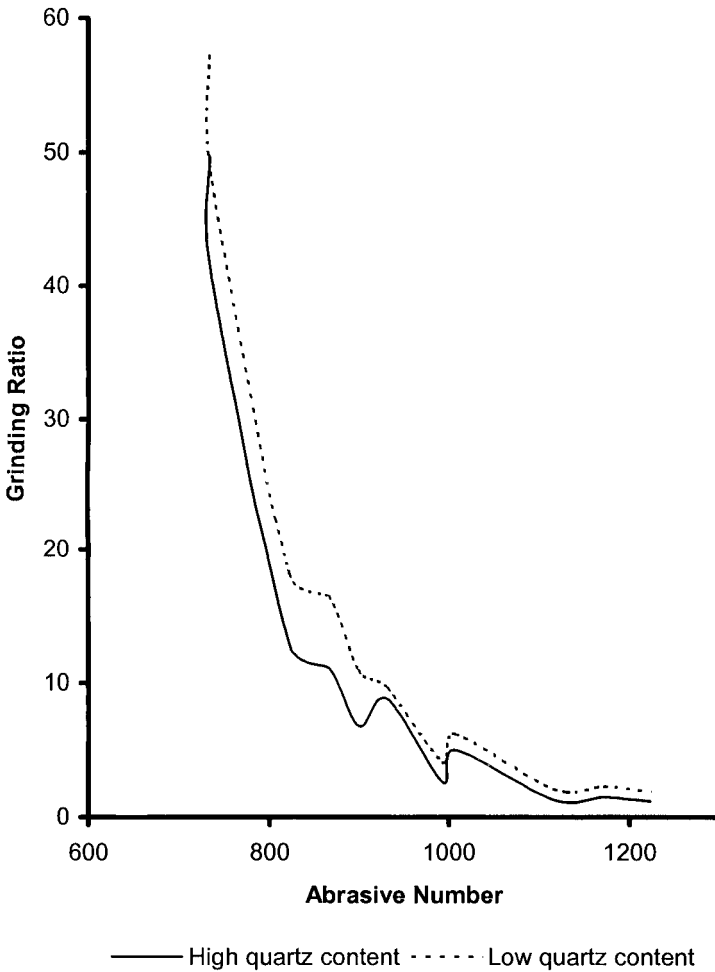


Fig. 10.23. Effect of the abrasive number on the grinding ratio for a high-quartz content and a low quartz-content bonding system

10.7 Laser Dressing of Nanogrinding Tools

The processing of abrasive materials by locally restructuring their surface using a high power laser allows one to provide a localized heat source at high speed that produces surface features that are able to remove material at the nanoscale. The depth of thermal processing of the surface that allows the material to melt, solidify and cool is controlled by parameters such as fluence (energy per unit area), laser beam scanning speed, and input power. Previous studies on laser dressing of grinding wheels have resulted in the localized modification of the morphology of corundum abrasive materials [19-21]. The grinding wheel is initially made by sintering corundum grains with a low melting point binding material, which is subsequently melted, vaporized, and selectively removed using a concentrated beam of optical energy that changes surface topography and composition. The refinement of grain size, densification of grinding layer, and evolution of competitive grains with sharp vertices is shown to occur during laser dressing [19]. These changes result in an increase in grinding ratios, especially when grinding tool steels [19].

X-ray diffraction (XRD) of the laser dressed surface indicated that crystallographic texture occurs on the surface of the grinding wheel, and the identification of planar texture is considered important as it controls the formation of multifaceted grains that take part in removing workpiece material. Pole figure analysis of laser dressed corundum composite materials indicates that crystallographic texture is preferred along the (110) plane [19-21]. Grinding properties are particularly sensitive to preferred orientation and as such variations in grinding are apparent. To predict the performance of these materials, it is important to identify crystallographic texture using XRD techniques. Orientation imaging microscopy (OIM) is used to characterize micro-texture [22] as it gives phase specific crystallographic texture. The OIM technique uses Kikuchi patterns to predict crystallographic texture at various points on the surface of the laser dressed material. Microstructural variations are observed on the laser dressed surface owing to temperature gradients and variations in cooling rates. Corundum, or alumina, has poor thermal

conductivity compared to metals that allows thermal energy to be retained in the surface for a longer period of time compared to the workpiece material. The occurrence of porosity between grains also reduces thermal conductivity, which results in the retardation of heat lost from the surface of the abrasive material [23]. In addition to the effects of porosity, consolidation of the corundum abrasive material with the bonding material changes the thermal properties during laser dressing [24-26]. Therefore, the combined thermophysical properties of the composite material must be used. Table 10.7 shows the thermophysical properties of the abrasive material. It is important to quantify the cooling rate in order to understand how the microstructure evolves into preferred orientation during laser dressing. Many models have been generated that predict how microstructures form under rapid solidification conditions [27-29]. The chapter presents an understanding of how cooling rates affect the formation of multiple cutting points on the surface of the abrasive material and how it affects grindability of a hypereutectoid steel such as AISI 52100 bearing steel. This is achieved by observing cooling rates using a two-color pyrometer, by characterizing the microstructural texture using OIM, and by determining grinding ratios when grinding AISI 52100 bearing steel.

Table 10.7. Thermophysical properties of vitrified corundum abrasive material

Thermophysical property	Numerical value of property ^a
Density, ρ	$2.7 \times 10^3 \text{ kg/m}^3$
Melting temperature, T_m ,	2045 K
Latent heat of fusion, ΔH_m ,	$1.03 \times 10^6 \text{ J/mol}$
Specific heat, C_p ,	1137 J/kg K
Thermal diffusivity, D ,	$1.08 \times 10^{-6} \text{ m}^2/\text{s}$

^a Source: *Vitrified Technologies Inc., Central Research and Development Laboratory, P. O. Box 3724, West Lafayette, IN 47996*

10.7.1 Experimental Procedures

Vitrified corundum abrasive products were supplied by Vitrified Technologies Inc., and were composed of corundum grains doped with 0.25% wt. chromia that were bonded together using a bonding system composed of borosilicate glass and orthoclase feldspar. The chemical composition of the abrasive grain material is 99.52% Al_2O_3 , 0.18% Na_2O , 0.05% Fe_2O_3 , and 0.25% Cr_2O_3 . A 2.5kW Hobart continuous-wave Nd:YAG laser equipped with a fiber optic beam delivery system was used for dressing the surface of the grinding wheel. Laser power was varied from 400 W to 1000 W, whilst the overlap between dressed layers was less than 20%. The laser beam was scanned at a linear speed of 250 cm/min on the surface of the grinding wheel. Full experimental details of the dressing procedure are provided in references [19,21]. Laser dressed grinding wheels were finally compared to conventionally dressed grinding wheels grinding a hypereutectoid steel typically used for bearing applications that is capable of being superfinished.

Measurement of Dressing Temperatures

A two-color optical pyrometer was used to measure the temperature of the abrasive surface during dressing. The temperature range of the pyrometer is 600°C to 1500°C with a response time of 0.5 ms. The pyrometer is calibrated against National Institute standards to within 10°C over the range 800°C to 3000°C. A specially constructed telescope with filter was constructed in order to measure the laser beam temperature at the surface, and a program was written to directly record temperature against processing time. When the laser beam dresses the surface, a large plume of light is emitted that interferes with the intensity of the light collected by the telescope. To overcome the large emission of light, a delay was programmed in the software program to prevent the erroneous measurement of temperature. As the plume of light fades away, the pyrometer records the temperature. The temperature is measured at 400 W and 500 W of laser power, but at very high laser power such as 1000 W the temperature is almost impossible to record because of the intensity of

light. Therefore, data are presented at the lower values of laser power because the plume lasts for less than 1 second.

Orientation Imaging Microscopy

To gain high-quality Kikuchi patterns from laser dressed grinding wheels, samples were cross-sectioned by polishing with a water solution on SiC abrasive papers then followed by polishing with a diamond paste to achieve a fine surface. The samples were then carbon coated with a uniform thickness of 3 nm. Electron backscattered diffraction patterns (EBSD), or backscattered Kikuchi patterns, were generated using a Philips FEG SEM equipped with an orientation-imaging microscope [30-32]. OIM analysis was conducted at Oak Ridge National Laboratory. To produce crystallographic orientation maps, the electron beam is scanned over a selected surface area and the resulting EBSD patterns are automatically indexed and the local orientation is determined [33-34]. For the present study, a sample processed at 1000 W was used in order to provide a crystallographic map of the whole re-solidified layer. From XRD and energy dispersive analysis (EDS), it was found that the primary phase created was α -alumina [19-20] and so the hexagonal crystal structure of alumina was selected to index the EBSD Kikuchi patterns obtained during the analysis. For OIM analysis, the 1000W laser dressed surface was used whereas the lower power processed samples were used to measure cooling rates. This does not affect solidification behavior as all samples follow the same morphological features during solidification, the only variable being the depth of the re-solidified layer.

Nanogrinding Experiments

To characterize the differences between conventional abrasives, sol-gel abrasives, monocrystalline alumina abrasives and laser dressed chromium-doped alumina, a series of grinding experiments were conducted in order to confirm results gained in field trials. In order to duplicate the field trials, a series of controlled experiments were conducted under increasing feed rates. The experiments were terminated when a condition of severe burn, chatter, or grinding wheel

breakdown was reached. The initial trial wheels used were: angular white alumina wheel with low temperature bonding system (Wheel specification: 77A60JV); sol-gel and angular white abrasive mixture wheel with low temperature bonding system (Wheel specification: 73A60JV); monocrystalline alumina grinding wheel with a low temperature bonding system (Wheel specification: SA60JV); and laser dressed chromium-doped alumina bonded with a high temperature bonding system. All grinding wheels were manufactured with a vitrified bond, 60 mesh-size abrasive (approximately 220 μm in diameter), J- mechanical grade, and a fairly open structure. Experiments were performed on a Jones and Shipman series 10 cylindrical grinding machine using a 450 mm diameter grinding wheel rotating at 33 m/s surface speed. The mechanically-dressed wheels were dressed using a D25 blade tool supplied by Unicorn-Van Moppes, and the dressing conditions were: 3 passes at 0.15 mm/rev at a depth of 0.03mm plus one pass at 0.015 mm depth at the start of each batch. Stock removal was 0.25 mm on diameter grinding AISI 52100 ball bearing steel (59 HRC) using 2% concentration soluble oil at 0.5 bar pressure and a flow rate of 15 liters/minute. Forty experimental test pieces were ground per experiment. The laser dressed samples were mounted in a modified grinding wheel that holds segments of samples that have been laser dressed. The segmented grinding wheel acts in the same way as a conventional grinding wheel but has the advantages of quick and easy replacement of laser-processed samples. The most important measurements made during the grinding experiments are grinding power, surface roughness of the workpiece, and the wheel wear parameter, grinding ratio, which is the ratio of workpiece machined to the amount of grinding wheel lost during grinding.

10.7.2 Experimental Results and Discussion

Laser Dressing Temperatures

The rapid solidification of the laser dressed samples show that a refined microstructure and reduced segregation of phases is possible. Very high cooling rates are possible over a small region of the workpiece where non-equilibrium structures are produced owing to

rapid solidification of the material. High cooling rates can be achieved using a laser beam that tends to diminish as the laser beam moves along the track. Therefore, the microstructure will change at the edges of the track toward the unaffected part of the grinding wheel. Laser irradiation is considered to be a point source with heat energy flowing radially away from the point. The system is assumed to attain quasi-steady-state conditions when the melt velocity at the melt/solid interface becomes constant [35]. Incident radiation is partly reflected and absorbed by the abrasive material, whilst some absorbed energy is lost by re-radiation and convection and some is conducted into the material. The melt zone is heated from the surface at the center of the track, which established convection currents within the melt pool and transports heat away very quickly from the melt/solid interface (Figure 10.24).

Experimentally determined cooling rates during laser processing for processing at two different power levels (400 W and 500 W) are shown in Table 10.8. The data are calculated from temperature and time data collected using the two-color pyrometer. The data is obtained by curve fitting the time dependent equation for the processing temperature so that cooling rates can be estimated close to the melting point of the abrasive material. Experimental data is provided for two tracks and cooling rates are calculated at the melting temperature of the abrasive material (2045 K), which is assumed to be the maximum cooling rate (Figure 10.25). The cooling rates in samples processed at higher laser power are lower compared to that at lower laser power. This is explained by the fact that the abrasive material is a poor conductor of heat compared to metals. Therefore, an increase in laser beam power will provide a greater input of heat to the material that will provide a larger melt zone and an increase in the interaction volume. Thus, it takes more time to dissipate the heat built-up and causes a drop in cooling rates. Therefore, for high laser power the cooling rate is expected to be lower compared to those calculated for 400 W and 500 W.

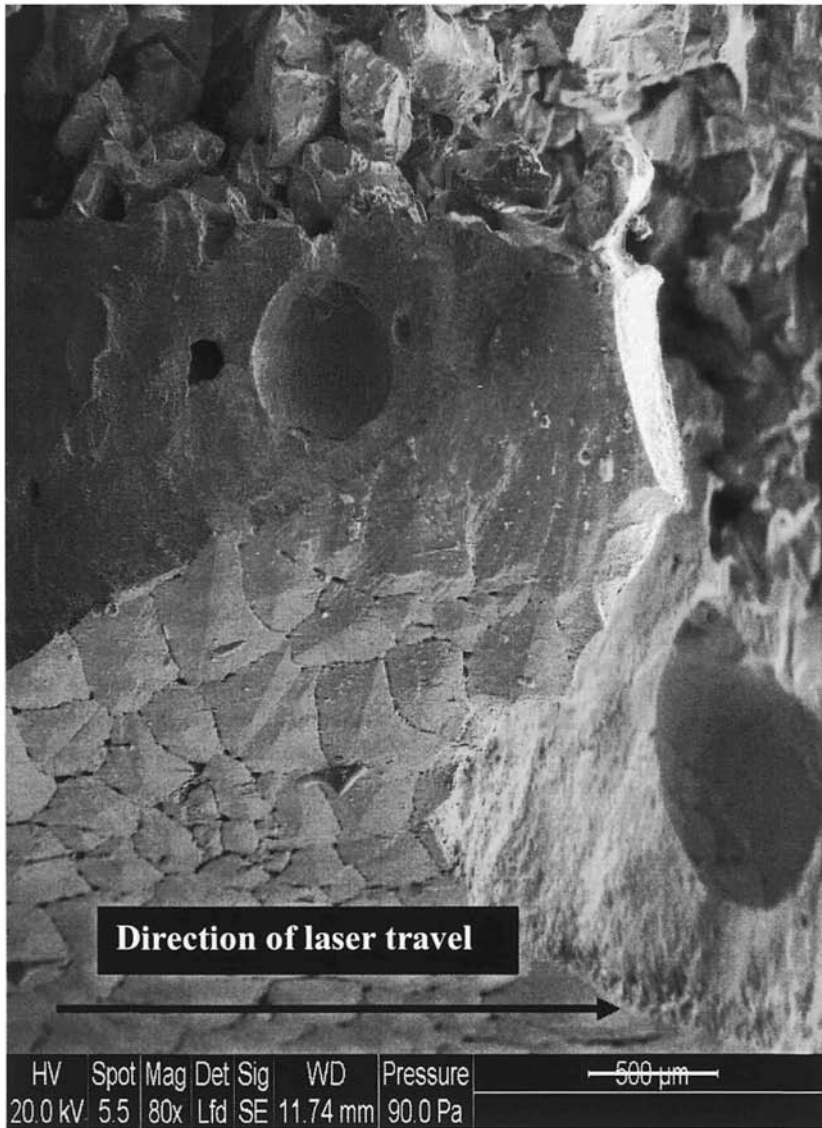


Fig. 10.24. Scanning electron micrograph showing center of laser processed track, resolidified layer, and original structure

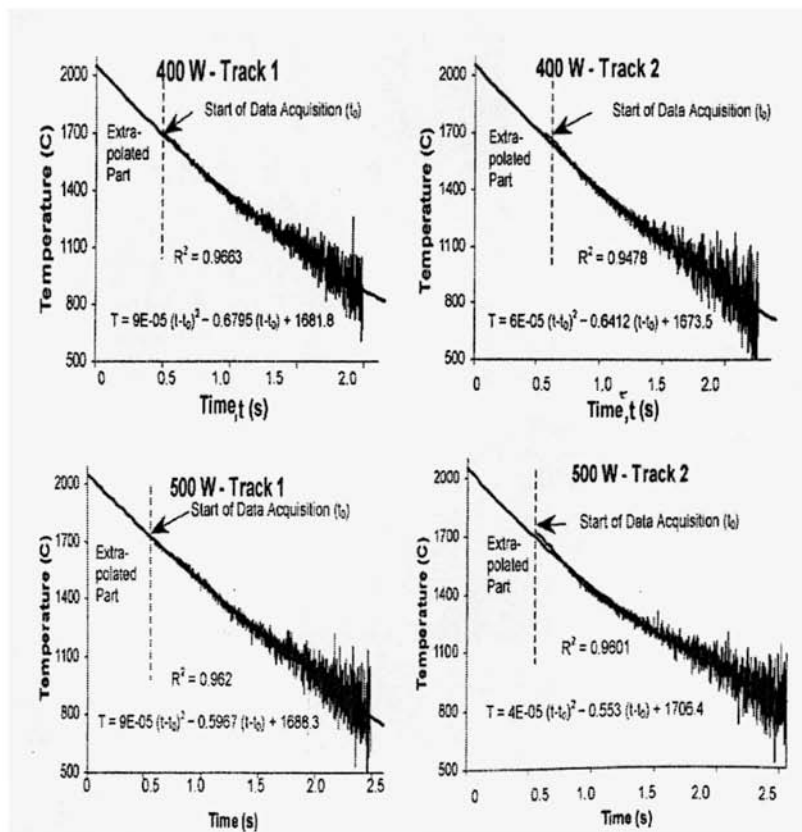


Fig. 10.25. Temperature and time profiles of laser processed tracks

Table 10.8. Cooling rates for laser processed grinding wheel

Laser power (W)	Maximum cooling rates, dT/dt , ($^{\circ}\text{C/s}$), for track 1 at the melting temperature	Cooling rates, dT/dt , ($^{\circ}\text{C/s}$), for track 1 at the start of solidification	Cooling rates, dT/dt , ($^{\circ}\text{C/s}$), for track 1 at the start of solidification	Cooling rates, dT/dt , ($^{\circ}\text{C/s}$), for track 2 at the start of solidification
400	-770.8	-437	-702.8	-382.2
500	-701.5	-401	-580.6	-299.7

The cooling rate in the second track is slightly lower than track 1 for both 400 W and 500 W samples. As the laser passes the over the first track it pre-heats the material adjacent to it that results in a reduced cooling rate for the second track owing to the decrease in the thermal gradient. Table 10.8 shows the cooling rate at 2.2 s after solidification, which corresponds to the temperature of the sample near to the lower calibrated temperature range of the pyrometer. The trend observed shows that the cooling rate is similar to that seen at the solidification temperature, but cooling rates are much lower due to thermal gradients and heat loss from the sample. Solidification occurs in directions that are opposite to the direction of heat extraction. It is also assumed that grain growth is equal in all directions owing to the fact that the directed laser energy is a point source of heat dissipation. Microstructural texture is assumed to form in accordance with the model of heat extraction. A full range of microstructures such as planar, cellular, and dendritic, are observed in laser processed samples [36-37].

A planar solidification front is observed when the interface is at the equilibrium liquidus temperature and when every point at the front of the interface is above the liquidus temperature. Any instability dissolves back in the melt and if it is supercooled, then the perturbation formed on the interface will grow fast into the liquid melt. Under the influence of a positive temperature gradient, constitutional supercooling is solute driven. The type of solidification microstructure formed during constitutional supercooling depends on the G/R ratio, where G is the thermal gradient and R is the solidification rate [36-37]. The solidification structure observed in the laser-processed tracks of the abrasive material changes the surface morphology. Referring to Figure 10.26, grains are multifaceted at the center of the laser track and are equiaxed possessing a dendritic structure. The edges of the tracks show elongated columnar grains that grow away from the point source in a direction normal to the laser beam. The columnar structures are similar to those reported by other authors [38-40] who have conducted laser based processing of alumina ceramics.

The heat transfer equation for a moving heat source is given by the following equation, where the substantial derivative of temperature, i.e., $T = T(y, t)$, and is given a partial derivative [41-44],

$$\frac{d}{dt}[t(y,t)] = \frac{\partial T}{\partial t} + \frac{\partial y}{\partial t} \cdot \frac{\partial T}{\partial y} = D \frac{\partial^2 T}{\partial y^2} + \frac{\dot{q}}{C_p \rho} \quad (10.55)$$

For the time-independent situation, i.e., quasi-steady state heat transfer for a moving boundary problem, the time derivative tends to zero in Equation 10.55. Hence, the surface cooling rate dT/dt in the direction opposite to the laser under the quasi-steady state ($T/t=0$) can be estimated as [43],

$$\frac{dT}{dt} = \frac{dT}{dy} \cdot \frac{dy}{dt} \quad \text{or,} \quad G = \frac{1}{v} \cdot \frac{dT}{dt} \quad (10.56)$$

Where v is the velocity of the laser beam.



Fig. 10.26. SEM image showing equiaxed grains with dendritic structure in the center of the track (A) and columnar growth of grains near the edge of the track (B)

Thus, the thermal gradients (G) are calculated from the temperature and time diagrams assuming quasi-steady state conditions using Eqn. 10.56. During solidification, the velocity of the liquid/solid interface or growth rate, R , is provided by the Neumann solutions to the Stefan problem [44]. Assumptions made include: strong convective currents exist in the melt pool and the total energy absorbed at the free surface of the liquid is transported to the interface by convection. The solution to the Stefan problem is,

$$V_i \rho \Delta H_m - \kappa_s \cdot \frac{\partial T}{\partial y} = V_i \rho [\Delta H_m + C_p (T_m - T_o)] = I_a \quad (10.57)$$

Where V_i is the liquid/solid interface velocity, and y is the distance in the melt pool. This equation gives the average velocity of the interface during the time that the treated zone solidifies. The solidification front velocity at the start of solidification is greater than Eqn. 10.57 estimates. Therefore, at the start of solidification the local temperature gradient is very large and this leads to a maximum interface solidification velocity that is approximated by [45]:

$$V_i^{\max} \approx \zeta \left(\frac{D}{\tau_1} \right)^{0.5} \quad (10.58)$$

Where τ_1 is the dwell time of the laser and ζ is provided by the solution of,

$$\zeta [1 + \operatorname{erf}(\zeta)] \exp(\zeta^2) = \frac{C_p (T_m - T_o)}{\sqrt{\pi} \cdot \Delta H_m} \quad (10.59)$$

It can be shown from Eqn. 10.59 that the average and maximum interface solidification rates are dependent on laser beam intensity and velocity. By using Equations 10.57 and 10.58, the velocity of the solid/liquid interface, or growth rate (R), is calculated at the center of the track. G/R ratios are calculated and are given in Table 10.9. The ratios are high near to the edge of the track where solidification starts and decreases toward the center of the track.

Table 10.9. G/R ratios for laser processing parameters

Track position	G/R ratio for laser power of 400W:	G/R ratio for laser power of 400W:	G/R ratio for laser power of 500W:	G/R ratio for laser power of 500W:
	Track 1	Track 2	Track 1	Track 2
Center	4.43×10^6	4.04×10^6	4.03×10^6	3.34×10^6
Edge ^a	1.74×10^9	1.74×10^9	1.74×10^9	1.74×10^9

^a*G/R ratios are the same for all conditions at the edge of the track because Eqn. 10.58 is used for calculating the growth rate, R, which is independent of G.*

The observed solidification structure varied from equiaxed grains with dendritic structure within the track to columnar grains at the edges of the track. Constitutional supercooling theory predicts that increasing the *G/R* ratio causes a progressive change in solidification structure from fully dendritic to cellular dendritic, then to cellular and then finally to a planar morphology. A similar trend is observed in the laser track. Therefore, the observed microstructure agrees with the predictions made by theory.

Orientation Imaging Microscopy of Laser-Dressed Materials

Figure 10.30 shows the image quality (IQ) micrograph obtained from the OIM. The area selected for analysis is of a cross-section of the re-solidified layer of one of the tracks. IQ represents the sharp character of the EBSD pattern and thus local crystal perfection. Hence, the IQ represents the real microstructure as demonstrated in an optical microscope.

The dark regions of the image are pores where the IQ intensity is zero. Grain boundaries are easily detected, which is in sharp contrast to a scanning electron microscopic image that does not resolve grain boundaries at that particular magnification. The growth direction is radial from the surface of the center of the track where the beam is focused. Figure 10.28 shows the inverse pole figure (IPF) map of the area shown in Figure 10.27.



Fig. 10.27. Image quality cross section of the laser processed track showing the re-solidified region laser dressed at 1000 W using OIM

The grains are color-coded that represents the crystallographic orientation of the normal surface. The key used for color-coding is provided in the stereographic triangle at the base of the figure. The orientation of some of the grains are in the form of the hexagonal cell for α -alumina. It is observed from the figure that growth takes place along the c-axis in the hexagonal α -alumina lattice during solidification of the molten abrasive bonding material. Grains numbered 1-4 possess an orientation that extends radially away from the center of the track as shown by the heat extraction model.

These grains lie within the re-solidified layer, whilst the outer grains lie parallel to the surface of the track. There are smaller grains that have their c-axes oriented differently than other smaller grains and not along the direction radially outward from the center of the laser-processed track.

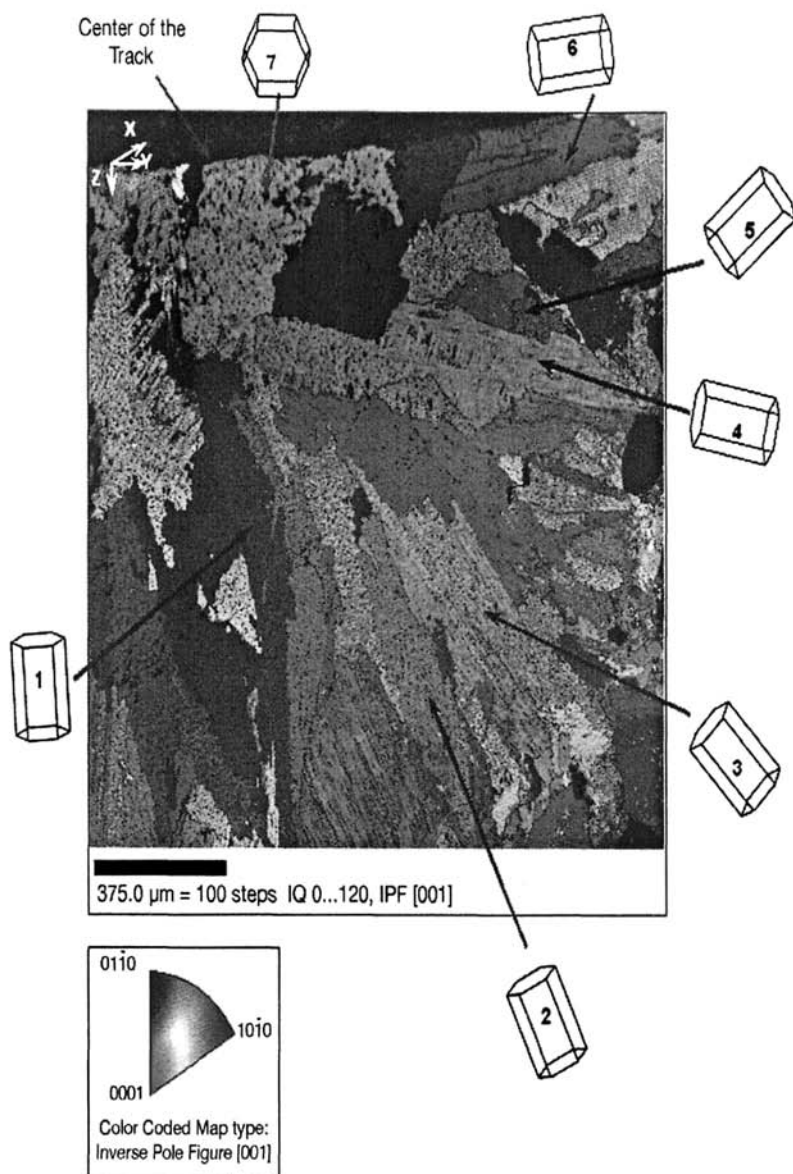


Fig. 10.28. Inverse pole figure (IPF) color-coded map of the resolidified region shown in Fig. 10.27 generated using a laser power level of 1000 W

These grains do not grow in size compared to other grains. Thus, a competitive growth mechanism is observed in which the growth is very fast for grains whose c-axis is parallel to the growth direction, and very slow for all other grains. Pole figure analysis and XRD during previous studies [18,19] indicated that a preferred orientation occurs on the (110) plane, as shown in Figure 10.29.

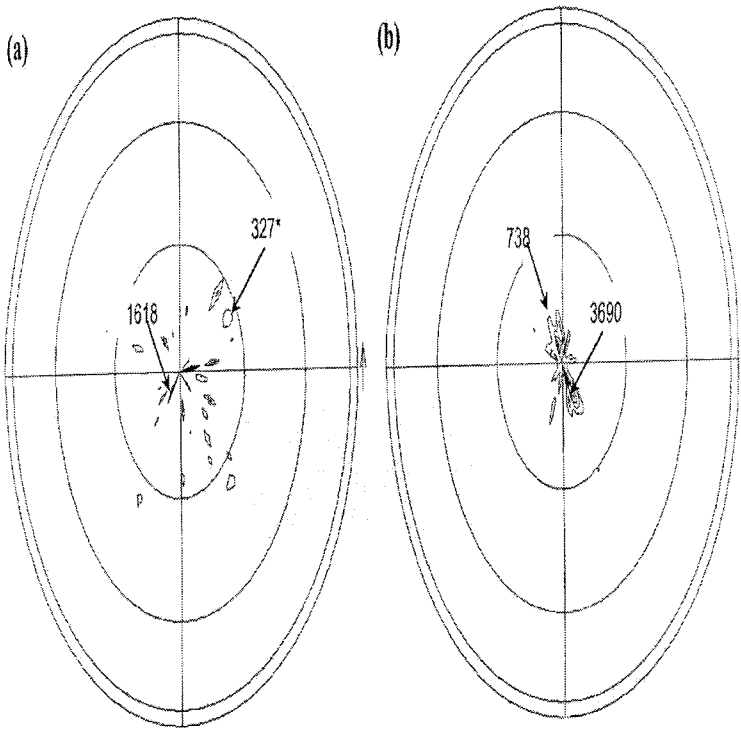


Fig. 10.29. Pole figure for (110) plane in (a) undressed sample and, (b) laser dressed sample (1000 W). Note : *Denotes intensity

The (110) planes are prismatic planes that are parallel to the c-axis in the hexagonal α -alumina cell. OIM maps suggest that growth takes place along the c-axis direction, which tends to favor (110) planes.

Nanogrinding Experiments

Figures 10.30-10.32 show the grinding results of mechanically-dressed and laser-dressed grinding wheels. None of the grinding wheels tested produced chatter or burn when grinding the experimental test pieces. Each experiment was terminated as a result of wheel breakdown, which showed itself as changes in grinding power, such as a rapid decrease in power or in the form of erratic fluctuations in power. At the lowest feed rate of 0.015 mm/s, all wheels gave a similar performance regarding power level, surface finish, and grinding ratio. At the intermediate feed rate of 0.02 mm/s, it was possible to differentiate between all three grinding wheels. The sol-gel abrasive wheel gave the best surface roughness and the highest grinding ratio (G-ratio) while the angular white alumina wheel gave the worst performance. At a feed rate of 0.03 mm/s, the white alumina (77A) wheel ground between 20 and 25 components satisfactorily and then the power became erratic and the surface roughness deteriorated, indicating wheel breakdown. The monocrystalline alumina wheel ground around 30 test pieces before surface roughness deteriorated, although grinding power showed a slight fluctuation. The sol-gel abrasive wheel showed no sign of breakdown. Subsequent tests were conducted up to 0.08 mm/s. However, only the sol-gel wheel could grind twenty test pieces after which it slowly broke down. In conclusion, although the sol-gel wheel operates at a higher power level, it is capable of working at much higher stock removal rates than either the white alumina or monocrystalline alumina grinding wheels. At moderately high stock removal rates, white alumina and monocrystalline alumina abrasives can remove metal at the same rate, but the monocrystalline alumina wheel tends to give a better surface finish and works longer before it requires dressing. At low stock removal rates there is no significant difference between sol-gel, angular white alumina, and monocrystalline alumina grinding wheels.

The effects of dressing conditions show interesting results in that laser-dressed grinding wheels require less grinding power at increasing feed rates (Figure 10.30). This implies that laser-dressed wheels are breaking down at a faster rate than mechanically-dressed grinding wheels as the feed rate increases, which is confirmed by the

reduction in grinding ratio as shown in Figure 10.32. However, even though more of the grinding wheel is lost through grinding, a significant improvement in surface roughness is gained at the expense of wheel loss.

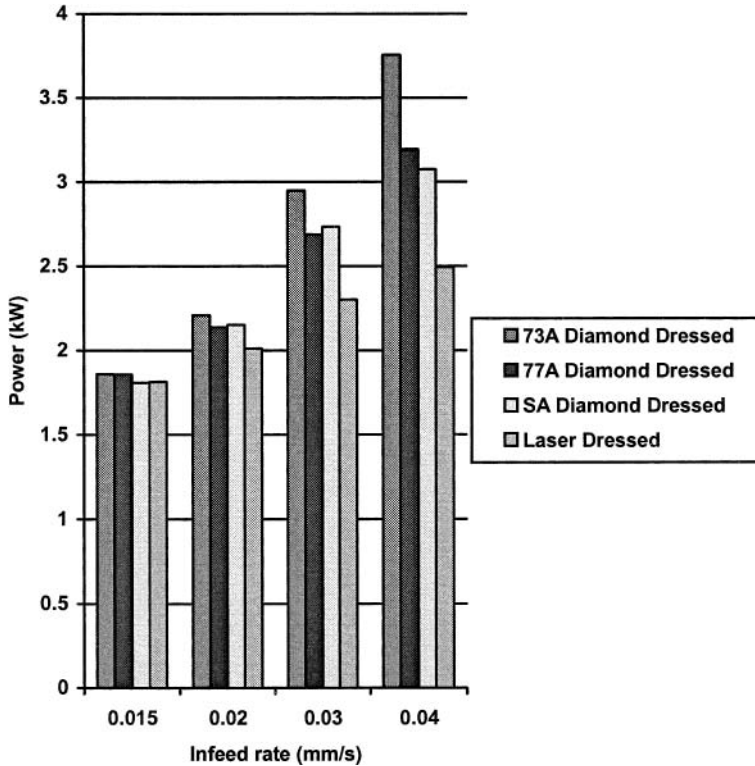


Fig. 10.30. Grinding power as function of feed rate for vitrified corundum grinding wheels with different types of abrasive and dressing conditions

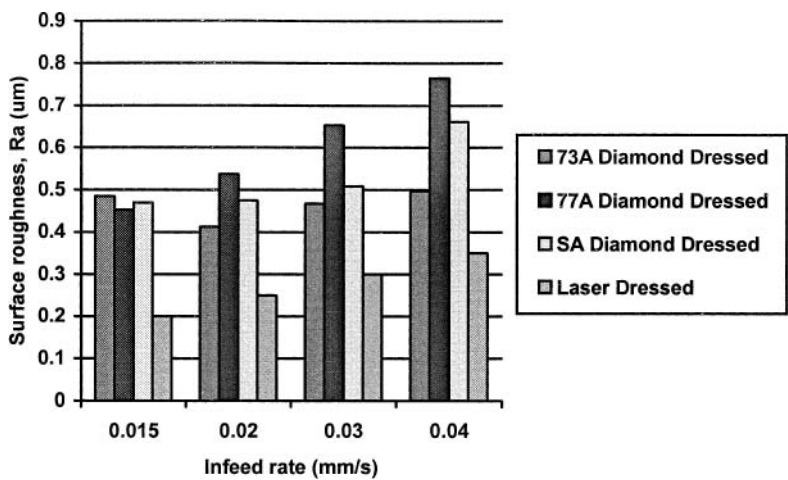


Fig. 10.31. Surface roughness as a function of feed rate for vitrified corundum grinding wheels with different types of abrasive and dressing conditions

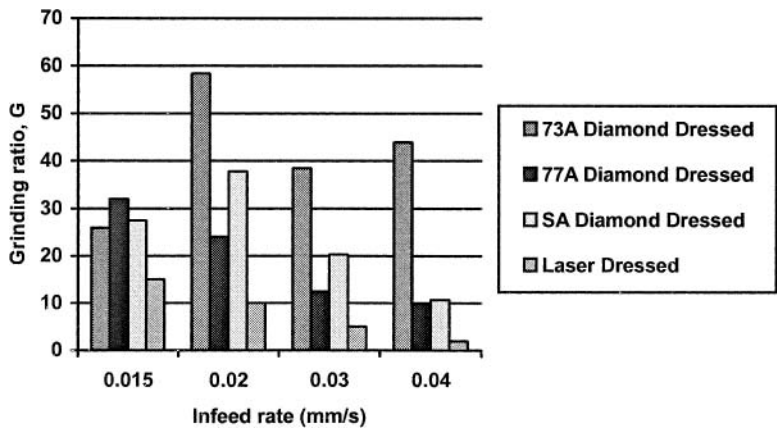


Fig. 10.32. Grinding ratio as a function of feed rate for vitrified corundum grinding wheels with different types of abrasive and dressing conditions

Figures 10.30 and 10.32 show that laser-dressed grinding wheels possess a free-cutting ability compared to the mechanically-dressed grinding wheels, but in contrast to those wheels they are able to provide a finer surface roughness to the workpiece due to the predominance of oriented vertices of α -alumina created by laser dressing that remove very small amounts of workpiece material. This process is known as “nanogrinding”.

10.8 Future Directions

For perfectly sharp diamond coated piezoelectric ceramic materials, grain fracture appears to be the dominant cause of abrasive material loss during a grinding operation. Grain fracture is much more likely to be caused by mechanically induced tensile stresses within abrasive grains than by mechanically induced compressive stresses. The best indicator of diamond grain performance during a nanogrinding operation under different operating conditions is the level of tensile stress established in abrasive grains. High tensile stresses are associated with grain fracture and low grinding ratios in perfectly sharp diamond-coated piezoelectric ceramic materials. Finite element models of perfectly sharp grinding grains can be applied to the piezoelectric nanogrinding process where the dominant wear mechanism is grain fracture. Piezoelectric nanogrinding is a process that has demonstrated its capability of being developed into a nanomanufacturing process of the future. The dissolution model derived by Jackson and Mills has been compared with experimental data using sintering and fusible vitrified bonding systems that are used extensively with high performance nanogrinding tools. The results predicted by the model compare well with the experimental results presented in this chapter. However, over longer periods of isothermal vitrification, the model becomes less accurate due to the assumptions made in the dissolution model. The model may be of use when predicting the mass fraction of quartz using high temperature firing cycles that are characterized by short soaking periods. The development of porous nanogrinding tools lies in their ability to be dressed using a directed photon beam that sharpens worn grains or promotes the formation of textured peaks from the vitreous bond-

ing system. The development of quartz-free bonding systems that has high corundum content is of paramount importance if porous nanogrinding tools are to be effective when machining engineering materials at the nanoscale. Cooling rates of the order of approximately 100°C/s are observed during laser dressing of vitrified corundum grinding wheels. High laser power tends to generate slower cooling rates because of the thermal properties of these complex ceramic materials. The observed solidification structures tend to be dendritic at the center of the laser-processed track, and columnar near to the edges of the track. OIM analyses of the laser processed tracks showed a preferred growth of grains along the c-axis and in a direction opposing heat flow. In association with XRD and pole figure analysis, preferred orientation favors growth on the (110) planes that are parallel to the c-axis in the hexagonal alumina cell. Competitive growth of grains takes place in the re-solidified layer during which time the grains with their c-axes not orientated from the center of the track are prevented from growing in their favored directions. Grinding experiments suggest that laser-dressed grinding wheels cut freely but produce lower surface roughness on AISI 52100 workpiece material owing to the predominance of oriented vertices of α -alumina that remove very small amounts of material even at increasing rates of feed.

10.9 Problems

1. Explain the process of piezoelectric nanogrinding.
2. How are stresses induced in diamond grains?
3. Derive the equations to predict radial stresses in nanogrinding grains.
4. Explain the nanogrinding procedure.
5. How are porous nanogrinding tools manufactured?
6. What is the effect of quartz in grinding tool bonds?
7. Explain how quartz is reduced in grinding tool bonding systems.
8. How are lasers used to shape vitrified grinding tools?
9. What is effect of focusing laser beams on the surface of a grinding wheel?
10. How does the laser beam change the texture and orientation of grains on the surface of the grinding wheel?

References

1. Zhao Q, Dong S, and Sun T (2001) Research on diamond tip wear mechanism in atomic force microscope-based micro-and nanomachining, *High Technology Letters*, **7**, (3), 84-89.
2. Ahao QL, Dong S, and Sun T (2001) Investigation of an atomic force microscope diamond tip wear in micro-and nanomachining, *Key Engineering Materials*, **202-203**, 315-350.
3. Jackson M J (2001) Vitrification heat treatment during the manufacture of corundum grinding wheels, *Journal of Manufacturing Processes*, **3**, 17-28.
4. Timoshenko SP, and Goodier JN (1970) *Theory of Elasticity*, 3rd Edition – International Student Edition, McGraw-Hill Kogakusha Ltd., p.p. 109-113, and p.p. 139-144.
5. Loladze TN (1967) Requirements of tool materials, *Proceedings of the 8th International Machine Tool Design and Research Conference*, Pergamon Press, 821-842.
6. Lundin ST, *Studies on Triaxial Whiteware Bodies*, (Almqvist and Wiksell, Stockholm, Sweden, 1959.
7. Storch W, Ruf H, and Scholze H, *Berichte Deut. Keram. Ges.*, 1984, **61**, 325.
8. Binns E, *Science of Ceramics*, 1962, **1**, 315.
9. Ford WF, and White J, *Trans. J. Brit. Ceram. Soc.*, 1951, **50**, 461.
10. Kirchoff G, Pompe W, and Bahr HA, *J. Mat. Sci.*, 1982, **17**, 2809.
11. Jackson MJ, and Mills B, *Dissolution of Quartz in Vitrified Ceramic Materials*, *J. Mat. Sci.*, 1997, **32**, 5295 - 5304.
12. Alexander IE, and Klug HP, *X-ray diffraction procedures*, *Anal. Chem.*, 1948, **20**, 886.
13. Khandelwal SK, and Cook RL, *Effect of alumina additions on crystalline constituents and fired properties of electrical porcelain*, *Amer. Ceram. Soc. Bull.*, 1970, **49**, 522 - 526.
14. Jander W, *Reaktion im festen zustande bei hoheren temperaturen (Reactions in solids at high temperature)*, *Z. Anorg. U. Allgem. Chem.*, 1927, **163**, 1-30.
15. Krause P, and Keetman E, *Zur kenntnis der keramischen brennvorgange (On combustion processes in ceramics)*, *Sprechsaal*, 1936, **69**, 45-47.
16. Monshi A, *Investigation into the strength of whiteware bodies*, Ph. D. Thesis, University of Sheffield, United Kingdom, 1990.
17. Jackson MJ, *A study of vitreous-bonded abrasive materials*, Ph. D. Thesis, Liverpool John Moores University, United Kingdom, December 1995.
18. M. J. Jackson, G. M. Robinson, N. Dahotre, A. Khangar, and R. Moss, *Laser Dressing of Vitrified Aluminium Oxide Grinding Wheels*, *British Ceramic Transactions*, 2003, **102**, 237-245.
19. A. Khangar and N. Dahotre, *Morphological Modification in Laser-Dressed Grinding Wheel Material For Microscale Grinding*, *Journal of Materials Processing Technology*, 2005, **170**, 1-10.

20. A. Khangar, N. B. Dahotre, M. J. Jackson, G. M. Robinson, Laser Dressing of Alumina Grinding Wheels, Proceedings of the International Surface Engineering Congress and Exposition, 2003, ASM International, p.p. 423-426.
21. D. J. Dingley and V. Randle, *J. Mat. Sci.*, 1992, **27**, 4585.
23. D. Triantafyllidis, L. Li, F. H. Stott, Surface Treatment of Alumina-based Ceramic Using Combined Laser Sources, *Appl. Surf. Sci.*, 2002, **186**, 140-144.
24. J. Lawrence, L. Li, J. T. Spencer, The Effects of High Power Laser Diode Laser Radiation on the Wettability, Adhesion, and Bonding Characteristics of an Alumina-Silica Based Oxide and Vitreous Enamel, *Surface and Coatings Technology*, 1999, **115**, 273-281.
25. Y. Yuanzheng, Z. Youlan, L. Zhengyi, C. Yuzhi, Laser Remelting of Plasma Sprayed Alumina Ceramic Coatings and Subsequent Wear Resistance, *Mater. Sci. and Engg.*, 2000, **A291**, 168-172.
26. L. Bradley, L. Li, F. H. Stott, Flame Assisted Laser Surface Treatment of Refractory Materials for Crack Free Densification, *Mater. Sci. and Engg.*, 2000, **A278**, 204-212.
27. W. Kurz, R. Trivedi, *Trans. ASME*, 1992, **114**, 450.
28. A. Kar, J. Mazumdar, *J. Appl. Phys.*, 1987, **61**, 2645.
29. M. Rappaz, S. David, J. M. Vitek, L. A. Boatner, *Metall. Trans. A*, 1989, **20A**, 1125.
30. D. J. Dingley, D.P. Field, *Mater. Sci. and Technology*, 1996, **12**, 1-9.
31. D. P. Field, *Ultramicroscopy*, 1997, **67**, 1-9.
32. B. K. Kim, J. A. Szpunar, *Scripta. Met.*, 2001, **44**, 2605.
33. J. Farrer, J. Michael, C. Carter, in *Electron Backscatter Diffraction in Materials Science*, Kluwer Academic Publishers, New York, 2000, p.299.
34. K. Z. Baba-Kishi, *J. Mater. Sci.*, 2002, **37**, 1715.
35. J. Mazumdar, W. M. Steen, *J. Appl. Phys.*, 1980, **51**, 941-947.
36. M. C. Fleming, *Solidification Processing*, McGraw-Hill, New York, 1974.
37. O. Esquivel, J. Mazumdar, M. Bass, S. M. Copeley, Microstructural Formation According to the Theory of Constitutional Supercooling, in *Rapid Solidification Processing, Processing and Technologies II*, Claitors, Baton Rouge, 1980, p.p. 150-173.
38. L. Bradley, L. Li, F. Stott, *Appl. Surf. Sci.*, 1998, **138-139**, 522-528.
39. S. Z. Lee, K. H. Ghar, *Mat. Wiss. Werkstofftech.*, 1992, **23**, 117-123.
40. J. Shieh, S. Wu, *Appl. Phys. Lett.*, 1991, **59**, 1512-1514.
41. D. Rosenthal, *Welding J. Supplement*, 1941, **20**, 220-234.
42. D. Rosenthal, *Trans. ASME*, 1946, **68**, 849.
43. H. Carslaw and J. C. Jaeger, *Conduction of Heat in Solids*, Clarendon Press, Oxford, 1962.
44. S. Kou, R. Mehrabian, in *Modelling of Casting and Welding Processes III*, The Metals and Minerals Society, TMS, Warrendale, PA, 1986.
45. D. Bauerle, *Laser Processing and Chemistry*, 3rd Edition, Springer-Verlag, Berlin, Germany, 2000, p.p. 168-176.

11. Nanomachining

11.1 Introduction

Nanotechnology is the creation and utilization of materials, structures, devices, and systems through the control of matters on the nanometer length scale. The essence of nanotechnology is the ability to work at these levels to generate large structures with fundamentally new molecular organization [1]. It is widely predicted that the nanotechnology area will lead to the next technological revolution [2]. Global investment in this area has been growing annually during the last decade and in the last few years not only from programs funded by research councils (EU 6th Framework Program, NSF nanomanufacturing program) and government bodies, but also from Venture Capitalists [3]. Although certain applications of nanotechnology, such as Giant Magnetoresistance (GMR) structures for computer hard disk read head and polymer displays have entered the marketplace, in general nanotechnology is still at a very early stage [4]. The barriers between nanotechnology and the marketplace lie in how to cut down the fabrication cost and how to integrate nanoscale assemblies with functional microscale and macro devices. Therefore, reliable mass production of nanostructures is currently one of the most crucial issues in nanotechnology. The commercialization of nanotechnology has to address the underlying necessities of predictability, repeatability, producibility and productivity in manufacturing at nanometer scale.

In this chapter nanometric machining refers only to the “top down” nanofabrication approach. To the author’s knowledge the concept of nanometric machining is more concerned with the precision rather than the characteristic size of the product. So nanometric machining is defined as the material removal process in which the dimensional accuracy of a product can be achieved is 100 nm or better, even towards 1 nm level. Nanometric machining can be classified into four categories:

- **Deterministic mechanical nanometric machining.** This method is to utilize fixed and controlled tools, which can specify the profiles of three-dimensional components by a well-defined tool surface and path. The method can remove materials in amounts as small as tens of nanometers. It includes typically diamond turning, micro milling and nano/micro grinding, etc.
- **Loose abrasive nanometric machining.** This method uses loose abrasive grits to removal a small amount materials. It consists of polishing, lapping and honing, etc.
- **Non-mechanical nanometric machining.** It comprises focused ion beam machining, micro-EDM, and excimer laser machining.
- **Lithographic method.** It employs masks to specify the shape of the product. Two-dimensional shapes are the main outcome; severe limitations occur when three-dimensional products are attempted [5]. It mainly includes X-ray lithography, LIGA, electron beam lithography.

The authors believe that the mechanical nanometric machining has more advantages than other methods since it is capable of machining complex 3D components in a more controllable and deterministic way. The machining of complex surface geometries is just one of the future trends in nanometric machining, which is driven by the integration of multiple functions in one product. For instance, the method can be used to machine micro molds/dies with complex geometric features and high dimensional and form accuracy, and even nanometric surface features. The method is indispensable to manufacturing complex micro and miniature structures, components and products in a variety of engineering materials. This chapter focuses on nanometric cutting theory, methods and its implementation and application perspectives.

11.2 Nanometric Machining

Single-point diamond turning and ultraprecision grinding are two major nanometric machining approaches. They are both capable of producing extremely fine cuts. Single-point diamond turning has

been widely used to machine nonferrous metals such as aluminum and copper. An undeformed chip thickness about 1 nm is observed in diamond turning of electroplated copper [6]. Diamond grinding is an important process for the machining of brittle materials such as glasses and ceramics to achieve nanometer levels of tolerances and surface finish. A repeatable optical quality surface roughness (surface finish < 10 nm Ra) has been obtained in nanogrinding of hard steel by Stephenson et al. using 76 μm grit CBN wheel on the ultra-precision grinding machine tool, the Tetraform C [7]. Recently, diamond fly-cutting and diamond milling have been developed for machining non-rotational non-symmetric geometrics, which has enlarged the product spectrum of nanometric machining [8]. In addition the utilization of ultra-fine grain hard metal tools and diamond coated micro tools represents a promising alternative for microcutting of even hardened steel [9].

Early envisaged applications of nanometric machining are in the mass production of some high precision parts for microproducts or microsystems. In fact, microproducts or microsystems will be the first path that enables nanoproducts to enter the marketplace since microproducts, or microsystems, have been dominating nanotechnology application markets worldwide. Figure 11.1 illustrates the promising application area of microproducts and microsystems [10]. It also anticipates that microproducts will have more and more requirements around the world. It is very interesting to see that the IT peripheral market is still the biggest market of microproducts. In 2005, the total turnover of microproducts is reached US \$38 billion, which is two times that of the total turnover in 2000. Nanometric machining can be applied in bulk machining of silicon, aluminum substrates for computer memory disks, etc. In other areas such as biomedical, automotive, household and telecommunication the total turnovers of microproducts are still steadily growing. Nanometric machining is also very promising in the production of sensors, accelerometer, actuators, micro-mirror, fiber optics connectors, and micro-displays. In fact applications of nanoproducts will enhance the performance of microproducts in the form of sensitivity, selectivity, and stability [11].

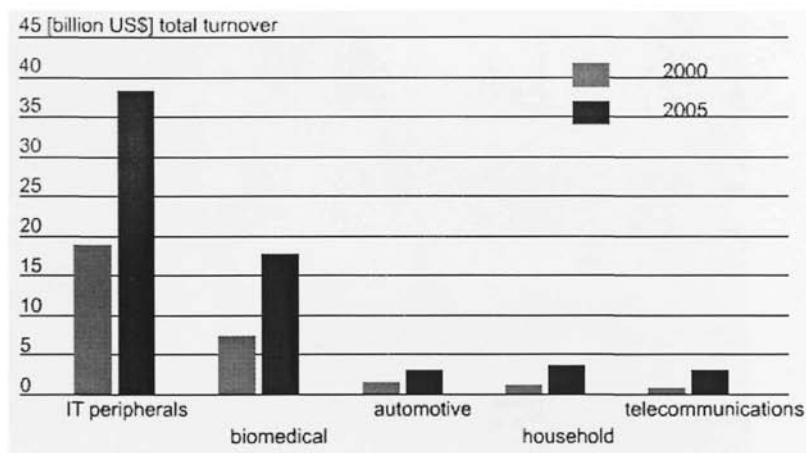


Fig. 11.1 Application market of microproducts and microsystems [10]

Although by 2006, IT is expected to lose this predominant position owing to new MEMS-based applications in sectors such as Biotechnology and Communication (optical and radio frequency switching for example will become a major growth area) [12]. Nanometric machining still has priority in this application area. The microproducts are normally integrated products of some electronics, mechanical parts and optical parts while in miniature or micro dimensions. In fact only small number of microproducts solely relies on electronics. The mechanical and optical parts are of significant importance for microproducts. Figure 11.2 obviously shows that the turnovers of mechanical and optical parts are dominant in the total turnover of microproducts. It provides confidence that the market figure of nanometric cutting technology, even taking account of unforeseen future applications in microproducts, will be high. The indispensable advantage of nanometric machining is its applicability to manufacture 3D complex components/devices including micro moulds, dies and embossing tooling for cheap mass production of optical and mechanical parts. Therefore, it is undoubtedly one of major enabling technologies for commercialization of nanotechnology in the future.

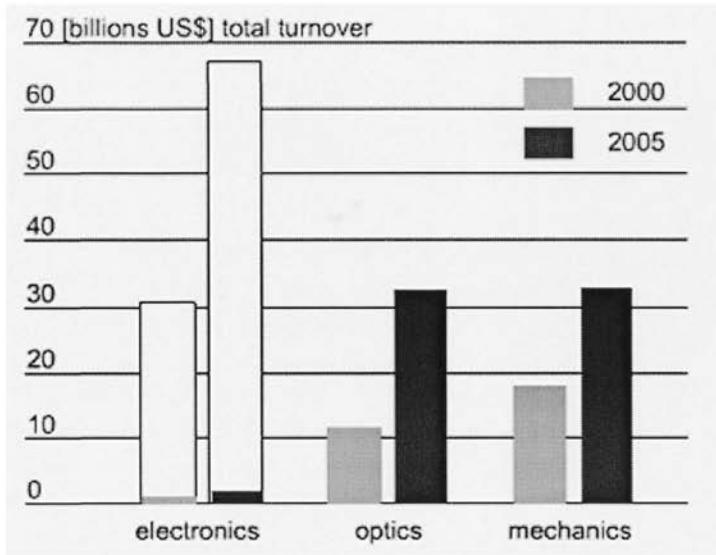


Fig. 11.2 Application market of microproducts by disciplines [10]

11.3 Theoretical Basis of Nanomachining

Scientific study of nanometric machining has been undertaken since late 1990s. Much attention to the study has been paid especially with the advance of nanotechnology [13]. The scientific study will result in the formation of the theoretical basis of nanometric machining, which enables the better understanding of nanometric machining physics and the development of its controllable techniques to meet the advanced requirements for nanotechnology and nanoscience.

11.3.1 Cutting Force and Energy

In nanomanufacturing, the cutting force and cutting energy are important issues. They are important physical parameters for understanding cutting phenomena as they clearly reflect the chip removal

process. From the aspect of atomic structures cutting forces are the superposition of the interactions forces between workpiece atoms and cutting tool atoms. Specific energy is an intensive quantity that characterizes the cutting resistance offered by a material [14]. Ikawa et al., and Luo et al. have acquired the cutting forces and cutting energy by Molecular Dynamics simulations [13-16]. Moriwaki and Lucca have carried out experiments to measure the cutting forces in nanometric machining [13]. Figure 11.3 shows the simulation and experimental results in nanometric cutting. Figure 11.3(a) illustrates the linear relation exists between the cutting forces per width and depth of uncut in both simulations and experiments. The cutting forces per width increase with the increment of the depth of cut.

The difference in the cutting force between the simulations and the experiments is caused by the different cutting edge radii applied in the simulations. In nanometric machining the cutting edge radius plays an important role since the depth of cut is similar in scale. Under the same depth of cut higher cutting forces are needed for a tool with a large cutting edge radius compared with a tool with a small cutting edge radius. The low cutting force per width is obviously the result of fine cutting conditions, which will decrease the vibration of the cutting system and thus improve the machining stability and will also result in better surface roughness.

A linear relationship between the specific energy and the depth of cut can also be observed in Fig. 11.3(b). The figure shows that the specific energy increases with a decreasing of depth of cut, because the effective rake angle is different under different depths of cut. In small depths of cut the effective rake angle will increase with the decreasing of depth of cut. Large rake angle results in the increasing of specific energy. This phenomenon is often called the “size effect”, which can be clearly explained by material data listed in Table 11.1. According to Table 11.1, in nanometric machining only point defects exist in the machining zone in a crystal, so it will need more energy to initiate the atomic-crack or atomic-dislocation. The decreasing of depth of cut will decrease the chance for the cutting tool to meet point defects and result in the increasing of the specific cutting energy.

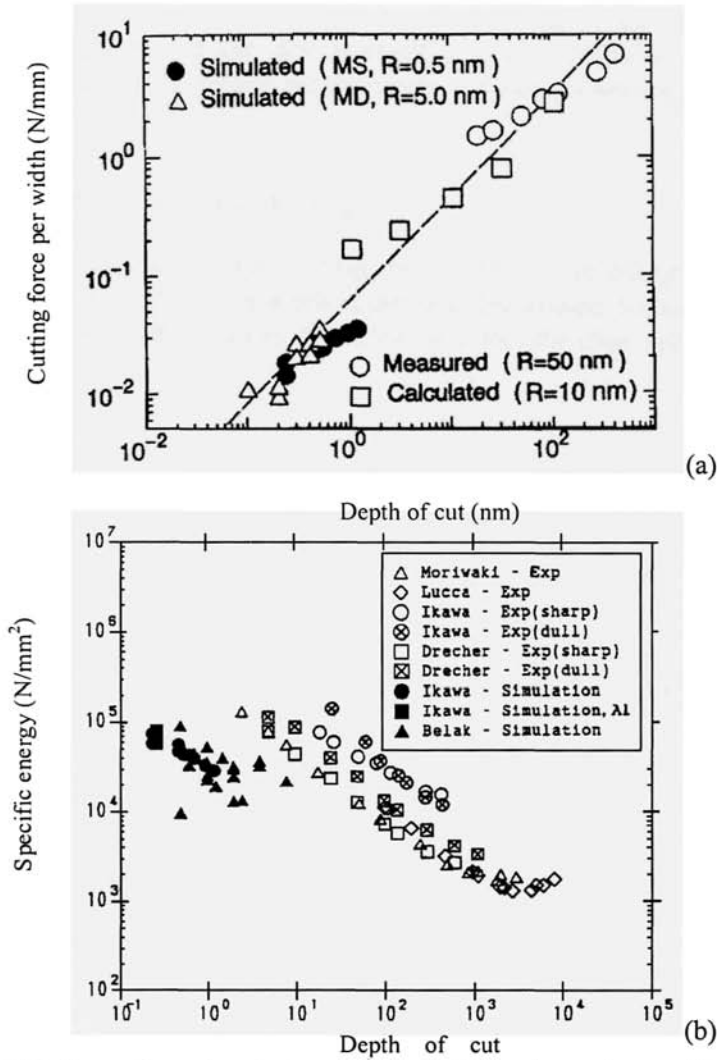


Fig. 11.3 Comparison of results between simulations and experiments: (a) cutting force per width against depth of cut; (b) specific energy against depth of cut [13]

Table 11.1 Material properties under different machining units [17]

		1nm – 0.1 μm	0.1 μm – 10 μm	10 μm – 1 mm
Defects/Impurities		Point defect	Dislocation/crack	Crack/grain boundary
Chip removal unit		Atomic cluster	Sub-crystal	Multi-crystals
Brittle fracture limit		10^4 J/m^3	10^3 J/m^3	10^2 J/m^3
		10^3 J/m^3	10^2 J/m^3	10^1 J/m^3
		Atomic-crack	Micro-crack	Brittle crack
Shear failure limit		10^4 J/m^3	10^3 J/m^3	10^2 J/m^3
		10^3 J/m^3	10^2 J/m^3	10^1 J/m^3
		Atomic-dislocation	Dislocation slip	Shear deformation

If the machining unit is reduced to 1 nm, the workpiece material structure at the machining zone may approach atomic perfection, so more energy will be required to break the atomic bonds. On the other hand when machining unit is higher than 0.1 μm , the machining points will fall into the distribution distances of some defects such as dislocations, cracks, and grain boundaries. The pre-existing defects will ease the deformation of workpiece material and result in a comparatively low specific cutting energy.

Nanometric cutting is also characterized by the high ratio of the normal to the tangential component in the cutting force [14, 16], as the depth of cut is very small in nanometric cutting, and the workpiece is mainly processed by the cutting edge. The compressive interactions will thus become dominant in the deformation of workpiece material, which will therefore result in the increase of friction force at the tool-chip interface and the relative high cutting ratio.

Usually the cutting force in nanometric machining is very difficult to measure due to its small amplitude compared with the noise (mechanical or electronic) [13]. A piezoelectric dynamometer or load cell is used to measure the cutting forces because of their high sensitivity and natural frequency. Figure 11.4 shows an experimental

force measuring system in micromilling process carried out by Dow et al [18]. The three-axis load cell, Kistler 9251, is mounted in a specially designed mount on the y-axis of a Nanoform 600 diamond turning machine. A piece of S-7 steel that has been ground flat on both sides is used as the workpiece and secured through the top of the load cell with a bolt preloaded to 30 N. The tool was moved in the +z direction to set the depth of cut and the workpiece was fed in the +y direction to cut the groove. The milling tool is mounted in a Westwind D1090-01 air bearing turbine spindle capable of speeds up to 60,000 rpm. The spindle is attached to the z-axis of the Nanoform 600. To determine the rotational speed of the tool and the orientation of each flute, an optical detector (Angstrom Resolver) was used to indicate a single rotation of the spindle by reading a tool revolution marker aligned with one flute. The measured 3D cutting forces under depth of cut of 25 μm , feed rate of 18.75 $\mu\text{m}/\text{flute}$, are in the scale of several Newton.

11.3.2 Cutting Temperature

In Molecular Dynamics simulation, the cutting temperature can be calculated under the assumption that cutting energy totally transfers into cutting heat and results in the rising of cutting temperature and kinetic energy of system. The lattice vibration is the major form of thermal motion of atoms. Each atom has three degrees of freedom. According to theorem of equi-partition of energy, the average kinetic energy of the system can be expressed as:

$$\bar{E}_k = \frac{3}{2} N k_B T = \sum_i \frac{1}{2} m (V_i^2) \quad (11.1)$$

Where \bar{E}_k is average kinetic energy in equilibrium state, K_B is Boltzmann's constant. T is temperature, m_i and V_i are the mass and velocity of an atom respectively, and N is the number of atoms.

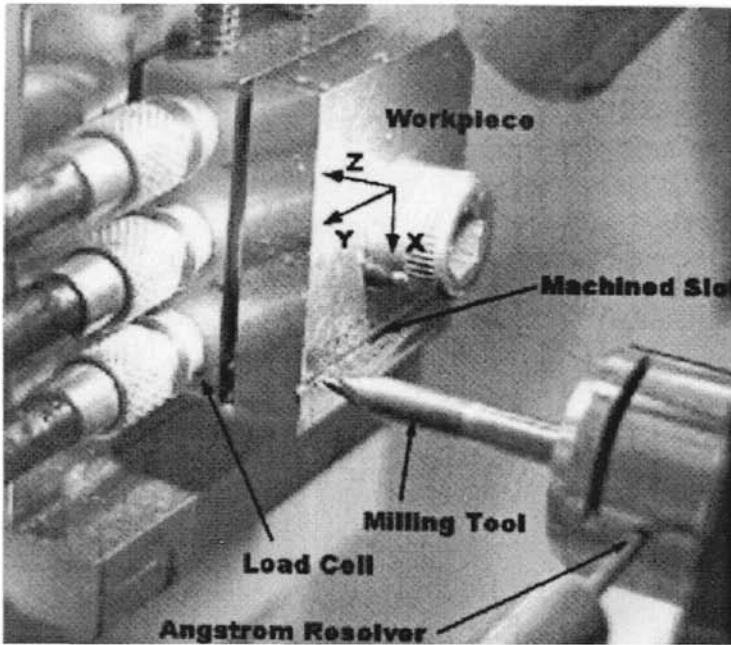


Fig. 11.4 Experimental force measurement system in micro-milling process [18]

The cutting temperature can be deduced as:

$$T = \frac{2 \bar{E}_k}{3 N k_B} \quad (11.2)$$

Figure 11.5 shows the variation of cutting temperature on the cutting tool in a Molecular Dynamics simulation of nanometric cutting of single crystal aluminum. The highest temperature is observed at cutting edge although the temperature at the flank face is also higher than that at the rake face. The temperature distribution suggests that a major heat source exists in the interface between cutting edge and workpiece and the heat is conducted from there to the rest of the cutting zone in workpiece and cutting tool. The reason is that because that most cutting actions take place at the cutting edge of the tool, the dislocation deformations of workpiece materials will

transfer potential energy into the kinetic energy and result in a rise in temperature. The comparative high temperature at the tool flank face is obviously caused by the friction between tool flank face and workpiece. The released energy due to the elastic recovery of the machined surface also contributes to the increment of temperature at tool flank face. Although there is also friction between the tool rake face and the chip, the heat will be taken away from the tool rake face by the removal of the chip.

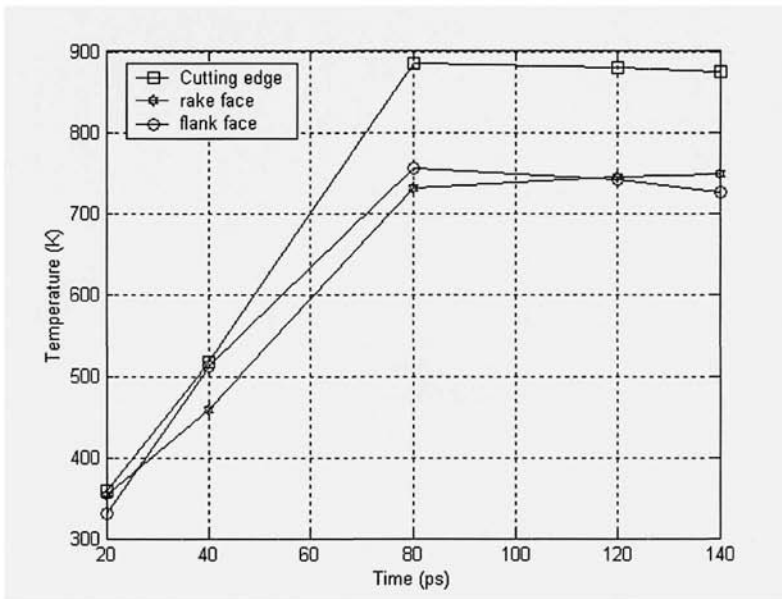


Fig. 11.5 Cutting temperature distribution of cutting tool in nanometric cutting (cutting speed = 20 m/s, depth of cut = 1.5 nm, cutting edge radius = 1.57 nm) [19]

Therefore, the temperature at tool rake face is lower than that at the tool cutting edge and tool flank face. The temperature value shows that the cutting temperature in diamond machining is quite low in comparison with that in conventional cutting, due to low cutting energy as well as the high thermal conductivity of diamond and the workpiece material. The cutting temperature is considered to govern the wear of a diamond tool in a Molecular Dynamics simula-

tion study by Cheng et al [19]. More in-depth experimental and theoretical studies are needed to find out the quantitative relationship between cutting temperature and tool wear although there is considerable evidence of chemical damage on diamond in which temperature plays a significant role [13].

11.3.3 Chip Formation and Surface Generation

Chip formation and surface generation can be simulated by Molecular Dynamics simulation. Figure 11.6 shows an MD simulation of a nanometric cutting process on single crystal aluminum. From Fig. 11.6(a) it is shown that after the initial plow of the cutting edge the workpiece atoms are compressed in the cutting zone near to the rake face and the cutting edge. The disturbed crystal lattices of the workpiece and even the initiation of dislocations can be observed in Fig. 11.6(b). Figure 11.6(c) shows the dislocations have piled up to form a chip. The chip is removed with the unit of an atomic cluster as shown in Fig. 6(d). Lattice disturbed workpiece material is observed on the machined surface.

Based on the visualisation of the nanometric machining process, the mechanism of chip formation and surface generation in nanometric cutting can be explained. Owing to the plowing of the cutting edge, the attractive force between the workpiece atoms and the diamond tool atoms becomes repulsive. Because the cohesion energy of diamond atoms is much larger than that of Al atoms, the lattice of the workpiece is compressed. When the strain energy stored in the compressed lattice exceeds a specific level, the atoms begin to rearrange so as to release the strain energy. When the energy is not sufficient to perform the rearrangement, some dislocation activity is generated. Repulsive forces between compressed atoms in the upper layer and the atoms in the lower layer are increasing, so the upper atoms move along the cutting edge, and at the same time the repulsive forces from the tool atoms cause the resistance for the upward chip flow to press the atoms under the cutting line. With the movement of the cutting edge, some dislocations move upward and disappear from the free surface as they approach the surface.

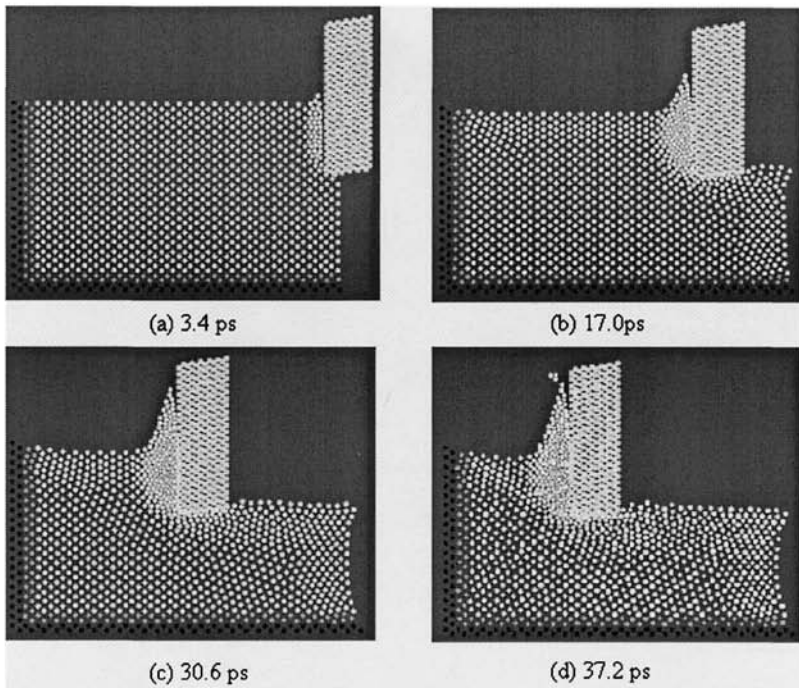


Fig. 11.6. MD simulations of the nanometric machining process (Cutting speed = 20 m/s, depth of cut = 1.4 nm, cutting edge radius = 0.35 nm) [19]

This phenomenon corresponds to the process of the chip formation. As a result of the successive generation and disappearance of dislocations, the chip seems to be removed steadily. After the passing of the tool, the pressure at the flank face is released. The layers of atoms move upwards and result in elastic recovery, so the machined surface is generated. The conclusion can therefore be drawn that the chip removal and machined surface generation are in nature the dislocation slip movement inside the workpiece material crystal grains. In conventional cutting the dislocations are initiated from the existing defects between the crystal grains, which will ease the movement of dislocation and result in smaller specific cutting forces compared with that in nanometric cutting.

The height of the atoms on the surface layer of the machined surface create the surface roughness. For this, 2-D MD simulation R_a

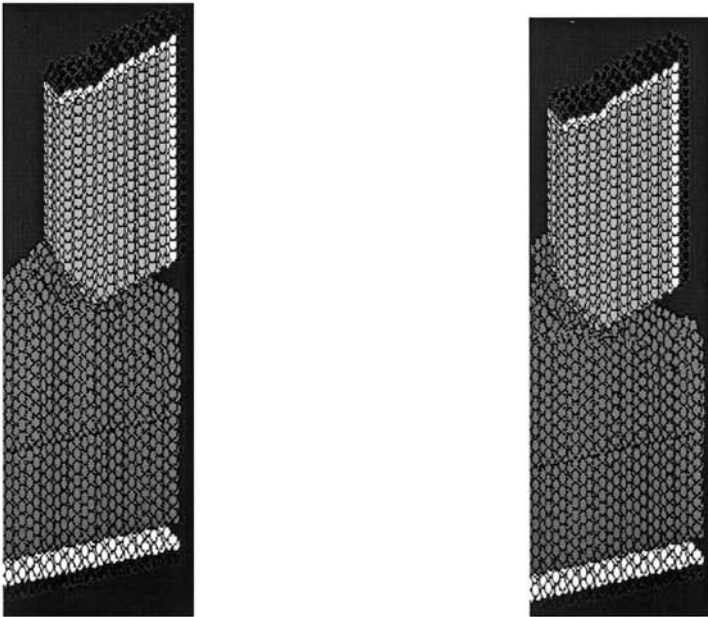
can be used to assess the machined surface roughness. The surface integrity parameters can also be calculated based on the simulation results. For example, the residual stress of the machined surface can be estimated by averaging the forces acting on the atoms in a unit area on the upper layer of the machined surface.

Molecular Dynamics (M.D.) simulation has been proved to be a useful tool for the theoretical study of nanometric machining [20]. At present the MD simulation studies on nanometric machining are limited by the computing memory size and speed of the computer. It is therefore difficult to enlarge the dimension of the current MD model on a personal computer. In fact, the machined surface topography is produced as a result of the copy of the tool profile on a workpiece surface that has a specific motion relative to the tool. The degree of the surface roughness is governed by both the controllability of machine tool motions (or relative motion between tool and workpiece) and the transfer characteristics (or the fidelity) of tool profile to workpiece [13]. A multi-scale analysis model, which can fully model the machine tool and cutting tool motion, environmental effects and the tool-workpiece interactions, is much needed to predict and control the nanometric machining process in a determinative manner.

11.3.4 Minimum Undeformed Chip Thickness

Minimum undeformed chip thickness is an important issue in nanometric machining because it relates with the ultimate machining accuracy. In principle the minimum undeformed chip thickness will be determined by the minimum atomic distance within the workpiece. But in ultra-precision machining practices, it much depends on the sharpness of the diamond cutting tool, the capability of the ultra-precision machine tool and machining environment. The diamond turning experiments of non-ferrous work materials carried out at LLNL show the minimum undeformed chip thickness, down to 1 nm, is attainable with a specially prepared fine diamond cutting tool on a highly reliable ultra-precision machine tool [6]. Based on the tool wear simulation, the minimum undeformed chip thickness is further studied in this chapter. Figure 11.7 illustrates chip formation

of single crystal aluminum with the tool cutting edge radius of 1.57 nm. No chip formation is observed when the undeformed chip thickness is 0.25 nm. But the initial stage of chip formation is apparent when the undeformed chip thickness is at 0.26 nm. In nanometric cutting, as the depth of cut is very small, the chip formation is related to the force conditions on the cutting edge. Generally, chip formation is mainly a function of tangential cutting force.



(a) Undeformed chip thickness = 0.25 nm (b) Undeformed chip thickness = 0.26 nm

Fig. 11.7. Study of minimum undeformed chip thickness by MD simulation [19]

The normal cutting force makes little contribution to the chip formation since it has the tendency to penetrate the atoms of the surface into the bulk of the workpiece. The chip is formed on condition that the tangential cutting force is larger than the normal cutting

force in theory. The relationships between the minimum undeformed chip thickness, cutting edge radius, and cutting forces are studied via MD simulations. The results are highlighted in Table 11.2. The data show that the minimum undeformed chip thickness is about $1/3$ to $1/6$ of the tool cutting edge radius. The chip formation will be initiated when the ratio of tangential cutting force to normal cutting force is larger than 0.92.

11.3.5 Critical Cutting Edge Radius

It is widely accepted that the sharpness of the cutting edge of a diamond cutting tool directly affects the machined surface quality. Previous MD simulations show that the sharper the cutting edge is, the smoother the machined surface becomes. But this conclusion is based on no tool wear. To study the real effects of cutting edge radius, the MD simulations on nanometric cutting of single crystal aluminum are carried out using a tool wear model [20].

In the simulations the cutting edge radius of the diamond cutting tool varies from 1.57 nm to 3.14 nm with depth of cut of 1.5 nm, 2.2 nm and 3.1 nm respectively. The cutting distance is fixed at 6 nm. The root-mean-square deviation of the machined surface and mean stress on the cutting edge are listed in Table 11.3.

Figure 11.8 shows the visualization of the simulated data, which clearly indicates that surface roughness increases with the decreasing cutting edge radius when the cutting edge radius is smaller than 2.31 nm. The tendency is obviously caused by the rapid tool wear when a cutting tool with small cutting edge radius is used. But when the cutting edge is larger than 2.31 nm, the cutting edge is under compressive stress and no tool wear happens. Therefore, it shows the same tendency that the surface roughness increases with decreasing the tool cutting edge radius as in the previous MD simulations.

Table 11.2. Minimum undeformed chip thickness against the tool cutting edge radius and cutting forces [19]

Cutting edge radius (nm)	1.57	1.89	2.31	2.51	2.83	3.14
Minimum undeformed chip thickness (nm)	0.26	0.33	0.42	0.52	0.73	0.97
Ratio of minimum undeformed chip thickness to tool cutting edge radius	0.17	0.175	0.191	0.207	0.258	0.309
Ratio of tangential cutting force to normal cutting force	0.92	0.93	0.92	0.92	0.94	0.93

Table 11.3 The relationship between cutting edge radius and machined surface quality [19]

	Cutting edge radius (nm)	1.57	1.89	2.31	2.51	2.83	3.14
Depth of cut: 1.5 nm	S_q (nm)	0.89	0.92	0.78	0.86	0.98	1.06
Depth of cut: 2.2 nm	S_q (nm)	0.95	0.91	0.77	0.88	0.96	1.07
Depth of cut: 3.1 nm	S_q (nm)	0.97	0.93	0.79	0.87	0.99	1.08
Mean stress at cutting edge (GPa)		0.91	0.92	-0.24	-0.31	-0.38	-0.44

The MD simulation results also illustrate that it is not true that the sharper the cutting edge, the better the machined surface quality. The cutting edge is destined to wear and results in the degradation of the machined surface quality if its radius is smaller than a critical value. But when the cutting edge radius is higher than the critical

value, the compressive stress will take place at the tool edge and the tool condition is more stable. As a result a high quality machined surface can be achieved. Therefore, there is a critical cutting edge radius for stably achieving high-quality machined surfaces. For cutting single crystal aluminum the critical cutting edge radius is at 2.31 nm. The MD simulation approach is applicable for acquiring the critical cutting edge radius for nanometric cutting of other materials.

11.3.6 Properties of Workpiece Materials

In nanometric machining the microstructure of the workpiece material will play an important role in affecting the machining accuracy and machined surface quality. For example, when machining polycrystalline materials, the difference in the elastic coefficients at the grain boundary and interior of the grain causes small steps formed on the cut surface since the respective elastic “rebound” varies [21]. The study by Lee and Chueng shows the shear angle varies with the crystallographic orientation of the materials being cut. This will produce a self-excited vibration between cutting tool and workpiece and result in a local variation of surface roughness of a diamond turned surface [22].

A material’s destructive behavior can also be affected by nanometric machining. In nanometric machining of brittle materials it is possible to produce plastically deformed chips, if the depth of cut is sufficiently small [23]. It has been shown that a “brittle-to-ductile” transition exists when cutting brittle materials at low load and penetration levels [24]. The transition from ductile to brittle fracture has been widely reported and is usually described as the “critical depth of cut” [23], i.e. generally small up to 0.1 to 0.3 μm . They will result in relatively slow material removal rates [23].

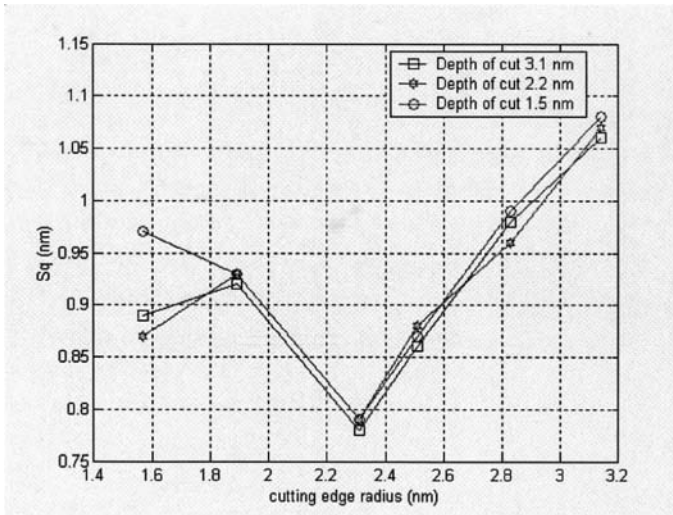


Fig. 11.8. Cutting edge radius against machined surface quality [19]

However, it is a cost-effective technique for producing high quality spherical and non-spherical optical surfaces, with or without the need for lapping and polishing [23].

The workpiece materials should also have a low affinity with the cutting tool material. If bits of the workpiece material are deposited onto the tool, this will cause tool wear and adversely affect the finished surface (surface finish and surface integrity). Therefore, workpiece materials chosen must process an acceptable machinability on which nanometric surface finish can thus be achieved.

Diamond tools are widely used in nanometric machining because of their excellent characteristics. The materials currently turned with diamond tools are listed in Table 11.4. The materials that can be processed via ductile mode grinding with diamond wheels are listed in Table 11.5.

Table 11.4. Current diamond turned materials [23]

Semiconductors	Metals	Plastics
Cadmium telluride	Aluminum and alloys	Acrylic
Gallium arsenide	Copper and alloys	Fluoroplastics
Germanium	Electroless nickel	Nylon
Lithium niobate	Gold	Polycarbonate
Silicon	Magnesium	Polymethylmethacrylate
Zinc selenide	Silver	Propylene
Zinc sulfide	Zinc	Styrene

Table 11.5. Materials that can be processed via ductile mode diamond grinding [23]

Ceramics/intermetallics	Glasses
Aluminium oxide	Titanium aluminide
Nickel aluminide	Titanium carbide
Silicon carbide	Tungsten carbide
Silicon nitride	Zirconia
	BK7 or equivalent
	SF10 or equivalent
	ULE or equivalent
	Zerodur or equivalent

11.3.7 Comparison of Nanometric Machining and Conventional Machining

Table 11.6 summarizes the comparison of nanometric machining and conventional machining in all major aspects of cutting mechanics and physics.

Table 11.6. The comparison of nanometric machining with conventional machining [16]

		Nanometric machining	Conventional machining
Fundamental cutting principles		Discrete molecular mechanics/micromechanics	Continuum elastic/plastic /fracture mechanics
Workpiece material		Heterogeneous (presence of microstructure)	Homogeneous (ideal element)
Cutting physics		Atomic cluster or micro-element model $q_i = \frac{\partial H}{\partial p_i} \quad i=1, 2, \dots, N$ $p_i = -\frac{\partial H}{\partial q_i}$	Shear plane model (continuous points in material)
		First principal stress $\sigma = \frac{1}{S} \sum_{i=1}^{N_s} \sum_{j=1}^{N_s} f_{ij} - \frac{1}{S} \sum_{i=1}^{N_s} \sum_{j=1}^{N_s} f_{0ij}$ (crystal deformation included)	Cauchy stress principle $\tau_s = \frac{F_s}{A}$ (constant)
Cutting force and energy	Energy consideration	Interatomic potential functional $U(r^N) = \sum_i \sum_{<i} u(r_{ij})$	Shear/friction power $P_s = F_s \cdot V_s$ $P_u = F_u \cdot V_c$
	Specific energy	High	Low
	Cutting force	Interatomic forces $F_I = \sum_{j \neq i}^N F_{ij} = \sum_{j \neq i}^N -\frac{du(r_{ij})}{dr_{ij}}$	Plastic deformation/friction $F_c = F(b, d_c, \tau_s, \beta_a, \phi_c, \alpha_r)$
Chip formation	Chip initiation	Inner crystal deformation (point defects or dislocation)	Inter crystal deformation (grain boundary void)
	Deformation and stress	Discontinuous	Continuous
Cutting tool	Cutting edge radius	Significant	Ignored
	Tool wear	Clearance face and Cutting edge	Rake face
Surface generation		Elastic recovery	Transfer of tool profile

The comparison highlighted in the table is by no means comprehensive, but rather provides a starting point for further study on the physics of nanometric machining.

11.4 Implementation of Nanomachining

The key to implementing nanometric machining procedures include highly reliable ultra-precision machine tools, high quality cutting tools, advanced nanometrology techniques, and correctly chosen machining variables.

11.4.1 Ultraprecision Machine Tools

The requirements from micro-engineering and nanotechnology applications, together with demands to minimize production costs, have led to significant developments in the generation of ultra-precision machine tools. A wide range of commercially available ultraprecision diamond turning and grinding machines are developed at Moore Nanotechnology Systems (Nanotech machines), and Precitech (Nanoform series). Some ultraprecision machine tools capable of nanometric tolerances on microcomponents and high precision large components have also been developed in some national labs, universities, and research institutes, for instance, Large Optics Diamond Turning Machine (LODTM) at Lawrence Livermore National Laboratory (LLNL), Cranfield Nanocenter, Tetra Form C ultraprecision grinding machine, and a 3-axis ultra-precision milling machine - UPM 3 at IPT Aachen. More recently the 5-axis machine tools have been developed in order to meet the demand of machining complex parts. Those machines include the high-precision 5-axis CNC machining centers - MICROMASTER MM[®] from Kugler and Robonano from Fanuc. The characteristics of these ultra-precision machine tools can be classified as:

- Machine tool structure with high loop stiffness, high natural frequency, and good damping characteristics
- High thermal and mechanical stability
- Low vibration
- High precision motion of the axis
- High precision control

An ultra-precision machine tool consists of four major sub-systems. They are mechanical structure, spindle and drive system, control and algorithms, and measurement and inspection system. These sub-systems are essential in maintaining the machine performance.

Mechanical Structure

Mechanical structure consists of stationary and moving bodies. The stationary bodies include machine base, column and spindle box housing. They usually carry moving bodies, such as worktables, slide, spindles and carriages.

The structural design is critical since the structure of a machine provides the mechanical support for all of the machine's components. When considered in the context of the design of the machine as a system, some of the major design issues include [25]:

- Stiffness and damping
- Structural configuration
- Structural connectivity

With regard to the proper functioning of moving axes and operational stability the structural design will follow the following principles:

- High structural loop stiffness. The structural loop includes the spindle shaft, the bearing and housing, the slide way and frame, the drives, and the tool and work-holding fixtures. All mechanical components and joints in the propagation path from the drive to the point of reaction, e.g., the end-effector (cutting tool) or the

center of gravity, must have a high stiffness to avoid deformation under changing load [26].

- Good damping property. This can be achieved by choosing high damping capability material as machine bed and slideway materials or filling structure's cavities with lead shot and oil for viscous and mass damping or concrete for mass damping. Some methods, such as shear plate and tuned mass damper, can also be applied to damp structures [25].
- Symmetry and closed loop structural configuration. "T" configuration is popularly used for most of the ultraprecision turning and grinding machines. Recently, a novel tetrahedron structure proposed by NPL in England, has been applied in an ultraprecision grinding machine tool - Tetraform C. It utilizes an internally damped space frame with all the loads carried in closed loop. The design generates a very high static stiffness coupled with exceptional dynamic stiffness [7].
- Minimize thermal and elastic structural loops to decrease the influence of spatial thermal gradients and make the system quickly reach and maintain a stable equilibrium.
- Minimization of heat deformation. Reduction of thermal deformation from the viewpoint of the structural design rather than the remedy by using the control technique. The methods include separating heat sources from the machine, quickly expelling the heat generated within the machine and maintaining the fluid used for heat removal at a constant temperature, using zero or low thermal expansion materials. LODTM developed at LLNL employs several ingenious methods removing the heat-related errors. For instance, the LODTM is enclosed in a container within which the air temperature is maintained at $20 \pm 0.010^{\circ}\text{C}$. The measurement frame is made from Superinvar and covered by a shell in which water maintained at $20 \pm 0.001^{\circ}\text{C}$ is circulated. The housing for the main spindle bearing incorporates a coolant conduct in which temperature controlled water is circulated to remove any heat generated by bearing before it causes excessive deformation. As a result of these measures, the maximum drift due to heat deformation over a 24-hour period is less than 25 nm [25].

- Isolation environmental effects. Closed-machining environment is essential to isolate the disturbances coming from outer circumstance surrounding the machine, e.g. vibration from the floor, fluctuation of room temperature, heat transfer from other machines, floating dust and so on [27].

The choice of materials for a machine tool is one of key factors in determining final machine performance. Many criteria may be considered, including temporal stability, specific stiffness, homogeneity [26]. Table 11.7 lists the mechanical properties of some structural materials.

Cast iron and granite are most widely used materials for machine base and slideway because of their good wear resistance, low thermal expansions, low stress-caused deformation, and high vibration damping capacity. The drawback of granite is that it can absorb moisture so it is used in dry environment. For this reason many builders seal the granite with epoxy resin. For obtaining light weight with high damping capacity and rigidity, polymer concrete becomes popular especially for some precision instruments and small types of machine tools. In one of the special purpose cases, structural materials of low thermal expansion coefficient and high dimensional stability have been used; among those are super-invar, synthetic granite, ceramics, and Zerodur [13].

The spindle is a key part of mechanical structures of machine tools because the spindle motion error will have significant effects on machined surface quality. The most often used spindles in precision machine tools are air-bearing spindles and oil hydrostatic bearing spindles. They have high motion accuracy and capable of high rotational speed. An air-bearing spindle has lower stiffness than an oil hydrostatic bearing spindle, but it has lower thermal deformation than oil hydrostatic bearing spindles. Air-bearing spindles are widely used in machine tools with middle and small loading capacity while hydrostatic bearing spindles are applied in large machine tools.

Table 11.7. Material properties of some structural materials

Materials Properties	Cast iron	Granite	Epoxy granite	Invar	Al ₂ O ₃
Young's modulus (GPa)	100	40	33	140	240
Density (g/cm ³)	7.3	2.6	2.5	8.2	3.4
Specific stiffness	1.4	1.5	1.3	1.7	7
Vibration damping ratio	1-3	6	20	N/A	0.6
Thermal expansion coefficient (10 ⁻⁶ /K)	12	8.3	12	0.6	16
Thermal conductivity (W/mk)	53.5	3.8	0.47	10.5	

Recently, groove technique has been used in the design of air bearing. The grooved hybrid air bearing combines aerostatic and aerodynamic design principles to optimize ultra-high-speed performance. Aerostatic lift is generated by feeding the bearing with pressurized air through orifice restrictors as in the conventional bearing design [28]. Aerodynamic lift is controlled by the additional helical grooves machined into the shaft or bearing journal. The benefits of grooves in the bearing include significantly changing the pressure distribution within the bearing and improving load carrying capability and stiffness. The groove also changes the air velocity gradients in the bearing affecting the basic mechanism of whirl instability, which usually improves the threshold from which the instability occurs [28].

Figure 11.9 shows the air-bearing spindle developed by Fraunhofer IPT, Philips, Zeiss and Cranfield Precision for UPM 3. Com-

bining the spiral groove technology with an externally pressurized bearing type, a maximum rotational speed of 100,000 rpm and radial stiffness of 30 N/ μm are achieved in radial direction with a total error motion below 100 nm.

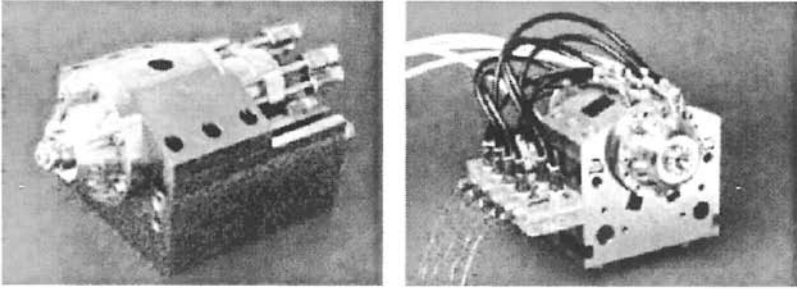


Fig. 11.9. Hybrid air bearing milling spindle for UPM 3 [8]

Air bearing slideways, air/magnetic bearing slideways, oil hydrostatic bearing slideways, and air-bearing rotary tables are widely used in state-of-the-art ultraprecision machine tools as they are capable of high motion accuracy. Oil hydrostatic bearings are often used in large machine tools because of their high load capability.

Drives

The moving mechanism is grouped into spindle and feed drives in machine tools. The spindle drive provides sufficient angular speed, torque and power to a rotating spindle held in the spindle housing with magnetic or air bearings. The electric AC motor and DC brushless motor for high-speed spindles are always built into the spindle to reduce the inertia and friction produced by the motor-spindle shaft coupling. The air turbine spindle is also applied in ultraprecision machine tools.

Piezoelectric actuators are a kind of short stroke actuator. It is very promising for application in the rotary table drive and slideway drive because of its high motion accuracy and wide response bandwidth. Currently, piezoelectric actuators have been applied in the

design of the fine tool-positioning system in order to obtain high precision motion of the cutting tool.

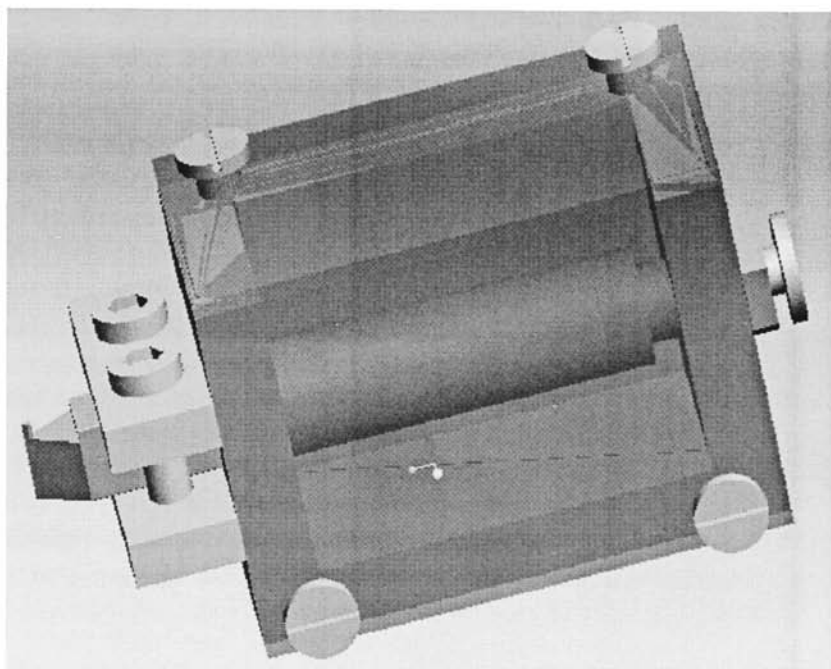


Fig. 11.10. A piezoelectric actuator for diamond cutting tool positioning

The piezoelectric actuator combined with mechanical flexure hinge is often used for positioning control of the diamond cutting tool. More recently, Fast Tool Servo (FTS) system has been introduced for diamond turning products with structured and non-rotationally symmetric surfaces such as laser mirrors, ophthalmic lenses, and lens molds. Figure 11.10 shows a schematic of a fine tool-positioning system mainly consists of a piezoelectric (PZT) actuator (Pzt 1505/20 Pizeomechanik) and a mechanical structure with flexure hinge. Strain gauge sensor is built inside the PZT by manufacture for sensing the deformation. A diamond tool is mounted in the front of the flexure hinge. The actuator system is

controlled with a computer-controlled amplifier (LE 150/025) through PID algorithms. In setting up the PZT is preloaded by the preload screw. When a voltage controlled by the PID controller is applied on the PZT actuator, the actuator will expand and push forward the front end of the flexure hinge, and thus to achieve the fast tool micro-displacement. The positioning accuracy, bandwidth, and stiffness of the designed actuator are 0.67 nm, 583 Hz and 25 N/ μm , respectively.

Linear motor direct drive and friction drive are two kinds of long stroke drives used on ultraprecision machine tools. Friction drives are predictable and reproducible due to a prescribed level of preload at the statically determinate wheel contacts, thereby superior machining an optically smooth surface. One of the good applications of friction drives is the UPM 3 with a friction wheel drive for the x-axis, which has form accuracy $< 0.2 \mu\text{m}$ per 100 mm [29].

Control

The control sub-system includes motors, amplifiers, switches, and the controller that are used to energize the electrical parts in a controlled sequence and time. High-speed, multi-axis CNC controllers are essential for efficient control of, not only servo drives in high precision position loop synchronism for contouring, but also thermal and geometrical error compensation, optimized tool setting, and direct entry of the equation of shape (avoiding lengthy post-processing) [13]. By applying feedback control the control resolutions in nanometer even sub-nanometer scales could be obtained. The use of advanced PC based control systems will be the trend for ultra-precision machine tools in the future.

Metrology and Inspection System

Metrology and inspection systems are the basis for nanometric machining to be widely applied in industry. On the other hand, high-level accuracy assurance in metrology and inspection is also a drive for nanometric machining towards higher precision requested for future engineering industry.

Laser metrology incorporated into the machine tool is widely used for feed and position control at the resolution down to nanometer or sub-nanometer level. Capacitance gages, LVDT (Linear Variable Differential Transducer), and photoelectric sensors are normally employed in the detection of nanometric displacement over small working distances [13].

Laser interferometric metrology system is shown in Fig. 11.11. the tool tip must be precisely positioned in the X and Z directions. In order to satisfy Abbe's principle, the laser interferometer shown in Fig. 11.11 is used for the tool position control. For the X direction, a pair of straightedges, one on each side of the tool bar, acts as the kinematic reference. To measure the position in the X direction, two beams are directed against each of the straightedges (i.e., a total of four beams). The tool bar's pitch angle error is corrected using the upper and lower laser beams, while the mean value of the measurements from both sides is used to eliminate errors caused by axisymmetric expansion of the frame [21].

For measurements in the z-direction (the tool's height), a pair of laser beams is directed against a pair of straightedges parallel to the tables as the kinematic reference. With a mirror attached to the bottom face of the tool bar (to get as close to the tool tip as possible), a third laser beam in the z-direction measures the tool's position. The earlier pair of laser beams in the z-direction is used to eliminate errors of the tool bar rotating about the x-axis [21].

In addition to incorporating Abbe's principle, this laser interferometer has another special design for high precision measurement, i.e., the laser beam conduits contain a vacuum [21].

11.4.2 Cutting Tools

Diamond cutting tools are the most popularly used cutting tool in ultra-precision machining. Advantages offered by diamond tooling include:

- Crystalline structure, which enable very sharp cutting edge to be produced [23].
- High thermal conductivity [23].

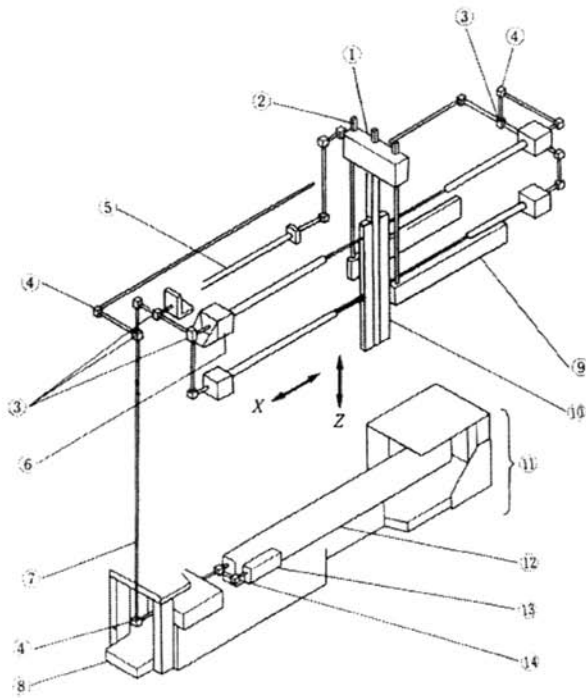


Fig. 11.11. Construction of the device for measuring displacement of sliding surface on LODTM [21]

1. Upper optics box three interferometer in vacuum system 2. Detector (three)

3. Beam splitter 4. Swing mirror 5. Bellows, at six locations within the vacuum system 6. Interferometer cover (4) and detector (4) within 7. Beam cover 8. Optics bench 9. z-axis straightedge 10. x-axis straightedge 11. support for laser optics unit 12. SP 125 helium/neon laser 13. Helium/neon laser with stabilized iodine 14. Feedback detector

- High hardness and wear resistance.

- High elastic and shear moduli, which reduce tool deformation during machining [23].

The limitations of a diamond tool are its affinity with ferrous material and lack of toughness. Figure 11.12 shows the diamond cutting tools manufactured by Contour Fine Tooling Ltd. The tools have controlled waviness down to 50 nm, which indicates that the radius shape deviates from a true circle by a guaranteed value. Therefore, a very sharp cutting edge in tens of nanometers can be achieved. Conical or cylindrical clearance is available in these tools to achieve better surface roughness and surface integrity. A diamond cutting tool can be provided either as an insert, or bounded directly to a suitable tool shank.

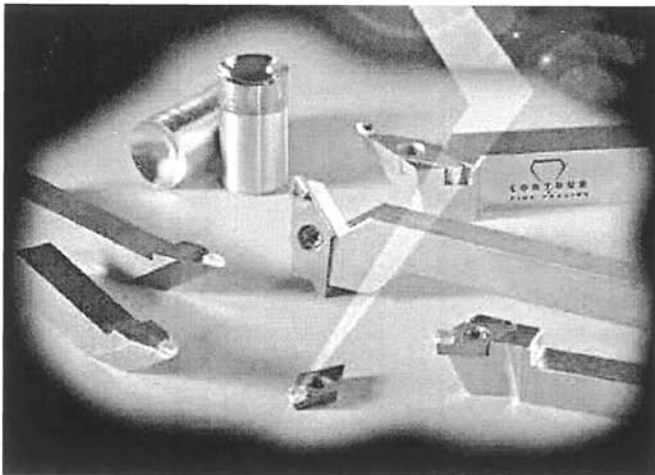


Fig. 11.12. Diamond cutting tools manufactured by Contour Fine Tooling Ltd [30]

Figure 11.13 shows micro-milling cutters (Jabro Tools Ltd, Germany) [18]. The tools are made from tungsten carbide coated with titanium carbide to improve their wear resistance [18]. The diameters are in the range of $\Phi 0.2$ mm to $\Phi 1.5$ mm.

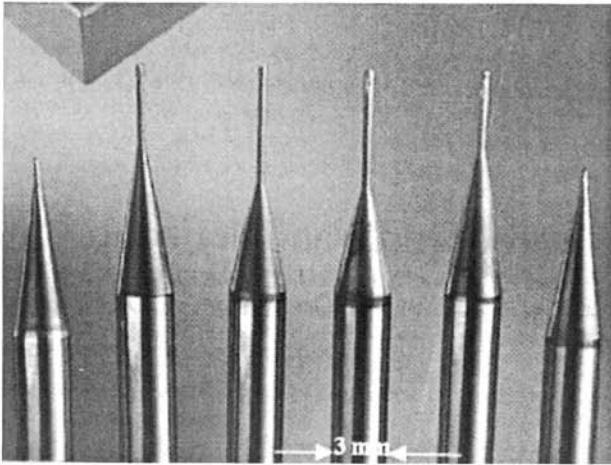


Fig. 11.13. Micro-milling tools (Jabro Tools Ltd, Germany) [18]

Diamond grinding wheels bonded with metal, and cBN grinding wheels bonded with resin are usually used in nanometric grinding. The theoretical and experimental studies of nanometric diamond grinding of glasses show that the average grain size of the wheel is the most significant factor. If a wheel of average grain size is less than $10\text{ }\mu\text{m}$ is used, the grinding of optical glasses in ductile mode grinding can be obtained and the crack will be removed [31]. The application of electrolytic in-line dressing (ELID) technique in nanometric grinding provides a significant machining cost reduction [7].

11.4.3 Nanometrology

The high precision measurement of dimension, form, surface texture and surface integrity plays a key role in the efficient and effective implementation of nanometric machining. A knowledge of the perfection of surface texture at the nanometer and sub-nanometer level is essential if many highly specialized nanotechnology applications intend to operate correctly, e.g., x-ray optical components and mirrors used in laser gyroscopes [32]; Perfection of geometrical

form is another key requirement for some components to meet their design specifications [32]; The achievement of functional performance of a product/component much depends on its surface conditions, i.e. the surface integrity, including their geometric properties, physical and chemical properties. Therefore, nanometrology for surface integrity is important, which is indispensable in characterization and control of the surface functionality and integrity in nanometric machining [33].

Displacement and Position Measurement

Laser interferometers are based on the interference of two beams, i.e., a reference and a measurement beam, emitted by a coherent laser source. The measurement resolution can be in sub-nanometer scale. The system accuracy is limited by the stability of the wavelength of the laser light. Another source of error is nonlinearity in the interpolations in optics [26].

The scales are based on a repetitive pattern of a reflective transmissive-conductive – or magnetic materials embedded in a substrate, giving a period signal. The measuring resolution of some linear scales can be in nanometer scale. The resolution for angular encoder can go down to 0.01 arc of a second.

Surface Texture Measurement

Currently optical profiler and scanning probe microscope are two kinds of major equipment used for surface texture measurement. The NT series optical profilers manufactured by Veeco Metrology Group and Newview series optical profiles from Zygo Corporation are popularly used worldwide. They are based on white light interferometry, or phase shift interferometry. Both of their products can achieve sub-nanometer vertical resolution.

Furthermore, the atomic force microscope (AFM) and scanning tunneling microscope (STM) are the best known examples of SPM have been developed to meet the requirement of measuring surfaces at the atomic level with adequate horizontal resolution.

Form Measurement

In some cases the technical requirements for a measurement are the departure from a perfect shape, for instance, the roundness and flatness of a component are typical examples [26]. Form accuracy is especially important for complex optics since the form error will significantly affect the performance of the optics. Interferometric techniques such as phase stepping have led to major advantages in the metrology of complex shapes such as astronomical mirrors where conformity to complex shapes at a fraction of the wavelength of light, which is a key element for the telescope to meet its design requirements [26].

Surface Integrity Measurement

Currently there is a trend to utilize the diamond tip of an SPM as an indenter to measure the material properties. The technique can thus be employed in surface integrity measurement. Veeco Metrology Group has added indentation module and scratching module in their Dimension 3100 SPM to measure the mechanical properties of machined surface. This makes the SPM operate very convenient for indentation and scratching experiments.

Recently, L.O.T. Orient Ltd, has developed NanoTest System to measure material properties, which is shown in Fig. 11.14. The function of the system is similar to those on an AFM, except the scanning module, indentation module, and impact module included with it. Therefore, it is capable of measuring a wide variety of material properties including [34]:



Fig. 11.14. NanoTest System (Courtesy of L.O.T. Orient Ltd [34])

- Elastic modulus
- Micro-hardness
- Adhesive failure
- Creep and relation
- Contact fatigue
- Fracture toughness
- Impact resistance
- Loss and storage moduli
- Nanoscale wear resistance
- Stress-strain rate
- Surface friction and topography

11.4.4 Machining Process Variables

The selection of machining process variables is very important in nanometric cutting. A selection and control strategy is needed to achieve the predictive production in the light of product performance. Figure 11.15 shows a promising control approach for the selection and control of machining variables. The function of the approach is described below.

According to the series of the specifications of the product, the controller classifies the surface functionalities and then decides on a number of surface parameters that will meet the functional demands on the finished product in regard to friction, wear resistance, lubrication, light scatter, and so on. Those parameters then will be translated into machining parameters to control the machining process in order to actually produce a surface with the desired functionalities. Therefore a multi-scale machining process model for understanding the nanometric machining process, optimization and control algorithms are needed to be developed in the future to achieve the high efficient and low cost nanometric machining.

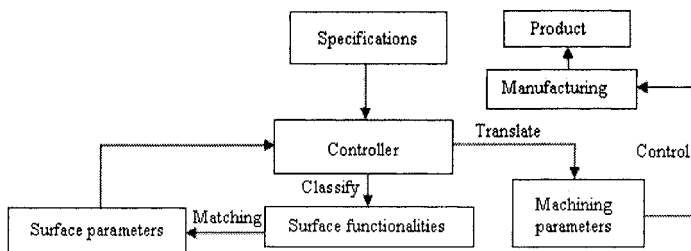


Fig. 11.15. A control approach for the selection and control of machining variables

11.4.5 Practical Nanometric Machining (Turning, Milling and Grinding)

Single Point Diamond Turning

Figure 11.16 shows an off-axis parabolic mirror fabricated at the LLNL for NASA's SPARCLE, a Space Shuttle experiment to measure wind speeds from space. The mirrors were finish-turned on the

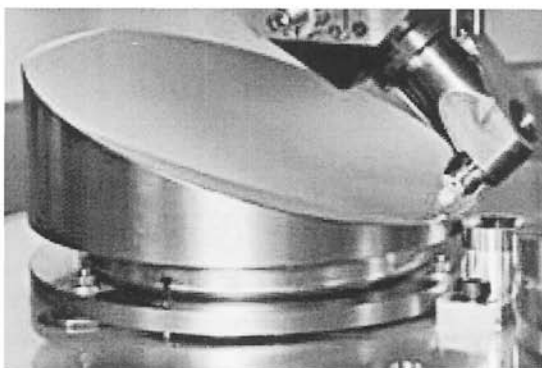


Fig. 11.16. An off-axis parabolic mirror machined on the LODTM [35]

LODTM in an electroless nickel coating on aluminum substrates. The final figure error on the mirrors was 150 nm peak-to-valley [35].

Figure 11.17 shows the optics of a chemical laser machined on the LODTM. The optics will make up the laser cavity for the Alpha chemical laser. The four separate surfaces were turned to the required 28 nm RMS tolerances [35].

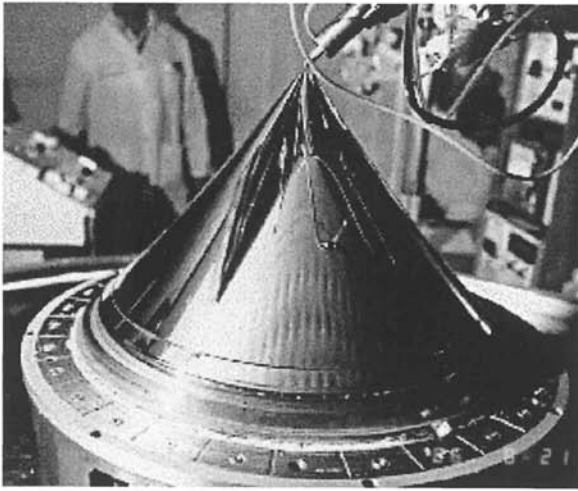
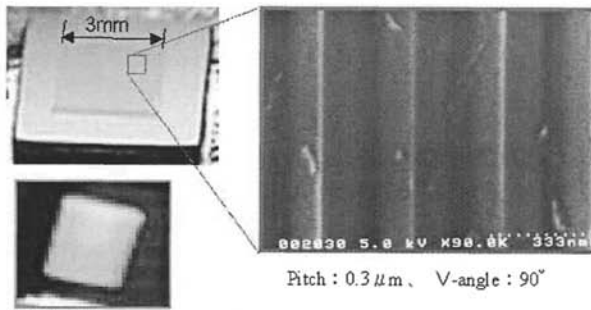


Fig. 11.17. Chemical laser cavity optics machined on the LODTM [35]



Bluish diffraction phenomenon

Fig. 11.18. A diffraction grating machined on the Robonano [36]

Diamond Milling of Complex Molds

Figure 11.18 shows a diffraction grating with a pitch of sub-micron dimensions, which is one of the typical nanomachining samples using a FANUC ROBONANO machine [36]. It can be observed that each edge of the groove is sharp and no burrs appear on the surface.

Nanogrinding

Figure 11.19 shows the resulting nanometric grinding of optical glass, the work is undertaken at the Center of Optics and Manufacturing at the University of Rochester. The nanometric grinding is carried out on a Nanotech 500 FG using a diamond wheel bonded with metal. An optical device with a 2.7 nm RMS surface roughness and 0.375 P-V surface form accuracy is obtained [37].

11.5 Conclusions

In this chapter, the theory, methods, and implementation techniques are formulated for nanometric machining research and practices. Nanometric cutting and nanogrinding are the kernel of nanometric machining technology. Nanometric machining research is timely and of great significance for future engineering industry. The technology is essential for mass manufacturing of miniature and micro components and 3D devices from a variety of engineering materials, which is also leading to the new challenges for manufacturing science and practices.

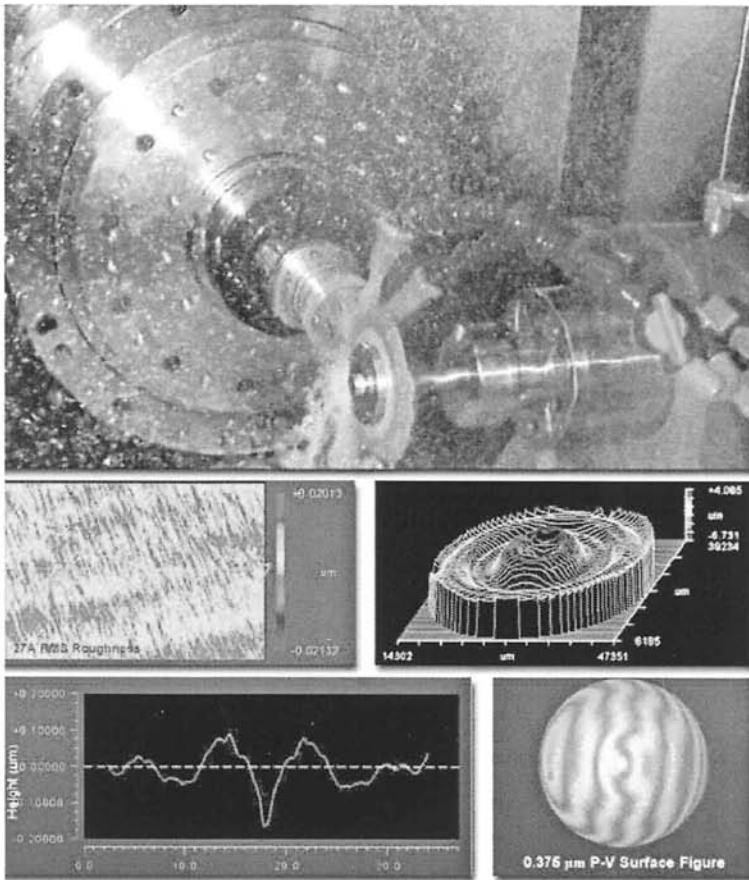


Fig. 11.19. Nanometric grinding of optical glass [37].

11.6 Problems

1. What is nanomachining?
2. What are the application markets for nanomachined products?
3. What is the theoretical basis of nanomachining?
4. What effect does energy have on the nanomachining process?

5. How are chips formed in nanomachining.
6. Describe the minimum undeformed chip thickness.
7. Describe the properties of workpiece materials and how they affect the nanomachining process.
8. What is the difference between single-point diamond turning and ductile mode grinding?
9. Compare nanometric and conventional machining processes.
10. Describe the mechanical structure required to nanomachine.
11. Describe the cutting tools used for nanomachining.
12. Describe nanometrology and how one can measure nanoscale features.

References

- [1] Committee on Technology National Science and Technology Council, "National Nanotechnology initiative: Leading to the next industrial revolution, Washington D. C. 2000.
- [2] Snowdon K, Mcneil C, Lakey J. Nanotechnology for MEMS components. *mstNews* 2001; (3): 9-10.
- [3] El-Fatraty A, Correial A. Nanotechnology in Microsystems: potential influence for transmission systems and related applications. *mstNews* 2003; (3): 25-26.
- [4] Werner M, Köhler T, Grünwald W. Nanotechnology for applications in microsystems. *mstNews* 2001; (3): 4-7.
- [5] El-Hofy H, Khairy A, Masuzawa T, McGeough J. Introduction. In: McGeough J eds. *Micromachining of Engineering Materials*. New York: Marcel Dekker, 2002.
- [6] Donaldson R, Syn C, Taylor J, Ikawa N, Shimada S. Minimum thickness of cut in diamond turning of electroplated copper. UCRL-97606 1987.
- [7] Stephenson DJ, Veselovac D, Manley S, Corbett J. Ultra-precision grinding of hard steels. *Precision Engineering* 2001; 15: 336-345.
- [8] Rübenach O. Micro technology – applications and trends. Euspen online training lecture. <http://www.euspen.org/training/lectures/course2free2view/02MicroTechApps/demolecture.asp> (accessed July 2006).
- [9] Diamond milling processes for the generation of complex optical mold inserts. <http://www.lfm.uni-bremen.de/html/res/res001/res108.html> (accessed July 2006).

-
- [10] Weck M. Ultraprecision machining of microcomponents. *Machine Tools* 2000; 113-122.
- [11] Andreas Schütze, Lutz-Günter John. Nano sensors and micro integration. *mstNews* 2003; **3**: 43-45.
- [12] Ayman El-Fatraty, Antonio Correial. Nanotechnology in Microsystems: potential influence for transmission systems and related applications. *mstNews* 2003; **3**: 25.
- [13] Ikawa N, Donaldson R, Komanduri R, König W, Mckeown PA, Moriwaki T, Stowers I. Ultraprecision metal cutting – the past, the present and the future. *Annals of the CIRP* 1991; **40**(2): 587-594.
- [14] Shaw MC. *Principles of Abrasive Processing*. New York: Oxford University Press, 1996.
- [15] Komanduri R, Chandrasekaran, Raff L. Effects of tool geometry in nanometric cutting: a molecular dynamics simulation approach. *Wear* 1998; **219**: 84-97.
- [16] Luo X, Cheng K, Guo X, Holt R. An investigation on the mechanics of nanometric cutting and the development of its test-bed. *International Journal of Production Research* 2003; **41** (7): 1449-1465.
- [17] Taniguchi N. *Nanotechnology*. New York: Oxford University Press, 1996.
- [18] Dow T, Miller E, Garrard K. Tool force and deflection compensation for small milling tools. *Precision Engineering* 2004; **28** (1): 31-45.
- [19] Cheng K, Luo X, Ward R, Holt R. Modelling and simulation of the tool wear in nanometric cutting. *Wear* 2003; **255**: 1427-1432.
- [20] Shimada S. Molecular dynamics simulation of the atomic processes in microcutting. In McGeough J, eds. *Micromachining of Engineering Materials*. New York: Marcel Dekker, 2002: 63-84.
- [21] Nakazawa H. *Principles of Precision Engineering*. New York: Oxford University Press, 1994.
- [22] Lee W, Cheung C. A dynamic surface topography model for the prediction of nano-surface generation in ultra-precision machining. *International Journal of Mechanical Sciences* 2001; **43**: 961-991.
- [23] Corbett J. Diamond micromachining. In McGeough J, eds. *Micromachining of Engineering Materials*. New York: Marcel Dekker, 2002: 125-146.
- [24] Bifano TG, Dow TA, Scattergood RO. Ductile-regime grinding: a new technology for machining brittle materials. *Transactions of ASME: Journal of Engineering for Industry* 1991; **113**: 184-189.
- [25] Slocum AH. *Precision Machine Design*. Englewood Cliffs: Prentice-Hall 1992.
- [26] Schellekens P, Rosielle N. Design for precision: current status and trends. *Annals of the CIRP* 1998; **47**(2): 557-584.

- [27] Shinno H, Hashizume H, Ito Y, Sato C. Structural configuration and performances of machining environment-controlled ultraprecision diamond turning machine 'capsule'. *Annals of the CIRP* 1992; **41**(1): 425-428.
- [28] Stanev P, Wardle F, Corbett J. Grooved hybrid air bearings. <http://www.loadpoint.co.uk/site2/grooved.pdf> (accessed July 2006).
- [29] Leifheim B. Precision and ultra precision machine tools. Euspen online lecture. <http://www.euspen.org/training/lectures/course2free2view/03PrecisionUltraTool/demolecture.asp> (accessed July 2006).
- [30] <http://www.contour-diamonds.com/> (accessed on April 2006).
- [31] Chen M, Li D, Dong S, Zhang F. Factors influencing the surface quality during ultra-precision grinding of brittle materials in ductile mode. *Key Engineering Materials* 2003; 257-258.
- [32] Corbett J, Mckeown P, Peggs G, Whatmore R. Nanotechnology: international developments and emerging products. *Annals of the CIRP* 2000; **49**(2): 1-23.
- [33] Cheng K, Luo X, Ward R, Liu X, Modelling and control of the surface integrity and functionality in precision machining. *Proceedings of the 3rd euspen International Conference, Eindhoven Holland, May 26-30 2002*, pp. 221-224.
- [34] NanoTest System brochure, L.O.T. Orient Ltd
- [35] http://www-eng.llnl.gov/lodtm/success_pg2.html (accessed on July 2006).
- [36] <http://www.fanuc.co.jp/en/product/robonano/index.htm> (accessed on July 2006).
- [37] <http://www.opticsexcellence.org/index.htm> (accessed on July 2006).

12. Micro-and Nanomanufacturing

12.1 Introduction

The future of micro-and nanomanufacturing lies in the ability to convert micro-and nanofabrication techniques into mass production manufacturing processes where small-scale products can be economically manufactured in a short period of time. This may be achieved by combining micro-and nanoscale processes, or by combining “top down” and “bottom up manufacturing techniques. The development of so-called hybrid manufacturing processes is set to take center stage in the future development of micro-and nanomanufacturing processes. This chapter focuses on current developments in the field of micro-and nanomanufacturing.

12.2 Micromanufacturing

12.2.1 Electroplating

The fabrication of master molds in preceding chapters was focused on the use of lithographic techniques such as LiGA, deep x-ray lithography, wet etching, dry etching using plasmas, etc. These techniques, although widely used, are very slow at producing master molds. An alternative technique that is proving to be slightly faster is electroplating that can produce master molds from a variety of

materials and is an established way of manufacturing precision products.

The object to be plated must be metallized and/or masked to define regions that require the addition of metals to their planar surfaces. Electrodeposition is based on the principle of electrolysis, which means that many metals can be deposited. The process of electroplating is very simple and can be performed using very basic equipment such as a laboratory beaker, electrodes, an electrolytic solution, and a power supply. Electroplating can deposit up to 1mm of metal in a reasonably short timescale. Electrolytic solutions can contain salts of metals, water, anions, and cations, and the solution can be buffered to control the pH level.

The density of parts produced using electrodeposition is typically 1-4% below the theoretical value that accounts for voids, inclusions, porosity, and impurities. Once electroplated, products are usually annealed to increase the density close to 100%. The influencing factors of a good quality micropart include a deposited thin film thickness that can be in the range between 12 – 18 μm . Stresses in these parts are caused by the interference of interacting grains and the use of high current densities when electroplating. The adhesion of plated films is dependent upon the match between substrate and electrodeposited film, the type of oxide film on the substrate, and on hydrogen embrittlement that can be promoted by the reduction reaction at the cathode that releases hydrogen into the electroplating cell. A selection of microscale parts produced by electroplating is shown in Fig. 12.1. Electroplating can be adapted very easily to produce microscale parts and mold masters with relative simplicity and is considered as a future micromanufacturing process for producing metallic microscale parts and components, and masters for dies and molds that can be used for the subsequent molding of polymeric microparts and components.

12.2.2 Casting

Casting is another large-scale manufacturing process that can be adapted to operate at the microscale. The process of casting microstructures is widespread in the academic world but is not widely

used for the production of microparts in industry. Casting offers a low cost solution to the manufacture of planar microstructures with intricate features and is typically used with silane elastomers such as polydimethylsiloxane (PDMS). The casting of PDMS is performed by initially mixing the PDMS elastomer with a curing agent in a 10:1 weight ratio. The pre-polymer mixture must be degassed, typically at 20-50 mTorr for 1 hr in a desiccator with a vacuum pump. The critical step is to remove any air bubbles in the mixture. Mixing PDMS at different ratios with the curing agent will affect the resulting mechanical properties, i.e., 10:1 PDMS has $E = 750$ kPa and 5:1 PDMS has $E = 868$ kPa.

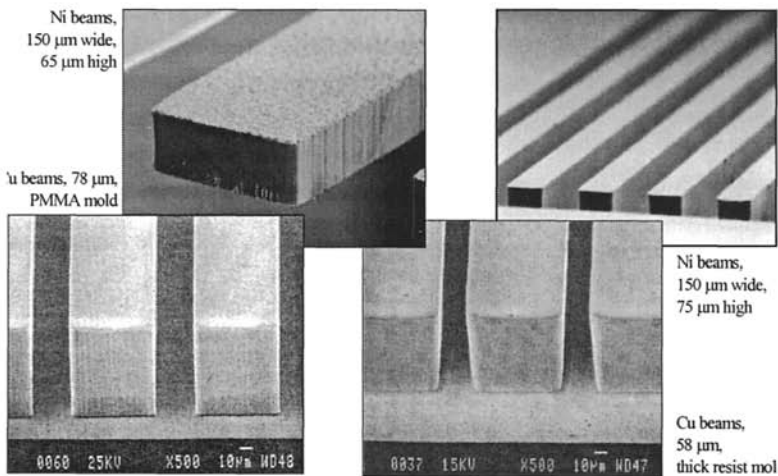


Fig. 12.1. A variety of mold components made from copper and nickel by electrodeposition

The compound is poured on to a master pattern and is allowed to set for three hours at 100°C . The master pattern can be silicon-based material or any other material for that matter. PDMS can also be cast on to photoresist material such as SU-8 and AZ4620. The cast elastomer can be peeled off the master pattern and be used many times to deposit microscale particles that form microscale features. The cast PDMS is typically 1mm thick but can be thicker. It can be attached to a rigid body so that it can be used as a stamp

when stamping microscale features. The fact that the stamp can be used multiple times makes it a micromanufacturing process that can be used for depositing micro-(and nano) scale particles, molecules, etc. This type of technology can be used to create features for microfluidic channels simply by casting PDMS layers to act as valves and switches on the surface of microchannels (Fig. 12.2).

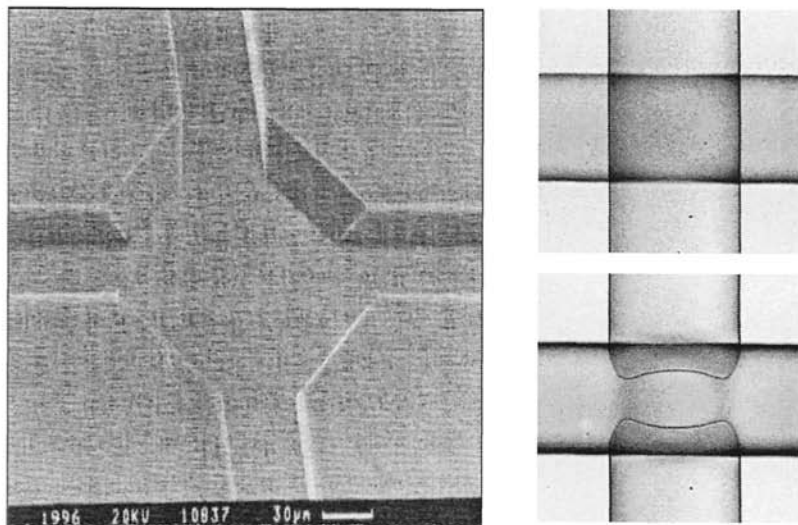
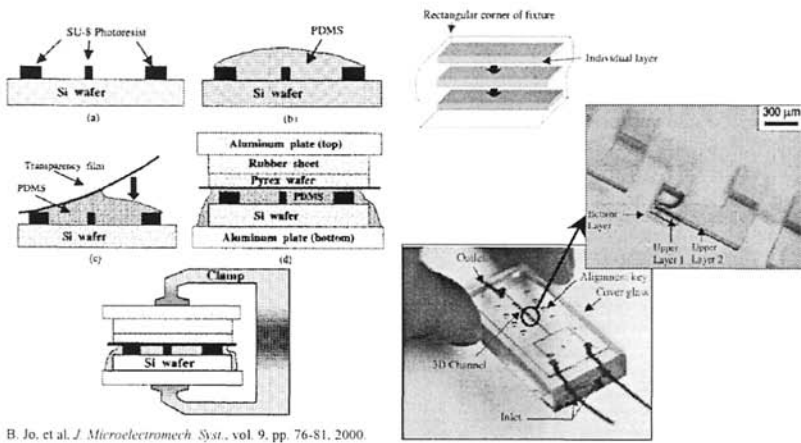


Fig. 12.2. Microchannels etched in silicon with a layer of PDMS deposited to act as a flow valve to control the flow of liquid in a microfluidic chamber

PDMS can also be cast to form soft tools that are used in micro-molding processes such as hot embossing. The casting of thin layers of PDMS can be performed to provide three-dimensional features, which is especially important in the proper functioning of micro-and nanofluidic flows. Figure 12.3 shows the casting of thin layers of PDMS in a three-dimensional microfluidic device.

The versatility of this material has not yet been realized in many micro-and nanofabrication processes. However, the future development of micro-and nanomanufacturing processes will certainly be aided by the extensive use of PDMS stamps, molds, and tools. The

casting of microparts in metals such as zinc and aluminum alloys has already started in the U.S. castings sector. The complexities of casting metals before they freeze in the molds they fill will lead to the development of warm casting processes or hybrid developments that may include semi-solid casting of microparts at low temperatures. A new wave of low temperature castable alloys will be required to meet these demands.



B. Jo, et al. *J. Microelectromech. Syst.*, vol. 9, pp. 76-81, 2000.

Fig. 12.3. The casting of thin layers of PDMS between silicon and SU-8 photoresist shows how three-dimensional microfluidic devices can be manufactured simply by casting and clamping [1]

12.2.3 Molding

The process of molding microparts individually is extremely widespread at the present time but has yet to be optimized for manufacturing microparts. The molding process has rapidly developed in the area of PDMS molding using silicon masters that have been produced using techniques such as LiGA, deep x-ray lithography, etching, etc.

Figure 12.4 shows the process of forming a PDMS molding using PDMS as a molding that can be used in microfluidic systems. In

order to convert the fabrication of PDMS molding to manufacturing PDMS moldings, the future manufacturing of these moldings will require the development of injection molding and hot embossing techniques. Hot embossing is a technique that is rapidly gaining popularity in producing microscale features in thermoplastic materials. The three stages of manufacture involve heating the polymer, embossing the polymer to the shape of the pattern, de-embossing to produce the molding. The embossing temperature is typically between 50 and 100°C. The overall embossing time is approximately ten minutes. Commercial embossing equipment is shown in Fig. 12.5.

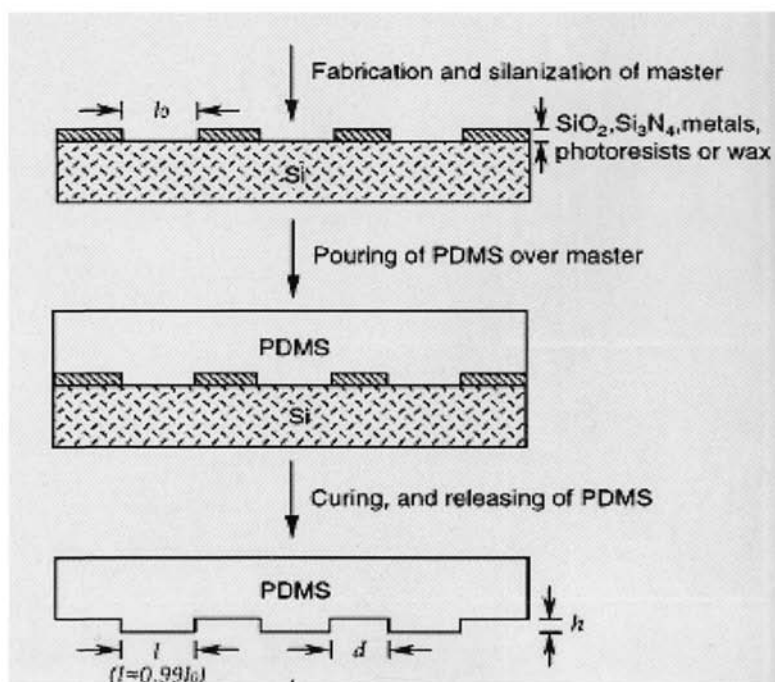


Fig. 12.4. Formation of a PDMS molding from a master pattern. Courtesy of G. Whitesides, Harvard University

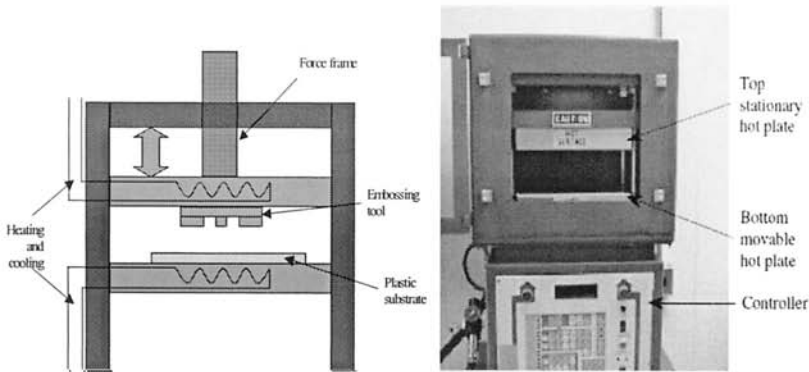


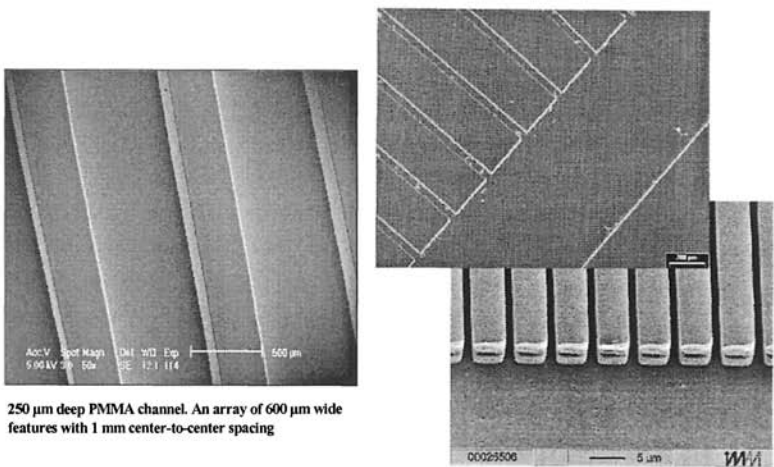
Fig. 12.5. Schematic view of hot embossing and commercial embossing equipment

The success of the hot embossing technique is dependent on the tool or pattern that is being embossed. Hard tools are prepared by machining, electroplating, dry or wet etching of silicon, or using LiGA. A comparison of tools created using these technologies is shown in Table 12.1. Figure 12.6 shows a selection of microscale products created using hot embossing. The products are produced on a mass scale and the typical embossing time for producing these parts was 8 minutes. Typical products produced using this micro-manufacturing process include lab-on-a-chip products such as ACLARA's Labcard as shown in Fig. 12.7.

The development of three-dimensional microdevices has prompted the recent development of hot embossing with soft tools [2,3]. The process involves coating a pattern with PDMS elastomer, allowing the PDMS soft tool to set, the using the soft tool to form an impression in a thermoplastic material by applying a direct force on to the surface of the polymer via the soft tool during hot embossing. The schematic outline of the process is shown in Fig. 12.8 with a scanning electron image of the soft PDMS tool and the embossed PMMA material in Fig. 12.9.

Table 12.1. Comparison of hard molding tools produced using various methods

	Silicon	UV-LIGA	LIGA	CNC	SU-8
Aspect ratio	Low(~1 to 2)	High(~ 6)	Very high(~100)	Very low(~1)	Low(~1 to 2)
Feature size	?5 μm	?25 μm	~0.1 μm	?100 μm	?25 μm
Lifetime	~30	~100	~50	>100	Few tens
Stiction	Yes	No	No	No	Yes
Finish	High (dry) Low (wet)	Moderate	Low (~10nm)	High	Moderate
Time to fabricate	Long (slow etch)	Moderate	Long (slow growth)	Short	Moderate (Bake time)



J. Narasimhan and I. Papautsky, *J. Micromech. Microeng.*, vol. 14, pp. 96–103, 2004.
H. Becker and C. Gerner, "Electrophoresis," vol. 21, pp. 12–26, 2000.

Fig. 12.6. Hot embossed microproducts [2,3]

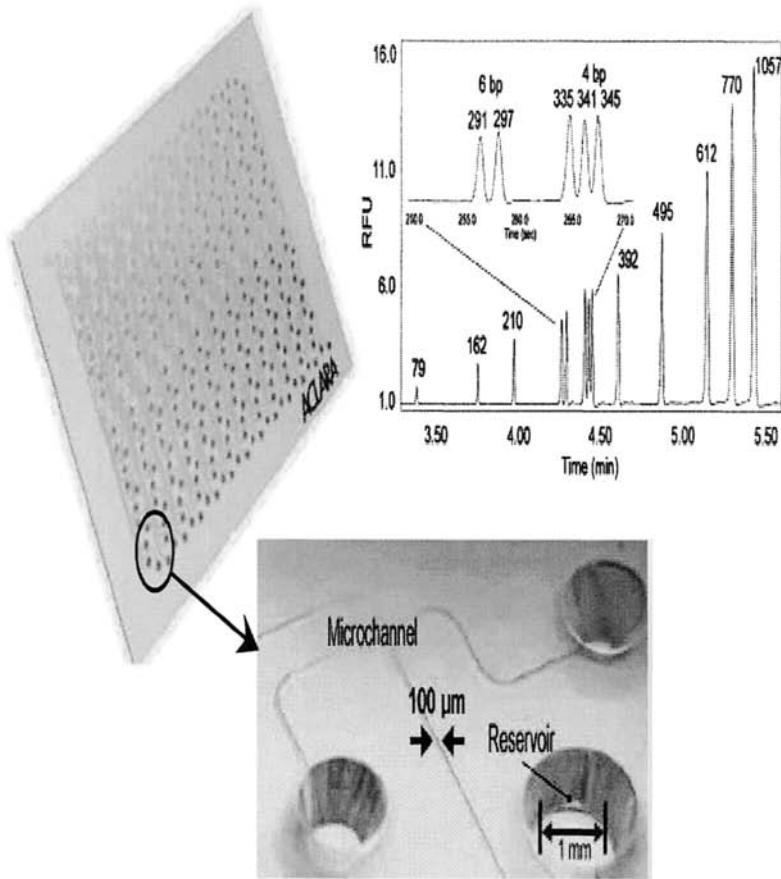


Fig. 12.7. Labcard product by ACLARA showing hot embossed microchannels and reservoirs.

The development of fabricating three-dimensional microfluidic devices has led to the development of orthogonal hot embossing with soft tools for manufacturing on the mass scale. This technique is shown in Figures 12.10 and 12.11 and is leading the way to the future development of hot embossing three-dimensional microstructures.

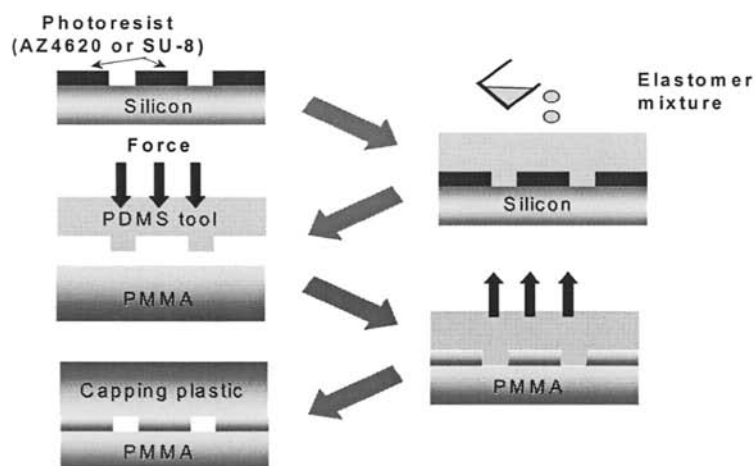
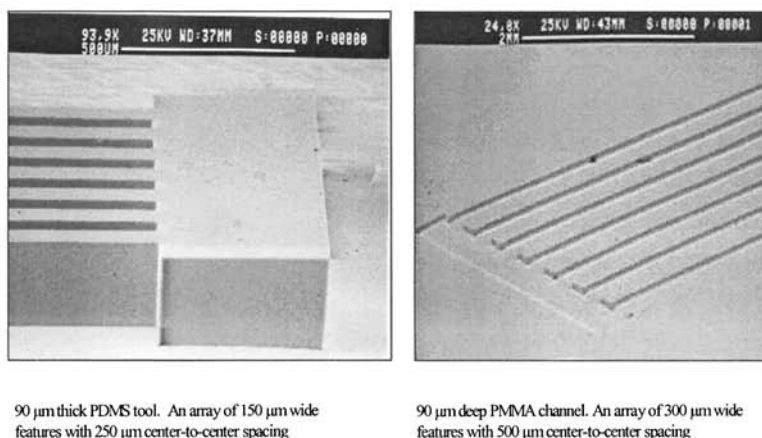


Fig. 12.8. Hot embossing with soft PDMS tools



90 μm thick PDMS tool. An array of 150 μm wide features with 250 μm center-to-center spacing

90 μm deep PMMA channel. An array of 300 μm wide features with 500 μm center-to-center spacing

J. Narasimhan and I. Papautsky, *J. Micromech. Microeng.*, vol. 14, pp. 96–103, 2004.

Fig. 12.9. Soft PDMS tool showing impression left after embossing PMMA thermoplastic material [2]

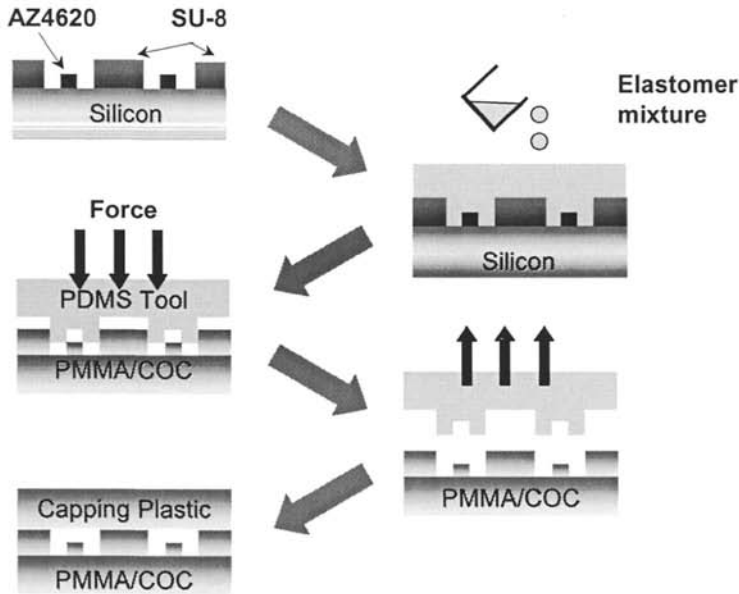
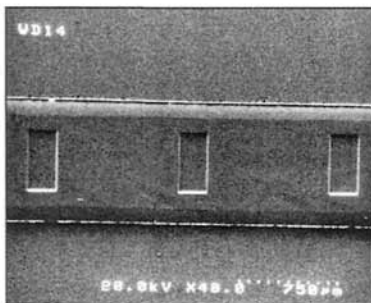
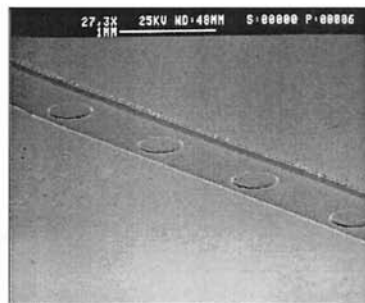


Fig. 12.10. Orthogonal hot embossing with soft PDMS tools



PDMS embossing tool illustrating the 20 μm deep rectangular indents (250 μm x 500 μm) on the 110 μm thick structure



Embossed orthogonal 3-D PMMA channel

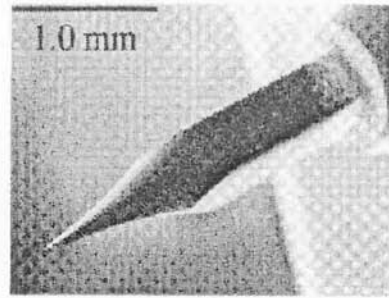
J. Narasimhan and I. Papautsky, *J. Micromech. Microeng.*, vol. 14, pp. 96–103, 2004.

Fig. 12.11. PDMS embossing tools and orthogonal channel in PMMA material [2]

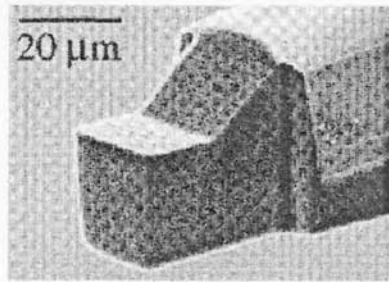
The critical issue for the future development of micromolding techniques such as hot embossing with soft tools is concerned with the faithful replication of the master pattern during hot embossing, which requires the application of a uniform force for the appropriate cycle time on the tool-polymer sandwich. This criterion in turn requires the embossing tool to be uniform in thickness throughout, which is achieved by casting on a highly flat and leveled hot plate. The embossing parameters are different from those normally used with Ni or Si tools, in part due to a much lower thermal conductivity of PDMS (~ 0.2 W/mK) compared with Ni ($\sim 150 - 500$ W/mK) or Si (157 W/mK) and the soft nature of the tool itself. The lifetime of soft tools have also been determined to last approximately twenty moldings with aspect ratios between 2 and 4, creating a minimum feature size of about $10\text{ }\mu\text{m}$. The use of soft tools and polymers looks set to open up future opportunities for creating all polymer transistors, circuits, and microprocessors.

12.2.4 Machining

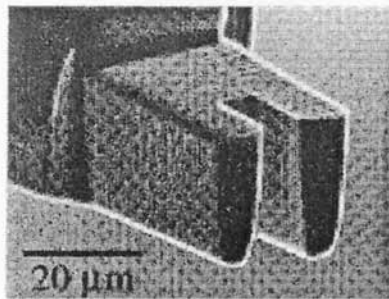
The process of machining has always been a strong contender for playing a role in the future of micromanufacturing. The ability to machine any material guarantees that micromachining will continue to be a micromanufacturing process of choice. In recent years, the size of the cutting tool has become smaller and smaller, and as such very small tools are now being fabricated by laser micromachining and ion beam milling processes [4]. Figure 12.12 shows a collection of cutting tools fabricated by ion beam milling. Laser micromachining shows promise in being able to remove very small areas of material using extremely high fluences. This can be achieved using femtosecond pulsed lasers and future applications of this type of laser may include sharpening very small diamonds that can be attached to tips such as AFM probes. The AFM may be developed as a nanomachining tool that can cleave the bonds between atoms.



(a)



(b)



(c)

Fig. 12.12. Focused ion beam milled diamond cutting tools [4]

Diamond and titanium based cutting tools are required to machine a wide variety of engineering materials. Developments in PVD and CVD coating technologies will also be fundamental to the future development of micromachining cutting tools. The future development of very stiff machine tools will also figure significantly in

the future too. Developments in this area have already begun by various research institutions in the United States and are described as “meso-micro machine tools” (mMTs).

12.2.5 Future Developments in Micromanufacturing

The development of micromanufacturing processes that use silicon-based materials are already highly developed. The next stage in the development of micromanufacturing processes lies in the ability to manufacture micro-products from engineering materials such as metals and ceramics. Processes that show promise in promoting the next stage of development include selective laser sintering of metals, laser micromachining using pulsed femto- and attosecond lasers, droplet-based manufacturing, and cold gas dynamic molding and spraying of microparts. Combinations of these techniques and established methods of manufacturing that produce hybrid manufacturing processes will create the short term “stepping stones” required to meet the demand generated to economically manufacture microscale products.

12.3 Nanomanufacturing

12.3.1 Semiconductor Manufacturing

Semiconductor manufacturers have made great strides in the past few years overcoming the diffraction limit of light waves to produce nanoscale transistors. The scale of engineering the limit to favor the semiconductor industry involves the use of extreme ultra violet light sources and soft “x-rays”. However, the use of photolithographic processes to produce transistors at length scales of the order of tens of nanometers will be reached within the next 5 years. Alternative manufacturing methods are required to produce features sizes in the range of tens of nanometers. A number of processes are emerging from universities and research institutes that will form the basis of future nanomanufacturing processes. The following descriptions of

processes form the basis of the future direction of nanomanufacturing.

12.3.2 Soft Lithographic Manufacturing

Soft lithographic processes are currently being developed for nanomanufacturing of semiconductor and non-semiconductor applications and include techniques such as microcontact printing (minimum feature size of 35 nm), replica molding (minimum feature size of 30 nm), microtransfer molding (minimum feature size of 500 nm), micromolding in capillaries (minimum feature size of 350 nm), and solvent assisted micromolding (minimum feature size of 60 nm) amongst others. Micro-contact printing is a non-photolithographic method that routinely forms patterned self assembled monolayers. An elastic stamp made from PDMS is used to transfer inks of molecules or colloids of nanoparticles to the surface of the substrate being printed. The process can be made into a “manufacturing” process by adding a roller to form a rolling stamp. Figure 12.13 shows the principle of the process. Contact times of less than 30ms are required to deposit molecules to the surface of the substrate making microcontact printing a relatively fast process. Deposition on the surface of silver appears to be better than gold owing to silver’s reactivity to etchants and its high electrical conductivity. Multilayers possess fewer defects than gold layers and edge distortions are less because the deposited layers are 1 – 3 nm in thickness. PDMS stamp require rigid backings so that the stamp does not lose form during printing. The development of higher quality elastomers may be necessary although reinforcing existing elastomers such as Sylgard 184 with metal particles may be the answer. The patterning of non-planar surfaces is possible with this mechanical form of lithography compared to the optical techniques. The development of microcontact printing as a nanomanufacturing process depends on the ability to deposit a variety of materials. So far, organic molecules and colloids of metals such as palladium have been successfully deposited. Future development of this process lies in the deposition of materials to substrates other than silicon and glass.

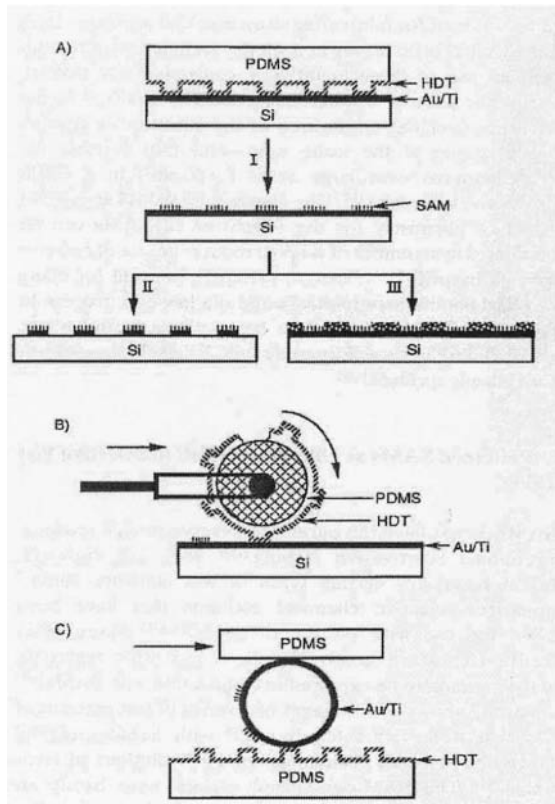


Fig. 12.13. Schematic diagram of microcontact printing of self-assembled monolayers (hexadecanethiol, HDT) to a gold surface: (a) printing a planar surface with a planar stamp; (b) large area planar printing with a rolling stamp; and (c) printing on a non-planar surface with a planar stamp [5]

Microcontact printing can also be performed to produce three-dimensional structures such as microfluidic devices using the sandwich method of printing. A PDMS master stamp is coated with a drop of PDMS pre-polymer which is stamped against the master pattern of a silicon substrate. Masters are aligned with features just touching where the PDMS pre-polymer cures under pressure. The resulting membrane is peeled off the master and can be laid on top of each other in order to build a three-dimensional device (Fig. 12.14).

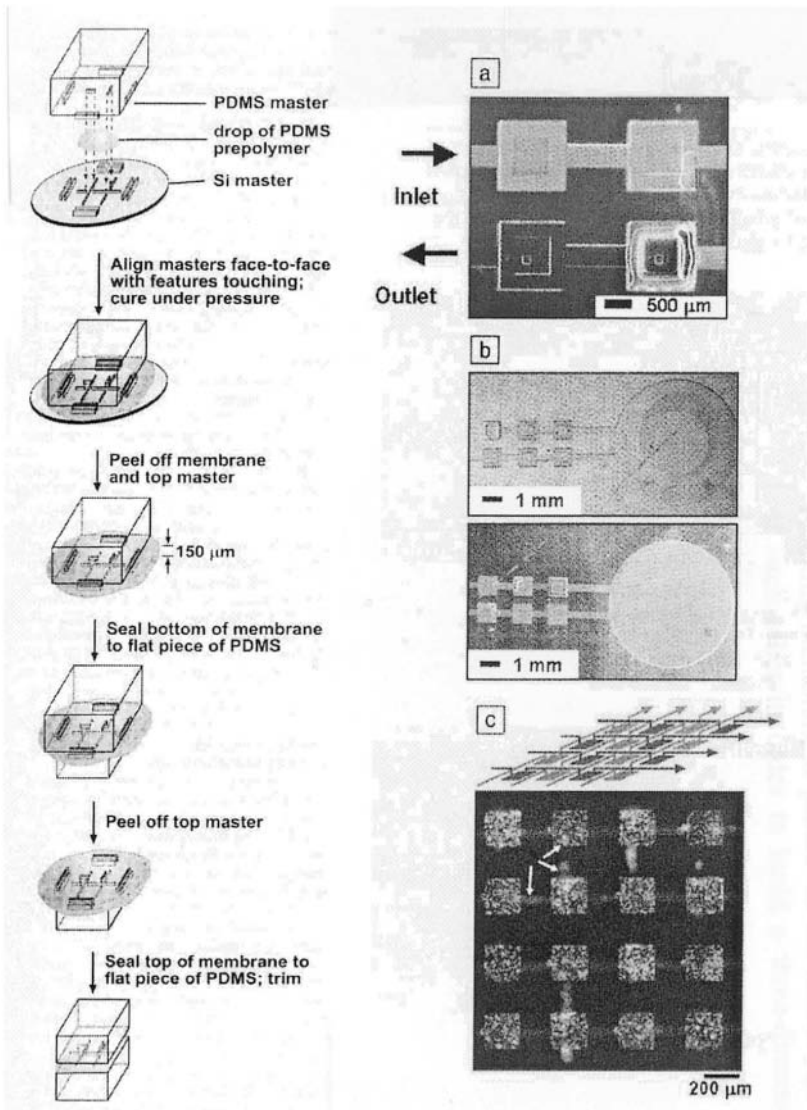


Fig. 12.14. Membrane sandwich method for producing three-dimensional microfluidic devices. The figure to the right shows flapper valves, a reciprocating pump, and channel systems fabricated using the membrane sandwich method [6]

12.3.3 Nanomanufacturing by Molding

Nanomanufacturing by use of micromolding techniques has recently been demonstrated as a viable future process for nanomanufacturing. Micromolding applied to the nanoscale is comprised of processes such as replica molding, microtransfer molding, micromolding in capillaries, and solvent assisted micromolding. Figure 12.15 shows the basic process procedures.

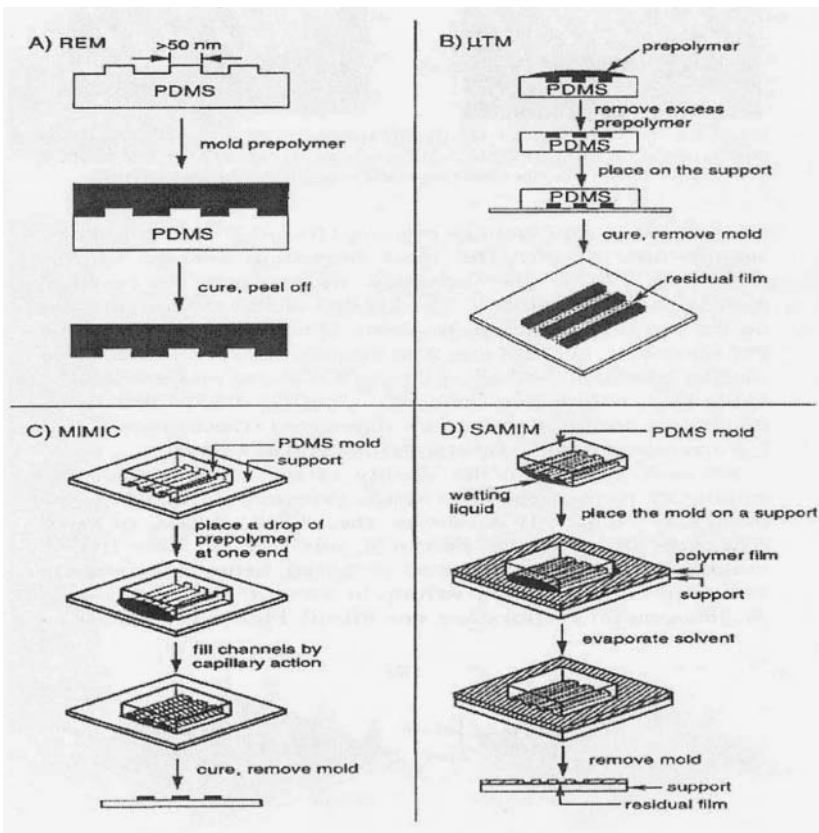


Fig. 12.15. Nanomanufacturing procedures associated with molding techniques: (a) replica molding; (b) microtransfer molding; (c) micromolding in capillaries; (d) solvent assisted micromolding [5]

Replica molding is used to make topographically complex structures using a soft PDMS stamp to replicate non-conformal surfaces on substrates. The process has been used to produce diffraction gratings, chirped, blazed diffraction gratings on curved surfaces, patterned microfeatures on hemispherical domes, and arrays of rhombic microlenses. Figure 12.16 shows the process procedure for making a variety of structures.

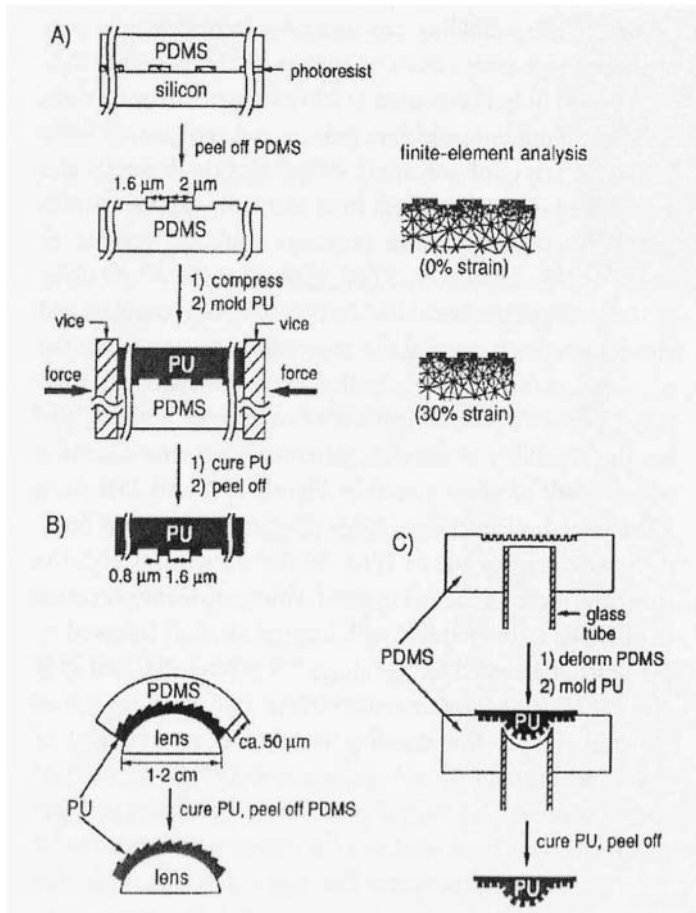


Fig. 12.16. Schematic illustration of replica molding against an elastomeric PDMS mold under: (a) mechanical compression; (b) bending; and (c) stretching [5]

Microtransfer molding is a process that produces very thin layers of patterned surfaces that can be used to build three-dimensional products with nanoscale features. A selection of products made using this technique is shown in Fig. 12.17.

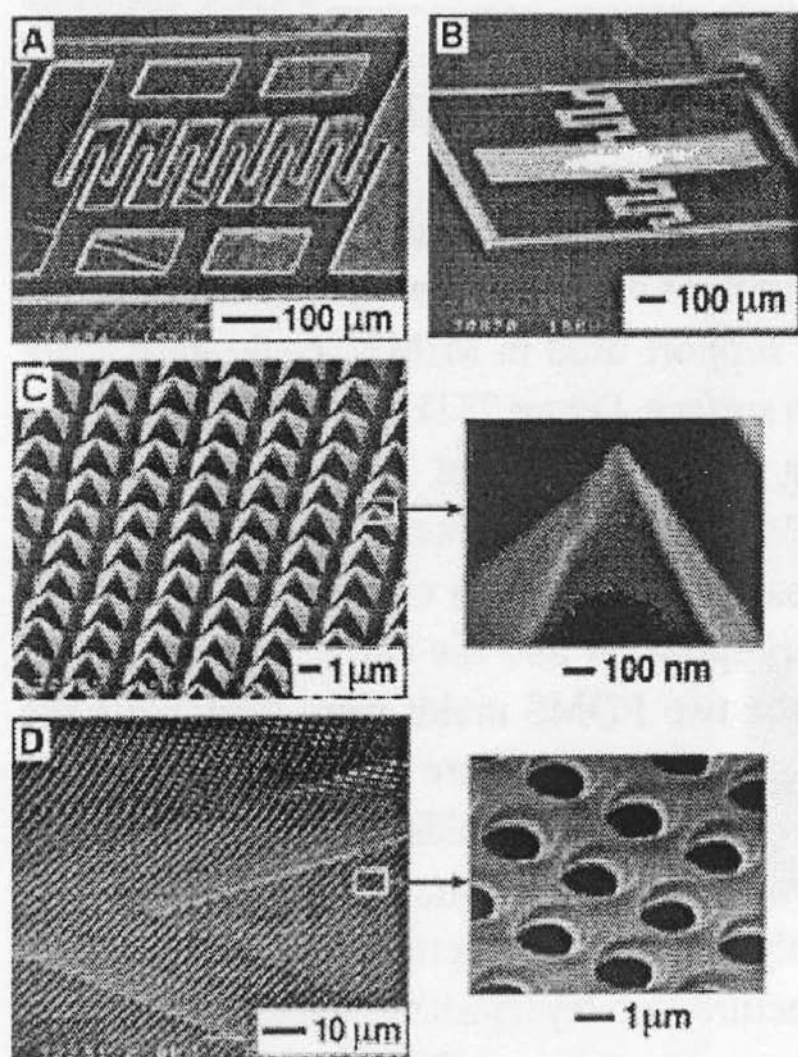


Fig. 12.17. Images of structures produced using microtransfer molding [5]

Another future method of nanomanufacturing is micromolding in capillaries (MIMIC). The process allows non-planar surfaces to be patterned using a network of channels that are filled with pre-polymer which is cured and forms a solid network of small-scale features. This process has been used with materials such as ceramics, biological materials, functional and structural polymers, inorganic salts, polymer beads, colloids, and sol-gel materials. Functional devices have been created using MIMIC and are described in depth by Xia and Whitesides [5]. The devices made include: Schottky diodes, GaAs/AlGaAs FETs, and silicon MOSFETs.

SAMIM is a process that uses solvents to form small channels in micro-and nanoscale products that is also a contender for development into a nanomanufacturing process [6]. The process can be used for making MEMS and NEMS devices such as micro-and nanofluidic devices as shown in Fig. 12.18.

Nanomanufacturing by molding will become more prevalent in the future because of the replication and reproducibility of feature size achievable using mechanical methods of lithography, and due to the fact that non-planar, convex and concave surfaces can be patterned with ease compared to optical lithographic methods. The molding of polymeric materials will experience the largest growth due to the construction of all polymer transistor circuits and micro-processors [7,8].

12.3.4 Nanoimprint Lithography

Nanoimprint lithography is a very promising low-cost nanomanufacturing process that involves two steps. The first step is “imprinting” and this relies on deforming a thin resist film using a mold with nanostructures imprinted on it. In the “pattern transfer” step, an etching process such as reactive ion etching (RIE) is used to remove residual resist material. The resist can be a thermoplastic, thermal curable polymer, or other deformable material. The process is a mechanical deformation process as opposed to soft lithography that imparts ink with colloidal fluid or self-assembled molecules to the substrate. The resolution is dependent on the mechanical strength of the mold but resolution as low as 5 nm are achievable.

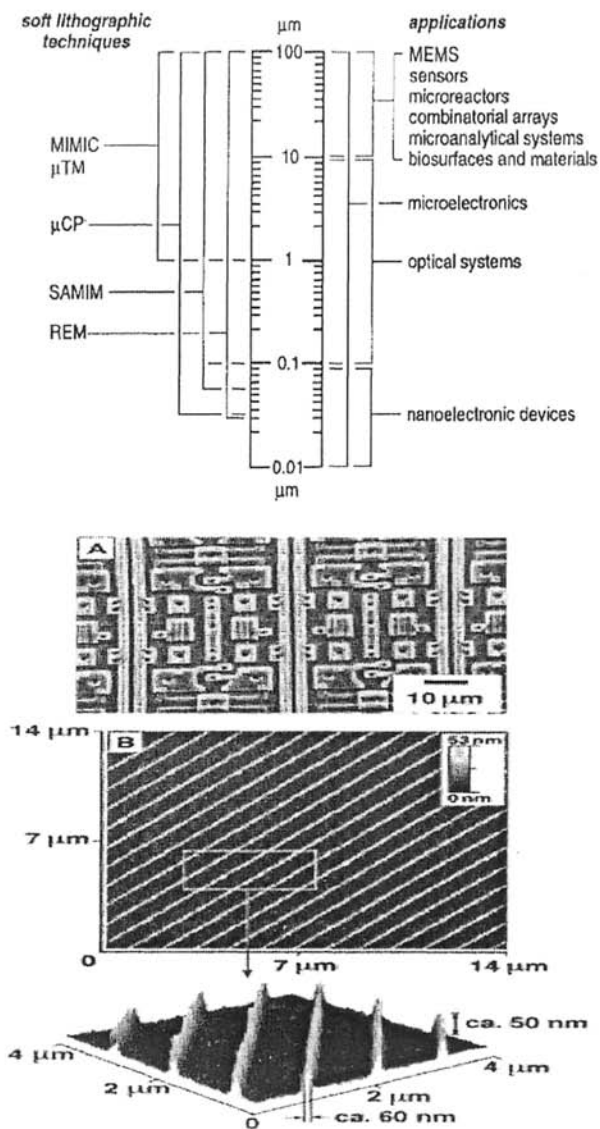


Fig. 12.18. Images of nanostructures created using MIMIC and a comparison of the micromolding techniques with their respective application to the micro- and nanoscales [5]

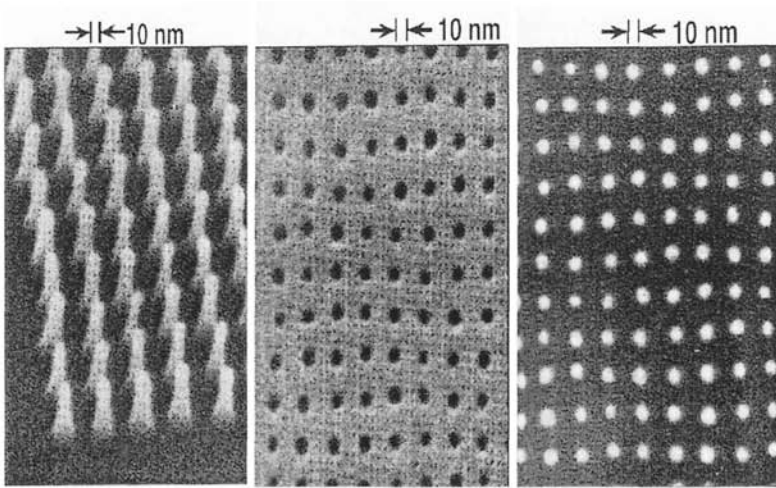


Fig. 12.19. Silicon mold with 10 nm diameter pillars that have imprinted holes into pieces of PMMA that are 60 nm deep and 40 nm apart from each other [9]

In general small holes are easier to imprint than pillars because they tear off the mold quite easily. Figure 12.19 shows images of molds and imprinted materials.

Nanoimprint lithography can be performed in one operation as a nanofabrication process but its future lies in its development as a nanomanufacturing process. This has recently been achieved by developing the roller nanoimprint lithography technique that uses a rolling mill to create nanofeatures.

Such features have been created in the form of microwave transistors T-gates and PMMA gratings. Figure 12.20 shows the roller nanoimprint process and transistor T-gates manufactured using the process. An interesting review of nanoimprint lithography has recently been published by Guo [10] who advances the ideas created by Chou [9] by commenting on the development of step-and-flash nanoimprint lithography, and combining processes such as photolithography and nanoimprint lithography to form hybrid processes such as reverse nanoimprint lithography.

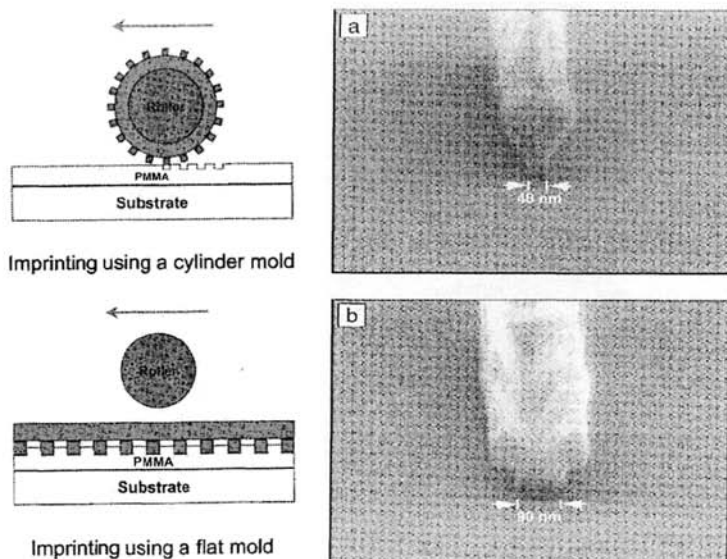


Fig. 12.20. Schematic diagram of roller nanoimprint lithography and two images of microwave transistor T-gates with footprints of 40 nm and 90 nm, respectively [9]

When combined with polymer inking techniques, a process is created that has common features associated with soft lithography and nanoimprint lithography. The simplicity associated with nanoimprint lithography has made it a strong candidate for a future nanomanufacturing process that can imprint nanoscale features and deposit a wide range of colloidal particles and self-assembled monolayers.

12.3.5 Lithographically Induced Self-Assembly

A variation of the nanoimprint lithography process is the lithographically induced self-assembly process, LISA (Fig. 12.21). This process allows pillars to “grow” from the surface of a viscous liquid between substrate and a mask. The self-formation of pillars forms a pillar array that can be the basis of creating three-dimensional

nanostructures. A variety of patterns have been observed depending on the template shape and size as well as the polymer used in the experiments. Processing conditions are also of vital importance when creating nanostructures. When processing conditions change, concentric rings are formed under certain conditions. Dynamic growth of the pillars has been observed using video techniques that show that pillars form one-by-one at the corner of the mask then at the edges propagating to the center. Figure 12.22 shows the protruding triangular pattern on the mask along with an AFM image of the surface of the features produced.

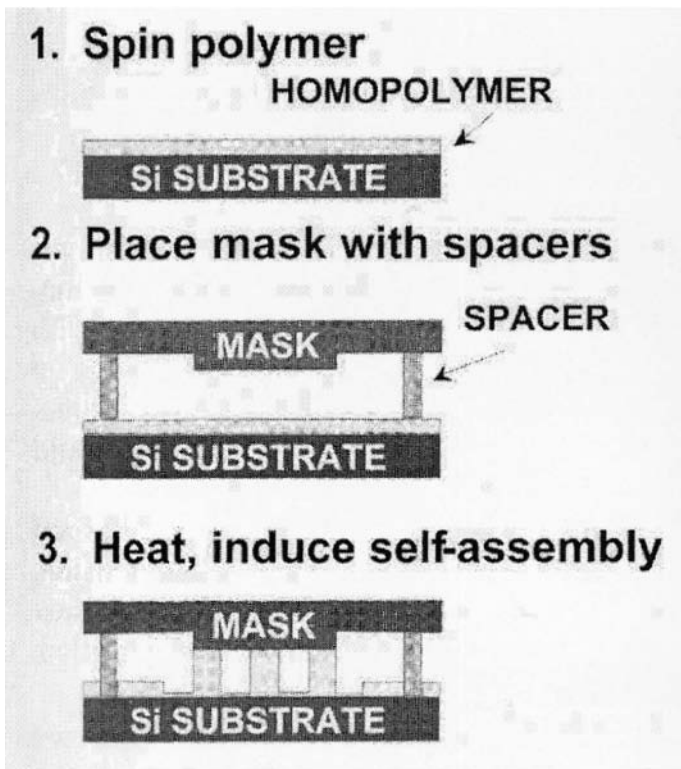


Fig. 12.21. Lithographically induced self-assembly process [9]

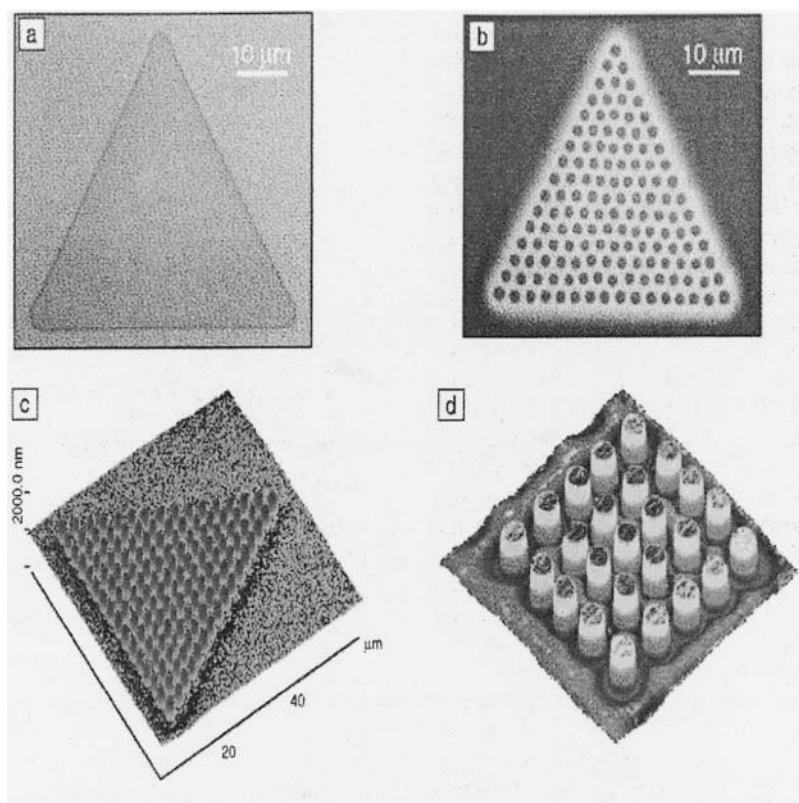


Fig. 12.22. LISA process showing: (a) protruding triangular pattern; (b) PMMA pillar array formed under the triangular pattern; (c) AFM image of pillar array; and (d) Shape and size of pillar arrays, which are 310 nm height, 5 μ m diameter, and 9 μ m spacing [9]

Applications of LISA include semiconductors, metal nanostructures, and biological arrays. Periodic arrays created by LISA are useful in memory devices, photonic materials, and biological structuring of hard and soft tissue. The future of both nanoimprint lithography and LISA lies in their ability to be adapted to manufacturing large-scale nanostructures using rollers and stamps.

12.3.6 Dip Pen Nanomanufacturing

Dip pen nanolithography can be adapted to deposit self-assembled monolayers in a manufacturing context by simply adding additional dip pen probes to the cantilever beam and adding reservoirs in order to deposit a multitude of nanoscale particles such as colloidal metals, molecules, and carbon nanotubes etc. This type of arrangement can be used to form nanoscale features very quickly by modifying an atomic force microscope. Figure 12.23 shows the construction of an array of “nanopens” that can directly write “ink” to the surface. The deposition of molecules by the nanoplotted is shown in Fig. 12.24. The process involves depositing the ink to a surface then selectively etching around the molecules to create trenches and removing the residue left behind. The resulting structure is viewed using the atomic force microscope to check topographic features of the nanostructure that has been created [11].

Another promising way of creating nanofeatures using a deposition process is ink jet printing, which was first used for depositing microstructures to substrates by Sachs at MIT.

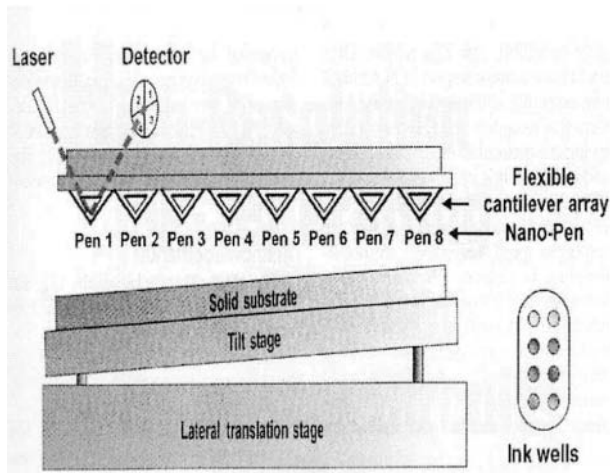


Fig. 12.23. Dip pen nanomanufacturing using the nanoplotted that dispenses a variety of inks, or one ink deposited multiple times [11]

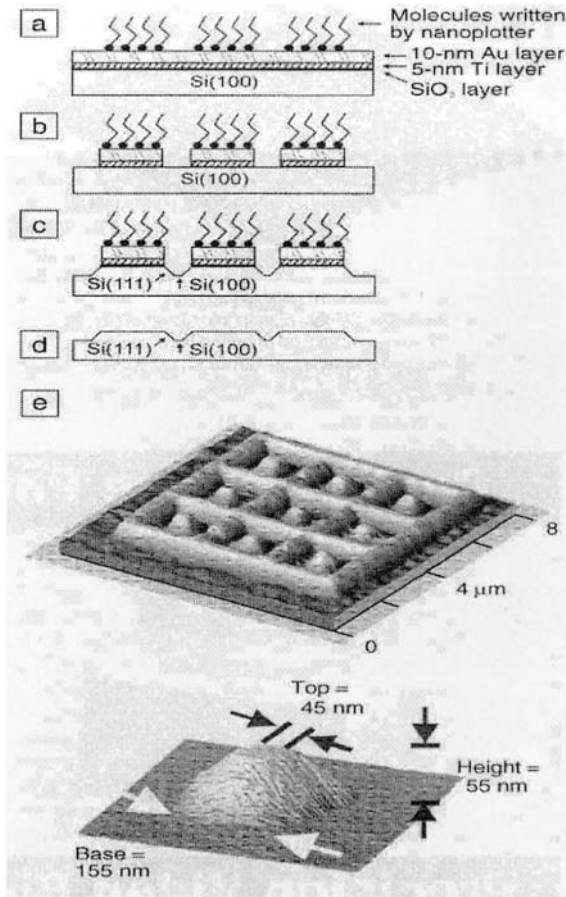


Fig. 12.24. Deposition of molecules written by the nanoplotter on to a gold layer on silicon. The AFM topographic image shows the nanometer resolution afforded by the process [11]

The ink jet printing of polymer transistors has resulted in a remarkable level of resolution and is a non-contact printing technique that is environmentally friendly and can be adapted for nanomanufacturing processing by adding more nozzles to the ink jet printer. Ink jet printing allows the precise control of liquid droplets forming on the surface of the substrate. Figures 12.25 and 12.26 show the resulting structures created by ink jet printing [12].

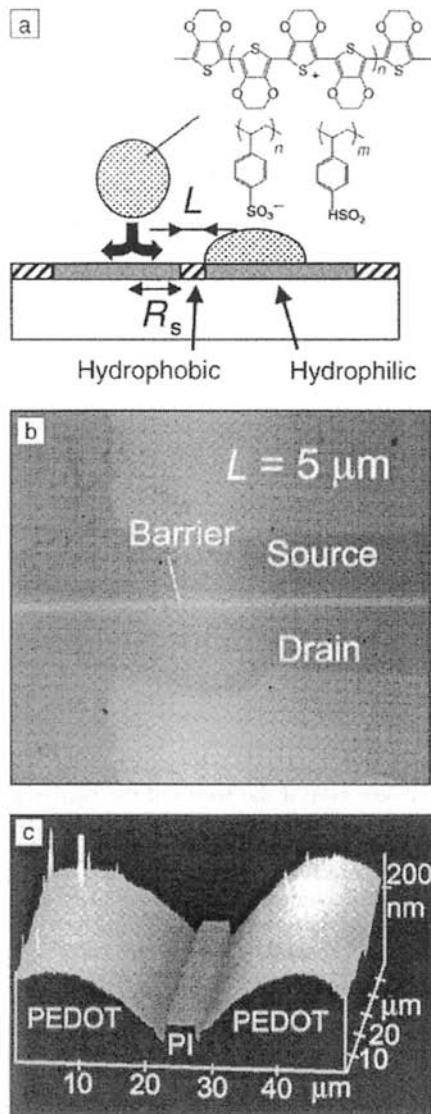


Fig. 12.25. Schematic diagram of high-resolution ink jet printing of source and drain electrodes of a polymer transistor [12]

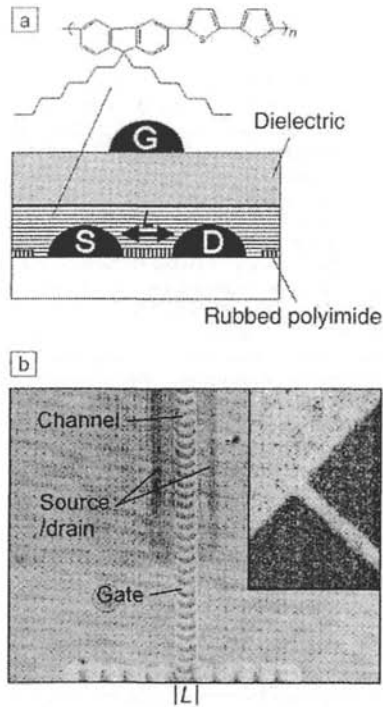


Fig. 12.26. Schematic diagram of a top-gate ink jet printed transistor showing the enlargement of the channel region [12]

12.3.7 Nanomanufacturing by Machining

Nanostructured materials such as metals have high hardness, strength, and ductility. However, their method of manufacture has inhibited their wider use. Nanostructured metals are typically manufactured by condensation from the vapor phase and by high-energy ball milling. The particulates produced are compacted and sintered to bulk form. The cost of these materials is typically hundreds of dollars per pound. Methods to produce a cheaper alternative include production by severe plastic deformation to achieve microstructural refinement such as rolling, drawing, equal channel angular extrusion (ECAE), and high-pressure torsional straining. Machining is one method to produce nanostructured metals [13-15]. Chip formation

produces high shear strains in the range between 2 and 10, strain rates up to 10^6 s^{-1} , and shear plane temperatures up to $0.7 T_m$. The production of chips creates these nanocrystals and is shown via the quick stop technique in Figure 12.27.

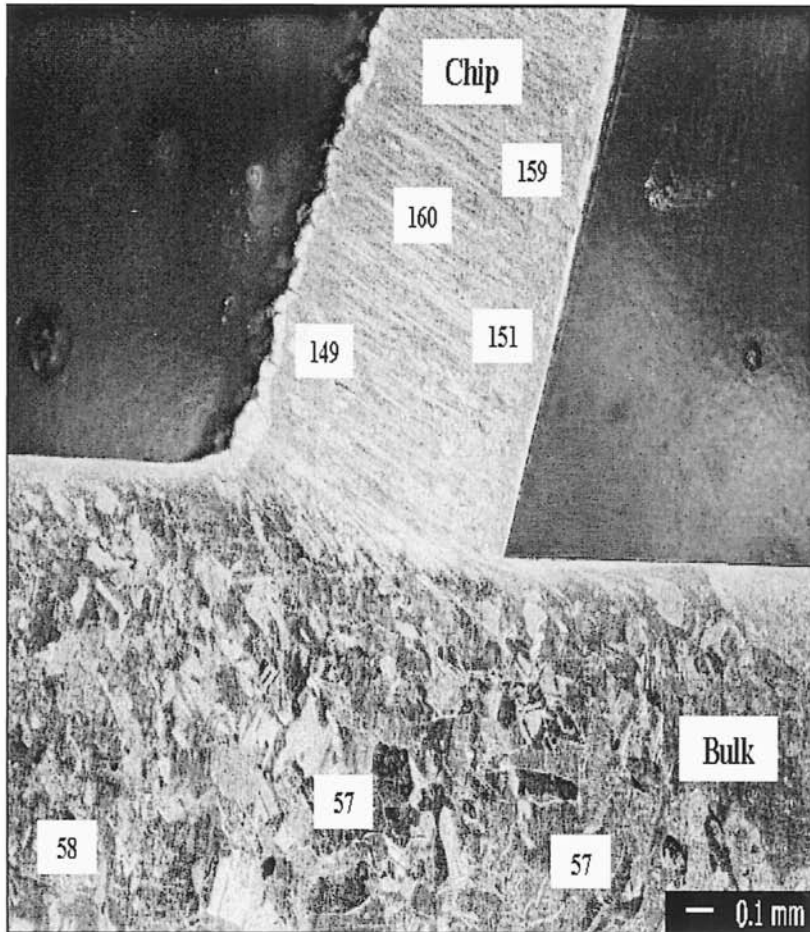
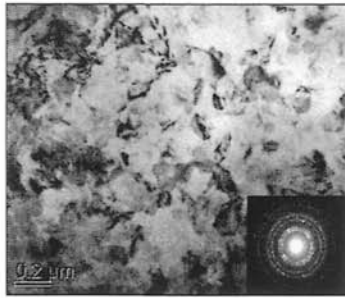
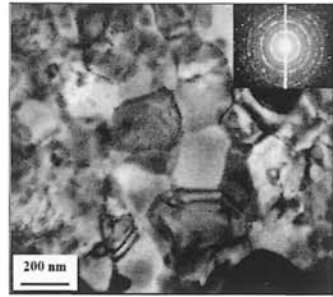


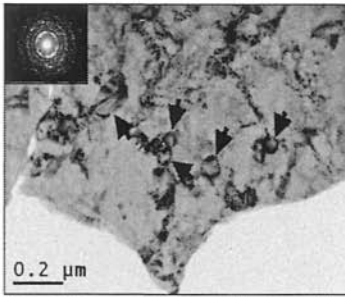
Fig. 12.27. Microstructure of partially formed chips produced using the quick stop device. The superposed Vickers' hardness values show the difference between bulk and chip material. The lack of visible grain structure in the chip illustrates the existence of sub-micron sized grains. Courtesy of S. Chandrasekara.



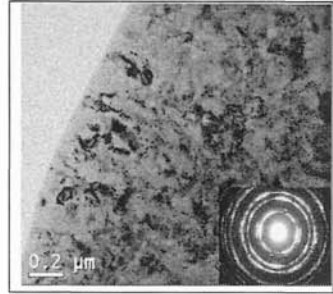
Al6061-T6, grain size: 75 nm



52100 steel, grain size: 330 nm



Ti, grain size: 90 nm



Inconel-718, grain size: 90 nm

Fig. 12.28. TEM images of various machining chips showing nanocrystalline structure. Regions of high dislocation density can be seen. This suggests that grains are highly deformed. Courtesy of S. Chandrasekara.

Figure 12.28 shows bright TEM images of machined chips and the corresponding selected area diffraction patterns. There are numerous grains with nanostructured features and elongated morphologies. Examination of the image suggests that grains are severely deformed and are under 1000 nm in size. Furthermore, grains are severely distorted with very high dislocation density. Distinct changes in aspect ratio have taken place, and convergent beam electron diffraction images show that nanostructured grains have both low- and high-angle grain boundaries.

Pure Aluminum

Transition from
elongated grains to
equiaxed grains with
high angle grain
boundaries

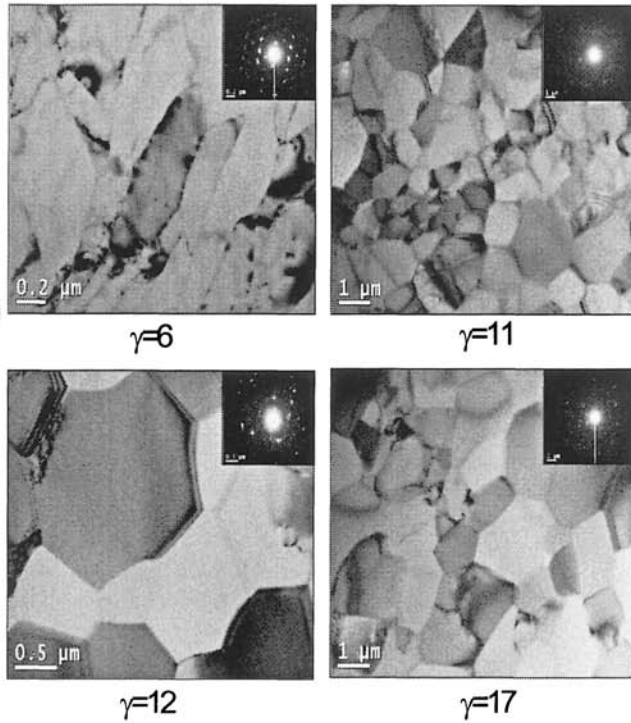


Fig. 12.29. Bright field TEM images of pure aluminum at increasing shear strains. Courtesy of S. Chandrasekara.

Figure 12.29 shows the bright-field TEM image of aluminum chips produced under increasing shear strains. The image shows the transition from elongated grains to equiaxed grains with high angle grain boundaries. The process of machining at increasing shear strains also increases the relative hardness of the chip compared to the bulk of the material. Figure 12.30 shows the difference between the chip and the bulk of the material. The chip is typically 2-3 times harder than the bulk material.

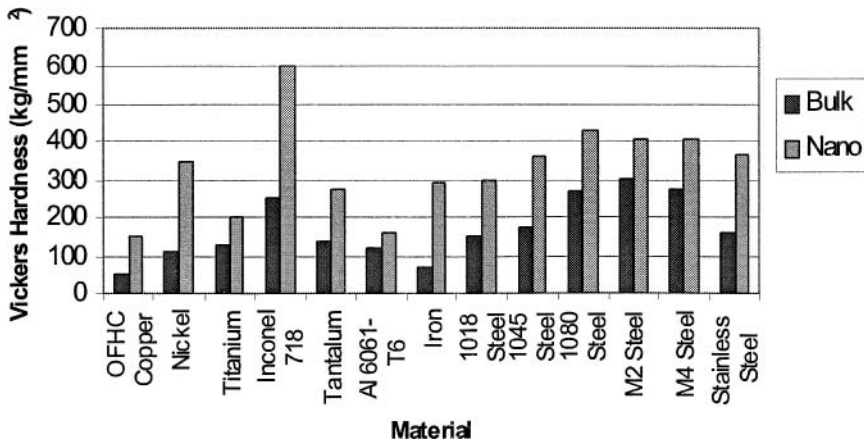


Fig. 12.30. Comparison between the hardness of the chip and the bulk material for various metals. Courtesy of S. Chandrasekara.

Conventional turning operations tend to produce chips that cannot subsequently be processed efficiently for forming nanocrystalline particulate products. For this purpose, modulation-assisted machining has been developed to produce unitary chips of the right shape and size. The process involves modulating the machining process to produce chips that can be used for infiltrating micro- and macroscale products. The production of unitary chips is shown in Figure 12.31. The figure shows the modification a spindle to machine with intermittent cuts. Figure 12.32 shows the effect of modulation on chip formation processes. The additional of adequate lubrication shows that segmented chips can be produced with grain sizes in the nanometer range. The process can machine a wide range of alloys and metals, provides an economic way to produce nanostructured products, eliminates secondary comminution, and provides an economic way of manufacturing large-scale particulate products.

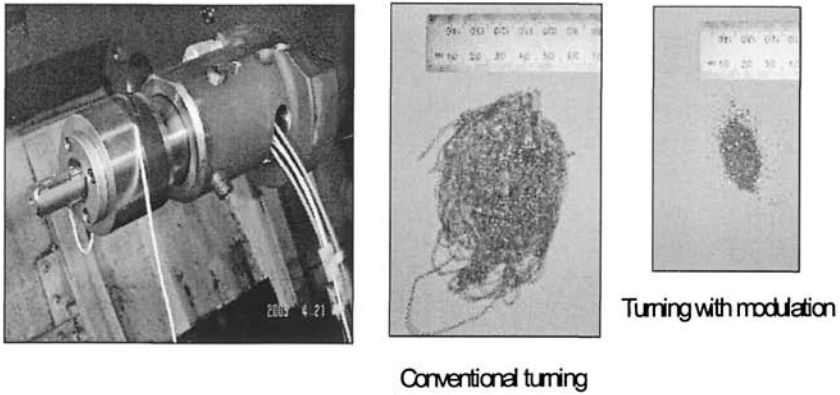


Fig. 12.31. Machine tool spindle retrofitted to perform modulation-assisted machining. Chip segments produced are shown

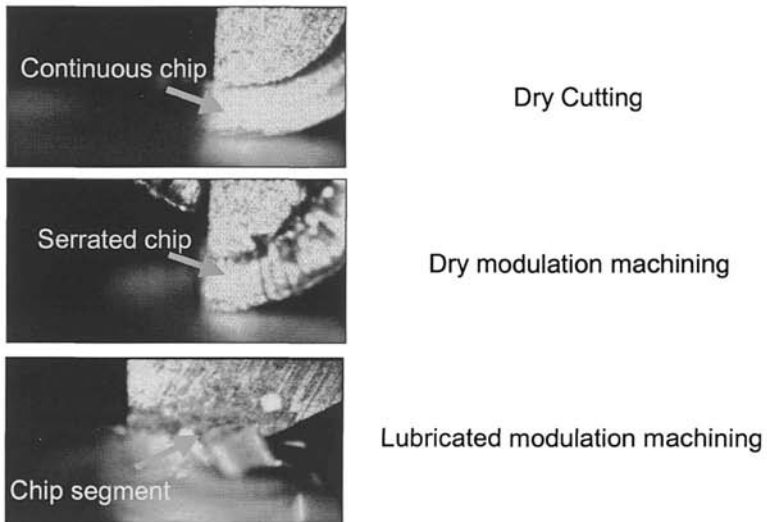


Fig. 12.32. Images of chips produced by dry cutting, dry modulation machining, and lubricated modulation machining. Courtesy of S. Chandrasekara.

The production of chips of different shape and forms can be accomplished using modulation-assisted machining. Figure 12.33 shows the types of chips created using modulation. The chips forms created are needles, platelets, and equiaxed forms and have aspect ratios between 1 and 200, and particle sizes ranging from 10 μm to 2 mm.

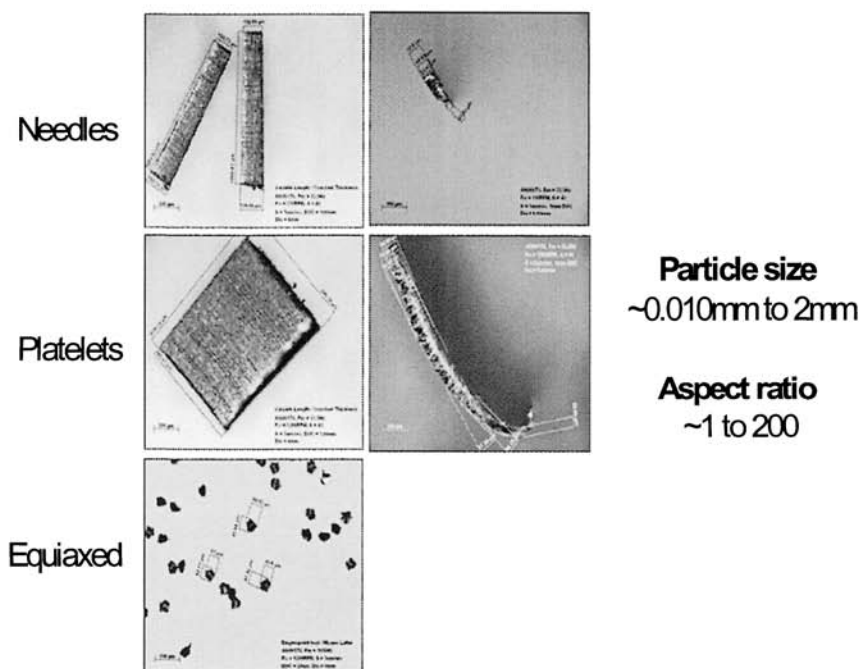


Fig. 12.33. Chip forms produced by modulation-assisted machining. Courtesy of S. Chandrasekara.

The advantages of producing nanostructured metals using these techniques clearly show how economically viable nanostructured products can be produced. The direct production of nanocrystalline particulates produces a wide range of metals and alloys with chip forms that have variable aspect ratios and sizes. Potential applications include: structural and wear components, spray applications,

thin and thick film coatings, ferromagnetic alloys, and metal and polymer matrix alloys. Nanostructured metals can be used to manufacture a wide variety of products by extrusion, vibratory compaction, cold spray, dynamic compaction, thermal spray, and sintering techniques. Nanomanufacturing by machining appears to be an extremely promising and economic way of improving the properties of micro- and macroscale products using nanostructured metals.

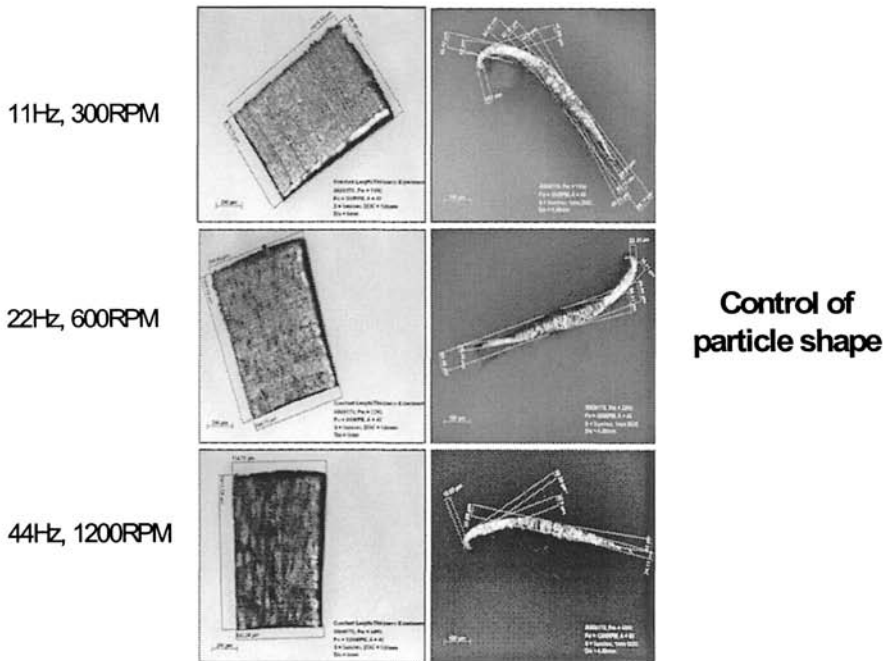


Fig. 12.34. Control of particle shape using modulation-assisted machining. Courtesy of S. Chandrasekara.

12.4 Commercialization Issues of Micro- and Nanotechnologies

This section is devoted to the key issues associated with the commercialization of products and services developed by Micro-NanoTechnologies (MNT). Research, prototype development, manufacturing, and marketing are intrinsic to any commercialization strategy. The availability of an appropriate infrastructure that bridges the gap between research and manufacture thus providing a seamless flow from concept to product realization is key to success. Very few nations have such an ideal infrastructure.

Historically, MNT are a set of enabling technologies that have evolved from the semiconductor industry, which was based entirely on silicon as a material. Product based MEMS, microsystems, or micromachining technologies really came into the market in the early 1980s because of their acceptance by the American automotive industry for use in automobiles. These products were manifold pressure sensors and fuel injector nozzles. They had to be ultra-reliable low cost products that could be mass produced and truly commercial. The 1990s gave birth to more commercially successful devices that sensed, actuated, and were smart. Sensors therefore became the largest market for microproducts since they pervaded almost every sector. Integration and packaging technologies had to be developed to meet market demand for new products such as the air accelerometer and ink-jet print head. The actual assembly, connection, integration and packaging of components to manufacture a useful product added a dimension of complexity and presented challenge to the designers and manufacturers. The emergence of nanotechnology and nanosystems, i.e., a two to three orders of magnitude smaller in dimensions greatly increases the magnitude of this challenge. Like microsystems, nanosystems will be disruptive so new manufacturing paradigms are required. They will be capable of realizing a limitless range of new products and systems; some will have a significant impact on societies.

Commercialization is about having a sustainable and marketable product at the right time. The performance at the technology-product interface produces the competitive advantage. This first has to clearly defined and understood by companies if they are to embrace

these technologies. The issues of market-demand versus technology push, which still haunt the strategist, also must be carefully examined before any new developments are pursued.

Unlike more conventionally produced products, markets for MNT products have unique characteristics, like the products themselves. For example, the markets for more conventional products in which microsystems are embedded can be leveraged by a factor in excess of 50 through enhancement and innovation. This is partly the reason for variability in the estimates of market growth for products, particularly in areas such as IT, medicine, and healthcare. Realistic roadmaps and market surveys can be of great value in formulating market strategies. They help reduce risks but do not eliminate them. The basic issues associated with developing a new MNT product and taking it to market is outlined below.

12.4.1 Commercialization Issues

The full market exploitation of a technology requires a clear path to commercialization. Such a path has many steps, which need to be taken and understood before progress can be made in taking a new product to market. MNT is really a set of novel enabling technologies that have product platforms extending across many domains. While the mass production of components, particularly sensors based largely on established IC technology is well developed; the full production of new systems is inhibited by lack of manufacturing capability and maturity. Commercialization requires a seamless transition from the laboratory-scale and prototype development to production capability; both for batch processing for small to medium scale and continuous processing for large-scale manufacture. MNT-based products have special needs; the lack of human intervention and the need for integrated manufacturing will require new methodologies. As nanotechnology develops, and if ever self-replication becomes a reality, manufacturing will face profound new challenges and take on new dimensions.

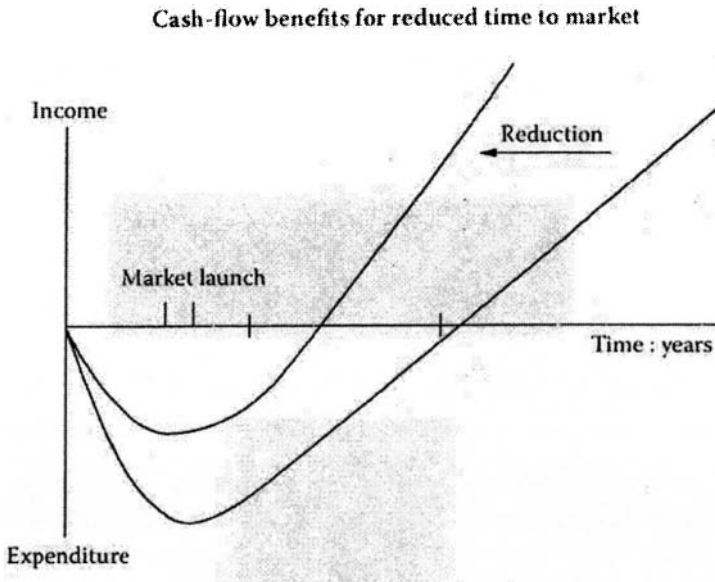
12.4.2 Product -Market Interface

Micro- and nanotechnology will revolutionize manufacturing for many existing industries. These technologies stimulate innovation and have the potential to provide an unlimited range of new products and services by leveraging skills from many different sectors. For example, in the ink-jet printer the innovation is the design of the microfluidic jetting system. It revolutionized printing by replacing conventional methods almost immediately with the result of producing a step-change in industry and eventually producing a greatly increased market. This paradigm shift also resulted in changes to work practices and the pattern of home activities. Printing was no longer just for the office or professional environment but could be done at home. The almost simultaneous development of the portable desktop computer, enable people to do their own printing. This empowerment enables people to work from home, resulting in new types of self-employment. Both these products have many embedded micro-components and microsystems that are linked by a common market.

Pressure sensors are another example of product with generic application areas. They are imbedded into products used across many sectors of industry from applications in automobiles to diagnostic instruments in medicine. The leveraging effect they can have will substantially increase the value of the product and the size of its market. This ubiquitous nature of microsystems makes them universally useful. Once generic designs are established, customization is less costly. Most of the cost is transferred to packaging, which can represent up to 80% of the cost of production.

MNT can provide a single solution to problems across multiple industries rather than a single, market-driven application. This can change a company's strategic approach to product development as many applications and markets can be pursued for one product thus increasing market share at a reduced cost. In excess of 60 industries have been identified as early adopters of MNT and have gained market benefits. The challenge for commercialization is reduction of the time-to-market and a profitable return on investment [16]. Figure 12.35 illustrates the movement across a timeline that is necessary for an investor to show in a viable business plan. This is particularly

relevant for small companies where cash flow dominates profitability and survival of the business.



12.4.3 Commercialization Infrastructure

It has now accepted that one of the barriers to commercialization of MNT is the lack of suitable infrastructure for supporting R&D, product development and manufacturing of an end product. A number of Government support programs and projects exist in some European and Asia-Pacific countries and in the United States for building or improving deficient infrastructure. But these are often not focused to provide the necessary range of equipment, expertise and facilities to meet the challenges of manufacturing. Recent large-scale funding support by many Governments for supporting

nanotechnology R&D has boosted confidence but it will take some time for this funding to filter down and benefit the manufacturing industry. The support for nanotechnology has distorted the development process as most companies still require further funded development for microdevices and systems. They see nanotechnology products as being too far in the future. The initial rush of investors has been curtailed by the long-term reality.

Nanotechnology, like its larger scale microtechnology, is disruptive. It is unstructured with uncertain technological outcomes making commercialization difficult to quantify and justify financially. However, although MNT products can be technologically revolutionary in nature, commercialization of them is usually incremental. This at least makes incorporating it into an existing business regime less risky. The rate of incorporation is governed by market demand. It is sometimes easy to identify a market but not to enter it.

Customers do not like change, particularly where legislation and regulation issues are involved which is the reason the medical market has been cautious and slow to react. The opposite situation can occur, however, as in the optical communications market where technological innovation exceeded market demand resulting in over capacity of supply and many companies becoming financially over committed and failing. It produced a knock-on effect resulting in massive decline in the industry, which adversely affected many large and small companies. This taught the industry a hard lesson that will make the next product push move more slowly. It will be in the health care diagnostic market where regulation and public acceptance will dictate the pace of market growth.

The acceptance level of MNT is different for companies of different sizes. Small companies are more adaptable to change as their management structure is able to make quicker decisions, sometimes survival may depend on bringing a new product to market to fill a niche. Large companies often have an infrastructure and a management system in which a Board of Directors make decisions. This can often produce a delay and even prevent new product innovation from being implemented thus losing a competitive edge in the market. The organization of a nation's commercial infrastructure and the extent of the free market economy also determine market growth in particular sectors. In countries where health care has a higher pri-

ority than automobiles then suppliers will be seeking appropriate products. This will then drive new developments.

12.4.4 Supply Chain Networks

A supply chain network is an important element in building a commercialization infrastructure. This must incorporate technology and knowledge support, training, design, prototyping, manufacture, and marketing. Each one of these areas can be divided up into segments. This gives opportunities to small companies and start-ups to become parts of the supply chain. A point of entry and a clear path to market are essential, particularly for small to medium size companies. Each step in the commercialization process as shown in Fig. 12.36 must be understood.

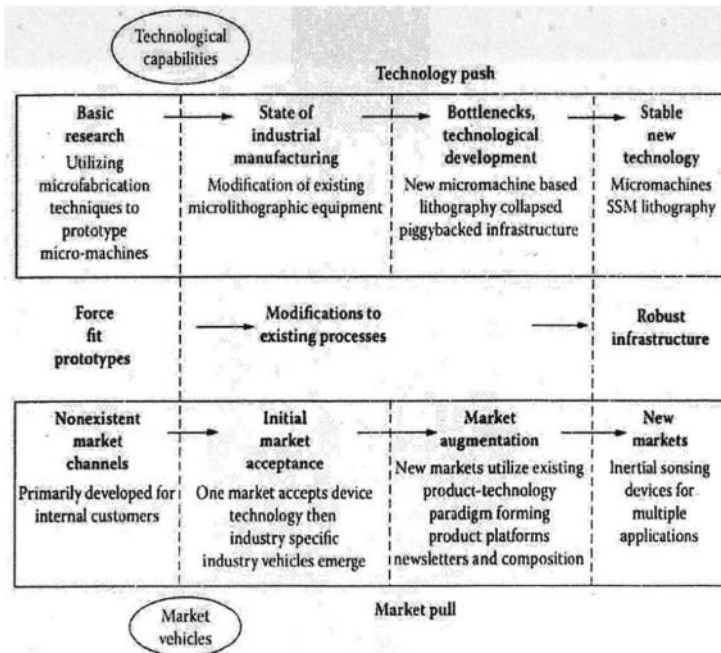


Fig. 12.36. Infrastructure model for discontinuous innovations

Stage 1 is basic research and non-existent markets. Existing technologies need to be modified for non-silicon processes to force fit between manufacturers and markets. In Stage 2, the technology-market-product paradigm starts. Business entrepreneurs enter and small numbers of products emerge. At Stage 3 bottlenecks occur as a result of technology development and market augmentation issues. New products possibilities are reviewed and investments made. Production and market issues such as packaging and capital equipment suppliers and customers are important. Stage 4 is where the technology and markets are stable and a robust infrastructure emerges. Large companies now take over from small companies and start-ups. The entrepreneur is replaced by the sales engineer and strategic market planning exists.

12.4.5 Product Manufacture

Packaging, Testing, and Standardisation

Design and packaging technology is key to the manufacture of commercial microproducts and can represent up to 80% of their cost. It is fundamental to product functionality and is required to inter-connect, protect and provide an interface between microsystems and the macroworld to facilitate human interaction in the working and living environment.

Packaging is the less developed of all micromanufacturing technologies and is currently considered to be the major obstacle to microproduct and microsystems commercialization. Until recently packaging was considered only after a component or sub-systems had been designed and developed as a concept. This inevitably causes problems at the assembly and packaging stage owing to a variety of incompatibility problems. Packaging solutions must be integral to the design process and significantly reduce manufacturing costs.

Four levels of packaging can be required to enable micro-components to be inter-connected and integrated into a fully func-

tional end product. For microsystems, they are: die, wafer level processing, subsystem, and assembly of subsystems to system (product). These are analogous to chip, card, board, and system in the silicon-based integrated circuit.

Design, assembly, bonding, encapsulation processes, materials, reliability, environmental issues, and functionality all provide major challenges to packaging. This is why design and packaging technologies constitute the largest proportion of manufacturing costs.

The lack of agreed standardization is serious disadvantage to wide-scale manufacture. It inhibits expansion of a market sector as suppliers cannot acquire compatible components and sub-systems. Various international groups such as SEMI and NEXUS have set up standards committees that are becoming proactive in attempting to obtain agreement between manufacturers on standards. This is in response to users demands for standards in interfaces, signal connectors and microfluidic connections. Other important areas include electromagnetic compatibility (EMC), electromagnetic interfacing (EMI) and radio frequency interface (RFI) standards to be applied at the design stage. Currently industry generally follows IC standards but many of these are inadequate or unsuitable for microproducts.

12.4.6 Manufacturing Centers

There are very few, if any, centers in the world dedicated to the development of manufacturing technologies, whereas in almost all countries extensive R&D facilities and centers exist. This over emphasis on R&D driven by academic research has been a principal reason for the retardation in commercialization. Most of the knowledge and experience resides in such centers. Manufacturing is in the domain of industry. Prototyping and the R&D needed to achieve success are often expensive and lacking. Very few small companies can afford to carry this out and therefore are excluded from the market unless they collaborate commercially with larger companies or have access to central facilities. This lack of pre-production prototyping facilities has now been extensively recognized as a barrier to commercialization and has stimulated some countries to initiate

plans to build such centers. An example of such a proposal is outlined below

12.4.7 The UK-NMPC Proposal

A proposal to develop a National Microsystems Packaging Center (NMPC) in the North West of England, now reaching its final stage, was made by the North West Development Agency in 2003. This will fill a much-needed gap in the UK infrastructure and will be a model for others to follow. If successfully completed it will place the UK in a leading and competitive position for prototype development and realization.

The NMPC will provide customers access to a competitive and comprehensive microsystems packaging service to realise manufacturable products for specific applications from conceptual designs through to pre-production prototypes and low volume pilot production, as visualised in Fig. 12.37.

The Center will be established primarily to supply customer needs through a commercially based service by providing design, modeling and simulation, prototyping, assembly, test and reliability facilities. Combined with volume-manufacturing techniques, it will enable products to be scaled down for high volume. Opportunities for limited volume production will be made available. This is particularly important for customers with products of high value but low in volume.

Actual development of the microstructures or microsystems will be carried out elsewhere as the Center will be mainly concerned with design, prototyping, and pre-production work for product qualification and any supporting R&D that is required.

The overriding benefit of the Center will be its effect on cash outlay and product development costs. It will obviate the need for customers to invest in expensive development equipment, thereby saving both manpower and capital; it will reduce the time-to-market, and hence increase the return on investment of new microsystems-based products. This is an essential element to any commercialization strategy.

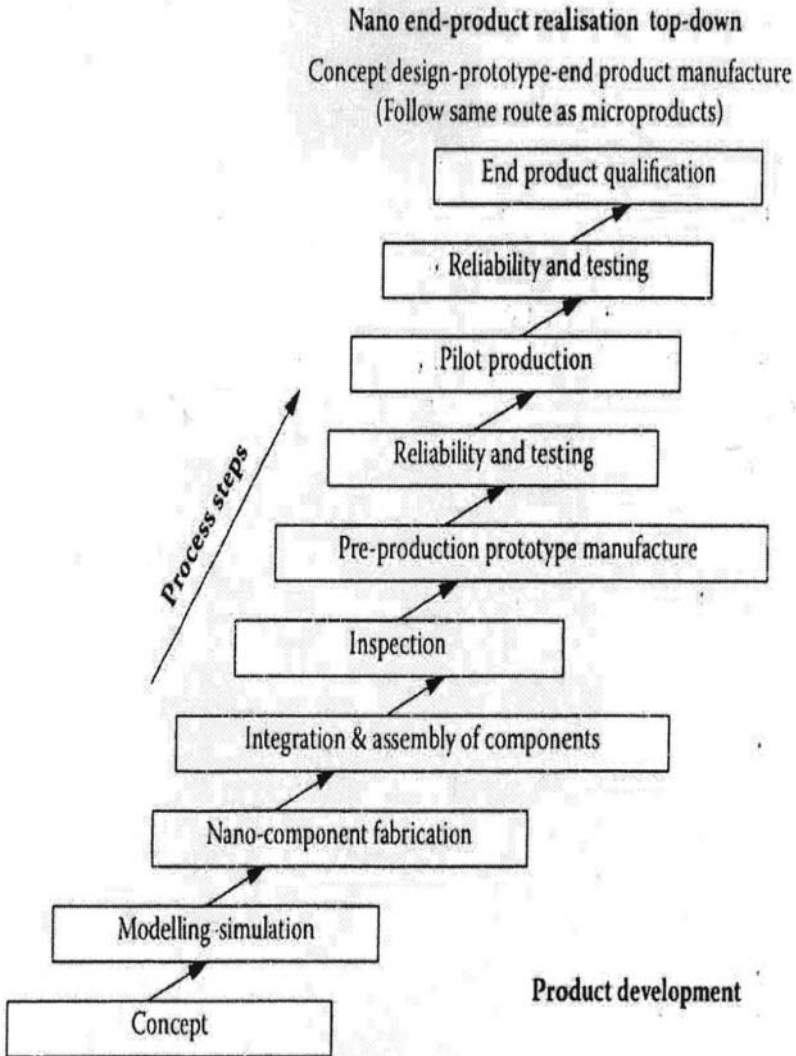


Fig. 12.37. Model adopted by the NMPC to realize product development and manufacture of micro-and nanotechnology products

12.4.8 Micro-Nanotechnology Markets

Market information and guidance material for strategists can be found in a number of market surveys and roadmaps that have been recently published. Technology and market roadmaps are particularly useful as they present a 'state-of-the-art' of the various technologies and give useful insight and foresight for information. Walsh [17] carried out the first a detailed study on international roadmapping for a disruptive technology focused on microtechnology and a top-down nanotechnology. This provided the basis for the development and publication of the first international roadmap on the subject, by MANCEF (Micro-and Nanotechnology Commercialization Educational Foundation), involving 400 people over a period of 5 years [18]. This stimulated the publication of another international Product-Technology Roadmap by NEXUS [19] the European organisation, (Network of Excellence in Multifunctional Microsystems).

NEXUS also published a market analysis [20] carried out by its Task Force. This predicts a rapid increase in the growth for microsystem-based products, from a global figure of about \$40 billion in 2002 to \$68 billion in 2005. Emerging new products and applications are expected to produce a 20% annual growth in the market. In Europe the market alone for products based on the use of micro-devices has increase to \$550 billion since 1996. These figures are linked to more than 70 different application areas. The mass markets and main fields of application are dominated by IT peripherals, biomedical, automotive, and telecommunications. Ink-jet printers, displays, and data storage for computers and sensors for automotive applications were early adopters and drivers of microsystem technology; biomedical diagnostic and health care products are expected to lead in the near future. RF-based microsystems will likely spearhead the drive for new products.

Market forecasts are driven by business and policy specialists eager to gain a competitive advantage and unfortunately are often out of phase with reality. It is generally agreed that anticipated market sizes, growth rates, and the development of new markets are very different for different applications of MNT products. Market predictions or forecasts must therefore always be viewed with qualification

and an understanding of the nature of both the technology and societal needs. An unexpected urgent demand, for example, for particular air pollution monitor or a biological sensor may temporarily distort a market prediction. As terrorism and climate change become more urgent issues, demands on MNT to deliver new innovative products will increase. These types of market demands are difficult to predict in advance.

12.5 Future Developments

The future of nanomanufacturing looks incredibly promising when one looks at processes such as soft lithography and nanoimprint lithography. The deposition of colloids and nanoinks of self-assembled monolayers, and the impression of nanostructures on soft materials ensures that industries such as the semiconductor industry will be presented with processes that will overcome the problems associated with the diffraction limit in optical lithographic processes. The greatest challenge to nanomanufacturers is the development of manufacturing processes that can be applied to engineering materials such as metal alloys and ceramics. Manufacturing processes for these materials appear to be relatively abundant at the microscale but do not appear to be available at the nanoscale.

Emerging nanomanufacturing processes will almost certainly be used to produce semiconducting devices using carbon nanotubes, nanostructured catalysts, lighter and stronger nanomaterials, improved pharmaceuticals with features such as programmed drug delivery at desired targets, reliable filters for water decontamination, efficient solar energy convertors, efficient fuel cells, durable composite materials, high-altitude long endurance space vehicles, nanoscale sensors, and coatings that will reflect heat and resist oxidation.

12.6 Problems

1. Describe how electroplating produces microcomponents.
2. How do casting processes produce microcomponents.
3. Explain how molding processes will be advanced to produce nanometer scale features.
4. How are thin layers cast to produce microfluidic devices.
5. Compare hard molding tools.
6. What is hot embossing?
7. What are the future developments in micromanufacturing?
8. Describe how semiconductors will be manufactured in the future.
9. What is soft lithography and how will it aid the manufacture the semiconductors?
10. Describe nanomanufacturing by molding.
11. What is nanoimprint lithography?
12. How do machining processes generate nanocrystals?
13. How are nanometal products manufactured?
14. Describe how micro-and nanotechnology products are commercialized.

References

1. Jo B et al., *J. Microelectromechanical Systems*, **9**, p.p. 76 – 81, 2000.
2. Narasimhan J and Papautsky I, *J. Micromech. Microengg.*, **12**, p.p. 96 – 103, 2004.
3. Becker H and Garner C, *Electrophoresis*, **21**, p.p. 12 – 26, 2000.
4. Tseng A, *J. Micromech. Microengg.*, **12**, p.p. R15-R34, 2004.
5. Xia Y and Whitesides GM, *Angew. Chem. Int.*, **37**, p.p. 550 – 575, 1998.
6. Love JC, Anderson JR, and Whitesides GM, *MRS Bulletin*, **26**, p.p. 523 – 528, July 2001.
7. Huck W, *Int. J. of Nanotechnology*, **1**, p.p. 119 – 129, 2004.
8. Hamley IW, *Nanotechnology*, **12**, p.p. R39-R54, 2003.
9. Chou SY, *MRS Bulletin*, **26**, p.p. 512 – 517, July 2001.

10. Guo LJ, J. Phys. D.:Appl. Phys., **37**, p.p. R123 – R121, 2004.
11. Mirken CA, MRS Bulletin, **26**, p.p. 535 – 538, July 2001.
12. Sirringhaus H, Kawase T, and Friend RH, MRS Bulletin, **26**, p.p. 539 – 543, July 2001.
13. Brown TL, Swaminathan S, Chadrasekar S, Compton WD, King AH, Trumble KP, J. Mater. Res., **17**, Number 10, October 2002.
14. Swaminathan S, Swanson C, Brown TL, Kezar RF, Chandrasekar RF, Compton WD, Trumble KP, Mat. Res. Soc. Symp. Proc., **821**, P9.5.1-9.5.6., 2004.
15. Swaminathan S, Swanson C, Brown TL, Kezar RF, Chandrasekar RF, Compton WD, Trumble KP, Mat. Res. Soc. Symp. Proc., **821**, P8.27.1-8.27.6., 2004.
16. Tolfree D and Eijkel K, Reducing Time-to-market for Micro-Nanotechnology Base Products; Presented at World Nano--Economic Congress- Europe, London, 6 November 2003.
17. Walsh ST, Roadmapping a Disruptive Technology, Technology Forecasting and Social Change, **71**, Issue 1-2, January – February 2004.
18. MANCEF Roadmap, by Micro-Nanotechnology Commercialisation Educational Foundation, Published 2002, Naples, Florida, US.
19. NEXUS -Product Technology Roadmap, Sept 2003, CEA Grenoble, France.
20. NEXUS – ‘Market Analysis for Microsystems 2000-2005’, February 2002, CEA Grenoble, France.

Subject Index

A

Abbe's principle, 221-225
Abrasive materials, 261-266
Absolute machining threshold velocity, 482-492
Addition phase, 5-10
Adsorption, active species, 99-102, 337-342
AFM, see Atomic force microscopy (AFM)
AISI steel, 144-149, 154-178
Alignment, x-ray mask to substrate, 58-78
Alumina, 261-274, 569-584
Aluminium oxide, 261-274, 569-584
AM-AFM, nanofabrication, 33
American Society of Precision Engineers, 600
AMTV, see Absolute machining threshold velocity (AMTV)
Anisotropic etching, 103
ANSYS software, 499-515
Apparatus
 diamond nanogrinding, 522, 535
 mechanical micro-machining, 208-218
Applications
 micromolding, 120
 nanocrystalline diamond, 524-527, 535-544
 nanometric machining, 592
Archimedes' law, 544-568

Armchair nanotubes, 40
Aspheric surface generation, 299-314
Astigmatic focusing error, 305-310
Atomic force microscopy (AFM), 30-42, 648-670
 carbon nanomaterials, 38-41
 laser nanofabrication, 464-467
 lithographically induced self-assembly, 654-664
 machining, 1-46
 nanofabrication, 2-32
 surface texture measurement, 15-40, 612-631
Axsun, LIGA services, 59

B

Beam characteristics, 387, 388-393
BEG, see Bias-enhanced growth (BEG)
BEN, see Bias-enhanced nucleation (BEN)
Beryllium mask materials, 83
Bias-enhanced growth (BEG), 345-356
Bias-enhanced nucleation (BEN) 346-365
CVD diamond technology, 345
Deposition routes, 356
Binderless wheels, 299

BioMEMS devices, 191
 Blades, mechanical micro-
 machining, 226-249
 Bonding bridges, 496-518
 Bonding systems, 240-251,
 496-518
 Bond materials, 245, 496-519
 Bottling, high-aspect ratio mi-
 crostructures, 100-114
 Bottom-up manufacturing, 1-
 50, 625
 Boundary conditions, me-
 chanical micromachining, 179
 Boundary region, high-aspect
 ratio microstructures, 96
 Bowing, high-aspect ratio mi-
 crostructures, 100-114
 Brittle-to-ductile transition,
 434

C

CAIBE, see Chemical-assisted
 ion beam etching (CAIBE)
 CAMD, see Center for Advanced
 Microstructures and Devices
 (CAMD)
 Cancellous bone, 220
 Carbon nanomaterials, 39-46
 Carbon nanotubes, see Carbon
 nanomaterials
 Casting, 635-646
 Center for Advanced Micro-
 structures and Devices (CAMD),
 95
 Centerless grinding opera-
 tions, 275-279
 Center of Optics Manufactur-
 ing, 629

CFD, see Computational fluid
 dynamics (CFD) approach
 CFX software, 217-229
 Chemical-assisted ion beam
 etching, 115-126
 Chemical vapor deposition
 (CVD) diamond technology
 advantages/disadvantages,
 323, 336
 basics, v, 323-327
 bias-enhanced nucleation,
 349
 DC plasma-enhanced, 333
 filament assembly modifica-
 tion, 334
 heteroepitaxial growth, 324-
 326
 historical developments,
 326-329
 homoepitaxial growth, 324-
 328
 hot filament, 334
 machining, 366-368
 mask materials, 336
 materials, substrates, 337-
 341
 metallic (Mo) wires, 356
 metastable diamond growth,
 329, 350
 microdrills, 357-359, 367
 microwave plasma-
 enhanced, 332
 modified hot filament CVD,
 354
 Mo/Si substrate, 339
 nanocrystalline diamond,
 377
 nucleation and growth, dia-
 mond, 348-355
 performance studies, 367-
 368
 plasma-enhanced CVD, 334

- pretreatment, substrates, 338
- process condition, 323-325
- process types, 324-326
- properties, diamond, 325
- RF plasma-enhanced CVD, 324
 - Si/Mo substrate, 339, 357
 - substrates, 337
 - synthesis, diamond, 326-329
 - technology development, 326-336
 - temperature influence, 351
 - three-diamond substrates, 356
 - time-modulated CVD, 372-380
 - WC-Co, 339, 342-344, 357
 - Chip formation
 - mechanical micro-machining, 191
 - nanometric machining, 591
 - Chiral nanotubes, 46
 - Chirped pulse amplification, 387-403
 - Chromatic aberrations, 300
 - Circumferential damage, 480, 493, 495
 - CIRP, see International Institute for Production Engineering Research (CIRP)
 - Clays and clay-based fluxes, 545-568
 - Closed-form solution model, 458-460
 - Closed-loop structural configuration, 612-630
 - CNC, see Computer Numerically Controlled (CNC) machines,
 - Coanda effect, 191-192
 - COC, see Cyclo-olefin copolymer,
 - Commercialization issues
 - basics, 672
 - infrastructure, 673
 - manufacturing centers, 683
 - markets, 672-674
 - product manufacture, 677
 - product-market interface, 678
 - supply chain networks, 672-682
 - Complex molds, nanometric machining, 592
 - Computational fluid dynamics (CFD) approach, 233-251
 - Computer Numerically Controlled (CNC) machines, 93, 221-225, 299-313
 - COMS2004 conference, 672
 - Concentration, grinding wheels, 261
 - Conducting layers, 1-8
 - Constant height mode, 1-50
 - Contour Fine Tooling, 629
 - Control, nanometric machining, 594, 613-628
 - Conventional grinding, 275-280
 - Conventional machining comparison, 277-280
 - Coulomb forces, 57-64
 - CPA, see Chirped pulse amplification (CPA)
 - Cranfield Unit for Precision Engineering (CUPE), 630
 - Creep-feed grinding, 275-280
 - Critical depth, cuts, 255-314
 - Cropping operations, 278

Cubic, boron nitride, 261, 279-288

CUPE, see Cranfield Unit for Precision Engineering (CUPE)

Cut-off grinding wheels, 280

Cut-off operations, 277

Cutting edge radius, 182-188, 595-611

Cutting tools, 182-186, 195-208, 323, 625-627

Cyclo-olefin copolymer (COC), 55-95

Cylindrical grinding operations, 279

Czochralski process, 1-43

D

Damping properties, 499, 595-615

Daresbury synchrotron source, 56

DC plasma-enhanced CVD, 336

Decomposition, adsorbed species, 99-135

Deep reactive ion etching (DRIE), see also Reactive ion etching (RIE)

Deep x-ray lithography (DXRL), 58

Deposited doses, 78-87

Design

grinding wheels, 255, 545-567

micromolds, 121-131

water-based machine

tools, 499

Deterministic mechanical nanometric machining, 592

Diamond, abrasive properties, 255-260, 325, 524

Diamond nanogrinding, see also Micro- and nanogrinding apparatus,

basics, 521

bonding bridges and systems, 496

dissolution models, 549-559

fracture-dominated wear model, 534

fusible bonding systems, 545-557

future directions, 589

Jackson and Mills' model, 500-512

Jander's model, 500-512

Krause and Keetman's model, 545-556

laser dressing, nanogrinding tools, 569

loaded nanogrinding grains, 524-535

Monshi's model, 545-556

nanogrinding, 521-588

nanogrinding wheels, 545

nomenclature, 524

piezoelectric nanogrinding, 522

porous nanogrinding tools, 545

procedure, 524-529

quartz, 545-555

refractory bonding systems, 554

stress analysis, 545-553

x-ray diffraction, 545-550

Diamond technology, CVD

advan-
 tages/disadvantages, 323, 334
 basics, 323-325
 bias-enhanced nuclea-
 tion, 349
 DC plasma-enhanced
 CVD, 333
 filament assembly modi-
 fication, 338
 heteroepitaxial growth,
 324-333
 historical developments,
 326-329
 homoepitaxial growth,
 298-299
 hot filament CVD, 334
 materials, substrates,
 337-346
 metallic (Mo) wires, 356
 metastable diamond
 growth, 331, 322
 microdrills, 357-360,
 367
 microwave plasma-
 enhanced CVD, 333
 modified hot filament
 CVD, 343
 Mo/Si substrate, 339
 nucleation and growth,
 diamond, 340-347
 performance studies,
 367-370
 pretreatment, substrates,
 338
 process conditions, 323-
 327
 process types, 324-325
 properties, diamond, 324
 RF plasma-enhanced
 CVD, 329
 Si/Mo substrate, 339, 349
 substrates, 337

synthesis, diamond, 325-
 330
 technology development,
 325-336
 temperature influence,
 351
 three-dimensional sub-
 strates, 356
 WC-Co, 339, 341-343,
 357
 Dicing operations, 278
 Diode lasers, 387-473
 Dip pens, 35-50, 648
 Dirac delta function, 499-501
 Direct-current (DC) plasma-
 enhanced CVD, 324
 Displacement, nanometric
 machining, 612-620
 Disruption mechanisms, etch-
 ing, 1-20, 99-107
 Dissolution models, 546-563
 Double-disk grinding, 278
 DRIE, see Deep reactive ion
 etching (DRIE)
 Drives, nanometric machining,
 591
 Dry etching, 99
 Ductile regime, 255, 294-308
 DXRL, see Deep x-ray lithog-
 raphy (DXRL)
 Dynamic stress intensity fac-
 tor, 482

E

EDM, see Electric discharge
 machining (EDM)
 Elastic structural loop minimi-
 zation, 591-632

Electric discharge machining (EDM), 53

Electrolytic in-process dressing (ELID) 299-324
 cutting tools, 300
 micro- and nanogrinding, 255-305, 521-598
 ultraprecision surface grinding, 299-303

Electroplating, 635

Electrostatic forces, 635-645

ELID, see Electrolytic in-process dressing (ELID)

EMC, see Electromagnetic compatibility (EMC) standards

EMI, see Electromagnetic interfacing (EMI) standards

Etching, 1-46, 99-118

 basics, 1-8, 99-100, 103

 botling, 115

 bowing, 114-115

 disruption mechanisms,

111

 effects, 113

 inhibitor depletion, 119

 ions, 118-119

 micrograss, 119

 radical depletion, 119

 reflection, 118-119

 RIE, 100-102

 TADTOP, 117

 tilting, 114

 trenches, 99-110

 volume transport, 108

Excimer lasers, 402

Experimental approaches

 mechanical micro-machining, 191

 pulsed water drop micromachining, 475

 Exposure, x-ray lithographic microfabrication, 95

F

Fanuc, 591

Far point, 255

Fast axial flow lasers, 387

Fast Tool Servo (FTS) system, 613

FEA, see Finite element analysis (FEA) model

FEM codes and calculations, 499-503

Femtosecond laser pulses, 460-473

Femtosecond pulse microfabrication, 456-464

Field effect transistors (FETs) 1-46

 microfabrication, 1

 nanofabrication, 30-45

Filament assembly modification, 332

Fillet surfaces, 255

Film formation, 323-353

Finite element analysis (FEA) model, 498

Finite element model, 499-503

Five-axis CNC jig grinders, 279

Five-axis CNC machining centers, 279-282

Flow topology, 191

Fluid flow analysis, 191-200, 226-252

Fluid-like flow, 143-188

Fluid models, 226-252

FM-AFM, 1-45

Fracture-dominated wear model, 534

Free-form optics, 300-305

Frequency response function (FRF), 500-504

Fresnel number, 255-306
 FRF, see Frequency response
 function (FRF)
 FTS, see Fast Tool Servo
 (FTS) system
 Fusible bonding systems, 545-
 567
 Fusion bonding, 1-15
 Future directions
 basics, 51
 casting, 683
 diamond nanogrinding,
 587
 dip pen nanomanufactur-
 ing, 683
 electroplating, 683
 lithographically induced
 self-assembly, 683
 machining, 138, 182,
 253, 518, 632, 683
 mechanical micro-
 machining, 252
 micromanufacturing, 687
 molding, 138, 686
 nanoimprint lithography,
 49, 688
 nanomanufacturing, 687
 semiconductor manufac-
 turing, 51, 687
 soft lithographic manu-
 facturing, 687
 x-ray lithographic micro-
 fabrication, 95

G

Grades, grinding wheels, 261
 Griffith's criterion, 534
 Grit size, grinding wheels, 261
 Growth, diamond, 344

H

Hagen-Poiseuille pressure
 drop effects, 191
 Hard turning, 255
 HARMST conference, 672-
 687
 HEMA, see Hydroxyethyl-
 methacrylate (HEMA)
 Heteroepitaxial growth, 323-
 327, 345
 HFCVD, see Hot filament
 CVD (HFCVD)
 High-aspect ratio microlitho-
 graphy, 99
 High-aspect ratio microstruc-
 tures 99-136
 High-speed multi-axis CNC
 controllers, 612
 High-speed air turbines, 226,
 231-242
 High-speed rotors 233-251
 High structural loop stiffness,
 221, 499-508, 612-620
 Historical developments, CVD
 diamond technology, 326
 Hot embossing, 1-50
 Hot filament CVD (HFCVD)
 330, 363
 Housing, mechanical micro-
 machining, 225
 Hydroxyethylmethacrylate
 (HEMA), 83

I

IADF, see Ion angular distri-
 bution function (IADF)
 IBARE, see Ion beam-assisted
 radical etching (IBARE)

IBE, see Ion beam etching (IBE)

IBM, see International Business Machines (IBM)

IC chip manufacturing, 255-315

IEDF, see Ion energy distribution function (IEDF)

Implementation, nanometric machining, 612

Infrastructure, commercialization issues, 672-687

Inhibitor depletion, trenches, 98-111

Inhomogeneous strain, 178

Initial chip curl modeling, 195

Injection compression molding, 119

Injection molding, 119

Ink-jet printers, 1-30, 255-308

Inlets, mechanical micro-machining, 222

Inspection systems, nanometric machining, 612-628

Institut für Mikrostrukturtechnik (FZK) Karlsruhe and Antwenderzentrum BESSY, 53-96

Internal grinding operations, 255-283

International Business Machines (IBM), 1-50

International Institute for Production Engineering Research (CIRP), 255

International Mezzo, LIGA services, 55-91

Ion angular distribution function (IADF), 103, 111

Ion beam-assisted radical etching (IBARE), 99, 111

Ion beam etching (IBE), 99, 112

Ion energy distribution function (IEDF), 103, 111

Ions, high-aspect ratio micro-structures, 105, 109-112

J

Jabro Tools, 616

Jackson and Mills' model, 551

Jander's models, 550-555

Jig grinding, 280-299

K

Kapton preabsorber filters, 85-89

Kececioğlu's model, 164

Knudsen number, 106

Krause and Keetman's model, 552

L

Labcard, 1-35

Lab-on-a-chip, 20-28

Large Optics Diamond Turning Machines (LODTM), 627-629

Large plastic flow, 154-168

Laser-based micro- and nano-fabrication 387-473

Laser dressing, nanogrinding tools, 569-570

Lateral jetting, 480

LEED, see Low-energy electron diffraction (LEED) study

LIGA process, 55

Limitations, micromolding,
131

LISA, 648-671

Lithographically induced self-
assembly, 648-671

Lithographic method, 1-45,
55-58, 636

Lithographic processes, see
also X-ray lithographic micro-
fabrication

Loaded nanogrinding grains,
524-528

LODTM, see Large Optics
Diamond Turning Machine
(LODTM)

M

Machining, see also High-
aspect ratio microstruc-
tures

Machining thresholds, modeling,
482

Machining thresholds velocity
(MTV), 482-519

Magnesium fluoride, 494-495

MANCEF, see Micro and
Nanotechnology Commer-
cialisation Educational
Foundation (MANCEF)

Manipulative techniques, nano-
fabrication, 23-47

Manufacturing centers, commer-
cialization issues, 687

Marangoni forces, 387-403

Markets, commercialization is-
sues, 673

Masks, materials, 55-95

Master micromold fabrication,
93-94

MD, see Molecular dynamics
(MD) simulation

Mechanical micromachining,
191-252

Mechanical structure, nanometric
machining, 592

MEMO, see Methacryloxypropyl
trimethoxy silane (MEMO)

Me-Scope software, 504

Meso machine tools (mMTs)
220-221

Metal cutting chip formation,
143-188, 195-207, 662-671

Metallic (Mo) wires, 356

Metastable diamond growth,
330,350

Methacryloxypropyl trimethoxy
silane (MEMO), 55-94

Metrology, nanometric machin-
ing, 591-632

Micro- and nanogrinding, see
also Diamond nanogrinding

Micro and Nanotechnology
Commercialisation Educa-
tional Foundation
(MANCEF), 672

Microcrystalline diamond
(MCD) films, 323-340

Microdrills, 3357-362, 366

Microfabrication, see also Laser-
based micro- and nanofabri-
cation

Microfabrication, x-ray lithogra-
phy, 55

Microfluidic devices, 191

Microfluidic systems, 192

Micrograss, 119

Micromachining, see also Pulsed
water drop micromachining,
475

Micromachining, mechanical,
191

Micromachining, size effect, 143-144
 Micromanufacturing, 635
 Micromilling, 191-250, 323-382
 Micromolding, 120
 Micromolding in capillaries (MIMIC), 649
 Micro-nanotechnology (MNT), see also Commercialization issues
 Microwave plasma CVD (MPCVD), 332
 MIMIC, see Micromolding in capillaries,
 Minimum undeformed chip thickness, 192, 255, 591
 Modeling, see also Simulation
 Mode shapes, tetrahedral structures, 504
 Modified hot filament CVD, 317
 Mounted wheels, 275
 MPCVD, see Microwave plasma CVD (MPCVD)
 MTV, see Machining threshold velocity (MTV)
 Multiple spin coats, resist application, 83-85
 Multi-wall carbon nanotubes (MWCNTs), 30-40

N

Nano- and microgrinding, see also Diamond nanogrinding
 Nanocrystalline diamond, 297-352
 Nanocrystalline diamond (NCD) films, 323-382

Nanofabrication, see also Laser-based micro- and nanofabrication
 Nanogrinding, see also Diamond nanogrinding; Micro- and nanogrinding
 Nanogrinding wheels, 521
 Nanoimprint lithography, 1-46
 Nanomanufacturing, 648
 Nanometric machining 647
 Nanometrology, 613
 Nd:YAG lasers, 387
 Nonaxisymmetric aspheric mirrors, 255
 Non-mechanical nanometric machining, 591
 North West Development Agency, 672
 Nucleation, 345
 Numerical control (NC) jig grinding, 273-288

O

Optics, laser-based micro- and nanofabrication, 387-388
 Optimal wavelength, 388-402
 Oxychloride, 255-260

P

Packaging, commercialization issues, 672
 Paraboloids, 255-298
 Partial ductile mode grinding, 255-298
 PAS, see Polyalkensulfone (PAS)

PDMS, see Polydimethylsiloxane (PDMS)
 Pentium 4 microprocessor, 1-50
 Picosecond pulse microfabrication, 387-473
 Piezoelectric nanogrinding, 522
 PLG, see Poly(lactide-coglycolide) (PLG)
 PMI, see Polymethacrylimide (PMI)
 PMMA, see Polymethylmethacrylate (PMMA)
 Polishing time reduction, 255-299
 Polyalkensulfone (PAS), 62-83
 Polyamide (PA), 64-80
 Polydimethylsiloxane (PDMS), 3-45, 62-83, 648-685
 Poly(lactide-coglycolide) (PLG), 62-83
 Polymethacrylimide (PMI), 63-84
 Polymethylmethacrylate (PMMA), 62-82
 Polyoxymethylene (POM), 61-82
 Polysulfone (PSU), 66-87
 Polytetrafluoroethylene (PTFE), 61-82
 POM, see Polyoxymethylene (POM)
 Porous nanogrinding tools, 545
 Practical nanometric machining, 611-633
 Precision grinding processes, 277
 Precision micro- and nanogrinding, see Micro- and nanogrinding
 Procedures, diamond nanogrinding, 521-588
 Product manufacture, 675
 Product-market interface, 673

Product-Technology Roadmap (NEXUS), 672-674
 Properties, diamond, 325
 PSU, see Polysulfone (PSU), 61-82
 PTFE, see Polytetrafluoroethylene (PTFE), 61-82
 Pulsed liquid impact theory, 475
 Pulsed water drop micro-machining, 475-485
 Pyrex glass, 255-270

Q

Q-switched lasers, 387
 Quality, optical, 390
 Quantum corrals, 1-45
 Quartz, 255-308, 521-536
 Quasi-static stress intensity, 482

R

Rayleigh surface waves, see Pulsed water drop micromachining
 Reaction injection molding, 121-128
 Reactive ion etching (RIE), see also Deep reactive ion etching (DRIE)
 Refractory bonding systems, 549-563
 Resinoid-bonded wheels, 255-258
 Resinoid materials, 256-257
 Resists, 72-82

RF plasma-enhanced CVD, 332

RIE, see Reactive ion etching (RIE)

Robonano, 591

Rubber, 255

S

SAE steel, 144-149, 154-173

SAMIM, 635

SAMs, see Self-assembled molecules (SAMs)

Scanning tunneling microscopy, 1-50

Self-assembled molecules (SAMs), 1-45

Semiconductor manufacturing, 1-45, 648-685

Shellac, 255

Shielding gas, 387-472

"The Significant Structure Theory," 144-159

Silicate, 265-260

Silicon, pulsed water drop micromachining, 493-495

Silicon carbide, 255-260

SRS, see Synchrotron radiation sources (SRS)

Standardization, commercialization issues, 672-682

Stepped microstructures, 55

Stimulated emission, 387

STM, see Scanning tunneling microscopy (STM)

Structure, grinding wheels, 255

Synchrotron radiation, 58

Synchrotron radiation sources (SRS), 58-63

Synthesis, diamond, 331

T

TADTOP, 117

Testing, commercialization issues, 672

Tetra Form C ultraprecision grinding machine, 591

Tetrahedral desktop machine tool, 300

Tetrahedral structures, 499-507

Three-axis ultraprecision grinding machines, 300

Three-axis ultraprecision milling machine (UPM 3), 593

Three-dimensional substrates, 336

Threshold curves, 482-493

Tilting, 112

Time-modulated CVD (TMCVD), 372-381

Tip angles, 233-245

Ti:sapphire lasers, 404-414

TMCVD, see Time-modulated CVD (TMCVD)

Tools, 323

Top down manufacturing, 635-684

Topography mode, nanofabrication, 5-31

Trenches, 98-111

U

Ultraprecision grinding, 299, 521-589

Ultraprecision machine tools,
221,307, 499-516, 611-630

Ultrashort picosecond pulses,
403-463

V

Vitrified materials, 545-567

Voice coil-actuated mMTs,
221

Volume transport, 106

W

Water drop impact, 480

Water drop micromachining,
see Pulsed water drop micro-
machining

WC-Co, 323-341

Workpiece material proper-
ties, 143-179

X

X-ray diffraction, 520-534

X-ray lithographic microfabri-
cation, 57-69

X-ray lithography, 57

X-ray masks, 69-94

Y

Young's modulus, 69, 480

Z

Zhang and Bagchi's model,
174



Dr. Mark J. Jackson

Professor of Mechanical Engineering
College of Technology
Purdue University

C. Eng., Engineering Council of London, U.K., 1998

M. A. Status, Natural Sciences, University of Cambridge, U.K., 1998

Ph. D., Mechanical Engineering, Liverpool, U.K., 1995

M. Eng., Mechanical & Manufacturing Engineering, Liverpool, U.K., 1991

O.N.D., Mechanical Engineering, Halton College, U.K., 1986

O.N.C. Part I, Mechanical Engineering, Halton College, U.K., 1984

Doctor Jackson began his engineering career in 1983 when he studied for his O.N.C. part I examinations and his first-year apprenticeship-training course in mechanical engineering. After gaining his Ordinary National Diploma in Engineering with distinctions and I.C.I. prize for achievement, he read for a degree in mechanical and manufacturing engineering at Liverpool Polytechnic and spent periods in industry working for I.C.I. Pharmaceuticals, Unilever Industries, and Anglo Blackwells. After graduating with a Master of Engineering (M. Eng.) degree with Distinction under the supervision of Professor Jack Schofield, M.B.E., Doctor Jackson subsequently read for a Doctor of Philosophy (Ph. D.) degree at Liverpool in the field of materials engineering focusing primarily on microstructure-property relationships in vitreous-bonded abrasive materials under the supervision of Professor Benjamin Mills. He was subsequently employed by Unicorn Abrasives' Central Research & Development Laboratory (Saint-Gobain Abrasives' Group) as materials technologist, then technical manager, responsible for product and new business development in Europe, and university liaison projects concerned with abrasive process development. Doctor Jackson then became a research fellow at the Cavendish Laboratory, University of Cambridge, working with Professor John Field, O.B.E., F.R.S., on impact fracture and friction of diamond before becoming a lecturer in engineering at the University of Liverpool in 1998. At

Liverpool, Dr. Jackson established research in the field of micromachining using mechanical tools, laser beams, and abrasive particles. At Liverpool, he attracted a number of research grants concerned with developing innovative manufacturing processes for which he was jointly awarded an Innovative Manufacturing Technology Center from the Engineering and Physical Sciences Research Council in November 2001. In 2002, he became associate professor of mechanical engineering and faculty associate in the Center for Manufacturing Research, and Center for Electric Power at Tennessee Technological University (an associated university of Oak Ridge National Laboratory), and a faculty associate at Oak Ridge National Laboratory. Dr. Jackson was the academic adviser to the Formula SAE Team at Tennessee Technological University. In 2004 he moved to Purdue University as Associate Professor of Mechanical Engineering in the College of Technology.

Doctor Jackson is active in research work concerned with understanding the properties of materials in the field of microscale metal cutting, micro- and nanoabrasive machining, and laser micro machining. He is also involved in developing next generation manufacturing processes and biomedical engineering. Doctor Jackson has directed, co-directed, and managed research grants funded by the Engineering and Physical Sciences Research Council, The Royal Society of London, The Royal Academy of Engineering (London), European Union, Ministry of Defense (London), Atomic Weapons Research Establishment, National Science Foundation, N.A.S.A., U. S. Department of Energy (through Oak Ridge National Laboratory), Y12 National Security Complex at Oak Ridge, Tennessee, and Industrial Companies, which has generated research income in excess of \$15 million. Dr. Jackson has organized many conferences and currently serves as General Chair of the International Surface Engineering Congress. He has authored and co-authored over 150 publications in archived journals and refereed conference proceedings, has edited a book on “microfabrication and nanomanufacturing”, is guest editor to a number of refereed journals, and is currently editing a book on “surgical tools and medical devices” and on “commercializing micro- and nanotechnology products”. He is the editor of the newly established “*International Journal of Nanomanufacturing*”, and is on the editorial board of the “*International Journal of Machining and Machinability of Materials*” and the “*International Journal of Manufacturing Research*”.